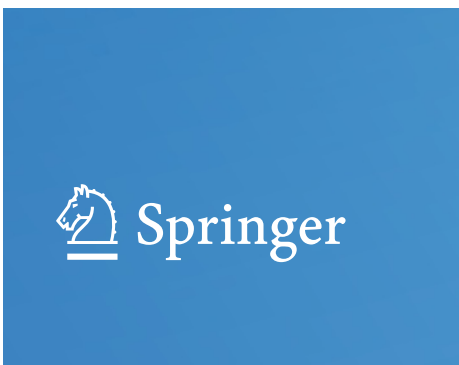
Springer

Quantitative Ultrasound in Soft Tissues

Jonathan Mamou · Michael L. Oelze
Editors

Quantitative Ultrasound in Soft Tissues

Springer

Editors
Jonathan Mamou
F. L. Lizzi Center for Biomedical Engineering
Riverside Research
New York, NY
USA

Michael L. Oelze
Department of Electrical and Computer Engineering
University of Illinois at Urbana-Champaign
Urbana, IL
USA

ISBN 978-94-007-6951-9 ISBN 978-94-007-6952-6 (eBook)
DOI 10.1007/978-94-007-6952-6
Springer Dordrecht Heidelberg New York London

Library of Congress Control Number: 2013943986

Printed on acid-free paper

Springer is part of Springer Science+Business Media (www.springer.com)

Preface

In the 1970s, Holasek, Gans, Purnell, and Sokollu expressed the notion that the frequency content of medical-ultrasound echo signals might be exploited to characterize soft tissue; they developed a method of color-encoding of B-scan images to depict spectral content of RF echo signals and termed the method "spectra color." By characterize, they essentially meant to distinguish one type of soft tissue from another, for example, to distinguish a cancerous lesion from a benign one, to track changes in tissue over time, or to monitor the progression or regression of disease. Unfortunately, the available analog technology of that era made testing, validating, and implementing this concept practically impossible. However, the notion of characterizing soft tissue based on features that could be extracted from echo signals caught the imagination of many other investigators, and several innovative efforts were launched in attempts to extract information from echo signals in a quantitative manner for the purpose of characterizing tissue with the then-available, essentially analog technology.

Those early efforts tended to concentrate on a single, echo-signal feature, such as attenuation, and to associate differences in estimates of the value of that feature with differences in tissue type or status. At about the same time, a young researcher named Frederic ("Fred") Lizzi was assigned by his managers in the Laboratories Division of Riverside Research to a project analyzing patterns of surface waves in the ocean. This project was intended to identify patterns or perturbations that could be used to detect underwater objects. While it was a stimulating and interesting project, it gave Fred considerable insight into signal analysis, Fourier methods, and power spectra.

Just about the time that Fred was wrapping up his project, Riverside Research was approached by an ophthalmologist from the Columbia Presbyterian Hospital named D. Jackson ("Jack") Coleman to see whether the technology Riverside had developed for fabricating piezoelectric transducers for acousto-optic modulators could be applied to ultrasonic imaging of the eye. It was indeed applicable; and Riverside Research built the first clinical, 10-MHz eye scanner for Jack. Fred became heavily involved in that effort, which led to more than 30 years of collaborative research between Fred and Jack.

Their collaboration began with studies to evaluate the safety aspects of using ultrasound at frequencies that were an order of magnitude higher than frequencies then used for clinical ultrasound scanning. Those studies established thresholds for damage induced by focused ultrasound in the eye using cow eyes ex vivo and rabbit eyes in vivo, and firmly established that diagnostic levels being used at 10 MHz were quite safe, and the damage thresholds also established a foundation for using focused ultrasound for therapeutic purposes.

Once safety was adequately established, Fred and Jack used the newly developed ophthalmic system to investigate the feasibility of using spectrum analysis of ultrasound echo signals for soft-tissue characterization. Their early work employed a manually dithered 10-MHz transducer that swept over an elevated region of the retina to determine whether the "bump" visible to the ophthalmologist was caused by underlying fluid or solid soft tissue. If the cause of the bump was solid tissue, then an analog spectrum analyzer generated the average logarithmic power spectrum of the dithered echo signals. A paper recorder traced the spectrum, which was then manually entered into a large central computer. To take transducer and electronic-system contributions to the spectrum into account, the logarithmic power spectrum of echo signals obtained from the surface of a "perfect" reflector—an optically flat glass plate normal to the incident ultrasound beam at the center of the transducer focal region—also was generated, manually digitized, and subtracted from the logarithmic power spectrum of the tissue echo signals. The result was termed the "normalized" or "calibrated" logarithmic power spectrum of the tissue echo signals, and a linear-regression approximation to the normalized spectrum produced associated slope, intercept, and midband spectral-parameter values, and the method we now term quantitative ultrasound or "QUS" was born.

The ensuing years saw considerable refinement by Fred and others, beginning with the initial exploitation of digital technology, for example, using Biomation analog-to-digital converters struggling to digitize linearly amplified echo signals at a sampling rate of 50 MS/s with 6-bit resolution and using DEC PDP-11/60 and similar minicomputers for signal processing and imaging. Employing the newly emerging digital technology, Fred and Jack established that linear combinations of slope and intercept values could distinguish among different histological types of primary choroidal metastatic melanomas. This basic empirical approach was applied with increasing technological capability over many succeeding years by Fred and his collaborators to characterization of liver and kidney tissue and differentiation of diffuse liver diseases. My collaborators and I subsequently applied this approach to characterization of intravascular thrombi and plaque, to imaging of prostate cancer, and to detection of metastases in lymph nodes.

In the meantime, in 1983, Fred and his co-workers published a theoretical framework for spectrum analysis of ultrasound echo signals from soft tissue that took into account the properties of the beam profile, the nature of the gating function, and the three-dimensional impedance distributions of the tissue scatterers. The underlying assumptions of the framework were that scattering is weak and

consistent with the Born approximation, and that the ultrasound field is reasonably uniform, ideally, at or beyond the focal zone. If these approximations applied, then the theory related the spectral slope value to an effective scatterer size (once attenuation was taken into account) and the spectral intercept value to effective scatterer size and the product of scatterer number concentration and relative acoustic impedance squared, i.e., the so-called "acoustic concentration." Of course, once size was estimated from the attenuation-compensated slope value, acoustic concentration could be estimated readily. Using this theory, Fred was able to show that the size estimate derived from the backscattered signals of intraocular tumors correlated nicely with their primary or metastatic nature. And QUS finally had a theoretical foundation underlying its slowly progressing, but very encouraging, empirical results.

Although Fred's theoretical framework assumed scatterers that were spheres with a distinct surface or that had a radially symmetric spatial autocorrelation function that could be expressed as an exponential or a logarithmic function, his theory estimated scatterer properties based only on the straight-line parameters, i.e., on the slope, intercept, and midband values. In 1990, Michal Insana and Timothy Hall advanced the theory of ultrasound scattering in soft tissue by going beyond the simple linear approximation to the empirical spectrum and introducing a form factor into the theory that permitted better fitting the observed spectrum to an assumed scatterer model, most typically an exponential model. With this improvement, QUS began to make progress in many additional laboratories. First, at the University of Illinois under the mentorship of William ("Bill") O'Brien, Michael Oelze and Timothy Bigelow expanded the underlying theory and applied it to tumor models in animals. Jonathan Mamou continued in that vein by inferring 3D distributions of acoustic impedance from tumor histology to further validate the theory underlying QUS. Gregory Czarnota and Michael Kolios and students they have mentored applied QUS theory to cell pellets in order to identify the actual histological scatterers, and concluded that cell nuclei were the best candidates for that role. And so the momentum for QUS built further through the turn of the century.

Today, QUS is being applied to a wide range of topics, including detection and imaging of cancers in the prostate, detection of metastases in lymph nodes, assessment of apoptosis and necrosis in treated tissue, and monitoring of therapy. QUS also is expanding to include estimates other than those derived from power spectra. For example, Tadashi Yamaguchi utilizes statistical estimates derived from the envelope of the backscattered signals to distinguish among types of liver tissue, and envelope-statistics estimates are now being applied to other soft tissues as well, for example, to lymph nodes by Jonathan Mamou and his colleagues. Destrempes and his colleagues are advancing the theoretical framework of envelope-statistics models in QUS, and Yoshifumi Saijo is relating QUS estimates to acoustic microscopy features. Roberto Lavarello and Michael Andre are incorporating QUS in their theoretical and applied studies of ultrasound tomography,

and Eric Strohm and his colleagues are investigating individual cells using acoustic microscopy at very high frequencies. Hence, the term QUS applies to a broad field that has matured in many ways while it continues to grow and advance in others. The chapters of this book have been contributed by current and historical leaders in QUS, and they cover the field comprehensively; however, they provide only a snapshot showing where rapidly evolving QUS stands today, barely one decade into the twenty-first century.

New York, NY, USA

Ernest J. Feleppa
Lizzi Center for Biomedical Engineering
Riverside Research

Contents

Introduction

Diagnostic Ultrasound

Diagnostic ultrasound has gained wide acceptance for a comprehensive range of medical applications. It is routinely used for gynecological applications, cardiac applications, and also a wide range of internal imaging applications (e.g., kidneys, abdominal, etc.). The ability of current ultrasound technology to easily form images in real-time with a small portable machine has significantly contributed to this trend. Furthermore, ultrasound remains one of the most inexpensive medical imaging modalities, is easy-to-use, and uses non-ionizing radiation. Therefore, because of these characteristics, ultrasound will continue to play a prominent role in medical practice worldwide.

Typical clinical ultrasound machines employ linear- or phased-array probes with center frequencies ranging from 1 to 10 MHz to form conventional (i.e., B-mode) images. These images have spatial resolution on the order of a wavelength (i.e., around 0.15–1.5 mm). The contrast mechanism in these images is the change in acoustic properties (speed of sound and density) of the different soft tissues encountered by the propagating ultrasound waves. The ability of these images to display morphology has gained wide acceptance in gynecology, cardiology, oncology, and others. It is often said that because of their "grainy" nature, or speckle noise, conventional B-mode images are not as "nice" or easy to interpret as medical images obtained from other modalities (e.g., X-ray computed tomography and magnetic resonance).

In addition, conventional B-mode images lack functional information and quantitative information is limited because images are highly dependent on machine settings. Although some quantitative studies are conducted from B-mode images (e.g., cyst size measurements, limb measurements during pregnancies, etc.) and some functional information can be inferred from Doppler methods which can map blood flow (e.g., echocardiography), current ultrasound imaging techniques lag far behind functional and quantitative information provided by magnetic resonance imaging and X-ray computed tomography.

In the past two decades, immense progress in technology has yielded a significant improvement in transducer technology, ultrasound image quality, and

image-formation algorithms and provided a basis for the development of more-complex imaging modes, like blood-flow imaging, contrast-agent-enhanced ultrasound, and, of course, quantitative ultrasound (QUS). For example, most QUS techniques rely on the availability of the raw unprocessed radio-frequency (RF) ultrasound backscattered signals. In the past, scanners would only deliver video images, which were obtained after envelope detection and post-processing operations such as time-gain compensation and log compression. These ultrasound images were inherently user-dependent and also were devoid of the frequency-dependent information originally contained in the raw (unprocessed) RF data. The next generation of clinical ultrasound scanners allowed access to the envelope-detected signals which were obtained after analog quadrature demodulation of the raw RF signals. By demodulation, significantly lower frequency content of the signals could be used and less expensive (i.e., slower) circuitry and electronics could be used. Currently, more and more ultrasound scanners have the necessary hardware to obtain and digitize the raw RF data, although the "research mode" which permits access to the data often needs to be unlocked by the manufacturer. The availability of these research modes will permit novel QUS techniques to be implemented on clinical devices and these new techniques to be exploited for improving diagnostic ultrasound.

Quantitative Ultrasound in Soft Tissues

The general research field of QUS in soft tissues deals with the development of measurements methods which can yield quantitative tissue properties that are independent of instrumentation and the operator. These QUS estimates can be used to form new parametric images (i.e., QUS images), where QUS estimates may be color-coded and overlaid above the conventional B-mode image. Therefore, QUS image contrast is entirely dictated by the underlying tissue properties, which may be different from the sound speed and density, and consequently, the interpretation of QUS images can be made in a much richer sense than conventional B-mode images.

At the simplest level, and at any scale, soft tissue can be understood as being formed by tissue components having shapes, spatial organization, and mechanical properties unique to tissue type and state encountered. The hope of QUS is to specifically estimate some of these properties by using appropriate models and the well-established theory of how ultrasound interacts with soft tissues. The ultrasound frequency chosen for a particular application drives the sensitivity of QUS to a specific scale of tissue structures, typically smaller than the wavelength. Consequently, higher frequency permits the interrogation of smaller tissue components. The field of QUS was born from these simple concepts, but challenges were quick to emerge when dealing with soft tissues because they present a natural complexity.

Over three decades ago, initial QUS studies developed the theories on how to process ultrasound signals to remove system dependence and obtain QUS estimates

describing soft tissue extensively. For QUS methods based on the backscatter coefficient, the most noteworthy studies were the theoretical frameworks developed by Lizzi et al. (1983, 1987) and Insana et al. (1990). These works not only provided a strong theoretical foundation, but they also presented encouraging experimental results.

Following these foundational studies, a wide range of QUS methods were developed to perform noninvasive tissue characterization. Initial basic studies have been performed in blood (Yu and Cloutier 2007; Franceschini et al. 2011), individual cells (Baddour et al. 2005), cell pellets (Oelze and Zachary 2006), and well-calibrated tissue-mimicking scattering phantoms (Madsen et al. 1999; Wear et al.). Preclinical and clinical studies were performed in characterizing prostate cancer (Feleppa et al. 2002), ocular tumors (Coleman and Lizzi 1983; Coleman et al. 1985, 1995), liver diseases (King et al. 1985), thrombi (Sigel et al. 1990), plaques (Lee et al. 1998; Noritomi et al. 1997a, b), cardiac abnormalities (Lizzi et al. 1997), and lymph nodes (Mamou et al. 2010, 2011).

Concurrently, other QUS studies were performed which relied on measurement approaches not directly related to the backscatter coefficients. Among these studies include using scanning acoustic microscopy, inverse and forward scattering models of ultrasound tomography, and also envelope-statistics modeling and quantification. These QUS methods are all addressed in this book. A remaining important QUS field is ultrasound elastography, where ultrasound signals are processed to obtain QUS estimates of tissue stiffness. Elastography techniques rely on perturbing the tissue (e.g., deformation) and measuring how tissue responds to these perturbations. Therefore, QUS techniques can be divided into techniques based on estimating unperturbed properties of tissues and on measuring properties from perturbed tissues. This book will focus on the former QUS techniques where signals from unperturbed tissues are quantified and related to tissue properties. Several works on elastography methods in ultrasound are available in the literature for the interested reader.

This Book

This book is organized into four major themes of active QUS research. The first theme deals with QUS studies based on the quantification of the ultrasound backscatter coefficient and is strongly emphasized in this book. The backscatter coefficient is essentially a function of frequency and tissue properties which indicate with a high degree of detail how a medium reflects sounds. In this first theme, Chap. 1 of the book reviews the state-of-the-art methods for estimating the backscatter coefficients experimentally. This chapter is intended for readers who do not have a background in ultrasound scattering theory and provides an important literature review of the progress in the field. Chapter 2 provides a historic review of QUS successes and provides an important overview of early attempts and also details the most successful studies to date. This chapter is intended for readers who do not have a background in QUS.

Chapter 3 deals with the important issue of QUS estimate statistics. QUS estimates are in nature stochastic and for estimates to be meaningful they must be estimated from a region-of-interest (ROI) of the ultrasound data. The chapter provides an excellent review of the methods used to choose the appropriate sample size, and also proposes ideas on how to reduce the sample size without compromising the QUS estimates. The sample sizes necessary to obtain good QUS estimates ultimately drive QUS image spatial resolution. Therefore, a tradeoff exists between spatial resolution and accuracy and precision of QUS estimates. This chapter is also insightful on how QUS estimates should be interpreted.

Chapter 4 reviews the different methods available to estimate and compensate for attenuation in the context of QUS. Ultrasound attenuation is frequency-dependent, and therefore, inappropriate compensation can drastically change the shape of the backscatter coefficient and yield erroneous QUS estimates. In addition, local attenuation within the soft tissue sample can in itself be used as a QUS estimate to provide quantitative information about tissue.

Chapters 5–8 cover four successful recent biomedical applications of QUS in soft tissues. These chapters represent the culmination of three decades of research and provide an encouraging view of what the future of QUS methods could be. Chapters 5 and 6 present preclinical QUS studies to assess individual cells and red blood cells. Comparatively, Chaps. 7 and 8 present clinical studies in oncology dealing with the detection of cancer in the prostate and lymph nodes. Both clinical studies presented extremely encouraging results.

Chapter 9, the final chapter of the first theme of the book, presents an innovative and modern QUS topic. It deals with QUS methods to monitor the real-time application of therapy and to detect the early response of tumors to therapy. An ongoing clinical challenge is the proper monitoring of the therapy, sparing healthy tissues and early detection of therapeutic response. This chapter investigates how QUS estimates could potentially be used to benefit this research theme.

The second theme of the book is interested in QUS methods which rely on envelope statistics. These methods are fundamentally different from backscatter coefficient-based methods because they do not require the raw RF data. Mathematical models can be used to describe ultrasound scattering phenomenon in terms of envelope statistics. Tissue properties and QUS estimates can then be obtained by fitting these models to specified statistics estimated within ROIs. Chapter 10 provides a comprehensive review of these mathematical models and also presents algorithms to estimate model parameters. This chapter also clearly describes how in the realm of ultrasound scattering these QUS estimates can be related to physical parameters pertaining to soft tissue organization and microstructure. Chapter 11 presents an elegant clinical application of QUS based on envelope statistics. Methods are presented which quantify the differences between a sample tissue ROI and a Rayleigh-distributed ROI. Rayleigh statistics are expected from a medium containing numerous randomly located sub-resolution identical scatterers. In this chapter these methods were successfully applied to the characterization of liver fibrosis.

The third theme of the book focuses on acoustic microscopy studies which estimate quantitative tissue properties. Chapter 12 presents our view of a wide range of acoustic microscopy methods to estimate several acoustic properties of soft tissues (i.e., speed of sound, density, attenuation, etc.) using high and very-high frequency transducers. Acoustic microscopy relies on 2D scanning of a thin tissue sample or the surface of a thicker sample. These QUS images typically have very-high spatial resolutions (i.e., 1–10 μm) and provide very comprehensive information about soft tissues. Chapter 13 presents recent acoustic microscopy studies conducted on individual cells using transducers with center frequencies up to 1 GHz. The QUS images obtained are high quality in detail and spatial resolution and provide acoustic properties of cells which cannot be obtained by any other method.

The fourth theme of the book presents QUS approaches using ultrasound tomography techniques. Ultrasound tomography methods are inherently complex due to the diffraction, refraction, and attenuation of the ultrasound waves. In recent years, better forward and inverse scattering models have been developed, and techniques have reached a certain maturity with the help of more powerful and efficient computers and reconstruction algorithms. Chapter 14 reviews the state-of-the-art methods and proposes a comprehensive view of the literature on the topic, from the initial theoretical studies to the currently applied studies. Finally, Chap. 15 presents one of the most promising biomedical applications of ultrasound tomography, the QUS imaging of breast-cancer patients.

Jonathan Mamou
Michael L. Oelze

References

Baddour RE, Sherar MD, Hunt JW, Czarnota GJ, Kolios MC (2005) High-frequency ultrasound scattering from microspheres and single cells. J Acoust Soc Am 117:934–943

Coleman DJ, Lizzi FL (1983) Computerized ultrasonic tissue characterization of ocular tumors. Am J Ophthalmol 96:165–175

Coleman DJ, Lizzi FL, Silverman RH, Helson L, Torpey JH, Rondeau MJ (1985) A model for acoustic characterization of intraocular tumors. Invest Ophthalmol Vis Sci 26:545–550

Coleman DJ, Rondeau MJ, Silverman RH, Folberg R, Rummelt V, Woods SM, Lizzi FL (1995) Correlation of microcirculation architecture with ultrasound backscatter parameters of uveal melanoma. Eur J Ophthalmol 5:96–106

Feleppa EJ, Ennis RD, Schiff PB, Wuu CS, Kalisz A, Ketterling J, Urban S, Liu T, Fair WR, Porter CR, Gillespie JR (2002) Ultrasonic spectrum-analysis and neural-network classification as a basis for ultrasonic imaging to target brachytherapy of prostate cancer. Brachytherapy 1:48–53

Franceschini E, Metzger B, Cloutier G (2011) Forward problem study of an effective medium model for ultrasound blood characterization. IEEE Trans Ultrason Ferroelectr Freq Control 58(12):2668–2679

Insana MF, Wagner RF, Brown DG, Hall TJ (1990) Describing small-scale structure in random media using pulse-echo ultrasound. J Acoust Soc Am 87:179–192

King DL, Lizzi FL, Feleppa EJ, Wai PM, Yaremko MM, Rorke MC, Herbst J (1985) Focal and diffuse liver disease studied by quantitative microstructural sonography. Radiology 55:457–462

Lee DJ, Sigel B, Swami VK, Justin JR, Gahtan V, O'Brien SP, Dwyer-Joyce L, Feleppa EJ, Roberts AB, Berkowitz HD (1998) Determination of carotid plaque risk by ultrasonic tissue characterization. Ultrasound Med Biol 24:1291–1299

Lizzi FL, Greenebaum M, Feleppa EJ, Elbaum M, Coleman DJ (1983) Theoretical framework for spectrum analysis in ultrasonic tissue characterization. J Acoust Soc Am 73:1366–1373

Lizzi FL, Ostromogilsky M, Feleppa EJ, Rorke MC, Yaremko MM (1987) Relationship of ultrasonic spectral parameters to features of tissue microstructure. IEEE Trans Ultrason Ferroelectr Freq Control 34:319–329

Lizzi FL, Astor M, Liu T, Deng C, Coleman D, Silverman RH (1997) Ultrasonic spectrum analysis for tissue assays and therapy evaluation. Int J Imaging Syst Technol 8:3–10

Madsen EL, Dong F, Frank GR, Garra BS, Wear KA, Wilson T, Zagzebski JA, Miller HL, Shung KK, Wang SH, Feleppa EJ, Liu T, O'Brien WD Jr, Topp KA, Sanghvi NT, Zaitsev AV, Hall TJ, Fowlkes JB, Kripfgans OD, Miller JG (1999) Interlaboratory comparison of ultrasonic backscatter, attenuation, and speed measurements. J Ultrasound Med 18:615–631

Mamou J, Coron A, Hata M, Machi J, Yanagihara E, Laugier P, Feleppa EJ (2010) Three-dimensional high-frequency characterization of cancerous lymph nodes. Ultrasound Med Biol vol 36:361–375

Mamou J, Coron A, Oelze ML, Saegusa-Beecroft E, Hata M, Lee P, Machi J, Yanagihara E, Laugier P, Feleppa EJ (2011) Three-dimensional high-frequency backscatter and envelope quantification of cancerous human lymph nodes. Ultrasound Med Biol 37(3):345–357

Noritomi T, Sigel B, Gahtan V, Swami V, Justin J, Feleppa E, Shirouzu K (1997a) In vivo detection of carotid plaque thrombus by ultrasonic tissue characterization. J Ultrasound Med 16:107–111

Noritomi T, Sigel B, Swami V, Justin J, Gahtan V, Chen X, Feleppa EJ, Roberts AB, Shirouzu K (1997b) Carotid plaque typing by multiple-parameter ultrasonic tissue characterization. Ultrasound Med Biol 23:643–650

Oelze ML, Zachary JF (2006) Examination of cancer in mouse models using high-frequency quantitative ultrasound. Ultrasound Med Biol 32:1639–1648

Sigel B, Feleppa EJ, Swami V, Justin J, Consigny M, Machi J, Kikuchi T, Lizzi FL, Kurohiji T, Hui J (1990) Ultrasonic tissue characterization of blood clots. Surg Clin North Am 70:13–29

Wear KA, Stiles TA, Frank GR, Madsen EL, Cheng F, Feleppa EJ, Hall CS, Kim BS, Lee P, O'Brien WD Jr, Oelze ML, Raju BI, Shung KK, Wilson TA, Yuan JR (2005) Interlaboratory comparison of ultrasonic backscatter coefficient measurements from 2 to 9 MHz. J Ultrasound Med 24:1235–1250

Yu FT, Cloutier G (2007) Experimental ultrasound characterization of red blood cell aggregation using the structure factor size estimator. J Acoust Soc Am 122(1):645–656

Part I
Ultrasound Backscatter Coefficient

Chapter 1
State of the Art Methods for Estimating Backscatter Coefficients

Goutam Ghoshal, Jonathan Mamou and Michael L. Oelze

Abstract Ultrasound, which is routinely used for diagnostic imaging applications, is mainly qualitative. However, novel quantitative ultrasound techniques are being developed for diagnosing disease, classifying tissue, and assessing and monitoring the application of therapy. Ultrasound is a propagating wave that interacts with the medium as a function of the spatially-dependent mechanical properties of the medium. By analyzing the backscattered wave, various properties of the propagating media can be inferred. The backscatter coefficient, which is a fundamental material property, can be estimated from backscattered ultrasound signals and can be further parameterized for quantifying tissue properties and classifying disease. In this chapter, the history of estimating backscatter coefficients will be explored and different methods and their underlying assumptions for estimating the backscatter coefficient will be compared.

Keywords Backscatter coefficients · Spectral normalization

G. Ghoshal · M. L. Oelze (✉)
Department of Electrical Engineering, University of Illinois at Urbana-Champaign,
405 N. Mathews, Urbana, IL 61801, USA
e-mail: oelze@illinois.edu

G. Ghoshal
e-mail: ghoshal2@gmail.com

J. Mamou
F. L. Lizzi Center for Biomedical Engineering, Riverside Research, 156 William St.
9th floor, New York, NY 10038, USA
e-mail: jmamou@riversideresearch.org

J. Mamou and M. L. Oelze (eds.), *Quantitative Ultrasound in Soft Tissues*, DOI: 10.1007/978-94-007-6952-6_1,

1.1 Introduction

Ultrasonic scattering from biological tissue is relevant to noninvasive tissue characterization and medical diagnosis. Ultrasound is a propagating pressure wave at frequencies above the audible range in a medium that scatters and reflects acoustic energy based on the mechanical properties of different tissues. Conventional ultrasonic B-mode images are constructed from the envelope-detected, time-domain signals scattered from different tissue structures. In an ultrasonic B-mode image, the frequency dependent information resulting from the scattering media is not utilized. However, by transforming the scattered signals in the frequency domain using a Fourier transform method before B-mode processing, the frequency dependence of the scattered signals can be related to structural properties of the biological media. Often statistical modeling techniques are employed to extract sub-resolution microstructural information using ultrasound with wavelengths larger than the length scale of heterogeneity in the scattering media. To extract microstructural features, such as an effective scatterer size of the dominant microstructure, accurate estimation of the backscatter coefficient (BSC) versus frequency is necessary.

The BSC is defined as the time-averaged scattered intensity in the backward direction per unit solid angle per unit volume normalized by time-averaged incident intensity (cm^{-1} Sr^{-1}). Therefore, it is a fundamental quantity of a material from which microstructural properties, such as shape, size, organization, concentration and impedance mismatch between scatterers and the surrounding media, can be estimated. BSCs can be used to estimate both microstructural and acoustical properties of the tissues.

BSC-based quantitative ultrasound (QUS) has been successfully used to characterize different aspects of tissue microstructure. Numerous researchers have estimated the BSC from different organs and tissues such as ocular, liver, prostate, pancreas, spleen, renal, myocardial tissue, cardiac tissues and lymph nodes (Nicholas 1982; O'Donnell and Miller 1981; Miller et al. 1983; Lizzi et al. 1983, 1987; Fei and Shung 1985; Insana et al. 1991; Maruvada et al. 2000; Mamou et al. 2011). Topp et al. (2001) differentiated between neoplastic and healthy tissues by studying the frequency-dependent BSC from in vivo rat mammary tumors. Kabada et al. (1980) estimated BSCs to differentiate different excised canine tissues in the frequency range of 1–10 MHz. They observed a higher frequency dependence of BSC in heart (left ventricle) muscle tissue than in liver tissues. Other researchers have used BSCs to differentiate between normal dog hearts and heart tissue from dogs subjected to ischemic injury by coronary occlusion (O'Donnell et al. 1981). They hypothesized that the ultrasonic scattering was sensitive to concentration of molecular collagen and the organizational state of the structural protein. Miller et al. (1983) estimated BSC both in vitro and in vivo and observed differences between normal and ischemic dog myocardium.

Nicholas (1982) published BSCs from various human excised tissues over a frequency range of 0.7–7 MHz. The author used a power law to fit the experimental backscatter from excised human liver, spleen and brain (white matter).

The author suggested two basic scattering sites in these tissues on the order of 1 mm and 20–40 μm, respectively. D'Astous and Foster (1986) found that the BSC from tumor tissues in the female breast were virtually inseparable from those of fat at low frequencies, but began to separate at higher frequency regimes. The BSC for parenchyma of the breast was about an order of magnitude above those of fat and infiltrating ductal carcinoma.

Wear et al. (1995) published estimates of BSCs from in vivo human liver and kidney in the frequency range of 2–4 MHz. Lu et al. (1999) estimated BSC in normal human livers and human livers with diffuse diseases in vivo. Maruvada et al. (2000) estimated BSCs from bovine tissues in the frequency range of 10–30 MHz. The authors observed similar frequency dependence in BSCs between kidney and liver. Recently, Ghoshal et al. (2011) observed changes in BSCs from excised beef and rabbit livers with increasing temperature in the frequency range of 10–28 MHz. The authors observed changes in frequency dependence and amplitude of BSC with increasing temperature.

Fei and Shung (1985) used a broadband substitution technique to estimate the BSC of bovine kidney. Turnbull et al. (1989) estimated the BSC in human renal tissue and three types of renal tumors over a frequency range of 3.5–7 MHz. The authors could not differentiate between renal cell carcinoma and normal kidney tissue. Insana et al. (1991) estimated BSCs from dog kidneys using a higher frequency range of 1–15 MHz. They estimated the BSC at different angles with respect to the predominant nephron orientation and observed a frequency dependence of 1.98–2.3 depending upon the angle of incidence.

Variation in BSCs was also observed from the same in vitro tissue depending upon the histochemical fixation process. Bamber et al. (1979) demonstrated that the BSCs were different between fixed and unfixed mammalian tissue using formalin, ethyl alcohol and potassium dichromate as histochemical fixing solution. The authors suggested 4 % formalin and 5 % potassium dichromate are good for consistently preserving the ultrasonic properties within a few percent of those of the fresh tissues.

Many other researchers have utilized the BSC to classify tissues and characterize tissue states. Table 1.1 provides a compilation of some BSC results acquired by various researchers from various tissues and tissue states. Therefore, the plethora of BSC applications found in the literature suggests that the accurate and precise calculation of the BSC from ultrasonic measurements is highly important.

When correctly implemented, the estimation of the BSC is system and user independent and the BSC is only a function of the tissue properties. To estimate system- and user-independent BSCs it is necessary to account for attenuation and system effects accurately. The typical steps involved in estimating the BSC are shown in Fig. 1.1. Radio-frequency (RF) signals are acquired from a scattering media and gated using a windowing function such as Hanning or rectangular window. Next, the power spectrum of a gated signal is calculated using the Fourier transform. To improve the estimate of the BSC, the power spectra from several gated signals can be averaged providing an average power spectrum. The average power spectrum is divided by a calibration spectrum and then compensated for

Table 1.1 BSCs in soft tissues reported by various researchers

Tissue types	BSC ($\sigma_b = 10^{-6} \times af^n$ cm^{-1} Sr^{-1})			Reference
	a	n	Freq. (MHz)	
Canine liver (excised)	–	2.1	1–10	(Kabada et al. 1980)
Canine heart (excised)	–	3.3	1–10	
Dog myocardium (in vivo)	58	3.1	2–7	(Miller et al. 1983)
Dog kidney (in vitro)	1.9	2.2	1–15	(Insana et al. 1991)
Dog myocardium (in vitro)	25	3.1	1–15	(O'Donnell et al. 1981)
Bovine kidney (in vitro)	31	2.3	2–7	(Fei and Shung 1985; Shung 1993)
Bovine heart (in vitro)	0.3	3.5	10–30	(Maruvada et al. 2000)
Bovine kidney (in vitro)	4	2.5	10–30	
Bovine liver (in vitro)	5	2.4	10–30	
Human kidney (in vitro)	6.6	1.7	3.5–7	(Turnbull et al. 1989)
Human liver (excised)	270	1.2	0.7–7	(Nicholas 1982)
Human spleen (excised)	120	1.7	0.7–7	
Human brain (white matter, excised)	20	1.2	0.7–7	
Human liver (in vivo)	45	1.6	2–4	(Wear et al. 1995)
Human kidney (in vivo)	23	2.1	2–4	
Human epidermis (excised)	5	3.8		(Moran et al. 1995)
Human dermis (excised)	1.8	2.8		

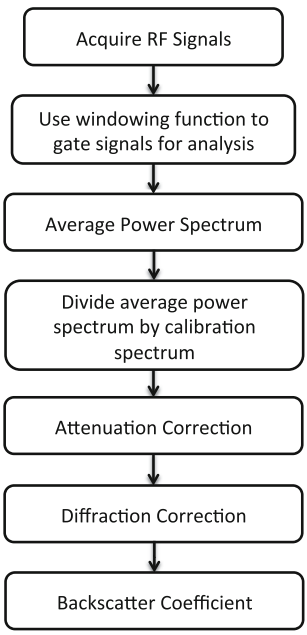

Fig. 1.1 Flowchart for estimating the BSC

attenuation and diffraction effects. The resulting frequency-dependent function is known as the BSC. The main challenge to estimating the BSC is to compensate for diffraction and attenuation effects accurately.

The ability to correctly estimate the BSC has been extensively tested across different transducers and systems. In one study, ten laboratories participated in an interlaboratory study to estimate BSCs from well-calibrated tissue-mimicking phantoms using each laboratory's respective ultrasonic systems, operators and techniques (Madsen et al. 1999). The conclusion of the study was that considerable differences in BSC estimates from tissue mimicking phantoms with the same properties existed between laboratories. These differences were attributed to the different measurement techniques adopted by each group and different methods for calculating the BSC. A better agreement was observed in a subsequent interlaboratory study to compare BSCs from tissue mimicking phantoms (Wear et al. 2005). In this study, the estimated BSCs were compared with theoretical values. The theoretical BSCs were calculated using an exact solution for the scattering from the phantoms (micrometer-sized glass beads were the scatterers) and the properties of the phantoms (Faran 1951).

From the apparent lack of agreement between laboratories, more extensive studies of BSC estimation were conducted to determine the sources of error observed between different groups when estimating the BSC. In one of the subsequent studies, BSCs from tissue-mimicking phantoms, where glass beads were used as scatterers, were conducted between two laboratories (Anderson et al. 2010). The main aim was to investigate the interlaboratory comparison of the theoretical model (Faran 1951) to predict BSCs in the frequency range 1–12 MHz from glass spheres embedded in a uniform agar-based background. Overall, the results of the study demonstrated good agreement between the two laboratories (Anderson et al. 2010). Further interlaboratory comparison of BSCs from tissue-mimicking phantoms with glass beads as scatterers were conducted using four different clinical array-based imaging systems (Nam et al. 2012a, b) and again good agreement was observed.

The first interlaboratory studies demonstrated that if attenuation and diffraction effects are not accounted for accurately, the estimate of the BSC can be biased. However, later studies demonstrated that careful measurement techniques along with careful BSC calculation could provide reasonable agreement between groups suggesting that the BSC can be system and user independent. Various researchers have developed analytical and numerical methods to accurately compensate for attenuation and diffraction effects and to estimate the BSC. In this chapter, the different techniques to estimate the BSC will be examined along with the performance associated with each technique.

1.2 Methods to Estimate System Independent BSCs

1.2.1 Estimating the BSC Using Single-Element Sources

Sigelmann and Reid (1973) developed the method of estimating backscatter power from a volume of randomly distributed scatterers using a single-element planar transducer. The authors used a substitution method where the backscattered signal from a sample and planar rigid reflector are compared to estimate the volumetric backscattering cross-section. A few years later, Bamber et al. (1979) used a cylindrical tissue sample positioned with its long axis normal to the sound propagation path and recorded the backscattered signal at different angles using a planar transducer that acted both as a source and receiver. The expression for estimating the backscatter cross-section from the cylindrical tissue sample is given by (Sigelmann and Reid 1973; Bamber et al. 1979)

$$\sigma_b(\omega) = \frac{4\alpha\xi}{\Omega e^{-4\alpha r}\left[e^{\alpha c\tau} - e^{-\alpha c\tau}\right]}\frac{W_S}{W_R} \tag{1.1}$$

where α is the frequency-dependent attenuation coefficient, r is the radius of the tissue cylinder, c is the speed of sound in the tissue, τ is the duration of the time gate, Ω is the solid angle subtended by the transducer face at the center of the specimen, W_S and W_R are the measured power scattered from the tissue and the total power returned by a plane reflector and ξ is the reflection coefficient of the plane reflector.

In a later study, Nicholas et al. (1982) used the substitution method to derive the BSC given by

$$\sigma_b(\omega) = \frac{W_r}{W_i}\frac{2\eta R^2}{\beta^2 A}\left[\frac{\lambda_0}{\lambda}\right]^2 \frac{2\alpha}{e^{-2\alpha z_1}\left[1 - e^{\alpha c\tau}\right]} \tag{1.2}$$

where W_r is the total power received at the transducer face due to scattering, W_i is the total power received from a planar reflector, η is the intensity reflection coefficient for the reference interface, β is the intensity transmission coefficient for the water/tissue interface, τ is the gate duration, c is the sound speed in the tissue, R is the distance from the transducer face to the gated volume, and z_1 is the distance from the surface of the tissue to the beginning of the gated region.

D'Astous and Foster (1986) used a plane wave approximation at the focus to develop the method of computing BSCs for focused transducers. According to their calculation, the BSC may be written as

$$\sigma_b(\omega) = \frac{R_q}{2\pi(1 - \cos\theta_T)z}\frac{|S'(\omega)|^2}{|S'_0(\omega)|^2} \tag{1.3}$$

where R_q is the intensity reflectance of the water quartz interface, θ_T is the half angle of the transducer subtended at its focus, $S'(\omega)$ is the energy spectrum of the

gated, attenuation corrected signal, $S_0'(\omega)$ is the Fourier transform of the reference echo signal measured using a planar surface, and Δz is the axial length of the range gated volume.

Ueda and Ozawa (1985), derived the reference power spectrum using the boundary integral wave equation under the first order Born approximation. An approximate closed form solution for estimating the BSC assuming a Gaussian profile for the transducer radiation pattern was proposed and developed by the authors and is given by

$$\sigma_b^G(\omega) = 1.9964 \frac{(G_p/2)^2}{1 + (G_p/2)} \frac{\gamma^2 R_1^2}{A_0 \Delta z} |S(\omega)|^2 \tag{1.4}$$

where ω is the frequency, A_0 is the aperture area of the transducer, Δz is the axial length of the range gated volume, R_1 is the on-axis distance between the transducer and the proximal surface of the gated volume, γ is the pressure reflection coefficient of the planar reflector, $G_p = kr^2/2R_1$ is the pressure focusing gain of the transducer (Chen et al. 1993, 1994), and a is the radius of the transducer. The power spectrum is defined by

$$|S(\omega)|^2 = \frac{\langle |S_m(\omega)|^2 \rangle}{|S_0(\omega)|^2} e^{-4(\alpha_m - \alpha_0)(R_1 + \Delta z/2)} \tag{1.5}$$

where $S_m(\omega)$ is the Fourier transform of the sample echo signal, $S_0(\omega)$ is the Fourier transform of the reference echo signal measured using a planar surface, and $\langle |S_m(\omega)|^2 \rangle$ is the average of the power spectrum of several adjacent, gated scan lines $s_m(t)$. The attenuation coefficients for the sample and the reference media are denoted by α_m and α_0, respectively. The authors also derived the BSC for a circular piston transducer given by

$$\sigma_b(\omega) = \left(\frac{L(ka, kR_1)}{0.919} \right) 1.9964 \frac{(G_p/2)^2}{1 + (G_p/2)} \frac{\gamma^2 R_1^2}{A_0 \Delta z} |S(\omega)|^2 \tag{1.6}$$

where $L(ka, kR_1)$ is a frequency-dependent correction factor, which can be calculated numerically for respective transducer characteristics (Ueda and Ozawa 1985).

Insana and co-workers (Insana et al. 1990; Insana and Hall 1990) used a volumetric integral wave equation derived under the first order Born approximation to estimate the power spectrum of both weakly scattering random media and the planar reflector. The BSC can be estimated using

$$\sigma_b(\omega) = 0.3625 \frac{\gamma^2 R_1^2}{A_0 \Delta z} |S(\omega)|^2. \tag{1.7}$$

Equation (1.7) was derived assuming a Hanning window to gate the RF data. Lavarello et al. (2011) noted an inconsistency in the derivation given by Insana et al. (1990) by a factor of 16. In particular, the source function corresponding to a

planar reflector was defined as $\gamma(r_0) = \gamma' h(z_0 - z_c)$ (Insana et al. 1990, Eq. (32)) with $h(z_0 - z_c)$ a step function located at the center of the gate and γ' defined to be the planar reflection coefficient by the authors. However, if $\kappa' = \kappa_0(1 + \delta\kappa)$ and $\rho' = \rho'(1 + \delta\rho)$ and under the weak scattering assumption (i.e., $\delta\kappa, \delta\rho << 1$) used by the authors (Insana et al. 1990), then $\gamma' = 4\gamma$. Therefore, γ' is equal to four times the pressure reflection coefficient of the planar reflector and not to γ as stated in Insana et al (1990). As a result, the expression in Eq. (1.7) is off by a factor of 16. Therefore, Eq. (1.7) should be corrected by multiplying it by 16 (Lavarello et al. 2011).

Chen et al. determined the reference power spectrum using the mirror image method assuming a perfectly reflecting plate and derived the BSC using (Chen et al. 1994, 1997)

$$\sigma_b(\omega) = 2.17 \frac{\gamma^2 R_1^2}{A_0 \Delta z} \left\{ \left| e^{-} jG_p \left[J_0(G_p) + jJ_1(G_p) \right] - 1 \right| \right\} |S(\omega)|^2 \tag{1.8}$$

where $J_m(.)$ is the mth order Bessel function and $|S(\omega)|^2$ is given in Eq. (1.5).

These different formulations for calculating the BSC were constructed for single-element transducers. The variations in these different formulations can explain some of the variations observed in BSC estimates in interlaboratory comparisons of BSCs from tissue-mimicking phantoms. Additional methods for calculating BSCs from ultrasonic arrays required different normalization procedures.

1.2.2 Estimating the BSC Using Arrays

Insana and co-workers developed a method to estimate BSCs using array transducers by analyzing the transducer beam directivity function for linear, two-dimensional and annular-array transducers (Insana et al. 1994). The BSC is given by

$$\sigma_b(\omega) = \frac{2}{3L} \left(\frac{\lambda R}{A} \right)^2 \frac{W(f)}{B_H(0,0)} \tag{1.9}$$

where L is the range gate length, R is the focal length, A is the active area of the transducer, W is the normalized power density spectrum and B_H is the autocorrelation function for beam directivity. The authors provided the analytical expressions for beam directivity functions and BSC for linear, two-dimensional and annular-array transducers.

Yao et al. (1990) derived the BSC from a sample by comparing the echo data acquired from the sample with the data from a well-characterized reference sample whose BSCs and attenuation coefficients were known, i.e., the reference phantom technique. The BSC using the reference phantom technique is given by

Table 1.2 Equations for calculating the BSC developed by different authors

References	BSC ($\sigma_b(\omega)$)	Remarks
(Sigelmann and Reid 1973; Bamber et al. 1979)	$\frac{4\alpha\xi}{\Omega e^{-4\alpha r}\left[e^{\alpha c\tau}-e^{-\alpha c\tau}\right]}$	Single-elemenet transducer
(Nicholas 1982)	$\frac{W_r}{W_i}\frac{2\eta R^2}{\beta^2 A}\left[\frac{\lambda_0}{\lambda}\right]^2\frac{2\alpha}{e^{-2\alpha z_1}\left[1-e^{\alpha c\tau}\right]}$	Substitution technique
(D'Astous and Foster 1986)	$\frac{R_q}{2\pi(1-\cos\theta_T)z}\frac{\lvert S'(\omega)\rvert^2}{\lvert S'_0(\omega)\rvert^2}$	Single-element focused transducer
(Ueda and Ozawa 1985)	$1.9964\frac{(G_p/2)^2}{1+(G_p/2)}\frac{\gamma^2R_1^2}{A_0\Delta z}\lvert S(\omega)\rvert^2$	Single-element focused transducer, Gaussian beam
	$\left(\frac{L(ka,kR_1)}{0.919}\right)1.9964\frac{(G_p/2)^2}{1+(G_p/2)}\frac{\gamma^2R_1^2}{A_0\Delta z}\lvert S(\omega)\rvert^2$	Circular focused transducer
(Insana et al. 1990; Insana and Hall 1990)	$0.3625\frac{\gamma^2R_1^2}{A_0\Delta z}\lvert S(\omega)\rvert^2$	Single-element focused circular piston transducer
(Chen et al. 1994, 1997)	$2.17\frac{\gamma^2R_1^2}{A_0\Delta z}\lvert S(\omega)\rvert^2$	Single-element focused piston transducer
	$\times\left\{\lvert e^{-}jG_p\left[J_0(G_p)+jJ_1(G_p)\right]-1\rvert\right\}$	
(Insana et al. 1994)	$\frac{2}{3L}\left(\frac{\lambda R}{A}\right)^2\frac{W(f)}{B_H(0,0)}$	Array transducer
(Yao et al. 1990)	$\sigma_b^R(\omega)e^{-4z(\alpha_R(\omega)-\alpha_S(\omega))}\frac{\lvert S_S(\omega)\rvert^2}{\lvert S_R(\omega)\rvert^2}$	For any source/receiver characteristics

$$\sigma_b(\omega)=\sigma_b^R(\omega)e^{-4z(\alpha_R(\omega)-\alpha_S(\omega))}\frac{\lvert S_S(\omega)\rvert^2}{\lvert S_R(\omega)\rvert^2} \tag{1.10}$$

where z is the depth, $\sigma_b^S(\omega)$ and $\alpha_S(\omega)$ are the backscatter and attenuation coefficients of the sample, respectively. Similarly, $\sigma_b^R(\omega)$ and $\alpha_R(\omega)$ are the backscatter and attenuation coefficients of the reference sample, respectively. The frequency domain signal from the sample and the reference sample are denoted by $S_S(\omega)$ and $S_R(\omega)$, respectively. This technique is applicable for any transducer geometry such as single-element focused/unfocused and array systems. The method assumes that the speed of sound is approximately similar both in the sample and in the reference sample.

The various methods to estimate BSCs from backscatter measurements are listed in Table 1.2. This table provides a list of the different diffraction related corrections associated with the BSC estimation.

1.2.3 Attenuation Correction

Attenuation correction is one of the major steps to estimate BSCs accurately as shown in Fig. 1.1. Typically, the frequency-dependent attenuation modifies the shape of the power spectrum which will lead to poor estimation of the BSC. Using Eq. (1.5), the normalized power spectrum is written as

$$|S(f)|^2 = \frac{|S_m(f)|^2}{|S_0(f)|^2} A(f) \tag{1.11}$$

where $A(f)$ is the frequency-dependent attenuation correction function. Extensive research has been conducted to develop attenuation correction functions. Point attenuation correction can be used for short-gated segments and low attenuation coefficients given by Oelze and O'Brien (2002)

$$A_{PC}(f) = e^{4\alpha_T(f)z_T + 2\alpha(f)L} \tag{1.12}$$

where z_T is the distance between the source and the gated region, L is the length of the gated region, and $\alpha_T(f)$, $\alpha(f)$ are the frequency-dependent attenuation coefficients in Np/cm for the intervening medium and over the gated region, respectively. Specifically, the first term accounts for the round-trip frequency-dependent attenuation losses between the gated region and the source, and the second term account for the attenuation within the gated region. The attenuation over the gated region is assumed to be constant. The point correction term also works well when using a Hanning or Hamming window to gate the RF signal.

O'Donnell and Miller (1981) used similar approximations of small gate length and low attenuation ($\alpha L > 1$) to derive an attenuation correction function given by

$$A_{OM}(f) = e^{4\alpha_T(f)z_T} \left[\frac{4\alpha(f)L}{1 - e^{-4\alpha(f)L}} \right]. \tag{1.13}$$

The above attenuation correction function is derived using a rectangular gating function. The authors chose a short gate length such that the beam function was approximately the same over the length of the gate for each frequency analyzed. The term in the square bracket accounts for frequency-dependent attenuation losses over the gated region.

Oelze and O'Brien (2002) derived another attenuation correction function by averaging the power spectra after integrating an attenuation function over the entire gate. The Oelze and O'Brien attenuation correction function is given by

$$A_{OO}(f) = e^{4\alpha_T(f)z_T} \left[\frac{2\alpha(f)L}{1 - e^{-2\alpha(f)L}} \right]^2. \tag{1.14}$$

The authors (Oelze and O'Brien 2002) demonstrated better performance than the O'Donnell and Miller (1981) model for $\alpha L < 1$ to estimate the normalized backscatter power spectrum. The authors also derived the attenuation correction function for a Hanning window given by Oelze and O'Brien (2002)

$$A_{OO}^{Han}(f) = A_{OO}(f) \left[1 + \left(\frac{2\alpha(f)L}{2\pi} \right)^2 \right]^2. \tag{1.15}$$

Bigelow and O'Brien (2004) derived attenuation correction functions by coupling the windowing function, beam pattern and attenuation coefficients. The authors

used a single order Gaussian function to model the transducer beam pattern in the focal region. The attenuation correction function is given by

$$A_{OB}(f) = e^{4\alpha_T(f)z_T}\left[\int_{-L/2}^{L/2} dz\; g_{\text{win}}(z)e^{-4\frac{z^2}{w_z^2}+4\alpha(f)z}\right]^{-1} \tag{1.16}$$

where g_{win} is the windowing function and w_z is the width of the Gaussian beam in the focal region.

Attenuation correction is one of the major components in estimating BSCs accurately. The frequency-dependent attenuation correction for some of the methods explained above are shown in Fig. 1.2a, b using $L = 1$ cm, $z_T = 0.5$ cm. The comparison between different methods for low ($\alpha_T = \alpha = 0.2$ dB/cm/MHz) and high ($\alpha_T = \alpha = 1.0$ dB/cm/MHz) attenuation coefficients is shown in Fig. 1.2a, b, respectively. The results clearly show that all the methods agree with each other for low attenuation values and start deviating as the attenuation coefficient in the sample increases. Specifically, the Oelze and O'Brien attenuation correction function lies in between the point attenuation and the O'Donnell and Miller attenuation correction function. Therefore, some attenuation correction

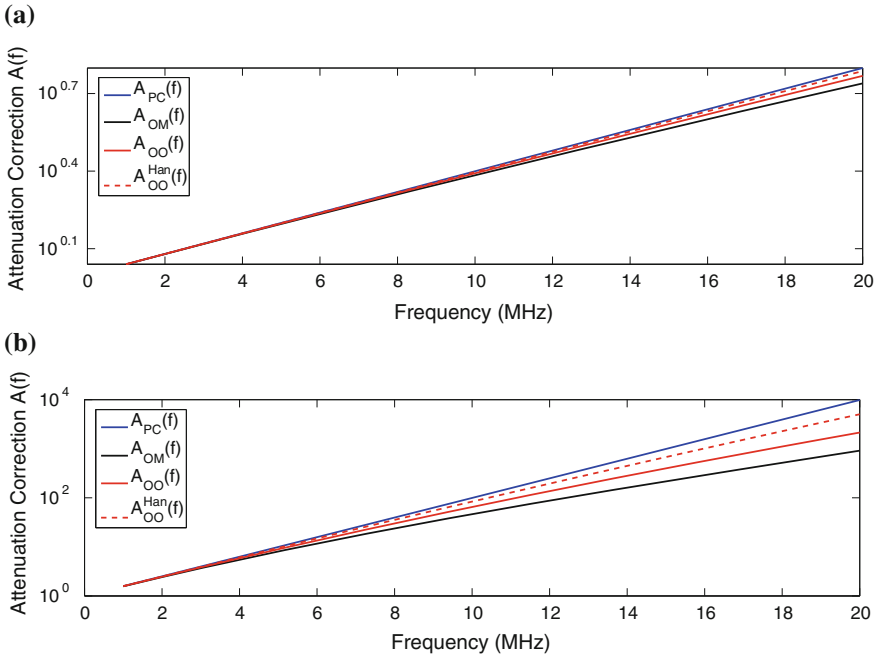

Fig. 1.2 Frequency dependent attenuation correction functions for (**a**) low attenuating and (**b**) high attenuating tissues

Table 1.3 Attenuation correction functions

References	Attenuation correction function ($A(f)$)	Remarks
(Oelze and O'Brien 2002)	$e^{4\alpha_T(f)z_T+2\alpha(f)L}$	Point attenuation correction
(O'Donnell and Miller 1981)	$e^{4\alpha_T(f)z_T}\left[\frac{4\alpha(f)L}{1-e^{-4\alpha(f)L}}\right]$	Small gate length and low attenuation
(Oelze and O'Brien 2002)	$A_{OO}(f)=\frac{e^{4\alpha_T(f)z_T-2\alpha(f)L}}{L}\left[\frac{2\alpha(f)L}{1-e^{-2\alpha(f)L}}\right]^2$	For small ($\alpha L<1$) and large ($\alpha L>1$) attenuation coefficients
	$A_{OO}(f)\left[1+\left(\frac{2\alpha(f)L}{2\pi}\right)^2\right]^2$	Hanning window
(Bigelow and O'Brien 2004)	$e^{4\alpha_T(f)z_T}\left[\int_{-L/2}^{L/2} dz\, g_{\text{win}}(z)e^{-4\frac{z^2}{w_z^2}+4\alpha(f)z}\right]^{-1}$	Coupled window function, beam pattern and attenuation coefficient

functions may over- or under-compensate while normalizing the power spectrum to estimate the BSC. A table of the different attenuation correction techniques that have been developed are provided in Table 1.3.

Researchers have also developed techniques to simultaneously estimate BSC and attenuation slopes using a least squares method (Nam et al. 2011). The authors used a power law model for BSCs and developed a three-parameter model to incorporate backscatter and attenuation coefficients. A least squares technique was employed to estimate backscatter and attenuation coefficients simultaneously. By simultaneously estimating the BSC and attenuation, there was no need to compensate for attenuation effects. The authors used a glass bead phantom to compare theoretical and experimental results.

1.3 Accuracy of Methods to Estimate BSCs

Given the availability of several methods for BSC estimation, it becomes of high importance to evaluate the feasibility of obtaining accurate and consistent BSC estimates. Some of the analytical models developed by various researchers are explained briefly in this chapter. Over the years, authors have developed models to predict BSCs accurately based on their experimental configurations. Lavarello et al. (2011) recently provided a comparison using three different techniques (Insana et al. 1990; Chen et al. 1997; Ueda and Ozawa 1985) shown in Eqs. (1.7), (1.8) and (1.4), respectively, to estimate BSCs from two well-characterized glass bead phantoms using multiple transducers with a wide range of focal properties and frequency bandwidths.

The basic difference between the three formulations for calculating BSCs are in the terms used to correct for diffraction effects. If these diffraction effect terms are isolated, then comparisons of their relative contributions can be conducted.

The frequency-dependent functions that are proportional to diffraction correction for each of the three formulations are given by

$$\begin{aligned} D_1(G_p) &= 1 \\ D_2(G_p) &= \left| e^{-jG_p} \left[J_0(G_p) + jJ_1(G_p) \right] - 1 \right|^2 \\ D_3^G(G_p) &= 0.92 \, \frac{(G_p/2)^2}{1 + (G_p/2)^2} \\ D_3(ka, kR_1) &= \frac{1}{0.92} \, D_3^G(G_p) L(ka, kR_1) \end{aligned} \tag{1.17}$$

where D_1, D_2, D_3^G, D_3 can be derived from Eqs. (1.7), (1.8), (1.4) and (1.6), respectively. The pressure focusing gain is given by $G_p = kr^2/2R_1$. The authors investigated the frequency dependence of three different calibration techniques as shown in Fig. 1.3. At low G_p it can be observed that all the frequency dependent calibrations terms are similar except D_1 (Insana et al. 1990) which does not have the frequency dependence.

Interestingly, all the frequency dependent calibration curves asymptotically agree with D_1 at high G_p. Specifically, the curve corresponding to D_3^G had good agreement with D_2 and D_3 for low G_p values and with D_1 for large G_p values as shown in Fig. 1.3. The curves corresponding to D_2, D_3 and D_3^G agreed with D_1 to within 1 dB for $G_p > 25$, $G_p > 25$, and $G_p > 5$, respectively. The authors demonstrated that different estimation methods introduced varying frequency-dependent effects to BSC curves, which could have noticeable effects when estimating other parameters from the BSC such as correlation length and scattering strength.

Estimates of the BSC from the two phantoms using: (1) the different transducers to cover a large frequency range, (2) a large range of G_p values, and (3) the three methods (with the Insana et al. 1990 method corrected) are plotted in Fig. 1.4. Two agar phantoms with glass bead inclusions, labeled as "41 μm phantom," contained 47 glass spheres/mm^3 ranging in diameter from 36 to 48 μm, and a second phantom labeled as "150–180 μm phantom," contained 20 g/l of glass spheres (approximately 3.2 glass spheres/mm^3) ranging in diameter from 144 to 204 μm

Fig. 1.3 Comparison of the frequency-dependent calibration terms to estimate system independent BSCs. [Figure taken from Lavarello et al. (2011)]

(a) **(b)**

Fig. 1.4 BSC estimates from a (**a**) 41 μm diameter and (**b**) a 150–180 μm diameter glass bead phantom normalized using the three methods with the theoretical BSC for the respective phantoms. The BSCs are denoted as η_1−(Insana et al. 1990), η_2−(Chen et al. 1997), η_3−(Ueda and Ozawa 1985), η_3^G−(Ueda and Ozawa 1985) assuming a Gaussian beam, and η_{th}−Farans model. [Figure taken from (Lavarello et al. 2011)]

were used for the experiments. All techniques gave similar overall BSC trends; however, there were differences in terms of the magnitude and slight differences in the frequency dependence of the BSC curves using the different methods. These differences were found to provide different estimates of scatterer size, but most estimates of scatterer size based on the BSC curves were within the range of sizes present in the phantoms as long as the *ka* range (acoustic wavenumber times the scatterer radius) was above 0.5.

In summary, the authors investigated several BSC normalization methods experimentally in order to isolate and determine potential differences in BSC. From experimental results, it was found that significant BSC amplitude differences may be observed depending on the normalization method used, which has a direct effect on scattering strength estimates. The differences in BSC frequency dependence introduced by all methods may result in noticeable variations in effective scatterer size estimates, especially when considering transducers with low G_p values and imaging targets with low *ka* products. The choice of normalization method may explain much of the variations reported in earlier inter-laboratory comparisons of BSC estimation (Madsen et al. 1999; Wear et al. 2005) and the results suggest that trying to use transducers with a larger G_p value when estimating BSCs will provide the most accurate and consistent results.

1.4 Conclusion

The ultrasonic BSC is a fundamental system-independent material quantity that can be used to characterize tissues, and monitor and assess therapies. Researchers have used BSCs to characterize different organs/tissues of the body and published

results from various mammalian tissues are available for reference for both in vitro and in vivo experimental configurations. For spectral-based QUS techniques to be successful, the BSC is one of the major parameters that needs to be estimated accurately. This is due to the fact that the BSC can be used to infer microstructural parameters such as correlation length and scattering strength. Often, correlation length can be related to cell size, as various researchers have hypothesized cells may be a dominant source of scattering in specific tissues. The scattering strength can be related to the acoustical properties of the tissue.

Due to the importance of estimating system- and user-independent BSCs accurately, numerous studies have been conducted to compensate for system effects and attenuation effects. Depending on the application, particular methods to estimate the BSC may be more appropriate based on experimental configuration and tissue types. We hypothesize that coupling attenuation and diffraction effects in an integral form (Bigelow and O'Brien 2004) can be used to estimate BSCs accurately. The method developed by Chen et al. (1997) is a robust method and used widely to estimate the BSC for focused single-element transducer systems. The reference phantom technique (Yao et al. 1990) is a very powerful technique because modeling of the diffraction pattern of the beam is not required, but the sound speed in the unknown and the reference sample need to be similar for the method to be most effective. The reference phantom technique can be used for both single-element and array transducer systems. The evidence of vast experimental and theoretical investigations conducted to estimate BSCs to infer tissue properties suggests that the BSC can be used for diagnostic and therapeutic applications.

References

Anderson JJ, Herd MT, King MR, Haak A, Hafez ZT, Song J, Oelze ML, Madsen EL, Zagzebski JA, O'Brien WD Jr, Hall TJ (2010) Interlaboratory comparison of backscatter coefficient estimates for tissue-mimicking phantoms. Ultrasonic Imaging 32(1):48–64

Bamber JC, Hill CR, King JA, Dunn F (1979) Ultrasonic propagation through fixed and unfixed tissues. Ultrasound in Med and Biol 5:159–165

Bigelow TA, O'Brien WD (2004) Scatterer size estimation in pulse-echo ultrasound using focused sources: Theoretical approximation and simulation analysis. J Acoust Soc Am 116:578–593

Chen X, Schwarz KQ, Parker KJ (1993) Radiation pattern of a focused transducer: A numerically convergent solution. J Acoust Soc Am 94:2979–2991

Chen X, Schwarz KQ, Parker KJ (1994) Acoustic coupling from a focused transducer to a flat plate and back to the transducer. J Acoust Soc Am 95:3049–3054

Chen X, Phillips D, Schwarz KQ, Mottley JG, Parker KJ (1997) The measurement of backscatter coefficient from a broadband pulse-echo system: A new formulation. IEEE Trans Ultrason Ferroelectr Freq Control 44:515–525

D'Astous FT, Foster FS (1986) Frequency dependence of ultrasound attenuation and backscatter in breast tissue. Ultrasound in Med and Biol 12(10):795–808

Faran JJ Jr (1951) Sound scattering by solid cylinders and spheres. J Accoust Soc Am 23:405–418

Fei DY, Shung KK (1985) Ultrasonic backscatter from mammalian tissues. J Accoust Soc Am 78:871–876

Ghoshal G, Luchies AC, Blue JP, Oelze ML (2011) Temperature dependent ultrasonic characterization of biological media. J Acoust Soc Am 130(4):2203–2211

Insana MF, Hall TJ (1990) Parametric ultrasound imaging from backscatter coefficient measurements: Image formation and interpretation. Ultrasonic Imag 12:245–267

Insana MF, Wagner RF, Brown DG, Hall TJ (1990) Describing small-scale structure in random media using pulse-echo ultrasound. J Accoust Soc Am 87:179–192

Insana MF, Hall TJ, Fishback JL (1991) Identifying acoustic scattering sources in normal renal parenchyma from the anisotropy in acoustic properties. Ultrasound in Med and Biol 17(6):613–626

Insana MF, Hall TJ, Cook LT (1994) Backscatter coefficient estimation using array transducers. IEEE Trans Ultrason Ferroelectr Freq Control 41:714–723

Kabada MP, Bhagat PK, Wu VC (1980) Attenuation and backscattering of ultrasound in freshly excised animal tissues. IEEE Trans Biomed Eng 27:76–83

Lavarello R, Ghoshal G, Oelze ML (2011) On the estimation of backscatter coefficients using single-element focused transducers. J Acoust Soc Am 129:2903–2911

Lizzi FL, Greenabaum M, Feleppa EJ, Elbaum M, Coleman DJ (1983) Theoretical framework for spectrum analysis in ultrasonic tissue characterization. J Accoust Soc Am 73:1366–1373

Lizzi FL, Ostromogilsky M, Feleppa EJ, Rorke MC, Yaremko MM (1987) Relationship of ultrasonic spectral parameters to features of tissue microstructure. IEEE Trans Ultrason Ferroelectr Freq Control 34:319–329

Lu ZF, Zagzebski JA, Lee FT (1999) Ultrasound backscatter and attenuation in human liver with diffuse disease. Ultrasound Med Biol 25(7):1047–1054

Madsen EL, Dong F, Frank GR, Gara BS, Wear KA, Wilson T, Zagzebski JA, Miller HL, Shung KK, Wang SH, Feleppa EJ, Liu T, O'Brien WD Jr, Topp KA, Sanghvi NT, Zaitsen AV, Hall TJ, Fowlkes JB, Kripfgans OD, Miller JG (1999) Interlaboratory comparison of ultrasonic backscatter, attenuation and speed measurements. J Ultrasound Med 18:615–631

Mamou J, Coron A, Oelze ML, Saegusa-Beecroft E, Hata M, Lee P, Machi J, Yanagihara E, Laugier P, Feleppa EJ (2011) Three-dimensional high-frequency backscatter and envelope quantification of cancerous human lymph nodes. Ultrasound in Med and Biol 37:345–357

Maruvada S, Shung KK, Wang SH (2000) High frequency backscatter and attenuation measurements of selected bovine tissue between 10 and 30 MHz. Ultrasound Med Biol 26(6):1043–1049

Miller JG, Perez JE, Mottley JG, Madaras EI, Johnston PH, Blodgett ED, Thomas LJ III, Sobel BE (1983) Myocardial tissue characterization: an approach based on quantitative backscatter and attenuation. Ultrasonic Symp Proc 2:782–793

Moran CM, Bush NL, Bamber JC (1995) Ultrasonic propagation properties of excised human skin. Ultrasound in Med and Biol 21:1177–1190

Nam K, Zagzebski JA, Hall TJ (2011) Simultaneous backscatter and attenuation estimation using a least square method with constraints. Ultrasound in Med and Biol 37(12):2096–2104

Nam K, Rosado-Mendex IM, Wirtzfeld LA, Kumar V, Madsen EL, Ghoshal G, Pawlicki AD, Oelze ML, Lavarello RJ, Bigelow TA, Zagzebski JA, O'Brien WD Jr, Hall TJ (2012a) Cross-imaging system comparison of backscatter coefficients estimates from tissue-mimicking material. J Acoust Soc Am 132:1319–1324

Nam K, Rosado-Mendex IM, Wirtzfeld LA, Pawlicki AD, Kumar V, Madsen EL, Ghoshal G, Lavarello RJ, Oelze ML, Bigelow TA, Zagzebski JA, O'Brien WD Jr, Hall TJ (2012b) Ultrasonic attenuation and backscatter coefficient estimates of rodent-tumor mimicking structures: Comparison of results among clinical scanners. Ultrasonic Imag 33:233–250

Nicholas D (1982) Evaluation of backscattering coefficients for excised human tissues: Results, interpretation, and associated measurements. Ultrasound Med and Biol 8:17–28

O'Donnell M, Miller JG (1981) Quatitative broadband ultrasonic backscatter: An approach to nondestrutive evaluation in acoustically inhomogeneous materials. J Appl Phys 52(2):1056–1065

O'Donnell M, Mimbs JW, Miller JG (1981) Relationship between collagen and ultrasonic backscatter in myocardial tissue. J Accoust Soc Am 69(2):580–588

Oelze ML, O'Brien WD Jr (2002) Frequency-dependent attenuation-compensation functions for ultrasonic signals backscattered from random media. J Acoust Soc Am 111:2308–2319

Shung KK (1993) In vitro experimental results on ultrasonic scattering in biological tissues. In: Thieme GA (ed) Shung KK. CRC Press, Ultrasonic Scattering in Biological Tissues, pp 75–124

Sigelmann RA, Reid JM (1973) Analysis and measurement of ultrasound backscattering from an ensemble of scatterers excited by sine-wave bursts. J Acoust Soc Am 53:1351–1355

Topp KA, Zachary JF, O'Brien WD Jr (2001) Quantifying B-mode images of in vivo rat mammary tumors by the frequency dependence of backscatter. J Ultrasound Med 20:605–612

Turnbull DH, Wilson SR, Hine AL, Foster FS (1989) Quantifying B-mode images of in vivo rat mammary tumors by the frequency dependence of backscatter. Ultrasound in Med and Biol 15:241–253

Ueda M, Ozawa Y (1985) Spectral analysis of echoes for backscattering coefficient measurements. J Accoust Soc Am 77(38–47):

Wear KA, Gara BS, Hall TJ (1995) Measurements of ultrasonic backscatter coefficients in human liver and kidney in vivo. J Acoust Soc Am 98:1852–1857

Wear KA, Stiles TA, Frank GR, Madsen EL, Cheng F, Feleppa EJ, Hall CS, Kim BS, Lee P, O'Brien WD Jr, Oelze ML, Raju BI, Shung KK, Wilson TA, Yuan JR (2005) Interlaboratory comparison of ultrasonic backscatter coefficint measurements from 2 to 9 MHz. J Ultrasound Med 24:1235–1250

Yao LX, Zagzebski JA, Madsen EL (1990) Backscatter coefficient measurements using a refernce phantom to extract depth-dependent instrumentation factors. Ultrasonic Imag 12:58–70

Chapter 2
Quantitative Ultrasound History and Successes

Goutam Ghoshal, Michael L. Oelze and William D. O'Brien Jr.

Abstract Ultrasound has been used for imaging and diagnostics for more than 50 years. During that time, the number of medical applications for ultrasonic imaging has increased dramatically. These increases in applicability have come with improved device technology, improved understanding of ultrasound interaction with tissues, and improved processing techniques. Over the past three decades, quantitative ultrasound (QUS) techniques have been explored to further improve medical diagnostics and monitor/assess therapeutic responses. The acceptance of QUS techniques has been slower in common medical practice than conventional ultrasonic imaging techniques like B-mode or Doppler. This is due mainly to a lack of technological capabilities to make use of these unique and beneficial imaging modes. However, with modern ultrasonic imaging devices, QUS techniques have found a new acceptance and are poised to make significant contributions to diagnostic medicine. In this chapter, we will examine the history of QUS techniques and their evolution over time along with significant contributions and successes that have been demonstrated over the years.

Keywords Quantitative ultrasound · Tissue characterization · Spectral analysis

G. Ghoshal · M. L. Oelze · W. D. O'Brien Jr. (✉)
Department of Electrical and Computer Engineering, University of Illinois at Urbana-Champaign, 405 N. Mathews, Urbana, IL 61801, USA
e-mail: wdo@uiuc.edu

G. Ghoshal
e-mail: ghoshal2@gmail.com

M. L. Oelze
e-mail: Delze@illinois.edu

J. Mamou and M. L. Oelze (eds.), *Quantitative Ultrasound in Soft Tissues*, DOI: 10.1007/978-94-007-6952-6_2,

2.1 Introduction

The earliest history of the science of sound has been recorded by Hunt (1978) in his manuscript that was completed following his untimely death. Another interesting and readable history of acoustics was prepared by Lindsey (1966). Hunt recounts the period from antiquity to the age of Newton, and Lindsey brings us mostly to the age of Rayleigh with special emphasis on Rayleigh's impact on modern acoustics. Sir Isaac Newton put forth the first serious theory regarding sound being a wave in his 1687 *Principia Mathematica* (Newton 1687). Modern acoustics as we know it today was first formulated in the classic 1877 work *The Theory of Sound* by Lord Rayleigh (Rayleigh 1945).

The development of diagnostic ultrasound applications dates back to the 1930s (Gohr and Wedekind 1940). The Dussik brothers developed a through-transmission differential attenuation method to image the brain (Dussik 1942, 1948, 1949; Dussik et al. 1947), although their technique was never widely developed for clinical application. Shortly thereafter, Firestone's patent (1942) for flaw detection in metals, and his later demonstration, is considered the first modern pulse-echo ultrasound technique for flaw detection (Firestone 1945, 1946; Firestone and Frederick 1946), and the basis for pulse-echo imaging in medicine. The development of diagnostic ultrasound instrumentation as we know it today was initiated around the time of the end of the Second World War; a time when fast electronic circuitry was becoming available as a result of the wartime RADAR and SONAR efforts, both of which utilized the pulse-echo principle. In the late 1940s and early 1950s, it was demonstrated that tissue interfaces could be detected in ultrasound echoes (Howry 1952), that tissue structure could be differentiated (cancer from benign) in ultrasound echoes (Wild 1950; Wild et al. 1950; French et al. 1950; Wild and Neal 1951), and that gall stones could be detected in ultrasound echoes (Ludwig and Struthers 1950), all of these being A-mode applications. Later, Howry and Bliss (1952) and Wild and Reid (1952a, b) independently built and successfully demonstrated the earliest B-mode, bistable, ultrasound scanners.

By the early to mid 1950s, the basic ideas of producing and acquiring reflected ultrasound echoes using either water path or direct contact methods, and displaying them in either A-mode or B-mode formats had been identified. These early investigators made their observations and findings public through presentations and publications which no doubt stimulated others to pursue pulse-echo system improvements and/or diagnostic imaging applications in, for example, echoencephalography (Leksell 1955; Gordon 1958; Tanaka et al. 1960), ophthalmology (Mundt and Hughes 1956; Baum and Greenwood 1958a, b), echocardiography (Elder and Hertz 1954; Elder and Gustafson 1957), obstetrics and gynecology (Donald and Brown 1961; Donald 1974), breast (Hayashi et al. 1962), direct-contact two-dimensional ultrasonic scanner (Donald 1964; Holmes et al. 1965), ultrasonic scanner with two articulated arms (Wells 1966; Filipczynski et al. 1966) and dynamic focusing (Reid and Wild 1957). However, progress was modest and the bistable images were often challenging for diagnostic interpretation in the late

1950s and 1960s. It was a time when most of the progress was being made in the university and/or hospital settings by true pioneers.

The 15-year period between the early 1970s and mid 1980s witnessed the greatest expansion of diagnostic ultrasound imaging capabilities, starting with bistable, static and ending with grey-scale, real-time capabilities. One of the major ultrasonic image quality advances was the introduction of the grey scale (Kossoff and Garrett 1972; Kossoff et al. 1974). Another major advance was the ability to display images in real time, wherein there were a number of approaches including the mechanical scanner (Griffith and Henry 1974), the linear array (Bom 1973; Bom et al. 1973), the phased array (Somer 1968; von Ramm and Thurston 1972; Thurston and von Ramm 1974), and the water-path scanner (Carpenter and Kossoff 1977). Scan converter developments played an important role with the implementation of both grey-scale and real-time capabilities (Fry et al. 1968; Yokio and Ito 1972).

2.2 Attenuation and Propagation Speed

Along with advances in ultrasound scanner technology came a deeper understanding of the wave propagation properties of tissues, which would define image contrast mechanisms and the fundamental limits of penetration depth and frame rate. One of the earliest reports of ultrasonic propagation properties in tissue was the observation of a nearly linear dependence of the attenuation coefficient on frequency (Pohlman 1939), later verified by Heuter (1948). Hueter also observed that attenuation in muscle tissue was anisotropic due to structural features of striated muscle. The first significant reports of propagation speed and impedance in high-water-content tissues observed that these values did not vary greatly from those of water, and that anisotropic structural features did not significantly affect these parameters (Ludwig 1950).

Researchers had investigated the relationship between macromolecular components of tissue and ultrasound wave propagation to understand ultrasonic absorption in biological tissues. Carstensen et al. (1953) discovered that the absorption and sound speed in blood were due to the amount of protein content of the blood, whether the protein is in solution or contained within cells. Another investigation indicated that a small fraction of the absorption arose due to the cellular organization of the blood (Carstensen and Schwan 1959). Schwan (1959) suggested that the macromolecular components may be responsible for the frequency dependence of acoustical properties in biological media. Pauly and Schwan (1971) showed that approximately two-thirds of the absorption in liver occurred at the macromolecular level, with the remaining one-third being attributed to macroscopic structures in the frequency range of 1–10 MHz. The authors showed that the ultrasonic absorption also depends on *p*H and protein denaturation. The authors observed specific absorption in liver tissue as 0.027 dB/cm per gram of solid component in 100 cm^3 at 1 MHz. Interestingly, the specific absorption in ground, homogenate, sediment, supernatant and nuclei all derived from liver were

0.023, 0.020, 0.027, 0.011 and 0.040 dB/cm per gram solid component in 100 cm^3 at 1 MHz, respectively. Therefore, destruction of the solid tissue resulted only in a moderate change in absorption, indicating that the absorption may be due to the macromolecules rather than the structure of the solid tissue.

Researchers observed variations in absorption by approximately an order of magnitude from one type of substance to another (Pauly and Schwan 1971; Smith and Schwan 1971). Smith and Schwan (1971) measured acoustic absorption of liver cell nuclei and observed that sound absorption per weight percentage of protein content varied from one type of protein to another. In a review article, Wells (1975) suggested that absorption and dispersion in biological materials were due to relaxation processes distributed over a range of frequencies. O'Brien and Dunn (1971, 1972b) suggested that the relaxation processes may be due to solvent-solute interactions and disturbances in H-bonding equilibria. Other researchers investigated the interaction between macromolecules in suspension of erythrocytes (Kremkau et al. 1973). The authors suggested that electrostatic interaction may be important in the sound absorption process. They observed increases in absorption with increasing organization or interaction of biological systems due to chemical and structural relaxations (Kremkau et al. 1973).

Kremkau and Cowgill (1984) measured absorption of several sugars, polysaccharides, amino acids and proteins to determine the importance of molecular weights in biomacromolecular absorption. The authors observed that absorption increases with increasing molecular weight only in the approximate molecular weight range of 500–1,500 daltons. Their results showed that proteins have higher absorption than solutions of amino acids of which they are made, which may be due to higher order structural characteristics present in proteins. In another study, Kremkau and Cowgill (1985) concluded that absorption in globular proteins is insensitive to structural characteristics while in linear proteins it depends upon the amount of $\alpha-$helix content. They suggested that the tertiary structure in the globular protein reduces absorption due to inhibited solvent interactions.

It was established that proteins are largely responsible for absorption in tissues. To understand the underlying mechanism, researchers studied the solutions of this chemical species, of their components and of somewhat related chemical species. O'Brien and Dunn (1972a) investigated propagation of ultrasound through solutions of biological polymers as the first step to understand ultrasonic propagation through tissue microstructure. Specifically, researchers have investigated the absorption in various chemical species such as amino acids, polypeptides, proteins, carbohydrates, bases, nucleotides and nucleosides, nucleic acids and lipids (Dunn and O'Brien 1978).

It was hypothesized that biological tissues act as a composite material whose ultrasonic propagation is mainly governed by the acoustic properties of collagen and globular proteins (Goss et al. 1980a). Pohlhammer and O'Brien (1980) compared ultrasonic attenuation and speed to the concentration of water, collagen, proteins, and fat, given in wet weight percent. Their study concluded that ultrasonic propagation properties of tissue are, indeed, functions of the constituent's concentrations. Water is the most abundant tissue constituent, making up as much as 70–80 % of

many tissues. The water concentration is nonuniformly distributed throughout the body such that adipose tissue and blood are about 10 and 83 % water, respectively. The ultrasonic absorption in water at 37 °C is given by Pinkerton (1949)

$$\alpha = 15.7 \times 10^{-17} f^2, \tag{2.1}$$

where f is the frequency in Hz, and α is the absorption coefficient in Np/cm. The ultrasonic attenuation coefficients in tissues were characterized according to their water concentration given by Goss (1978)

$$\alpha = 9 \times 10^{-12} f W^{-0.74}, \tag{2.2}$$

where W is the water concentration. Using a least squares linear regression, a power function relationship between the ultrasonic attenuation in the 1–10 MHz range and the wet weight percentage of collagen in a tissue was developed (O'Brien 1977a). To the first approximation this yielded

$$\alpha = 0.11 C^{0.51}, \tag{2.3}$$

where C is the wet weight percentage of collagen. Similarly, the authors derived the relationship between ultrasonic speed and collagen concentration given by

$$v = 1588 + 32 \ln C, \tag{2.4}$$

where v is the speed in m/s (O'Brien 1977a).

Collagen plays an important role in the acoustical properties of tissues due to its high tensile strength and it exhibits a wide range of acoustical properties from those of the other common tissue constituents (Pohlhammer and O'Brien 1980). Collagenous fibers exhibit a static elastic modulus approximately 1,000 times higher than other tissues (Fields and Dunn 1973). Because ultrasonic speed is proportional to the square of the elastic modulus, the ultrasonic speed would be significantly greater than other tissue constituents. Due to a higher elastic modulus, collagen is hypothesized to be responsible for much reflection and scattering of ultrasound. Fields and Dunn (1973) suggested that collagen is largely responsible for the echographic visualizability of soft tissues. Other investigators have shown in excised, unfixed breast tissue that fat yields the lowest attenuation and lowest velocity compared to all other surrounding tissue (Greenleaf et al. 1975, 1976). They observed that normal parenchymal breast tissue exhibited relatively high attenuation and moderately high velocity, infiltrating medullary carcinoma exhibited an attenuation between fat and normal breast tissue and high velocity, and connective tissue associated with muscle boundaries of a scirrhous carcinoma clearly exhibited the highest attenuation and velocity. These results clearly infer a relationship between increasing structural protein concentration and increasing ultrasonic speed and attenuation.

Several studies of the relationship between attenuation and collagen concentration in infarcted tissues have been conducted. A quantitative study of the attenuation in normal and infarcted canine myocardium, which was made around two months after the infarct and over the frequency range of 2–10 MHz, indicated

that attenuation increased in the infarcted tissue (Yuhas et al. 1976; Mimbs et al. 1977). O'Brien (1977b) observed that the attenuation in most soft tissue appears to be an increasing function of the collagen content. In another study, O'Donnell et al. (1979) observed a direct correlation between attenuation and collagen concentration. The authors measured frequency-dependent attenuation in the frequency range of 2–11 MHz with respect to collagen content in hearts from normal dogs and in hearts from dogs subjected to ischemic injury by coronary occlusion. The authors detected elevated attenuation in regions of myocardial infarction. The results clearly suggest a correlation between increases in attenuation and increases in collagen in infarcted tissue. Other investigators measured ultrasonic attenuation and sound speed in four different types of tissue elements present in acute myocardial infarction using an acoustic microscope in the frequency range 100–200 MHz (Saijo et al. 1997). The authors measured very low attenuation and sound speed of degenerated myocardium compared with normal myocardium. Furthermore, attenuation and sound speed were very high in fibrotic tissue. From the results, it was suggested that the ultrasonic properties of acute myocardial infarction were due to density, intra- and intercellular structure and bulk elasticity of the tissue element.

O'Brien et al. (1981) characterized cutaneous wound tissue using a 100-MHz scanning laser acoustic microscope. Results of this study indicated that there was an increase in sound speed and attenuation with an increase in the age of the scar tissue. The authors suggested that the increase in the acoustical parameters was caused by both increases in collagen concentration and the changes in nature of the collagen. In another study, researchers documented the normal progression of wound maturation in a canine model using tensile strength measurements, light microscopy, collagen biochemistry and acoustical properties (Olerud et al. 1987). The authors observed a strong correlation between ultrasound speed and attenuation with tissue collagen content [$r = 0.80$ and $r = 0.56$, respectively ($p < 0.001$)]. They also found that ultrasonic speed and attenuation were inversely correlated with tissue water content [$r = -0.57$ and $r = -0.73$, respectively ($p < 0.001$)]. The tensile strength was also correlated significantly with ultrasonic speed and attenuation [$r = 0.90$ and $r = 0.58$, respectively ($p < 0.001$)].

Fat or lipid is a tissue which is almost water free. Generally, at least 10 % of the body weight of the normal mammal is due to lipid. The attenuation in fat is similar to most soft tissue except collagen-high tissues. Ultrasonic speed in fat is approximately 50–100 m/s less than most other tissues, and there is evidence to suggest that sound speed in subcutaneous fat, in particular, is as much as 300–600 m/s lower (O'Brien et al. 1981). Hammes and Roberts (1970), in a study undertaken to examine membrane models, observed excess attenuation only in the presence of the phospholipids in the frequency range of 10–165 MHz at a temperature of 25 °C. The authors postulated four main classes of mechanisms by which ultrasonic energy interacts with phospholipids dispersions: (1) liposomal aggregation, (2) breaking the reforming liposomes, (3) intraliposomal conformational changes and (4) liposome hydration sphere equilibria. Greenleaf and co-workers showed that in excised, unfixed specimens, fat yields the lowest attenuation and lowest sound speed of any of the breast tissues (Greenleaf et al. 1975, 1976). Kossoff et al. (1973) found that

the speed of sound in post-menopausal fatty breast tissue was 7 % lower than that in pre-menopausal breast tissue, with the difference being attributed to a proliferation of fat that occurs as the glandular tissue deteriorates during and following menopause. Thus, these authors suggested that it was possible to distinguish between different states of the breast as well as to identify various benign and malignant conditions by measuring the ultrasonic speed through the tissue.

In fatty liver, fat invades the hepatocytes causing them to balloon which are distributed throughout the organ. Pohlhammer and O'Brien (1980) hypothesized that due to lower ultrasonic speed of fat, these droplets may cause a significant amount of scattering, thereby causing an increase in attenuation with increases in fat content in the liver. Bamber et al. (1981) observed increased attenuation and backscattering with increasing fat content in livers. The authors observed decreased speed of sound with increasing fat content (Bamber and Hill 1981). Other investigators studied the effects of increasing fat in a rat liver on ultrasonic propagation properties using a scanning laser acoustic microscope at 100 MHz (O'Brien et al. 1988). The authors observed that as hepatic lipid increased, ultrasonic attenuation at 100 MHz increased temporally from a normal range of 12–14 dB/mm to a maximum of 54 dB/mm and ultrasonic speed decreased from a normal rage of 1,553–1,584 m/s to a minimum of 1,507 m/s. Thus, quantitative ultrasound (QUS) techniques have been used to quantify properties of the liver in both in vitro and in vivo studies (Bamber and Hill 1981; Fei and Shung 1985; Wear et al. 1995). Researchers have examined the use of attenuation and backscatter coefficients to monitor the stages of the liver remodeling in mice (Guimond et al. 2007; Gaitini et al. 2004). Lu and co-workers demonstrated that the backscatter coefficient and attenuation in patients with diffuse liver disease were higher than in patients with healthy livers (Lu et al. 1999). Suzuki and co-workers observed that the ultrasonic attenuation depends on fatty infiltration of the liver and to a lesser extent on fibrosis (Suzuki et al. 1992).

Another method or ultrasound imaging mode that has been developed to image and quantify sound speed and attenuation is ultrasound computed tomography. The concept of ultrasound time-of-flight computed tomography was first introduced by Greenleaf et al. (1974, 1975). Glover (1977) constructed a two-dimensional velocity distribution in tomographic slices transaxial to the breast from transmission time-of-flight projections with an objective to detect malignant and benign lesions. Dines and Kak (1979) constructed ultrasound attenuation tomograms from formalin-fixed dog heart using various attenuation estimation algorithms. Carson et al. (1981) observed that carcinoma tissues appeared as a bright circular mass of sound speed 1,531 m/s compared to fatty background sound speed of 1,445 m/s in a sound speed tomogram. Greenleaf and Bahn (1981) observed low velocity of 1,400–1,450 m/s in the subcutaneous zone compared to 1,500–1,520 m/s in cysts. They observed that extremely fibrous or schirrous carcinomas tended to have high sound speeds of 1,530 m/s (Greenleaf and Bahn 1981).

Several commercial ultrasound tomography imaging systems are available today (Jeong et al. 2005; Duric et al. 2005; Johnson et al. 2007; Li et al. 2008). Researchers have used a spectral target detection method based on a constrained

energy minimization technique to construct attenuation tomograms and developed a High Resolution Ultrasonic Transmission Tomography (HUTT) system (Jeong et al. 2005). Researchers at the Karmanos Cancer Institute developed a Computerized Ultrasound Risk Evaluation (CURE) device to record reflected, transmitted and diffracted ultrasound signals from the breast to construct sound speed and attenuation tomograms (Duric et al. 2005, 2007). The CURE device operates at a center frequency of 1.5 MHz with 256 transducer elements with a minimum detectable sound speed of 5 m/s. The device has a spatial resolution of 4 mm in sound speed and attenuation tomograms (Duric et al. 2007). The CURE device estimated the sound speeds of fatty and glandular tissues as $1,409 \pm 17$ m/s and $1,472 \pm 37$ m/s , respectively and 75 % of masses >1 cm in size were detected by a combination of reflection and transmission images (Duric et al. 2007). Li et al. (2008) used bent-ray time-of-flight ultrasound tomography to reconstruct sound speed and complex energy ratio to construct attenuation tomograms. Johnson and co-workers used inverse scattering algorithms assuming propagation in fluid media to construct sound speed and attenuation tomograms (Johnson et al. 2007). Unlike previous approaches to ultrasound tomography, the inverse scattering techniques accounted for diffraction, refraction, and multiple scattering effects.

Several researchers have provided comprehensive compilations of available data for the acoustical properties of tissues such as sound speed and attenuation (Goldman and Hueter 1956; Chivers and Parry 1978; Goss et al. 1978, 1980b). The experimental results presented by numerous researchers suggest that ultrasound absorption depends on the macromolecular constituents of tissues. According to the research conducted by numerous researchers, ultrasonic absorption is attributed mainly to the relaxation processes. Nevertheless, more research is necessary to explicitly understand the variation of sound speed and attenuation with tissue properties.

2.3 Quantitative Backscattered Ultrasound Analyses

Conventional B-mode images are derived from backscattered radio frequency (RF) echo signals. The RF echoes are created by reflections from interfaces between acoustically different regions (macrostructure) and by coherent and incoherent scattering from tissue microstructures. Those echo signals contain frequency-dependent information about the smaller scale tissue structures (< wavelength). B-mode image processing hides the frequency-dependent information available in the RF echoes. Conventional B-mode images display large-scale structures (> wavelength) but, to display and quantify smaller-scale structures, the frequency-dependent information must be utilized.

Frequency-dependent scattering from small structures ($\approx$ wavelength) has been used to extract information about properties of different materials in addition to its investigation in medical imaging. Laser scattering has been used to examine glass

and polymer structures (Miyazaki 1974), and neutron scattering has been used to measure molecular bond lengths (Egelstaff et al. 1975). In acoustics, low-frequency sound (<1 kHz) has been used to measure the size and distribution of turbulence in the atmosphere (Wilson et al. 1999).

The RF echoes backscattered from biological tissues contain information about the microstructural properties of the tissues. Preliminary attempts to relate QUS scatterer property estimates to tissue microstructure identified from optical microscope images of the same tissues has met with success. The backscattered signal is a superposition of wavelets scattered from numerous small structures confined within the volume of insonified tissue. The frequency-dependent backscattered signal depends on the average tissue properties (size, shape, number, compressibility, density) of the scatterers within the insonified region relative to the compressibility and density of the medium surrounding the scatterers. The backscattered signal is, therefore, modeled as that resulting from a statistical distribution of scatterers.

The goal of QUS is to estimate parameters, such as effective scatterer diameter (ESD), effective acoustic concentration (EAC), number density and attenuation, from backscattered data from tissues, and associate these parameter values with specific tissue structures. QUS images of scatterer parameters, like ESD and EAC, have been constructed for test phantoms (Insana and Hall 1990) and tissues (Insana et al. 1993). The most simple models that can be used to parameterize the backscattered power spectrum are fitting a line to the spectra and estimating the spectral slope, mid-band fit and spectral intercept (Lizzi et al. 1983). However, the backscattered power spectrum, if modeled correctly, can lead to better QUS estimates of specific scatterer properties.

The ESD, EAC, and number density are values that can be related to microscopic optical histological evaluation. Relating ultrasound backscatter measurements to optical microscope images has been conducted for a variety of tissues (Waag et al. 1983). Specifically, estimates of ESD have been related to the average size of cellular structures in murine models of mammary carcinoma and subcutaneous sarcomas as estimated from their optical microscope images (Oelze et al. 2004). Volume representations from histological sections of scattering tissues can be constructed that are hypothesized to be able to identify the size and distribution of possible scattering sources. The significance of the approach is threefold: (1) QUS estimates can be compared with optical histology findings (validation of the model truth), (2) better models then can be constructed based on comparisons with optical histology and (3) improvement in modeling based on optical histology can increase ability of QUS to diagnose disease.

There have been notable QUS successes. Acoustic scattering theories for biological tissues assume that the tissues can be modeled as either discretely or continuously varying distributions of mass density and bulk compressibility (Insana and Brown 1993). Scattering occurs when an acoustic wave propagates across a region that has local variations in density and/or compressibility. Scattering from simple shapes (spheres and cylinders) has been solved analytically including the effects of shear (Faran 1951). If the scatterers size is comparable to

or smaller than the wavelength and the relative impedance mismatch between scatterer and background is small, then scattering may be modeled using the Born approximation by a spatial autocorrelation function (SAF) (Insana and Hall 1990; Lizzi et al. 1987; Chen 1994).

QUS backscattering techniques have been successfully used to characterize different aspects of tissue microstructures. Noteworthy are the pioneering works that demonstrated theoretically and experimentally the ability to ultrasonically quantify ocular, liver, prostate, renal and cardiac tissues (Miller et al. 1983; Lizzi et al. 1983; Insana et al. 1991).

Feleppa et al. (1986) found that the ESD in ocular tumors was a strong indicator of malignancy. Larger scatterer sizes were observed in malignant tumors when compared with surrounding normal tissues. EAC was also integral to diagnostically distinguishing between ambiguous cases (Lizzi et al. 1987). Feleppa et al. (1996) and Balaji et al. (2002) also demonstrated that QUS parameters provided greater diagnostic accuracy in prostate-cancer detection and lesion localization than all other noninvasive techniques combined.

QUS scattering studies in renal tissues found that changes in the scattering strength (EAC) were responsible for the anisotropy of backscatter and not changes in ESD (Insana et al. 1991) and was, thus, an important parameter for characterizing the anisotropy of backscatter in tissues. The glomeruli ($\approx 200\ \mu$m) and afferent and efferent arterioles ($\approx 50\ \mu$m) were identified as the principal structures responsible for scattering. ESD and sound speed were the most stable QUS parameters for characterizing the tissues. These early studies were the basis of investigations into the ability of QUS images using the scatterer properties to detect changes in renal microanatomy (Insana et al. 1992, 1993, 1995; Garra et al. 1994; Hall et al. 1996). QUS imaging techniques were demonstrated to be capable of differentiating among conditions that caused increased cortical echogenicity and structural changes like glomerular hypertrophy, and QUS measurements agreed well with measurements of those structures in biopsy samples.

For almost 30 years, Coleman and colleagues (Coleman and Lizzi 1983; Coleman et al. 1987, 1990, 1991, 2004; Silverman et al 2001, 2003) strived to develop QUS techniques to diagnose/classify primary malignant melanoma of the choriod and ciliary body to preserve vision without increasing the risk to the patient's life. Earlier, they showed that backscatter properties were correlated with survival in patients with uveal malignant melanoma (Coleman et al 1990, 1991). More recently (Coleman et al. 2004), they successfully demonstrated that QUS parameters of extravascular matrix patterns (EMP) correlated with histologic EMP patterns to discriminate between lethal and less lethal tumors.

Also, for almost 30 years, cardiac studies investigating the cyclic variation in integrated backscatter (Miller et al. 1983; Tamirisa et al. 2001) have demonstrated that this was a useful measure of cardiac function and viability. This work successfully identified the extracellular matrix (Hall et al. 2000) and myocytes (Landini and Santarelli 1995; Recchia et al. 1995) to be the dominant sources of scattering in the heart.

In addition, QUS frequency-dependent backscatter from tissues has been used to enhance B-mode images (Feleppa et al. 1997; Lizzi et al. 1997; Golub et al. 1993; Zagzebski et al. 1993; Topp et al. 2001). Different tissue regions with different scattering properties had their respective, possibly unique, slope and intercept parameters extracted from the scattered power spectrum. Enhanced images were formed by colored pixels in an image corresponding to the local slope and intercept parameters of the power spectrum (Feleppa et al. 1997; Lizzi et al. 1997). The goal of these studies was to use the enhanced QUS images to differentiate between diseased and healthy tissues.

Estimating the number of scatterers per unit volume has also been investigated using a variety of approaches. Wear et al. (1997), Dumane and Shankar (2001) and Shankar (2000) have shown that when the number density of scatterers was small (< 2/ resolution cell), the number of scatterers could be estimated using backscattered envelope statistics. Using fractional order moments of the backscattered envelope (Dutt and Greenleaf 1995), number density could be estimated for scatterer number densities up to 10/resolution cell. The estimates of scatterer number density and EAC could then be used to extract the relative impedance difference between the scatterers and background.

Another example of successful QUS is the work of Donohue and colleagues (Gefen et al. 2003; Varghese and Donohue 1993; Huang et al. 2000) using the generalized spectrum to classify breast tumors. Their results demonstrated that computer-generated features of the RF echo data operated with a true-positive fraction of 100 % and a false-positive fraction of 32 % suggesting the potential for avoiding biopsy of benign breast lesions.

Numerous investigators have pursued QUS breast-imaging techniques with promising results. D'Astous and Foster (1986) found that the attenuation coefficient and its frequency dependence were different for infiltrating ductal cancer (IDC), parenchyma, and fat (3–8 MHz) and those differences increased (due to higher frequency dependence of scattering in IDC) with increasing frequency. They also found that the backscatter coefficient (BSC) for fat and IDC was about the same but was beginning to separate near the upper frequency limit. The BSC for parenchyma was about an order of magnitude above those of fat and IDC, and also exhibited higher frequency dependence. They also found that a two-parameter analysis (attenuation and BSC) was sufficient to separate the three distinct tissue types they studied.

Landini et al. (1987) measured relative backscatter and found similar results to those reported by D'Astous and Foster. A significant difference was that Landini et al. separated fatty tissues into subcategories of fatty and fibro-fatty and found that the backscatter for fatty tissue was between that of scirrhosis carcinoma and medullary carcinoma (4–14 MHz). More significantly, they estimated the correlation functions for five breast-tissue types (the four above plus fibrosis) and found distinct correlation functions (analogous to the ESDs) for each tissue type.

Mortensen et al. (1996) used a feature set consisting of sound speed, attenuation and backscatter parameters to classify in vitro breast-tissue samples as either normal, benign, or malignant with a variety of classifiers. Their best performance,

obtained using an artificial neural network, achieved a diagnostic accuracy of about 93 % even though their data acquisition system did not provide image guidance for ROI selection and operated at relatively low frequencies (3–8 MHz). Their diagnostic accuracy far exceeded the 0.729 found by Stavros et al. (1995) for standard clinical sonography.

Insana et al. (1995) used QUS techniques to follow renal vascular changes in anesthetized dogs during local intra-arterial infusion of a potent vasoconstrictor, endothelin-1 (ET-l). The authors analyzed the backscatter spectra in the frequency range of 5–15 MHz to estimate scatterer size. They observed changes in scatterer size with changes in renal hemodynamics, and increase in attenuation with increasing ET-1 concentration. The authors verified the changes in hemodynamics using Doppler techniques. Insana used a transverse isotropic correlation function to predict backscattering from kidney microstructure (Insana 1995). The author suggested that by analyzing different frequency regimes of the backscatter, structure of different sizes, number densities and scattering strength could be characterized.

Mamou and co-workers used high-frequency ultrasound to estimate different QUS parameters for detecting cancer in excised lymph nodes (Mamou et al. 2011). The authors estimated ESD, EAC, intercept and slope by analyzing the backscatter coefficient from lymph nodes. They used Nakagami and homodyned-K distributions to estimate another four parameters by analyzing the statistics of the envelope of the backscatter signal. The authors obtained a specificity and sensitivity of 95 % by combining ESD and envelope parameters to detect small metastatic foci in dissected lymph nodes.

Recently, cell pellets made of Chinese hamster ovary (CHO) cells were used to understand ultrasound wave propagation in biological media (Teisseire et al. 2010). An analytical scattering model was used to predict the sound speed in nucleus and cytoplasm as 1,802 m/s and 1,952 m/s, respectively, at a low number density of 1.3×10^6 cells/mL. They used a concentric sphere scattering model to predict the scattering in nucleus and cytoplasm. In a subsequent study, Han et al. (2011) estimated the attenuation in CHO cell pellets at low concentration as $0.021f^{1.6}$ dB/cm using a power law fit in the frequency range of 20–100 MHz. The authors observed different attenuation slopes as the concentration of cells increased in the cell pellets. With better attenuation compensation and improved data-processing strategies and scattering models from those used by Teisseire et al. (2010), Han et al. (2011) estimated the sound speed in nucleus and cytoplasm around 1,600 m/s and 1,550 m/s, respectively, at the lower number densities in CHO cell pellets.

QUS techniques relying on normalized backscattered power spectra have been used to assess apoptosis and necrosis of tumors undergoing both thermal therapy and chemotherapy (Czarnota et al. 1999; Kolios et al. 2002; Banihashemi et al. 2008; Vlad et al. 2009). Czarnota and coworkers used high-frequency (40 MHz) ultrasound to quantify the changes in the backscatter amplitude from cells in vitro undergoing apoptosis due to anticancer agents, apoptosis in tissues ex vivo and

apoptosis in tumors in live animals (Czarnota et al. 1999). They observed large changes in backscatter amplitude from regions of cell death compared to surrounding viable tissues. Kolios et al. (2002) estimated spectral slope and midband fit parameters from backscattered power spectra to monitor apoptosis in in vitro and in vivo experiments due to chemotherapy. The authors observed increases in spectral slope and midband fit with respect to time after drug exposure. Banihashemi et al. (2008) also observed increases in backscattered power with respect to time after application of photodynamic therapy. The authors correlated the QUS parameters to apoptosis and histologic variations in cell nuclear size and observed changes in spectral slope with respect to changes in nuclear size. Similarly, Vlad et al. (2009) observed changes in backscatter spectral parameters due to changes in cellular microstructure with application of radiotherapy. These results clearly suggest that QUS imaging can be used to monitor therapy response.

All of the above work aimed at quantifying backscattered signals through system-independent techniques to quantify the backcattered power. Other investigators have implemented different approaches to QUS that do not provide system-independent results. For example, Garra et al. (1993) digitized the video output of an ultrasound scanner and analyzed the statistics of the B-mode image texture. Although their patient population was small, they only used 5 and 7.5 MHz transducers, and had comparatively poor-quality data, they were able to correctly identify 78 % of the fibroadenomas, 73 % of the cysts, and 91 % of the fibrocystic nodules while maintaining 100 % sensitivity for cancer. Using similar data acquisition, image texture parameters and an artificial neural network, Chen et al. (1999) obtained a diagnostic accuracy of 95 % and with the sensitivity set at 98 %, they achieved a specificity of 93 %, positive predictive value of 89 % and negative predictive value of 99 %. Although very encouraging, these results are nonetheless system dependent. Nevertheless, their success demonstrates that measures of texture statistics (including co-occurrence matrix, run length, etc.) have merit for differentiating among breast diseases

The obvious step to translate QUS imaging to the clinics is to test the feasibility of estimated parameters to be reproducible across different transducers and systems. Several studies have been conducted to compare QUS parameters by different systems and users from the same sample. Ten laboratories participated in an interlaboratory study to estimate backscatter coefficients from tissue–mimicking phantoms using individual laboratory's systems, operators and techniques (Madsen et al. 1999). The study found considerable differences in backscatter coefficient estimates between laboratories, which may be related to the accuracy of the techniques used by each group. A better agreement was observed in a subsequent interlaboratory study to compare backscatter coefficients from tissue–mimicking phantoms (Wear et al. 2005). In this study, the estimated backscatter coefficients were compared with theoretical values. Another interlaboratory study of backscatter coefficients from tissue–mimicking phantoms, where glass beads were used as scatterers, was conducted between two laboratories (Anderson et al. 2010). The main aim was to investigate the interlaboratory comparison of Faran's theoretical model (Faran 1951) to predict backscatter coefficients in the frequency range 1–12 MHz from

glass spheres embedded in a uniform agar-based background. The results of the study demonstrated good agreement between the two laboratories and the theoretical model except for one of the tissue–mimicking phantoms (Anderson et al. 2010). Further interlaboratory comparison of backscatter coefficients from tissue-mimicking phantoms with glass beads as scatterers were conducted using four different clinical array-based imaging systems (Nam et al. 2012a, b). Another interlaboratory study was conducted to develop tissue-mimicking phantoms with weak scatterers and compare theoretical prediction of backscatter coefficient with experimental results in the frequency range of 1–13 MHz (King et al. 2010). The study concluded with good agreement between the two laboratory experimental results and theoretical predictions of backscatter coefficients. The scattering properties of these weakly scattering phantoms represent biological tissue better than glass bead phantoms (King et al. 2010). Good agreement was found between the laboratories and theoretical predictions demonstrating that these QUS parameters based on the backscatter coefficients from different scattering media are reproducible and can be system and operator independent.

Interlaboratory studies to estimate the backscatter coefficient from in vivo spontaneous rat mammary tumors (fibroadenoma and carcinoma) acquired by different research groups using three clinical array systems and a single-element laboratory scanner system were conducted (Wirtzfeld et al. 2010). The results were encouraging from this first in vivo study to compare QUS parameter estimates by different laboratories and systems scanning the same tumor in vivo. Better agreement in backscatter coefficients was observed from in vivo spontaneous rat mammary tumors in the second joint study by the same group of laboratories (Wirtzfeld et al. 2013). In this study the researchers used functional ANOVA to compare the frequency dependence of the backscatter coefficients across different systems (Wirtzfeld et al. 2013).

The successes, outlined above, in applying QUS techniques to improve diagnosis have not yet led to broad application. Part of the reason is that the techniques were either too computationally intensive for existing hardware, or not extensive enough to be robust for everyday clinical use. Furthermore, correcting effects of attenuation have been problematic to date. However, recent progress has been made in developing algorithms to accurately predict the attenuation in tissues. Therefore, the main roadblocks to clinical implementation have been largely overcome in recent years. The success to date places QUS techniques on the cusp of broad clinical applicability.

2.4 Conclusion

The QUS technology and successes outlined in this chapter will form a new imaging capability that will be used as an optional mode to augment standard B-mode imaging, analogous to the use of ultrasound-based flow estimation. The successes outlined in this chapter demonstrate that the QUS techniques can

provide new sources of contrast for improved image diagnostics. We do not expect that QUS will solve all of the limitations of current imaging modalities. However, the new information provided through QUS will likely improve performance of diagnostic ultrasound. We anticipate that QUS information will be part of a multimode analysis that augments B-mode imaging, (e.g., spectral Doppler, color-flow imaging, elasticity imaging, etc.). Just as modalities such as MRI can acquire image information based on different tissue properties, we believe that ultrasound machines will provide useful diagnostic information when QUS parameters are displayed to augment the time-honored B-mode image. Transducer technology, beamforming flexibility, and information-processing capacity are now emerging that will enable the development of this new generation of machines. The history of successes for QUS to detect, quantify and diagnose a host of different diseases and tissue conditions suggests that QUS techniques have an important role to fill in ultrasound medical diagnostics. Interlaboratory studies have demonstrated that these techniques can be system and user independent. Therefore, future clinical machines will likely include different QUS imaging modes.

Acknowledgments The work was supported by NIH Grant R01EB008992, R01CA111289 and R21CA139095 (National Institutes of Health, Bethesda, MD).

References

Anderson JJ, Herd MT, King MR, Haak A, Hafez ZT, Song J, Oelze ML, Madsen EL, Zagzebski JA, O'Brien WD Jr, Hall TJ (2010) Interlaboratory comparison of backscatter coefficient estimates for tissue-mimicking phantoms. Ultrason Imaging 32(1):48–64

Balaji KC, Fair WR, Feleppa EJ, Porter CR, Tsai H, Liu T, Kalisz A, Urban S, Gillespie J (2002) Role of advanced 2 and 3-dimensional ultrasound for detecting prostate cancer. J Urol 168(6):2422–2425

Bamber JC, Hill CR (1981) Acoustic properties of normal and cancerous human liver-I. dependence on pathological condiction. Ultrasound Med Biol 7:121–133

Bamber JC, Hill CR, King JA (1981) Acoustic properties of normal and cancerous human liver - II dependence on tissue structure. Ultrasound Med Biol 7:135–144

Banihashemi B, Vlad R, Debeljevic B, Giles A, Kolios MC, Czarnota GJ (2008) Ultrasound imaging of apoptosis in tumor response: Novel preclinical monitoring of photodynamic therapy effects. Cancer Res 68:8590–8596

Baum G, Greenwood I (1958a) The application of ultrasonic locating techniques to ophthalmology. Arch Ophthalmol 60(2):263–279

Baum G, Greenwood I (1958b) The application of ultrasonic locating techniques to ophthalmology: theoretical considerations and acoustic properties of ocular media. (i) reflective properties. Am J Ophthalmol 46:319–329

Bom N (1973) A multi-element system and its application to cardiology. Excerpta Medica 227(2)

Bom N, Lancée CT, van Zwieten G, Kloster FE, Roelandt J (1973) Multiscan echocardiography. i. technical description. Circulation 48:1066–1074

Carpenter DA, Kossoff G (1977) The u. i. octoscan - a new class of ultrasonic echoscopes. In: White D, Brown RE (eds) Ultrasound in medicine, vol 3B, pp 1785–1786

Carson PL, Meyer CR, Scherzinger AL, Oughton TV (1981) Breast imaging in coronal planes with simultaneous pulse echo and transmission ultrasound. Science 214(4):1141–1143

Carstensen EL, Schwan HP (1959) Absorption of sound arising from the presence of intact cells in blood. J Acoust Soc Am 31(2):185–189

Carstensen EL, Li K, Schwan HP (1953) Determination of the acoustic properties of blood and its components. J Acoust Soc Am 25(2):286–289

Chen DR, Chang RF, Huang YL (1999) Computer-aided diagnosis applied to us of solid breast nodules by using neural networks. Radiology 213(2):407–412

Chen JF (1994) Statistical parameter estimation in ultrasound backscattering from tissue mimicking media. PhD thesis, University of Wisconsin

Chivers RC, Parry RJ (1978) Ultrasonic velocity and attenuation in mammalian tissues. J Acoust Soc Am 63(3):940–953

Coleman DJ, Lizzi FL (1983) Computerized ultrasonic tissue characterization of ocular tumors. Am J Ophthalmol 96(2):165–175

Coleman DJ, Rondeau M, Silverman R, Lizzi F (1987) Computerized ultrasonic biometry and imaging of intraocular tumors for monitoring of therapy. Trans Am Opthalmol Soc 85:48–81

Coleman DJ, Silverman RH, Rondeau MJ, Lizzi FL, McLean JW, Jakobiec FA (1990) Correlations of acoustic tissue typing of malignant melanoma and histopathologic features as a predictor of death. Am J Ophthalmol 110(4):380–388

Coleman DJ, Silverman RH, Rondeau MJ, Coleman JA, Rosberger D, Ellsworth RM, Lizzi FL (1991) Ultrasonic tissue characterization of uveal melanoma and prediction of patient survival after enucleation and brachytherapy. Am J Ophthalmol 112(6):682–688

Coleman DJ, Silverman RH, Rondeau MJ, Boldt HC, Lloyd HO, Lizzi FL, Weingeist TA, Chen X, Vangveeravong S, Folberg R (2004) Noninvasive in vivo detection of prognostic indicators for high-risk uveal melanoma: Ultrasound parameter imaging. Ophthalmology 111(3):558–564

Czarnota GJ, Kolios MC, Abraham J, Portnoy M, Ottensmeyer FP, Hunt JW, Sherar MD (1999) Ultrasonic imaging of apoptosis: high-resolution non-invasive imaging of programmed cell death in vitro, in situ and in vivo. British J Cancer 81:520–527

D'Astous FT, Foster FS (1986) Frequency dependence of ultrasound attenuation and backscatter in breast tissue. Ultrasound Med Biol 12(10):795–808

Dines KA, Kak AC (1979) Ultrasonic attenuation tomography of soft tissue. Ultrason Imaging 1:16–33

Donald I (1964) Ultrasonography in two dimensions. Med Biol Illustr 14:216–224

Donald I (1974) Sonar - the story of an experiment. Ultrasound Med Biol 1:109–117

Donald I, Brown TG (1961) Demonstration of tissue interfaces within the body by ultrasonic echo sounding. Brit J Radiol 34:539–545

Dumane VA, Shankar PM (2001) Use of frequency diversity and nakagami statistics in ultrasonic tissue characterization. IEEE Trans Ultrason Ferroelectr Freq Contr 48(4):1139–1146

Dunn F, O'Brien WD Jr (1978) Ultrasonic absorption and dispersion. In: Fry FJ (ed) Ultrasound: Its application in medicince and biology. Elsevier, Amsterdam, pp 393–439

Duric N, Littrup P, Babkin A, Chambers D, Azevedo S, Kalinin A, Pevzner R, Tokarev M, Holsapple E, Rama O, Duncan R (2005) Development of ultrasound tomography for breast imaging: Technical assessment. Med Phys 32(5):1375–1386

Duric N, Littrup P, Holsapple E, Rama O, Glide C (2007) Detection of breast cancer with ultrasound tomography: First results with the computed ultrasound risk evaluation (cure) prototype. Med Phys 34(2):773–785

Dussik KT (1942) Uber die moglichkeit hochfrequente mechanische schwingungen als diagnostisches hilfsmittel zu verwerten (about the possibility of using ultrasound as a diagnostic aid). Z Neurol Psychiat 174:153–168

Dussik KT (1948) Ultraschall diagnostik, in besondere bei gehirnerkrankungen, mittels hyperphongraphie (ultrasound diagnostics, in particular of brain diseases, by using hyperphonography). Z Phys Med 1:140–145

Dussik KT (1949) Zum heutigen stand der medizinischen ultraschallforschung (state of the art of medical ultrasound research). Wien Klin Wochenschr 61:246–248

Dussik KT, Dussik F, Wyt L (1947) Auf dem wege zur hyperphonographie des gehirnes (en route to hyperphonography of the brain). Wien Med Wochenschr 97:425–429
Dutt V, Greenleaf JF (1995) K distribution model of ultrasound speckle: fractional order SNRs and log compression variance. In: Proceeding of the IEEE Ultrasonic Symposium, vol 2, pp 1375–1378
Egelstaff PA, Gray CG, Gubbins KE, Mo KC (1975) Theory of inelastic neutron scattering from molecular fluids. J Stat Phys 13:315–330
Elder I, Gustafson A (1957) Ultrasonic cardiogram in mitral stenosis. Acta Med Scand 154:85–90
Elder I, Hertz CH (1954) The use of the ultrasonic reflectoscope for the continuous recording of the movements of heart walls. Kungl Fysiograf Sällsk Lund Förhandl 24:5
Faran JJ Jr (1951) Sound scattering by solid cylinders and spheres. J Accoust Soc Am 23:405–418
Fei DY, Shung KK (1985) Ultrasonic backscatter from mammalian tissues. J Accoust Soc Am 78:871–876
Feleppa EJ, Lizzi FL, Coleman DJ, Yaremko MM (1986) Diagnostic spectrum analysis in opthalmology: A physical perpestive. Ultrasound Med Biol 12:623–631
Feleppa EJ, Kalisz A, Sokil-Melgar JB, Lizzi FL, Liu T, Rosado AL, Shao MC, Fair WR, Wang Y, Cookson MS, Reuter VE, Heston WDW (1996) Typing of prostate tissue by ultrasonic spectrum analysis. IEEE Trans Ultrason Ferroelectr Freq Contr 43(4):609–619
Feleppa EJ, Liu T, Shao MC, Fleshner N, Reuter V, Fair WR (1997) Ultrasonic spectral-parameter imaging of the prostrate. Int J Imaging Syst Technol 8:11–25
Fields S, Dunn F (1973) Correlation of echographic visualizability of tissue with biological composition and physiological state. J Acoust Soc Am 54:809–812
Filipczynski L, Etienne J, Lypacewicz G (1966) Visualizing the inside of the abdomen by means of ultrasound. Proc Vibr Probl 7:211–220
Firestone FA (1942) Flaw detecting device and measuring instrument. US Patent 2(280):226
Firestone FA (1945) The supersonic reflectoscope for interior inspection. Metal Progress 48:505–512
Firestone FA (1946) The supersonic reflectoscope, an instrument of inspecting the interior of solid parts by means of sound waves. J Acoust Soc Am 17:287–299
Firestone FA, Frederick JR (1946) Refinements in supersonic reflectoscopy. polarized sound. J Acoust Soc Am 18:200–211
French LA, Wild JJ, Neal D (1950) Detection of cerebral tumors by ultrasonic pulses. pilot studies on postmortem material. Cancer 3(4):705–708
Fry WJ, Leichner GH, Okuyama D, Fry FJ, Fry EK (1968) Ultrasonic visualization system employing new scanning and presentation methods. J Acoust Soc Am 44:1324–1338
Gaitini D, Baruch Y, Ghersin E, Veitsman E, Kerner H, Shalem B, Yaniv G, Sarfaty C, Azhari H (2004) Feasibility study of ultrasonic fatty liver biopsy: texture vs. attenuation and backscatter. Ultrasound Med Biol 30:1321–1327
Garra BS, Krasner BH, Horii SC, Ascher S, Mun SK, Zeman RK (1993) Improving the distinction between benign and malignant breast lesions: the value of sonographic texture analysis. Ultrason Imaging 15(4):267–285
Garra BS, Insana MF, Sesterhenn IA, Hall TJ, Wagner RF, Rotellar C, Winchester J, Zeman RK (1994) Quantitative ultrasonic detection of parenchymal structural change in diffuse renal disease. Invest Radiol 29(2):134–140
Gefen S, Tretiak OJ, Piccoli CW, Donohue KD, Petropulu AP, Shankar PM, Dumane VA, Huang LX, Kutay MA, Genis V, Forsberg F, Reid JM, Goldberg BB (2003) Roc analysis of ultrasound tissue characterization classifiers for breast cancer diagnosis. IEEE Trans Medical Imaging 22(2):170–177
Glover GH (1977) Computerized time-of-flightultrasonic tomography for breast examination. Ultrasound Med Biol 3:117–127
Gohr H, Wedekind T (1940) Der ultraschall in der medizin. Wien Klin Wochenschr 19:25–29
Goldman DE, Hueter TF (1956) Tabular data of the velocity and absorption of high-frequency sound in mammalian tissues. J Acoust Soc Am 28:35–37

Golub RM, Parsons RE, Sigel B, Feleppa EJ, Justin J, Zaren HA, Rorke M, Sokilmelgar J, Kimitsuki H (1993) Differentiation of breast-tumors by ultrasonic tissue characterization. J Ultrasound Med 12(10):601–608

Gordon D (1958) Echo-encèphalographie. Rev Neurol 99:652

Goss SA (1978) The role of collagen in the ultrasonic properties of tissues. PhD thesis, University of Illinois at Urbana-Champaign, Urbana, Illinois, USA

Goss SA, Johnston RL, Dunn F (1978) Comprehensive compilation of empirical ultrasonic properties of mammalian tissue. J Acoust Soc Am 64:423–457

Goss SA, Frizzell LA, Dunn F (1980a) Dependence of the ultrasonic properties of biological tissue on constituent proteins. J Acoust Soc Am 67(3):1041–1044

Goss SA, Johnston RL, Dunn F (1980b) Compilation of empirical ultrasonic properties of mammalian tissues ii. J Acoust Soc Am 68:93–108

Greenleaf JF, Bahn RC (1981) Clinical imaging with transmissive ultrasonic computerized tomography. IEEE Trans Biomed Eng 28(2):177–185

Greenleaf JF, Johnson SA, Lee SL, Herman GT, Wood EH (1974) Algebric reconstraution of spatial distribution of acoustic absorption within tissue from their two dimensional acoustic projections. Acoust Holography 5:591–603

Greenleaf JF, Johnson SA, Samayoa WF, Duck FA (1975) Algebric reconstruction of spatial distribution of acoustical velocities in tissue from their time-of-flight profiles. Acoust Holography 6:71–90

Greenleaf JF, Johnson SA, Bahn RC, Samayoa WF, Hansen CR (1976) Images of acoustic refractive index and on attenuation: relationships to tissue types within excised female breast. First World Federation of Ultrasound in Medicine and Biology, San Francisco

Griffith JM, Henry WL (1974) A sector scanner for real time two-dimensional echocardiography. Circulation 49:1147–1152

Guimond A, Teletin M, Garo E, D'Sa A, Selloum M, Champy MF, Vonesch JL, Monassier L (2007) Quantitative ultrasonic tissue characterization as a new tool for continuous monitoring of chronic liver remodeling in mice. Liver Int 27:854–864

Hall CS, Scott MJ, Lanza GM, Miller JG, Wickline SA (2000) The extracellular matrix is an important source of ultrasound backscatter from myocardium. J Acoust Soc Am 107(1):612–619

Hall TJ, Insana MF, Harrison LA, Cox GG (1996) Ultrasonic measurement of glomerular diameters in normal adult humans. Ultrasound Med Biol 22(8):987–997

Hammes GG, Roberts PB (1970) Ultrasonic attenuation measurements in phospholipid dispersion. Biochim Biophys Acta 203:220–227

Han A, Abuhabsah R, Blue JP Jr, Sarwate S, O'Brien WD Jr (2011) Ultrasonic backscatter coefficient quantitative estimates from high-concentration chinese hamster ovary cell pellet biophantoms. J Acoust Soc Am 130(6):4139–4147

Hayashi S, Wagai T, Miyazawa R, Ito K, Ishikawa S, Uomatsu K, Kikuchi Y, Uchida R (1962) Ultrasonic diagnosis of breast tumor and cholelithiasis. Western J Surg Obstet Gynec 70:34–40

Holmes JH, Wright W, Meyer EP, Posakony GJ, Howry DH (1965) Ultrasonic contact scanner for diagnostic application. Am J Med Electron 4(4):147–152

Howry DH (1952) The ultrasonic visualization of soft tissue structures and disease processes. J Lab Clin Med 40:812–813

Howry DH, Bliss WR (1952) Ultrasonic visualization of soft tissue structures of the body. J Lab Clin Med 40:579–592

Huang L, Donohue KD, Genis V, Forsberg F (2000) Duct detection and wall spacing estimation in breast tissue. Ultrason Imag 22(3):137–152

Hueter TF (1948) Messung der ultraschallaborption in tierischen geweben und ihre abhangigkeit von der frequenz (measurement of ultrasonic absorption in animal tissues and its dependence on frequency). Naturwiss 35:285–287, [English translation in Ultrasonic Biophysics, Dunn F, O'Brien W. D. Jr (eds) (1976) Benchmark Papers in Acoustics, vol 7 (Dowden, Hutchinson and Ross, Stroudsburg, PA)].

Hunt FV (1978) Origins of Acoustics. Yale University Press, New Haven
Insana MF (1995) Modeling acoustic backscatter from kidney microstructure using an anisotropic correlation function. J Acoust Soc Am 97:649–655
Insana MF, Brown DG (1993) Acoustic scattering theory applied to soft biological tissues. In: Shung KK, Thieme GA (eds) Ultrasonic Scattering in Biological Tissues. CRC Press, Boca Raton, pp 75–124
Insana MF, Hall TJ (1990) Parametric ultrasound imaging from backscatter coefficient measurements: Image formation and interpretation. Ultrason Imaging 12:245–267
Insana MF, Hall TJ, Fishback JL (1991) Identifying acoustic scattering sources in normal renal parenchyma from the anisotropy in acoustic properties. Ultrasound Med Biol 17(6):613–626
Insana MF, Wood JG, Hall TJ (1992) Identifying acoustic scattering sources in normal renal parenchyma in vivo by varying arterial and ureteral pressures. Ultrasound Med Biol 18:587–599
Insana MF, Hall TJ, Wood JG, Yan ZY (1993) Renal ultrasound using parametric imaging techniques to detect changes in micrstructure and function. Invest Radiol 28:720–725
Insana MF, Wood JG, Hall TJ, Cox GG, Harrison LA (1995) Effects of endothelin-1 on renal microvasculature measured using quantitative ultrasound. Ultrasound Med Biol 21(9):1143–1151
Jeong JW, Kim TS, Shin DC, Do S, Singh M, Marmarelis VZ (2005) Soft tissue differentiation using multiband signatures of high resolution ultrasonic transmission tomography. IEEE Trans Medical Imaging 24(3):399–408
Johnson SA, Abbott T, Bell R, Berggren M, Borup D, Robinson D, Wiskin J, Olsen S, Hanover B (2007) Non-invasive breast tissue characterization using ultrasound speed and attenuation. Acoust imaging 28:147–154
King MR, Anderson JJ, Herd M, Ma D, Haak A, Wirtzfeld LA, Madsen EL, Zagzebski JA, Oelze ML, Hall TJ, O'Brien WD Jr (2010) Ultrasonic backscatter coefficients for weakly scattering, agar spheres in agar phantoms. J Acoust Soc Am 128:903–908
Kolios MC, Czarnota GJ, Lee L, Hunt JW, Sherar MD (2002) Ultrasonic spectral parameter imaging of apoptosis. Ultrasound Med Biol 28:589–597
Kossoff G, Garrett WJ (1972) Ultrasonic film echoscopy for placental localization. Aust N Zeal J Obstet Gynaecol 12(2):117–121
Kossoff G, Fry EK, Jellins J (1973) Average velocity of ultrasound in the human female breast. J Acoust Soc Am 53:1730–1736
Kossoff G, Garrett WJ, Radovanovich G (1974) Grey scale echography in obstetrics and gynecology. Australian Radiol 18(1):63–111
Kremkau FW, Cowgill RW (1984) Biomolecular absorption of ultrasound: I. molecular weight. J Acoust Soc Am 76(5):1330–1335
Kremkau FW, Cowgill RW (1985) Biomolecular absorption of ultrasound: Ii. molecular structure. J Acoust Soc Am 77(3):1217–1221
Kremkau FW, Carstensen EL, Aldridge WG (1973) Macromolecular interaction in the absorption of ultrasound in fixed erthrocytes. J Acoust Soc Am 53(5):1448–1451
Landini L, Santarelli MF (1995) A regression-model of ultrasound reflectivity from normal myocardium. Med Eng Phys 17(2):141–144
Landini L, Sarnelli R, Salvadori M, Squartini F (1987) Orientation and frequency-dependence of backscatter coefficient in normal and pathological breast tissues. Ultrasound Med Biol 13(2):77–83
Leksell L (1955) Echo-encephalography: detection of intracranial complications following head injury. Acta Chir Scand 110:301
Li C, Duric N, Huang L (2008) Breast imaging under transmission ultrasound: Reconstructing tissue parameters of sound speed and attenuation. In: 2008 International Conference on BioMedical Engineering and Informatics, pp 708–712
Lindsey RB (1966) The story of acoustics. J Acoust Soc Am 39:629–644
Lizzi FL, Greenabaum M, Feleppa EJ, Elbaum M, Coleman DJ (1983) Theoretical framework for spectrum analysis in ultrasonic tissue characterization. J Accoust Soc Am 73:1366–1373

Lizzi FL, Ostromogilsky M, Feleppa EJ, Rorke MC, Yaremko MM (1987) Relationship of ultrasonic spectral parameters to features of tissue microstructure. IEEE Trans Ultrason Ferroelectr Freq Contr 34:319–329

Lizzi FL, Astor M, Liu T, Deng C, Coleman DJ, Silverman RH (1997) Ultrasonic spectrum analysis for tissue assays and therapy evaluation. Int J Imaging Syst Technol 8:3–10

Lu ZF, Zagzebski JA, Lee FT (1999) Ultrasound backscatter and attenuation in human liver with diffuse disease. Ultrasound Med Biol 25(7):1047–1054

Ludwig GD (1950) The velocity of sound through tissues and the acoustic impedance of tissues. J Acoust Soc Am 22:862–866

Ludwig GD, Struthers FW (1950) Detecting gallstones with ultrasonic echoes. Electronics 23:172–178

Madsen EL, Dong F, Frank GR, Gara BS, Wear KA, Wilson T, Zagzebski JA, Miller HL, Shung KK, Wang SH, Feleppa EJ, Liu T, O'Brien WD Jr, Topp KA, Sanghvi NT, Zaitsen AV, Hall TJ, Fowlkes JB, Kripfgans OD, Miller JG (1999) Interlaboratory comparison of ultrasonic backscatter, attenuation and speed measurements. J Ultrasound Med 18:615–631

Mamou J, Coron A, Oelze ML, Saegusa-Beecroft E, Hata M, Lee P, Machi J, Yanagihara E, Laugier P, Feleppa EJ (2011) Three-dimensional high-frequency backscatter and envelope quantification of cancerous human lymph nodes. Ultrasound Med Biol 37:345–357

Miller JG, Perez JE, Mottley JG, Madaras EI, Johnston PH, Blodgett ED, Thomas LJ III, Sobel BE (1983) Myocardial tissue characterization: an approach based on quantitative backscatter and attenuation. Ultrason Symp Proc 2:782–793

Mimbs JW, Yuhas DE, Miller JG, Weiss AN, Sobel BE (1977) Detection of myocardial infarction in vitro based on altered attenuation of ultrasound. Cir Res 41:192–198

Miyazaki Y (1974) Light scattering of laser beams by random micro-inhomogeneities in glasses and polymers. Japanese J Appl Phys 13:1238–1248

Mortensen CL, Edmonds PD, Gorfu Y, Hill JR, Jensen JF, Schattner P, Shifrin LA, Valdes AD, Jeffrey SS, Esserman LJ (1996) Ultrasound tissue characterization of breast biopsy specimens: expanded study. Ultrason Imaging 18(3):215–230

Mundt GH, Hughes WF (1956) Ultrasonics in ocular diagnosis. Am J Ophthalmol 41(3):488–498

Nam K, Rosado-Mendex IM, Wirtzfeld LA, Kumar V, Madsen EL, Ghoshal G, Pawlicki AD, Oelze ML, Lavarello RJ, Bigelow TA, Zagzebski JA, O'Brien WD Jr, Hall TJ (2012a) Cross-imaging system comparison of backscatter coefficients estimates from tissue-mimicking material. J Acoust Soc Am 132:1319

Nam K, Rosado-Mendex IM, Wirtzfeld LA, Pawlicki AD, Kumar V, Madsen EL, Ghoshal G, Lavarello RJ, Oelze ML, Bigelow TA, Zagzebski JA, O'Brien WD Jr, Hall TJ (2012b) Ultrasonic attenuation and backscatter coefficient estimates of rodent-tumor mimicking structures: comparison of results among clinical scanners. Ultrason Imaging 33:233–250

Newton I (1687) Philosophiae Naturalis Principia Mathematica. Royal Society London, Cambridge

O'Brien WD Jr (1977a) The relationship between collagen and ultrasonic attenuation and velocity in tissue. In: Proceedings of the ultrasonics international '77, IPC science and technology press Ltd., Guildford, England, pp 194–205

O'Brien WD Jr (1977b) The role of collagen in determining ultrasonic propagation properties in tissue. Acoust Holography 7:37–50

O'Brien WD Jr, Dunn F (1971) Ultrasonic examination of hemoglobin dissociation process in aqueous solutions of guanidine hydrochloride. J Acoust Soc Am 50:1213–1215

O'Brien WD Jr, Dunn F (1972a) Ultrasonic absorption by biomacromolecules. In: Proceedings of the workshop on interaction of ultrasound and biological tissues, pp 15–19

O'Brien WD Jr, Dunn F (1972b) Ultrasonic absorption mechanisms in aqueous solutions of bovine hemoglobin. J Phys Chem 76:528–533

O'Brien WD Jr, Olerud J, Shung KK, Reid JM (1981) Quantitative acoustical assessment of wound maturation with acoustic microscopy. J Acoust Soc Am 69(2):575–579

O'Brien WD Jr, Erdman JW Jr, Hebner TB (1988) Ultrasonic propagation properties (@100 mhz) in excessively fatty rat liver. J Acoust Soc Am 83(3):1159–1166

O'Donnell M, Mimbs JW, Miller JG (1979) The relationship between collagen and ultrasonic attenuation in myocardial tissue. J Acoust Soc Am 65(2):512–517

Oelze ML, O'Brien WD Jr (2004) Differentiation and characterization of rat mammary fibroadenomas and 4T1 mouse carcinomas using quantitative ultrasound imaging. IEEE Trans Med Imaging 23:764–771

Olerud JE, O'Brien WD Jr, Riederer-Henderson MA, Steiger D, Forster FK, Daly C, Ketterer DJ, Odland GF (1987) Ultrasonic assessment of skin and wounds with the scanning laser acoustic microscope. J Invest Dermatol 88:615–623

Pauly H, Schwan HP (1971) Mechanism of absorption of ultrasound in liver tissue. J Acoust Soc Am 50(2):692–699

Pinkerton JMM (1949) The absorption of ultrasonic waves in liquids and its relation to molecular constitutions. Proc Phys Soc B 62:129–141

Pohlhammer JD, O'Brien WD Jr (1980) The relationship between ultrasonic attenuation and speed in tissues and constituents: Water, collagen, protein and fat. In: Fullerton G, Zagzebski JA (eds) Medical physics of CT and ultrasound: tissue imaging and characterization. Medical Physics, New York, pp 409–435

Pohlman R (1939) Uber die absorption des ultraschalls im menschlichen geweben und ihre abhangigkeit von der frequenz (on the absorption of ultrasound in human tissues and their dependence upon frequency). Physik 40:159–161

von Ramm OT, Thurston FL (1972) Improved resolution in ultrasound tomography. In: Proc. 25th Annual Conf. Engr. Med. Biol., p 141

Rayleigh L (1945) Theory of sound. Dover Publications, New York

Recchia D, Hall CS, Shepard RK, Miller JG, Wickline SA (1995) Mechanisms of the view-dependence of ultrasonic backscatter from normal myocardium. IEEE Trans Ultrason Ferroelectr Freq Contr 42(1):91–98

Reid JM, Wild JJ (1957) Current developments in ultrasonic equipment for medical diagnosis. IRE Trans Ultrason Eng PGUE 5:44–58

Saijo Y, Tanaka M, Okawai H, Sasaki H, Nitta SI, Dunn F (1997) Ultrasonic tissue characterization of infarcted myocardium by scanning acoustic microscopy. Ultrasound Med Biol 23(1):77–85

Schwan HP (1959) Absorption of ultrasound by tissues and biological matter. Proc IRE 47(11):1959–1962

Shankar PM (2000) A general statistical model for ultrasonic backscattering from tissues. IEEE Trans Ultrason Ferroelectr Freq Contr 47(3):727–736

Silverman RH, amd BG, Ursea FLL, Rondeau MJ, Eldeen NB, Kaliscz A, Lloyd HO, Coleman DJ (2001) High-resolution ultrasonic imaging and characterization of the ciliary body. Invest Ophthalmol Visual Sci 42(5):885–894

Silverman RH, Folberg R, Rondeau MJ, Boldt HC, Lloyd HO, Chen X, Lizzi FL, Weingeist TA, Coleman DJ (2003) Spectral parameter imaging for detection of prognostically significant histologic features in uveal melanoma. Ultrasound Med Biol 29(7):951–959

Smith A, Schwan HP (1971) Acoustic properties of cell nuclei. J Acoust Soc Am 49:1329–1330

Somer JC (1968) Electronic sector scanning for ultrasonic diagnosis. Ultrasonics 6(3):153–159

Stavros AT, Thickman D, Rapp CL, Dennis MA, Parker SH, Sisney GA (1995) Solid breast nodules: use of sonography to distinguish between benign and malignant lesions. Radiology 196(1):123–134

Suzuki K, Hayashi N, Sasaki Y, Kono M, Kasahara A, Fusamoto H, Imai Y, Kamada T (1992) Dependence of ultrasonic attenuation of liver on pathologic fat and fibrosis: Examination with experimental fatty liver and liver fibrosis models. Ultrasound Med Biol 18(8):657–666

Tamirisa PK, Holland MR, Miller JG, Perez JE (2001) Ultrasonic tissue characterization: Review of an approach to assess hypertrophic myocardium. Echocardiogr J Cardiovas Ultrasound Allied Tech 18(7):593–597

Tanaka K, Kikuchi S, Ito K, Ishii M, Katsumi S, Wagai T, Kikuchi Y, Uehida R (1960) Ultrasonic diagnosis of intracranial disease. J Jpn Surg Soc 61:761

Teisseire M, Han A, Abuhabsah R, Blue JP Jr, Sarwate S, O'Brien WD Jr (2010) Ultrasonic backscatter coefficient quantitative estimates from chinese hamster ovary cell pellet biophantoms. J Acoust Soc Am 128(5):3175–3180

Thurston FL, von Ramm OT (1974) A new ultrasound imaging echnique employing two-dimensional electronic beam steering. Acoust Holography 5:249

Topp KA, Zachary JF, O'Brien WD Jr (2001) Quantifying b-mode images of in vivo rat mammary tumors by the frequency dependence of backscatter. J Ultrasound Med 20:605–612

Varghese T, Donohue KD (1993) Characterization of tissue microstructure scatterer distribution with spectral correlation. Ultrason Imag 15(3):238–254

Vlad RM, Brand S, Giles A, Kolios MC, Czarnota GJ (2009) Quantitative ultrasound characterization of responses to radiotherapy in cancer mouse models. Clin Cancer Res 15:2067–2075

Waag RC, Nilsson JO, Astheimer JP (1983) Characterization of volume scattering power spectra in isotropic media from power spectra of scattering by planes. J Acoust Soc Am 74(5):1555–1571

Wear KA, Gara BS, Hall TJ (1995) Measurements of ultrasonic backscatter coefficients in human liver and kidney in vivo. J Acoust Soc Am 98:1852–1857

Wear KA, Wagner RF, Brown DG, Insana MF (1997) Statistical properties of estimates of signal-to-noise ratio and number of scatterers per resolution cell. J Acoust Soc Am 102(1):635–641

Wear KA, Stiles TA, Frank GR, Madsen EL, Cheng F, Feleppa EJ, Hall CS, Kim BS, Lee P, Oelze ML, Raju BI, Shung KK, Wilson TA, Yuan JR (2005) Interlaboratory comparison of ultrasonic backscatter coefficint measurements from 2 to 9 MHz. J Ultrasound Med 24:1235–1250

Wells PNT (1966) Developments in medical ultrasonics. World Med Electron 4:272

Wells PNT (1975) Absorption and dispersion of ultrasound in biological tissue. Ultrasound Med Biol 1:369–376

Wild JJ (1950) The use of ultrasonic pulses for the measurement of biological tissues and the detection of tissue density changes. Surgery 27:183–188

Wild JJ, Neal D (1951) Use of high frequency ultrasonic waves for detecting changes in texture in living tissue. Lancet 1:655–657

Wild JJ, Reid JM (1952a) Application of echo-ranging techniques to the determination of structure of biological tissues. Science 115:226–230

Wild JJ, Reid JM (1952b) Further pilot echographic studies on the histologic structure of tumors of the living intact human breast. Am J Path 28(5):839–861

Wild JJ, French LA, Neal D (1950) Detection of cerebral tumours by ultrasonic pulses: pilot studies on postmortem material. Cancer 3(4):705–708

Wilson DK, Brasseur JG, Gilbert KE (1999) Acoustic scattering and the spectrum of atmospheric turbulence. J Acoust Soc Am 105:30–34

Wirtzfeld LA, Ghoshal G, Hafez ZT, Nam K, Labyed Y, Anderson JA, Herd M, Haak A, He Z, Miller RJ, Sarwate S, Zagzebski JA, Bigelow TA, Oelze ML, Hall TJ, O'Brien WD Jr (2010) Cross-imaging platform comparison of ultrasonic backscatter coefficient measurements of live rat tumors. J Ultrasound Med 29:1117–1123

Wirtzfeld LA, Nam K, Labyed Y, Ghoshal G, Haak A, Sen-Gupta E, He Z, Hirtz NR, Miller RJ, Sarwate S, Simpson DG, Zagzebski JA, Bigelow TA, Oelze ML, Hall TJ, O'Brien WD Jr (2013) Techniques and evaluation from a cross-platform imaging comparison of quantitative ultrasound parameters in an in vivo rodent fibroadenoma model. IEEE Trans Ultrason Ferroelectr Freq Control (in press)

Yokio H, Ito K (1972) Ultrasonic diagnostic equipment with color display unit for simultaneous tomogram method. Toshiba Rev 14–21

Yuhas DE, Mimbs JW, Miller JG, Weiss AN, Sobel BE (1976) Correlation between changes in the frequency dependence of ultrasonic attenuation and regional cpk depletion associated with myocardial infarction. Reflections p 114.

Zagzebski JA, Lu ZF, Yao LX (1993) Quantitative ultrasound imaging: in vivo results in normal liver. Ultrason Imageing 15(4):335–351

Chapter 3
Statistics of Scatterer Property Estimates

Michael L. Oelze

Abstract Quantitative ultrasound (QUS) techniques are based on providing parameter estimates from ultrasound backscattered signals that can be related to different properties of the tissue. Parameter estimates based on analyzing the spectrum of the ultrasound backscattered signal or the amplitude distribution of the envelope require a certain number of samples to produce meaningful estimates in terms of bias and variance of estimates. For example, calculation of the periodogram is used to approximate the true backscattered power spectrum of the ultrasound signal. Typically, the larger the samples size the better the periodogram represents the backscattered power spectrum and the better the bias and variance of QUS estimates. Analysis of the statistics of parameter estimation for spectral-based parameters and envelope statistics will allow the tradeoff between sample size and estimate bias and variance to be quantified. This chapter discusses the statistics of QUS property estimation, the effects of estimate bias and variance on the resolution of QUS parameter imaging, and techniques to reduce the variance of different QUS property estimates.

Keywords Statistics · Spatial resolution · Estimate bias · Estimate variance

3.1 Introduction

Quantitative ultrasound (QUS) techniques have been employed to provide additional diagnostic information from ultrasound backscattered signals beyond conventional B-mode imaging. QUS techniques include estimation of spectral features of the backscattered ultrasound, estimation of the ultrasonic attenuation

M. L. Oelze (✉)
Beckman Institute, Department of Electrical and Computer Engineering, University of Illinois at Urbana-Champaign, 405 N. Mathews, Urbana, IL 61801, USA
e-mail: oelze@illinois.edu

J. Mamou and M. L. Oelze (eds.), *Quantitative Ultrasound in Soft Tissues*, DOI: 10.1007/978-94-007-6952-6_3,

and sound speed, parameterizing the statistics of the envelope of backscattered ultrasound, ultrasound elastography, ultrasound microscopy, and ultrasound computed tomography. Quantitative parameters derived from the ultrasonic signals can provide new sources of image contrast, can improve the sensitivity of ultrasound to detect disease and monitor therapy, can improve the specificity of ultrasound, and can be correlated to underlying tissue microstructure.

While a variety of parameter estimates can be obtained using different QUS techniques, their usefulness ultimately depends upon the statistical properties of the estimates (Lizzi 1997a). Good accuracy and precision of the estimator are vital to classifying a tissue based on a set of estimated features or parameters. For example, assume that two parameters A and B are proposed to classify a tissue as either diseased or normal. If a group of subjects with known diagnoses are examined using the technique, a feature analysis plot can be constructed to demonstrate the ability of the parameters to uniquely classify the tissue. Figure 3.1 shows three feature plots of parameter A versus parameter B for a fictional sample set. In Fig. 3.1a, the two groups (tissue 1 and tissue 2) have different mean values but large overlap between estimates because of the large variance of the estimates. Therefore, the two parameters would not make a good classifier based on the degree of overlap and the large variance of the estimates (low precision). In Fig. 3.1b, the variance of the estimates for both tissue 1 and tissue 2 are greatly reduced due to a better estimator; the mean values of the parameters are different for the two tissue types (but approximately the same as in Fig. 3.1a). Therefore, the two parameters would result in a better classifier because the degree of overlap is minimal between the two groups of tissues. In the final scenario, Fig. 3.1c, the variances of the estimates are still small (same as in Fig. 3.1b), but the mean values of the parameters for both groups of tissues are close to each other. Therefore, while the spread of the estimates is low, the amount of overlap in parameters between the different tissues is high leading to a poor classifier.

The ability to uniquely classify tissues from QUS parameters depends on the variance and mean values of the estimated parameters. The mean value of the estimates depends on the tissue properties but also on the model being used to deduce estimates, the number of samples of data used to provide an estimate, the

Fig. 3.1 **a** Feature analysis plot with estimates of high variance and large differences in mean values, **b** feature analysis plot with low variance of estimates and large differences in mean values and **c** feature analysis plot of estimates with low variance but low separation in the mean values

signal-to-noise ratio (SNR) and the estimator. Biases in estimates can occur if the model used to provide the estimates is incorrect, if the estimator is flawed or too little data exists. The variance of estimates can depend on the biological variability of different subjects, on faulty modeling of signals, on a low number of samples in the data, and on SNR. Even if the optimal estimator is utilized for a specific set of parameters, if the biological contrast is too low and the biological variability is too high, the ability to classify a tissue based on the set of parameters will be poor.

The biological variability and biological contrast are inherent properties of the entity being imaged and, therefore, reducing biological variability and improving the biological contrast may not be possible. However, the variance and bias of parameter estimates also depend on factors related to the measurement and estimation process. Different techniques can be utilized to improve the bias and variance of estimates and thereby improve the ability of parameters to classify tissues. In addition, fundamental tradeoffs exist between the spatial resolution of parameter maps and the bias and variance of estimates. In this chapter, a framework for describing the statistical properties of QUS estimates (spectral-based parameters and envelope statistics) will be provided based on several studies available in the literature and techniques to improve the statistical attributes of these estimates will be examined.

3.2 Description of Statistics of Spectral-Based QUS Parameters

3.2.1 Spectral-Based Estimation Techniques

Several foundational studies have been published in assessing the statistical attributes of different spectral-based estimates in ultrasonic tissue classification (Huisman 1996; Chaturvedi 1996; Lizzi 1997a, b; Oelze 2002, 2004a, b; Gerig 2003; Lizzi 2006). In general, spectral-based imaging requires the estimation of the power spectrum of the backscattered signal. Because an infinite number of signal samples cannot be obtained, the power spectrum is estimated through the periodogram. If the ultrasound backscattered signal is represented by $r(t)$ with a finite number of samples, then the periodogram is given by

$$|R(f)|^2 = |\mathrm{FT}\{r(t)\}|^2 \tag{3.1}$$

where FT represents the Fourier transform of a finite sampled time signal and f represents the frequency. Assuming a stationary signal, as the number of samples increases the better the periodogram represents the true power spectrum of the signal.

The estimate of the power spectrum can be modeled as a function of system-dependent features and sample-dependent features,

$$r(t) = h(t) * d(t,z) * s(t,z) * a(t,z) \tag{3.2}$$

where $h(t)$ is the pulse-echo impulse response of the transducer, $d(t,z)$ represents the spatially-dependent diffraction pattern of the transducer, $s(t,z)$ is the spatially-dependent scattering function of the tissue sample, $a(t,z)$ is spatially-dependent attenuation function that encompasses losses in the tissue medium, z represents the distance from the transducer and * represents the convolution. In the power spectral domain the signal is represented by

$$|R(f)|^2 = |H(f)|^2|D(f,z)|^2|S(f,z)|^2|A(f,z)|^2. \tag{3.3}$$

To acquire tissue-dependent parameters, the system-dependent parameters must be taken into account through a calibration spectrum and calculation of the normalized power spectrum. To account for the volume scattering effects, the backscatter coefficient (BSC) can be calculated from the normalized spectrum. The BSC is the basis for many spectral-based QUS parameters and is a unique characteristic of the tissue itself. The BSC is defined as

$$\sigma_{bsc}(f) = \frac{R_1^2}{V}\frac{\langle I_{sc}(f)\rangle}{I_{inc}(f)} \propto W(f) \tag{3.4}$$

where R_1 is the distance to the scattering volume of interest, V is the scattering volume defined by the beam width and range gate length, $I_{sc}(f)$ and $I_{inc}(f)$ are the scattered and incident intensity fields, respectively, and $W(f)$ is the normalized power spectrum. Therefore, the BSC is both operator and system independent. In regions where the scattering is uniform, the BSC can be parameterized to yield estimates of the scatterer properties, which can then provide a geometrical interpretation of the underlying tissue microstructure.

3.2.2 Statistics of the BSC and Attenuation Estimation

Several authors have examined the statistical properties of estimating attenuation and the backscatter coefficient from ultrasound backscattered signals (Yao 1991; Huisman 1996). From Eq. (3.3), Huisman and Thijssen defined the attenuation function as

$$A(f,z) = 10^{-0.05a(f)z} \tag{3.5}$$

where $a(f)$ is the attenuation coefficient [dB/cm]. By assuming that the attenuation coefficient could be approximated by a linear model, then

$$a(f) = a_0 + a_1(f - f_c), \tag{3.6}$$

where a_0 is the attenuation intercept [dB/cm] at the center frequency f_c, and a_1 is the attenuation slope [dB/cm/MHz]. They also modeled the scattering function of the tissue as

$$|S(f,z)|^2 = 10^{0.05b(f)} \tag{3.7}$$

where $b(f)$ was defined as a backscatter function [dB] and also described by a line as

$$b(f) = b_0 + b_1(f - f_c) \tag{3.8}$$

with b_0 defined as the backscatter intercept [dB] at the center frequency f_c, and b_1 defined as the backscatter slope [dB/MHz].

To examine the statistics of estimating these two functions, a log converted averaged periodogram of the data was first calculated after correcting for the transducer effects and is given by

$$W_L(f) = 20\log\left[\frac{\overline{|R(t)|^2}}{|H(t)|^2|D(t,z)|^2}\right] = 20\log\left[|S(t,z)|^2|A(t,z)|^2\right]$$

$$W_L(f) = 2\hat{a}(f)z + \hat{b}(f) + \varepsilon \tag{3.9}$$

where the $\wedge$ indicates the estimated variable and ε represents zero mean Gaussian noise. The averaged periodogram was estimated by averaging the periodograms estimated from independent adjacent scan lines.

Averaging the periodogram over a longer signal and from several independent samples will provide a better estimate of the true power spectrum related to the sample. In a practical sense, this is accomplished with the ultrasound backscattered data by windowing a segment of the signal and averaging the estimated power spectra from several independent windowed scan lines. Scan lines are considered to provide independent samples when they are at least a beamwidth apart. Assuming that the scan lines are parallel and separated by a beamwidth, then the averaged periodogram comes from a data block. Figure 3.2 shows an image of a data block used for the estimate of the normalized power spectrum. The normalized power spectrum estimate can then be associated with a backscatter function and parameterized. The parameter estimates can be correlated to a

Fig. 3.2 Diagram of a data block used to provide a localized estimate of the BSC

specific sample region corresponding to the data block locations. A map or image of the parameter estimates can then be constructed based on spatially correlating parameter estimates with the data block locations.

If the tissue is modeled as a collection of nearly identical scatterers with random spatial locations, then the echo envelope and amplitude spectrum can be modeled using a Rayleigh probability distribution function (pdf). For a Rayleigh pdf, the standard deviation of the echo amplitude at a frequency f can be represented by (Papoulis 1991)

$$\sigma_f \approx \mu_f / 1.91 \tag{3.10}$$

where μ_f is the mean of the echo amplitude at frequency f. The standard deviation of the echo amplitude at a frequency f can be decreased by averaging amplitude spectra (periodograms). Assuming a large number of periodograms are averaged, then the standard deviation decreases as

$$\sigma_f \approx \mu_f / 1.91 / \sqrt{N} \tag{3.11}$$

where N is the number of independent periodograms used in the average. Relating this back to Eq. (3.9), where the estimate of the power spectrum was log converted, gives

$$\sigma_{W_L(f)} \approx 8.686 \sigma_f / \mu_f = \frac{4.54}{\sqrt{N}}. \tag{3.12}$$

From this estimate of the standard deviation of the log averaged and normalized periodogram, Huisman and Thijssen determined that

$$\sigma_{\hat{a}(f)} \approx \frac{\sqrt{3}\sigma_{W_L(f)}}{\Delta z N^{3/2}} \simeq \frac{7.86}{\Delta z N^2} \tag{3.13}$$

and

$$\sigma_{\hat{b}(f)} \approx \frac{9.08}{N} \sqrt{1 + 3\delta + 3\delta^2 - \frac{3 + 6\delta}{2N}} \tag{3.14}$$

where Δz represents the length of the gated region (assuming a rectangular windowing function) and δ is defined as the relative distance to the range gate [$\delta = z_1/(\Delta z N)$] and z_1 is the distance to the start of the range gate. The analysis assumes that the backscatter function estimate is corrected for attenuation losses based on the attenuation estimate. Therefore, the variance of the backscatter function estimate increases as the depth location of the sampled data increases due to dependence of the attenuation estimate on depth, z.

The results of the analysis by Yao et al. (1991) and Huisman and Thijssen (1996) predict several statistical attributes of spectral-based estimation of attenuation and backscatter functions. First, the standard deviation of the attenuation estimate is inversely proportional to the number squared of independent

periodograms used in the average and the length of the range gate used in the estimate. Therefore, there exists a tradeoff between the number of independent samples acquired from the data and the precision of the estimate. If parametric image maps are constructed from data blocks, then the spatial resolution of the parametric images depends on the size of the data blocks. From the Huisman and Thijssen analysis, the variance of the attenuation estimate can be reduced by increasing the range gate length and the number of independent periodograms in the average. However, a much larger reduction in variance is obtained by using a larger number of independent periodograms in the average than by increasing the length of the windowed segment. Second, the analysis predicts that the variance of an estimate of the BSC will decrease in proportion to the number of independent periodograms that are averaged. To a lesser degree, increasing the range gate length can also reduce the variance of an estimate of the BSC.

3.2.3 Statistics of Parameter Estimation

Once a BSC has been calculated and corrected for attenuation effects, the BSC as a function of frequency can be parameterized. To parameterize the BSC, models of scattering from the underlying tissue must be adopted. In the simplest case, the BSC or normalized power spectrum can be parameterized as a straight line and estimates of the spectral slope (SS), spectral intercept (SI), and midband fit (MBF) can be obtained (Lizzi 1997a, b). Only two of these parameters combined yield independent information. In more complex models, the scatterers can be modeled as spheres, cylinders or other more complex structures (Insana 1995). From more complex models, estimates of the effective scatterer diameter (ESD) and effective acoustic concentration (EAC) have been adopted (Lizzi 1987; Insana 1990a, b; Oelze 2002).

In the analysis of the statistics of spectral-based parameters (SS, SI, and MBF), Lizzi et al. (1997a, b) first examined the statistics of the power spectrum estimation, using a similar approach to Yao et al. (1991) and Huisman and Thijssen (1996), to produce estimates of the variance of the spectral-based parameters. Because the spectral-based estimates were calculated by using a standard, linear-regression technique, standard procedures could be used to calculate the variances (standard deviations) of the different parameters. The standard deviations of the MBF and SS were derived and given by

$$\sigma_{MBF} = \frac{\sigma_{dB}(N)}{\sqrt{M}} \tag{3.15}$$

and

$$\sigma_{SS} = \sqrt{\frac{12}{M(M^2-1)}}\frac{\sigma_{dB}(N)}{\Delta f} \tag{3.16}$$

where Δf is the correlation bandwidth and is approximately equal to the inverse of the gate length $\left(\approx {}^{1}/_{L}\right)$, M is equal to the number of independent frequency samples in the analysis bandwidth $\left(\approx {}^{B}/_{\Delta f}\right)$, B is the analysis bandwidth, N represents the number of independent spectra averaged from N independent scan lines, and $\sigma_{dB}(N)$ is the standard deviation of the averaged power spectrum estimate in a dB scale and given by Lizzi et al. (1997a) as,

$$\sigma_{dB}(N) \approx \frac{4.34}{\sqrt{N}}. \tag{3.17}$$

From the estimates of the standard deviations for the MBF and SS, the standard deviation of the SI was also calculated,

$$\sigma_{SI} = \left[\sigma_{MBF}^2 + f_c^2 \sigma_{SS}^2\right]^{1/2} \tag{3.18}$$

where f_c is the center frequency of the analysis bandwidth.

From these results it could be concluded that statistical traits observed for the parameter estimates were similar to statistical traits for estimates of the BSC. Increasing the number of independent scan lines in the periodogram average resulted in improved standard deviation of estimates. From the analysis it was also concluded that for a given bandwidth, a longer window would result in smaller standard deviation of the estimates and a larger analysis bandwidth would result in improved standard deviation.

In a later study, Lizzi et al. (2006) examined the role of the windowing function used to calculate the MBF, SS, and SI parameters. For a window length of L, the spectral resolution of the Hanning window will be much less than the spectral resolution provided by the rectangular window. Provided the biases produced by the window function are small, then the standard deviation of the spectral-based estimates will be smaller for the rectangular function compared to a tapered window function. For example, σ_{MBF} and σ_{SS} are approximately 1.4 times larger for a Hamming window function compared to a rectangular windowing function (Lizzi 2006).

More complex models have also been examined for the ability to classify tissues and the statistical features of these estimates have also been examined (Chaturvedi 1996; Oelze 2002; Gerig 2003). For example, Chaturvedi and Insana (1996) calculated the statistical attributes of estimating the ESD using a spherical Gaussian model. In that work, they compared predicted error from measurements with the method-independent lower bound on estimation error found from the Cramer-Rao inequality.

The ESD was estimated from the backscattered power spectrum by utilizing a form factor model (Insana 1990b). The backscattered power spectrum (corrected for attenuation) is related to the form factor by

$$|R(f)|^2 = Cf^4 |H(f)|^2 F(f, \mathrm{ESD}) \tag{3.19}$$

where C is a frequency-independent constant and $F(f, \mathrm{ESD})$ is the form factor which is a function of the frequency and ESD. The ESD was estimated by minimizing the mean-square difference between the theoretical form factor for the tissue scatterer size and the measured form factor, $\hat{F}$, described by the equation

$$\widehat{\mathrm{ESD}} = \arg\min_{\mathrm{ESD}} \chi^2 \tag{3.20}$$

where

$$\chi^2 = \sum_{i=1}^{M} \frac{1}{\mathrm{var}\ \hat{F}(f_i)} \left\{ \hat{F}(f_i) - \exp\left(-3.04 f_i^2 \mathrm{ESD}^2\right) \right\} \tag{3.21}$$

and M is the number of points included in the analysis bandwidth. By taking the derivative of Eq. (3.21) with respect to ESD and setting it equal to zero, Eq. (3.20) can be solved,

$$\sum_{i=1}^{M} \frac{f_i^2}{\mathrm{var}\ \hat{F}(f_i)} \exp\left(-3.04 f_i^2 \mathrm{ESD}^2\right) \left\{ \hat{F}(f_i) - \exp\left(-3.04 f_i^2 \mathrm{ESD}^2\right) \right\} = 0. \tag{3.22}$$

The estimate of ESD is the value of ESD that satisfies Eq. (3.22). When the ratio of $ka \sim 1$ (the acoustic wavenumber times the effective scatterer radius), then the form factor is a smooth function of frequency and is sensitive to small changes in scatterer size (Insana 1990a). For this ka regime, Chaturvedi (1996) showed that

$$\mathrm{var}\ \widehat{\mathrm{ESD}} \approx \sum_{i=1}^{M} \left\{ \mathrm{var}\ \hat{F}(f_i) \left(\frac{\partial \mathrm{ESD}}{\partial \hat{F}(f_i)} \right)^2 \right\}. \tag{3.23}$$

To evaluate this variance, an expression for the derivative of the ESD with respect to $\hat{F}$ was derived by differentiating Eq. (3.22) with respect to $\hat{F}(f_i)$. When the gated signal is large, the variance of the ESD can be estimated as

$$\mathrm{var}\ \widehat{\mathrm{ESD}} \approx \frac{C}{\mathrm{ESD}^2} \left\{ \sum_{i=1}^{M} \left[\frac{f_i^4}{q(f_i)} \right] \right\}^{-1} \tag{3.24}$$

with

$$q(f_i) = \left[1 + \left(\frac{\sin(2\pi f_i K \Delta t)}{K \sin(2\pi f_i \Delta t)} \right)^2 \right] \tag{3.25}$$

where Δt is the sampling rate of the time signal and K is the number of points in the time signal. The significance of Eq. (3.24) is that the variance of the estimate is inversely proportional to the size of the ESD (within the range that $ka \sim 1$). Therefore, larger values of ESD will result in smaller variance of the estimate for a given bandwidth and variance will be smaller for larger bandwidth.

Extending the analysis conducted by Chaturvedi and Insana (1996), Oelze et al. (2002) calculated the variance of an ESD estimate for a novel estimator using linear regression of a log reduced power spectrum. Using the best-fit line approach, the variance of the estimator was calculated as

$$\operatorname{var}\widehat{\mathrm{ESD}} \approx \frac{2.09 \times 10^{-2}}{\mathrm{ESD}^2}\left\{\sum_{i=1}^{M}\left[f_i^4 - M\overline{f^2}^2\right]\right\}^{-1}. \tag{3.26}$$

As before, larger ESD resulted in smaller variances and smaller variances were also associated with estimates conducted at high center frequencies and over a larger bandwidth.

This work was further extended to include measurement variances inherent in using a reference phantom method for normalization of the backscattered power spectrum (Yao 1991; Gerig 2003). When using a reference phantom technique to estimate the BSC, the variance in the estimate of the power spectrum from the reference phantom must also be taken into account. In the reference phantom method, the sample BSC is estimated by calculating the power spectrum from a sample and normalizing by the BSC calculated for a reference phantom,

$$\widehat{\mathrm{BSC}}_s(f) = \frac{\overline{S_s(f)}}{\overline{S_r(f)}}\mathrm{BSC}_r(f)e^{4z[\alpha_s(f)-\alpha_r(f)]} \tag{3.27}$$

where $\overline{S(f)}$ represents the power spectrum averaged from independent gated rf signals from a scattering medium, z is the depth of the range-gated segment used for spectral estimation, α represents an attenuation coefficient (Np/m), and the subscripts s and r represent the sample and reference medium, respectively. In general, neglecting windowing functions the variance of a spectrum is given by (Chaturvedi 1996),

$$\operatorname{var}\left[\hat{S}(f)\right] \approx S(f)^2 \tag{3.28}$$

where $S(f)$ is an arbitrary power spectrum. From this result and Eq. (3.27), Gerig et al. (2003) calculated that the estimated variance of a BSC estimate using the reference phantom is given by,

$$\operatorname{var}\left[\widehat{\mathrm{BSC}}_s(f)\right] \approx \left(\frac{N_s + N_r}{N_s N_r}\right)\mathrm{BSC}_s^2(f) \tag{3.29}$$

where N_s and N_r represent the number of sample and reference waveforms used to calculate the spectral averages, respectively. From this result, the variance of the BSC estimate from a sample using the reference phantom technique is reduced when using a large number of waveforms in the average of the reference phantom spectra. Using a similar procedure as in Oelze et al. (2002), the variance of the estimate of the ESD using a reference phantom technique was derived, giving

$$\operatorname{var}\widehat{\mathrm{ESD}} \approx \frac{C}{\mathrm{ESD}^2}\left(\frac{N_s+N_r}{N_sN_r}\right)\sum_{i=f_{\min}}^{f_{\max}}\left[\frac{f_i^2-\overline{f^2}}{\sum_{j=f_{\min}}^{f_{\max}}\left(f_j^2-\overline{f^2}\right)^2}\right]^2 \tag{3.30}$$

where the summation is over the analysis bandwidth. These results provide similar variance estimates as found by Chaturvedi and Insana (1996) and Oelze et al. (2002) in terms of being inversely proportional to the ESD squared and dependent on the bandwidth. However, in the reference phantom technique, increasing the number of spectra used in the average spectra from the reference results in a reduction in variance of the ESD estimate. Therefore, in using a reference phantom technique, it is advantageous to average as many spectra from independent scan segments from the reference phantom as possible to reduce the variance of spectral-based estimates like the ESD. This is not a problem because typically one is not concerned with spatial resolution in a reference phantom, i.e., a data block from the reference phantom can be as large as the dimensions of the phantom to provide a very good estimate of the power spectrum because the phantom ideally has uniform scattering properties throughout. Furthermore, additional scan lines for averaging can be obtained by moving the probe in the elevational direction.

3.2.4 Simulation and Experimental Validation

Simulation studies and studies with physical phantoms have also been conducted to examine the tradeoffs between bias and variance of spectral-based estimates and the size of the data blocks used to produce an estimate. From Fig. 3.2 the data block size is defined axially by a range gate length and laterally by the number of scan lines used in the spectral estimate times the separation between the scan lines. In QUS imaging, each data block corresponds to a pixel in an image and can be color-coded corresponding to a particular estimate value. An example of a QUS image using the ESD is shown in Fig. 3.3. The image depicts a B-mode image of a mouse sarcoma tumor followed by a QUS image superimposed on the B-mode image. The spatial resolution of the QUS image is much worse than the spatial resolution of the B-mode image. This loss in spatial resolution is necessitated by the requirement to obtain enough samples to get a good periodogram estimate to have low bias and variance of the resulting spectral estimates. Different structures of the tumor can be visualized by choosing data blocks and therefore pixels as small as possible but large enough to retain good variance and bias of estimates. If the data block size is larger, the bias and variance tend to be smaller as long as the data block encompasses uniform scattering properties. However, as the data block size becomes larger, the greater the likelihood that the data block may encompass tissue regions with distinct scattering properties. This will tend to increase the bias and variance of subsequent estimates for that data block. Therefore, it is important

Fig. 3.3 (*left*) Ultrasound B-mode image of a subcutaneous sarcoma tumor and (*right*) QUS image of the tumor using an ESD map superimposed on the B-mode image

to make the data blocks as small as possible to retain good spatial resolution and the ability to clearly distinguish different tissue regions from one another in an image. But at the same time sufficient data samples are required for good bias and variance. Too small of a data block size will result in increased bias and variance of estimates and subsequent QUS images will tend to have large streaks or noisy characteristics.

Simulation and experimental studies were conducted to examine the specific tradeoffs between estimate bias and variance and the spatial resolution of QUS imaging (using the ESD) in media with uniform scattering properties (Oelze 2004b). A resolution cell of an ultrasonic imaging system (B-mode) is defined by the pulse length times the cross-sectional area of a beam. In the simulation and experimental studies (Oelze 2004b), data block sizes were defined laterally by the number of beamwidths and axially by the number of pulse lengths. Because the estimate variance has been shown to be dependent on the bandwidth and the pulse length is proportional to the bandwidth, for statistical considerations the axial resolution should be defined in terms of the number of pulse lengths. Therefore, the data block could be defined in terms of the number of resolution cells of the ultrasonic imaging system. The spatial resolution of a B-mode image is given by one resolution cell volume.

In the simulations, estimates of the power law of the ultrasonic backscattered signal from a collection of point scatterers at a number density of 64 mm^{-3} were obtained using various data block sizes. A point scatterer will scatter sound as f^4 (Faran 1951). Estimates of the power law from simulated data were obtained versus the data block size. The percent error in the estimate (bias) and the standard deviation (variance) as a percent of the estimate mean were plotted versus different data block sizes. Figure 3.4 shows the graphs of the errors in the estimates of the power law versus the data block size.

From these simulations studies several things can be observed and concluded. First, as predicted by theory, the bias and variance of the estimates is increased as the data block size is decreased. Second, a similar bias and variance can be

Fig. 3.4 (*top*) Percent error in the estimate of the power law dependence of the backscattered signal versus data block size and (*bottom*) standard deviation as a percent of the mean value of the estimate versus data block size. *Black* represents error values above 10 %. Figures taken from (Oelze 2004b)

obtained for a range of data block sizes, i.e., a minimum data block size is required in terms of the number of resolution cells needed to get good bias and variance of estimates. Therefore, the data block does not need to be a perfect square but can be rectangular in shape or even circular. Third, at a minimum, to get low bias and variance of estimates (better than 10 %), the axial length must be at least five to six

pulse lengths long and the lateral size must be three beamwidths wide. Based on these simulations, if the smallest possible data block is desired while still retaining within 5 % accuracy and precision, a data block size of 15 pulse lengths by five beamwidths was suggested (Oelze 2004b).

Experiments with physical phantoms containing glass bead scatterers were also conducted to examine the tradeoffs between data block size and the statistics of scatterer property estimates (Oelze 2004b). The phantoms contained glass bead scatterers with diameters ranging from 45 to 53 μm, sound speed in the phantom was approximately 1540 m/s and the attenuation coefficient of the phantom was approximately 0.5 dB/MHz/cm. The phantom was scanned with a single-element weakly-focused transducer (f/4) with a center frequency of 10 MHz and a -6-dB bandwidth of 6.5 MHz. Parallel scan lines from the phantoms were taken at intervals of less than a quarter beamwidth separation. From the backscattered ultrasound scan lines, the averaged spectra were acquired from data blocks and the ESD was estimated from the averaged spectra using the theory of Faran (1951). Figure 3.5 shows the graphs of the error plots versus different data block sizes. The results correlate well with simulation results presented in Fig. 3.4. Therefore, the experiments support the conclusion that there exists a tradeoff inherent between data block size and bias and variance of spectral-based estimates.

3.3 Description of Statistics of Envelope Statistics Parameters

A number of models for the statistics of the envelope of acoustic and optical signals have been proposed over the past few decades with applications to sea echo, medical ultrasound, and laser scattering (Dutt 1994; Hruska 2009a). Some of these distributions include the Rayleigh distribution, the Rician distribution, the K distribution, the homodyned K distribution, and the Nakagami distribution. A comprehensive review of the different distributions that have been applied for ultrasonic tissue characterization has been published, (e.g., Destrempes 2010).

Work has been conducted to quantify the bias and variance of estimates of the envelope statistics. Specifically, Dutt and Greenleaf examined the bias and variance of estimates for the parameters of the K distribution when using fractional order moments (Dutt 1995). They concluded that the use of fractional order moments reduced the variance of estimates derived from the K distribution resulting in an extended tradeoff between the number of samples needed for the estimate and the estimate performance in terms of bias and variance.

Hruska and Oelze (2009b) developed a novel estimator for the homodyned K distribution based on using fractional order moments to estimate the k and μ parameters. The k parameter describes the ratio of coherent to incoherent energy in the signal. If a medium has a significant specular scatterer or the medium has periodic structure, the k parameter is larger. If the medium is full of diffuse

Fig. 3.5 (*top*) Percent error in the estimate of the power law dependence of the backscattered signal versus data block size and (*bottom*) standard deviation as a percent of the mean value of the estimate versus data block size. Figures taken from Oelze (2004b)

scatterers with random spatial locations, the k parameter is smaller. The μ parameter quantifies the number of scatterers per resolution cell. If the volume of a resolution cell is known or can be approximated, then the number density of scatterers can be estimated. When the number of scatterers per resolution cell approaches 10, the sensitivity of the μ parameter decreases rapidly, i.e., it is

difficult to distinguish 10 scatterers per resolution cell from 100 scatterers per resolution cell. This is because when there are many scatterers per resolution cell, the pdf begins to look more and more like the Rayleigh distribution and the shape of the distribution depends less and less on the number density of scatterers (Weng 1991). The Rayleigh distribution is a limiting case of fully developed speckle where only the magnitude of the backscattered energy can be extracted from the envelope statistics. Therefore, reliable estimation of the μ parameter is restricted to cases where the number density is sufficiently low.

To examine the sensitivity and bias of an estimate of the μ parameter based on the homodyned K distribution, simulations were conducted. In the simulations, software phantoms were constructed with scatterers placed spatially at random with number densities corresponding to 1.0–10 scatterers per resolution cell of a simulated ultrasonic source. For each scatterer number density, 10 independent phantoms were constructed to examine the bias and variance of the μ parameter estimate. Figure 3.6 shows a graph of the actual scatterers per resolution cell versus the estimated number of scatterers per resolution cell. From the figure it can be observed that lower values of the μ parameter result in lower standard deviations of the estimate whereas the higher the value of the μ parameter the larger the standard deviation of the estimate. Therefore, the results indicate that the precision of the estimate of the μ parameter is highly dependent on the actual value of the μ parameter. As the estimate of the μ parameter becomes large, the validity of that estimate becomes suspect. From Fig. 3.6, the bias of the estimate is also observed to increase as the μ parameter increases. For example, when the number of scatterers per resolution cell is 10, the estimator provides a μ parameter estimate of 7.2. The trend is that as the number of scatterers per resolution cell continues to increase, the bias will also continue to increase. Therefore, if an estimate above 10 scatterers per resolution cell occurs, the confidence in that estimate is not high. When conducting characterization of a tissue using the μ parameter, estimates above the 10 threshold should be used with caution as they may not reliably describe underlying tissue structure.

The size of the sample required to obtain good estimates of the k and μ parameters from the homodyned K distribution using the technique developed by

Fig. 3.6 Estimate bias of the μ parameter via simulation. The *solid line* represents the estimated parameter and the *dashed line* represents the actual value. The *error bars* represent mean estimates from 10 samples. Figure taken from Hruska (2009a)

Hruska and Oelze (2009b) was also examined. Like the spectral-based estimates, estimates of the k and μ parameters are associated with a data block with lateral dimensions related to the number of scan lines separated by a beamwidth and axially by the range gate used to segment the data. All else being equal, when a larger data block is used, a greater number of envelope samples are available for estimation.

As a first step towards examining the effects of sample size on estimate bias and variation, independent and identically distributed samples of the homodyned K distribution were generated. Because the samples are statistically independent and follow the desired distribution exactly, this analysis should establish a best-case theoretical limit. Sets of samples were generated for a variety of model parameters: μ ranging from 1.0 to 10 and k ranging from 0.25 to 1.0. For each sample size and pair of parameter values, 50 independent estimation trials were performed. The absolute relative bias and the normalized standard deviation of the parameter estimates were calculated. The absolute relative bias is defined as

$$B_{\hat{x}} = \left| \frac{\bar{\hat{x}} - x}{x} \right| \tag{3.31}$$

where x represents the parameter being estimated. Likewise, the normalized standard deviation is defined as

$$SD_{\hat{x}} = \frac{\sqrt{\text{var}[\hat{x}]}}{x}. \tag{3.32}$$

For each sample size, the average absolute relative bias was computed by averaging together the absolute relative bias obtained from the 50 trials for each set of parameter values. The average normalized standard deviation was obtained similarly. The absolute relative bias (given by the absolute value) was used instead of the relative bias to allow meaningful averaging of the biases from different trials. The results, plotted in Fig. 3.7, follow expectations, i.e., as the sample size increases, the bias and variance of the parameter estimates decrease.

Like the spectral-based parameters, QUS images utilizing the k and μ parameters from the homodyned K distribution can be constructed. The data blocks used to provide an estimate can also be associated with pixel colors and superimposed on B-mode images to create a mapping of the parameters. Because the data blocks require a number of samples to obtain adequate bias and variance of the estimates, the spatial resolution of QUS images utilizing the envelope statistics are also less than for ultrasonic B-mode imaging. The same tradeoffs associated with the spectral-based imaging also apply for the envelope statistics. The same data blocks used for spectral-based imaging can be used for imaging with the k and μ parameters from the homodyned K distribution with similar bias and variance of estimates. Figure 3.8 shows an example of a QUS image of a mammary tumor in a rat utilizing the k parameter.

Fig. 3.7 Average absolute relative bias and average normalized SD of estimated model parameters versus sample size

Fig. 3.8 Parametric image of k parameter enhancing a B-mode image of a rodent tumor (MAT II-B)

3.4 Methods to Improve the Scatterer Property Statistics

Several processing methods can be used to improve the spectral-based estimates in terms of bias and variance and extend the tradeoff between spatial resolution of an image and quality of the estimates. These different techniques include compounding (i.e., averaging of spectra or estimates from independent realizations) and windowing techniques. Additional filtering techniques may be available to improve either the bias (Oelze 2002, 2004a) or variance of estimates, but these filtering techniques will not be discussed here.

3.4.1 Discrete Model Analysis

To understand how compounding and windowing techniques can result in improvements in the statistical attributes of spectral-based estimates, a discrete model of scattering will be used. In the discrete model of scattering, the signal is assumed to arise from many discrete, sub-resolvable and nearly identical scatterers with random spatial locations. This scenario is represented by Fig. 3.9. The scattering from these sub-resolution scatterers gives rise to a complex interference pattern, i.e., speckle that can be observed in B-mode images.

The signal from the collection of scatterers can then be represented by

$$r(t) = p(t) * s'(t) * a(t), \tag{3.33}$$

where $r(t)$ is the received signal, $p(t)$ is the pulse-echo impulse response but also incorporates the system-dependent effects (i.e., the transmit voltage level, diffraction effects, etc.), $a(t)$ is a function that accounts for the frequency-dependent attenuation of the signal and

$$s'(t) = s(t + t_1) + s(t + t_2) + \cdots + s(t + t_N) \tag{3.34}$$

relates the scatter function in time domain for N scatterers located at different temporal locations (depths in the tissue). Essentially, pulses are arriving at different times because scatterers are located at different distances from the transducer and their arrival pulses sum together coherently at the transducer surface. The scattered pulses will sum to make the backscattered time train. Equivalently,

$$r(t) = p(t) * [s(t - t_1) + s(t - t_2) + \cdots + s(t - t_N)] * a(t). \tag{3.35}$$

Taking the Fourier transform of the above relation gives

$$R(f) = P(f)S'(f)A(f) \tag{3.36}$$

or

$$R(f) = P(f)A(f)S(f)\left[e^{-j2\pi ft_1} + e^{-j2\pi ft_2} + \cdots + e^{-j2\pi ft_N}\right]. \tag{3.37}$$

An estimate of the power spectrum can be obtained by taking the magnitude squared of the above relation,

$$|R(f)|^2 = |P(f)|^2|A(f)|^2|S'(f)|^2. \tag{3.38}$$

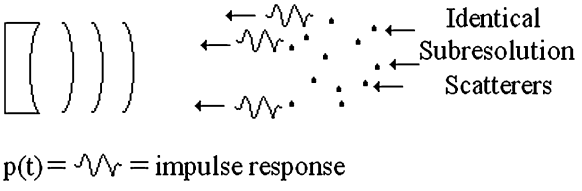

Fig. 3.9 Graphic depiction of discrete but sub-resolvable scatterers and the scattered ultrasound pulse

By considering each scatterer contribution individually, this can be further reduced to

$$|R(f)|^2 = |P(f)|^2|A(f)|^2|S(f)|^2\left[N + 2\sum_{n>m=1}^{N}\cos(2\pi f[t_n - t_m])\right]$$
$$|R(f)|^2 = |G(f)|^2\left[N + 2\sum_{n>m=1}^{N}\cos(2\pi f[t_n - t_m])\right]. \tag{3.39}$$

The first term on the right is called the incoherent scattering term and depends only on the scattering function and the number of scatterers contributing to the power spectrum estimate. The first term does not depend on the spatial locations of the scatterers. The second term is called the coherent scattering term and depends on the scattering function and the spatial locations of the scatterers. For large numbers of randomly spaced scatterers, the second term acts as noise to the incoherent spectrum when trying to parameterize the BSC. The noise increases bias and variance of scatterer property estimates. It is the second term that is reduced in its contribution to the BSC estimate by compounding and windowing techniques, which will lead to improvements in the bias and variance of estimates.

3.4.2 Spectral Smoothing with Compounding

In the case of compounding, the power spectrum, given by $|R(f)|^2$, is estimated by averaging the spectra from several independent samples. Assume that M different spectra were obtained from M independent scan line segments having the same scattering properties but with different scatterer location realizations. This could be represented by the set of equations

$$|R(f)|_1^2 = |G(f)|^2\left[N + 2\sum_{n>m=1}^{N}\cos(2\pi f[t_n - t_m])\right]$$
$$|R(f)|_2^2 = |G(f)|^2\left[N + 2\sum_{o>p=1}^{N}\cos\big(2\pi f\big[t_o - t_p\big]\big)\right]$$
$$\vdots$$
$$|R(f)|_M^2 = |G(f)|^2\left[N + 2\sum_{q>r=1}^{N}\cos\big(2\pi f\big[t_q - t_r\big]\big)\right].$$

If these spectra are then compounded together, the resulting spectrum is

$$\overline{|R(f)|^2} = |G(f)|^2 \left[N + \frac{1}{M} \left\{ 2 \sum_{n>m=1}^{N} \cos(2\pi f[t_n - t_m]) + \cdots + 2 \sum_{q>r=1}^{N} \cos\left(2\pi f\left[t_q - t_r\right]\right) \right\} \right]. \tag{3.40}$$

In this case, the number of coherent terms has been increased by a factor of M but the magnitude of the coherent terms has also been decreased by a factor of M. This results in a much smaller contribution of the coherent "noise" to the estimation of the incoherent part of the spectrum and will result in a marked improvement in the variance of the spectral-based estimates.

Compounding to improve spectral-based estimates can be accomplished through several mechanisms: spatial compounding, angular compounding (Gerig 2004), and deformational compounding (Herd 2011). In spatial compounding, the spectra from independent scan lines are used to reduce the variance of the estimate at the tradeoff of spatial resolution. Independent scan lines are separated by at least a beamwidth.

Angular compounding can be used to improve the variance of spectral estimates without the loss in spatial resolution if scattering is isotropic. Angular compounding works by acquiring several estimates from a single region of space where each estimate is obtained by interrogating the region from a different "look" angle. The different look angles cause the orientation of the scatterers with respect to each other and the transducer to be different leading to different coherent terms at each angle. Figure 3.10 shows a scenario where the scatterers examined from two different angles result in two different signal realizations. If scattering is isotropic with angle, the effect of the orientation change is that the coherent terms from Eq. (3.39) will be different for each angular look angle providing independent spectra that can then be averaged provided the angle of separation is large enough. If the scattering is anisotropic with scattering, then different "look" angles will result in different coherent and incoherent scattering terms. If the angles of orientation for the measurements are too close together, the spectra will not be completely independent and the averaging will produce less reduction in the coherent spectrum. Because the spectra come from the same spatial location, no significant loss in spatial resolution will be observed compared with spatial

Fig. 3.10 Signal received by looking at a set of scatterers from two different angular orientations

Fig. 3.11 ESD estimates from a simulated phantom consisting of two cylindrical regions using data block sizes of 1.2 mm by 1.2 mm. The ESD estimates were obtained using data from one (*left*) and 64 (*right*) angles of view with 360° coverage. Figure taken from Lavarello (2008)

compounding for QUS. Figure 3.11 shows an example of angular compounding for QUS and the improvements in variance of the estimates without the loss of spatial resolution of the QUS image. The compounded image has a center region with different scattering properties than the outer region. In the first image, the variance of the estimates is too noisy to clearly make out the central region. After angular compounding, the QUS image is much less noisy and the contrast of the center target is clear and more observable.

Finally, deformational compounding works by compressing the tissue and then taking a new measurement from the same location in space (Herd 2011). Because the scatterers have shifted in location from one another and with respect to the transducer due to compression of the tissue, the spectra from each measurement at each deformation will have different coherent spectra realizations. Averaging the spectra at each compression results in the reduction in magnitude of the coherent part of the spectrum. Like the angular compounding, the spatial resolution can be preserved with the reduction in the coherent part of the spectrum. However, if the deformation is not enough, the spectra from the different compressions will not be completely independent.

3.4.3 Spectral Smoothing with Windowing Methods

Another method for smoothing the estimate of the BSC, which can result in improvements in the variance of spectral-based parameter estimates from the BSC, are windowing methods such as the Welch's method or multi-taper methods (Wu 2010). To understand how the windowing methods reduce the variance of the BSC estimate, consider a medium with only four identical scatterers spaced at random spatial locations and the corresponding time signal produced by these scatterers

Fig. 3.12 **a**) Signal from *four scatterers* using a simple rectangular gate and **b**) using a Welch's technique with rectangular window functions

(Fig. 3.12a). If a rectangular window is used to segment the time signal including all of the scatterers, then the power spectrum of the signal can be represented by

$$|R(f)|^2 = |G(f)|^2 \left[\begin{array}{c} 4 + 2\cos(2\pi f[t_1 - t_2]) + 2\cos(2\pi f[t_1 - t_3]) + 2\cos(2\pi f[t_1 - t_4]) \\ + 2\cos(2\pi f[t_2 - t_3]) + 2\cos(2\pi f[t_2 - t_4]) + 2\cos(2\pi f[t_3 - t_4]) \end{array} \right]. \tag{3.41}$$

Instead of using a simple single rectangular window to segment the data, another technique developed by Welch calculates the power spectrum from a length of signal by creating sub-windows to further segment the data (Welch 1967). The spectra from the sub-windows are then averaged together to smooth the average spectrum estimate and reduce the variance of parameter estimates based on the average spectrum. The Welch's method reduces the variance of the spectrum estimate by reducing the number of coherent terms included in the estimate. Consider the case where the signal from the four scatterers shown in Fig. 3.12b is segmented by two non-overlapping rectangular windows. By summing together the two spectra from the sub-windows, the corresponding power spectrum estimate is given by

$$|R(f)|^2 = |G(f)|^2[4 + 2\cos(2\pi f[t_1 - t_2]) + 2\cos(2\pi f[t_3 - t_4])]. \tag{3.42}$$

Comparing Eq. (3.42) with Eq. (3.41), it can be observed that the number of coherent terms in the Welch's technique is greatly reduced. Specifically, the cross terms between the two gates that are present in Eq. (3.41) are not present in the Welch's method. The Welch's technique breaks the coherence of the scattering terms in the power spectrum between the sub-windows. Therefore, the number of coherent terms contributing to the estimate of the power spectrum is greatly reduced. In this example, non-overlapping rectangular windows were used; however, typically in the Welch's technique overlapping Hanning windows (50 % overlap) are used providing a good reduction in the variance of BSC and parameter estimates.

A similar method that can be used to reduce the variance of the power spectrum estimate is the multi-taper method (Thomson 2001). Consider again the four scatterers with random spatial locations except that now the resulting signal is windowed using two different window segments as shown in Fig. 3.13. The first window is a simple rectangular window and can be thought of as two rectangular

Fig. 3.13 Illustration of two window functions used to segment the scattered signal. The *top figure* corresponds to a simple rectangular window and the *bottom figure* corresponds to a window of the same length but with the first half given by +1 and the second half given by −1

windows of the same length connected together. The second window can be thought of as two rectangular windows of the same length connected together except the second one is multiplied by −1. The first window can be represented by [1, 1] and the second by [1, −1]. If a power spectrum is calculated using each of these windowed signals, then it can be described mathematically by

$$|R(f)|^2_{[1,1]} = |G(f)|^2 \left[\begin{array}{l} 4 + 2\cos(2\pi f[t_1 - t_2]) + 2\cos(2\pi f[t_1 - t_3]) + 2\cos(2\pi f[t_1 - t_4]) \\ \quad + 2\cos(2\pi f[t_2 - t_3]) + 2\cos(2\pi f[t_2 - t_4]) + 2\cos(2\pi f[t_3 - t_4]) \end{array} \right] \tag{3.43}$$

and

$$|R(f)|^2_{[1,-1]} = |G(f)|^2 \left[\begin{array}{l} 4 + 2\cos(2\pi f[t_1 - t_2]) - 2\cos(2\pi f[t_1 - t_3]) - 2\cos(2\pi f[t_1 - t_4]) \\ \quad - 2\cos(2\pi f[t_2 - t_3]) - 2\cos(2\pi f[t_2 - t_4]) + 2\cos(2\pi f[t_3 - t_4]) \end{array} \right]. \tag{3.44}$$

Averaging the power spectra from the two windows yields the same result as Eq. (3.42), the Welch's technique result. Therefore, the multi-taper method reduces the variance of the power spectrum estimate by also reducing the number of coherent terms contributing to the power spectrum estimate. This reduction in terms will improve the variance of parameter estimates based on the averaged power spectrum.

In the illustration provided here, the windowing functions used were not tapered. The technique is called the multi-taper method because typically a set of tapered window functions with positive and negative lobes are used to produce the power spectrum estimate. The best known set of tapers used for signal processing is the Slepian sequences or the discrete prolate spheroidal segments (DPSS) (Slepain 1978). A graph of these window functions is shown in Fig. 3.14. These windows comprise an orthonormal set of window functions. Each window

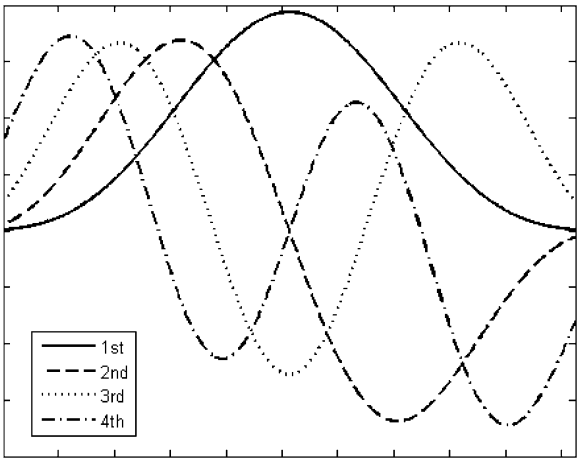

Fig. 3.14 First *four Slepian* sequences

function is used to obtain a power spectrum estimate. These spectra are then averaged together to provide a smoothed power spectrum or BSC.

Different windowing techniques can be used to smooth the estimate of the power spectrum, which results in a reduction of the variance of the estimate of the power spectrum. These windowing techniques improve the estimate by reducing the number of coherent spectrum terms that contribute to the estimate of the power spectrum. Specifically, these techniques reduce the number of coherent terms by breaking the coherence between scatterers. If the sub-windows used to produce the power spectrum estimates are too small, then bias is introduced into the power spectrum estimate. Therefore, there is a limitation in the number and size of the sub-windows that can be used in these windowing methods.

In terms of reducing the variance of estimates, compounding techniques provide a larger reduction in variance compared to the windowing techniques. However, by combining these two techniques, significant reduction in estimate variance can be produced.

3.5 Conclusions

The statistics of QUS techniques involving spectral-based estimates and envelope statistics estimates were examined. The bias and variance of both spectral-based estimates and the estimates from the envelope statistics depend on the size of the data blocks used to make the estimate, i.e., number of samples of the signal used to make the estimate. Several authors have suggested data block sizes for QUS imaging to balance the spatial resolution versus estimate bias and variance. For example, Oelze (2004b) suggested that to keep bias and standard deviation below 10 %, a data block size of 10 pulse lengths by five beamwidths should be used. This corresponds to a data block size that is 50 resolution cells in size meaning that

the spatial resolution of the resulting QUS image is approximately 50 times worse than a corresponding B-mode image. Wu and Zagzebski (2010) suggested a data block size with approximately 10 scan lines contributing to the estimate and an axial length corresponding to 10 wavelengths of the center frequency of the insonifying pulse (or approximately 30–70 resolution cells). Therefore, as a rule of thumb with basic processing procedures, sample sizes should be around 50 resolution cell sizes to provide a good tradeoff between spatial resolution of QUS estimates and good statistical features of the estimate.

ESD estimates were also analyzed and found to depend on the actual ESD size, i.e., a larger ESD size corresponds to a lower variance of the ESD estimate. Furthermore, a larger bandwidth results in a decrease in the variance of ESD estimate. However, the bandwidth consideration is included in the idea of choosing a sample size that is a large number of resolution cells. The bandwidth in pulsed sources is inversely proportional to the pulse length and, therefore, the resolution cell size. The larger the bandwidth the smaller the resolution cell size.

Additional compounding and windowing techniques can further reduce the variance of power spectrum estimates and spectral-based estimates such as the ESD. By applying angular compounding techniques, the tradeoff between spatial resolution and good statistical features for the estimates will be extended, i.e., a sample size could be smaller than 50 resolution cells. Using a Welch's approach or a multi-taper method may also reduce variance of estimates at the cost of some bias introduced. If reducing estimate variance is more important than reducing estimate bias, which may be the case when trying to discriminate tissues with parameters have small mean differences, then choosing small Welch windows or a larger number of tapers may improve the variance without increasing the spatial resolution associated with the QUS estimate.

References

Chaturvedi P, Insana MF (1996) Error bounds on ultrasonic scatterer size estimates. J Acoust Soc Am, 100:392–399

Destrempes F, Cloutier G (2010) A critical review and uniformized representation of statistical distributions modeling the ultrasound echo envelope. Ultrasound Med Biol, 36:1037–1051

Dutt V, Greenleaf JF (1994) Ultrasound echo envelope analysis using a homodyne K distribution signal model. Ultrason Imaging, 16:265–287

Dutt V, Greenleaf JF (1995) Speckle analysis using signal to noise ratios based on fractional order moments. Ultrason Imaging, 17:251–268

Faran JJ (1951) Sounds scattering by solid cylinders and spheres. J Acoust Soc Am, 23:405–418

Gerig A, Zagzebski J, Varchese T (2003) Statistics of ultrasonic scatterer size estimation with a reference phantom. J Acoust Soc Am, 113:3430–3437

Gerig AL, Varghese T, Zagzebski JA (2004) Improved parametric imaging of scatterer size estimates using angular compounding. IEEE Trans Ultrason, Ferroelect, Freq Contr, 51:708–715

Herd MT, Hall TJ, Jiang J, Zagzebski JA (2011) Improving the statistics of quantitative ultrasound techniques with deformation compounding: an experimental study. Ultrasound Med Biol, 37:2066–2074

Hruska DP (2009a) Improved techniques for statistical analysis of the envelope of backscattered ultrasound using the homodyne K distribution. M.S. Thesis, University of Illinois at Urbana-Champaign, Urbana

Hruska DP, Oelze ML (2009b) Improved parameter estimates based on the homodyne K distribution. IEEE Trans Ultrason, Ferroelect, Freq Contr, 56:2471–2481

Huisman HJ, Thijssen JM (1996) Precision and accuracy of acoustospectographic parameters. Ultrasound Med Biol, 22:855–871

Insana MF (1995) Modeling acoustic backscatter from kidney microstructure using and anisotropic correlation function. J Acoust Soc Am, 97:649–655

Insana MF, Hall TJ (1990a) Parametric ultrasound imaging from backscatter. Ultrason Imaging, 12:245–267

Insana MF, Wagner RF, Brown DG, Hall TJ (1990b) Describing small-scale structure in random media using pulse-echo ultrasound. J Acoust Soc Am, 87:179–192

Lavarello RJ, Sanchez JR, Oelze ML (2008) Improving the quality of QUS imaging using full angular spatial compounding. In: Proceedings 2008 IEEE Ultrasonics Symposium, pp 32–35

Lizzi FL, Ostromogilsky M, Feleppa EJ, Rorke MC, Yaremko MM (1987) Relationship of ultrasonic spectral parameters to features of tissue microstructure. IEEE Trans Ultrason, Ferroelect, Freq Contr, 34:319–329

Lizzi FL, Astor M, Feleppa EJ, Shao M, Kalisz A (1997a) Statistical framework for ultrasonic spectral parameter imaging. Ultrasound Med Biol, 23:1371–1382

Lizzi FL, Feleppa EJ, Astor M, Kalisz A (1997b) Statistics of ultrasonic spectral parameters for prostate and liver examinations. IEEE Trans Ultrson, Ferroelec, Freq Contr, 44:935–942

Lizzi FL, Alam SK, Mikaelian S, Lee P, Feleppa EJ (2006) On the statistics of ultrasonic spectral parameters. Ultrasound Med Biol, 32:1671–1685

Oelze ML, O'Brien Jr WD (2002) Method of improved scatterer size estimation and application Method of improved scatterer size estimation and application. J Acoust Soc Am, 112:3053–3063

Oelze ML, O'Brien Jr WD (2004a) Improved scatterer property estimates from ultrasound backscatter for small gate lengths using a gate-edge correction factor. J Acoust Soc Am, 116:3212–3223

Oelze ML, O'Brien Jr. WD (2004b) Defining optimal axial and lateral resolution for estimating scatterer properties from volumes using ultrasound backscatter. J Acoust Soc Am, 115:3226–3234

Oelze ML, Zachary JF, Obrien JR WD (2002) Characterization of tissue microstructure using ultrasonic backscatter: theory and technique for optimization using a Gaussian form factor. J Acoust Soc Am, 112:1202–1211

Papoulis A (1991) Probability, random variables, and stochastic processes. Mcgraw-Hill, New York

Slepian J (1978) Prolate spheroidal wave-functions, Fourier-analysis, and uncertainty. V. The discrete case. Bell Syst Tech J, 57:1371–1430

Thomson DJ (2001) Multi-taper analysis of nonstationary and nonlinear. In: Fitzgerald R, Smith R, Walden A, Young P, Nonlinear and nonstationary signal processing. Cambridge University Press, Cambridge

Welch PD (1967) The use of fast fourier transform for the estimation of power spectra: A method based on time averaging over short, modified periodograms. IEEE Trans Audio Electroacoust, 15:70–73

Weng L, Reid JM, Shankar PM, Soetanto K (1991) Ultrasound speckle analysis based on the K distribution. J Acoust Soc Am, 89:2992–2995

Wu L, Zagzebski JA (2010) Trade-offs in data acquisition and processing parameters for backscatter and scatterer size estimations. IEEE Trans Ultrason, Ferroelect, Freq Contr, 57:340–352

Yao LY, Zagzebski JA, Madsen EL (1991) Statistical uncertainty in ultrasonic backscatter and attenuation coefficients determined with a reference phantom. Ultrasound Med Biol, 17:187–194

Chapter 4
Attenuation Compensation and Estimation

Timothy A. Bigelow and Yassin Labyed

Abstract Estimating the losses of ultrasound signal energy with propagation depth as a function of frequency is essential for quantifying tissue properties. Specifically, ultrasound attenuation is used to correct for spectral distortion prior to estimating quantitative ultrasound parameters to assess the tissue. Ultrasound attenuation can also be used independently to characterize the tissue. In this chapter, we review the primary algorithms for estimating both the local attenuation within a region of interest as well as the total attenuation between a region of interest and an ultrasound source. The strengths and weaknesses of each algorithm are also discussed.

Keywords Attenuation · Local attenuation · Total attenuation · Spectral difference method · Spectral-log difference method · Hybrid method · Spectral-fit method · Multiple filter method

4.1 Introduction

When attempting to characterize tissue based on the frequency spectrum of backscattered ultrasound echoes, it is critically important to correctly compensate for attenuation. Because both scattering and attenuation impact the frequency spectrum, the effects of attenuation must be removed before the scattering properties can be extracted for diagnostic purposes. For the purpose of tissue characterization, there are two different attenuation parameters to be considered. First, there is the **local attenuation**. The local attenuation is the attenuation within a

T. A. Bigelow (✉)
Iowa State University, 2113 Coover Hall, Ames, IA 50011, USA
e-mail: bigelow@iastate.edu

Y. Labyed
Los Alamos National Lab, Los Alamos, NM, USA

J. Mamou and M. L. Oelze (eds.), *Quantitative Ultrasound in Soft Tissues*, DOI: 10.1007/978-94-007-6952-6_4,

Fig. 4.1 Illustration of tissue when performing ultrasound tissue characterization

region of interest and is used primarily to quantify the tissue properties of that region. It can also be used to improve the accuracy of scatterer property estimates, e.g., scatterer size and acoustic concentration, as will be discussed in more detail later in this chapter. The second and most important type of **attenuation is the total attenuation**. The total attenuation is the effective attenuation along the propagation path from the source thru the intervening tissue layers to the region of interest. Figure 4.1 shows an image of the different regions corresponding to the local and total attenuation. It is more difficult to obtain accurate estimates of the backscatter coefficient and corresponding scatterer property estimates derived from the backscatter coefficient without an accurate estimate for the total attenuation. In this chapter, we will review how the attenuation impacts the backscattered power spectrum as well as summarize the basic algorithms that have been developed to estimate both total and local attenuation.

4.2 Impact of Attenuation on Backscattered Power Spectrum

Before discussing the various algorithms that have been developed to estimate the total and local attenuation, we will briefly review how these attenuation parameters relate to the backscattered power spectrum. The backscattered power spectrum from a region of interest in an unknown sample is given by Bigelow (2004) and Bigelow and O'Brien (2004a, b)

$$S_s(f) \propto \left[\begin{array}{c} f^4 |H(f)|^4 |V_{inc}(f)|^2 \exp(-4\alpha_{tot}(f) z_T) \\ \times M_\gamma \cdot F_\gamma\left(f, a_{eff}\right) D(f, \alpha_{loc}) \end{array} \right] \tag{4.1}$$

In this equation, f is frequency, $H(f)$ is the dimensionless filtering characteristics of the ultrasound source, $|V_{inc}(f)|$ is the power spectrum of the voltage pulse applied to the ultrasound source, and z_T is the distance from the ultrasound source to the beginning of the region of interest in the tissue. The term $\alpha_{tot}(f)$ is the total attenuation along the propagation path, as was described previously, and is given by

$$\alpha_{tot}(f) = \left(\sum_{j=1}^{N-1} \alpha_j(f) \frac{\Delta z_j}{z_T} \right) \tag{4.2}$$

where α_j is the attenuation in each of the intervening tissue layers of thickness Δz_j. Also, $F_\gamma\left(f, a_{eff}\right)$ is the form factor which captures the frequency dependence of the scattering while M_γ is the acoustic concentration (Insana et al. 1990). Typical form factors for tissue and tissue-mimicking phantoms include the Gaussian form factor, the fluid-filled sphere form factor, and the spherical-shell form factor.

$$\begin{aligned} F_{\gamma\_Gaussian}\left(f,\ a_{eff}\right) &= \exp\left(-0.827\left(k \cdot a_{eff}\right)\right) \\ F_{\gamma\_Sphere}\left(f,\ a_{eff}\right) &= \left[\frac{j_1\left(2k \cdot a_{eff}\right)}{(2/3)k \cdot a_{eff}}\right]^2 \\ F_{\gamma\_Shell}\left(f,\ a_{eff}\right) &= \left[j_o\left(2k \cdot a_{eff}\right)\right]^2 \end{aligned} \tag{4.3}$$

The development of more complicated form factors to accurately model tissue is the subject of current study (Oelze and O'Brien 2006).

The remaining term from Eq. (4.1), $D(f,\ \alpha_{loc})$ takes into account both the diffraction of the acoustic waves (i.e., focusing) and the local attenuation, $\alpha_{loc}(f)$ of the tissue in the region of interest and is given by

$$\begin{aligned} D(f, \alpha_{loc}) = &\exp(-4\alpha_{loc}(f)z_o) \\ &\times \int_{-L/2}^{L/2} \left[g_{win}(s_z) \exp(-4\alpha_{loc}(f)s_z) D_{focus}(f, s_z)\right] ds_z \end{aligned} \tag{4.4}$$

where the variable of integration, s_z, increases as we move away from the source. In this equation, g_{win} is the windowing function used to gate the backscattered echoes when selecting an analysis region. Common windowing functions include rectangular, Hamming, and Hanning windows. Also, L is the length of the windowing function expressed as a distance and z_o is the distance from the beginning of the region of interest (ROI) to the center of the current windowed analysis region within the ROI. We distinguish here between the larger ROI, or the region over which the attenuation estimate is obtained, and the smaller windowed analysis region, or the region where the power spectrum is estimated. The attenuation estimation algorithms require finding multiple power spectra from different analysis regions within the ROI in order to find the attenuation of the ROI. The windowed analysis region is illustrated in Fig. 4.2.

Fig. 4.2 Illustration showing coordinates when defining variables in backscattered power spectrum

The term within the integral $D_{focus}(f, s_z)$ takes into account focusing and is given by

$$D_{focus}(f, s_z) = \left[\begin{array}{c} \exp\left(\frac{-2((z_T+z_o-F_{transmit})+s_z)^2}{(w_{z\_transmit}(f))^2}\right) \\ \times \exp\left(\frac{-2((z_T+z_o-F_{rcv})+s_z)^2}{(w_{z\_rcv}(f))^2}\right) \end{array} \right] \tag{4.5}$$

assuming the beam profile on transmit and receive can be approximated by a Gaussian function; an approximation that is reasonable for most sources (Barber 1991; Bigelow 2004; Bigelow and O'Brien 2004a, b). In this equation, $F_{transmit}$ and F_{rcv} are the distance from the aperture plane to the transmit and receive foci respectively. Also, $w_{z\_transmit}(f)$ and $w_{z\_rcv}(f)$ are the effective Gaussian depths of focus for the transmit and receive foci, respectively. For a spherically focused source, w_z is approximately equal to $6.01\lambda(\text{f\#})^2$ where λ is the wavelength and f# is the f-number for the source.

From Eq. (4.4), it is clear that the impact of local attenuation on the backscattered power spectrum is coupled with the diffraction of the acoustic field via the integral expression. This coupling can make the assessment of backscatter more challenging. As a result, various investigators have attempted to isolate the local attenuation and focusing effects on the spectrum so that each can be corrected independently. The most common approach, termed **point compensation**, assumes that the size of the windowing function is so small that g_{win} can be approximated by an impulse function (Oelze and O'Brien 2002; Bigelow 2004; Bigelow and O'Brien 2004a, b). Under this approximation, Eq. (4.4) becomes

$$D(f, \alpha_{loc}) = \exp(-4\alpha_{loc}(f)z_o)\left[\begin{array}{c} \exp\left(\frac{-2(z_T+z_o-F_{transmit})^2}{(w_{z\_transmit}(f))^2}\right) \\ \times \exp\left(\frac{-2(z_T+z_o-F_{rcv})^2}{(w_{z\_rcv}(f))^2}\right) \end{array} \right] \tag{4.6}$$

where the local attenuation term and diffraction terms have been decoupled.

Another approach to decouple the local attenuation and diffraction is to use an approximate value for the local attenuation within the integral (Bigelow and O'Brien 2006). This approach is used in all tissue characterization methods that divide the power spectrum from the sample by the power spectrum from a reference phantom as will be discussed in more detail later in the chapter. Under this approximation Eq. (4.4) becomes

$$D(f,\alpha_{loc}) = \exp(-4\alpha_{loc}(f)z_o) \times \int_{-L/2}^{L/2} \left[g_{win}(s_z)\exp\left(-4\alpha_{approximate}(f)s_z\right)D_{focus}(f,s_z)\right]ds_z \tag{4.7}$$

The optimal choice for $\alpha_{approximate}(f)$ was shown to be given by

$$\alpha_{approximate}(f) \cong \sqrt{\frac{\alpha_{high}^2(f)+\alpha_{low}^2(f)}{2}} \tag{4.8}$$

where $\alpha_{high}(f)$ and $\alpha_{low}(f)$ are the largest and smallest attenuation values expected in the tissue region (Bigelow and O'Brien 2006).

4.3 Local Attenuation Estimation Algorithms

Now that we have reviewed how local and total attenuation impacts the backscattered power spectrum, we can review some of the algorithms used to estimate the attenuation within a region of interest. While this local attenuation can be used to improve the estimate of the scattering properties for the tissue, it is typically used independently to characterize the tissue for diagnostic purposes. We will focus on four of the most common local attenuation estimation algorithms.

4.3.1 Spectral Shift Algorithm for Local Attenuation Estimation

One of the most common algorithms for estimating the attenuation within a region of interest is the spectral-shift algorithm. This algorithm uses the down shift in center frequency of the power spectrum versus propagation depth to estimate the attenuation slope, α_0, where the local attenuation is assumed to have the form $\alpha_{loc}(f) = \alpha_0 f + \beta_b$ (Narayana and Ophir 1983a, b; Oosterveld et al. 1991; Baldeweck et al. 1993, 1994, 1995; Girault et al. 1998; Kim and Varghese 2007). This algorithm has been implemented in both the frequency and the time domain, where the time-domain implementation requires utilizing an autoregressive

approach (Baldeweck et al. 1993, 1994, 1995; Girault et al. 1998). We will derive the algorithm in the frequency domain because focusing has not been accounted for in the autoregressive approach.

The spectral shift algorithm begins by assuming that the backscattered power spectrum can be approximated by a Gaussian function. As a result, Eq. (4.1) can be written as

$$S_s(f) \propto \exp\left(-\frac{(f-f_o)^2}{2\sigma_\omega^2}\right) D(f,\ \alpha_{loc}). \tag{4.9}$$

Traditionally, the spectral-shift algorithm has been implemented assuming weakly-focused sources where diffraction effects in the ROI can be neglected. In addition, small windows are typically used resulting in the assumption that point compensation is valid. Hence, Eq. (4.9) can be written as

$$S_s(f) \propto \exp\left(-\frac{(f-f_o)^2}{2\sigma_\omega^2}\right) \exp(-4\alpha_o \cdot f z_o). \tag{4.10}$$

However, multiplying the Gaussian function by the decaying exponential is just a Gaussian transformation resulting in a new Gaussian function.

$$S_s(f) \propto \exp\left(-\frac{\left(f-\tilde{f}_o(z_o)\right)^2}{2\sigma_\omega^2}\right) \tag{4.11}$$

where

$$\tilde{f}_o(z_o) = f_o - 4\sigma_\omega^2 \alpha_o \cdot z_o. \tag{4.12}$$

Therefore, the attenuation slope can be found by selecting multiple windows within a ROI (i.e., different z_o). The power spectrum for each window is then calculated and fit by a Gaussian function to find the center frequency, $\tilde{f}_o$, and bandwidth, σ_ω^2. The attenuation slope can then be calculated from the change in center frequency with depth,

$$\alpha_o = -\frac{1}{4\sigma_\omega^2}\frac{\partial \tilde{f}_o}{\partial z_o}. \tag{4.13}$$

Importance of Finding the Usable Frequency Range: When fitting a function to a spectrum it is critically important to perform the fit only with values from the spectrum that are not dominated by noise. Therefore, the first step in any frequency domain algorithm is to first find the usable frequency range from the power spectrum. One can do this from either a visible inspection of the spectrum or using a computer program that identifies the noise floor for the spectral data and always operates above this noise floor.

Hint on Finding Center Frequency and Bandwidth: When finding the center frequency and bandwidth from a fit to a Gaussian function, we have found that a more accurate fit can be obtained by performing the fit in the log domain. Therefore, we find the values of $\tilde{f}_o$ and σ_ω^2 that minimize the function in Eq. (4.14).

$$mse = \underset{f}{\text{mean}}\left[\left(\begin{array}{l}\log\left(e^{\left(-\frac{(f-\tilde{f}_o)^2}{2\sigma_\omega^2}\right)}\right) - \log\left(\frac{S_s(f)}{\max\limits_f(S_s(f))}\right) \\ -\underset{f}{\text{mean}}\left(\log\left(e^{\left(-\frac{(f-\tilde{f}_o)^2}{2\sigma_\omega^2}\right)}\right) - \log\left(\frac{S_s(f)}{\max\limits_f(S_s(f))}\right)\right)\end{array}\right)^2\right]. \quad (4.14)$$

The expression derived in Eq. (4.13) is valid only when diffraction effects can be neglected (Bigelow et al. 2008; Kim and Varghese 2008). Otherwise, a correction needs to be applied as indicated in Fig. 4.3 taken from Bigelow et al. (2008).

From this figure, it is clear that without focusing compensation, ROIs before the focus underestimate the attenuation slope while ROIs beyond the focus overestimate the attenuation slope. When the windowed regions is close to the focus, we use the following correction

Fig. 4.3 Error in attenuation estimate both with and without focusing compensation for a simulated 33 MHz spherically focused transducer intended to assess cervical ripening in rats taken from Bigelow et al. (2008). The source had a focal length 9 mm and $z_o = 0$ in this figure corresponds to the focus

$$\left[\exp\left(\frac{2(z_T + z_o - F_{transmit})^2}{(w_{z\_transmit}(f))^2}\right) \cdot \exp\left(\frac{2(z_T + z_o - F_{rcv})^2}{(w_{z\_rcv}(f))^2}\right)\right] \tag{4.15}$$

before finding the center frequency. This correction is based on the assumption that the beam can be approximated by a Gaussian function in the focal region (Bigelow et al. 2008).

4.3.2 Spectral Difference Method for Local Attenuation Estimation

Another common algorithm for estimating the local attenuation from an ROI is the spectral difference method (Parker and Waag 1983; Parker et al. 1988; Yao et al. 1990). The spectral difference method is sometimes referred to as the reference-phantom method because it uses a well-characterized reference phantom to correct for diffraction effects. In the spectral difference method, multiple overlapping windows are positioned throughout the ROI as shown in Fig. 4.4. An overlap of 50 % between adjacent windows is common; however, other overlap values have been used. Power spectra from corresponding windows in a reference phantom are also acquired.

Importance of Sound Speed: It is important to use a tissue-mimicking phantom with a sound speed similar to the expected sound speed of the tissue so that the diffraction properties are similar when estimating the attenuation.

After obtaining the power spectrum from each window for the sample and the reference, the power spectra are divided to give

Fig. 4.4 Illustration of windowed regions within ROI when implementing the spectral difference algorithm

$$\frac{S_s(f)}{S_{ref}(f)} \propto \left[\frac{\exp(-4\alpha_{tot}(f)z_T) \cdot M_\gamma F_\gamma(f) D(f,\, \alpha_{loc})}{\exp\left(-4\alpha_{ref}(f)z_T\right) \cdot M_{\gamma\_ref} F_{\gamma\_ref}(f) D\left(f,\, \alpha_{ref}\right)} \right] \tag{4.16}$$

where $\alpha_{ref}(f)$ is the attenuation of the reference phantom and $F_{\gamma\_ref}(f)$ is the form factor describing the frequency dependence of the scattering from the phantom. Using the approximation in Eqs. (4.7) and (4.16) simplifies to

$$\frac{S_s(f)}{S_{ref}(f)} \propto \left[\begin{matrix} \exp\left(-4\left(\alpha_{tot}(f) - \alpha_{ref}(f)\right)z_T\right) \\ \exp\left(-4\left(\alpha_{loc}(f) - \alpha_{ref}(f)\right)z_o\right) \frac{M_\gamma F_\gamma(f)}{M_{\gamma\_ref} F_{\gamma\_ref}(f)} \end{matrix} \right]. \tag{4.17}$$

Taking the natural logarithm of the above relation gives,

$$S(f) = \ln\left(\frac{S_s(f)}{S_{ref}(f)}\right) = 4\left(\alpha_{ref}(f) - \alpha_{loc}(f)\right)z_o + C(f) \tag{4.18}$$

where $C(f)$ is a function of frequency that depends on the scattering properties and total attenuation of the sample and reference phantoms. $C(f)$ does not depend on z_o provided the ROI is homogeneous. The attenuation of the sample is calculated from the change in $S(f)$ with z_o, i.e.,

$$\alpha_{loc}(f) = \alpha_{ref}(f) - \frac{1}{4}\frac{\partial S(f)}{\partial z_o}. \tag{4.19}$$

Importance of Homogeneous Region: The spectral difference method cannot be used to estimate the attenuation when the scattering properties change within the ROI as this would make $C(f)$ also a function of z_o (Labyed and Bigelow 2011).

4.3.3 Spectral Log Difference Method for Local Attenuation Estimation

A slightly modified form of the spectral-difference method is the spectral-log-difference method (Kuc and Schwartz 1979; Kuc 1980, 1984; Insana et al. 1983). This method is slightly less dependent on changes in the scattering properties of the medium (Labyed and Bigelow 2011). The method begins by finding the backscattered power spectrum from two windowed regions within an ROI; one at the proximal edge of the ROI, z_{op}, and one at the distal edge of the ROI, z_{od}, as shown in Fig. 4.5. Once again the power spectra from the windowed regions of the sample are divided by corresponding spectra from a reference phantom yielding

Fig. 4.5 Illustration of windowed regions within ROI when implementing the spectral log difference algorithm

$$S_p(f) = \ln\left(\frac{S_s(f, z_{op})}{S_{ref}(f, z_{op})}\right) = 4\left(\alpha_{ref}(f) - \alpha_{loc}(f)\right)z_{op} + C\left(f, z_{op}\right) \tag{4.20}$$

$$S_d(f) = \ln\left(\frac{S_s(f, z_{od})}{S_{ref}(f, z_{od})}\right) = 4\left(\alpha_{ref}(f) - \alpha_{loc}(f)\right)z_{od} + C(f, z_{od}) \tag{4.21}$$

where the subscript p refers to the proximal windowed region and the subscript d refers to the distal windowed region. Subtracting Eqs. (4.20) and (4.21) yields

$$S_\Delta(f) = S_p(f) - S_d(f) = \begin{bmatrix} 4\left(\alpha_{ref}(f) - \alpha_{loc}(f)\right)\left(z_{op} - z_{od}\right) \\ + C\left(f, z_{op}\right) - C(f, z_{od}) \end{bmatrix}. \tag{4.22}$$

Also, if we assume that the frequency dependence of the scattering does not change within the ROI for the sample (only possibly the acoustic concentration), then

$$C\left(f, z_{op}\right) - C(f, z_{od}) \cong C_\Delta\left(z_{op}, z_{od}\right) \tag{4.23}$$

which is independent of frequency (Labyed and Bigelow 2011). Therefore, the local attenuation within the ROI can be estimated by finding

$$\left[\frac{S_\Delta(f)}{4\left(z_{od} - z_{op}\right)} + \alpha_{ref}(f)\right] = \alpha_{loc}(f) + \frac{C_\Delta\left(z_{op}, z_{od}\right)}{4\left(z_{od} - z_{op}\right)} \tag{4.24}$$

and then performing a fit as a function of frequency to eliminate the C_Δ term. The most common approach is to assume a frequency dependence of $\alpha_{loc}(f) = \alpha_0 f + \beta_b$, and then perform a linear fit as a function of frequency to determine α_0.

ROI Size needed for Spectral Log Difference Method: A good rule of thumb is to have $(z_{od} - z_{op}) > 15$ pulse lengths and at least 15 independent echoes when using a linear approximation for the attenuation with the spectral-log-difference method. Smaller values tend to produce large variance of the estimates. However, these values are also dependent on the frequency range available for obtaining the estimates.

4.3.4 Hybrid Method for Local Attenuation Estimation

A third method for estimating the attenuation within an ROI is the hybrid method (Kim and Varghese 2008). The hybrid method has very similar performance to the spectral log-difference method (Labyed and Bigelow 2011). The hybrid method once again begins by calculating the power spectra for multiple windowed regions within an ROI and a corresponding reference phantom. The sample and reference power spectra are then divided yielding

$$\frac{S_s(f,z_o)}{S_{ref}(f,z_o)} \propto \begin{bmatrix} \exp\left(-4\left(\alpha_{tot}(f)-\alpha_{ref}(f)\right)z_T\right) \\ \exp\left(-4\left(\alpha_{loc}(f)-\alpha_{ref}(f)\right)z_o\right)\frac{M_\gamma(z_o)F_\gamma(f)}{M_{\gamma\_ref}(z_o)F_{\gamma\_ref}(f)} \end{bmatrix} \tag{4.25}$$

where once again we have assumed that the frequency dependence of the scattering **does not change** within the ROI. Note that a change in the acoustic concentration $M_\gamma(z_o)$ within the ROI does not impact the attenuation estimate. The power-spectra ratio for each window is then multiplied by a Gaussian function and corrected for the attenuation of the reference phantom to yield

$$\begin{aligned} GRS(f,\,z_o) &= \exp\left(-\frac{(f-f_c)^2}{2\sigma_c^2}\right)\frac{S_s(f,\,z_o)}{S_{ref}(f,\,z_o)}\exp\left(-4\alpha_{ref}(f)z_o\right) \\ &\propto \begin{bmatrix} \exp\left(-\dfrac{(f-f_c)^2}{2\sigma_c^2}\right)\exp\left(-4\left(\alpha_{tot}(f)-\alpha_{ref}(f)\right)z_T\right) \\ \exp(-4\alpha_{loc}(f)z_o)\dfrac{M_\gamma(z_o)F_\gamma(f)}{M_{\gamma\_ref}(z_o)F_{\gamma\_ref}(f)} \end{bmatrix} \end{aligned} \tag{4.26}$$

which is approximately equal to

$$GRS(f,\,z_o) \propto \left[\exp\left(-\frac{\left(f-\tilde{f}_c\right)^2}{2\tilde{\sigma}_c^2}\right)\exp(-4\alpha_{loc}(f)z_o)\right] \tag{4.27}$$

because of the frequency dependence of total attenuation and scattering. If we assume that the attenuation within the ROI has the form $\alpha_{loc}(f) = \alpha_0 f + \beta_b$, then Eq. (4.27) becomes

$$GRS(f,z_o) \propto e^{-\frac{(f-\tilde{f}_c)^2}{2\tilde{\sigma}_c^2}}e^{-4\alpha_o f z_o} \propto \exp\left(-\frac{\left(f-\tilde{f}_c'(z_o)\right)^2}{2\tilde{\sigma}_c^2}\right) \tag{4.28}$$

where

$$\tilde{f}_c'(z_o) = \tilde{f}_c - 4\tilde{\sigma}_c^2\alpha_o \cdot z_o. \tag{4.29}$$

Therefore, the attenuation slope can be calculated as

$$\alpha_o = -\frac{1}{4\tilde{\sigma}_c^2}\frac{\partial \tilde{f}_c'}{\partial z_o}. \tag{4.30}$$

Selection of f_c and $\tilde{\sigma}_c$ for Hybrid Method: f_c is often chosen as the frequency where the spectral peak of $GRS(f, z_o)$ is approximately in the middle of the usable frequency range. Similarly, $\tilde{\sigma}_c$ is chosen as the bandwidth of the received echoes from the ROI.

4.3.5 Comparison of Spectral Difference, Spectral Log-Difference, and Hybrid Methods for Local Attenuation Estimation

Before concluding our discussion of local attenuation estimation, we will briefly compare the performance of the three algorithms that utilize a reference phantom as was originally reported in Labyed and Bigelow (2011). These algorithms were selected for comparison because they are the easiest to implement when using modern ultrasound clinical array transducers. We use computer simulations to evaluate the dependence of the algorithms on the number of independent echoes and the number of pulse lengths utilized to obtain the estimates. The simulations utilized a 10 MHz source with a 5 cm focal length and a 50 % −3-dB bandwidth. We assume that the local attenuation has the form $\alpha_{loc}(f) = \alpha_0 f$. Figure 4.6 shows the variance of the estimates as a function of ROI size.

From this figure, it is clear that for any given ROI size, the spectral-difference method has the lowest variance. However, the spectral-difference method is also significantly impacted by any heterogeneities in the tissue (Kim and Varghese 2008; Labyed and Bigelow 2011). The spectral-log difference method and the hybrid method have comparable performance both in terms of variance (Fig. 4.6) and in terms of their robustness to tissue heterogeneity (Labyed and Bigelow 2011). Neither the spectral log-difference nor the hybrid method are impacted by changes in acoustic concentration within the ROI. However, a bias will be introduced when there is a change in the frequency dependence of the scattering. If we assume that the change in frequency dependence results from a variation in the effective scatterer diameter, then the bias is approximately given by

$$Error(Np/cm - MHz) \cong \frac{16.32\, f_{mid}\left(a_{eff}^2(z_p) - a_{eff}^2(z_d)\right)}{c^2\left(z_p - z_d\right)} \tag{4.31}$$

where f_{mid} is the middle frequency of the usable frequency range.

Fig. 4.6 The standard deviation (STD) in the percent error of the attenuation coefficient estimates that were obtained using the spectral difference method from the homogeneous sample, versus the number of pulse lengths and the number of echoes per ROI for the (**a**) spectral difference algorithm, (**b**) the spectral-log difference algorithm, and (**c**) the hybrid algorithm

4.4 Total Attenuation Estimation Algorithms

When performing ultrasound tissue characterization, it is critically important to correct for the frequency dependence of the attenuation along the propagation path. Therefore, in this section we will summarize the two types of algorithms that have been proposed for this purpose. Both of these algorithms assume that the **total attenuation for the sample has a linear frequency dependence** give by $\alpha_{tot}(f) = \alpha_s f$. A third approach, which will not be discussed in detail, would be to use estimates of local attenuation in each of the intervening tissue layers and then sum the estimates to calculate the total attenuation from Eq. (4.2) directly. While this third approach works for some applications with clearly identifiable and relatively thick layers, it tends to have problems when the intervening tissue layers are more complex.

4.4.1 Multiple Filter Algorithm for Total Attenuation Estimation

The first type of algorithm that will be discussed is the multiple-filter algorithm. This algorithm requires either applying multiple Gaussian filters to the backscattered waveforms or using multiple transmit frequencies that span the bandwidth of the transducer (Bigelow 2008, 2010a, b; Labyed and Bigelow 2010). Because most modern tissue characterization applications utilize a clinical array transducer, we will focus our discussion on the use of multiple filters. We use echoes from a reference phantom to correct for diffraction effects.

The algorithm begins with finding the power spectra from a single windowed region in the tissue sample and from the corresponding region in a well-characterized reference phantom. After correcting for the attenuation in the reference phantom, the ratio of the spectra is given by

$$\frac{S_s(f)}{S_{ref}(f)} e^{-\alpha_{ref}(f) z_T} \propto \exp(-4\alpha_s f z_T) \frac{F_\gamma(f)}{F_{\gamma\_ref}(f)} \tag{4.32}$$

where we can assume that the window is located at $z_o = 0$ without loss of generality. We then assume that the frequency dependence of the scattering is approximately given by $F_\gamma(f) \propto \exp(-Af^n)$ where n is approximately equal to 2. While this is clearly true for the Gaussian form factor, it is also true over a limited ka_{eff} range for other common form factors as shown in Fig. 4.7 taken from Bigelow (2010a, b).

In this figure, the fits for each form factor are given by

$$\begin{aligned} F_{\gamma\_Sphere}\left(f,\ a_{eff}\right) &\cong \exp\left(-1.11\left(ka_{eff}\right)^{2.167}\right) \\ F_{\gamma\_Shell}\left(f,\ a_{eff}\right) &\cong \exp\left(-2\left(ka_{eff}\right)^{1.914}\right), \end{aligned} \tag{4.33}$$

and the fit was performed for ka_{eff} from 0 to 1.2 because ka_{eff} values less than 1.2 are of the greatest interest when quantifying the tissue microstructure.

If we then multiply Eq. (4.32) by a series of Gaussian filters, we can show that

$$\frac{S_s(f)}{S_{ref}(f)} e^{-\alpha_{ref}(f) z_T} \exp\left(-\frac{(f-f_c)^2}{2\sigma_c^2}\right) \cong C_1 \exp\left(-\frac{\left(f-\tilde{f}_c\right)^2}{2\sigma_c^2}\right) \tag{4.34}$$

Fig. 4.7 Form factor with fit of the form $\exp(-Af^n)$ for (**a**) fluid filled sphere and (**b**) spherical shell taken from Bigelow (2010a, b)

where

$$\begin{aligned}\tilde{f}_c &\cong \left[1-2\tilde{\sigma}_c^2(A_s-A_r)\right]f_c + 4\tilde{\sigma}_c^2 z_T \alpha_s \\ \tilde{\sigma}_c^2 &= \frac{\sigma_c^2}{1-2\sigma_c^2(A_s-A_r)}\end{aligned} \tag{4.35}$$

using a derivation similar to that performed for the hybrid method discussed previously. Therefore, for each filter applied, we can find

$$\xi(f_c) = \frac{\left(f_c - \tilde{f}_c\right)}{4\tilde{\sigma}_c^2 z_T} \cong \frac{(A_s - A_r)}{2z_T} f_c - \alpha_s. \tag{4.36}$$

The intercept of $\xi(f_c)$ with respect to f_c will give the slope of the frequency dependence for the total attenuation.

One of the challenges when using the multiple-filter method is determining the optimal number of filters. In an early work, the use of four filters was examined (Bigelow 2010a, b; Labyed and Bigelow 2010). For the first three filters, the center frequency of each filter was calculated as

$$\begin{aligned}f_{c1} &= f_{\min} + \frac{f_{\max} - f_{\min}}{4} \\ f_{c2} &= f_{c1} + \frac{f_{\max} - f_{\min}}{4} \\ f_{c3} &= f_{c2} + \frac{f_{\max} - f_{\min}}{4}\end{aligned} \tag{4.37}$$

where f_{min} and f_{max} were the smallest and largest frequencies of the usable frequency range, respectively. The usable frequency range is the range of frequencies in the power spectrum for which the power spectrum exceeds some level (for example -20 dB) based on the noise level of the received echoes. Once these center frequencies were set, the bandwidths were determined by finding the percent bandwidth such that f_{min} corresponded to the -10 to -15 dB bandwidth for the filter as calculated from

$$\sigma_{c1}^2 = \left(\frac{10(f_{c1} - f_{\min})^2}{2\ln(10)(-BW_{dB})}\right) \tag{4.38}$$

where BW_{dB} is the desired bandwidth (i.e. -10 or -15 dB) for the first filter that would correspond with f_{min}. The bandwidths of the other three filters were then selected to have the same -3-dB percent bandwidth as the first filter. The remaining 4th filter was then selected to span the entire usable frequency range of the backscattered echoes.

Recently, a statistical analysis study was performed on the multiple-filter algorithm to derive an expression for the standard deviation of the total attenuation estimate as a function of ROI size, bandwidth, and number of Gaussian filters (Labyed 2010). The focus was on the variance of the estimates as this is the

limiting criterion when estimating the total attenuation (Bigelow and O'Brien 2005a, b; Bigelow et al. 2005; Bigelow 2008, 2010a, b; Labyed and Bigelow 2010). While it is trivial to get the attenuation correct on average, it is much more challenging to obtain precise estimates especially when the ROI is small. The statistical analysis used non-overlapping (independent) filters to simplify the mathematics and found that the variance in the total attenuation estimate was proportional to

$$\mathrm{var}(\alpha_s) \propto \frac{(N_s + N_r)}{N_s N_r} \frac{1}{\left\{\sum_{j=1}^{K}\left[\sum_{i=1}^{M}(f_i - f_c(j))^2\right]\right\} - \frac{\left\{\sum_{j=1}^{K}\left[\sum_{i=1}^{M}(f_i - f_c(j))^2\right] f_c(j)\right\}^2}{\sum_{j=1}^{K}\left\{\left[\sum_{i=1}^{M}(f_i - f_c(j))^2\right] f_c(j)^2\right\}}} \quad (4.39)$$

where f_i are the individual frequency components of the spectrum, $f_c(j)$ is the center frequency of the jth Gaussian filter when a total of K filters are used, and N_s and N_r are the number of independent echoes used to estimate the power spectra of the sample and reference, respectively.

Precision of Total Attenuation Estimation Algorithms: The precision of the total attenuation estimation algorithms is strongly influenced by the bandwidth of the source and the number of independent echoes used to obtain the estimate. There is also some dependence on the size of the windowed region used to estimate the power spectrum as this can influence the accuracy of the power spectra estimate.

The results of the statistical analysis also revealed that the optimal number of non-overlapping filters is equal to two. In addition, the standard deviation of the total attenuation estimate decreases with increasing ROI size, i.e., with increasing number of independent echo lines used to compute the power spectra, and increasing time window length used to gate the echo lines. Note that the total attenuation is estimated from the power spectrum that is obtained by averaging the power spectra of the windows within the ROI. Therefore, using a large number of echo lines improves the estimate of the power spectrum, and hence improves the estimate of the total attenuation.

The results of the statistical analysis were validated using numerical simulations. Backscattered signals were simulated for a sample and a reference that had attenuation coefficients of 0.7 and 0.5 dB/cm-MHz, respectively. The sample scatterers had a Gaussian Form Factor with a 20 μm effective radius, while the reference had spherical shell scatterers with 10 μm radii. Both the sample and the reference had a scattering density of 100 mm^{-3}, corresponding to approximately 10 scatterers per resolution cell, which is adequate for fully developed speckle.

Fig. 4.8 Plots of the theoretical and calculated standard deviation of the total attenuation estimate from the simulated backscattered signals, obtained with the multiple-filter method using an ROI length of 10 pulse lengths and an ROI width of 60 independent echo lines, with respect to the number of non-overlapping filters

Figure 4.8 shows plots of the theoretical and calculated standard deviation of the total attenuation estimate from the simulated backscattered signals as a function of the number of non-overlapping filters. It is clear that using two independent Gaussian filters yields the smallest standard deviation in the estimate of the total attenuation. As shown in Fig. 4.9, the STD in the total attenuation estimate decreased with increasing number of independent echoes.

Fig. 4.9 Plots of the theoretical and calculated standard deviation of the total attenuation estimate from the simulated backscattered signals, obtained using the multiple filter method with two Gaussian filters and an ROI length (time window size) of 10 pulse lengths with respect to the number of independent of echoes per ROI

4.4.2 Spectral Fit Algorithm for Total Attenuation Estimation

The second type of algorithm used for obtaining the frequency-dependent attenuation along the propagation path involves estimating the frequency dependence of the backscatter and the attenuation simultaneously. Initially, the tissue was assumed to satisfy a Gaussian form factor $\left(F_{\gamma\_Gaussian}\left(f,\ a_{eff}\right) = \exp\left(-0.827\left(k \cdot a_{eff}\right)\right)\right)$ and a fit was performed to estimate both α_s and a_{eff} (Bigelow and O'Brien 2005a, b; Bigelow et al. 2005). Other authors have extended the algorithm to allow for a more general form for the backscatter $(BSC(f) = bf^n)$ and then perform a fit for b, n, and α_s (Nam et al. 2011). However, we will focus on the original spectral fit algorithm where only two parameters were estimated.

The spectral fit algorithm begins by dividing the spectra from the windowed region of the sample by the spectra from the windowed region of a known reference. Initially, a planar target was used as a reference, but a reference phantom has also been used. Our derivation here will assume a reference phantom is used. After dividing the spectra, the result is multiplied by the attenuation and backscatter terms for the reference as given by

$$S_{fit}(f) = \frac{S_s(f)}{S_{ref}(f)} e^{-\alpha_{ref}(f) z_T} BSC_{ref}(f) \propto \exp(-4\alpha_s f z_T) F_\gamma(f). \tag{4.40}$$

Assuming a Gaussian form factor for $F_\gamma(f)$, the natural log of Eq. (4.40) will yield

$$-\ln\left(S_{fit}(f)\right) = 0.827\left(\frac{2\pi}{c} a_{eff}\right)^2 f^2 + 4\alpha_s f z_T + Constant \tag{4.41}$$

where a simple polynomial fit will yield both the total attenuation slope, α_s, and the effective scatterer radius, a_{eff}.

When implementing the spectral fit algorithm, more accurate and precise estimates are obtained as the frequency range ($\Delta f = f_{max} - f_{min}$) used to obtain the attenuation estimate increases, similar to the case for the multiple filter method (Labyed 2010). Figure 4.10 shows average error and the deviation as a function of frequency range for attenuation values of 0, 0.3, 0.5, and 1 dB/cm-MHz with a_{eff} of 5–105, 5–75, 5–85, and 5–150 μm, respectively taken from Bigelow and O'Brien (2005a, b). Also, shown are the results for a 25 μm a_{eff} and attenuation values varying from 0 to 1 dB/cm-MHz. The results were obtained using a 3 mm Hamming window (~13.5 pulse lengths) and 25 independent echoes. Regardless of the scattering and attenuation properties of the sample, a consistent variance is achieved provided the same Δf is used to obtain the estimates. Figure 4.10 also reiterates that when finding the total attenuation, achieving good accuracy is much easier than achieving small variance.

Fig. 4.10 Plots of the **a** accuracy and **b** precison for a range of attenuations and scatterer sizes taken from Bigelow and O'Brien (2005a, b) estimated from simulated backscattered signals illustrating the importance of the frequency bandwidth when estimating the total attenuation using the spectral fit algorithm

Methods to Improve Usable Frequency Range: Because the total attenuation estimation algorithms are highly dependent on bandwidth. One way of increasing the bandwidth is to use higher frequency transducers. Using higher frequency transducers however, limits the penetration depth into tissue. Recently, methods that are based on coded excitation and pulse compression have been shown to improve the bandwidth and penetration depth (Oelze 2007). Surface micro-machined capacitive ultrasonic transducers are new designs that demonstrated a big improvement in the bandwidth (Ladabaum et al. 1998; Ergun et al. 2003). Some ultrasound clinical systems, however, allow the transducer to be excited at three different center frequencies. This feature can be used to increase the usable frequency range in the power spectrum of the backscattered signal.

4.4.3 Comparison of Spectral Fit Algorithm and Multiple Filter Algorithm

As described in Sect. 4.4.1, the optimal number of filters for the multiple-filter method is two. However, that result was only valid when the Gaussian filters were non-overlapping. Therefore, it is important to test whether using overlapping filters can improve the attenuation estimates. A comparison of the performance between the multiple-filter method and the spectral-fit method is also important to consider.

Fig. 4.11 Plots of the **a** bias, **b** STD, and **c** MSE of the estimate α_s, which was obtained using the multiple filter method with two independent Gaussian filters, the multiple filter method with four overlapping Gaussian filters, and the spectral-fit method, with respect to the number of independent of echoes per ROI for an ROI length of 10 pulse lengths

In this section, we compare the bias, STD, and mean squared error (MSE) of the total attenuation estimates obtained with the spectral-fit method, the multiple-filter method that uses two non-overlapping filters, and the multiple-filter method that uses four overlapping filters as described in (see Sect. 4.4.1). We use the numerical simulations described in Sect. 4.4.1 to perform these tests. Figure 4.11 shows the results as a function of number of independent echoes in the sample while Fig. 4.12 gives the results as a function of number of pulse lengths used to estimate the backscattered power spectrum. The results indicate that the variance strongly depends on the number of echoes with only a weak dependence on the number of pulse lengths. However, a slight bias is introduced for smaller pulse lengths that is not observed when the number of independent echoes tends towards zero.

Fig. 4.12 Plots of the **a** bias, **b** STD, and **c** MSE of the estimate α_s, which was obtained using the multiple filter method with two independent Gaussian filters, the multiple filter method with four overlapping Gaussian filters, and the spectral-fit method, with respect the number of pulse lengths per ROI for an ROI that has 50 independent echo lines

ROI Size needed for Total Attenuation Algorithms: A good rule of thumb is to have a windowed region of at least 10 pulse lengths and at least 25 to 35 independent echoes. However, these values are also dependent on the frequency range available for obtaining the estimates.

Based on the two figures below, the MSE is comparable for both the spectral fit method and the multiple filter method with two independent Gaussian filters. However, the spectral fit method provides a slightly smaller STD and a slightly larger bias compared to the two independent filter method. The figures also show in the multiple filter method, that using three overlapping Gaussian filters and a fourth filter that spans the entire usable frequency range gives better results than using only two independent Gaussian filters. This latter result demonstrates that

the multiple filter method could potentially be improved to yield smaller errors in the attenuation estimates by using two overlapping filters.

References

Baldeweck T, Laugier P et al (1993) Application of autoregressive spectral analysis for ultrasound attenuation: interest in highly attenuating medium

Baldeweck T, Herment A et al (1994) Attenuation estimation in highly attenuating media using high frequencies: a comparison study between different mean frequency estimators

Baldeweck T, Laugier P et al (1995) Application of autoregressive spectral analysis for ultrasound attenuation estimation: interest in highly attenuating medium. IEEE Trans Ultrason Ferroelectr Freq Control 42(1):99–110

Barber FE (1991) The scanning acoustic microprobe: I. Analysis and synthesis of a spherically symmetric point spread function. J Acoust Soc Am 90(1):1–10

Bigelow TA (2004) Estimating the medical ultrasound in vivo power spectrum. PhD, Electrical Engineering. University of Illinois, Urbana, p 243

Bigelow TA (2008) Ultrasound attenuation estimation using backscattered echoes from multiple sources. J Acoust Soc Am 124(2):1367–1373

Bigelow TA (2010a) Estimating the total ultrasound attenuation along the propagation path by applying multiple filters to backscattered echoes from a single spherically focused source. IEEE Trans Ultrason Ferroelectr Freq Control 57(4):900–907

Bigelow TA (2010b) Improved algorithm for estimation of attenuation along propagation path using backscattered echoes from multiple sources. Ultrasonics 50(4–5):496–501

Bigelow TA, O'Brien WD Jr (2004a) Scatterer size estimation in pulse-echo ultrasound using focused sources: calibration measurements and phantom experiments. J Acoust Soc Am 116(1):594–602

Bigelow TA, O'Brien WD Jr (2004b) Scatterer size estimation in pulse-echo ultrasound using focused sources: theoretical approximations and simulation analysis. J Acoust Soc Am 116(1):578–593

Bigelow TA, O'Brien WD Jr (2005a) Evaluation of the spectral fit algorithm as functions of frequency range and Dka_{eff}. IEEE Trans Ultrason Ferroelectr Freq Control 52(11):2003–2010

Bigelow TA, O'Brien WD Jr (2005b) Signal processing strategies that improve performance and understanding of the quantitative ultrasound SPECTRAL FIT algorithm. J Acoust Soc Am 118(3):1808–1819

Bigelow TA, O'Brien WD Jr (2006) Impact of local attenuation approximations when estimating correlation length from backscattered ultrasound echoes. J Acoust Soc Am 120(1):546–553

Bigelow TA, Oelze ML et al (2005) Estimation of total attenuation and scatterer size from backscattered ultrasound waveforms. J Acoust Soc Am 117(3):1431–1439

Bigelow TA, McFarlin BL et al (2008) In vivo ultrasonic attenuation slope estimates for detecting cervical ripening in rats: preliminary results. J Acoust Soc Am 123(3):1794–1800

Ergun AS, Yaralioglu GG et al (2003) Capacitive micro machined ultrasonic transducers: theory and technology. J Aerosp Eng 16(2):76–84

Girault JM, Ossant F et al (1998) Time-varying autoregressive spectral estimation for ultrasound attenuation in tissue characterization. IEEE Trans Ultrason Ferroelectr Freq Control 45(3):650–659

Insana M, Zagzebski J et al (1983) Improvements in the spectral difference method for measuring ultrasonic attenuation. Ultrason Imaging 5(4):331–345

Insana MF, Wagner RF et al (1990) Describing small-scale structure in random media using pulse-echo ultrasound. J Acoust Soc Am 87(1):179–192

Kim H, Varghese T (2007) Attenuation estimation using spectral cross-correlation. IEEE Trans Ultrason Ferroelectr Freq Control 54(3):510–519

Kim H, Varghese T (2008) Hybrid spectral domain method for attenuation slope estimation. Ultrasound Med Biol 34(11):1808–1819

Kuc R (1980) Clinical application of an ultrasound attenuation coefficient estimation technique for liver pathology characterization. IEEE Trans Biomed Eng BME 27(6):312–319

Kuc R (1984) Estimating acoustic attenuation from reflected ultrasound signals: comparison of spectral-shift and spectral-difference approaches. IEEE Trans Acoust Speech Signal Process 32(1):1–6

Kuc R, Schwartz M (1979) Estimating the acoustic attenuation coefficient slope for liver from reflected ultrasound signals. IEEE Trans Sonics Ultrason 26(5):353–361

Labyed Y (2010) Optimization and application of ultrasound attenuation estimation algorithms. PhD Electrical and computer engineering. Iowa State University, Ames, 179

Labyed Y, Bigelow TA (2010) Estimating the total ultrasound attenuation along the propagation path by using a reference phantom. J Acoust Soc Am 128(5):3232–3238

Labyed Y, Bigelow TA (2011) A theoretical comparison of attenuation measurement techniques from backscattered ultrasound echoes. J Acoust Soc Am 129(4):2316–2324

Ladabaum I, Xuecheng J et al (1998) Surface micromachined capacitive ultrasonic transducers. IEEE Trans Ultrason Ferroelectr Freq Control 45(3):678–690

Nam K, Zagzebski JA et al (2011) Simultaneous backscatter and attenuation estimation using a least squares method with constraints. Ultrasound Med Biol 37(12):2096–2104

Narayana PA, Ophir J (1983a) A closed form method for the measurement of attenuation in nonlinearly dispersive media. Ultrason Imaging 5:17–21

Narayana PA, Ophir J (1983b) On the validity of the linear approximation in the parametric measurement of attenuation in tissues. Ultrasound Med Biol 9(4):357–361

Oelze ML (2007) Bandwidth and resolution enhancement through pulse compression. IEEE Trans Ultrason Ferroelectr Freq Control 54(4):768–781

Oelze ML, O'Brien WD Jr (2002) Frequency-dependent attenuation-compensation functions for ultrasonic signals backscattered from random media. J Acoust Soc Am 111(5):2308–2319

Oelze ML, O'Brien WD Jr (2006) Application of three scattering models to characterization of solid tumors in mice. Ultrason Imaging 28(2):83–96

Oosterveld BJ, Thijssen JM et al (1991) Ultrasound attenuation and texture analysis of diffuse liver disease: methods and preliminary results. Phys Med Biol 36(8):1039–1064

Parker KJ, Waag RC (1983) Measurement of ultrasonic attenuation within regions selected from B-Scan images. IEEE Trans Biomed Eng BME 30(8):431–437

Parker KJ, Lerner RM et al (1988) Comparison of techniques for in vivo attenuation measurements. IEEE Trans Biomed Eng 35(12):1064–1068

Yao LX, Zagzebski JA et al (1990) Backscatter coefficient measurements using a reference phantom to extract depth-dependent instrumentation factors. Ultrason Imaging 12(1):58–70

Chapter 5
Quantitative Ultrasound and Cell Death

Omar Falou, Ali Sadeghi-Naini, Azza Al-Mahrouki, Michael C. Kolios and Gregory J. Czarnota

Abstract This chapter surveys the structural and physical changes that occur during cell death along with novel non-invasive techniques recently developed for the detection of such changes utilizing mid- to high-frequency ultrasound. Cell death introduces structural changes in the cell's nucleus including nuclear condensation and fragmentation. These result in differentiable echogenicities of living cells and cells dying of programmed cell death (apoptosis). Quantitative ultrasound (QUS) methods have exhibited good capabilities to detect cell death, particularly apoptosis, resulting from exposure to anticancer therapies in cell pellets in vitro, in liver samples ex vivo, and in cancer mouse models in vivo. Experimental results demonstrate that there is a strong correlation between changes in ultrasound backscatter characteristics and tumor regions that have responded to treatment. Recent emerging data from clinical applications of this work have also

O. Falou · A. Sadeghi-Naini · A. Al-Mahrouki · G. J. Czarnota (✉)
Department of Radiation Oncology, and Physical Sciences, Sunnybrook Health Sciences Centre, and Sunnybrook Research Institute, 2075 Bayview Avenue, TB-064, Toronto, ON M4N 3M5, Canada
e-mail: Gregory.Czarnota@sunnybrook.ca

O. Falou
e-mail: Omar.Falou@sunnybrook.ca

A. Sadeghi-Naini
e-mail: Ali.Sadeghi-Naini@sunnybrook.ca

A. Al-Mahrouki
e-mail: Azza.Almahrouki@sunnybrook.ca

O. Falou · A. Sadeghi-Naini · A. Al-Mahrouki · G. J. Czarnota
Department of Radiation Oncology, University of Toronto, Toronto, ON, Canada

O. Falou · A. Sadeghi-Naini · A. Al-Mahrouki · M. C. Kolios · G. J. Czarnota
Department of Medical Biophysics, University of Toronto, Toronto, ON, Canada

M. C. Kolios
Department of Physics, Ryerson University, Toronto, ON, Canada
e-mail: mkolios@ryerson.ca

J. Mamou and M. L. Oelze (eds.), *Quantitative Ultrasound in Soft Tissues*, DOI: 10.1007/978-94-007-6952-6_5,

demonstrated that QUS techniques can distinguish between clinically responding or non-responding breast cancer patients during the course of neo-adjuvant treatment. As such, QUS at conventional frequencies is expected to provide rapid, non-invasive, and quantitative functional information, in real time for evaluating responses to a specific therapy.

Keywords Cancer · Treatment monitoring · Therapy response · Apoptosis · Quantitative ultrasound · Cell characterization · Tissue characterization

5.1 Introduction

The reality of cancer therapy is that there is no unique solution for all patients, and hence, cancer treatments include the use of chemotherapy drugs, ionized radiation, hormone therapy, immunotherapy, gene therapy, and surgery, or a combination of some of these treatments. Further, recent studies have shown that there are variations in responses to a given therapy from one patient to another due to the complexity of the biological systems (Notta et al. 2011). For instance, studies have demonstrated that the genetic variations in leukemia stem cells have led to the production of diverse cells, which in turn is the reason behind poorer therapy outcomes. In other types of cancers, resistance or desensitization to therapy is another challenge, which is caused by different factors such as the low level of reactive oxygen species in cancer stem cells (Diehn et al. 2009). Such challenges make it hard to follow one specific course of treatment with the hope of a good therapy outcome. This necessitates the need for an efficient early monitoring modality to effectively evaluate the response to treatment, which would ultimately improve the outcome of therapy by facilitating treatment customization. Imaging, in general, is non-invasive and cost effective approach that could have a significant impact in assessing and choosing the appropriate type of treatment in the early stages of the therapy, so the disease may be contained. This can be achieved through the detection of cell death using an imaging modality, which would reflect the level of response to a specific treatment. Cancer imaging is a very valuable tool when used in different cancer management stages, which include detection and monitoring of tumor progression under treatment (de Torres et al. 2007; Sarkeala et al. 2008; Lee et al. 2004; Ferme et al. 2005; Ashamalla et al. 2005; Brindle 2008; Keidar et al. 2004). This helps in providing physicians with informed clinical decision-making that can save lives. Advances in the various imaging modalities have allowed the quantification of a wide range of different cellular components that provide molecular, biochemical, functional, morphological, and structural information (Brindle 2008; Fass 2008; von Schulthess et al. 2006; Artemov et al. 2003; Sipkins et al. 1998). In this chapter, we will discuss subcellular changes that lead to gross morphological and structural alterations, and can be detected with quantitative methods in ultrasound imaging. We will also

review the advancements made in cancer imaging in general with specific focus on imaging cell death, particularly apoptosis. With special focus on the advances made to date in the detection and treatment monitoring using QUS, we will discuss recent in vitro, ex vivo, in vivo and clinical studies.

5.2 Apoptosis

Cellular transformation, where cell death pathways or tumor suppression genes are altered along with a failure of immunological control, can lead to malignancy. Numerous studies have targeted immunological (Quezada et al. 2011; Ferguson et al. 2011) and cell death signaling pathways (Denicourt and Dowdy 2004; Hunt and Evan 2001) as well as changes in oncogenes (Levine and Puzio-Kuter 2010; Visvader 2011) in order to control cancer. These therapies can induce multiple forms of cell death such as apoptosis, necrosis, autophagy and mitotic catastrophe. We will briefly discuss the different cellular changes involved with apoptotic cell death as it is a common pathway induced by many anti-cancer treatments.

Apoptosis or programmed cell death is a vital process in development and normal cell turnover. It is an essential cellular homeostatic mechanism in organs and tissues, and has a defense role in the function of the immune system as well as eliminating diseased cells. However, when this process is disrupted, it becomes a factor in different disease conditions, such as various cancers, neurodegenerative and auto-immune diseases (Elmore 2007; Ding et al. 2011; Burguillos et al. 2011; Chen et al. 2006). Different physiological or pathological stimuli can trigger apoptosis by inducing various pathways in cells, which explains why not all cells exposed to the same stimulus will undergo apoptosis. Regardless of the stimuli or the pathway, complex cascades lead to the production of a number of cysteine proteases (caspases) that result in the demise of cells. This process is accompanied by several morphological changes that include the condensation of cells and their chromatin, where the cytoplasm becomes dense and the cellular organelles are tightly packed. Membrane blebbing follows and the cellular fragments separate into apoptotic bodies (Fig. 5.1). Chromatin is cleaved into fragments by specific enzymes resulting in apoptotic laddering. The formed apoptotic bodies are then engulfed by macrophages or neighboring cells and thus the cellular fragments are not released into the interstitial surroundings nor are anti-inflammatory cytokines produced (Zullig and Hengartner 2004). Furthermore, tumorigenesis is related to resistance to apoptosis, which can translate to resistance to anti-cancer therapies.

Inducing apoptosis alone has proved not to be the only solution in cancer treatment, indicating a role for non-apoptotic mechanisms such as autophagy and mitotic catastrophe (Hanahan and Weinberg 2011) all of which result in necrosis (dead cells). In mitotic catastrophe, which can be induced by mitotic-arresting drugs such as taxotere or ionizing radiation, which interfere with mitotic spindle formation, nuclear material undergoes irreversible condensation of chromatin (pyknosis) with multiple genome copies of material accumulating in cells that

Fig. 5.1 Morphological changes of apoptotic cells. **a** Human umbilical vein endothelial cells (HUVEC) exposed to ultrasound activated microbubbles and ionizing radiation to induce apoptosis (scale bar = 5 μm), **b** Hematoxylin and eosin straining of a section from prostate xenograft tumor; treated similarly, and **c** TUNEL staining of a section from prostate xenograft tumor; treated as in **b**; *arrows* in both **b** and **c** point to apoptotic cells, and scale bars = 50 μm

survive. Cells that die after mitotic catastrophe go on to die either through apoptosis or non-apoptotic death. In autophagy, cells digest themselves and are characterized by clustering of the phagolysosome membrane-associated protein LC3. These different forms of cellular changes, which are associated with malignant tumor cells and the targeted therapies, are manifested through different characteristic morphological modifications which result in cells adopting different physical properties. The associated cellular changes therefore can be detected with different imaging modalities both in vitro and in vivo, and will be discussed further in this chapter in the context of imaging.

5.3 Advances in the Detection of Cell Death Using Different Imaging Modalities

The earlier the evaluation of a cancer treatment outcome, the better is the prognosis for patients because treatment alterations can be made or salvage regimens instituted, especially in aggressive diseases such as lung or brain cancers. Alteration and deregulation of cell death is characteristic of cancer; therefore, many cancer therapies induce different forms of cell death including apoptosis. In order to assess the effectiveness of a therapy non-invasively by monitoring cellular changes, a number of imaging modalities have been investigated. This includes positron emission tomography (PET), where a number of radiolabeled PET tracers are being developed to target cell proliferation and apoptosis (Nguyen and Aboagye 2010). Evading apoptosis has been described as being a hallmark of cancer (Evan and Vousden 2001), whereas inducing apoptosis is an important therapeutic approach. Apoptosis, as described earlier, is characterized by morphological changes that include cell shrinkage, membrane blebbing, condensation of chromatin, and the formation of apoptotic bodies. The morphological changes are the outcome of various molecular and biochemical changes that include: (1) the activation of death receptors or mitochondrial effectors to activate caspases, and (2) the exposure of plasma membrane phosphatidylserine, which consequently label cells for clearance by phagocytes. Based on the biochemical changes in apoptotic cells, a number of PET probes have been developed such as Annexin-V, a protein that binds to phosphatidylserine (Blankenberg 2008). Another molecular imaging approach to detect cellular changes is single photon emission computed tomography (SPECT), which is similar to PET imaging by using an optical or radioisotope labeled reporting molecule, but with less sensitivity. Combined modality imaging using SPECT/CT has also been utilized. A recently characterized tracer, 4-(N-(S-glutathionylacetyl)amino) phenylarsonous acid (GSAO), which is abundant in the cytosol of dying cells and binds covalently to Hsp90, was shown to identify cell death with high sensitivity compared to other tracers when scanned with SPECT/CT (Park et al. 2011). Using MRI to image apoptosis has also been investigated (Blankenberg 2008; Zhao et al. 2001; Schellenberger et al. 2002; Vangestel et al. 2011; Hiller et al. 2006; Bailey et al. 2009), where Gd-DTPA-labeled annexin V was used to detect apoptosis. Although the above described modalities are not invasive, they employ the use of radioisotope probes that can be limited in their use, and need to be fully evaluated before use in clinical trials. As such, imaging of cell death without using a contrast agent or a tracer is favorable, and the use of diffusion-weighted MRI (DWI) is an alternative (Blankenberg 2008; Charles-Edwards and deSouza 2006). Other methods that do not require contrast agents, such as ultrasound, rely on the microstructural changes associated with cell death to generate the contrast being detected.

Clinical ultrasound imaging is the most frequently used imaging modality in the world accounting for almost 25 % of all imaging procedures (Forsberg 2004). Ultrasound imaging has the advantage of low cost, rapid imaging speed, portability

and high spatial resolution. Unlike many clinical imaging modalities that are based on the contrast-agent interaction with body fluids or tissues; diagnostic ultrasound is based on the scattering and reflection of acoustic waves and does not have adverse bioeffects. However, despite its safety and popularity, relatively unsophisticated pulse echo techniques are still the basis of this imaging modality. Advances in ultrasound instrumentation over the last decade have led to the rapid expansion of clinical ultrasound. Furthermore, new developments in transducer technology have increased available frequencies to 20–80 MHz providing better image spatial resolution at the expense of reduced ultrasound penetration depth. The associated ultrasound wavelengths and resultant spatial resolutions are 20–75 μm, on the order of the size of cells. Nevertheless, individual cells cannot be resolved but the speckle pattern visualized in ultrasound images is a result of constructive and destructive interference effects which are related to cellular structure. This suggests an increased sensitivity to statistical features related to the structure, size and organization of cells. For over two decades it has been known that the necrotic core of living spheroids has an increased ultrasound echogenicity that can be detected using high-frequency ultrasound as shown in Fig. 5.2 (Sutherland 1988; Sherar et al. 1987). Such increases were not produced by the introduction of exogenous contrast agents as required by many other imaging modalities, but rather by the mechanism of cell death itself. This was confirmed by analyzing histology of regions of cell death which correlated well with regions of

Fig. 5.2 Ultrasound images of MCF-7 spheroids taken with 25 (*top*) and 55 (*bottom*) MHz transducers using the VEVO 770 ultrasound scanner. B-scan images (x–z plane) in the *left* hand panel, and two c-scan images (x–y planes, *middle* and *right* panels, chosen within *red* area denoted in *dotted line* in B-scan images) at different depths. Images illustrate an increased echogenicity (>6 dB) for both 25 and 55 MHz transducer data, illustrating contrast between necrotic and viable spheroid regions (scale bar = 100 μm)

increased ultrasound signal intensity. These early investigations were a precursor to specific studies on apoptotic cell death and quantitative analyses using specialized methods in spectroscopic signal analysis of ultrasound signals.

5.4 Quantitative Ultrasound Techniques

Conventional ultrasound produces images related to tissue echogenicity. Changes in image brightness may occur as a result of tissue properties but like any medical imaging device can be affected by instrument parameters which can be modified from imaging session to imaging session. This makes it extremely difficult to compare images between different ultrasound machines and even for the same machine when different settings are used. Another major disadvantage of conventional ultrasound is its high degree of user dependence since it requires specialized education in image optimization techniques and proper understanding of the interactions that occur between the ultrasonic beam and the organs. Quantitative parameters based on the ultrasound-backscatter radiofrequency (RF) have been developed in order to eliminate instrument dependence and to provide low levels of user dependence. In addition, QUS techniques have aimed to increase the diagnostic sensitivity and specificity of ultrasound, thus providing more functional imaging rather than classic grayscale anatomical-based imaging (Guglielmi et al. 2009; McPherson 1991; Skorton and Collins 1988). Early parameters investigated include integrated backscatter (related to image intensity), ultrasound attenuation, and speed of sound. Because the last two parameters are difficult to measure in vivo, another method of characterization relies on the characterization of tissue power spectra, normalized to correct for the effect of the system transfer function, as developed by the late Lizzi et al. (1997, 1983). While both approaches analyze the same backscattered signal, the latter is more suitable for in vivo imaging. Moreover, attenuation and speed of sound are more dependent on molecular tissue composition than backscatter, which is more dependent on tissue structure rather than molecular composition (Sarvazyan and Hill 2004) making it more suitable for the detection of gross morphological changes that accompany cell death. QUS methods originally developed at lower frequencies, and later applied at high frequencies to cell death, can be classified as either spectroscopic or methods that examine the statistics of the backscattered signal intensity. Ultrasound backscatter spectroscopy can be used to estimate tissue acoustic parameters through analysis of the frequency (spectral) content of backscattered signals (Lizzi et al. 1996, 1997) which are related to the tissue microstructure (Feleppa et al. 1986; Mamou et al. 2005). In addition, researchers have been able to estimate the size, shape and acoustic properties of “effective” scatterers in tissue utilizing theoretical models (Insana 1995, 1996). Changes in the size and/or acoustical parameters of scatterers are reflected in the power spectra. These methods were first applied clinically in the 1970s to applications other than cell death, with limited success due to relatively early imaging equipment, limited computational resources needed for

performing digital signal processing and poorly controlled biology. Moreover, many of these investigations were attempting to detect benign from malignant tissue which is a more subtle and complex problem because there are less apparent differences between normal and malignant tissue than between viable and dead tissue. In the majority of work published on the use of ultrasound to detect cell death, higher frequencies are used to detect differences in cell morphology (living versus apoptotic or necrotic). We hypothesized that the use of mid- to high-frequency ultrasound, with wavelengths on the order of the size of cells, make quantitative ultrasound more sensitive to cell structure and the spatial distribution of cells, and therefore to the structural changes that occur during cell death. However, recent evidence also demonstrates that conventional frequency ultrasound may be used to detect cell death. Much of the preliminary research conducted at high-frequency and now low-frequency has relied on pre-clinical in vitro research conducted using centrifuged cell-pellet models as a model system for in vivo tumors, with comparisons of observed scattering to theory.

In terms of theory, two general approaches have been used to model ultrasound backscatter: continuous and discrete (Mo and Cobbold 1992). In the discrete model, backscattered wavelets from discrete weak scatterers are coherently summed at the ultrasonic source to generate the total backscattered signal. In the continuous model, because there are many scatterers in the resolution volume of an ultrasound transducer, the medium is modeled as a continuum for which fluctuations of tissue density and compressibility give rise to the scatter. In the case of the continuum model, a correlation length can be estimated from the backscattered power spectrum, which can be related to an effective scatterer size (Oelze and O'Brien 2002). In the discrete approach, the backscattered power spectrum can be inverted to provide estimates of the scatterer properties, such as an effective scatterer size. The continuum model requires randomly spaced scatterers and many scatterers per resolution cell in order to provide scatterer property estimates from theory. While most analysis to date of scattering from tumors and cells have utilized a continuum model for estimation of scatterer properties, the idea that cells are the prominent source of scattering in tumors suggests that a discrete model may better describe the generation of the backscattered signal.

For complex structures like tissue, the extracellular matrix, nerves, blood vessels and lymphatics may play a role in tumor backscatter. However, of key importance is the observation, by our group and others (Oelze and Zachary 2006; Oelze and O'Brien 2006), that for tumors with high cellular content, ultrasound backscatter from pellets of cells exhibit similar frequency-dependent ultrasound backscatter as xenograft tumors in mice formed from the same cell type (Fig. 5.3). This attests to the suitability of cell pellet models for investigating the basic biophysical mechanisms of scattering, i.e., it is a good model used in numerous studies for investigating tumor ultrasound scattering (Taggart et al. 2007).

In the context of the work described below, quantitative ultrasound parameters were calculated as follows: RF data within the region-of-interest (ROI) were obtained and multiplied by a Hamming function to suppress undesired spectral lobes. The power spectrum calculated using a Fourier transform of the resultant

Fig. 5.3 Normalized power spectra, hematoxylin and eosin stains and ultrasonic images for FaDu derived tumor cells: a viable cell pellet sample and tumor xenograft. **a** Normalized power spectra compensated for frequency dependent attenuation within the intervening sample, computed from FaDu tumor (*solid*) and cell sample (*dotted*). **b** Hematoxylin and eosin staining for a section through a FaDu cell sample and **c** FaDu tumor. The scale bar = 20 μm. **d** Ultrasonic images for FaDu viable cell sample and **e** Tumor xenograft. Gains are not similar in the two images, but in **a** the scattering strength can be compared as the data are normalized. The scale bar = 1 mm. Adapted from Vlad (2009)

data for each line segment within the ROI and subsequently averaged. The resulting power spectrum was divided by the power spectrum computed from a flat quartz calibration plate (in vitro, in vivo data, and ex vivo data) or a glass bead phantom (human data) to remove the effects of system and transducer transfer functions and to calculate the normalized power spectrum. The integrated

backscatter and integrated backscatter coefficient were calculated by integrating the normalized power spectrum and the frequency-dependent backscatter coefficient (Turnbull et al. 1989) over the −6 dB bandwidth of the transducer, respectively. Linear regression analysis was performed within the −6 dB bandwidth to calculate the spectral slope of the best fit line, its mid-band fit, and corresponding 0-MHz intercept described by the ultrasonic spectrum analysis framework (Lizzi et al. 1983, 1997). The backscatter amplitudes were calculated by multiplying the pixel intensities in the B-mode image by the inverse of the transfer function of the ultrasound instrument provided by the manufacturer (Czarnota et al. 1997). The backscattered signal intensity was estimated by averaging the pixel intensities in the B-mode image (Kolios et al. 2003).

5.5 Quantitative Ultrasound Detection of Cell Death

The majority of work in QUS has been focused on tissue characterization (Mamou et al. 2006; Oelze et al. 2004; Takiuchi et al. 2000; Vered et al. 1987). The use of QUS techniques for the detection of morphological changes associated with cell death is a new advancement (Kolios et al. 2002). Early work on acute myeloid leukemia (AML) cell pellets (tightly packed aggregates of cells) in vitro exposed to the chemotherapeutic agent cisplatin and imaged at high frequency ultrasound (20–60 MHz) has demonstrated large increases (up to ∼6 folds) in the ultrasound backscatter amplitude 24 h after exposure associated with cell death (Czarnota et al. 1997, 1999). Further work has demonstrated that treated regions can clearly be differentiated from untreated ones due to the changes in ultrasound backscattered signal intensity as shown in Fig. 5.4 (Kolios et al. 2003). The sensitivity of the ultrasound detection method to the number of cells responding to treatment was assessed by mixing treated acute myeloid leukemia cells with untreated cells to form mixtures containing 0, 2.5, 5, 10, 20, 40, 60, 80 and 100 % treated cells (not all the treated cells respond to the treatment; therefore, the percentages represent an upper bound to the concentration of treated cells). It was found that the ultrasound technique could differentiate between untreated cells and a mixture of 2.5 % treated cells, indicating that the technique is sensitive to very low levels of apoptosis (Tunis et al. 2005). The application of this technique to liver samples ex vivo demonstrated a strong correlation between ischemic cell death and increases in the integrated backscatter (4–9 dBr) (Vlad et al. 2005). In addition, we have applied the ultrasonic characterization techniques to several cell lines to examine how integrated backscatter coefficient, attenuation and speed of sound were dependent on cell structure. Integrated backscatter coefficient, attenuation and speed of sound were estimated through measurements from cell pellets using a novel container. The data strongly suggest that integrated backscatter coefficient is correlated with the size of the nucleus in these experiments (Taggart et al. 2007). This finding is of particular significance because the nucleus is the cell organelle that undergoes the most significant changes when the cell undergoes apoptosis and

Fig. 5.4 Ultrasonic images (8 × 8 mm) of a three layer AML pellet (normal-treated-normal) using the **a** 20 MHz and **b** 40 MHz transducers (scale bars = 1 mm). The treated layer can clearly be differentiated due to the increase in the backscattered signal intensity (~11 dB). The *bottom row* shows hematoxylin and eosin stains of the pellet from the boundary between the unexposed top and cisplatin exposed middle layers **c** Nuclear condensation and cytoskeletal disruption can be seen in the treated region on the *left* hand side of the Hematoxylin and eosin stain. There is excellent correspondence between the area of treated and untreated cells and backscatter increase. In panel **b** the *bottom layer* could not be visualized due to the ultrasound attenuation effect. The scale bar = 20 μm. Adapted from Kolios et al. (2003)

other forms of cell death. The same techniques were applied to several cancers in vivo using different treatment methods to test the robustness of the ultrasound techniques and applicability in other cell lines. In recent work, we have demonstrated that these techniques may be used to differentiate between responding and non responding regions within a tumor in animal models (Banihashemi et al. 2008; Vlad et al. 2009). Moreover, we have shown that despite the existence of other structures within the tumor (e.g., blood vessels or lymphatics), these techniques may be used to non-invasively monitor treatment. Time-dependent increases in mid-band fit, consistent with increases in ultrasound backscattered signal intensity, at high ultrasound frequency were observed in xenograft malignant melanoma tumors after photodynamic therapy (Banihashemi et al. 2008). Such increases correlated well with morphological changes associated with apoptotic cell death after treatment. Similar experiments were conducted on xenograft tumors in vivo

Fig. 5.5 Ultrasound imaging of in vivo tumor response to radiation. Ultrasound images of C666-1 tumors presenting areas with increased echogenicity at 24 after treatment and corresponding to the areas of cell death indicated in TUNEL staining (**a**, **b**). 0 Gy signifies the image before treatment. (**c**) A particular case of another tumor type (FaDu) in which a portion of the tumor exhibited increased echogenicity that corresponded very well with the TUNEL staining (scale bar = 1 mm). In many cases (depending on the tumor type) such variable responses are seen (scale bar = 500 μm) (**d**) High scale magnifications of region in *black box* in part (**c**) illustrate pattern of cell death, similar to that seen in the cell pellet system; scale bar = 100 μm. Adapted from Vlad et al. (2009)

imaged at 10–30 MHz after radiotherapy (Vlad et al. 2009). Large hyperechoic regions appeared in two mouse models (FaDu and C666-1) at 24 h after treatment as demonstrated in Fig. 5.5. In these models, the integrated backscatter increased by 6.5 and 8.2 dBr for the FaDu and C666-1 tumors, respectively. The spectral slopes increased from 0.54 to 0.78 dBr/MHz for the FaDu tumors and from 0.77 to 0.90 dBr/MHz for the C666-1 tumors, in these regions compared with pre-treatment tumors. The hyperechoic regions in the ultrasound images in such studies have corresponded to areas of cell death assessed by histology. This further indicates that ultrasound imaging may potentially be used as a non-invasive technique for treatment monitoring.

5.6 Emerging Clinical Studies

QUS has recently been proposed for imaging cancer therapy response which can facilitate personalized medicine in cancer treatment procedures. Personalized medicine is predicated on changing an ineffective therapy to one which is more efficacious for a specific patient. Therapy response monitoring using appropriate imaging methods is paramount in personalized medicine. In cancer treatment, standard anatomical based imaging can detect macroscopic changes in tumor size but these often take many weeks to months to develop. Functional imaging methods which probe tumor physiology have recently been demonstrated capable of detecting tumor responses from days to weeks after starting therapy. They could be used to non-invasively guide changes in treatment, after days of use instead of waiting many months, in order to optimize the chances of cure.

Patients with locally advanced breast cancer (LABC) represent a typical patient population which could highly benefit from changing ineffective therapies to more efficacious treatments. Locally advanced breast cancer is an aggressive form of breast cancer which continues to have poor outcomes despite the development of new therapies. LABC has variable definitions, including Stage III or inoperable disease. This cancer accounts for 5–20 % of all new breast cancer diagnosed in North America (American Cancer Society 2007; Mankoff et al. 1999; Giordano 2003). Most of the fatalities are young women typically between 20 and 45 years old with large bulky inoperable breast cancers and represent a majority of the years-lost-to-disease in breast cancer due to their young age. LABC carries a much poorer prognosis compared to early stages with only 55 % of LABC patients surviving at 5 years because of the high risk for metastatic spread (Giordano 2003). Also, despite aggressive therapeutic combinations including chemotherapy, surgery and radiation treatment (RT) the loco-regional recurrence rate remains high at 10–20 % (Giordano 2003). LABC is often inoperable and current guidelines recommend treatment "up-front" with aggressive neo-adjuvant chemotherapy. The neo-adjuvant therapy is then followed by surgery that is generally a mastectomy with axillary nodal clearance, followed by radiotherapy and possibly Herceptin and/or hormonal manipulation if indicated (De Lena et al. 1981; Esteva and Hortobagyi 1999; Hortobagyi 1990). Clinical and pathological complete responses to neo-adjuvant chemotherapy have been reported by several groups as an important marker of better outcomes, with survival rates reaching 70 % (Chollet et al. 1997; Smith et al. 2002). However, response to the neo-adjuvant treatment is assessed clinically over the course of several months, relying on subjective measurement of the palpable tumor size. Unfortunately, this is an unreliable measure and a poor predictor of residual disease and patient outcome. Changes in palpable tumor size often occur late in treatment regimens (months) whereas functional changes in tumor physiology, can occur much earlier (weeks). A reliable measure of tumor response soon after the initiation of treatment, e.g., apoptosis, would allow treatment to be tailored. This would enable the selection of more effective therapy

earlier, in order to better control not only the primary disease but also metastatic spread during treatment, and thus improve patient outcomes.

Various imaging modalities have recently been developed to evaluate treatment response (Brindle 2008; Sadeghi-Naini et al. 2012a). Diffuse optical imaging (DOI), using near-infrared light to provide functional information related to tissue microstructure and biomechanical composition, has been shown to predict tumor response in breast cancer patients undergoing neo-adjuvant within 1–4 weeks after treatment initiation (Cerussi et al. 2007; Soliman et al. 2010). However, this technique may only be applied to tissues with low attenuation, such as brain and breast. Dynamic contrast-enhanced magnetic resonance imaging (DCE-MRI) is sensitive to tissue microvasculature changes and can be used to assess the effectiveness of tumor treatments (Padhani and Husband 2001). However, its utility in treatment monitoring is limited due to lack of a standard quantification approach. Radionuclide imaging has been shown to detect treatment response with high sensitivity and specificity (Kim et al. 2004). This technique, however, remains limited due to the high cost of radionuclides production. Finally, dynamic contrast-enhanced ultrasound (DCE-US) using microbubbles can measure blood perfusion and is hence used to monitor tumor response (Lamuraglia et al. 2010). However, clinical approval of microbubbles is still pending in many countries. The need for an accessible imaging methodology of treatment monitoring has motivated researchers to consider QUS which was previously demonstrated capable of probing apoptosis in this context (Fig. 5.6). In contrast with other imaging modalities, ultrasound imaging and therefore QUS imaging, have the advantage of low cost, rapid imaging speed, portability and high spatial resolution. Moreover, as stated earlier, unlike the other modalities being investigated for treatment monitoring, no injections of contrast agents are needed because the image contrast and changes in normalized power spectrum are caused by changes in the physical properties of dying cells.

QUS at conventional frequencies has recently been applied in our research laboratory for the evaluation of tumor cell death response in LABC patients receiving neo-adjuvant chemotherapy (Sadeghi-Naini et al. 2013). Conventional ultrasound data were acquired prior to treatment onset and at four times during treatment. Several QUS parameters were applied as measures of tumor response during the course of neo-adjuvant treatment. The parameters included spectral slope, 0-MHz intercept, mid-band fit (Lizzi et al. 1983, 1997; Feleppa et al. 1986; Oelze and O'Brien 2002), and parameters associated with fitting the Rayleigh (Molthen et al. 1998) and Generalized Gamma (Tunis et al. 2005) distributions to the RF signal envelope. Obtained results ($n = 24$ patients) have demonstrated a close association between average changes in QUS parameters after one to two cycles of chemotherapy (few weeks) and clinical response in the tumor many months later. More specifically, patients who had a significant clinical response demonstrated considerable changes in mean values of QUS parameters consistent with cell death, while women with no substantial changes in QUS parameters demonstrated no ultimate clinical response (Fig. 5.7). In addition, texture analysis techniques on QUS parametric maps are currently being investigated. The preliminary results obtained suggested that these techniques may distinguish between

Fig. 5.6 Parametric imaging of breast tumors. These panels demonstrated the feasibility of using ultrasound to image breast cancer and to monitor treatment responses. Panel **a** presents clinical ultrasound data from a woman with a large locally-advanced breast cancer, imaged at 10 MHz. The focus is set at 1.75 cm depth and the total field of view is 4 cm. The skin is at the top of the image. The *blue line* outlines the radiological extent of disease which shows a central mass with spiculated extensions. Panel **b** shows a magnified view of panel **a** reconstructed from the raw RF data. The *left panel* is from the same patient imaging session as in Panel **a** whereas the *right panel* shows the same nominal region one week after the administration of Adriamycin-Cyclophosphamide chemotherapy. Panel **c** shows mid-band fit parametric overlays on both images. There is a 5 dBr increase in mean backscatter mid-band fit over the region of interest. This is consistent with experiments in vitro in pre-clinical models where cell death is concurrently detected. Scale bars in **b** and **c** = 0.5 cm

clinically responding and non-responding patients more robustly (Sadeghi-Naini et al. 2012b). Texture analysis techniques provide second order statistics for the parametric maps through a number of textural parameters such as energy, correlation, contrast, and homogeneity (Haralick et al. 1973). As observed in Fig. 5.7, textural changes are clearly detectable in the 0-MHz parametric maps generated for the clinically responding patient, whereas they remain negligible in the case of

Fig. 5.7 Monitoring tumor cell death response in LABC patients receiving neo-adjuvant chemotherapy using conventional frequency QUS. **a**, **b**: Representative parametric 0-MHz intercept images of a large tumor during neo-adjuvant chemotherapy for a **a** clinically responding patient, **b** clinically non-responding patient (scale bars = 1 cm.). Scans 1, 2, 3, and 4 are pre-treatment, week 1, week 4, and week 8 scans, respectively. In the clinically responding patient the continuous changes are detectable in the 0-MHz intercept images over the course of treatment. In the case of the clinically non-responding patient there is no striking change in the 0-Mhz intercept during the majority of therapy compared to the case of clinically responding patient. **c** The whole mount histopathology corresponding to the clinically responding patient indicates just a small residual mass in the mastectomy specimen (10 cm wide). **d** The whole mount histopathology corresponding to the clinically non-responding patient indicates a large compact residual mass in the mastectomy specimen (8 cm wide). Adopted from Sadeghi-Naini et al. (2012a)

clinically non-responding patient during the course of neo-adjuvant chemotherapy. These early findings indicate that QUS can potentially be used to non-invasively monitor treatment response in patients.

5.7 Concluding Remarks

In summary, we have demonstrated that the amplitude and the frequency dependence of the ultrasonic backscatter are sensitive to the structural and physical changes that cells undergo during cell death. During apoptosis induced by exposure to cisplatin or cell death due to radiation exposure, the ultrasonic backscatter

amplitude of in vitro samples has been demonstrated to increase by a factor of four creating a large contrast between treated and untreated regions. Similar ultrasonic contrast between normal and damaged tissues has also been detected in other models of tissue damage/remodeling ex vivo, e.g., organ preservation. In vivo, we have demonstrated that there is an excellent correspondence between tumor regions that have responded to treatment and the changes in the ultrasonic backscatter characteristics similar to those observed in vitro. Recently, we have investigated clinical applications for the ultrasonic detection of breast tumor cell death in LABC patients undergoing neo-adjuvant chemotherapy. Results have demonstrated that QUS techniques may distinguish between clinically responding or non-responding patients early during the course of neo-adjuvant treatment. These promising results pave the way for establishing protocols for the clinical applications of the conventional frequency QUS techniques in therapy response monitoring.

References

American Cancer Society (2007) Cancer facts and figures 2007. American Cancer Society, Atlanta

Artemov D, Mori N, Ravi R, Bhujwalla ZM (2003) Magnetic resonance molecular imaging of the HER-2/neu receptor. Cancer Res 63(11):2723–2727

Ashamalla H, Rafla S, Parikh K, Mokhtar B, Goswami G, Kambam S, Abdel-Dayem H, Guirguis A, Ross P, Evola A (2005) The contribution of integrated PET/CT to the evolving definition of treatment volumes in radiation treatment planning in lung cancer. Int J Radiat Oncol Biol Phys 63(4):1016–1023

Bailey C, Giles A, Czarnota GJ, Stanisz GJ (2009) Detection of apoptotic cell death in vitro in the presence of Gd-DTPA-BMA. Magn Reson Med 62(1):46–55

Banihashemi B, Vlad R, Debeljevic B, Giles A, Kolios MC, Czarnota GJ (2008) Ultrasound imaging of apoptosis in tumor response: novel preclinical monitoring of photodynamic therapy effects. Cancer Res 68(20):8590–8596

Blankenberg FG (2008) In vivo detection of apoptosis. J Nucl Med 49(Suppl 2):81S–95S

Brindle K (2008) New approaches for imaging tumour responses to treatment. Nat Rev Cancer 8(2):94–107

Burguillos MA, Deierborg T, Kavanagh E, Persson A, Hajji N, Garcia-Quintanilla A, Cano J, Brundin P, Englund E, Venero JL, Joseph B (2011) Caspase signalling controls microglia activation and neurotoxicity. Nature 472(7343):319–324

Cerussi A, Hsiang D, Shah N, Mehta R, Durkin A, Butler J, Tromberg BJ (2007) Predicting response to breast cancer neoadjuvant chemotherapy using diffuse optical spectroscopy. Proc Natl Acad Sci USA 104(10):4014–4019

Charles-Edwards EM, deSouza NM (2006) Diffusion-weighted magnetic resonance imaging and its application to cancer. Cancer Imaging 6:135–143

Chen M, Wang YH, Wang Y, Huang L, Sandoval H, Liu YJ, Wang J (2006) Dendritic cell apoptosis in the maintenance of immune tolerance. Science 311(5764):1160–1164

Chollet P, Charrier S, Brain E, Cure H, van Praagh I, Feillel V, de Latour M, Dauplat J, Misset JL, Ferriere JP (1997) Clinical and pathological response to primary chemotherapy in operable breast cancer. Eur J Cancer 33(6):862–866

Czarnota GJ, Kolios MC, Vaziri H, Benchimol S, Ottensmeyer FP, Sherar MD, Hunt JW (1997) Ultrasonic biomicroscopy of viable, dead and apoptotic cells. Ultrasound Med Biol 23(6):961–965

Czarnota GJ, Kolios MC, Abraham J, Portnoy M, Ottensmeyer FP, Hunt JW, Sherar MD (1999) Ultrasound imaging of apoptosis: high-resolution non-invasive monitoring of programmed cell death in vitro, in situ and in vivo. Br J Cancer 81(3):520–527

De Lena M, Varini M, Zucali R, Rovini D, Viganotti G, Valagussa P, Veronesi U, Bonadonna G (1981) Multimodal treatment for locally advanced breast cancer. Result of chemotherapy-radiotherapy versus chemotherapy-surgery. Cancer Clinical Trials 4(3):229–236

de Torres JP, Bastarrika G, Wisnivesky JP, Alcaide AB, Campo A, Seijo LM, Pueyo JC, Villanueva A, Lozano MD, Montes U, Montuenga L, Zulueta JJ (2007) Assessing the relationship between lung cancer risk and emphysema detected on low-dose CT of the chest. Chest 132(6):1932–1938

Denicourt C, Dowdy SF (2004) Medicine. Targeting apoptotic pathways in cancer cells. Science 305(5689):1411–1413

Diehn M, Cho RW, Lobo NA, Kalisky T, Dorie MJ, Kulp AN, Qian D, Lam JS, Ailles LE, Wong M, Joshua B, Kaplan MJ, Wapnir I, Dirbas FM, Somlo G, Garberoglio C, Paz B, Shen J, Lau SK, Quake SR, Brown JM, Weissman IL, Clarke MF (2009) Association of reactive oxygen species levels and radioresistance in cancer stem cells. Nature 458(7239):780–783

Ding Z, Wu CJ, Chu GC, Xiao Y, Ho D, Zhang J, Perry SR, Labrot ES, Wu X, Lis R, Hoshida Y, Hiller D, Hu B, Jiang S, Zheng H, Stegh AH, Scott KL, Signoretti S, Bardeesy N, Wang YA, Hill DE, Golub TR, Stampfer MJ, Wong WH, Loda M, Mucci L, Chin L, DePinho RA (2011) SMAD4-dependent barrier constrains prostate cancer growth and metastatic progression. Nature 470(7333):269–273

Elmore S (2007) Apoptosis: a review of programmed cell death. Toxicol Pathol 35(4):495–516

Esteva FJ, Hortobagyi GN (1999) Locally advanced breast cancer. Hematology/Oncology Clinics of North America 13(2):457–472, vii

Evan GI, Vousden KH (2001) Proliferation, cell cycle and apoptosis in cancer. Nature 411(6835):342–348

Fass L (2008) Imaging and cancer: a review. Mol Oncol 2(2):115–152

Feleppa EJ, Lizzi FL, Coleman DJ, Yaremko MM (1986) Diagnostic spectrum analysis in ophthalmology: a physical perspective. Ultrasound Med Biol 12(8):623–631

Ferguson TA, Choi J, Green DR (2011) Armed response: how dying cells influence T-cell functions. Immunol Rev 241(1):77–88

Ferme C, Vanel D, Ribrag V, Girinski T (2005) Role of imaging to choose treatment. Cancer Imaging 5 Spec No A:S113–S119

Forsberg F (2004) Ultrasonic biomedical technology; marketing versus clinical reality. Ultrasonics 42(1–9):17–27

Giordano SH (2003) Update on locally advanced breast cancer. Oncologist 8(6):521–530

Guglielmi G, Adams J, Link TM (2009) Quantitative ultrasound in the assessment of skeletal status. Eur Radiol 19(8):1837–1848

Hanahan D, Weinberg RA (2011) Hallmarks of cancer: the next generation. Cell 144(5):646–674

Haralick RM, Shanmuga K, Dinstein I (1973) Textural features from image classification. IEEE Trans Syst Man Cybern SMC3(6):610–621

Hiller KH, Waller C, Nahrendorf M, Bauer WR, Jakob PM (2006) Assessment of cardiovascular apoptosis in the isolated rat heart by magnetic resonance molecular imaging. Mol Imaging 5(2):115–121

Hortobagyi GN (1990) Comprehensive management of locally advanced breast cancer. Cancer 66(6 Suppl):1387–1391

Hunt A, Evan G (2001) Apoptosis. Till death us do part. Science 293(5536):1784–1785

Insana MF (1995) Modeling acoustic backscatter from kidney microstructure using an anisotropic correlation function. J Acoust Soc Am 97(1):649–655

Insana MF (1996) Ultrasonic imaging of microscopic structures in living organs. Int Rev Exp Pathol 36:73–92

Keidar Z, Haim N, Guralnik L, Wollner M, Bar-Shalom R, Ben-Nun A, Israel O (2004) PET/CT using 18F-FDG in suspected lung cancer recurrence: diagnostic value and impact on patient management. J Nucl Med 45(10):1640–1646

Kim SJ, Kim SK, Lee ES, Ro J, Kang S (2004) Predictive value of [18F] FDG PET for pathological response of breast cancer to neo-adjuvant chemotherapy. Ann Oncol 15(9):1352–1357

Kolios MC, Czarnota GJ, Lee M, Hunt JW, Sherar MD (2002) Ultrasonic spectral parameter characterization of apoptosis. Ultrasound Med Biol 28(5):589–597

Kolios MC, Taggart L, Baddour RE, Foster FS, Hunt JW, Czarnota GJ, Sherar MD (2003) An investigation of backscatter power spectra from cells, cell pellets and microspheres. In: 2003 IEEE ultrasonics symposium, Honolulu, HI, US

Lamuraglia M, Bridal SL, Santin M, Izzi G, Rixe O, Paradiso A, Lucidarme O (2010) Clinical relevance of contrast-enhanced ultrasound in monitoring anti-angiogenic therapy of cancer: current status and perspectives. Crit Rev Oncol/Hematol 73(3):202–212

Lee KS, Jeong YJ, Han J, Kim BT, Kim H, Kwon OJ (2004) T1 non-small cell lung cancer: imaging and histopathologic findings and their prognostic implications. Radiographics 24(6):1617–1636; discussion 1632–1636

Levine AJ, Puzio-Kuter AM (2010) The control of the metabolic switch in cancers by oncogenes and tumor suppressor genes. Science 330(6009):1340–1344

Lizzi FL Ultrasonic scatterer-property images of the eye and prostate. In: 1997 IEEE ultrasonics symposium, Toronto, ON, Canada pp 1109–1117

Lizzi FL, Greenebaum M, Feleppa EJ, Elbaum M, Coleman DJ (1983) Theoretical framework for spectrum analysis in ultrasonic tissue characterization. J Acoust Soc Am 73(4):1366–1373

Lizzi FL, Astor M, Kalisz A, Liu T, Coleman DJ, Silverman R, Ursea R, Rondeau M (1996) Ultrasonic spectrum analysis for assays of different scatterer morphologies: theory and very-high frequency clinical results. In: 1996 IEEE ultrasonics symposium. San Antonio, TX

Lizzi FL, Astor M, Feleppa EJ, Shao M, Kalisz A (1997a) Statistical framework for ultrasonic spectral parameter imaging. Ultrasound Med Biol 23(9):1371–1382

Lizzi FL, Astor M, Liu T, Deng C, Coleman DJ, Silverman RH (1997b) Ultrasonic spectrum analysis for tissue assays and therapy evaluation. Int J Imaging Syst Technol 8(1):3–10

Mamou J, Oelze ML, O'Brien WD Jr, Zachary JF (2005) Identifying ultrasonic scattering sites from three-dimensional impedance maps. J Acoust Soc Am 117(1):413–423

Mamou J, Oelze ML, O'Brien WD, Zachary JF (2006) Perspective on biomedical quantitative ultrasound imaging. IEEE Signal Process Mag 23(3):112–116

Mankoff DA, Dunnwald LK, Gralow JR, Ellis GK, Drucker MJ, Livingston RB (1999) Monitoring the response of patients with locally advanced breast carcinoma to neoadjuvant chemotherapy using [technetium 99 m]-sestamibi scintimammography. Cancer 85(11):2410–2423

McPherson DD (1991) Tissue characterization by ultrasound: what is possible now? What will be possible? Echocardiography 8(1):77–91

Mo LY, Cobbold RS (1992) A unified approach to modeling the backscattered Doppler ultrasound from blood. IEEE Trans Biomed Eng 39(5):450–461

Molthen RC, Shankar PM, Reid JM, Forsberg F, Halpern EJ, Piccoli CW, Goldberg BB (1998) Comparisons of the Rayleigh and K-distribution models using in vivo breast and liver tissue. Ultrasound Med Biol 24(1):93–100

Nguyen QD, Aboagye EO (2010) Imaging the life and death of tumors in living subjects: preclinical PET imaging of proliferation and apoptosis. Integr Biol (Camb) 2(10):483–495

Notta F, Mullighan CG, Wang JC, Poeppl A, Doulatov S, Phillips LA, Ma J, Minden MD, Downing JR, Dick JE (2011) Evolution of human BCR-ABL1 lymphoblastic leukaemia-initiating cells. Nature 469(7330):362–367

Oelze ML, O'Brien WD Jr (2002) Method of improved scatterer size estimation and application to parametric imaging using ultrasound. J Acoust Soc Am 112(6):3053–3063

Oelze ML, O'Brien WD Jr (2006) Application of three scattering models to characterization of solid tumors in mice. Ultrason Imaging 28(2):83–96

Oelze ML, Zachary JF (2006) Examination of cancer in mouse models using high-frequency quantitative ultrasound. Ultrasound Med Biol 32(11):1639–1648

Oelze ML, O'Brien WD Jr, Blue JP, Zachary JF (2004) Differentiation and characterization of rat mammary fibroadenomas and 4T1 mouse carcinomas using quantitative ultrasound imaging. IEEE Trans Med Imaging 23(6):764–771

Padhani AR, Husband JE (2001) Dynamic contrast-enhanced MRI studies in oncology with an emphasis on quantification, validation and human studies. Clin Radiol 56(8):607–620

Papanicolau N, Dent R, Spayne J, Kolios MC, Sofroni E, Iradji S, Czarnota GJ (2010) Conventional frequency evaluation of tumor cell death response in locally advanced breast cancer patients to chemotherapy treatment administration. J Acoust Soc Am 128(4):2365

Park D, Don AS, Massamiri T, Karwa A, Warner B, MacDonald J, Hemenway C, Naik A, Kuan KT, Dilda PJ, Wong JW, Camphausen K, Chinen L, Dyszlewski M, Hogg PJ (2011) Noninvasive imaging of cell death using an Hsp90 ligand. J Am Chem Soc 133(9):2832–2835

Quezada SA, Peggs KS, Simpson TR, Allison JP (2011) Shifting the equilibrium in cancer immunoediting: from tumor tolerance to eradication. Immunol Rev 241(1):104–118

Sarkeala T, Heinavaara S, Anttila A (2008) Breast cancer mortality with varying invitational policies in organised mammography. Br J Cancer 98(3):641–645

Sarvazyan A, Hill CR (2004) Physical chemistry of the ultrasound-tissue interaction in physical principles of medical ultrasonics. In: Hill CR, Bamber JC, Haar G (eds) Wiley, Chichester, UK pp 223–236

Sadeghi-Naini A, Falou O, Hudson JM (2012a) Imaging innovations for cancer therapy response monitoring. Imag in Med 4:311–327. doi:10.2217/iim.12.23

Sadeghi-Naini A, Falou O, Czarnota GJ (2012b) Quantitative ultrasound spectral parametric maps: Early surrogates of cancer treatment response. 34th Annual International Conference of the IEEE Engineering in Medicine and Biology Society (EMBC). IEEE, San Diego, CA, USA, pp 2672–2675

Sadeghi-Naini A, Papanicolau N, Falou O (2013) Quantitative ultrasound evaluation of tumour cell death response in locally advanced breast cancer patients receiving chemotherapy. Clin Canc Res 19:2163–2174. doi:10.1158/1078-0432.CCR-12-2965

Schellenberger EA, Bogdanov A Jr, Hogemann D, Tait J, Weissleder R, Josephson L (2002) Annexin V-CLIO: a nanoparticle for detecting apoptosis by MRI. Mol Imaging 1(2):102–107

Sherar MD, Noss MB, Foster FS (1987) Ultrasound backscatter microscopy images the internal structure of living tumour spheroids. Nature 330(6147):493–495

Sipkins DA, Cheresh DA, Kazemi MR, Nevin LM, Bednarski MD, Li KC (1998) Detection of tumor angiogenesis in vivo by alphaVbeta3-targeted magnetic resonance imaging. Nat Med 4(5):623–626

Skorton DJ, Collins SM (1988) Clinical potential of ultrasound tissue characterization in cardiomyopathies. J Am Soc Echocardiogr 1(1):69–77

Smith IC, Heys SD, Hutcheon AW, Miller ID, Payne S, Gilbert FJ, Ah-See AK, Eremin O, Walker LG, Sarkar TK, Eggleton SP, Ogston KN (2002) Neoadjuvant chemotherapy in breast cancer: significantly enhanced response with docetaxel. J Clin Oncol 20(6):1456–1466

Soliman H, Gunasekara A, Rycroft M, Zubovits J, Dent R, Spayne J, Yaffe MJ, Czarnota GJ (2010) Functional imaging using diffuse optical spectroscopy of neoadjuvant chemotherapy response in women with locally advanced breast cancer. Clin Cancer Res 16(9):2605–2614

Sutherland RM (1988) Cell and environment interactions in tumor microregions: the multicell spheroid model. Science 240(4849):177–184

Taggart LR, Baddour RE, Giles A, Czarnota GJ, Kolios MC (2007) Ultrasonic characterization of whole cells and isolated nuclei. Ultrasound Med Biol 33(3):389–401

Takiuchi S, Rakugi H, Honda K, Masuyama T, Hirata N, Ito H, Sugimoto K, Yanagitani Y, Moriguchi K, Okamura A, Higaki J, Ogihara T (2000) Quantitative ultrasonic tissue characterization can identify high-risk atherosclerotic alteration in human carotid arteries. Circulation 102(7):766–770

Tunis AS, Czarnota GJ, Giles A, Sherar MD, Hunt JW, Kolios MC (2005) Monitoring structural changes in cells with high-frequency ultrasound signal statistics. Ultrasound Med Biol 31(8):1041–1049

Turnbull DH, Wilson SR, Hine AL, Foster FS (1989) Ultrasonic characterization of selected renal tissues. Ultrasound Med Biol 15(3):241–253

Vangestel C, Peeters M, Mees G, Oltenfreiter R, Boersma HH, Elsinga PH, Reutelingsperger C, Van Damme N, De Spiegeleer B, Van de Wiele C (2011) In vivo imaging of apoptosis in oncology: an update. Mol Imaging 10(5):340–358

Vered Z, Barzilai B, Mohr GA, Thomas LJ 3rd, Genton R, Sobel BE, Shoup TA, Melton HE, Miller JG, Perez JE (1987) Quantitative ultrasonic tissue characterization with real-time integrated backscatter imaging in normal human subjects and in patients with dilated cardiomyopathy. Circulation 76(5):1067–1073

Visvader JE (2011) Cells of origin in cancer. Nature 469(7330):314–322

Vlad RM (2009) Quantitative ultrasound characterization of responses to radiotherapy in vitro and in vivo. Department of Medical Biophysics. University of Toronto, Toronto, Ontario, Canada

Vlad RM, Czarnota GJ, Giles A, Sherar MD, Hunt JW, Kolios MC (2005) High-frequency ultrasound for monitoring changes in liver tissue during preservation. Phys Med Biol 50(2):197–213

Vlad RM, Brand S, Giles A, Kolios MC, Czarnota GJ (2009) Quantitative ultrasound characterization of responses to radiotherapy in cancer mouse models. Clin Cancer Res 15(6):2067–2075

von Schulthess GK, Steinert HC, Hany TF (2006) Integrated PET/CT: current applications and future directions. Radiology 238(2):405–422

Zhao M, Beauregard DA, Loizou L, Davletov B, Brindle KM (2001) Non-invasive detection of apoptosis using magnetic resonance imaging and a targeted contrast agent. Nat Med 7(11):1241–1244

Zullig S, Hengartner MO (2004) Cell biology. Tickling macrophages, a serious business. Science 304(5674):1123–1124

Chapter 6
Modeling of Ultrasound Backscattering by Aggregating Red Blood Cells

Emilie Franceschini and Guy Cloutier

Abstract This chapter provides a review of the last 15 years on the use of quantitative ultrasound (QUS) techniques to characterize red blood cell (RBC) aggregation (i.e., aggregate size, structure and packing organization). The paper focuses on studies aimed at explaining factors affecting the frequency dependent backscatter coefficient (BSC). The theoretical structure factor model of ultrasound backscatter by aggregated RBCs is presented. Computer simulations based on this model are then described to understand the impact of the RBC aggregate size and packing organization on the frequency-dependent BSC. Two QUS cellular imaging methods, based respectively on the structure factor size estimator and the effective medium theory combined with the structure factor model, are compared to estimate the structural aggregate parameters. Finally, in vitro and in vivo results are presented with an optimization method to take into account the attenuation effects of intervening tissues between the probe and the blood flow.

Keywords Cellular imaging · Blood · Red blood cell aggregation · Backscatter coefficient · Structure factor · Effective medium theory · Tissue attenuation

E. Franceschini
Laboratoire de Mécanique et d'Acoustique LMA, CNRS, UPR 7051, Aix-Marseille University, Marseille Cedex 20, Centrale Marseille F-13402, France
e-mail: franceschini@lma.cnrs-mrs.fr

G. Cloutier (✉)
Laboratory of Biorheology and Medical Ultrasonics, University of Montreal Hospital Research Centre (CRCHUM), 2099 Alexandre de Sève (Room Y-1619), Montreal, Quebec H2L 2W5, Canada
e-mail: guy.cloutier@umontreal.ca

G. Cloutier
Department of Radiology, Radio-Oncology and Nuclear Medicine, and Institute of Biomedical Engineering, University of Montreal, Montreal, Quebec, Canada

J. Mamou and M. L. Oelze (eds.), *Quantitative Ultrasound in Soft Tissues*, DOI: 10.1007/978-94-007-6952-6_6,

6.1 Introduction

Blood is a heterogeneous suspension of erythrocytes, leukocytes, and platelets in a fluid plasma. The scattering of ultrasound by blood is mainly attributed to the erythrocytes, also called red blood cells (RBCs), because they constitute the vast majority (97 %) of the cellular content of blood and occupy a large volume fraction (hematocrit) of 35–45 % under normal conditions. RBCs in normal blood flowing through human vessels constitute reversible aggregates. Aggregates usually form rouleaux or complex three-dimensional structures. The mechanisms of aggregate formation and dissociation are complex and depend on the shearing conditions of the flow, the concentration of protein macromolecules in plasma (such as fibrinogen) (Chien 1975; Meiselman 1993; Armstrong et al. 2004) and the RBC aggregability (Rampling et al. 2004). The aggregation phenomenon is normal and occurs in the circulation of many mammalian species. However, hyperaggregation, i.e. an abnormal increase in RBC aggregation, is a pathological state associated with several circulatory diseases such as vascular thrombosis (Chabanel et al. 1994), coronary artery disease (Neumann et al. 1991), diabete mellitus (Poggi et al. 1994; Le Dévéhat et al. 1996), myocardial infarction and cerebrovascular accidents (Hayakawa and Kuzuya 1991; Vayá et al. 2004). The fact that these diseases and their complications generally occur in specific locations of the vascular system suggest a pathological micro- and/or macro-circulatory hemodynamic contribution to their etiologies.

Currently, indices of aggregation can be measured in vitro on samples obtained by venipuncture using different techniques including viscosimetry, erythrocyte sedimentation rate, electrical impedance and light scattering (Stoltz and Donner 1991). Contrary to these techniques needing a withdrawal of blood and the analysis in a laboratory instrument, the ultrasound backscattering method has the potential to measure RBC aggregation under both in vivo and in situ flow conditions. This imaging modality could significantly contribute to the hemorheology field especially at high ultrasound frequencies, since it allows characterization of RBC aggregation in space and in time, as demonstrated by its sensitivity to measure aggregate formation kinetics (Cloutier et al. 2004, 2008) and its ability to follow cyclic aggregation and disaggregation states under pulsatile flows (De Kroon et al. 1991; Nguyen et al. 2008). The ultrasound backscattering method would certainly stimulate prospective clinical studies aimed at elucidating the role of RBC aggregation in the development of cardiovascular diseases and it can also help to improve our basic understanding of the relationship between the hemodynamic of the circulation and RBC aggregation.

Ultrasound and Scatterer Size Estimation

In the ultrasonic blood characterization field, the aim is to obtain quantitative parameters that reflect the RBC aggregation state. One of this relevant quantitative parameter is the aggregate size. It is thus interesting to quickly recall the main quantitative ultrasound (QUS) techniques allowing to estimate scatterer size.

For years, many investigators have attempted to estimate the tissue structure properties (i.e. scatterer size and concentration) by analyzing the power spectra of the radio frequency (RF) data. The access to RF data from laboratory instruments and, increasingly, from clinical scanners allows application of a normalization procedure (Madsen et al. 1984; Wang and Shung 1997) to obtain the backscattering coefficient (BSC), defined as the power backscattered by a unit volume of scatterers per unit incident intensity per unit solid angle. The spectral content of the RF data (and therefore the BSC) contains information about the size, shape, concentration and acoustic impedance of the scattering objects within the tissues. A spectral analysis approach consists in estimating two spectral parameters: the spectral slope and intercept (Lizzi et al. 1986, 1996). The spectral slope is the linear slope of the BSC as a function of frequency on a log-log scale and the spectral intercept is the extrapolation of the BSC linear fit to zero frequency. The slope is related to the effective scatterer size, and the intercept is determined by the scatterer size and acoustic concentration (the acoustic concentration is the product of the scatterer concentration times the square of the relative impedance difference between the scatterers and surrounding tissue). Another QUS method used to extract effective scatterer size and acoustic concentration relies on theoretical scattering models (such as the spherical gaussian model) in order to fit the BSC to an estimated BSC by an appropriate model (Insana et al. 1990). Both spectral analysis and fitting approaches considered random structures, i.e. a low density of scatterers (Lizzi et al. 1986; Insana et al. 1990). These QUS approaches have been successfully used for the characterization of the eye (Feleppa et al. 1986), the prostate (Feleppa et al. 1997), apoptotic cells (Kolios et al. 2002), the breast (Oelze and Zachary 2006) and cancerous lymph nodes (Mamou et al. 2010). However, as will be discussed later (Sect. 6.2), it is not possible to apply these QUS techniques on blood because it is an extremely dense medium (5 million erythrocytes/mm^3) that cannot be considered as random.

Challenges of Ultrasonic Blood Characterization

Besides the high cellular number density of blood, another difficulty for modeling blood backscattering is to consider clustering particles such as RBC aggregates, characterized by specific size, structure and packing organization. Indeed, the structure and packing organization are also relevant QUS parameters for the blood characterization since the structure differs between normal and pathological human RBC aggregates. This was shown by Schmid-Schönbein et al. with microscopic observations of blood samples from normal and diabetic patients (Schmid-Schönbein et al. 1976, 1990) (see Fig. 6.1). The structures of RBC aggregates have the tendency to form clumps (i.e. isotropic structures) in pathological human blood such as in diabetes mellitus, whereas these structures are rouleaux in normal blood (i.e. anisotropic structures).

The aim of the present chapter is to provide a review with an emphasis on the last fifteen years or so on the use of the frequency dependent BSC to characterize RBC aggregation (i.e. aggregate size, structure and packing organization). Before

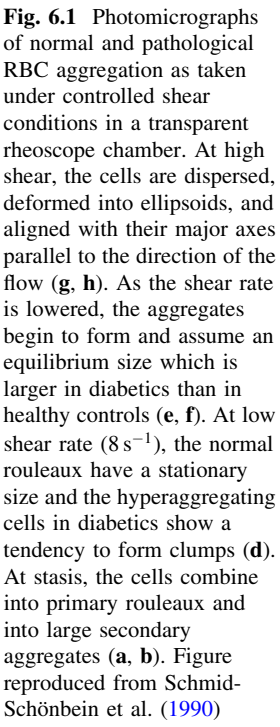

Fig. 6.1 Photomicrographs of normal and pathological RBC aggregation as taken under controlled shear conditions in a transparent rheoscope chamber. At high shear, the cells are dispersed, deformed into ellipsoids, and aligned with their major axes parallel to the direction of the flow (**g**, **h**). As the shear rate is lowered, the aggregates begin to form and assume an equilibrium size which is larger in diabetics than in healthy controls (**e**, **f**). At low shear rate ($8\,s^{-1}$), the normal rouleaux have a stationary size and the hyperaggregating cells in diabetics show a tendency to form clumps (**d**). At stasis, the cells combine into primary rouleaux and into large secondary aggregates (**a**, **b**). Figure reproduced from Schmid-Schönbein et al. (1990)

that, the mean backscattered power or the mean BSC was more generally studied, and the reader can refer to the article of Cloutier and Qin (1997) to have a review on the use of the backscattered power to characterize aggregating RBCs. Section 6.2 presents the structure factor model (Savery and Cloutier 2001; Fontaine et al. 2002) used for modeling aggregated RBCs. In Sect. 6.3, computer simulations of ultrasound backscattering by blood are described based on the structure factor model established in Sect. 6.2. The use of computer simulations allowed to provide information on the impact of the RBC aggregate size and packing organization on the frequency dependent BSC, information that cannot easily be obtained experimentally. In Sect. 6.4, two theoretical backscattering models for the estimation of the structural aggregate parameters are described and their performance are compared based on the computer simulations addressed in Sect. 6.3. Finally, in vitro and in vivo results are presented in Sect. 6.5.

6.2 Backscattering Theory

To model ultrasound backscattering by blood, some simplifying assumptions (but nevertheless acoustically realistic) are necessary. First, it is assumed that shear wave propagation and wave mode conversion are neglected such that only

compressional waves are taken into account. Secondly, attenuation of the backscattered ultrasound blood echoes due to viscous losses is also ignored. As a consequence, the RBCs and plasma are acoustically described as fluid and non-viscous media. Moreover, contrary to the majority of soft tissues, backscattering by blood is also time dependent because of the flow conditions. Nevertheless, one can consider that blood movement is much slower that sound propagation (around 1,540 m/s in blood) such that the insonified blood is quasi-stationary (Mo and Cobbold 1993).

Under the above conditions, two major difficulties for modeling blood backscatter are the high volume concentration of RBCs (i.e. hematocrit) and the clustering of particles. In this section, we indicate how these difficulties have been achieved by presenting successively the ultrasound backscattering from a single RBC, a collection of disaggregated RBCs and aggregated RBCs.

6.2.1 Backscattering Cross Section by a Single RBC Under Rayleigh Condition

Before modeling the ultrasound backscattering by an ensemble of interacting RBCs, it is instructive to model backscattering by a single RBC. A parameter characterizing the ultrasonic signal backscattered by a single scatterer is the differential backscattering cross section per unit volume σ_b, which is the power backscattered by one particle per unit incident intensity per unit solid angle (Mo and Cobbold 1993).

The hemoglobin solution encapsulated by the RBC membrane is acoustically described as a fluid and non-viscous medium, characterized by a compressibility $\kappa_1 = 3.41 \times 10^{-10}\,\mathrm{Pa}^{-1}$ and a density $\rho_1 = 1.092$ g/ml (or equivalently an impedance $z_1 = 1.766$ MRayl and a sound speed $c_1 = 1{,}617$ m/s) (Shung 1982; Savery and Cloutier 2007). The effect of the RBC membrane on acoustical backscattering is neglected because of the small membrane thickness of around 10 nm. The plasma is acoustically described as a fluid and non-viscous medium, characterized by a compressibility $\kappa_2 = 4.09 \times 10^{-10}\,\mathrm{Pa}^{-1}$ and a density $\rho_2 = 1.021$ g/ml (or equivalently an impedance $z_2 = 1.580$ MRayl and a sound speed $c_2 = 1{,}547$ m/s) (Shung 1982; Savery and Cloutier 2007). The RBC is thus considered as a weak scattering medium with a relative contrast of acoustical impedance between the RBC and the plasma equals to $\gamma_z = (z_1 - z_2)/z_2 = 0.13$.

Typical human RBCs are flexible biconcave disks having a diameter of approximately 8 μm and a thickness of 2.2 μm. In most clinical experiments, the ultrasound frequency is in the range of 5–30 MHz, i.e. a wavelength in the range of 50–300 μm. Since the incident wavelength is larger than the size of a RBC, scattering follows the Rayleigh theory. This theory predicts that the backscattering cross-section is proportional to the fourth power of the incident wave frequency and to the square of the scatterer volume, a behavior that does not depend on the

shape of the scatterer (Coussios 2002). Under the Rayleigh scattering theory, the backscattering cross-section σ_b of a single weak scattering RBC is given by (Mo and Cobbold 1993):

$$\sigma_b(-2k) = \frac{k^4 V_s^2}{16\pi^2}\left(\gamma_\kappa - \gamma_\rho\right)^2, \tag{6.1}$$

where k is the wavenumber, V_s the RBC volume, γ_κ the relative contrast in compressibility $\gamma_\kappa = (\kappa_1 - \kappa_2)/\kappa_2$ and γ_ρ the relative contrast in density $\gamma_\rho = (\rho_1 - \rho_2)/\rho_1$. Note that the dependence of σ_b in $(-2k)$ indicates the backscattering configuration where the wave vector is the opposite of the incident wave vector **k**.

In the case of weak scattering, when γ_κ and γ_ρ are very small, the difference between γ_κ and γ_ρ approximates to $\left(\gamma_\kappa - \gamma_\rho\right) \approx -2\gamma_z$. Therefore Eq. 6.1 reduces to:

$$\sigma_b(-2k) = \frac{k^4 V_s^2}{4\pi^2}\gamma_z^2. \tag{6.2}$$

The RBCs are often modeled as scatterers of simple shape such as spheres of equivalent volume. The typical volume of a RBC being 94 μm^3, one RBC can be approximated by a sphere of radius $a = 2.82$ μm. In order to take into account a spherical shape, a spherical form factor F can be added in the expression of σ_b as follows (Insana and Brown 1993; Savery and Cloutier 2007):

$$\sigma_b(-2k) = \frac{k^4 V_s^2 \gamma_z^2}{4\pi^2} F(k) = \frac{k^4 V_s^2 \gamma_z^2}{4\pi^2}\left(3\frac{\sin(2ka) - 2ka\cos(2ka)}{(2ka)^3}\right)^2. \tag{6.3}$$

Savery and Cloutier (2007) compared a semi-analytical model of the backscattering cross section of a realistic biconcave RBC with analytical models of simple shapes (sphere, cylinder, ellipsoid) mimicking a RBC (see Figs. 6.2 and 6.3). This study shows that for frequencies below 21 MHz (i.e. $ka < 0.21$), a RBC can be considered as a sphere of equivalent volume as given in Eq. (6.3). Beyond that limit, the shape and orientation of a RBC could modify the behavior of the backscattering cross-section. However, in practice, when a collection of RBCs randomly oriented is studied, the behavior of the mean backscattering cross section should depend on a mean form factor of the collection of RBCs randomly oriented, such that the limit frequency for the expression of σ_b using the spherical form factor should be above 21 MHz. That is why a collection of non-aggregating RBCs at hematocrits between 6 and 30 % shows experimentally a fourth power frequency-dependence of backscatter up to 30 MHz (Wang and Shung 1997).

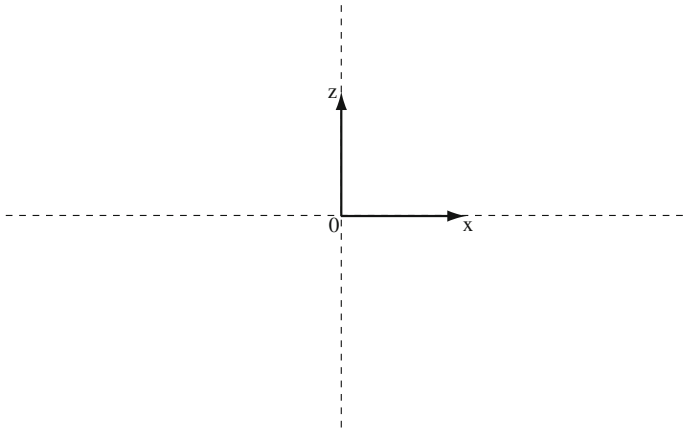

Fig. 6.2 Geometric cross sections of a red blood cell and equivalent descriptive shapes (Figure modified from Savery and Cloutier 2007)

Fig. 6.3 Normalized backscattering cross section with respect to $4\pi a^2$ as a function of the frequency ka for different descriptive shapes and incident wave directions along Oz ($k = k_z$) and Ox ($k = k_r$) (Figure from Savery and Cloutier 2007)

6.2.2 Backscattering by Disaggregated RBCs: The Particle Model

The ability of a tissue to generate acoustical echoes is often quantified by the frequency-dependent BSC. In this subsection, we consider a simple case of non-aggregating cells.

For a dilute, random suspension where the volume concentration of particles is typically less than a few percents, each particle equally and individually contributes to the backscattered power. It means that each particle scatters the incident

waves unaffected by the presence of the other particles. The BSC is thus proportional to the average number of scatterers per unit volume n (also called the scatterer density related to the hematocrit ϕ as $n = \phi/V_s$) as follows:

$$BSC(-2k) = n\sigma_b(-2k) \tag{6.4}$$

where σ_b is the backscattering cross section of a single scatterer obtained from Eq. (6.3). However, for human blood at a normal hematocrit (≈ 40 %), even in the absence of aggregation, the RBCs are densely packed. It means that the positions of any pair of scatterers are neither uncorrelated nor perfectly correlated in space and time, such that the RBCs cannot be treated as independent scatterers. In the absence of aggregation, a few stochastic scattering models (Angelsen 1980; Mo and Cobbold 1986, 1992; Twersky 1987; Fontaine et al. 1999), described next, were proposed to better understand the ultrasound backscattered power properties.

Two classical approaches are known as the particle and continuum models. The particle model (PM) consists of summing contributions from individual RBCs and modeling the RBC interaction by an analytical packing factor expression (Mo and Cobbold 1986; Twersky 1987). The continuum model (CM) considers that scattering arises from spatial fluctuations in the density and compressibility of the blood continuum (Angelsen 1980). A hybrid model generalizing the PM and CM frameworks was later proposed by Mo and Cobbold (1992). The RBCs are treated as a single scattering unit within a voxel, which size is defined as a fraction of the acoustic wavelength. The contribution from each single scattering unit is then determined as in the PM, and the contribution from all voxels is then summed by considering the influence of the mean number of scatterers per voxel and its variation in numbers between voxels. A complete description of these models can be found in a review by Mo and Cobbold (1993). Herein we only present in details the PM, which was used as a framework in Fontaine et al. (1999).

The classical approach known as the PM consists of summing contributions from individual RBCs, all considered much smaller than the acoustic wavelength, and modeling the RBC interaction by a packing factor W (Mo and Cobbold 1986; Twersky 1987). Based on this approach, the BSC is given by:

$$BSC_{PM}(-2k) = n\sigma_b(-2k)W. \tag{6.5}$$

The packing factor W can be expressed in terms of the statistical pair-correlation function $g(\mathbf{r})$, which is the probability of finding two particles separated by a distance $\mathbf{r}$:

$$W = 1 + n\int (g(\mathbf{r}) - 1)d\mathbf{r}. \tag{6.6}$$

An example of a pair-correlation function g is shown in Fig. 6.4. The function g is zero at short separations ($r < 2a$), since the particles are impenetrable. Then g oscillates around the value of 1 with several peaks in the range of $r \geq 2a$, with a maximum at $r = 2a$. The occurrence of these peaks at a large range ($r > 2a$)

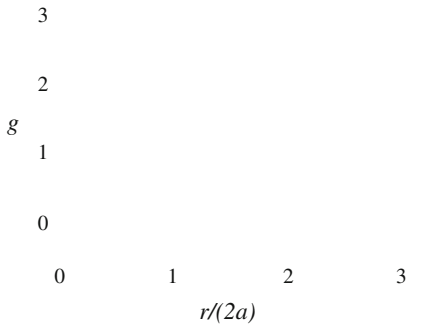

Fig. 6.4 Example of a pair-correlation function g

indicates a high degree of ordering. As the distance r increases, the oscillation of the peaks becomes weak and g tends to a value of 1. Physically, the packing factor W is a measure of orderliness in the spatial arrangement of RBCs. At very low hematocrits, when the RBC positions are completely random, $(g(\mathbf{r}) - 1)$ is equal to 0 and W is equal to unity such that the BSC is simply the sum of the backscattering cross section σ_b from all RBCs. As the hematocrit increases, W decays gradually to zero since closer packing will invariably lead to a greater orderliness in the RBC spatial arrangement. The most often used packing factor expression is based on the Percus-Yevick pair-correlation function for identical, unpenetrable and radially symmetric particles in the m-dimensional (slabs, circles and spheres for $m = 1, 2$ and 3, respectively) (Twersky 1987). The Perkus-Yevick packing factor W_{PY} is dependent on the hematocrit but independent on the frequency. Its value for spheres ($m = 3$) was first applied to blood by Shung (1982) and is given by Twersky (1987):

$$W_{PY} = \frac{(1-\phi)^4}{(1+2\phi)^2}. \tag{6.7}$$

Several studies compared the theoretical BSC_{PM} as a function of the hematocrit with experimental observations (Shung 1982; Lucas and Twersky 1987; Yuan and Shung 1988; Berger et al. 1991). For porcine RBCs suspended in a saline suspension that do not exhibit aggregation (i.e. aggregation does not occur in saline), the PM succeeded to explain the nonlinear relationship between the backscatter amplitude and hematocrit, as shown in Fig. 6.5 (Yuan and Shung 1988). The ultrasonic backscatter versus the hematocrit curve peaks around 13 % as it was expected by the PM using the Perkus-Yevick packing factor given by Eq. 6.7. Comparisons were also conducted on aggregating blood from different species (Yuan and Shung 1988). It is worth noting that the RBC aggregation tendency varies among species (Zijlstra and Mook 1962; Weng et al. 1996a). For example, horse blood has an excessive tendency to aggregate; porcine, dog and normal human bloods have a moderate tendency; and bovine blood forms no aggregate. For bovine whole blood, Yuan and Shung (1988) found that experimental and

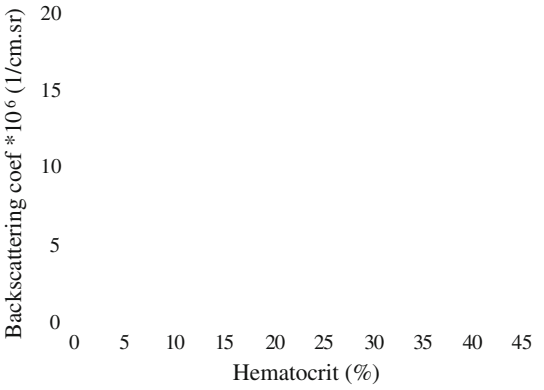

Fig. 6.5 The ultrasonic backscatter from porcine RBC suspensions as a function of the hematocrit. *Solid line* represents theoretical curves calculated from Eq. (6.5) using the Perkus-Yevick packing factor W_{PY}. *Triangles* represent typical experimental results for a laminar flow (Figure modified from Yuan and Shung 1988)

theoretical curves of BSC as a function of hematocrit were qualitatively in good agreement, since the tendency of aggregation is minimal for this blood species. However, to date, no data obtained under RBC aggregation conditions were fitted to the PM.

6.2.3 Backscattering by Aggregated RBCs: The Structure Factor Model

A major difficulty for modeling blood backscattering is to consider clustering particles as RBC aggregates. The aforementioned approach failed to predict the magnitude and frequency dependence of backscatter echoes observed in in vitro experiments when considering aggregating RBCs (Yuan and Shung 1988). Indeed, it was experimentally demonstrated that the aggregated RBCs did not follow a fourth-order frequency dependence contrary to the disaggregated case (Yuan and Shung 1988; Savery and Cloutier 2001). That is why Savery and Cloutier (2001) proposed the Structure Factor Model (SFM) to predict backscattering by aggregating RBCs, by considering first a low hematocrit. This model was later generalized to a normal hematocrit of 40 % (Fontaine et al. 2002). The SFM sums the contributions from individual RBCs and models the RBC interaction by a statistical mechanics structure factor S as follows (Savery and Cloutier 2001; Fontaine et al. 2002):

$$BSC_{SFM}(-2k) = n\sigma_b(-2k)S(-2k) = \frac{\phi}{V_s}\sigma_b(-2k)S(-2k). \tag{6.8}$$

The aggregation phenomenon is only affecting the structure factor S since RBC properties (i.e. σ_b and V_s) and the systemic hematocrit ϕ are expected to remain constant in the modeled region of interest. The structure factor S is by definition linked to the three-dimensional (3D) Fourier transform of the total correlation function $(g(\mathbf{r}) - 1)$:

$$S(-2k) = 1 + n \int (g(\mathbf{r}) - 1) e^{-2j\mathbf{kr}} d\mathbf{r}. \tag{6.9}$$

It can be easily seen by considering the particular case, of an incident plane wave in the x direction of a Cartesian coordinate system (x, y, z) that Eq. (6.9) becomes:

$$S(-2k) = 1 + n \int (g(x, y, z) - 1) e^{-2jkx} dx\, dy\, dz. \tag{6.10}$$

In Eq. (6.10), the structure factor is linked to the standard Fourier transform of the projection, on the ultrasound propagation axis, of the total correlation function. The Fourier transform of the projection is, by the Fourier projection-slice theorem, a line of the 3D Fourier transform of the total correlation function (see appendix of Fontaine et al. 1999). That is why the structure factor S depends only on the modulus k of the wave vector $\mathbf{k}$. Note that the low frequency limit of S is by definition the packing factor W used under Rayleigh conditions. For non-aggregated RBCs under Rayleigh conditions, Eq. (6.8) therefore directly reduces to Eq. (6.5). It is important to emphasize that the structure factor cannot analytically be calculated contrary to the packing factor (Twersky 1987).

The SFM was largely used to perform simulation studies on RBC aggregation as described in the next Sect. 6.3.

6.3 Computer Simulations of Ultrasound Backscattering by Aggregated RBCs

Computer simulation studies have been proposed to better understand mechanisms of ultrasound backscattering by various RBC distributions. First, the backscatter by non-aggregated RBCs as a function of the hematocrit was studied using one-dimensional (1D) and two-dimensional (2D) computer simulations (Routh et al. 1987; Zhang et al. 1994). In these studies, the RBCs are represented by slabs or circles, respectively in 1D or 2D, randomly positioned one by one. Following these studies, Lim and Cobbold (1999) performed 3D computer simulations for non-aggregated RBCs (represented by spheres) and 2D computer simulations for aggregated RBCs. In 3D, the backscattered power of non-aggregated RBCs peaked at around 12 % hematocrit, which corresponds to the PM theoretical prediction and experimental results (Yuan and Shung 1988). In 2D, the mean backscattered power by aggregated RBCs for frequencies below 5 MHz was computed to study the effects of the aggregate size, aggregate compactness and size distribution as a function of the hematocrit. Hunt et al. (1995) performed 1D and 2D computer simulations to study the differences in the backscattered power for several spatial distributions of the scattering sources. These simulations predicted that there would be a large reduction of the backscatter amplitudes if the scattering sources were regularly spaced and that backscatter amplitudes are very sensitive to the degrees of randomness (i.e. random or pseudo-random spatial distribution).

Later, our group performed computer simulations to predict the frequency dependence of the BSC from aggregated RBCs based on the SFM (Teh and Cloutier 2000; Savery and Cloutier 2001, 2005; Fontaine et al. 2002; Fontaine and Cloutier 2003; Saha and Cloutier 2008; Saha et al. 2011; Franceschini et al.2011), contrary to the works previously mentioned which have studied the mean BSC over the studied frequency bandwidth or the integrated backscatter. Our aim was to demonstrate that the use of the BSC frequency dependence would be more powerful than the indices generally used. Most of these simulations were based on particle dynamics or statistical mechanics to obtain the RBC spatial distributions (Savery and Cloutier 2001, 2005; Fontaine et al. 2002; Fontaine and Cloutier 2003; Saha and Cloutier 2008) and had the objective to mimic the rheological behavior of blood. The RBC distributions obtained showed aggregates with various sizes, shapes and compactness. Most of those studies were restricted to two dimensions (Savery and Cloutier 2001, 2005; Fontaine et al. 2002; Fontaine and Cloutier 2003) because of the computational load to generate aggregating RBC distributions. Besides techniques based on particle dynamics or statistical dynamics, another simple and fast method was to randomly generate non-overlapping and identical shaped aggregates (Teh and Cloutier 2000; Saha et al. 2011; Franceschini et al. 2011), as performed previously by Lim and Cobbold (1999). Although this method did not take into consideration realistic interactions between RBCs, it allowed to isolate the effects of hematocrit, aggregate size, shape and/or size distribution on the ultrasound backscattering. In this section, the BSC computation using the SFM is explained and a recent computer simulation that isolates the effects of aggregate size and compactness is presented.

6.3.1 BSC Computation Using the Structure Factor Model

The computation of the BSC_{SFM} using the SFM requires the knowledge of the structure factor S as described in Eq. (6.8). Since the structure factor S is by definition a statistical quantity, an average of all structure factors obtained from several particle distributions can give an estimated value of S.

For each distribution of RBCs, a density matrix M is computed by dividing the square simulation plane L^2 in N_p^2 pixels for a 2D computer simulation (or L^3 in N_p^3 pixels for a 3D simulation) and by counting the number of RBCs falling into each pixel. This matrix represents the microscopic density function defined by

$$M(\mathbf{r}) = \sum_{i=1}^{N} \delta(\mathbf{r} - \mathbf{r}_i) \tag{6.11}$$

where $\mathbf{r_i}$ are the position vectors defining the center of the ith RBC in space, N the number of RBCs in blood and δ the Dirac distribution. An equivalent expression of Eq. (6.9) for the structure factor S can be given in terms of the microscopic density distribution M as follows:

$$S(-2\mathbf{k}) = E\left[\frac{1}{N}\left|\int M(\mathbf{r})e^{-i2\mathbf{k}\mathbf{r}}d\mathbf{r}\right|^2\right] \tag{6.12}$$

where E is the ensemble average. The structure factor is thus computed by averaging 2D Fourier transforms for 2D computer simulations (or 3D Fourier transforms for 3D simulations) of several density matrices for averaging purpose. The FFTs give the structure factor values $S(-2\mathbf{k})$ on a centered grid of wave-vectors between $\pm\pi N_p/2L$ with a step of $\Delta k = \pi/L$.

6.3.2 *Effects of the Aggregate Size and Compactness on the BSC Frequency Dependence*

Computer simulations in 2D were recently performed by Franceschini et al. (2011) to isolate, for the first time, the effect of aggregate compactness ϕ_i (i.e. the RBC concentration within aggregates) on the BSC frequency dependence. The simulation algorithm was suitable for generating non-overlapping and isotropic RBC clusters. The locations of the RBCs inside each aggregate were generated randomly to give the desired compactness of aggregates such that the distribution of RBCs within each aggregate was different.

6.3.2.1 Effect of the Aggregate Compactness on the BSC

A key feature of these simulations was the possibility to have various compactnesses of aggregates ϕ_i with the same size of aggregates r_{ag}. Figure 6.6a and b illustrates spatial arrangements of RBCs for a constant value of $r_{ag}/a = 6.32$ (i.e. $r_{ag} = 17.39\,\mu m$), a constant systemic hematocrit $\phi = 20\,\%$ and two compactnesses of aggregates of 40 and 60 %. The corresponding backscattering coefficients BSC_{SFM} were computed with the SFM between 4 and 100 MHz for different aggregate compactnesses of 40, 50 and 60 % at a systemic hematocrit of 20 % (see Fig. 6.6c). As the compactness of aggregates ϕ_i increases, the BSC_{SFM} amplitude increases at low frequencies (< 23 MHz). The first peaks of the BSC_{SFM} are between 18.0 and 20.6 MHz for all simulated conditions.

6.3.2.2 Effect of the Aggregate Size on the BSC

Figure 6.7 shows BSC_{SFM} as a function of frequency for the disaggregated case ($r_{ag}/a = 1$) and for aggregated conditions with radii $r_{ag}/a = 3.16, 5.0$ and 7.07, at different hematocrits. In these simulations, the compactness of aggregates had a constant value of $\phi_i = 60\,\%$. For frequencies less than 20 MHz, the BSC_{SFM}

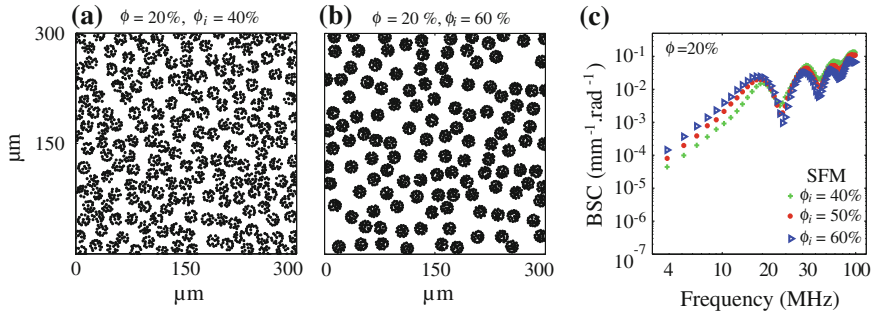

Fig. 6.6 **a** and **b** RBC distributions used in 2D computer simulations for a constant aggregated radius $r_{ag} = 6.32a = 17.32\,\mu m$ and a constant systemic hematocrit $\phi = 20\ \%$ at two aggregate compactnesses: **a** $\phi_i = 40\ \%$ and **b** $\phi_i = 60\ \%$. **c** Dependence of the backscattering coefficients on the compactness of aggregates: $r_{ag}/a = 6.32$ and $\phi = 20\ \%$ (Figure modified from Franceschini et al. 2011)

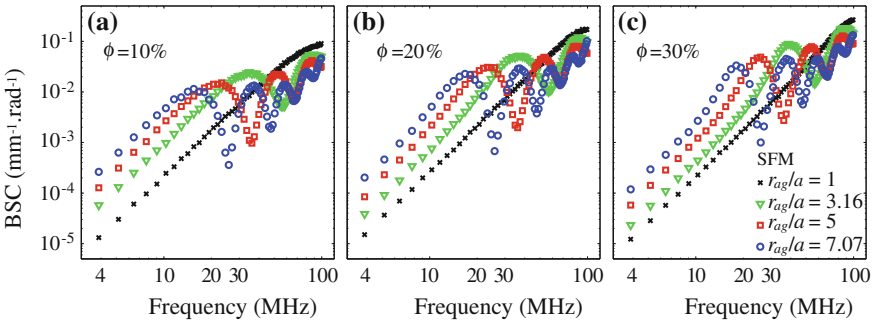

Fig. 6.7 Dependence of the backscattering coefficients for different aggregate sizes and a constant aggregate compactness $\phi_i = 60\ \%$ at systemic hematocrits of 10, 20 and 30 % (Figure modified from Franceschini et al. 2011)

amplitude increases with the size of aggregates. Moreover, the BSC_{SFM} peaks occur at lower frequencies as the aggregate radius increases.

To summarize, this study had provided some insights into the influence of the aggregate size and compactness on the BSC frequency dependence (Franceschini et al. 2011). The aggregate compactness as well as the aggregate size can greatly influence the BSC amplitude. The frequency position of the BSC first peak was found not to be significantly affected by changes in the aggregate compactness, whereas it was greatly affected by changes in the aggregate size. Note that other computer simulations putting emphasis on the influence of the aggregate shape (i.e. anisotropy) and of the aggregate size distribution on ultrasound backscattering can be found in the literature (Lim and Cobbold 1999; Fontaine et al. 2002; Savery and Cloutier 2005).

6.4 Ultrasound Backscattering Modeling for the Estimation of Structural Aggregate Parameters

As seen previously in Sects. 6.2.3 and 6.3, the SFM allows to simulate the BSC from RBCs whatever the RBC spatial distribution (i.e. disaggregated or aggregates with isotropic or anisotropic shape and/or with various aggregate sizes, shapes and compactnesses). However, the SFM can hardly be implemented to estimate structural parameters in the framework of an inverse problem formulation because of the intensive computational time to assess the structure factor by realizing distributions of RBCs with simulations. That is why two scattering theories, named the Structure Factor Size Estimator (SFSE) and the Effective Medium Theory combined with the Structure Factor Model (EMTSFM), have been recently developed in order to approximate the SFM for practical assessments of RBC structural features (i.e., in an inverse problem formulation). Both theories are based on some simplifying assumptions regarding the RBC spatial distributions:

- First, isotropic aggregates are assumed. In human blood, low shear rates can promote the formation of RBC aggregates having anisotropic (i.e. rouleaux) or isotropic (i.e. clump) structures, as seen in Fig. 6.1. The rouleaux like pattern is typically associated to normal blood. However, as the binding energy between RBCs increases with inflammation (Weng et al. 1996b), aggregates form clump structures such as in diabetes mellitus (Schmid-Schönbein et al. 1976, 1990). The assumption of isotropic aggregates is thus valid as far as we are concerned with the study of pathological states.
- Second, a minimal polydispersity in terms of aggregate sizes is assumed. Under in vivo conditions with ultrasound measurements on a blood vessel, the shear rate distribution varies with the radial position, and consequently, the aggregate size distribution too. That is why the backscattered echoes from blood are generally analyzed over a rectangular or a hamming window which is moved along the RF signal to examine the whole vessel at different depths (Yu and Cloutier 2007; Yu et al. 2009). For example, at a central frequency of 25 MHz, the window length was typically around 400 μm (Yu et al. 2009). RBC aggregates may thus be assumed to be locally identical, but variations can be considered within an ultrasound image by moving the measurement window.

6.4.1 Structure Factor Size Estimator

Yu and Cloutier (2007) and Yu et al. (2009) developed the SFSE scattering theory, which consists of using a second-order Taylor expansion of the structure factor as follows:

$$\begin{aligned} S(-2k) &\approx C_0 - 2kC_1 + (-2k)^2 C_2 \\ &\approx W - 4R_g^2 k^2 \\ &\approx W - \frac{12}{5}(kaD)^2 \end{aligned} \tag{6.13}$$

where C_0, C_1, and C_2 are simply the series coefficients. We have shown earlier that C_0 is the low frequency limit of the structure factor, named the packing factor W (see Eq. 6.6), here for aggregated RBCs. By considering isotropic aggregates, the second constant C_1 is equal to zero because the blood remains the same if the blood sample is turned around 180° (i.e. $S(-2k) = S(2k)$). By a dimensional analysis, the third constant C_2 is a surface in m^2 and is assumed to be the square of the mean aggregate gyration radius R_g^2, as usually performed in the field of crystallography using x-ray scattering (Guinier and Fournet 1955; Yu and Cloutier 2007). The diameter of an homogeneous spherical object in terms of number of RBCs can also be related to its radius of gyration as $D = \sqrt{5/3}R_g/a$ (Guinier and Fournet 1955; Yu and Cloutier 2007).

To summarize, the SFSE parameterizes the BSC by two structure indices, the packing factor W and the mean aggregate diameter D assumed to be isotropic, as follows:

$$\begin{aligned} BSC_{SFSE}(-2k) &= n\sigma_b(-2k)\left(W - \frac{12}{5}(kaD)^2\right) \\ &= \frac{\phi}{V_s}\frac{k^4 V_s^2 \gamma_z^2}{4\pi^2}\left(3\frac{\sin(2ka) - 2ka\cos(2ka)}{(2ka)^3}\right)^2\left(W - \frac{12}{5}(kaD)^2\right). \end{aligned} \tag{6.14}$$

Assuming that the hematocrit ϕ, the RBC radius of the equivalent sphere a and the impedance contrast γ_z are known *a priori*, the parameters W and D are estimated by fitting the measured BSC versus frequency with the theoretical BSC_{SFSE} given in Eq. (6.14).

6.4.2 *Effective Medium Theory Combined with the Structure Factor Model*

A new scattering theory, named an Effective Medium Theory (EMT) combined with the SFM (EMTSFM), was recently proposed by Franceschini et al. (2011). The EMT was initially developed by Kuster and Toksoz (1974) in the field of geophysics. Herein, the EMT assumes that aggregates of RBCs can be treated as individual homogeneous scatterers, which have effective properties determined by the concentration of RBCs within aggregates (i.e. the compactness of aggregates ϕ_i) and acoustical properties of blood constituents. The approximation of RBC

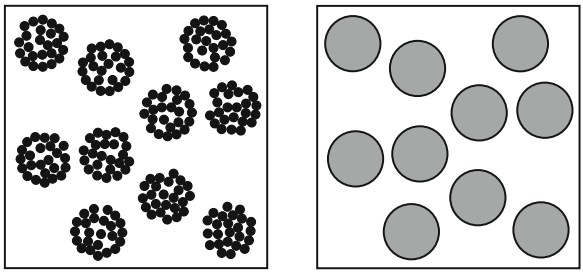

Fig. 6.8 Schematic representation of aggregates treated as individual scatterers. The aggregates of RBCs in blood (*left side*) are assumed to be homogeneous particles (*right side*) with effective properties that depend on the internal hematocrit, and density and compressibility of the RBCs within them (Figure from Franceschini et al. 2011)

aggregates as homogeneous effective particles is combined with the SFM to consider the concentrated blood medium. The effective particle interactions were thus modeled by a structure factor, as in Savery and Cloutier (2001) and Fontaine et al. (2002). The EMTSFM parameterizes the BSC by three indices: the aggregate radius, the concentration of RBCs within aggregates (also named aggregate compactness) and the systemic hematocrit. In the field of clinical hemorheology, assessing the compactness of RBC aggregates is of high clinical importance since it is related to the binding energy between cells. Normal RBC aggregates form rouleaux type structures, whereas pathologies associated with stronger binding energies result in clumps of RBCs (close to a spherical isotropic packing). A complete description of the EMTSFM is described below.

As a first approximation, we assume that all the RBCs are aggregated in blood, that the aggregates are identical and isotropic and that the RBCs within the aggregates are evenly distributed. The EMTSFM assumes that aggregates of RBCs can be treated as individual homogeneous scatterers as shown in Fig. 6.8. Each aggregate is thus approximated by an effective single particle. The density ρ_{ag} and compressibility κ_{ag} of the new effective particle are determined by considering the EMT (Kuster and Toksoz 1974). It means that ρ_{ag} and κ_{ag} are derived from the acoustical properties of the two fluids that constitute the aggregates (i.e. ρ_1, ρ_2, κ_1 and κ_2, where 1 indicates properties of RBCs and 2 those of plasma) and from the internal concentration of RBCs within the aggregates ϕ_i, as follows:

$$\begin{aligned} \rho_{ag} &= \phi_i \rho_1 + (1 - \phi_i)\rho_2 \\ \frac{1}{\kappa_{ag}} &= \frac{\phi_i}{\kappa_1} + \frac{1 - \phi_i}{\kappa_2} \end{aligned} \tag{6.15}$$

The BSC from blood is then obtained by summing contributions from individual effective particles of radius r_{ag} and modeling the effective particle interaction by a

statistical mechanics structure factor S_{ag}. The equivalent BSC expression is thus given by:

$$BSC_{EMTSFM}(-2k) = n_{ag}\sigma_{ag}(-2k)S_{ag}(-2k), \tag{6.16}$$

where n_{ag} is the number density of aggregates that is related to the effective volume fraction of aggregates ϕ_{ag}. The effective volume fraction of aggregates is equal to the volume fraction of RBCs in blood ϕ divided by the aggregate compactness ϕ_i: $\phi_{ag} = \phi/\phi_i$. The backscattering cross-section σ_{ag} of an effective single sphere can be determined using the fluid-filled sphere model developed by Anderson (1950). That model provides an exact solution for the backscattering of sound by a single fluid sphere, not necessarily small compared to the wavelength, in a surrounding fluid medium (i.e. the plasma). The structure factor S_{ag} corresponds here to a collection of N_{ag} identical and disaggregated particles (mimicking RBC aggregates) of radius r_{ag} randomly distributed.

By assuming that the RBC radius a and the acoustical properties of plasma and RBCs are known *a priori*, the unknown parameters are the aggregate radius r_{ag} and aggregate compactness ϕ_i. The unknown parameters can be estimated by matching the measured BSC with the theoretical BSC_{EMTSFM} given by Eq. (6.16).

6.4.3 Assessment of the Accuracy of Scattering Models in Determining the RBC Aggregate Size and Aggregate Compactness

To our knowledge, there is no means to experimentally assess aggregate sizes at 40 % hematocrit because RBCs at that hematocrit are opaque to light. The experimental assessment of accuracy of the SFSE was only performed at a low hematocrit of 6 % by comparing optical and acoustic measurements of RBC aggregate sizes (Yu and Cloutier 2007). That is why 3D computer simulations producing BSCs from RBC aggregates were recently performed to evaluate the accuracy of the SFSE method (Saha et al. 2011). In this subsection, we determine the performance of the EMTSFM to extract RBC aggregate sizes and compactnesses from simulated BSC_{SFM} and compare that with SFSE predictions. This comparison is based on 2D computer simulations using the SFM previously presented in Sect. 6.3. In the following, all the estimated parameters are denoted by a star.

The SFSE and EMTSFM are first examined when the aggregate size is fixed $r_{ag}/a = 6.32$ and aggregate compactnesses ϕ_i vary from 40 to 60 %. Figure 6.9a presents the BSC fitted curves with the SFSE and the EMTSFM to the simulated BSC_{SFM} already presented in Fig. 6.6. The fitted curves using the SFSE overestimate the BSC_{SFM} amplitude at low frequencies, whereas the EMTSFM provides good fittings to the simulated BSC_{SFM}. The values of the estimated parameters W^*

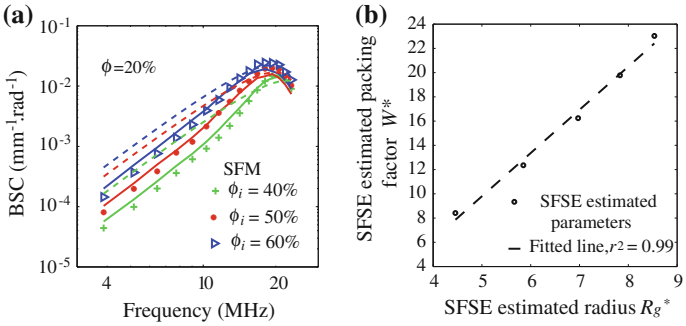

Fig. 6.9 **a** Frequency-dependent backscatter coefficients computed with the SFM for different aggregate compactnesses and a constant aggregate size $r_{ag}/a = 6.32$ at a systemic hematocrit of 20 %, and corresponding fitting with the SFSE (in *dashed lines*) and with the EMTSFM (in *solid lines*). **b** Linear relationship between estimated parameters W^* and R_g^* obtained with the SFSE

and R_g^* obtained with the SFSE and estimated parameters r_{ag}^*/a and ϕ_i^* obtained with the EMTSFM are reported in Table 6.1 for a systemic hematocrit of 20 %. Although the true radius is fixed, the estimated R_g^* increases with the aggregate compactness. A linear relation links also the estimated parameters W^* and R_g^* when the aggregate compactness varies (see Fig. 6.9b), as it was previously observed in Yu and Cloutier (2007) and Saha et al. (2011). Therefore there is no significant correlation between the actual fixed radius and the estimated radii. The SFSE cannot take into account a variation in aggregate compactnesses since a change in compacity is interpreted as a change in the aggregate size. On the other hand, the EMTSFM gives quantitatively satisfactory estimates with relative errors inferior to 8 % for the estimated aggregate size and inferior to 19 % for the estimated compactness.

The SFSE and EMTSFM are also evaluated when the aggregate size varies and the aggregate compactness is fixed to a high value: $\phi_i = 60$ %. Figure 6.10a presents the BSC fitted curves with the SFSE and the EMTSFM to the simulated BSC_{SFM} at a hematocrit of 30 %. The EMTSFM fits very well the simulated BSC_{SFM}, whereas the fitted SFSE curves over-estimate the simulated BSC_{SFM} in the low frequency range. For the SFSE, significant correlations between the estimated and true radii of aggregates with a correlation coefficient r^2 around 0.95 were found for all hematocrits (Fig. 6.10b). The EMTSFM gives quantitatively satisfactory estimates with relative errors inferior to 7 and 14 %, respectively, for the aggregate size and the aggregate compactness, whereas the relative errors for the estimated radii with the SFSE model are comprised between 24 and 62 % (see Table 6.2).

To conclude, although the SFSE did not provide good fits to the simulated data, significant correlations between the estimated and true radii of aggregates with r^2 around 0.95 were found when the aggregate compactness was fixed. However, the SFSE showed no significant correlation between the actual fixed radius and those

Table 6.1 Comparison of the SFSE and EMTSFM based on simulated BSCs for the following aggregating conditions: $r_{ag}/a = 6.32$, $\phi = 20\ \%$, ϕ_i varies

SFM		SFSE			EMTSFM			
Actual r_{ag}/a	Actual ϕ_i (%)	Estimated W^*	Estimated R_g^*	$\varepsilon_{R_g^*}$%	Estimated ϕ_i^* (%)	$\varepsilon_{\phi_i^*}$ (%)	Estimated r_{ag}^*/a	$\varepsilon_{r_{ag}^*}$ (%)
6.32	40	6.49	3.92	37.86	44.56	11.40	5.8	8.23
6.32	50	12.51	6.12	3.01	59.5	19.00	5.9	6.65
6.32	60	17.74	7.49	18.60	67.71	12.85	5.8	8.23

Values of the aggregate size r_{ag}/a and compactness ϕ_i used for computation of the simulated BSC_{SFM} from the SFM, and values of parameters found with the SFSE and EMTSFM and corresponding relative errors ε

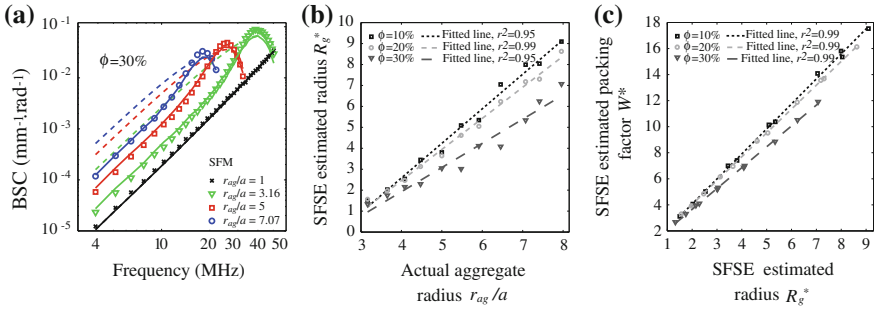

Fig. 6.10 **a** Frequency-dependent backscatter coefficients computed with the SFM for different aggregate sizes and a constant aggregate compactness $\phi_i = 60\ \%$ at a systemic hematocrit of 30 %, and corresponding fitting with the SFSE (in *dashed lines*) and with the EMTSFM (in *solid lines*). **b** Comparison of the estimated aggregate size R_g^* obtained with the SFSE to the true size r_{ag}/a for the three systemic hematocrits of 10, 20 and 30 %. **c** Linear relationship between W^* and R_g^*

estimated when the aggregate compactness varied (see Table 6.1), and the SFSE parameters W^* and R_g^* followed a linear relationship. It means that the BSC parameterization is reduced to one parameter physically linked to the aggregate size. On the other hand, the EMTSFM was the model that better matched the simulated data and gave quantitatively satisfactory estimates when the aggregate radius and compactness varied. At the moment, the SFSE is largely used because of a fast computation around 0.1 s to estimate parameters from a single BSC, against 1 s with the EMTSFM using Matlab programs (The MathWorks, Inc., Natick, MA). Also, the SFSE was developed to consider tissue attenuation for in vivo applications (Franceschini et al. 2008, 2010), whereas it is still not the case for the EMTSFM.

Table 6.2 Comparison of the SFSE and EMTSFM based on simulated BSCs for the following aggregating conditions: r_{ag}/a varies, $\phi = 30\,\%$, $\phi_i = 60\,\%$ (except in the case of diaggregated RBCs where $\phi_i = 100\,\%$)

SFM		SFSE			EMTSFM			
Actual r_{ag}/a	Actual ϕ_i (%)	Estimated W^*	Estimated R_g^*	$\varepsilon_{R_g^*}$ (%)	Estimated ϕ_i^* (%)	$\varepsilon_{\phi_i^*}$ (%)	Estimated r_{ag}^*/a	$\varepsilon_{r_{ag}^*}$ (%)
1	100	0.17	0.38	62.00	100	0.00	1.0	0.00
3.16	60	2.67	1.32	58.23	66	10.00	3.0	5.06
5	60	5.31	3.04	39.20	68	13.33	4.7	6.00
7.07	60	8.58	5.33	24.61	66	10.00	6.6	6.65

Values of the aggregate size r_{ag}/a and compactness ϕ_i used for computation of the simulated BSC_{SFM} from the SFM, and values of parameters found with the SFSE and EMTSFM and corresponding relative errors ε

6.5 In Vitro and In Vivo Experimental Studies

6.5.1 In Vitro Experiments

As seen previously in Sect. 6.3, computer simulations allowed to determine the influence of the aggregate size, shape and compactness on ultrasound backscattering. It is currently difficult to control all these parameters in in vitro experiments. An instructive in vitro experiment is to shear blood in a Couette flow device providing a linear velocity profile and a constant shear rate for a given rotational speed of the device (Foster et al. 1994; Van Der Heiden et al. 1995; Yu and Cloutier 2007; Yu et al. 2009). A homogeneous level of aggregation could thus be expected in such a controlled flow. Figure 6.11 shows the typical measured BSC_{meas} as a function of frequency for porcine blood at a systemic hematocrit of 40 % sheared at different shear rates in a Couette flow device (Franceschini et al. 2010). These experimental data were obtained using an ultrasound scanner Vevo 770, Visualsonics (Toronto, Canada) equipped with a 25 MHz-center frequency probe (RMV 710). The measured BSC_{meas} signifies here the experimental measure of the BSC. It was calculated here by a substitution method with a reference phantom (i.e. a sample of disaggregated RBCs suspended in saline at a 6 % hematocrit) to compensate the backscattered power spectra for the electromechanical system response, and the depth-dependent diffraction and focusing effects caused by the ultrasound beam. As observed in Fig. 6.11, the amplitude of the BSC_{meas} increases and the peak occurs at lower frequencies as the shear rate decreases (i.e. when the level of aggregation increases). Also represented are corresponding fitted curves obtained with the SFSE, as well as the corresponding values of W^*, D^* and the correlation coefficient r^2 to assess the goodness of fit between the model and the measured data. Note that in this section the aggregate sizes estimated by the SFSE correspond to the mean aggregate diameter D^* instead of the mean aggregate gyration radius R_g^* (see Eq. (6.13)). The SFSE provides good fits to the data and W^* and D^* increase when the shear rate decreases.

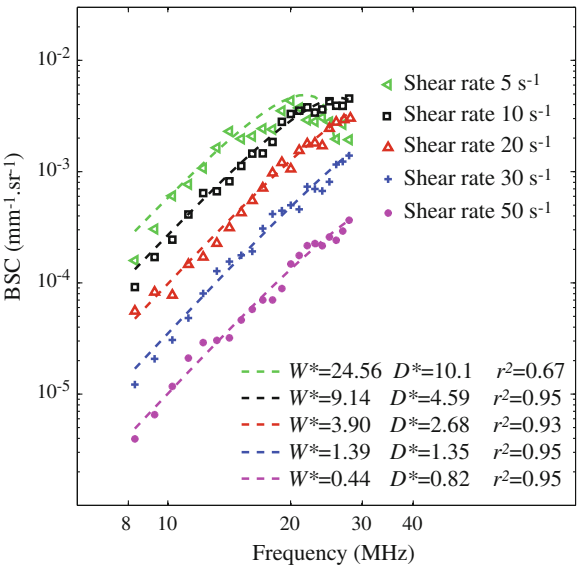

Fig. 6.11 Backscatter coefficients for blood sheared at different shear rates, and corresponding fitting with the SFSE (Figure modified from Franceschini et al. 2010)

The corresponding spatial maps of aggregate size and packing factor estimates (parametric images) for a shear rate of 10 s^{-1} are displayed in Fig. 6.12. The parametric images are superimposed on a conventional B-mode frame. The parametric images are useful for describing how aggregate structures vary in size as a function of depths. In the Couette flow experiments, the parametric images are quite homogenous as it was expected, since the level of aggregation is identical whatever the depth. Under in vivo conditions with ultrasound measurements on a blood vessel, the shear rate distribution varies with the radial position, and consequently, the aggregate size distribution too. An example of parametric images of porcine blood in a tubular in vitro experiment is displayed in Fig. 6.13.

6.5.2 In Vivo Experiments

The difficulty to apply the SFSE or the EMTSFM in vivo is that the spectral content of backscattered echoes is also affected by attenuation caused by intervening tissue layers (such as the skin) between the probe and the blood flow. To evaluate correctly microstructural parameters, it is thus of major interest to take into account tissue attenuation effects. Some groups (He and Greenleaf 1986; Oosterveld et al.1991) developed measurement techniques to evaluate the frequency-dependent attenuation in order to compensate *a posteriori* the backscattered power spectrum. Recently, Bigelow et al. (2005a, 2005b) introduced a new

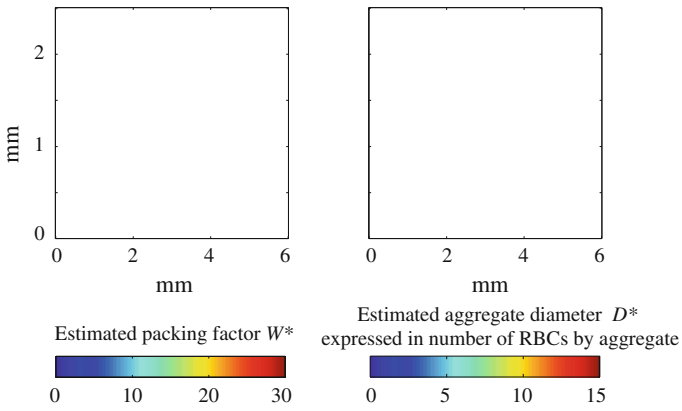

Fig. 6.12 Quantitative images of porcine blood sheared at 10 s^{-1} in a Couette device superimposed on the gray-scale B-mode images. Parameters W^* and D^* were estimated by the SFSE (Figure modified from Franceschini et al. 2010)

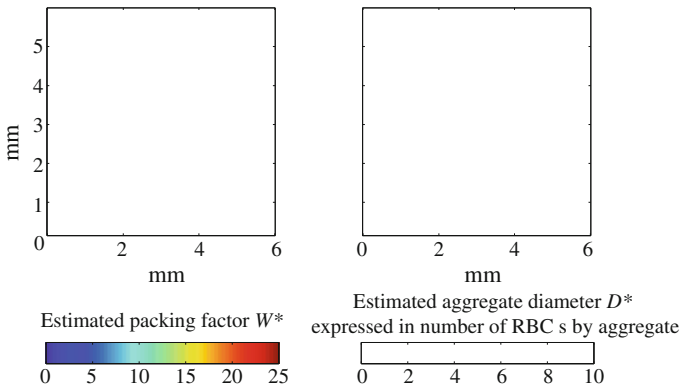

Fig. 6.13 Quantitative images of porcine blood sheared in a tube superimposed on the gray-scale B-mode images. Parameters W^* and D^* were estimated by the SFSE (Figure modified from Franceschini et al. 2010)

algorithm that has the advantage to estimate simultaneously the effective radius of the tissue microstructure and the total attenuation. These two parameters were determined by using a single minimization method that fits the spectrum of the backscattered RF echoes from the region of interest (ROI) to an estimated spectrum by an appropriate model. This last strategy was recently adapted for the estimation of RBC scatterer sizes by slightly modifying the SFSE and was named the Structure Factor Size and Attenuation Estimator (SFSAE) (Franceschini et al. 2008, 2010). The SFSAE allows to determine simultaneously blood structural parameters (i.e. W and D) and the total attenuation by modeling the theoretical backscattering coefficient of blood as follows (Franceschini et al. 2008):

$$\begin{aligned} BSC_{SFSAE}(-2k) &= n\sigma_b(-2k)\left(W - \frac{12}{5}(kaD)^2\right)A(-2k) \\ &\approx n\sigma_b(-2k)\left(W - \frac{12}{5}(kaD)^2\right)e^{\frac{-4\,\alpha_0\,kc}{8.68\,2\pi}} \end{aligned} \tag{6.17}$$

where A is the frequency-dependent attenuation function, c is the mean speed of sound in the intervening tissue layers and α_0 is the attenuation coefficient (in dB/MHz) defined by: $\alpha_0 = \sum_i \alpha_i e_i$, where α_i and e_i are respectively the intervening tissue layer attenuations (in dB/cm/MHz) and thicknesses. One can note in Eq. (6.17) the coefficient 8.68 that expresses unit conversion from dB to Neper: $\alpha_0[\text{Neper/MHz}] = \alpha_0[\text{dB/MHz}]/8.68$. According to the above equation, we thus assume that the attenuation increases linearly with the frequency f: $\alpha(f) = \alpha_0 f/8.68$. The packing factor W^*, aggregate diameter D^* and total attenuation along the propagation path α_0^* are determined by matching the measured BSC with the theoretical BSC_{SFSAE} given by Eq. (6.17), as performed previously with the SFSE model.

Note that the SFSAE allows to estimate a total attenuation, including the intervening tissues between the probe and the blood flow but also the blood attenuation itself. The skin is one of the most attenuating tissue layers during in vivo scanning. The attenuation of human dermis is around 0.21 dB/MHz at 14–50 MHz considering a 1-mm dermis thickness (Raju and Srinivasan 2001). On the other hand, the blood attenuation is smaller around 0.015 dB/mm/MHz for disaggregated blood and 0.053 dB/mm/MHz for large aggregating conditions (Franceschini et al. 2010).

With in vitro experiments (Franceschini et al. 2008, 2010) the method gave satisfactory estimates with relative errors below 25 % for attenuations between 0.115 and 0.411 dB/MHz and $D^* < 7.29$ (corresponding to a product $kr_{ag} < 2.08$). Measurements were also performed on an arm's vein of a normal subject using an ultrasound scanner equipped with a 25 MHz center frequency probe (Franceschini et al. 2009). The probe was positioned in longitudinal view to examine a complex flow in the vinicity of two closed venous valves. Regions were examined upstream and downstream from the two venous valves. Quantitative ultrasound parametric images of the aggregate diameter D^*, the packing factor W^* and the total attenuation α_0^* were constructed by using the SFSAE (Fig. 6.14). The black pixels in Fig. 6.14 correspond to rejected solutions of the optimization method, when the estimated packing factor W^* or diameter D^* was found equal to zero, which is unrealistic (see section V-D in Franceschini et al. 2010). For the two structural parameters D^* and W^*, statistically significant differences were observed between blood stagnation and circulation zones; whereas attenuation mean values were quite similar. This work shows the SFSAE ability to estimate blood structural properties in vivo and in situ, and opens the way to parametric imaging for clinical studies in abnormal blood conditions.

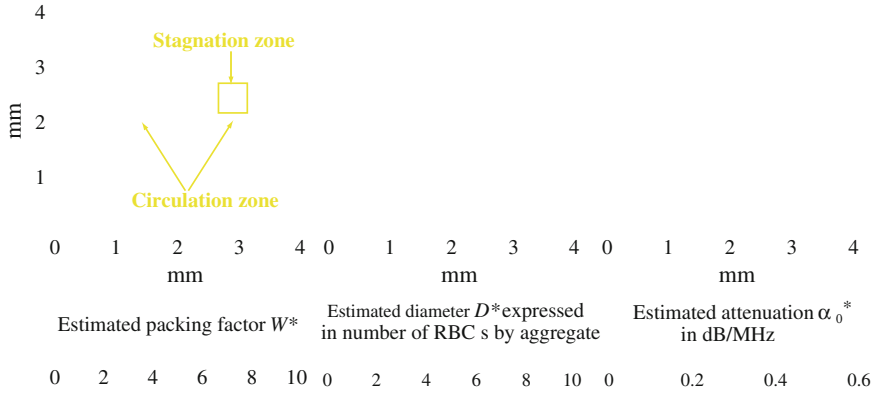

Fig. 6.14 Quantitative images of blood circulating in the vinicity of the two closed venous valves superimposed on the gray-scale B-mode images. Parameters W^*, D^* and α_0^* were estimated by the SFSAE (Figure modified from Franceschini et al. 2009)

6.6 Conclusion

This chapter has focused on the theoretical structure factor model of ultrasound backscattering by aggregated RBCs, on computer simulations to understand the impact of the aggregate structure on the frequency-dependent BSC and on two approximated theoretical models, the SFSE (or SFSAE) and the EMTSFM, allowing the estimation of blood structural properties. The SFSAE, i.e. the modified SFSE allowing to take into account the intervening tissue between the probe and the blood, has been shown able of estimating blood structural properties in vivo and in situ. Using the SFSAE, future works should focus on in vivo and in situ assessment of the pathophysiological impact of abnormal RBC aggregation on the cardiovascular system (see for example Yu et al. 2011).

The EMTSFM recently proposed is also a very promising model needing to be developed to speed the parameter estimation. Computed simulations show the superiority of the EMTSFM to estimate RBC aggregate size and compactness in comparison with the SFSE. An important contribution of this new model is the parameterization of the BSC with the aggregate compactness, which is a structural parameter not available in any other modeling strategies proposed in quantitative ultrasound imaging. The main limitation of the EMTSFM (as well as the SFSE) is the assumption of isotropic aggregates that limits the use of these models to pathological blood. In the future, improvements should consider incorporating the aggregate anisotropy and the possibility to simultaneously estimate the tissue attenuation, as for the SFSAE. It means that the EMTSFM could be slightly modified by introducing the attenuation term to estimate simultaneously the RBC aggregate size, compactness and the total attenuation.

Acknowledgments We acknowledge the continuous financial support of the Canadian Institutes of Health and Natural Sciences and Engineering Research Council of Canada, and the French National Center for Scientific Research (CNRS).

References

Anderson VC (1950) Sound scattering from a fluid sphere. J Acoust Soc Am 22:426–43

Angelsen BAJ (1980) Theoretical study of the scattering of ultrasound by blood. IEEE Trans Biomed Eng 27:61–67

Armstrong JK, Wenby RB, Meiselman HJ, Fisher TC (2004) The hydrodynamic radii of macromolecules and their effect on red blood cell aggregation. Biophys J 87:4259–4270

Berger NE, Lucas RJ, Twersky V (1991) Polydisperse scattering theory and comparisons with data for red blood cells. J Acoust Soc Am 89:1394–1401

Bigelow TA, Oelze ML, O'Brien WD (2005a) Estimation of total attenuation and scatterer size from backscatter ultrasound waveforms. J Acoust Soc Am 117:1431–1439

Bigelow TA, O'Brien WD (2005b) Signal processing strategies that improve performance and understanding of the quantitative ultrasound SPECTRAL FIT algorithm. J Acoust Soc Am 118:1808–1819

Chabanel A, Horellou MH, Conard J, Samama MM (1994) Red blood cell aggregability in patients with a history of leg vein thrombosis: influence of post-thrombotic treatment. Br J Haematol 88:174–179

Chien S (1975) Biophysical behavior of red cells in suspensions. In: Surgenor DM (ed) The red blood cell. Academic, New York

Cloutier G, Qin Z (1997) Ultrasound backscattering from non-aggregating and aggregating erythrocytes—a review. Biorheology 34:443–470

Cloutier G, Daronat M, Savery D, Garcia D, Durand LG, Foster FS (2004) Non-Gaussian statistics and temporal variations of the ultrasound signal backscattered by blood at frequencies between 10 and 58 MHz. J Acoust Soc Am 116:566577

Cloutier G, Zimmer A, Yu FT, Chiasson JL (2008) Increased shear rate resistance and fastest kinetics of erythrocyte aggregation in diabetes measured with ultrasound. Diabet Care 31:1400–1402

Coussios CC (2002) The significance of shape and orientation in single-particle weak-scatterer models. J Acoust Soc Am 112:906-915

De Kroon MGM, Slager CJ, Gussenhoven WJ, Serruys PW, Roelandt JRTC, Bom N (1991) Cyclic changes of blood echogenicity in high frequency ultrasound. Ultrasound Med Biol 17:723–728

Le Dévéhat C, Khodabandehlou T, Vimeux M, Aouane F (1996) Diabetes mellitus: its effects on blood rheological properties and microcirculatory consequences. Clin Hemorheol 16:677–683

Feleppa EJ, Lizzi FL, Coleman DJ, Yaremko MM (1986) Diagnostic spectrum analysis in ophthalmology: a physical perspective. Ultrasound Med Biol 12:623–631

Feleppa EJ, Liu T, Kalisz A, Shao MC, Fleshner N, Reuter V (1997) Ultrasonic spectral-parameter imaging of the prostate. Int J Imag Syst Technol 8:11–25

Fontaine I, Bertrand M, Cloutier G (1999) A system-based approach to modeling the ultrasound signal backscattered by red blood cells. Biophys J 77:2387–2399

Fontaine I, Savery D, Cloutier G (2002) Simulation of ultrasound backscattering by red blood cell aggregates: effect of shear rate and anisotropy. Biophys J 82:1696–1710

Fontaine I, Cloutier G (2003) Modeling the frequency dependence (5–120 MHz) of ultrasound backscattering by red cell aggregates in shear flow at a normal hematocrit. J Acoust Soc Amer 113:2893–2900

Foster FS, Obara H, Bloomfield T, Ryan LK, Lockwood GR (1994) Ultrasound backscatter from blood in the 30–70 MHz frequency range. In: Proceedings IEEE Ultrasonic Symposium, pp 1599–1602

Franceschini E, Yu FTH, Destrempes F, Cloutier G (2010) Ultrasound characterization of red blood cell aggregation with intervening attenuating tissue-mimicking phantoms. J Acoust Soc Amer 127:1104–1115

Franceschini E, Yu FTH, and Cloutier G (2008) Simultaneous estimation of attenuation and structure parameters of aggregated red blood cells from backscatter measurements. J Acoust Soc Am 123:EL85-91

Franceschini E, Yu FTH, Destrempes F, Cloutier G (2009) In vivo ultrasound characterization of red blood cell aggregation using the structure factor size and attenuation estimator. In: Proceedings IEEE ultrasonic symposium, pp 301–304

Franceschini E, Metzger B, and Cloutier G (2011) Forward problem study of an effective medium model for ultrasound blood characterization. IEEE Trans Ultras Ferroelectr Freq Control 58:2668–2679

Guinier A, Fournet J (1955) Small angle scattering of X-rays. Wiley Interscience, New York

Hayakawa M, Kuzuya F (1991) Effects of ticlopidine on erythrocytes aggregation in thrombotic disorders. Angiology 42:747–753

He P, Greenleaf JF (1986) Application of stochastic analysis to ultrasonic echoes—estimation of attenuation and tissue heterogeneity from peaks of echo envelope. J Acoust Soc Am 79:526–534

Hunt JW, Worthington AE, Kerr AT (1995) The subtleties of ultrasound images of an ensemble of cells: simulation from regular and more random distributions of scatterers. Ultrasound Med Biol 21:329–341

Insana MF, Wagner RF, Brown DG, Hall TJ (1990) Describing small-scale structure in random media using pulse-echo ultrasound. J Acoust Soc Am 87:179–192

Insana MF, Brown DG (1993) Acoustic scattering theory applied to soft biological tissues. In: Shung KK, Thieme GA (eds) Ultrasonic scattering in biological tissues. CRC, Boca Raton, FL

Kolios MC, Czarnota GJ, Lee M, Hunt JW, Sherar MD (2002) Ultrasonic spectral parameter characterization of apoptosis. Ultrasound in Med Biol 28:589–597

Kuster GT, Toksoz MN (1974) Velocity and attenuation of seismic waves in two-phase media: part I theoretical formulations. Geophysics 39:587–606

Lim B, Cobbold RSC (1999) On the relation between aggregation, packing and the backscattered ultrasound signal for whole blood. Ultrasound Med Biol 25:1395–1405

Lizzi FL, Ostromogilsky M, Feleppa EJ, Rorke MC, Yaremko MM (1986) Relationship of ultrasonic spectral parameters to features of tissue microstructure. IEEE Trans Ultrason Ferroelect Freq Contr 33:319–329

Lizzi FL, Astor M, Kalisz A, Liu T, Coleman DJ, Silverman R, Ursea R, Rondeau M (1996) Ultrasound spectrum analysis for different scatter morphologies: theory and very-high frequency clinical results. In: Proceedings IEEE Ultrason Symp, pp 1155–1159

Lucas RJ, Twersky V (1987) Inversion of ultrasonic scattering data for red blood cell suspensions under different flow conditions. J Acoust Soc Am 82:794–799

Madsen EL, Insana MF, Zagzebski JA (1984) Method of data reduction for accurate determination of acoustic backscatter coefficients. J Acoust Soc Am 76:913–923

Mamou J, Coron A, Hata M, Machi J, Yanagihara E, Laugier P, Feleppa E (2010) Three-dimensional high-frequency characterization of cancerous lymph nodes. Ultrasound Med Biol 36:361–375

Meiselman HJ (1993) Red blood cell role in RBC aggregation: 1963–1993 and beyond. Clin Hemorheol 13:575–592

Mo LYL and Cobbold RSC (1986) A stochastic model of the backscattered Doppler ultrasound from blood. IEEE Trans Biomed Eng 33:20–27

Mo LYL and Cobbold RSC (1992) A unified appraoch to modeling the backscattered Doppler ultrasound from blood. IEEE Trans Biomed Eng 39:450–461

Mo LYL, Cobbold RSC (1993) In: Shung KK, Thieme GA (eds) Ultrasonic scattering in biological tissues. CRC, Boca Raton, FL

Neumann FJ, Katus HA, Hoberg E, Roebruck P, Braun M, Haupt HM, Yillmanns H, Kubler W (1991) Increased plasma viscosity and erythrocyte aggregation: Indicators of an unfavorable clinical outcome in patients with unstable angina pectoris. Br Heart J 66:425–430

Nguyen LC, Yu FT, Cloutier G (2008) Cyclic changes in blood echogenicity under pulsatile flow are frequency dependent. Ultrasound Med Biol 34:664–673

Oelze ML, Zachary JF (2006) Examination of cancer in mouse models using high frequency quantitative ultrasound. Ultrasound Med Biol 32:1639–1648

Oosterveld BJ, Thijssen JM, Hartman PC, Romijn RL and Rosenbusch GJE (1991) Ultrasound attenuation and texture analysis of diffuse liver disease: methods and preliminary results. Phys Med Biol 36:1039–1064

Poggi M, Palareti G, Biagi R, Parenti M, Babini AC, Coccher S (1994) Prolonged very low calory diet in highly obese subjects reduces plasma viscosity and red cell aggregation but not fibrinogen. Int J Obes 18:490–496

Raju I, Srinivasan MA (2001) High-frequency ultrasonic attenuation and backscatter coefficients of in vivo normal human dermis and subcutaneous fat. Ultrasound Med Biol 27:15431556

Rampling MW, Meiselman HJ, Neu B, Baskurt OK (2004) Influence of cell-specific factors on red blood cell aggregation. Biorheology 41:91–112

Routh HF, Gough W, Williams RP (1987) One-dimensional computer simulation of a wave incident on randomly distributed inhomogeneities with reference to the scattering of ultrasound by blood. Med Biol Eng Comput 25:667–671

Saha RK, Cloutier G (2008) Monte Carlo study on ultrasound backscattering by three-dimensional distributions of red blood cells. Physical Review E 78:061919

Saha RK, Franceschini E, Cloutier G (2011) Assessment of accuracy of the structure-factor-size-estimator method in determining red blood cell aggregate size from ultrasound spectrum backscattering coefficient. J Acoust Soc Am 129:2269–2277

Savery D, Cloutier G (2001) A point process approach to assess the frequency dependence of ultrasound backscattering by aggregating red blood cells. J Acoust Soc Am 110:3252–3262

Savery D, Cloutier G (2005) Effect of red cell clustering and anisotropy on ultrasound blood backscatter: a Monte Carlo study. IEEE Trans Ultras Ferroelectr Freq Control 52:94–103

Savery D, Cloutier G (2007) High-frequency ultrasound backscattering by blood: analytical and semi-analytical models of the erythrocyte cross section. J Acoust Soc Amer 23:3963–3971

Schmid-Schönbein H, Gallasch G, Gosen JV, Volger E, Klose HJ (1976) Red cell aggregation in blood flow. I New methods of quantification. Klin Wschr 54:149–157

Schmid-Schönbein H, Malotta H, Striesow F (1990) Erythrocyte aggregation: causes, consequences and methods of assessment. Tijdschr NVKS 15:88–97

Shung KK (1982) On the ultrasound scattering from blood as a function of hematocrit. IEEE Trans Sonics Ultrason SU-29:327–331

Stoltz JF, Donner M (1991) Red blood cell aggregation: measurements and clinical applications. Tr J Med Sci 15:26–39

Teh BG, Cloutier G (2000) Modeling and analysis of ultrasound backscattering by spherical aggregates and rouleaux of red blood cells. IEEE Trans Ultras Ferroelectr Freq Control 47:1025–1035

Twersky V (1987) Low-frequency scattering by correlated distributions of randomly oriented particles. J Acoust Soc Am 81:1609–1618

Van Der Heiden MS, De Kroon MGM, Bom N, Borst C (1995) Ultrasound backscatter at 30 MHz from human blood: influence of rouleau size affected by blood modification and shear rate. Ultrasound Med Biol 21:817–826

Vayá A, Falcó C, Rganon E, Vila V, Martnez-Sales V, Corella D, Contreras MT, Aznar J (2004) Influence of plasma and erythrocyte factors on red blood cell aggregation in survivors of acute myocardial infarction. Thromb Haemost 91:354–359

Wang SH, Shung KK (1997) An approach for measuring ultrasonic backscattering from biological tissues with focused transducers. IEEE Trans Biomed Eng 44:549–554

Weng X, Cloutier G, Pibarot P, Durand LG (1996a) Comparison and simulation of different levels of erythrocyte aggregation with pig, horse, sheep, calf, and normal human blood. Biorheology 33:365–377

Weng X, Cloutier G, Beaulieu R, Roederer GO (1996b) Influence of acute-phase proteins on erythrocyte aggregation. Am J Physiol 271:H2346–H2352 (Heart and Circulatory, Physiology 40)

Yu FTH, Cloutier G (2007) Experimental ultrasound characterization of red blood cell aggregation using the structure factor size estimator. J Acoust Soc Am 122:645–656

Yu FTH, Franceschini E, Chayer B, Armstrong JK, Meiselman HJ, Cloutier G (2009) Ultrasonic parametric imaging of erythrocyte aggregation using the structure factor size estimator. Biorheology 46:343363

Yu FTH, Armstrong JK, Tripette J, Meiselman HJ, Cloutier G (2011) A local increase in red blood cell aggregation can trigger deep vein thrombosis: evidence based on quantitative cellular ultrasound imaging. J Thrombosis Haemostasis 9:481–488

Yuan YW, Shung KK (1988) Ultrasonic backscatter from flowing whole blood. I: dependence on shear rate and hematocrit. J Acoust Soc Am 84:52–58

Zhang J, Rose JL, Shung KK (1994) A computer model for simulating ultrasonic scattering in biological tissues with high scatterer concentration. Ultrasound Med Biol 20:903–913

Zijlstra WG, Mook GA (1962) Medical reflection photometry. In: Van Gorcum (ed) Assen, Netherlands

Chapter 7
Backscatter Quantification for the Detection of Metastatic Regions in Human Lymph Nodes

Jonathan Mamou, Alain Coron, Emi Saegusa-Beecroft, Masaki Hata, Eugene Yanagihara, Junji Machi, Pascal Laugier and Ernest J. Feleppa

Abstract Quantitative ultrasound (QUS) methods using high-frequency ultrasound offer a means of investigating biological tissue at the microscopic level. This chapter describes high-frequency, three-dimensional (3D) QUS methods to characterize freshly dissected lymph nodes of cancer patients. 3D ultrasound radio-frequency data were acquired from lymph nodes using a 25.6-MHz center-frequency transducer. Each node was inked prior to tissue fixation to recover orientation after sectioning for 3D histological evaluation. Backscattered echo signals were processed using 3D cylindrical regions-of-interest to yield four QUS estimates associated with tissue microstructure (i.e., effective scatterer size,

J. Mamou (✉) · E. J. Feleppa
F. L. Lizzi Center for Biomedical Engineering, Riverside Research, New York, NY, USA
e-mail: jmamou@riversideresearch.org

E. J. Feleppa
e-mail: efeleppa@riversideresearch.org

A. Coron · P. Laugier
UMR7623, Laboratoire d'Imagerie Paramétrique, CNRS, Paris, F-75006, France
e-mail: alain.coron@upmc.fr

P. Laugier
e-mail: pascal.laugier@upmc.fr

A. Coron · P. Laugier
UMR7623, LIP, UPMC Univ Paris 06, Paris, F-75005, France

E. Saegusa-Beecroft · M. Hata · E. Yanagihara · J. Machi
University of Hawaii and Kuakini Medical Center, Honolulu, HI, USA
e-mail: emilysaegusa@hotmail.com

M. Hata
e-mail: masakihata4999@yahoo.co.jp

E. Yanagihara
e-mail: kplety@earthlink.net

J. Machi
e-mail: junji@hawaii.edu

J. Mamou and M. L. Oelze (eds.), *Quantitative Ultrasound in Soft Tissues*, DOI: 10.1007/978-94-007-6952-6_7,

acoustic concentration, spectral intercept, and spectral slope). QUS estimates were computed following established methods using two scattering models. Then, the four QUS estimates were combined using linear-discriminant analysis to increase classification performance. Finally, the discriminant scores were used to compute *a posteriori* cancer probability. In this study, more than 400 lymph nodes acquired from more than 250 patients diagnosed with colon, breast, or gastric cancer were processed. Results indicated that metastatic and cancer-free lymph nodes of colon- and gastric-cancer patients could be well classified using these methods and that metastatic regions could potentially be detected and used to guide pathologists towards suspicious regions.

Keywords High-frequency ultrasound · Lymph node · Cancer · Metastases

7.1 Introduction

Quantitative ultrasound (QUS) imaging attempts to determine meaningful tissue properties in a robust, system-independent, and user-independent fashion. Currently, QUS approaches are being investigated by several research groups, and many tissue parameters have been estimated using a wide range of methods and algorithms. This chapter specifically focuses on QUS methods that analyze the backscattered spectrum of high-frequency ultrasound (HFU, > 20 MHz), radio-frequency (RF) echo signals. These QUS methods are derived from the theoretical framework of ultrasound scattering established in Lizzi et al. (1983) for biological tissues and subsequently expanded (Oelze et al. 2002; Insana et al. 1990; Feleppa et al. 1986; Mamou et al. 2008; Oelze and Zachary 2006). Since these pioneering studies, several groups have established QUS approaches to investigate ocular, liver, prostate, renal, blood, and cardiac tissues at conventional frequencies (i.e., < 10 MHz) for more than three decades (Perez et al. 1988; Lizzi et al. 1983, 1987; Insana et al. 1991; Feleppa et al. 2004; Franceschini et al. 2010; Saha et al. 2011).

This chapter describes QUS methods that are being used to characterize freshly excised human lymph nodes from histologically proven cancer patients. Specifically, the frequency-dependent information derived from the raw RF backscattered signals (Oelze et al. 2002; Insana et al. 1990; Feleppa et al. 1986) is used to assess tissue microstructural properties quantitatively and relate them to histological properties. Therefore, our hypothesis is that QUS estimates obtained using HFU may help to differentiate between cancer-containing (i.e., metastatic) nodes and cancer-free nodes. The QUS methods described in this chapter are able to quantify tissue properties based on theoretical assumptions about the nature of scattering. Accordingly, two scattering models were used to yield four QUS estimates. In previous lymph-node studies more than a decade ago, our group successfully used spectrum-analysis methods at 10 MHz to detect distinct differences between cancerous and cancer-free lymph nodes of breast- and colorectal-cancer patients

(Feleppa et al. 1997); in those preliminary studies at conventional frequencies (i.e., 10 MHz), a single attenuation-independent QUS estimate, spectral intercept, produced an area under the ROC curve (AUC) of 0.97 for identifying metastatic nodes.

In the current standard of care, lymph nodes dissected from a cancer patient are sent to a pathology laboratory for microscopic histological examination. Two different pathology procedures exist: (1) a postoperative complete histological preparation and evaluation, or (2) an intraoperative "touch-prep" procedure. The complete procedure involves bisection nodes that are 5 mm or smaller or cutting larger nodes into 3-mm pieces; fixing and embedding the cut pieces; preparing three to six thin (3-μm) sections from the exposed cut surfaces; placing thin sections on microscope slides; and staining and examining the slides. The complete procedure typically utilizes hematoxylin and eosin (H&E) stains, but also can employ more-sensitive immunohistochemical methods. Complete histological preparation and evaluation provide the definitive means of detecting metastases in lymph nodes; however, the procedure obviously is limited by sampling constraints. The entire volume of the node is not examined. The touch-prep procedure is used for rapid detection of metastases while the patient remains under anesthesia in the operating room. It essentially is a cytological procedure in which selected nodes are dissected and each dissected node is cut in half with a scalpel, and both cut surfaces are pressed on a microscope slide to transfer cells to the slide for microscopic examination. (Postoperatively, nodes that have undergone the intraoperative touch prep procedure also undergo a complete histology preparation and examination.) The touch-prep method is used primarily for sentinel lymph nodes—most commonly for the axillary nodes of invasive breast-cancer patients. If metastases are detected in a touch-prepped node, then a formal (complete) node dissection is performed during the same operation. However, because only cells from the two cut surfaces are examined, the touch-prep procedure presents a high probability of false-negative determinations.

Clearly, both pathology procedures suffer from sampling constraints that can result in false-negative determinations; clinically significant micrometastases (i.e., metastases between 0.2 and 2 mm in size) can be missed. In the touch-prep procedure, the pathologist only examines cells from two adjacent surfaces of the lymph node, and the cells derived from these surfaces may not reveal the presence of a small cancerous region within a metastatic node, i.e., there is a sampling problem. In the complete histological evaluation, the nodes are sectioned into blocks (2–3 mm thick), fixed and embedded, and then thin sections of the surfaces of the thick sections are obtained, histochemically stained, and evaluated under a microscope. Consequently, this method also suffers from a sampling problem; the method reliably detects nodal metastases that are present in the examined thin sections, but only a limited number (usually 2–3) of thin sections are obtained from the surfaces of thick sections. Furthermore, the postoperative histological procedure is time consuming (e.g., requiring 2–3 days).

Although the QUS methods that we are investigating eventually may allow reliable detection of nodal metastases in touch-prep specimens while the patient remains under anesthesia in the operating room, our immediate objective is to

develop high-frequency QUS methods capable of reliably detecting small metastases in freshly excised nodes so that histological examination can be directed toward suspicious regions of the node and small metastases that reside between thick-section surfaces can be detected. In particular, these methods could be used to evaluate all the dissected lymph nodes in their entirety.

In the remainder of this chapter, we present the methods we have developed to acquire and co-register three-dimensional (3D) ultrasound and 3D histological data, to estimate four QUS parameters (i.e., effective scatterer size, acoustic concentration (Oelze et al. 2002), slope and intercept (Lizzi et al. 1983)), to construct color-coded QUS images, or to display 3D interactive maps of cancer probability within the entire lymph node (Mamou et al. 2010). The chapter is organized into the following three sections: the Methods section presents our methods from surgery and lymph-node preparation to QUS image formation; the Results section presents results from a database of over 250 lymph nodes; finally, the Conclusions section presents a summary of the study to date and the next steps of the study. The Institutional Review Boards (IRBs) of the University of Hawaii and the Kuakini Medical Center (KMC) in Honolulu, HI, approved the protocols for participation of human subjects in the study. All participants were recruited at KMC and gave written informed consent as required by both IRBs.

7.2 Methods

7.2.1 Surgery and Ultrasound Data Acquisition

Patients with histologically proven primary cancers (e.g., breast, colon, and gastric cancers) were scheduled for lymphadenectomy. During the surgery, 5–20 lymph nodes were dissected at KMC. Dissected nodes were taken to the pathologist for gross preparation, which included isolating individual nodes and removing as much overlying fibroadipose (i.e., fatty) tissue as possible from each node. Following gross preparation, individual, manually defatted lymph nodes were placed in a water bath containing isotonic saline (0.9 % sodium chloride solution) at room temperature. RF ultrasound data were acquired with a focused, single-element transducer (PI30-2-R0.50IN, Olympus NDT, Waltham, MA) with an aperture of 6.1 mm and a focal length of 12.2 mm (i.e., an F-number of 2). The transducer had a center frequency of 25.6 MHz and a −6-dB bandwidth that extended from 16.4 to 33.6 MHz. Figure 7.1a shows the 3-axis scanning system with a lymph node being scanned. Figure 7.1b provides a closer view of the transducer and the lymph node pinned to the sound-absorbing material. The transducer was excited by a Panametrics 5900 pulser/receiver unit (Olympus NDT, Waltham, MA) used with an energy setting of 4 μJ. RF echo signals were digitized using an 8-bit A/D board (DB-105, Acqiris, Monroe, NY) at a sampling frequency of 400 MHz. A 3D scan of each lymph node

(a) **(b)**

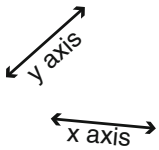

Fig. 7.1 The scanning system with a lymph node pinned to a piece of sound-absorbing material. Axis orientations are shown. (Reproduced from Mamou et al. 2010)

was obtained by scanning in a raster pattern with scan vectors separated by 25 μm in *x* and *y* directions to uniformly interrogate the entire lymph node.

7.2.2 Histology Data Acquisition

For this project, a non-standard histology procedure was required for two reasons. First, we needed fine spatial sampling to guarantee that no clinically significant metastases would be missed. Accurate determination of the presence and distribution of cancer foci was critical for developing and assessing classifiers and the ability to image clinically significant metastases. Second, we needed fine sampling to permit rapid co-registration of the 3D ultrasound volume with the 3D histology volume. Co-registration was critical to evaluate whether the QUS methods are able to detect the metastatic regions within the lymph nodes in a sufficiently reliable manner.

Accordingly, scanned nodes were inked immediately after ultrasound data acquisition to provide visual references for subsequent reassembly of histology into 3D volumes and spatial matching with volumes generated from the 3D HFU dataset and 3D QUS processing. Inked nodes then were prepared for histology. Figure 7.2a and c display a schematic and an actual lymph node after inking. Red and blue inks divided the surface of a whole node into two sections (i.e., to recover top and bottom) and a circle of black ink was placed at a junction between the two colored sections (i.e., to recover left and right). The complete node was photographed using a digital camera (FujiFilm FinePix S9100, Fuji Photo Film, Tokyo, Japan) equipped with Hoya +2 and +4 close-up lenses (Hoya Corp., Tokyo, Japan)

in order to estimate the size of the lymph node prior to histologic preparation including tissue fixation and subsequent shrinkage. In this study, we approximated each lymph node as an ellipsoid; sizing the lymph node consisted of measuring the length of the three main axes of the lymph-node-approximating ellipsoid as illustrated in Fig. 7.2c and e.

Following sizing, the node was cut longitudinally, approximately in half, perpendicular to the black-inked region and bisecting the node at the junction between the red and blue inks, as indicated in Fig. 7.2a. The two half-nodes were fixed in 10 % neutral-buffered formalin and embedded in paraffin with the flat cut surface oriented downward in the embedding cassette, as illustrated in Fig. 7.2b. After embedding, the two fixed half-nodes were microtomed into paired thin sections, placed on microscope slides and stained with H&E. Figure 7.2d and f show a cartoon and an actual pair of half-node histology sections adjacent to the flat cut plane, respectively. One cut plane is shown on Fig. 7.2b to d with two different shades of gray to illustrate how 3D histologic volumes were derived from histology sections. In most histology sections, orientation was easily recovered because the blue-, red-, and black-inked boundaries were visible at the edges of the remaining perinodal fibroadipose tissue. (In Fig. 7.2f, the visible blue, red, and black inks are enhanced digitally for display purposes.)

Each pair of stained thin sections was 3 μm thick and sets of 3 to 5 pairs were obtained 50 or 100 μm from the preceding set of sections depending on the size of the lymph node. (Steps of 50 μm were used for nodes smaller than 5 mm; 100 μm steps were used for larger nodes.) Digital images were made of each H&E-stained slide; each image contained the paired histologic images of the two lymph-node halves. These histological images were made using either the same digital camera used for sizing or a high-quality, high-throughput slide scanner (NanoZoomer, Hamamatsu, Japan) with a pixel resolution of 0.46 μm. (In conventional node evaluations, the pathologist characterizes each lymph node based on only 2 or 3 stained histology sections from each major cut surface, which typically is only the pair of surfaces exposed by the single node-bisecting central cut. However, in our study, the best-quality pair of thin sections at each step section were histologically evaluated; this typically involved 15 to 30 thin sections per node.)

7.2.3 Three-Dimensional Histologic Volume Reconstruction

The set of bitmap images of the histologic sections was used to reconstruct a 3D histological model of the node with an inter-section spacing that matched the original separations (i.e., 50 or 100 μm) between the thin sections obtained at each step. The 3D histology reconstruction enabled spatial matching of histologically proven, metastatic cancer foci with their signatures in QUS images.

To explain the spatial relationships between ultrasound scan planes and histology sections, three dashed lines are included on Fig. 7.2e to symbolize three parallel ultrasound scan planes. Their spatial locations are quantified by their y

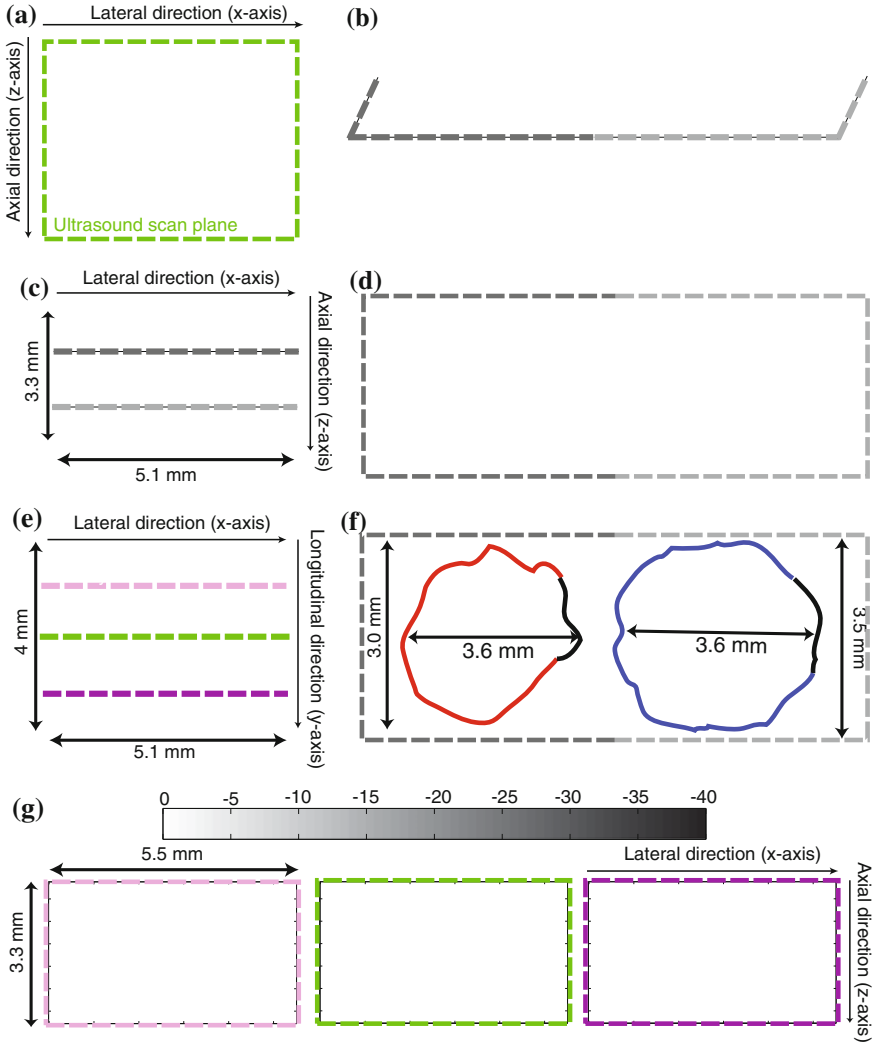

Fig. 7.2 Illustration of the geometry-conserving, histology, and sizing procedures of a lymph node: **a** inking cartoon; **b** sectioning cartoon prior to embedding for histology; **c** and **e** sizing photographs of a colon-cancer lymph node; **d** and **f** cartoon and sizing photographs of histology section; and **g** three conventional B-mode images (40-dB dynamic range) obtained at different y locations ($y = 0$ is the central section of the lymph node). Shrinkage due to fixation is estimated from the dimensional changes in **c** and **e** compared to **f**. The scanning planes are indicated by the *dashed pink*, *green*, and *purple lines* in Fig. 7.2e. The complete 3D ultrasound data set of this lymph node contains 160 sections. (Reproduced from Mamou et al. 2010)

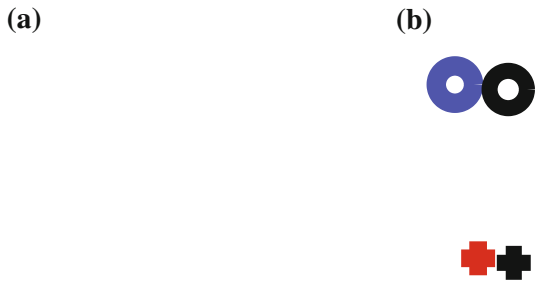

Fig. 7.3 **a** Extra digital image with the dots to recover the orientation with respect to the ultrasound data set. **b** Results of the automatic disc detection algorithm: the black and red crosses indicate where the two discs corresponding to the red half were found and the black and the blue discs indicate where the two discs corresponding to the blue half were found

coordinate in reference to the center plane depicted by the green dashed line. The center plane is also depicted in green on Fig. 7.2a. The ultrasound images corresponding to these three scan planes are shown in Fig. 7.2g. The colors used around the ultrasound images are the same as in Fig. 7.2e.

To permit accurate co-registration, an additional digital image was acquired of a central slice with orientation information added as blue, black, and red dots to identify the inked edges of the connective remnants of the perinodal fibroadipose tissue (Fig. 7.3a). From that information, we were able to recover the orientation of the HFU coordinate system with respect to the top (red) and bottom (blue) half-node sections. The four dots were detected automatically using a disc detection algorithm looking for discs of known *a priori* diameter and colors (i.e., one blue disc, one red disc and two black discs). The results of the disc detection algorithm are shown in Fig. 7.3b, where the two dots corresponding to the red half are symbolized by red and black crosses, and those corresponding to the blue half are symbolized by red and blue discs.

Then, in each digital image, we needed to isolate the separate histology sections from the two lymph-node halves. Isolation was accomplished using a segmentation algorithm that we expressed as a cost-minimization problem based on a parametric-shape modeling of the sections as ellipses. Thus, we searched for the position, size and orientation of two non-intersecting ellipses, $\mathscr{E}_1$, $\mathscr{E}_2$, one for each section and covered as much tissue as possible and as little background as possible (i.e., the cost function increased when more background tissue was included and decreased when more node tissue was included). From the estimated ellipses $\mathscr{E}_1$ and $\mathscr{E}_2$, the location of each section was extracted as well as a straight line to separate the two sections. This line was the bisector of the points $P_1 \in \mathscr{E}_1$ and $P_2 \in \mathscr{E}_2$ that minimized the Euclidian distance between the two ellipses.

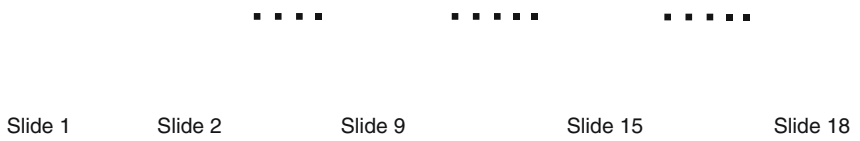

Fig. 7.4 Results of the section detection using the energy minimization approach on a lymph node from a colon-cancer patient. The ellipses minimizing the cost function are shown as well as the closest points, P_1 and P_2, from both ellipses. (Only five digital histology images of the 18 total images are shown)

Figure 7.4 illustrates the results of the segmentation algorithm on a lymph node from a colon-cancer patient. (Details about the energy minimization routine can be found in Coron et al. 2010.)

After the location of the sections was found in each digital image, we registered the saturation channel of each consecutive pair of sections in order to find the rigid transform that best aligned one image to the next. In order to minimize the background area, the images were limited to a bounding box slightly larger than the bounding box of the ellipses. The following two metrics were considered: normalized correlation and mutual information. This optimization problem was solved using `elastix` (Klein et al. 2010), a publicly available computer program for intensity-based medical image registration that includes a hierarchical strategy and adaptive stochastic gradient descent optimizer.

The rigid transformations were used to align each digital image with the image with the extra dots. Then, using the bisector of the ellipses and the previously estimated transforms, the sections were separated. Two new images were created (one for each section) from each digital image. Additionally, the sections of the top half-node needed to be reflected because of the discrepancy in the orientation of the HFU acquisition system and the image-coordinate system. In order to get an initial rigid transform for aligning the bottom and top half-nodes, the rotation and translation that best matched the two pairs of dots were estimated.

Because histology preparation potentially could lose portions of tissue or produce tears on the two central sections, they were not considered to be good candidates for registering the two half-nodes. Therefore, we constructed the "footprint" images of the top and bottom half-nodes. Then, the rigid transform that best aligned the half-nodes was estimated by registering these footprint images with `elastix`. The footprint of each half-node was defined as the maximum of the saturation value of each image belonging to each half.

Once the two half-nodes were reconstructed and registered, a final rigid transform was applied to the entire data set so that the detected dots matched the orientation of the ultrasound data as illustrated in Figs. 7.2 and 7.3. This final step led to a stack of histology images aligned with the 3D ultrasound data set.

7.2.4 Three-Dimensional Ultrasound Segmentation

Observation of the 3D ultrasound images revealed that some residual perinodal fibroadipose tissue often remained surrounding the lymph node. The thickness of the remaining layer varied among lymph nodes, and for most lymph nodes it was between 100 and 500 μm. The layer of intervening fibroadipose tissue could bias the QUS results because fibroadipose tissue could have a different attenuation than nodal tissue and also QUS processing needed to be limited to nodal tissue and to exclude fibroadipose tissue.

Therefore, a 3D segmentation algorithm was developed to detect the remaining fibroadipose tissue. The algorithm followed a region-based, semiautomatic approach which was implemented in MATLAB (The MathWorks, Inc., Natick, MA). First, the envelope of each RF line was downsampled by a factor of 8 by computing approximation coefficients with Mallat's pyramidal algorithm (Mallat 2009) and log-compressed. Then, the 3D watershed transform was applied to the 3D H-minima transform (Soille 2002) of the 3D Deriche gradient (Farnebäck and Westin 2006) of the log-compressed approximation coefficients.The watershed transform is a well-known segmentation approach known to oversegment (i.e., generate many regions). Therefore, the H-minima transform was used to remove local minima of the 3D gradient to reduce the number of regions returned by the watershed transform.

The 3D ultrasound data was segmented into three regions (i.e., saline, fibroadipose, and lymph-node tissue). In order to classify each watershed-deduced region as saline, node tissue or fibroadipose tissue, a pseudo-maximum-probability classifier was used. The mean echo amplitude of each region, $\bar{x}$, was used for classification because examination of the ultrasound data revealed that at a given depth, a saline voxel is almost certainly less echogenic than a node-tissue voxel, and a typical node-tissue voxel is less echogenic than a typical residual-fibroadipose voxel. The classifier used two thresholds, T_1 and T_2, to classify voxels based on which of the conditional probability density functions (PDFs), $p(x|C)$ with C being saline, node tissue, or fibroadipose tissue, was the greatest. Therefore, a region was classified as saline if $\bar{x} \leq T_1$, node tissue if $T_1 < \bar{x} \leq T_2$, and fibroadipose tissue if $\bar{x} > T_2$.

The PDF for the lymph-node tissue was estimated from voxels located in a small 3D region centered at the transducer focus and in the middle of the xy-plane; this volume usually was exactly at the center of the lymph node and therefore was entirely filled by lymph-node tissue. The saline PDF was estimated from voxels located in the top four corners of the 3D RF data set; these corners are always filled by saline because lymph nodes typically have an ellipsoidal shape. Finally, the residual-fibroadipose-tissue PDF was estimated using voxels from a 3D slice near the focal plane (i.e., at a value of z between 12.05 and 12.15 mm). Because fibroadipose voxels usually have a higher echo amplitude than the amplitude of node tissue or saline, the regions within this slice with the 10 % highest mean-intensity values were selected and used to estimate the residual-fibroadipose-tissue

PDF. To account for beam diffraction, T_2 was rendered depth (d) dependent: $T_2(d) = T_2 + K(d)$ where $K(d)$ is the maximum of a reference echo at depth d. Finally, residual artifacts (if any) of the 3D segmentation were corrected by an expert using our custom visualization software.

A previous study showed that even without human correction, the 3D segmentation algorithm produced satisfactory results on a limited, but representative, set of lymph nodes obtained from colorectal-cancer patients (Coron et al. 2008). However, most axillary lymph nodes obtained from breast-cancer patients had to be manually corrected because they were structurally more complex. In particular, some fatty deposits remained inside the lymph nodes. We are currently investigating novel approaches to segment the axillary lymph nodes automatically.

7.2.5 QUS Estimation

During the course of this project, several QUS methods were applied and many different QUS estimates were obtained (Mamou et al. 2010, 2011), but for this chapter we will only focus on the QUS methods that quantify the backscattered spectra. In total, four QUS estimates were obtained computed from using these methods. Specifically, two different ultrasound-scattering models were used, each leading to two QUS estimates. These four QUS estimates quantify microstructural tissue properties and were used to test the hypothesis that QUS estimates are statistically different between cancerous (i.e., metastatic) and non-cancerous tissue in lymph nodes.

7.2.5.1 Three-Dimensional Cylindrical Regions of Interest

To take advantage of the 3D RF data set, we used 3D regions of interest (ROIs) because they closely follow the beam shape and permit us to obtain normalized spectra with a high SNR (because more independent RF segments are used than in 2D ROIs having the same cross-section). The complete 3D RF data set was separated into overlapping 3D cylindrical ROIs having a diameter (in the xy plane) of 1 mm and a length (in the z direction) of 1 mm. The size of the ROI was based on the resolution cell size of our imaging system. Theory predicted the axial and lateral resolutions of the HFU imaging system to be 86 and 116 μm, respectively (Kino 1987). Therefore, a cylindrical ROI contained about 648 resolution cells, which allowed ample averaging of independent scattering contributions. The overlap between adjacent ROIs depended on the total number of voxels in the 3D RF data set; it was selected to permit smaller data sets to have sufficient ROIs for statistical stability while avoiding overly long computation times for larger data sets.

Figure 7.5 shows three cross-sectional B-mode images of a segmented lymph node obtained from a colon-cancer patient. The results of the 3D segmentation are depicted by the green and red highlights in all three cross-sections. Based on the

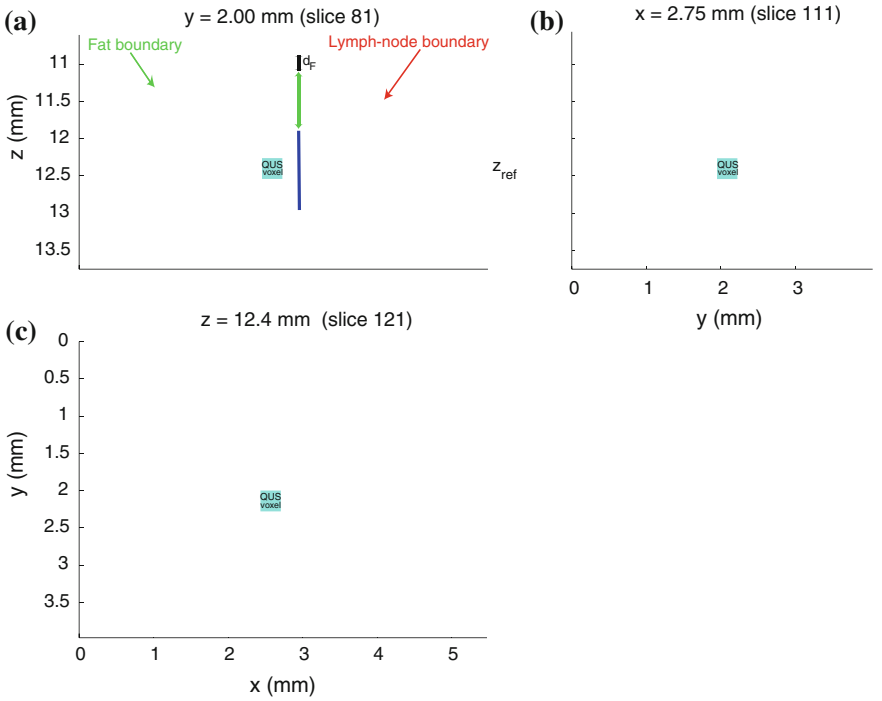

Fig. 7.5 Illustration of the QUS processing of a colon-cancer lymph node. **a** Cross-section at $y = 2.00$ mm, **b** cross-section at $x = 2.75$ mm, and **c** cross-section at $z = 12.4$ mm. (Reproduced from Mamou et al. 2010)

3D segmentation results, QUS estimates were computed only when the 3D ROI was entirely composed of lymph-node tissue (i.e., all of the 3D ROI was contained inside the red highlighted segmented border of the lymph-node tissue). The dark blue square in Fig. 7.5a and b and the light-blue circle in Fig. 7.5c depict a 3D cylindrical ROI ($L = 1$ mm). QUS parameters were estimated in each ROI to generate QUS images having a voxel size corresponding to the spacing between adjacent ROIs. The solid blue square in Fig. 7.5 depicts a QUS voxel corresponding to the surrounding cylindrical ROI.

7.2.5.2 Calibration

To remove system and user dependence, calibration was performed using the reflection of a planar reflector over a range of depths using the same instrument settings as those used during lymph-node data acquisition (Lizzi et al. 1987; Oelze et al. 2002; Insana et al. 1990). This calibration step is critical to obtain robust QUS estimates that depend only on underlying tissue properties and therefore can be used rigorously to assess tissue pathology.

Tissue is a weak reflector of sound because the acoustic impedance of the great majority of tissue scatterers is within a few percent of that of water (Duck 1990; Goss et al. 1978, 1980). To maintain the same digitizer and pulser settings for calibration and acquisition of echo signals from tissue, we used a weakly reflecting planar reflector that also is a weak reflector of sound for a calibration target. We used Dow Corning 710 oil (Dow Corning Corporation, Midland, MI) because it has acoustic properties close to those of water, but is more dense than water so that ultrasound from a transducer mounted above the interface can propagate through an aqueous medium to the weakly reflecting water-oil interface (Assentoft et al. 2001; Oelze et al. 2003). Maintaining the same digitizer and pulser settings guarantees a more accurate calibration, making the QUS estimates more system independent.

7.2.5.3 Attenuation Compensation

Because original theoretical frameworks assume that a plane wave is propagating through a non-attenuating medium, calibration reduces processing to the plane wave case (Insana et al. 1990; Lizzi et al. 1983), but attenuation compensation remains necessary. Frequency-dependent attenuation can lead to a bias in QUS estimates which is a function of depth and does not depend on the underlying tissue properties. Therefore, a critical part of the signal processing and the theoretical models underlying QUS is accurately compensating for attenuation (Oelze and O'Brien 2002).

In this study, attenuation compensation is particularly critical because HFU waves are attenuated more strongly than waves at more-commonly encountered lower frequencies. Attenuation compensation was performed by utilizing an attenuation-compensation function in the frequency domain. Attenuation compensation was conducted individually for every RF segment of each ROI.

Figure 7.5a shows the boundaries of the layer of external, node-enveloping, fibroadipose tissue (in green) and of the lymph node itself (in red). These boundaries were obtained by the segmentation algorithm summarized above. To reach the beginning of the RF segment, sound had to travel through two layers of attenuating material with different attenuation-coefficient values. The first was a layer of highly attenuating, residual, external fibroadipose tissue (of length d_F in Fig. 7.5a) and the second was an internal layer of lymph-node tissue (of length d_N in Fig. 7.5a). Note that values of d_F and d_N are different for each RF segment of the 3D ROI. (A uniform speed-of-sound value of 1485 m/s was assumed for saline, lymph-node tissue, and fibroadipose tissue.)

To compensate for the attenuation for each specific RF segment of each specific ROI, the following attenuation-compensation function was computed (Oelze and O'Brien 2002):

$$A(f) = e^{4\alpha_F(f)d_F} e^{4\alpha_N(f)d_N} \left[\frac{2\alpha_N(f)L}{1 - e^{2\alpha_N(f)L}}\right]^2 \left[1 + \left(\frac{\alpha_N(f)L}{\pi}\right)^2\right]^2, \tag{7.1}$$

where L is the length of the ROI in cm, and $\alpha_F(f)$ and $\alpha_N(f)$ are the attenuation coefficients in Np/cm at frequency f of the fibroadipose tissue and lymph-node tissue, respectively. In this study, the value of L was kept at 1 mm. The frequency-dependent attenuation coefficient of fibroadipose tissue was measured to be 0.97 dB/MHz/cm (using a spectral-difference method applied to backscattered echoes from the fat tissue of four lymph nodes) at 20 MHz, and the coefficient inside the lymph node was assumed to be 0.5 dB/MHz/cm which is typical of soft tissue (Goss et al. 1978, 1980). (The spectral-difference method consists of subtracting the spectra of two ROIs at different depths and estimating the attenuation as a function of frequency and distance (i.e., in dB/MHz/cm); this method is prone to large standard deviations. We are currently investigating more-robust substitution methods to estimate fibroadipose-tissue and lymph-node-tissue attenuation more accurately (van der Steen et al. 1991; D'Astous and Foster 1986)).

In Eq. (7.1), the first term accounts for the attenuation due to the fibroadipose-tissue layer (of length d_F); the second term accounts for the attenuation inside the lymph node to the beginning of the ROI (i.e., a distance of d_N traveled in the lymph node); the third term accounts for the attenuation within the ROI of length L; and the fourth term accounts for the effect of using a Hanning window over the length L of the ROI. A Hanning window was used to compute the power spectrum of every RF segment.

The attenuation-compensated power spectrum of the RF segment of this specific ROI was computed by:

$$S(f) = |FT[RF_L(t)H_L(t)]|^2 A(f), \tag{7.2}$$

where FT is the Fourier transform operator, RF_L is the raw RF-segment time-domain signal data, and H_L is the Hanning window of length L centered on the middle of the RF segment.

Finally, the attenuation-compensated power spectrum of the entire ROI, $S_{ROI}(f)$, was computed by averaging the attenuation-compensated power spectrum of each RF segment as:

$$S_{ROI}(f) = \frac{1}{N}\sum_{i=1}^{N} S_i(f), \tag{7.3}$$

where N is the number of RF segments within the ROI and $S_i(f)$ is the attenuation-compensated spectrum of the i th RF segment of the ROI computed using Eq. (7.2). In this study, N is equal to 1,251 because the adjacent A-lines were 25 μm apart and therefore the radius of a cylindrical ROI was composed of 20 A-lines and $\pi 20^2 \approx 1,251$.

7.2.6 QUS Estimation

Following averaging, $S_{ROI}(f)$ was divided by the calibration spectrum of the water-oil interface located at the center depth of the ROI (i.e., z_{ref} on Fig. 7.5a). The resulting spectrum was log-compressed to produce the normalized power spectrum (in dB) of the ROI (Oelze et al. 2002):

$$W_{ROI}(f) = 10\log[S_{ROI}(f)] - 10\log\left[S_{oil}(f, z_{ref})\right], \tag{7.4}$$

where

$$S_{oil}(f, z_{ref}) = \frac{4}{R(f)^2}\left|FT\left[RF_{oil}(t, z_{ref})\right]\right|^2, \tag{7.5}$$

and $RF_{oil}(t, z_{ref})$ is the RF time signal of length L obtained from the reflection of the water-oil interface at a depth z_{ref}. $R(f)$ is the frequency-dependent pressure-reflection coefficient of the water-oil interface. Numerical values of $R(f)$ were obtained from 1 to 100 MHz by fitting reflection-coefficient measurements to a reflection-coefficient model that included an attenuating medium (i.e., the oil has a complex impedance, see Eq. (8.3.3) of Kinsler et al. 2000). Using this normalization approach, $W_{ROI}(f)$ is dependent only upon tissue properties; system and user dependence have been entirely removed (Oelze et al. 2002; Insana et al. 1990; Lizzi et al. 1983).

To obtain QUS estimates, $W_{ROI}(f)$ was parameterized. Specifically, four QUS parameters were estimated by fitting two different models to Eq. (7.4) over an ROI-dependent frequency band (i.e., the fitting band). The first model was a straight line and led to estimates of spectral intercept (I) and spectral slope (S). The second model was a spherical Gaussian scattering model (i.e., a spherical Gaussian form factor (Insana et al. 1990)); this model yielded estimates of effective scatterer sizes (D in μm) and acoustic concentration (i.e., CQ^2 expressed in dB mm^{-3}). Briefly, $Q_{ROI}(f) = W_{ROI}(f) - 40\log(f)$ is fit to an affine function of f^2, i.e., $Q_{ROI}(f) \simeq Mf^2 + N$. Finally, D is estimated from M only and then CQ^2 is estimated from D and N (Oelze et al. 2002). The frequency band over which the models were fit to Q_{ROI} or W_{ROI} was varied between each ROI using an SNR-estimation algorithm. Theory predicts that standard deviations of QUS estimates decrease when the fitting band increases in width (Oelze et al. 2002; Chaturvedi and Insana 1996). Briefly, the algorithm estimates the backscattered spectrum which would be obtained from a virtual planar reflector placed at the center of the ROI. This estimation takes into account the transducer beam properties and also the attenuation along the propagation path to the ROI. The optimization bandwidth included the frequencies for which the estimated backscattered spectrum amplitude was > -12 dB when normalized by the spectrum from the oil at the natural focus of the transducer. Details about the SNR-estimation approach can be found in Mamou et al. (2010).

The estimation process was repeated for all ROIs within the entire segmented lymph-node tissue. 3D QUS images were formed by color-coding and overlaying the parameter values (i.e., D, CQ^2, I, or S) on the conventional B-mode volume. Also, ROIs that were not fully contained in depth between $z = 10.9$ mm and $z = 13.3$ mm were not processed because they were judged to be too far away from the nominal focal depth of the transducer.

7.2.7 Classification and Cancer-Probability Estimation

A set of uniform lymph nodes (i.e., either entirely devoid of metastatic tissues or essentially completely filled by metastatic tissue) was used to train the classifier. Specifically, the average values of all four QUS parameters for each lymph node of the training set were computed and a linear-discriminant (LD) function, Δ, was computed.

$$\Delta = \alpha_1 D + \alpha_2 CQ^2 + \alpha_3 I + \alpha_4 S = \vec{\alpha} \cdot \vec{E}, \tag{7.6}$$

where $\vec{\alpha}$ is the vector of linear coefficients and $\vec{E}$ is the vector formed by the four QUS estimates. The linear-coefficient vector was obtained using the Fisher LD approach which maximizes the ratio of the interclass variance to intraclass variance.

$$\vec{\alpha} = (\Sigma_1 + \Sigma_0)^{-1}(\vec{\mu}_1 - \vec{\mu}_0), \tag{7.7}$$

where Σ_1 and Σ_0 are the covariance matrices of $\vec{E}$ for cancer and non-cancerous lymph nodes, and $\vec{\mu}_1$ and $\vec{\mu}_0$ are the mean of $\vec{E}$ for cancerous and non-cancerous lymph nodes, respectively.

The LD approach was used to evaluate the classification performance of the combination of any two or three QUS estimates as well as all four QUS estimates together. The classification performance was evaluated by deriving ROC curves and computing the AUC for each individual QUS estimate and for all possible linear combinations of the four estimates.

Finally, Δ was used to compute *a posteriori* cancer probability for each ROI of each lymph node:

$$P(\delta) = \frac{e^{-(\delta-\Delta_1)^2/\sigma_\Delta^2}}{e^{-(\delta-\Delta_1)^2/\sigma_\Delta^2} + e^{-(\delta-\Delta_0)^2/\sigma_\Delta^2}}, \tag{7.8}$$

where Δ_1 and Δ_0 are the mean of the discriminant score for cancerous and non-cancerous nodes, σ_Δ is the total variance over the training set, and δ is the discriminant score for the ROI.

7.3 Results

More than 400 lymph nodes were processed with these QUS methods. For classifier-training purposes, nodes were separated by primary cancer organ (i.e., colorectal, gastric, and breast) and only uniform nodes were used; uniform nodes were nodes either essentially entirely filled with metastatic tissue or nodes devoid of any metastatic tissue.

7.3.1 Illustrative QUS Images

A powerful visualization software was developed in MATLAB to permit the exploration in 3D of each lymph node. The software allows visualization of three orthogonal cross-sections of the B-mode data, along with the segmentation results, any individual QUS estimate, the cancer probability, as well as the matching plane of co-registered histology.

To illustrate the visualization software, parametric images enhanced by effective scatterer sizes are shown in Figs. 7.6 and 7.7. In these figures, three panels show the ultrasound data while the fourth displays the co-registered histology that matches the presentation of the *xy* ultrasound plane. On the ultrasound panels, the segmentation results are shown by the green and red outlines that demarcate the fibroadipose and nodal tissue, respectively. Additionally, the estimated effective scatterer sizes for each ROI are color-coded and overlaid on the conventional B-mode data display. Finally, the fourth panel displays the histology images closest to the corresponding ultrasound section shown in the *xy* plane, i.e., at a constant *z*.

The lymph node shown in Fig. 7.6 was obtained from a colon-cancer patient and it did not contain any metastatic foci. The lymph node shown in Fig. 7.7 was obtained from a different colon-cancer patient and was entirely metastatic. To permit comparison, the color scale for the effective scatterer-size estimates is the same on the two figures. Specifically, the average scatterer-size estimates were 21.3 ± 1.6 μm for the non-metastatic node and 38.9 ± 3.0 μm for the metastatic node. These illustrative results suggest that a larger scatterer size may reliably indicate metastatic regions within lymph nodes of colon-cancer patients.

7.3.2 Classification Performance

In total, 267 uniform lymph nodes from 168 patients were entirely processed and used to train LD-based classifiers. Table 7.1 presents the classification performance results. For each organ, the first line shows the classification results expressed as ROC AUC values obtained using the single best QUS estimate and the second line shows the AUC results obtained by linearly combining the four

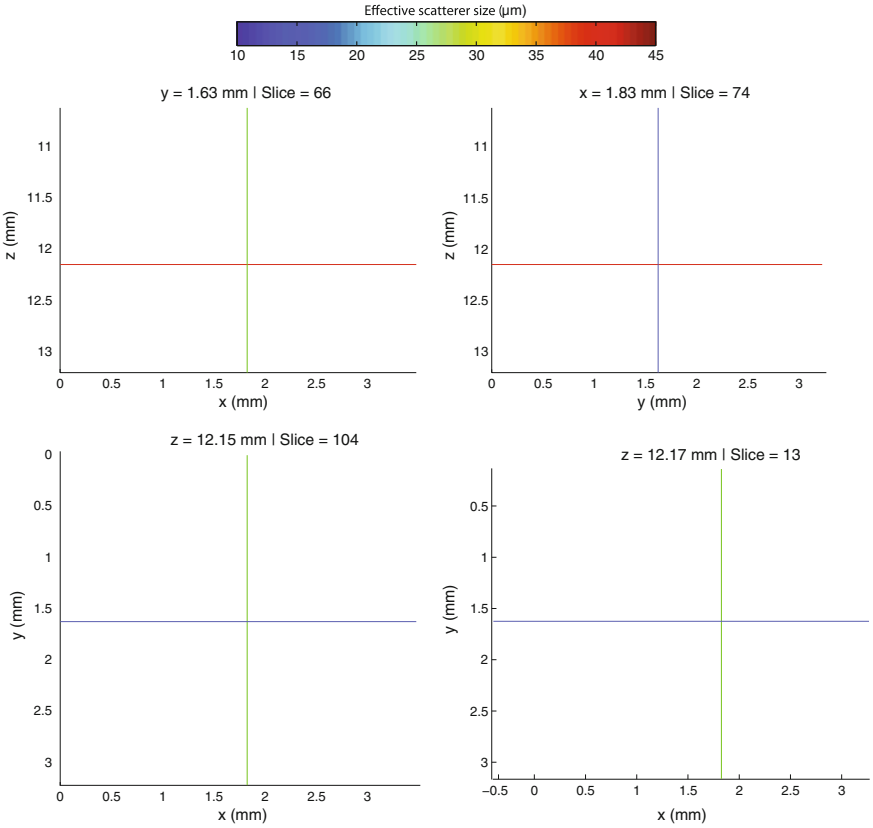

Fig. 7.6 3D cross-sectional parametric images of a non-metastatic lymph node from a colon-cancer patient. Effective scatterer-size estimates are color-coded and overlaid on the three conventional B-mode images. Co-registered histology is also shown

QUS estimates. Finally, the last two columns display sensitivity and specificity values obtained at a specific operating point on the corresponding ROC curve. This operating point was chosen to be clinically conservative (i.e., specifying a high sensitivity value to limit false-negative determinations at the expense of moderately-higher false-positive determinations).

The colorectal-cancer results are very satisfactory, and excellent classification performance was obtained with an AUC value of 0.950 using D alone. Note that LD analysis did not increase the performance significantly. The gastric-cancer results are similar and equally satisfactory when the four QUS estimates were combined, although because of the limited number of cases, greater uncertainty in the AUC value exists. In previous reports, the gastric-cancer nodes were analyzed in combination with the colorectal-cancer nodes because their histologic differences are minute (Mamou et al. 2011) and because the number of cases was insufficient for independent analysis. As the number of gastric-cancer cases

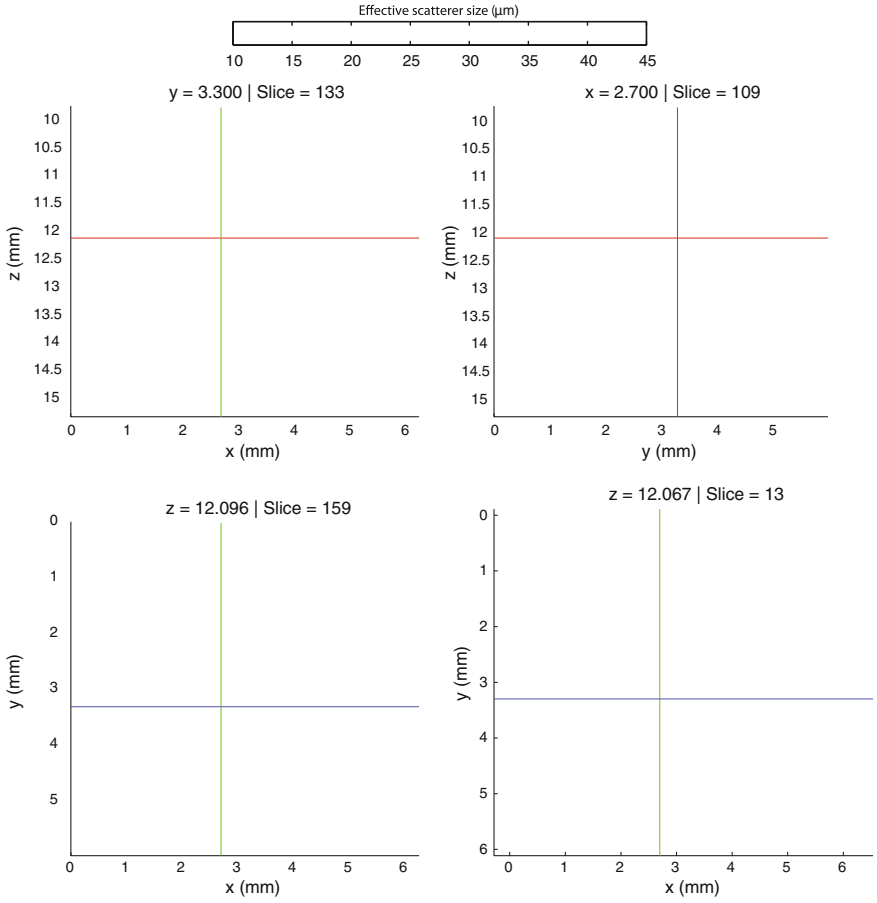

Fig. 7.7 3D cross-sectional parametric images of an entirely metastatic lymph node from a colon-cancer patient. Effective scatterer-size estimates are color-coded and overlaid on the three conventional B-mode images. Co-registered histology is also shown

increases, our methods will be tested for their ability to track these minute differences.

The axillary nodes of breast-cancer patients are structurally very different from the gastric- and colorectal-cancer nodes, and classification performance was much poorer; classifcation of axillary nodes gave an AUC of 0.752 using LD analysis. Note that the single best QUS estimate (i.e., D) produced a nearly random classification with an AUC value of 0.565, marginally above 0.500. This result may indicate that the scattering models being used are not well suited to lymph nodes obtained from breast-cancer patients.

The ROC curves obtained using LD analysis are displayed in Fig. 7.8. Clinically conservative operative points are also shown on the ROC curves in the same figure. These ROC curves illustrate how the QUS method potentially could be used

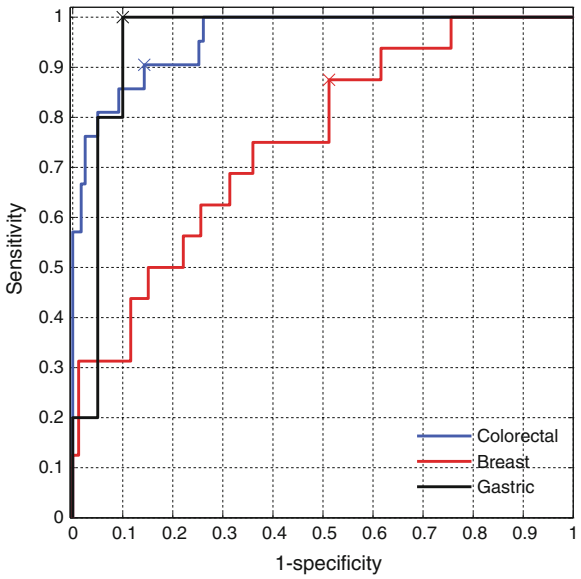

Fig. 7.8 ROC curves obtained using LD analysis

Table 7.1 Classification performance of QUS

Primary organ	Patient number	Total nodes	Cancerous nodes	Non-cancerous nodes	Parameter	ROC AUC	Sensitivity (%)	Specificity (%)
					D	0.958 ± 0.012	90.5	85.7
Colorectal	77	140	21	119	LD	0.958 ± 0.012	90.5	85.7
					D	0.880 ± 0.069	100	85.0
Gastric	17	25	5	20	LD	0.950 ± 0.044	100	90.0
					D	0.565 ± 0.061	87.5	36.0
Breast	74	102	16	86	LD	0.752 ± 0.065	87.5	48.8

Areas under the ROC curve (AUC)

clinically to drastically reduce the number of false-negative determinations obtained using current standard histopathology procedures.

7.3.3 Cancer-Probability Images and Pathology Guidance

Three-dimensional parametric images depicting cancer probability within lymph nodes were generated using the methods described in Sect. 7.2.7. These images permit a quick investigation of the entire lymph node using the 3D interactive display, and the images can be interpreted readily by clinicians and pathologists.

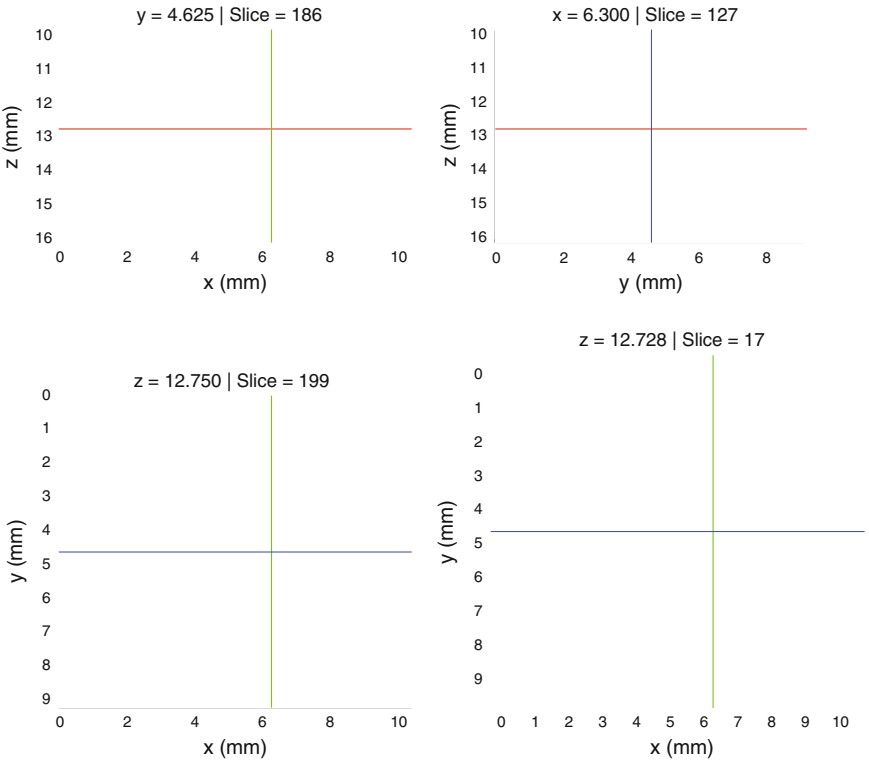

Fig. 7.9 Three-dimensional cross-sectional parametric images of a partially metastatic lymph node from a colon-cancer patient. Red highlights symbolize cancer probability greater than 50 %. Co-registered histology photomicrograph showing metastatic regions in green is also shown

Figure 7.9 displays an illustrative image of a partially metastatic lymph node obtained from a colon-cancer patient. This image is analogous to Fig. 7.6 except that regions in the lymph node having a QUS-derived cancer probability greater than 50 % are highlighted in red and cancerous regions in the histology image (bottom right panel) were outlined in green by the pathologist. Figure 7.9 indicates that the metastatic foci were well detected in the B-mode images augmented with the cancer-probability overlay.

7.4 Conclusions

The results of this study establish the potential of QUS-based detection of metastatic regions in dissected lymph nodes. For colorectal- and gastric-cancer nodes, the four QUS estimates were able to yield high sensitivity while maintaining satisfactory specificity. Therefore, the results to date suggest that these methods

have a superb potential for specific detection and localization of micrometastases often missed during conventional histology of this category of lymph nodes. However, for axillary nodes of breast-cancer patients, the results suggest that the two scattering models used to obtain the four QUS estimates might be inappropriate. New models should be investigated and heavily tested.

Although not presented in this chapter, our QUS methods have been augmented to include nine additional QUS estimates based on envelope statistics (Mamou et al. 2011, 2012). The inclusion of these envelope-based estimates significantly improved classification performance for breast-cancer nodes. Specifically, an AUC of 0.85 with a sensitivity of 93.8 % and a corresponding specificity of 55.8 % were obtained. Nevertheless, the results remained less satisfactory than results for the other node types. (The inclusion of the QUS estimates based on envelope statistics did not significantly improve the already excellent classification performance obtained for colorectal- and gastric-cancer lymph nodes.)

For axillary sentinel lymph nodes, which are cut in half prior to 3D ultrasound scanning during the touch-prep procedure, we also are investigating the use of higher-frequency ultrasound. We currently are scanning half-nodes obtained from sentinel lymph nodes with a single-element transducer having a center frequency around 35 MHz. The improved spatial resolution in QUS estimates obtained using this higher frequency potentially could benefit detection of smaller metastatic foci while also improving classification performance.

Additionally, in the presented studies, only LD methods were used for classification. Potentially, the results could be improved further by the use of more complex classifiers such as artificial neural networks or support vector machines. The use of support vector machines for this project is currently being investigated.

Finally, the 3D cancer-probability maps can serve as basis for development of a novel pathology tool. A low-cost, small-footprint device could be designed to scan lymph nodes quickly, obtain QUS estimates, derive cancer-probability values, and efficiently guide the pathologist towards suspicious regions. This device would include a 3D HFU scanner and a computer display that would allow interactive investigation of each lymph node over its entire volume in 3D (See Fig. 7.9). Such a tool could be invaluable for reducing the current rate of false-negative determinations and could significantly benefit the current standard of care of cancer patients undergoing lymphadenectomy.

References

Assentoft JE, Gregersenb H, O'Brien WD Jr (2001) Propagation speed of sound assessment in the layers of the guinea-pig esophagus in vitro by means of acoustic microscopy. Ultrasonics 39:263–268

Chaturvedi P, Insana MF (1996) Error bounds on ultrasonic scatterer size estimates. J Acoust Soc Am 100:392–399

Coron A, Mamou J, Hata M, Machi J, Yanagihara E, Laugier P, Feleppa EJ (2008) Three-dimensional segmentation of high-frequency ultrasound echo signals from dissected lymph nodes. In: Proceedings of the 2008 IEEE ultrasonics, symposium, pp 1370–1373

Coron A, Mamou J, Saegusa-Beecroft E, Hata M, Lee P, Machi J, Yanagihara E, Laugier P, Feleppa EJ (2010) Assembling 3D histology volumes from sections of cancerous lymph nodes to match 3D high-frequency quantitative ultrasound images. In: Proceedings of the 2010 IEEE ultrasonics, symposium, pp 2368–2371

D'Astous FT, Foster FS (1986) Frequency dependence of ultrasound attenuation and backscatter in breast tissue. Ultrasound Med Biol 12(10):795–808

Duck FA (1990) Physical properties of tissue. A comprehensive reference book. Academic Press, New York

Farnebäck G, Westin C-F (2006) Improving Deriche-style recursive Gaussian filters. J. Math. Imaging and Vis. 26:293–299

Feleppa EJ, Machi J, Noritomi T, Tateishi T, Oishi R, Yanagihara E, Jucha J (1997) Differentiation of metastatic from benign lymph nodes by spectrum analysis in vitro. In: Proceedings of the 1997 IEEE ultrasonics, symposium, pp 1137–1140.

Feleppa EJ, Lizzi FL, Coleman DJ, Yaremko MM (1986) Diagnostics spectrum analysis in ophthalmology: a physical perspective. Ultrasound Med Biol 12:623–631

Feleppa EJ, Porter CR, Ketterling J, Lee P, Dasgupta S, Urban S, Kalisz A (2004) Recent developments in tissue-type imaging (TTI) for planning and monitoring treatment of prostate cancer. Ultrason Imaging 26:163–172

Franceschini E, Yu FT, Destrempes F, Cloutier G (2010) Ultrasound characterization of red blood cell aggregation with intervening attenuating tissue-mimicking phantoms. J Acoust Soc Am 127(2):1104–15

Goss SA, Johnston RL, Dunn F (1978) Comprehensive compilation of empirical ultrasonic properties of mammalian tissues. J. Acoust. Soc. Am. 64:423–457

Goss SA, Johnston RL, Dunn F (1980) Compilation of empirical ultrasonic properties of mammalian tissues II. J Acoust Soc Am 68: 93–108

Insana MF, Wagner RF, Brown DG, Hall TJ (1990) Describing small-scale structure in random media using pulse-echo ultrasound. J Acoust Soc Am 87:179–192

Insana MF, Wood JG, Hall TJ (1991) Identifying acoustic scattering sources in normal renal parenchyma in vivo by varying arterial and ureteral pressures. Ultrasound Med Biol 17:613–626

Kino GS (1987) Acoustic waves. Prentice Hall, Englewoods Cliffs, NJ

Kinsler LE, Frey AR, Coppens AB, Senders JV (2000) Fundamental of acoustics, 4th edn. John Wiley and Sons, Hoboken, NJ

Klein S, Staring M, Murphy K, Viergever MA, Pluim JP (2010) Elastix: a toolbox for intensity-based medical image registration. IEEE Trans Med Imaging 29(1):196–205

Lizzi FL, Greenebaum M, Feleppa EJ, Elbaum M, Coleman DJ (April 1983) Theoretical framework for spectrum analysis in ultrasonic tissue characterization. J Acoust Soc Am 73:1366–1373

Lizzi FL, Ostromogilsky M, Feleppa EJ, Rorke MC, Yaremko MM (May 1987) Relationship of ultrasonic spectral parameters to features of tissue microstructure. IEEE Trans Ultrason Ferroelectr Freq Control 34:319–329

Mallat S (2009) A wavelet tour of signal processing—the sparse way, 3rd edn. Academic Press

Mamou J, Oelze ML, O'Brien WD Jr, Zachary JF (2008) Extended three-dimensional impedance map methods for identifying ultrasonic scattering sites. J Acoust Soc Am 123:1195–1208

Mamou J, Coron A, Hata M, Machi J, Yanagihara E, Laugier P, Feleppa EJ (2010) Three-dimensional high-frequency characterization of cancerous lymph nodes. Ultrasound Med Biol 36:361–375

Mamou J, Coron A, Oelze ML, Saegusa-Beecroft E, Hata M, Lee P, Machi J, Yanagihara E, Laugier P, Feleppa EJ (2011) Three-dimensional high-frequency backscatter and envelope quantification of cancerous human lymph nodes. Ultrasound Med Biol 37(3):345–57

Mamou J, Saegusa-Beecroft E, Coron A, Oelze M, Yamaguchi T, Machi J, Hata M, Yanagihara E, Laugier P, Feleppa EJ (2012) Three-dimensional quantitative high-frequency characterization of freshly-excised human lymph nodes. In: Proceedings of the 2011 IEEE ultrasonics, symposium, pp 37–40

Oelze ML, Zachary JF, O'Brien WD Jr (2002) Parametric imaging of rat mammary tumors in vivo for the purposes of tissue characterization. J Ultrasound Med 21:1201–1210

Oelze ML, Zachary JF, O'Brien WD Jr (2002) Characterization of tissue microstructure using ultrasonic backscatter: Theory and technique for optimization using a Gaussian form factor. J Acoust Soc Am 112:1202–1211

Oelze ML, O'Brien WD Jr (2002) Frequency-dependent attenuation-compensation functions for ultrasonic signals backscattered from random media. J. Acoust. Soc. Am. 111:2308–2319

Oelze ML, Miller RJ, Blue JP Jr, Zachary JF, O'Brien WD Jr (2003) Impedance measurements of ex vivo rat lung at different volumes of inflation. J Acoust Soc Am 114:3384–3393

Oelze ML, Zachary JF (2006) Examination of cancer in mouse models using high-frequency quantitative ultrasound. Ultrasound Med Biol 32:1639–1648

Perez JE, Barzilai B, Wickline SA, Vered Z, Sobel BE, Miller JG (1988) Quantitative characterization of myocardium with ultrasonic imaging. J Nucl Med Allied Sci 32:149–157

Saha RK, Franceschini E, Cloutier G (2011) Assessment of accuracy of the structure-factor-size-estimator method in determining red blood cell aggregate size from ultrasound spectral backscatter coefficient. J Acoust Soc Am 129(4):2269–77

Soille P (2002) Morphological image analysis–principles with applications, 2nd edn. Springer.

van der Steen AF, Cuypers MH, Thijssen JM, de Wilde PC (1991) Influence of histochemical preparation on acoustic parameters of liver tissue: a 5-mhz study. Ultrasound Med Biol 17(9):879–891

Chapter 8
Quantitative Ultrasound for Tissue-type Imaging of the Prostate: Implications for Planning and Guiding Biopsies and Delivering Focal Treatments

Ernest J. Feleppa and Christopher R. Porter

Abstract Improved means of imaging prostate cancer would enable more-effective biopsy and treatment guidance and potentially would provide a reliable means of monitoring non-surgical therapy. Current, commonly used, conventional means of imaging the prostate do not reliably depict cancerous lesions, and as a result, biopsy needles are placed with respect to visible anatomic features of the gland, treatment tends to involve the entire gland, and post-treatment monitoring of therapy is based predominantly on serum PSA levels, and in many cases, periodic biopsies. Conventional transrectal ultrasound is the most-commonly employed imaging modality for use in prostate biopsy and treatment procedures, but it offers no advantages in terms of reliably depicting cancerous regions of the gland. However, new methods of tissue-type imaging that are based on spectrum analysis of echo signals and that utilize non-linear methods for classification offer promise as a means of more-reliably distinguishing cancerous lesions from non-cancerous tissue in the prostate. Such advanced methods have produced areas under ROC curves exceeding 0.84 compared to an area of 0.64 for conventional assessments of the same locations in biopsy-guiding B-mode images. The potential improvement in imaging sensitivity implied by the ROC curves is more than 50 %. If current validation studies confirm these encouraging results, then an effective, inexpensive, noninvasive means of imaging prostate-cancer foci, and therefore of guiding biopsies and enabling focal treatments, will be available to urologists and radiation oncologists.

Keywords Prostate cancer · Focal therapy · Quantitative ultrasound · Tissue-type imaging · Spectrum analysis · Artificial neural networks · Support-vector machines · ROC curves

E. J. Feleppa (✉)
Lizzi Center for Biomedical Engineering, Riverside Research,
156 William Street, 9th floor, New York, NY 10038, USA
e-mail: efeleppa@riversideresearch.org

C. R. Porter
Department of Urology, Virginia Mason Medical Center, Seattle, WA, USA

J. Mamou and M. L. Oelze (eds.), *Quantitative Ultrasound in Soft Tissues*, DOI: 10.1007/978-94-007-6952-6_8,

8.1 Introduction

The American Cancer Society estimates that nearly 238,590 new cases of prostate cancer (PCa) will be detected in men in the United States during 2013, which makes PCa the most-commonly detected male cancer in the United States, excluding skin cancers (Cancer Facts and Figures 2013). The Society also estimates that nearly 30,000 men in the United States will die of PCa during 2013, which makes PCa the second-leading cause of death by cancer in the United States.

8.1.1 Current Needs

Definitive diagnosis of PCa is performed using core-needle biopsies obtained transrectally, and the most-common means of guiding transrectal biopsies of the prostate is conventional transrectal ultrasound (TRUS) imaging. However, TRUS does not reliably distinguish between cancerous and non-cancerous tissue in the prostate; therefore, TRUS-guided biopsies rely upon relatively well-imaged anatomical structures, such as the interface between the gland and periprostatic fibroadipose tissues, as spatial references for placing core needles in the gland. Because cancerous lesions are not reliably depicted on conventional images, biopsy sampling is done essentially blindly with respect to actual cancer foci, and a positive biopsy cannot be assured even in the presence of PCa foci. The probability of a positive core in a gland having small scattered cancer foci is unacceptably small. In fact, our analysis of published repeat-biopsy data for traditional sextant biopsies suggests that the actual sensitivity of the TRUS-guided biopsy procedure may be as low as 50 %; other studies draw similar conclusions (Haas et al. 2007; Applewhite et al. 2002; Feleppa et al. 2002). In other words, a significant fraction of the population of patients who actually have PCa have a negative biopsy result because of the current inability to image suspicious regions reliably, and consequently, the inability to target biopsy needles to cancerous tissue. Furthermore, all negative procedures, whether they are true or false, impose an unwarranted health risk as well as cost to the patient. This risk is associated with various side effects of the biopsy, including hemorrhage and particularly infection (Feliciano et al. 2008; Loeb et al. 2012). In addition, recent reports express concern that drug resistance is developing among the common pathogens associated with biopsy-related infections (Macchia 2007). Therefore, reducing the number of true negative biopsies would be beneficial to patients from the standpoint of reducing risk as well as cost.

A second concern derived from the limitations of current ultrasonic imaging methods is the difficulty encountered in selecting patients for focal therapy and planning the therapy with confidence that no cancer foci are missed. Most current forms of therapy are amenable to a focal approach; these methods include external-beam radiation therapy, brachytherapy, cryo-ablation, and high-intensity focused ultrasound (HIFU). Current cautious approaches to focal surgery

emphasize hemitherapy that excludes either the left or right side of the gland and attempts to spare the urethra, bladder, rectum, and the contralateral neurovascular bundle. Assuming no cancer foci are present in the untreated portion of the gland, the obvious benefits of focal therapy are reduction of side effects and maintenance of gland function, e.g., retention of reproductive functions. Patient selection and treatment planning for focal therapy now rely heavily on saturation transperineal biopsies that utilize 40 to as many as 80 cores to provide a reasonably good sense of where cancer is NOT present and therefore what regions, if any, can be spared from treatment. However, although it is minimally septic, the use of so many inserted needles is a significantly invasive and traumatic procedure. The availability of a reliable means of imaging cancer in the prostate would eliminate the need for saturation biopsies and would markedly enhance means of patient selection for focal therapy and planning the therapy itself.

An additional concern regarding ultrasonic imaging of PCa is the inability of TRUS to provide a reliable means of staging or estimating the aggressiveness of detected PCa. Because conventional ultrasound does not distinguish cancerous from non-cancerous prostate tissue, TRUS images cannot depict tumor proximity to the capsule, extra-capsular extensions, or seminal-vesicle invasion with certainty, and as a consequence, TRUS imaging does not contribute information of value to clinical staging estimations. Improved clinical staging is desirable because 20–30 % of radical prostatectomies show evidence of disease that is not gland confined, which retrospectively reveals that a significant number of surgical procedures are unwarranted (Epstein et al. 1994; Partin et al. 1997). Furthermore, a number of studies show that the benefits of treatment to many patients are minimal or non-existent (Ahmed et al. 2009, 2012; Wei 2010). However, treatment tends to be performed in the absence of a reliable means of determining whether a detected cancer is indolent or a threat to life because no reliable means exist for assessing disease aggressiveness. If a method were available to monitor untreated PCa with confidence, then changes indicating disease progression, such as tumor growth, could provide a basis for initiating required treatment; a static cancer could continue to be monitored noninvasively with confidence.

Ultrasound is not the only imaging modality deficient in its ability to distinguish cancerous regions from non-cancerous ones. While some advanced methods mentioned in this chapter show promise for overcoming existing limitations in the ability to visualize cancer in the prostate, all currently commonly used, conventional, clinical, imaging modalities are deficient in that regard; none can depict PCa reliably.

8.1.2 Quantitative Ultrasound

Ultrasonic spectrum analysis has been investigated by our group since the early 1970s as a means of extracting and utilizing information that is present in the raw "radio-frequency" (RF) echo signals derived from tissue during an ultrasound

scan. The conversion of RF signals to envelope-detected, video signals needed to generate high-definition, high-contrast, B-mode images discards or distorts much of the information present in the original RF signals. Spectrum analysis of linearly processed RF signals is one way of capturing and presenting the information that ordinarily is discarded in conventional ultrasound imaging. No way exists to know in advance whether the captured information can be of use for tissue typing and imaging, but in research undertaken by our group, spectrum analysis has in fact proven to be useful in distinguishing among tissue types of interest in the eye, liver, blood vessels, lymph nodes, and prostate (Coleman et al. 2004; Silverman et al. 2003; Lizzi et al. 1988, 1997; Lee et al. 1998; Noritomi et al. 1997a, b, 1998; Kolecki et al. 1995; Tateishi et al. 1998; Dasgupta et al. 2007; Feleppa et al. 1997, 1998, 2000, 2001, 2002, 2004, 2007). Because the methods used to compute spectra retain and exploit all quantitative information present in the original RF signals, the methods based on spectrum analysis have been termed quantitative ultrasound or "QUS." Although QUS originally was applied to spectrum analysis and estimates derived from spectrum analysis, the term now is becoming generalized to include any signal-processing approach that quantitatively exploits the information contained in the original echo signals, including for example, methods that derive estimates from the statistics of envelope signals that are computed in a linear quantitative manner from linearly processed RF data. Examples of the use of envelope statistics to characterize tissue are the studies to detect metastatic foci in lymph nodes described elsewhere in this book by Mamou (Chap.7, this volume).

8.2 Background

8.2.1 Spectrum Analysis

When used to characterize or type tissue, QUS based on spectrum analysis seeks to exploit the fact that different types of tissues may have different ultrasound-scattering properties. If those differences exist in tissues that need to be distinguished from each other or in tissues that change over time either in the course of surveillance or in response to treatment, then sensing those differences and expressing them quantitatively may have great medical value. Spectrum-analysis-based QUS offers a convenient, easy-to-implement method for representing the properties of tissues of interest as they are expressed in backscattered ultrasonic echo signals.

Spectrum analysis as the basis for the prostate tissue-type imaging (TTI) methods described here can trace its origins back to the work of many investigators in the 1960s and 1970s, including perhaps most notably the research of Purnell and Sokulu (Jones et al. 1976). These investigators coined the term "spectra-color" for an ultrasonic imaging technique that employed color to depict the frequency content of echo signals compared to those in the incident ultrasound pulse. However, spectrum analysis subsequently matured as a method of tissue typing

largely through the work of Lizzi and other pioneering investigators such as Zagzebski, Insana, and Wagner (Nicholas 1982; Zagzebski et al. 1983; Feleppa et al. 1986; Lizzi et al. 1983, 1987, 1997; Nassiri and Hill 1990; Insana et al. 1990; Insana and Hall 1990). Hosokowa et al. (1994) attempted to validate the theory underlying spectrum analysis using widely spaced, spherical cell clusters cultured in a collagen-based medium to represent ideal scatterers; they obtained results that matched theoretical predictions over a limited range of scatterer (i.e., cell-cluster) sizes. More recently, several younger investigators, such as Kolios, Oelze, Mamou, and Bigelow, have made valuable contributions to spectral methods by advancing insights into underlying mechanisms and by extending and refining the scattering theory associated with spectral behaviors (Bigelow and O'Brien 2004a, b, 2005, 2006; Mamou et al. 2005; Oelze et al. 2002a, b; Oelze and Zachary 2006; Kolios et al. 2001, 2002).

The basic theories of scattering in tissue assume that scattering is weak and the Born approximation applies (Wu and Ohmura 1962). In essence, this approximation considers scattering behavior to depend solely on the interaction between scatterers and the incident field; i.e., it assumes that the total field, which includes perturbations to the incident field by other scatterers, including components arising from scattering, can be replaced by the incident field alone because the contribution of the field to the total field can be ignored. The theoretical framework first published by Lizzi expressed the spectrum of the backscattered echo signals received at the transducer as the integral over three spatial autocorrelation functions: the two-way beam-directivity autocorrelation function, which expresses the behavior of the incident-beam profile in two dimensions transverse to the beam-propagation direction; the one-dimensional autocorrelation function of the time-domain window used to select backscattered signals for spectral processing; and the three-dimensional autocorrelation function of spatial variations in relative acoustic impedance, which expresses the properties of the scatterers themselves (Lizzi et al. 1983, 1987; Zagzebski et al. 1983; Feleppa et al. 1986). The fundamental equation derived by Lizzi et al. is

$$S = 4k^2 \iiint R_\zeta(\Delta\mathbf{x}) R_D(\Delta y, \Delta z) R_G(\Delta x) e^{j2k\Delta x} d\Delta x \, d\Delta y \, d\Delta z$$

where S is the normalized spectrum (corrected for the system transfer function), k is the wave number, $R_\zeta(\Delta\mathbf{x})$ is the spatial autocorrelation function of the distribution of the relative acoustic impedance of the scatterers, $R_D(\Delta y, \Delta z)$ is the autocorrelation function of the two-way ultrasound beam-directivity function, and $R_G(\Delta x)$ is the autocorrelation function of the gating function (typically a Hamming or Hanning window) (Lizzi et al. 1983). Normalization of the spectrum traditionally is performed by computing the spectrum of a "perfectly" reflecting surface (such as an optically flat glass plate) placed parallel to the planar wave front of the ultrasound pulse at the transducer focal point. More recently, a weakly reflecting water-oil interface is being used by our group to reduce reflected-signal amplitude and allow the use of identical instrument power and gain settings for

acquiring calibration and actual tissue echo-signal data. (The oil used has a density greater than that of water, so an ultrasound beam can be directed downward toward the interface through a weakly and linearly attenuating water path.) The reflectivity of the oil-water interface is well-defined so that calibration data acquired from it can be referenced to a perfect reflector.

In practice, this equation is applied using assumed autocorrelation functions for the scatterer acoustic impedance, typically Gaussian. For the Gaussian function, the equation predicts a gently curving spectrum when expressed in logarithmic form, i.e., in dB with respect to a perfectly reflecting calibration target. When approximated by a straight line over the available noise-limited bandwidth, the linear fit to a calibrated spectrum has two, basic, independent defining parameters: (1) a slope value that is dependent only on scatterer size and attenuation in the intervening medium and (2) an intercept value that depends on scatterer size, concentration, and acoustic impedance relative to the environment of the scatterers. An additional spectral parameter is the midband (or midband fit), which is the value of the straight-line approximation at the center of the noise-limited frequency band, i.e., it is the average value of the amplitude of the straight-line approximation over the usable frequency band. The midband parameter is equivalent to the integrated-backscatter parameter developed and investigated by Miller and his co-workers (O'Donnell et al. 1979; Lanza et al. 1996, 1998; Miller et al. 1998).

If attenuation is negligible or can be estimated, then an attenuation-corrected slope value can be computed easily, and from it, the effective size, d, of scatterers can be estimated. Once d is estimated using the attenuation-corrected slope value, then the combination of concentration, C, and relative acoustic impedance, Q, can be derived from the intercept value. That combination is termed CQ^2 or simply "acoustic concentration." Only two of the three spectral parameters, slope, intercept, and midband, are independent of each other. Their relationship is expressed by $y = af + y_0$ where y is the amplitude of the straight line, a is the slope of the line, f is frequency, and y_0 is intercept. However, slope and midband are affected by attenuation in intervening tissue, while in theory, intercept is independent of attenuation if attenuation is linear with frequency, which is an accepted approximation in soft tissue.

8.2.2 Classification

Once spectral-parameter values are computed for known tissue types, e.g., cancerous and non-cancerous tissues in the biopsied regions of the prostate, a classifier can be trained to assign a score for the likelihood of an unknown tissue being in one or the other tissue-type category. If the "truth" is known, e.g., if biopsy histology is available to serve as the gold standard, then the scores generated by the classifier can be compared to the true tissue type to determine the classification performance of the classifier. The most-accepted method of expressing classifier

performance is the ROC curve where ROC originally stood for "receiver-operator characteristics" when the method was first developed for technical purposes, e.g., to assess the ability to extract usable signals from noise. The ROC curve shows how effective a system is in classifying an unknown correctly into either of two possible groups, e.g., cancerous or noncancerous tissue in the prostate (Metz et al. 1998). The ROC curve expresses system performance as the tradeoff between the true-positive fraction (i.e., sensitivity) as a function of the false-positive fraction (i.e., 1 minus specificity). By reversing the abscissa, the curve directly expresses sensitivity as a function of specificity. This rarely used "reversed ROC curve" perhaps is a more appropriate representation for clinical evaluations.

A perfect classifier is one that has a sensitivity of 1.0 with a specificity of 1.0, i.e., a value of 1.0 for sensitivity at a value of 0.0 for 1 minus specificity. The sensitivity value of the ROC curve for such a classifier would be 1.0 for all values of 1 minus specificity, and the area under that ROC (AUC) curve would be 1.0. A classifier that is purely random in its determinations would have an ROC curve that begins at the origin and linearly goes to a value of 1.0 for sensitivity at a value of 1.0 for 1 minus specificity, and the AUC value for that classifier would be 0.5. In ROC-curve classifier-performance assessment, an AUC value of 1 indicates a perfect classifier and an AUC value of 0.5 indicates an entirely random classifier. Real classifier systems, including humans reading images such as X-ray, ultrasound, or magnetic-resonance images, typically produce AUCs in the range of 0.6 or poorer to 0.9 or better.

To utilize determinations made by classifiers such as linear-discriminant-analysis methods, nearest-neighbor methods, artificial neural networks (ANNs), or support-vector machines (SVMs) as inputs for ROC-curve calculations, the computations by the classifier produce a score for the likelihood of a positive, and this score is compared to a gold standard, such as the biopsy histology results serving as the gold standard in our prostate studies. Such scores can be "continuous" over a range determined by the classification software, but typically, scores are normalized to a range extending from 0 to $+1$ or -1 to $+1$. To utilize reader interpretations as inputs for ROC-curve calculations, reader determinations often are expressed as a "discrete" level of suspicion (LOS) for positives using 5 or more integer values. As an example, on a scale of 1–5, 1 would indicate the reader's virtual certainty of a negative finding, 5 would indicate virtual certainty of a positive finding, and 3 would indicate an indeterminate case with an equal likelihood of a positive or a negative finding. These LOS scores for cancer are compared to a gold standard to compute the ROC curve. In our studies, we use the LOS values assigned by the examining urologist to establish a baseline ROC curve for comparing the classifier being developed to the available conventional image-based classification method. Most available ROC-computing software accommodates discrete and continuous types of likelihood assignment. Such software also typically provides considerable information in addition to the AUC values such as the standard error in the AUC estimate and the 95 %-confidence-intervals of the AUCs.

When only a single parameter is needed for classification of two tissue types, then a simple histogram can be used to display the distributions of parameter values for the two types of interest. A decision-threshold value can be selected for assigning tissue type based on the values of that parameter, and a sensitivity and specificity can be computed for the distributions and the threshold point. Alternatively, an ROC curve can be generated from the parameter-value distributions; the overall classification performance of the single parameter can be determined from the AUC value, and the tradeoff between sensitivity and specificity can be determined from the curve shape (Metz et al. 1998). In our experience, a single parameter rarely is sufficient for reliable differentiation of tissue types, and this is emphatically the case in identifying PCa.

Typically, two or more parameters are required to differentiate between two tissue types. Because only two independent parameters are associated with the linear-regression approximation, the best two parameters usually are all that is needed for classification. For example, if effective scatterer size is an important tissue property, i.e., if size is significantly different in the two tissue types, then slope and intercept or slope and midband would be useful parameter combinations.

For useful clinical decision making, a single number is desirable for a decision threshold, and in the case of two or more relevant parameters, linear-discriminant analysis provides a single discriminant-function value for the threshold (McLachlan 1992). The distribution of discriminant-function values can serve as a basis for selecting the preferred trade-off between sensitivity and specificity, and the classification performance of the discriminant analysis can be expressed in an ROC curve. Linear-discriminant methods work well when the categories of interest occupy different, but separable regions of parameter space where discriminant analysis effectively can rotate the point of view of the observer to maximize the apparent separation among the classes. However, when the two categories of interest, e.g., cancerous and non-cancerous prostate tissue, include many sub-categories, e.g., different Gleason grades of cancerous tissue and the various types of benign tissues such as atrophic, hyperplastic, calcified, acutely inflamed, chronically inflamed, etc., linear methods have little hope of performing effective classification.

When the parameter values of subtypes of cancerous and non-cancerous tissues are intermingled in parameter space, linear methods become challenged and non-linear methods of classification have better hope of recognizing the possible clustering of values into sub-regions for each tissue type within the overall parameter space. Examples of such non-linear methods are nearest-neighbor analysis, ANNs, and SVMs (Shawe-Taylor and Cristianini 2000; Shakhnarovish and Indyk 2005; Keller et al. 1985; Cortes and Vapnik 1995; Theodoridis and Koutroumbas 2009). Our prostate classification and imaging studies to date have investigated the use of all three classification methods and have had the best success using SVMs, as discussed below. Like linear-discriminant methods, these non-linear methods produce scores that express the relative likelihood of an unknown tissue being cancerous or non-cancerous; the scores have a distribution for each tissue type, and classification performance can be represented in an ROC curve.

8.2.3 Imaging

A classifier that is trained to distinguish effectively between cancerous and non-cancerous tissue based on a set of parameters can be used to generate images that show the relative likelihood of cancer being present at a pixel location. Such a method can be applied to an entire image plane or to a subset of pixels in a region of interest (ROI) within the plane. A three-dimensional (3D) rendering can be generated from a set of properly registered two-dimensional (2D), TTI images to produce a TTI volume image. Parameter values can be generated to span the range of values found in the data for a given classification study, e.g., the spectral-parameter values for cancerous and non-cancerous prostate tissue. These artificial, parameter values then can serve as test values to be given cancer-likelihood scores by the trained classifier. The output is a lookup table (LUT) that contains a likelihood score for each of the combinations of parameter values that can be encountered in actual tissue. Then, when spectral parameters are computed at a pixel location in an image, the values can be referred to the matching parameter-value location in the LUT to obtain the corresponding likelihood score. The score then can be expressed as a pixel value in gray scale or false color. As discussed below, we have found in our studies that locally varying intercept and midband spectral-parameter values combined with the value of the patient's serum prostate-specific antigen (PSA) level provide good classification using either an ANN or an SVM for classification. The combination of local parameter values then can be translated into TTI pixel values using a multi-element LUT.

8.3 Ultrasonic Prostate Tissue-type Images

8.3.1 Database Development

Our first step toward generating tissue-type images of the prostate was to build a database of spectral-parameter values for RF echo signals acquired from tissue that was sampled by core-needle biopsies. The RF data were acquired immediately prior to firing the spring-loaded biopsy-needle gun and removing tissue. This method prevented corruption of the RF signals either by the needle itself or by the subsequent tissue trauma and hemorrhage along the needle track. Note that in transrectal prostate biopsies, the needle is in a fixed location with respect to the probe and as a result, the trajectory of the needle is well defined with respect to the scanned region.

In our initial studies, which used a B-K model 3535 scanner (B-K Medical, Peabody, MA), the needle traversed the probe at an angle and emerged from the probe near, but slightly proximal to the mechanically sector-scanning transducer, which was near the tip of the probe. In these studies, the urologist obtaining the biopsy held the probe in a fixed position once the desired biopsy location was

found, and advised an assistant to acquire data via the computer interfaced with the clinical ultrasound scanner. Data acquisition occurred over a single frame, and when the transfer of data to the computer memory was complete, as indicated by a tone from the computer, the urologist fired the biopsy-needle gun. In our more-recent studies, which used a Hitachi EUB-525 scanner (Hitachi Medical Systems America, Twinsburg, OH), all frames were digitized continuously, and the latest acquired frame was kept in the memory of the digitizer board. In these later studies, firing of the biopsy-needle gun was sensed to trigger data transfer from the digitizer board to computer memory automatically, and the computer stored the latest digitized frame from the digitizer board. In both studies, the acquired RF data could be spatially related with high precision to the actual site of the tissue sample. Also, in both studies, the full set of biopsy-plane scans for a given patient were digitized and retained in computer memory before being transferred to the hard disk. Retention of data in computer memory until completion of the examination permitted performing biopsies rapidly, with minimal overall examination time and patient discomfort. Upon completion of the examination, data then were transferred from memory to hard disk for permanent storage.

Each biopsy tissue sample, also termed a "core," was placed in an individual vial containing fixative, and the vial was labeled to indicate biopsy location, e.g., left-base-medial, or right-mid-lateral. Medial and lateral designations were used in the 12-core examinations of later studies, but were not relevant in the simpler, 6-core biopsies of earlier studies. These designations referred to biopsies of the prostate peripheral zone; the peripheral zone is the most highly glandular region of the prostate and therefore is the region most likely to contain prostatic adenocarcinoma, i.e., cancer of the prostatic secretory epithelium. The examinations also sometimes included biopsies of the prostate transition zone and, very rarely, the seminal vesicles.

In addition to acquiring RF echo-signal data from the biopsied tissue, these studies also document several patient variables, e.g., each patient's level of serum PSA, age, NIH-defined race, ethnicity, etc. (Race and ethnicity data are required for reporting purposes as well as having a possible role in tissue classification.)

To provide a baseline for comparing the performance of developed classifiers to conventional methods, the urologist performing the biopsy assigned a LOS for the tissue being biopsied based primarily on its appearance in the conventional B-mode, ultrasound image used to direct the needle, but also consciously combined with all other available information regarding the patient, e.g., the results of the palpation performed during the digital rectal examination (DRE), PSA level, gland size estimated from the B-mode image, family history, etc. The LOS values ranged from 1 for virtual certainty of non-cancerous tissue to 5 for virtual certainty of a cancerous tissue with 3 indicating an entirely indeterminate tissue.

Subsequently, the actual tissue type of each biopsy core was provided by the pathologist. Pathology reports specified the biopsy-core location as described above, which enabled matching the results of RF spectrum analysis to the tissue type determined by the pathologist. We used the pathologists' determinations as our gold standard, which we considered to be entirely correct. A limitation to this

approach was that the intense work load of the pathologists prevented them from specifying how much of a positive core consisted of cancerous tissue, or more-ideally, which quadrants of a core contained cancerous tissue. Occasionally, microscopic foci of cancer were identified, and we treated such cores as negative cases. We retained pre-cancerous prostatic intraepithelial neoplasia (PIN) and transition-zone data in our data base, but we have not used these tissue types in our classification studies to date.

8.3.2 Classifier Development

The complex and interwoven expressions of healthy and unhealthy prostate tissue suggest that simple, linear methods of classifying cancerous versus non-cancerous tissues in the gland are likely to be inadequate. For example, a range of grades exist for prostatic adenocarcinoma, with higher grades associated with a greater loss of differentiation and normal tissue architecture. Non-cancerous tissues include a wide range of age-dependent "normal" tissues as well as varying degrees of chronic and acute inflammation, glandular and stromal hyperplasia, glandular and stromal atrophy, and pre-cancerous tissue such as PIN. Therefore, as expected, our attempts to distinguish cancerous from non-cancerous prostate tissue based simply on the values of spectral parameters and clinical variables such as PSA level failed to produce acceptable results. However, our early investigations of non-linear methods such as nearest-neighbor classification techniques, showed promise and encouraged us to apply more-powerful ANN methods. We employed a variety of off-the-shelf and custom software. The ANN software that provided the best results, as ascertained using ROC analyses, was the MATLAB neural-network toolbox (The Mathworks, Inc., Natick, MA)-specifically, a MATLAB implementation of a multilayer-perceptron (MLP) ANN. Similar, but slightly poorer results were obtained using NConnect (SPSS, Chicago, IL) MLP and radial-basis-function ANNs.

Classification was performed using intercept and midband parameter values along with PSA, age, and race variables. Slightly superior performance was obtained using all parameters, but because the difference was not statistically significant and in order to reduce the number of classifier dimensions and thereby to maximize generality, we limited our final classification parameters to intercept, midband, and PSA-level values. To optimize the MLP configuration, we ran the ANN using a script that prescribed different numbers of hidden layers and nodes. The scores for the likelihood of cancer, along with the actual tissue types were evaluated using ROC methods to identify the best MLP configuration.

Classifier training was performed by using a leave-one-patient-out approach as well as a leave-one-biopsy-out approach. In the leave-one-biopsy-out approach, the MLP was trained using 90 % of the data and validated using 10 % of the data while a single biopsy was tested (i.e., assigned a score for the likelihood of cancer) by the trained MLP. This was repeated for every biopsy in the data set, and the scores for all the biopsies, along with their true tissue types, were input to the ROC

software. However, concern existed regarding the possibility of a favorable bias in apparent classification performance that might result if data associated with the multiple biopsies of a given patient were correlated and if some of those data were in the training set while some also were in the test set. Therefore, to eliminate any chance of such bias, we tested using all data for a given patient in the test set and repeated the classification run for every patient, drawing a different patient for each run and returning the previous test set to the training and validation sets. Again, the likelihood scores and true tissue types for all biopsies were input to the ROC software for assessment.

As a specific example, the data set from the Washington DC Veterans Affairs Medical Center included 64 patients and 617 biopsies. We ran our MLP using a leave-one-patient-out approach 64 times using the set of data for a different single patient each time and we randomly divided the remaining data into a training set (90 %) and a validation set (10 %). The scores and true tissue types were input to any one of a variety of ROC-software packages, including ROCkit by Charles Metz (http://xray.bsd.uchicago.edu/krl/KRL_ROC/software_index6.htm), MedCalc by Frank Schoonjans (http://www.medcalc.be/), or our own custom MATLAB-based ROC software. For all methods, computed ROC AUC values were essentially identical, and our best-performing MATLAB MLP classifier gave AUCs of 0.844 ± 0.018 (95 % CI: 0.806, 0.877) for the classifier and 0.638 ± 0.031 (95 % CI: 0.576, 0.697) for the corresponding B-mode-based classification using LOS assignments, as shown in Fig. 8.1. The standard errors (0.018 and 0.031) in the AUC estimates are very small compared to the AUC difference (0.206) between these ROC curves, and the lower 95 %-confidence value (0.806) of the MLP ROC is significantly greater than the upper value (0.697) of the LOS ROC. For the likely values of sensitivity for B-mode-guided biopsies of approximately 0.50, the corresponding sensitivity of the MLP ROC curve is

Fig. 8.1 ROC curves produced (1) by a MATLAB implementation of an MLP ANN using a leave-one-patient-out approach (*upper curve*) and (2) by LOS assignments primarily based on B-mode appearance (*lower curve*). The vertical axis is True-positive Fraction (*TPF*), which is equivalent to sensitivity; the horizontal axis is False-positive Fraction (*FPF*), which is equivalent to 1 minus specificity

approximately 0.80, i.e., the MLP sensitivity is superior to the B-mode-based sensitivity by approximately 60 %. If that classifier improvement could be translated into real-time images used for biopsy guidance, then a marked improvement in biopsy yield would be possible. Similarly, such images, whether generated in real time or off line, could make targeted or focal treatments a clinical reality.

A similar approach was used for developing and assessing the SVM classifier, which has the advantages of being less vulnerable with respect to false minima, overtraining, and excessive dimensionality. As was the case with ANN development, the data, consisting of intercept, midband and PSA values plus the actual histologically determined tissue type (cancerous vs. non-cancerous) were analyzed using SVM methods as implemented in the OSU SVM Toolbox for MATLAB using a radial-basis-function kernel. A grid search was performed to establish optimal values of the cost-function constant, C, and the radial-basis constant, γ. For each value of C and γ in the grid search, an SVM model was generated using a leave-one-patient-out approach, i.e., the model was determined using all data values except those for the one patient; the set of values for the specified patient were treated as the unknown. This process was iterated for all patients, an ROC analysis was performed, and an AUC value was estimated. The optimal C and γ values were selected on the basis of the maximal AUC.

8.3.3 TTI Development

TTIs are needed that can represent the likelihood of cancer at each pixel or voxel in a user-defined ROI. The ROI could be the entire scan plane, a biopsy-targeting window, the prostate only, a 3D representation of the gland, or some other user-specified region. Pixel or voxel values could be computed by running classifier software either by using the full available data set as the training set, by using a simpler classification algorithm based on the weights of a trained classifier, or by using an LUT. We chose to use an LUT to assign values to pixels in the ROI.

To generate the LUT, we examined our data set and determined what ranges of data values, i.e., values for intercept parameter, midband parameter and PSA level, were representative of the data. Although PSA levels for a few patients with extensive advanced disease exceeded 100, we limited PSA values to a range between 0 and 78; similarly, we limited midband values to a range between −0.47 and −0.65 dB and intercept values to a range between −0.35 and −0.65 dB, where dB denotes decibels with respect to a perfectly reflecting calibration target. For each variable, we divided the range into 40 steps in value, which resulted in 64,000 combinations of values. Clearly, not all value combinations are reasonable, e.g., an intercept value of −0.65 dB and a midband value of −0.47 dB have a corresponding slope value of 4.0 dB/MHz at a center frequency of 5.75 MHz, which is the center of the frequency range in our prostate studies: 3.5 MHz to 8.0 MHz. According to Lizzi et al., this slope value is not theoretically possible (Lizzi et al. 1983, 1987; Feleppa et al. 1986). (Over the bandwidth of 3.5 to 8.0 MHz,

the theoretical slope limit for isotropic Rayleigh scattering with an f^4 dependence on backscattered power is approximately 3 dB/MHz.) However, a midband value of −65 dB and an intercept value of −35 dB have a corresponding slope of −5 dB/MHz, and this slope value corresponds to a scatterer diameter of approximately 230 μm. Scatterers of this size are very likely to exist among the stromal and acinar elements of the prostate.

The 64,000 combinations were input to the best-performing MLP as unknowns, i.e., test cases. The full data set was used as the training set. Experience in optimizing the MLP showed that 250 epochs (iterations) were required for the MLP to converge to the best possible solution; therefore, 250 epochs were used to compute a likelihood-of-cancer score for each of the 64,000 combinations of intercept parameter, midband parameter and PSA level.

An SVM-based LUT was generated in a manner equivalent to the method used to generate the MLP-based LUT. Once optimal C and γ values were selected, the SVM was applied to the same 64,000 combinations of intercept, midband and PSA as were used in the ANN case to generate an SVM-based LUT. Figure 8.2 shows an SVM-based LUT surface plot for a PSA level of 7.5; the associated SVM utilized a C value of 2,000 and a γ value of 10,000. The surface plot depicts the relative likelihood of cancer on the vertical axis for the given PSA value and all 64,000 combinations of midband and intercept on the two horizontal axes. The relative likelihood of cancer shows a broad peak at midband values of

Fig. 8.2 An SVM-based LUT for a PSA value of 7.5 showing a broad peak in the score value for relative cancer likelihood at low (*negative*) intercept and intermediate midband parameter values. The vertical axis is the cancer-likelihood score; the horizontal axis on the *left* is the midband axis, with decreasing values toward the viewer; the horizontal axis on the *right* is the intercept axis with decreasing values toward the viewer

approximately −50 to −55 dB and at low intercept values. As PSA value increases, all likelihood values increase, but with less emphasis in any particular region of the midband-intercept space, i.e., the LUT surface plot tends to flatten as it rises with increasing PSA values.

To generate a TTI using an LUT, the patient's serum PSA level is entered into the TTI software, and the software computes spectral-parameter values at a pixel (or voxel) location in the ROI. These three values fall on a specific step for each of the 40 values of midband, intercept, and PSA. That step is located in the LUT, and the corresponding value for the relative cancer likelihood is returned. The likelihood value then is translated into a color-encoded or gray-scale pixel (or voxel) value in the TTI image. Figure 8.3 shows an example of a TTI for a prostate that was scanned in situ immediately prior to prostatectomy while the patient was in the operating room. Subsequent prostatectomy histology showed a 12-mm, previously unrecognized, anterior tumor as well as smaller cancer foci and some PIN tissue. The left image in Fig. 8.3 is the gray-scale TTI; the center image is a midband-parameter image of the same scan plane with superimposed TTI color encoding to display the regions of highest relative likelihoods for cancer; the right image is the approximately corresponding whole-mount histology section, which clearly shows the demarcated anterior tumor and some smaller foci of cancerous and PIN tissue. The planes of the ultrasound scans and whole-mount histology are not necessarily identical, but are at the widest gland cross section and clearly overlap in the region of the anterior tumor.

Additional examples of TTIs are the 3D versions of this same prostate, as shown in Fig. 8.4, and the biopsy-search-window TTIs of Fig. 8.5. In Fig. 8.4, the most-highly suspicious volumes are depicted in red. The representation of the gland in Fig. 8.4 was generated from a set of parallel scan planes acquired at 5 mm plane separations; 2D TTIs were generated for each plane; and the set of 2D TTIs

Fig. 8.3 TTI images compared to post-surgical histology. Gray-scale TTI image (*left image*) and a color-overlay TTI on a midband image (*center image*) show a high suspicion of cancer in a large anterior tumor and smaller nearby foci. (In the *color image*, *red* depicts the highest cancer likelihood and *orange* the second-highest likelihood.) Whole-mount prostatectomy histology (*right image*) shows demarcations made by the pathologist to indicate cancerous and precancerous neoplastic tissue, particularly a large (12-mm) anterior tumor that was not detected previously by conventional imaging or palpation. All views are from the apex: the patient's *right* is the viewer's *left*; his anterior is up. [Reproduced, with permission, from *Ultrasonic Imaging*]

Fig. 8.4 3D TTI of the gland shown in Fig. 8.3. Cancerous regions warranting dose escalation in ablative treatments or a conservative (*wide*) surgical margin are clearly indicated; regions that could be spared in ablative treatments or safely could undergo nerve-sparing surgery also are apparent. All views are from the base; i.e., the gland is rotated around its vertical axis compared to Fig. 8.3. [Reproduced, with permission, from *Ultrasonic Imaging*]

was assembled into a 3D rendering using manual demarcation of the gland surface and TTI color-encoding to demarcate the tumor surfaces automatically. (In Fig. 8.4, the gland is rotated so that it is viewed through the base rather than viewing it more conventionally from the apex as shown in Fig. 8.3.) This type of 3D rendering could be extremely useful in planning therapy. It clearly shows that a nerve-sparing approach could be applied with a tight margin on the right portion of the gland, but a more generous and cautious one on the left side. It also could provide inputs for planning focal or differential radiation, cryo-ablation, or high-intensity ultrasound treatments. The illustrative biopsy-guidance TTI windows of Fig. 8.5 were generated from two separate scans of the same biopsy patient. In this figure, five levels of relative cancer likelihood are shown with green indicating the lowest likelihood, yellow-green a slightly higher likelihood, yellow an intermediate likelihood, orange a moderately high likelihood, and red the highest likelihood. The left image in Fig. 8.5 was generated from a plane in which the biopsy subsequently proved to be positive; the right image was from a plane that had a negative biopsy. If such images had been available to guide the biopsies in real time, the needle certainly could have been targeted into the red and orange regions shown in the left image, but the green and yellow-green regions in the right image might have been spared.

Fig. 8.5 Illustrative biopsy-guidance images with a small TTI ROI window. Two planes from the same patient are shown. Color encoding is used to depict cancer likelihood; the highest likelihood is depicted in *red* and the lowest in *green*; the background *gray-scale* image is a midband image. The actual biopsy histology was positive in the *left* image and negative in the *right* one. This type of search-window TTI could be used to guide biopsies more effectively. [Reproduced, with permission, from *Ultrasonic Imaging*]

8.4 Discussion and Summary

Focal treatments of PCa that spare at least half the prostate or differential treatments that grade the delivery of ablative radiation, cryotherapy, or HIFU over the gland according to images that reliably present the spatial distribution of cancer within the gland can reduce treatment toxicity without degrading treatment efficacy. Similarly, biopsies that are guided by images that present the likelihood of cancer can improve the positive yields of core-needle biopsies while simultaneously reducing or eliminating the current need to insert the needle blindly into non-cancerous regions.

The studies described here use sophisticated, non-linear methods of classification to distinguish cancerous from non-cancerous tissues based on RF echo signals. At present, these methods rely on ANNs and SVMs, and although more than 600 samples are available from more than 60 patients in the data set cited above, only 17 % of the samples in our most-recent data set are cancerous. Considering the range of possible expressions of cancerous and non-cancerous prostatic tissues, further study certainly is required to increase the number of independent samples and to assure that the classifier has sufficient generality. Furthermore, a conservative perspective would consider the patients, and not the biopsy cores to be the independent samples; to take that perspective into account, a much larger data set is required to fully validate the method and allay concerns regarding the generality of the classifier.

Concerns regarding excessive dimensionality and vulnerability to false minima that are inherent when using ANN classifiers are less of an issue with SVMs. Our preliminary investigations of SVMs for classifying prostate tissue have given us very encouraging results, e.g., providing ROC AUCs equivalent or superior to what we achieved using ANNs, but with far lower dimensionality. A third option to pursue is identification of additional spatially varying parameters such as those

associated with the statistics of envelope or RF-signal amplitudes (Mamou Chap.7, this volume).

Confidence in reliable ultrasonic TTIs such as the ones under development and described here can enable detection and treatment of PCa to advance dramatically. The ultrasonic TTIs illustrated in this chapter can be applied clinically either as pure ultrasound techniques using existing digital technology to generate TTIs in real time or they can be used in combination with other modalities to produce even more-powerful methods of imaging PCa. For example, the inability of current imaging methods to depict suspicious regions reliably prevents many patients from choosing the option of watchful waiting or active surveillance. A reliable means of imaging cancerous foci would give such patients confidence that their diseases can be monitored safely and unnecessary treatment of indolent disease can be avoided. As a second example, TTI methods can be integrated into existing ultrasonic instruments that ablatively treat prostate diseases such as benign hyperplasia and cancer with HIFU. Integration would provide a single-modality instrument for targeting and guiding HIFU ablation of selected cancerous regions of the gland and sparing regions that present a low likelihood of being cancerous. As an additional example, the mechanical properties sensed by ultrasound and exploited in ultrasound-based TTIs also can be applied in conjunction with spatially matching chemical properties sensed by magnetic-resonance spectroscopy methods, with perfusion and diffusion properties sensed by contrast-enhanced magnetic resonance, or with metabolic properties sensed by positron-emission methods. Admittedly, such hybrid methods require reliable means of spatial co-registration, but modern image-processing technology seems to be on the verge of enabling such co-registration to be performed quickly and accurately. Once these QUS-based TTI methods are more-fully validated by the on-going studies cited in the acknowledgments below, clinical implementation will be straightforward.

Acknowledgments The studies described in this chapter were inspired, guided, and encouraged by the late Edgar A. Parmer, William R. Fair, and Frederic L. Lizzi. Paul Lee, Stella Urban, and Ronald Silverman made invaluable contributions to the classification aspects of the studies. The original prostate-TTI research was supported in part by NIH/NCI Grants CA053561 and the Riverside Research Fund for Biomedical Engineering. Current studies to integrate TTIs with prostate-HIFU instruments and to integrate US TTIs with MR methods are supported by NIH/NCI Grants CA135089 and CA140772, respectively. Current studies applying envelope statistics in combination with spectrum-analysis methods to distinguishing cancerous from non-cancerous tissue in lymph nodes are supported by NIH/NCI Grant CA100183.

References

Ahmed HU, Kirkham A, Arya M, Illing R, Freeman A, Allen C, Emberton M (2009) Is it time to consider a role for MRI before prostate biopsy? Nat Rev Clin Oncol 6(4):197–206

Ahmed HU, Emberton M, Kepner G, Kepner J (2012) A biomedical engineering approach to mitigate the errors of prostate biopsy. Nat Rev Urol 9(4):227–231

Applewhite J, Matlaga B, McCullough D (2002) Results of the 5-region prostate biopsy method: the repeat biopsy population. J Urol 168(2):500–503

Bigelow TA, O'Brien WD (2005) Evaluation of the spectral fit algorithm as functions of frequency range and Δka_{eff}. IEEE Trans Ultrason Ferroelect Freq Cont 52(11):2003–2010

Bigelow TA, O'Brien WD (2006) Impact of local attenuation approximations when estimating correlation length from backscattered ultrasound echoes. J Acoust Soc Am 120(1):546–553

Bigelow TA, O'Brien WD (2004a) Scatterer size estimation in pulse-echo ultrasound using focused sources: theoretical approximations and simulation analysis. J Acoust Soc Am 116(1):578–593

Bigelow TA, O'Brien WD (2004b) Scatterer size estimation in pulse-echo ultrasound using focused sources: calibration measurements and phantom experiments. J Acoust Soc Am 116(1):594–602

Cancer Facts and Figures (2013) American Cancer Society, Atlanta, p 10

Coleman DJ, Silverman RH, Rondeau MJ, Boldt HC, Lloyd HO, Lizzi FL, Weingeist TA, Chen X, Vangveeravong S, Folberg R (2004) Noninvasive in vivo detection of prognostic indicators for high risk uveal melanoma: ultrasound parameter imaging. Ophthalmology 111(3):558–564

Cortes C, Vapnik V (1995) Support-vector networks. Mach Learning 20:273–297

Dasgupta S, Feleppa EJ, Ramachandran S, Ketterling JA, Kalisz A, Haker S, Tempany C, Porter C, Lacrampe M, Isacson C, Sparks D (2007) Spatial co-registration of magnetic resonance and ultrasound images of the prostate as a basis for multi-modality tissue-type imaging. In: Yuhas MP (ed) Proceedings of 2007 IEEE international ultrasonics symposium. Institute of electrical and electronics engineers. Piscataway, pp 641–643

Epstein JI, Walsh PC, Carmichael M, Brendler CB (1994) Pathologic and clinical findings to predict tumor extent of nonpalpable (stage T1c) prostate cancer. JAMA 271(5):368–374

Feleppa EJ, Lizzi FL, Coleman DJ, Yaremko MM (1986) Diagnostic spectrum analysis in ophthalmology: a physical perspective. Ultrasound Med Biol 12(8):623–631

Feleppa EJ, Liu T, Kalisz A, Shao MC, Fleshner N, Reuter V (1997) Ultrasonic spectral-parameter imaging of the prostate. Int J Imaging Syst Technol 8:11–25

Feleppa EJ, Machi J, Noritomi T, Tateishi T, Oishi R, Yanagihara E, Jucha J (1998) Differentiation of metastatic from benign lymph nodes by spectrum analysis in vitro. In: Schneider S, Levy M, McAvoy B (eds) Proceedings of the 1997 ultrasonics symposium. Institute of electrical and electronics engineers. Piscataway, pp 1137–1142

Feleppa EJ, Fair WR, Liu T, Kalisz A, Balaji KC, Porter CR, Tsai H, Reuter V, Gnadt W, Miltner MJ (2000) Three-dimensional ultrasound analyses of the prostate. Mol Urol 4(3):133–141

Feleppa EJ, Ennis RD, Schiff PB, Wuu CS, Kalisz A, Ketterling J, Urban S, Liu T, Fair WR, Porter CR, Gillespie JW (2001) Spectrum-analysis and neural networks for imaging to detect and treat prostate cancer. Ultrasound Imaging 23:135–146

Feleppa EJ, Ketterling JA, Kalisz A, Urban S, Schiff PB, Ennis RD, Wuu CS, Porter CR, Fair WR, Gillespie JW (2002a) Application of spectrum analysis and neural-network classification to imaging for targeting and monitoring treatment of prostate cancer. In: Schneider S, Levy M, McAvoy B (eds) Proceedings of the 2001 ultrasonics symposium, IEEE. Piscataway, pp 1269–1272

Feleppa EJ, Ennis RD, Schiff PB, Wuu CS, Kalisz A, Ketterling JA, Urban S, Liu T, Fair WR, Porter CR, Gillespie JR (2002b) Ultrasonic spectrum-analysis and neural-network classification as a basis for ultrasonic imaging to target brachytherapy of prostate cancer. J Brachytherapy Intl 1(1):1–6

Feleppa EJ, Porter CR, Ketterling JA, Lee P, Dasgupta S, Urban S, Kalisz A (2004) Recent developments in tissue-type imaging (TTI) for planning and monitoring treatment of prostate cancer. Ultrasound Imaging 26:71–84

Feleppa EF, Porter CR, Ketterling J, Dasgupta S, Ramachandran S, Sparks D (2007) Recent advances in ultrasonic tissue-type imaging of the prostate: improving detection and evaluation. In: Andre MP (ed) Acoustical imaging, vol 28. Springer, Dordrecht, pp 331–339

Feliciano J, Teper E, Ferrandino M, Macchia RJ, Blank W, Grunberger I, Colon I (2008) The incidence of fluoroquinoline-resistant infections after prostate biopsy—are fluoroquinolines still effective prophylaxis? J Urol 179:952–955

Haas GP, Delongchamps NB, Jones RF, Chandan V, Serio AM, Vickers AJ, Jumbelic M, Threatte G, Korets R, Lilja H, Roza G, de la Roza G (2007) Needle biopsies on autopsy prostates: sensitivity of cancer detection based on true prevalence. J Natl Cancer Inst 99(19):1484–1489

Hosokowa T, Sigel B, Machi J, Kitamura H, Kolecki RV, Justin JR, Feleppa EJ, Tuszynski G, Kakegawa T (1994) Experimental assessment of spectrum analysis of ultrasonic echoes as a method for estimating scatterer properties. Ultrasound Med Biol 20(5):4763–4770

Insana MF, Hall TJ (1990) Parametric ultrasound imaging from backscatter coefficient measurements: image formation and interpretation. Ultrasound Imaging 12:245–267

Insana MF, Wagner RF, Brown DG, Hall TJ (1990) Describing small-scale structure in random media using pulse-echo ultrasound. J Acoust Soc Am 87:179–192

Jones JP, Holasek E, Jennings WD, Purnell EW (1976) Two dimensional display of spectral information and its application to diagnostic medicine. In: Proceedings of 1976 ultrasonics symposium, IEEE, vol 1, pp 58–59

Keller JM, Gray MR, Givens JA (1985) A k-nearest neighbor algorithm. IEEE Trans Syst, Man Cybern SMC 15:580–585

Kolecki RV, Sigel B, Justin J, Feleppa EJ, Parsons RE, Kitamura H, Machi J, Hayashi J, Taylor P, McGann L, Roberts AB (1995) Determining the acuteness and stability of deep venous thrombosis by ultrasonic tissue characterization. J Vasc Surg 21(6):976–984

Kolios MC, Czarnota GJ, Hussain M, Foster FS, Hunt JW, Sherar MD (2001) Analysis of ultrasound backscatter from ensembles of cells and isolated nuclei. In: Proceedings of 2001 ultrasonics symposium, IEEE, vol 2, pp 1257–1260

Kolios MC, Czarnota GJ, Lee M, Hunt JW, Sherar MD (2002) Ultrasonic spectral parameter characterization of apoptosis. Ultrasound Med Biol 28(5):589–597

Lanza GM, Wallace K, Scott MJ, Cachetis C, Abendschein D, Christy D, Sharkey A, Miller J, Gaffney P, Wickline S (1996) A novel site-targeted ultrasonic contrast agent with broad biomedical applications. Circulation 94:3334–3340

Lanza GM, Trousil RL, Wallace KD, Rose JH, Hall CS, Scott MJ, Miller JG, Eisenberg PR, Gaffney PJ, Wickline SA (1998) In vitro characterization of a novel, tissue-targeted ultrasonic contrast system with acoustic microscopy. J Acoust Soc Am 104:3665–3672

Lee DJ, Sigel B, Swami VK, Justin JR, Gahtan V, O'Brien SP, Dwyer-Joyce L, Feleppa EJ, Roberts AB, Berkowitz HD (1998) Determination of carotid-plaque risk by ultrasonic tissue characterization. Ultrasound Med Biol 24(9):1291–1299

Lizzi FL, Greenebaum M, Feleppa EJ, Elbaum M, Coleman DJ (1983) Theoretical framework for spectrum analysis in ultrasonic tissue characterization. J Acoust Soc Am 73(4):1366–1373

Lizzi FL, Ostromogilsky M, Feleppa E, Rorke MC, Yaremko MM (1987) Relationship of ultrasonic spectral parameters to features of tissue microstructure. IEEE Trans Ultrason Ferroelectr Freq Control 34(3):319–329

Lizzi FL, King DL, Rorke MC, Hui J, Ostromogilsky M, Yaremko MM, Feleppa EJ, Wai P (1988) Comparison of theoretical scattering results and ultrasonic data from clinical liver examinations. Ultrasound Med Biol 14(5):377–385

Lizzi FL, Feleppa EJ, Astor M, Kalisz A (1997a) Statistics of ultrasonic spectral parameters for prostate and liver examinations. IEEE Trans Ultrasound, Ferroelectr, Freq Control 44(4):935–942

Lizzi FL, Astor M, Liu T, Deng C, Coleman DJ, Silverman RH (1997b) Ultrasonic spectrum analysis for tissue assays and therapy evaluations. Int J Imaging Syst Technol 8:3–10

Loeb S, van den Heuvel S, Zhu X, Bangma CH, Schröder FH, Roobol MJ (2012) Infectious complications and hospital admissions after prostate biopsy in a European randomized trial. Eur Urol 61(6):1110–1114

Macchia R (2007) Resistant infections after prostate biopsy: are fluoroquinolones still effective prophylaxis. Presented on 11 Nov 2007 at the 2007 annual meeting of the New York section of the AUA in Buenos Aires, Argentina

Mamou J, Oelze ML, Brien WD, Zachary JF (2005) Ultrasound characterization of three animal mammary tumors from three-dimensional acoustic tissue models. In: Proceedings of 2005 ultrasonics symposium, IEEE, vol 2, pp 866–869

McLachlan GJ (1992) Discriminant analysis and statistical pattern recognition. Wiley, New York

Metz CE, Herman BA, Shen JH (1998) Maximum likelihood estimation of receiver operating characteristic (ROC) curves from continuously-distributed data. Stat Med 17(9):1033–1053

Miller JG, Perez JE, Wickline SJA, Baldwin SL, Barzilai B, Davila-Roman V, Fedewa RJ, Finch-Johnston AE, Hall CS, Handley SM, Huckett FD, Holland MR, Kovacs A, Lanza GM, Lewis SS, Marsh JN, Mobley J, Sosnovik DE, Trousil RL, Wallace KD, Waters KR (1998) Backscatter imaging and myocardial tissue characterization. In: Proceedings of the IEEE ultrasonics symposium. Sendai, Japan, pp 1373–1383

Nassiri DK, Hill CR (1990) The use of angular scattering measurements to estimate structural parameters of human and animal tissues. J Acoust Soc Am 87:179–192

Nicholas D (1982) Evaluation of backscattering coefficients for excised human tissues: results, interpretation and associated measurements. Ultrasound Med Biol 8:17–28

Noritomi T, Sigel B, Gahtan V, Swami V, Justin J, Feleppa EJ, Shirouzu K (1997a) In vivo detection of carotid plaque thrombus by ultrasonic tissue characterization. J Ultrasound Med 16(2):107–111

Noritomi T, Sigel B, Swami V, Justin J, Gahtan V, Chen X, Feleppa EJ, Roberts AB, Shirouzu K (1997b) Carotid plaque typing by multiple-parameter ultrasonic tissue characterization. Ultrasound Med Biol 23(5):643–650

Noritomi T, Machi J, Feleppa EJ, Yanagihara E, Shirouzu K (1998) In vitro investigation of lymph node metastasis of colorectal cancer using ultrasonic spectral parameters. Ultrasound Med Biol 24:235–243

O'Donnell M, Bauwens D, Mimbs JW, Miller JG (1979) Broadband integrated backscatter: an approach to spatially localized tissue characterization in vivo. In: Proceedings of the IEEE ultrasonics symposium 79 CH 1482–1489, pp 175–178

Oelze M, Zachary J (2006) Examination of cancer in mouse models using high-frequency quantitative ultrasound. Ultrasound Med Biol 32(11):1639–1648

Oelze ML, Zachary JF, O'Brien WD (2002a) Ultrasonic quantification of the tissue microstructure of spontaneous mammary tumors in rats. In: Proceedings of 2002 ultrasonics symposium, IEEE, vol 4, pp 1369–1372

Oelze ML, Zachary JF, O'Brien WD (2002b) Characterization of tissue microstructure using ultrasonic backscatter: theory and technique for optimization using a Gaussian form factor. J Acoust Soc Am 112:1202–1211

Partin AW, Kattan MW, Subong EN, Walsh PC, Wojno KJ, Oesterling JE, Scardino PT, Pearson JD (1997) Combination of prostate-specific antigen, clinical stage, and Gleason score to predict pathological stage of localized prostate cancer. A multi-institutional update. JAMA 277:1445–1451

Shakhnarovish D, Indyk E (eds) (2005) Nearest-neighbor methods in learning and vision. MIT Press, Cambridge

Shawe-Taylor J, Cristianini N (2000) Support vector machines and other kernel-based learning methods. Cambridge University Press, New York

Silverman RH, Folberg R, Rondeau MJ, Boldt HC, Lloyd HO, Chen X, Lizzi FL, Weingeist TA, Coleman DJ (2003) Spectral parameter imaging for detection of prognostically significant histologic features in uveal melanoma. Ultrasound Med Biol 29(7):951–959

Tateishi T, Machi J, Feleppa EJ, Oishi RH, Jucha J, Yanagihara E, McCarthy LJ, Noritomi T, Shirouzu K (1998) In vitro diagnosis of axillary lymph node metastases in breast cancer by spectrum analysis of radio frequency echo signals. Ultrasound Med Biol 24(8):1151–1159

Theodoridis S, Koutroumbas K (2009) Pattern recognition, 4th edn. Academic Press, New York

Wei JT (2010) Limitations of a contemporary prostate biopsy: the blind march forward. Urol Oncol 28(5):546–549
Wu TY, Ohmura T (1962) Quantum theory of scattering. Prentice Hall, Upper Saddle River
Zagzebski JA, Lu ZF, Yao LX (1983) Quantitative ultrasound imaging: in vitro results in normal liver. Ultrasound Imaging 15:335–351

Chapter 9
Therapy Monitoring and Assessment Using Quantitative Ultrasound

Michael L. Oelze, Jeremy P. Kemmerer, Goutam Ghoshal and Roxana M. Vlad

Abstract Quantitative ultrasound (QUS) techniques have demonstrated the ability to detect changes in tissue microstructure following the application of cancer therapy. In this chapter, QUS techniques, i.e., spectral-based analysis and envelope statistics, are examined for their ability to detect, image and quantify the therapeutic response of diseased and normal tissues ex vivo and in vivo. Specifically, high frequency QUS (>20 MHz) techniques were used to detect changes in the tumor microstructure of cancer mouse models following radiation therapy and changes in ex vivo liver tissue following thermal therapy. QUS parameter estimates were correlated with changes observed in photomicrographs of histological slides of stained tissues. Mouse tumors treated with radiation therapy demonstrated an increase in the ultrasound integrated backscatter of 6–8 dB in the treated regions compared to untreated regions. The treated regions can be clearly distinguished in ultrasound images as hyperechoic areas. When liver tissues were treated with heat, a change in the slope of the frequency dependence of the backscatter coefficient versus thermal dose was observed. QUS changes were examined versus transient elevations in temperature using a thermocouple in order to guide the application of thermal therapies in these samples. It was observed that some QUS parameters were capable of tracking changes in the temperature. This work provides means of using QUS to monitor and guide therapy application, and rapidly assess the response of tissues to different therapies.

Keywords Therapy monitoring · Therapy guidance · Therapy assessment · Quantitative ultrasound

M. L. Oelze (✉) · J. P. Kemmerer · G. Ghoshal
Department of Electrical and Computer Engineering, University of Illinois at Urbana-Champaign, Urbana, IL 61801, USA
e-mail: oelze@illinois.edu

R. M. Vlad
Walker Family Cancer Centre, Hamilton Health Sciences, St. Catharines, ON, Canada

J. Mamou and M. L. Oelze (eds.), *Quantitative Ultrasound in Soft Tissues*, DOI: 10.1007/978-94-007-6952-6_9,

9.1 Introduction

Quantitative ultrasound (QUS) techniques are based on processing radio-frequency (RF) ultrasound data. RF data are used to construct conventional medical ultrasound B-mode images by applying an envelope detection technique (Cobbold 2007). This type of processing removes the frequency-dependent information. B-mode images are good at displaying large-scale structures, larger than the wavelength, because simple tissue interfaces such as organ boundaries produce well-defined RF signals whose envelopes can be clearly detected. Most structures of interest, including organ parenchyma and tumors, have a complex spatial distribution of mechanical properties that result from the complex internal microstructure of biological tissues. B-mode images reflect this complexity, exhibiting an average gray-scale level that is related to the average scattering strength and results in a specific speckle pattern that depends on tissue characteristics. Clinicians interpret this speckle pattern on the basis of boundary geometry of specific structures, internal brightness and texture, but not much information can be inferred about the properties of the underlying tissue structure. Smaller scale structures, smaller than the ultrasound wavelength, could be characterized using the frequency-dependent information content from RF backscattered signals by extracting various parameters that could be related to specific tissues properties, e.g., size, density, compressibility and number of tissue scattering structures (Insana et al. 1990). QUS techniques incorporate this type of analysis. Since tissue microstructure changes follow disease processes or therapeutic interventions, it is possible to detect these changes using QUS techniques. QUS applications include characterization of cancer pathology in certain organs, i.e., prostate, lymph nodes and monitoring therapy response following cancer treatment, i.e., chemotherapy, photo-dynamic therapy and radiotherapy. QUS methods can detect changes in tissue before any changes in the size of the tumor are detectable in anatomical images.

The ability to detect tumor response to treatment addresses an important aspect in the field of cancer therapy. Often, poor prognosis in a patient is associated with a lack of response to a specific therapy. A patient may benefit from an earlier detection of a non-responsive treatment by a change to a more aggressive treatment earlier during the course of treatment and, thus, avoidance of side effects associated with prolonged ineffective treatments. Therefore, QUS techniques have the potential of advancing the methods of cancer diagnosis and lead to adaptive therapy approaches in the treatment of cancer.

The clinical management of cancer treatment remains a significant challenge because, tumors are phenotypically heterogeneous and, therefore, it is rare for all cancers of a particular type to respond to a specific therapy. Tumor responses to treatment are traditionally assessed by measurements of tumor size in clinical images using the response evaluation criteria in solid tumors (RECIST) guidelines (Jaffe 2006; Eisenhauer et al. 2009). Current methods to monitor tumor response include palpation, ultrasound, computed tomography and magnetic resonance

imaging (MRI). These techniques assess the response of a tumor to cancer by identifying changes in the size of the tumor. Measurement of tumor size is not ideal for predicting patient outcome because changes in tumor size appear late during the course of therapy. For instance, changes in tumor size could be observed at 6–8 weeks after a treatment starts (Michaelis and Ratain 2006). Furthermore, a change in the tumor size as indicated by a certain imaging modality might not correspond with the ground truth identified in the histopathology. For instance, in one study that compared response assessment by palpation, X-ray mammography, ultrasound, and MRI, it was found that agreement of tumor shrinkage with pathology was only 19, 26, 35, and 71 %, respectively (Yeh et al. 2005).

In recent years, the measurements of tumor size have been supplemented by imaging of tissue function, often termed molecular imaging, which aims to characterize biological processes at the cellular and molecular level in vivo. Dynamic contrast enhanced MRI (DCE-MRI) monitors the tumor perfusion by rapidly acquiring series of images that are used to follow the kinetics of a contrast agent into the tumor (Brindle 2008). DCE-MRI has been recently used to evaluate breast tumor response to neo-adjuvant chemotherapy but its application is limited by reduced availability and high cost. Positron emission tomography (PET) imaging using a glucose analogue, the radionuclide 2-[18F] fluoro-2-deoxy-d-glucose (FDG) is an established modality in the diagnosis and management of various malignancies (Brindle 2008). Studies of lung cancer (Weber et al. 2003), oesophageal cancer (Weber et al. 2001) and lymphoma (Spaepen et al. 2001) have demonstrated that reduced FDG uptake can identify early tumor response to treatment. Persistently increased FDG uptake after treatment is associated with a high risk for early disease recurrence and poor prognosis (Brindle 2008). These results have shown that PET imaging is a promising imaging modality to identify tumor response. However, PET imaging has the disadvantage of requiring complex resources, including special radiation safety considerations for the design of imaging facility, handling of the radionuclides and the need of having a cyclotron on site for the radionuclides production or ready access to these radionuclides.

Detecting early tumor response to therapy, and thus predicting the likely outcome of a treatment, requires suitable means to identify markers of the response. Markers of response may include: cell death, vascular damage, changes in metabolism or receptor expression associated with tumor cell death or inhibition of proliferation (Ian et al. 2004). For instance, increased tumor cell death, early during a course of treatment, is a good prognostic indicator of a treatment outcome (Symmans et al. 2000; Roberg et al. 2007).

Developing techniques that can rapidly assess treatment response in order to adapt cancer therapy to treatment response may solve an important clinical need. Recent advances in new ultrasonic imaging modes have yielded promise for early detection of the response of cancer to therapy. Specifically, QUS techniques have matured and research has been successfully conducted on the ability of these techniques to diagnose cancer and to detect cell death or tissue changes induced by therapy (Oelze and Zachary 2006; Vlad et al. 2008, 2009, 2010, 2011; Kolios and

Czarnota 2009; Kemmerer et al. 2010). This chapter will discuss applications of QUS techniques to monitor and assess therapeutic response.

9.2 QUS Techniques and Traditional Cancer Therapy

A non-invasive technique, e.g., ultrasound imaging enhanced by QUS parameters, capable of assessing early tumor responsiveness to therapy within days after the start of a treatment could aid clinicians in making decisions to guide treatment selection. This will help to select a treatment adapted to tumor aggressiveness and provide individualized patient therapy. It might lead to improved outcomes and the sparing of patients from unnecessary side effects related to ineffective prolonged cancer treatments.

Increased tumor cell death, early during a course of treatment, is a good prognostic indicator of a treatment outcome (Symmans et al. 2000; Roberg et al. 2007). Experimentally, ultrasound imaging and spectrum analysis techniques were applied for the first time by Czarnota et al. (1997, 1999), Kolios et al. (2002) to detect cell death in cell samples and tissues exposed to cancer therapies (e.g., chemotherapy and photodynamic therapy). Two parameters, Ultrasound integrated backscatter (UIB) and spectral slope (SS) calculated from the ultrasonic power spectra were used to monitor the responses of cells and tumors exposed to cancer treatment (Vlad et al. 2008, 2009, 2011). The UIB depends on size and acoustic properties (density and compressibility) of scatterers in a sample and the SS can be related to the effective scatterer size. Further details on the theoretical and signal analysis considerations and how spectral parameters are related to tissue microstructure can be found elsewhere (Lizzi et al. 1983). In the experiments performed on cell samples exposed to a chemotherapeutic drug, apoptotic cells exhibited up to a 16-fold increase in UIB in comparison with viable cells, as well as other measurable changes in ultrasonic parameters (Kolios et al. 2003; Tunis et al. 2005). The same technique can be used to detect oncotic cell death following ischemic injury when cells and tissues were deprived of essential nutrients. UIB increased up to eight-fold in rat livers exposed to ischemic injury (Vlad et al. 2005) and up to four-fold in cell samples left to die at room temperature (Kolios et al. 2003). These provide the groundwork for future investigations regarding the use of ultrasound in cancer patients to individualize treatments based on non-invasive imaging assessment of tumor responses to specific interventions.

In research conducted by Vlad et al. (2008), radiotherapy effects can be characterized by QUS methods in preclinical mouse cancer models, as early as 24 h after treatment administration. For instance, ultrasound imaging and ultrasound images enhanced by spatial maps of ultrasound spectral parameters enabled non-invasive assessment of cell death in tumor regions that responded to radiotherapy. The key advantage of the technique is that the image contrast and changes in UIB and SS are caused by changes in physical properties of cells undergoing death and, hence, responding to therapy. This is an important benefit of the technique, because it does not require injections of contrast agents or radioisotopes, unlike

Fig. 9.1 **a** Ultrasound image of a mouse tumor presenting regions with increased echogeneity after radiotherapy, **b** corresponding histological TUNEL stained section, indicating an area of cell death (*brown colored area*), **c** parametric image constructed from local estimates of the UIB and superimposed on the corresponding B-mode image. The increased echogeneity in the ultrasound image and greater UIB estimates in the parametric image corresponded to the area of cell death in histology. **d** Hematoxylin and Eosin histological staining at higher magnification demonstrating a clear delineation between the areas of cell death on the *left side* of the image, characterized by small condensed and fragmented nuclei indicated by the *black arrows*, and regions appearing as viable tissue on the right side of the image indicated by the *white arrows*. Scale bars are: (**a**, **b** and **c**) −1 mm and **d** −50 μm

other imaging modalities for treatment monitoring, e.g., DCE-MRI, single photon emission computed tomography and PET.

Figure 9.1 is an image from a representative head and neck cancer mouse model exposed to a radiation dose of 4 Gy in a single fraction. Data were collected with an ultrasound scanner using a broadband 25 MHz single element focused transducer with a −6 dB bandwidth of 12–30 MHz, 12.5 mm focal distance and 6 mm aperture. After exposure to radiotherapy, the tumor exhibited large hyperechoic areas corresponding to the brown colored regions in the TUNEL staining indicating cell death Fig. 9.1a, b. The local estimates of the UIB demonstrated values greater by 6–8 dB in the echogenic regions selected from mouse tumors treated with radiotherapy compared with the UIB estimates calculated from regions that did not respond to therapy, Fig. 9.1c, d.

Fig. 9.2 **a** Averaged normalized power spectra and spectral slopes of six head and neck tumors before treatment (XRT−) and 24 h following radiotherapy (XRT+); **b** corresponding feature analysis plot indicating a clear separation between the (XRT−) tumors and the (XRT+) tumors. Error bars in panel **a** represent the standard error of the averaged spectra for $n = 6$ animals

Figure 9.2 demonstrates the use of the ultrasound spectral parameters in characterization of tumor responses to radiotherapy in six head and neck cancer mouse models. The results indicate that the SS increased from 0.77 ± 0.03 dB/MHz before treatment to 0.90 ± 0.05 dB/MHz ($p < 0.05$) after treatment administration in hyperechoic regions selected from mouse tumors at 24 h after exposure to radiotherapy. As previously described, these changes in ultrasound images and spectral parameters were interpreted as direct consequences of cell death following radiotherapy (Vlad et al. 2008, 2009).

In order to adopt the ultrasound imaging and QUS methods in preclinical and clinical applications, it is essential to know how well the volume of cell death in ultrasound and parametric images corresponds to the true cell death in histology. Currently, stained histological sections are considered the gold standard for cancer diagnosis, detection of cell death and assessment of tumor response. For instance, the ability to know how well the margins of a region of cell death represented in ultrasound and parametric images correspond to the cell death as assessed from histology can result in the development of new clinical applications, e.g., guiding needle and surgical excision biopsies for diagnostic purposes using ultrasound methods.

Because changes calculated in the QUS parameters were mainly demonstrated by the hyperechoic regions in the ultrasound images following radiotherapy, a metric of comparison between the true cell death in histology and these hyperechoic regions was developed. An example of qualitative comparison between the volume and localization of cell death, assessed from histology, with the volume and localization of cell death surrogate assessed from the ultrasound images as hyperechoic regions for a mouse cancer model is presented in Fig. 9.3. This method used volumetric meshes to compare the volumes and the localization of cell death in histological and ultrasound images. The procedure was developed on seven mice and it has been presented elsewhere, Vlad et al. (2010). In the example from

Fig. 9.3, the method was applied to demonstrate the potential of mid-to-high frequency (10–20 MHz) ultrasound imaging to detect early tumor response 24 h after delivery of radiotherapy treatment. This technique, briefly described here, could be applied similarly to assess tumor response to other modalities of cancer treatment.

To construct the volumetric mesh model of tumor and cell death, the ultrasound and histological images were rigidly registered. The tumors and regions of cell death were manually outlined on the histological images. Similarly, the tumors and hyperechoic regions were outlined on the ultrasound images. Each set of contours from histology and ultrasound images was converted to a volumetric mask in order to compare the corresponding volumes. An in-house developed algorithm was used to calculate the mask volumes and the overlap of mask volumes for each representation of tumor and cell death in ultrasound and histology. Finally, to visualize the volumes and create models of tumor and cell death in each representation (ultrasound and histology), the mask files were converted to a triangular surface mesh, finite element model, using methodology described by Balter et al. (2005).

There are differences between the volume of tumor and cell death as assessed from ultrasound and histological images, Fig. 9.3c–f. Part of these differences can be attributed to tissue shrinkage during histopathological processing and deformation of tissue during cutting and mounting of each section. Considering that the size of the tumor in the ultrasound image is the ground truth, a scaling factor of ~ 17 % was calculated to account for differences in tumor size between the histological and ultrasound images. Using this factor, the histological images were scaled uniformly to compensate for tissue changes during histological processing. The average difference in the volume of tumors as represented in ultrasound and histology decreased from 17 ± 2 % to 3 ± 2 % after compensating for tissue shrinkage, (Vlad et al. 2010). The average overlap of the volumes of cell death assessed from ultrasound and histological images was 70 ± 12 % for the seven mice used to develop this method (Vlad et al. 2010). An illustrative example of this type of cell death overlap is presented in Fig. 9.3f. It can be observed that the differences resulted from the tumor representation in histology and ultrasound propagated to the cell death representation in the two modalities. In addition, factors linked to how well the ground truth of cell death in histology corresponded to the hyperechoic areas in the ultrasound images contributed to this difference.

The method indicated a good co-localization of cell death volume in the ultrasound and histological representation. The good agreement between cell death representation in histological and ultrasound images indicated that high frequency ultrasound imaging is capable of detecting early response to radiotherapy in these types of tumors. These results provide confidence in the capabilities of ultrasound imaging to detect cell death and support the basis for the application of mid-to high frequency ultrasound imaging and QUS methods to characterize early tumor responses to cancer radiotherapy.

A more precise co-localization between the cell death in histology and cell death identified by the ultrasound could be obtained by adding local estimates of QUS parameters to this analysis. QUS parameters, e.g., UIB and SS, were able to differentiate different modalities of cell death in well controlled laboratory

Fig. 9.3 **a** Representative ultrasound image of a mouse tumor 24 h after radiotherapy with 4 Gy in a single fraction, presenting a large hyperechoic region after treatment, **b** Corresponding Hematoxylin and Eosin image indicating an area of cell death of similar shape as the hyperechoic area in the ultrasound image. These types of images were used to contour the tumor and cell death in ultrasound imaging and corresponding histology. Volumetric mesh models of a tumor and cell death segmented from **c** ultrasound images and, **d** from corresponding histology. Volumetric mesh models **e** demonstrating the overlap between the tumor representation in ultrasound and histology and, **f** demonstrating the overlap of cell death representation in ultrasound and histology. Scale bars are 4 mm

conditions (Vlad et al. 2008). Rigorous QUS analysis might have the potential of differentiating cell death from early tissue reactions to radiotherapy, e.g., inflammation and edema, in the hyperechoic regions observed in ultrasound images following radiotherapy.

9.3 QUS Techniques Applied to Thermal Therapy

For more than 60 years the idea of noninvasive surgery has attracted the attention of medicine (Fry et al. 1954; Kennedy et al. 2003). The benefits of noninvasive surgery are the improved patient recovery time, the reduction in occurrence of post-operative infection, and the reduction of healthy tissues affected by the procedure. For almost as long, ultrasound has been suggested as a tool for conducting noninvasive surgical procedures through high intensity focused ultrasound (HIFU). The use of ultrasound to treat tumors has been investigated in the prostate (Madersbacher et al. 1995; Gelet et al. 1996; Chaussy et al. 2002; Sanghvi et al. 1996; Uchida et al. 1995; Foster et al. 1993), in tumors (ter Haar et al. 1991; Prat et al. 1995; Sibille et al. 1993; Yang et al. 1991), the kidney (Frizzell et al. 1977; Adams et al. 1996; Daum et al. 1999), the brain (Hynynen and Jolesz 1998; Sun and Hynynen 1999), and for various eye conditions (Lizzi et al. 1984).

HIFU has seen dramatic advancements in higher power transducer array designs using novel materials and driving systems (Clement 2004). Array designs have allowed improved focusing with narrower beams to better control the affected regions. The result is a decrease in treatment times, less distortion in beam characteristics, and improved lesion formation.

While improved technology for transducer array design has been important to the advancement of HIFU treatment of cancer, several significant roadblocks still exist for widespread clinical acceptance of this noninvasive treatment option. The clinical roadblocks faced by having a truly noninvasive HIFU treatment option are related to the monitoring and assessment of treatment. Noninvasive monitoring of HIFU during treatment requires an estimation of the temperature rise in the cancerous regions and surrounding normal tissues and an assessment of the therapy effectiveness. The goal is to treat cancerous regions while minimizing the effects on surrounding healthy tissue. Noninvasive assessment of the treatment refers to detecting the onset of cell or tissue death or coagulative necrosis due to the rise in tissue temperature and mapping out the regions where these effects occurred.

9.3.1 Monitoring of HIFU Therapy: Non Ultrasonic Techniques

Currently, monitoring can be done invasively through the placement of temperature probes in the tissues to be treated. However, aside from the complications involved with the invasiveness of the procedure, the placement of temperature probes leads to a sampling problem, i.e., only limited portions of the cancerous region and surrounding healthy tissues can be monitored. Second, viscous heating effects near the thermocouple result in local increases in temperature readings and unreliable temperature readings. Third, mapping out of cancerous regions and the assessment of treatment throughout the cancerous regions can only be

accomplished through a limited sampling when using an invasive procedure. In the treatment of cancer, it is vitally important to treat all of the cancerous lesions including microscopic disease, which requires knowledge of the extent of the cancer before treatment and residual microscopic disease after treatment.

In terms of monitoring the temperature rise in tissues treated with HIFU and guiding exposures, ultrasound, CT, and MRI have been investigated (Clement 2004). However, currently only MRI has been found to accurately monitor and quantify the temperature rises in tissues treated with HIFU in vivo noninvasively (Hynynen et al. 1996; Hazle et al. 2002; Huber et al. 1994; Chung et al. 1996; Smith et al. 1995). MRI can provide quantitative spatial maps of induced temperature rise in tissues with good accuracy and good spatial resolution (Gellerman et al. 2005; Bohris et al. 1999; Cline et al. 1995). Several groups have investigated MRI for use in monitoring temperature rises in vivo during HIFU treatment (Hynynen et al. 1996; Hazle et al. 2002; Huber et al. 1994; Chung et al. 1996; Smith et al. 1995). MRI has been used to correlate ablation volumes using HIFU treatment with pathology in a rabbit hepatocarcinoma model (Hazle et al. 2002; Weidensteiner et al. 2003). MRI has been used successfully with HIFU to guide and monitor the treatment of uterine fibroids and leiomyomas in vivo (Tempany et al. 2003). MRI has also been investigated as a technique to guide HIFU therapy in the brain (Hynynen and Jolesz 1998; Sun and Hynynen 1999; Hynynen et al. 2001).

While research in the area of MRI guided HIFU therapy continues, several issues limit its widespread clinical use. First, MRI can suffer from motion artifacts. However, progress continues to be made in the area of motion detection that should mitigate some or all of these effects (Clement 2004). Second, the lack of portability and the expense related to MRI devices limits the widespread use of MRI-guided HIFU treatment. Third, ultrasound equipment that is MRI-compatible is required to perform the procedures, which also limits the availability of the technique and raises the expense of the procedures. Finally, MRI does not allow inherently real-time mapping of temperature in vivo (Anand et al. 2007).

9.3.2 QUS Techniques for Monitoring HIFU

Ultrasound is attractive as an imaging modality to monitor and guide HIFU treatment because it is nonionizing, inexpensive, portable, real time, and convenient. Because of its attractiveness, several ultrasonic techniques have been investigated for monitoring, quantifying, and mapping the temperature rise induced in tissues by HIFU treatment. These techniques include quantifying the change in sound speed through cross-correlation of backscattered signals during treatment (Anand et al. 2007; Abolhassani et al. 2007; Daniels et al. 2007; Varghese et al. 2002a; Simon et al. 1998; Pernot et al. 2004; Maas-Moreno and Damianou 1996). As temperature increases in most tissues, the speed of sound also increases, which causes a slight time shift in backscattered echoes (Bamber and

Hill 1979). This time shift can be detected by cross-correlating signals from a region at one temperature with signals from the same region at a different temperature. A second route has utilized elastographic methods to examine the changes in tissue stiffness when undergoing temperature rises (Konofagou et al. 2003; Lizzi et al. 2003; Miller et al. 2002; Varghese et al. 2002a). Other techniques have examined the spectral content of the backscattered ultrasonic signals to quantify temperature rises in vivo during HIFU treatment (Seip and Ebbini 1995; Amini et al. 2005; Arthur et al. 2005; Trobaugh et al. 2008). All of these techniques have met with some success.

Several investigators have examined techniques to estimate changes in speed of sound and thermal expansion with temperature for the purposes of monitoring HIFU treatment using cross-correlation techniques (Anand et al. 2007; Abolhassani et al. 2007; Daniels et al. 2007; Varghese et al. 2002a; Simon et al. 1998; Pernot et al. 2004; Maas-Moreno and Damianou 1996). These investigators have claimed the ability to detect changes in temperature as small as 0.5 °C using cross-correlation to estimate time shifts in the RF backscattered signals with good spatial resolution (Anand et al. 2007). More recent advances have tracked changes in three-dimensional (3D) volumes as opposed to two-dimensional (2D) image planes. Finally, these techniques offer the possibility of real-time tracking of temperature changes in vivo.

However, time-domain cross-correlation methods are limited due to several factors. First, the time-domain cross-correlation methods are limited by motion in subsequent acquisition scans. Motion between the acquisition of imaging frames causes scan lines to become decorrelated resulting in large errors in the estimation of time shifts. Motion artifacts are especially predominant in abdominal organs, e.g., the liver or kidney, where centimeter-sized displacements can cause large estimate errors in micrometer-sized displacements due to sound speed changes. Recent attempts to combat these errors have met with some success by relying on fast frame rate imaging to detect and monitor shifts in sound speed due to motion artifacts (Liu and Ebbini 2010). Second, sound speed and thermal expansion coefficients do not always follow the same linear increase relative to temperature increases for every kind of tissue. For example, the speed of sound of fatty tissues will actually decrease with increasing temperature while the speed of sound in liver will increase monotonically with temperature until about 50 °C (Bamber and Hill 1979). Finally, the thermal lens effect, caused by the distortion of the focused beam, will introduce errors into the estimation of echo shifts (Simon et al. 1998).

Another ultrasound monitoring technique that has been investigated is the use of elastographic methods for estimating the changes in tissue stiffness versus temperature rise. In one technique investigators used an ultrasound stimulated acoustic emission technique to examine the shift in frequency of the acoustic emission stimulated by a radiation force (Konofagou et al. 2003). As the stiffness of the tissue increased with increased temperature, the frequency of the stimulated acoustic emission would increase. The technique was examined in simulation, agar gel phantoms, and muscle tissue and indicated that below the coagulative necrosis threshold the frequency shift increased with increasing temperature. While the

results were encouraging, the drawbacks to the proposed technique were the lack of sensitivity to tissue stiffness, the slow acquisition time, and differentiating shifts in frequency due to changes in the size of the lesion as a result of heating.

Other investigators examined traditional strain imaging techniques to estimate mechanical properties of tissues during or after HIFU therapy. Varghese et al. (2002b) used speckle tracking algorithms to estimate the changes in tissue mechanical properties and relate these estimates to tissue necrosis. Lizzi et al. (2003) investigated a radiation force technique to provide strain images related to changes in tissue stiffness due to HIFU treatment. Miller et al. (2002) quantified the limitation of strain imaging techniques to estimate the temperature rise in tissues such as the liver. They found that it was necessary to have large signal-to-noise ratios (SNRs) to acquire good estimates (>26 dB) and that motion during monitoring needed to be minimal. Further limitations were found for liver tissues with high fat concentration.

Other investigators have examined spectral techniques for monitoring the temperature increases in tissues treated with HIFU. In one technique, investigators hypothesized that the sound speed and density of subwavelength scatterers would change differently compared to the background when subjected to hyperthermia treatment (Arthur et al. 2005). Based on this theory, the investigators examined the changes in the backscatter energy versus temperature over the range of 37–50 °C. They found that the backscatter energy changed monotonically with temperature with either positive or negative slope depending on the location in the scanned region. However, like earlier techniques involving echo shifts, the technique to estimate changes in the backscatter energy depended on correlating tissue regions during temperature increases. Therefore, motion between the acquisition of imaging frames caused scan lines to become decorrelated and estimation errors to increase. In addition, these techniques have not been tested in in vivo situations.

Seip and Ebbini (1995) proposed another spectral-based technique for estimating temperature increases using a discrete scattering model. In their approach, the investigators hypothesized that backscattered spectra from tissues would have resonances due to semi-regularly spaced scatterers in the tissues. The resonances would shift as the temperature increased due to changes in the speed of sound and thermal expansion. The investigators used an autoregressive technique to estimate the shifts in the resonant frequencies and related these shifts to temperature increases. The technique was limited by the need to have regularly spaced scatterers, the need for two or more regularly spaced scatterers to be included in the range gated window used for estimation, the large bias and variance of frequency shift estimates, and appropriate choice of the autoregressive model order (Simon et al. 1998). Later studies estimated shifts in resonant frequencies using a unique spectral estimation routine based on state-covariance subspace analysis allowing high resolution in frequency analysis (Amini et al. 2005). Similar limitations existed with the improved spectral estimation routine except that the bias and variance of estimates could be reduced.

Silverman et al. (1986) developed spectral-based parameters to examine the changes induced in tumor xenografts treated ultrasonically to induce hyperthermia.

These spectral-based parameters were correlated to histological changes observed in the tumors. Subcutaneous tumors were treated with a spherically focused transducer having a center frequency of 4.6 MHz with the focus just above the skin surface of the tumor to insonify the whole tumor. Tumors were scanned both immediately prior and subsequent to treatment. The diagnostic ultrasound system employed a weakly-focused 10 MHz transducer. Raw RF data were acquired from the system allowing the power spectrum of the backscattered signal to be calculated. The normalized power spectrum from a data block was calculated using a planar reference spectrum (Lizzi et al. 1983). From the normalized backscattered power spectrum, the spectral slope and spectral intercept (SI) were estimated. In addition, the normalized power spectrum was further divided into a low bandwidth (5–8 MHz) and a high bandwidth (11–14 MHz) to create bandpass images and estimates. From these bandpass images a co-occurrence matrix was formed and these values compared between pre-treatment and post-treatment.

Estimates of the spectral-based parameters resulted in significant changes between pre- and post-treatment samples. The SS was observed to decrease from 0.261 dB/MHz pre-treatment to −0.147 dB/MHz post-treatment. The SI was observed to increase from −66.84 dB pre-treatment to −55.31 dB post-treatment immediately after ultrasonically induced hyperthermia. Co-occurrence matrices from pre- and post-treatment had different shapes. The treated case resulted in a shift upwards and to the right along the diagonal. The results of Silverman et al. (1986) suggested that histologic changes accounted for the changes observed in the spectral-based parameters. They observed that low frequency estimates followed deterministic structural elements (e.g., boundaries in the tumor) while higher frequency estimates were correlated to changes in cellular scattering, cytoplasmic vacuoles and widened intercellular spaces.

In a similar study to assess the effects of thermal therapy on tissues, QUS techniques involving spectral-based parameters [backscatter coefficient (BSC), effective scatterer diameter (ESD) and effective acoustic concentration (EAC)] were explored for their ability to correlate to tissue damage (Kemmerer and Oelze 2012). Scattering property estimates and attenuation estimates were generated from rat liver samples submersed in a saline bath heated to 37, 45, 50, 55, 60, 65, or 70 °C for 10 min. Ultrasonic scans were performed in a 37 °C saline bath using a weakly-focused (f/4) 20 MHz transducer. All scans were completed less than two hours after euthanasia to minimize the effects of tissue decomposition. From the results of the study, the attenuation coefficient was observed to increase monotonically with exposure temperature, increasing by 86 % for the highest temperature with respect to the non-treated case. Figure 9.4 displays graphs of the BSC estimates for the different thermal doses corrected using estimates of attenuation from the samples. The BSC had close agreement for all thermal doses from 8 to 15 MHz. Above 15 MHz, an increased BSC slope was observed for samples heated at and above 55 °C compared to lower temperature exposures. The BSC was then parameterized to provide estimates of the ESD and EAC assuming a spherical Gaussian model. When using a bandwidth above 15 MHz (Fig. 9.4 bottom), the ESD and EAC were able to distinguish treated from non-treated cases.

Fig. 9.4 (*left*) Graph of the BSC versus frequency for the lower thermal doses and (*right*) for the higher thermal applied doses and (*bottom*) blow up of the higher thermal applied doses (15–25 MHz). Figures taken from Kemmerer and Oelze (2012)

Figure 9.5 shows a plot of the ESD estimates for different thermal doses. The findings suggest that, in rat liver, the ultrasonic BSC (below 15 MHz) and the sound speed are relatively insensitive to tissue changes due to thermal therapy. Attenuation, BSCs above 15 MHz, and scatterer property estimates above 15 MHz were sensitive to tissue changes caused by thermal therapy and could potentially be used for therapy assessment.

Thermal lesions in rat livers were also produced by a HIFU transducer and the response of the tissue was quantified using QUS imaging. QUS techniques were used to scan the same area before and after producing the thermal lesion with HIFU. Lesions were verified via histological analysis using optical microscopy. Figure 9.6 shows parametric images of thermal lesions using the EAC. Decreases in the EAC were observed in liver lesions created using HIFU. A nominal attenuation value of 0.7 dB/MHz/cm was used in the estimates of EAC both before and after therapy. These changes were not observed when heating the liver via a water bath and at first glance suggest that different mechanisms may have caused the damage. Further examination revealed that the apparent decrease in EAC was associated with the region behind the lesion and was an artifact of

Fig. 9.5 Estimates of the average ESD for liver samples heated in a saline bath for different durations. Figure taken from Kemmerer and Oelze (2012)

undercompensated attenuation. Therefore, the decrease in the EAC observed behind the lesion was attributed to the increase in the attenuation within the lesion due to heating. EAC within the lesions did not change appreciably due to heating with HIFU similar to water bath heating of the liver.

Similar work was also conducted by Silverman et al. (2006) using spectral parameter imaging in both the fundamental and harmonic of backscattered RF data to visualize a HIFU lesion. B-mode images derived from a focused 9 MHz source were compared with spectral-parameter images based on the midband fit (MBF) created at the fundamental frequency (9 MHz) and at the harmonic (18 MHz). Lesions were formed using a HIFU system in freshly excised rabbit liver and in chicken breast. Images of HIFU-induced lesions constructed from the MBF had increased contrast of approximately 3 dB between tumor margins compared to images using traditional ultrasonic B-mode. MBF images derived from the harmonic had higher contrast in attenuated structures related to the lesions. In the image space, as the image shifts from untreated to treated regions, changes in the image features will occur. These changes are quantified by the rate of the change in image features across the boundary or the gradient of feature changes. The gradients between the lesion and surrounding untreated tissues were 3.4, 6.9 and 17.2 dB/mm for B-mode, MBF at the fundamental and MBF at the harmonic, respectively. These results suggest that spectral-based features can provide improved ability to visualize and perhaps quantify the extent of treatment due to HIFU exposure.

In another study, the backscatter coefficient and spectral-based parameters were quantified in fresh rabbit and beef liver during exposure to heat in a saline bath (Ghoshal et al. 2011) in order to quantify the changes in QUS parameters versus temperature. Samples were scanned using a 20 MHz single-element weakly-focused transducer. QUS parameters (ESD and EAC) were estimated from the backscatter coefficient estimates. QUS parameters were estimated from the samples versus increases in temperature from 37 to 50 °C in 1 °C increments.

Fig. 9.6 QUS images of lesions formed using HIFU. The *left* and *right panels* each represent one liver sample. The *top panels* are pre-exposure, the *middle panels* are post-exposure and the *bottom panels* are photographs of the exposed regions. The *red circles* indicate the location of the lesion

Fig. 9.7 Plots of the frequency versus backscatter coefficient at different temperatures for the (*left*) beef liver and the (*right*) rabbit liver. Figures taken from Ghoshal et al. (2011)

Fig. 9.8 Change in (*left panels*) ESD and (*right panels*) EAC versus temperature for the (*top*) beef liver samples and (*bottom*) rabbit liver samples. Figures taken from Ghoshal et al. (2011)

Changes in the backscatter coefficient versus frequency were observed at different temperature elevations. Figure 9.7 shows graphs of the backscatter coefficients for the rabbit and beef livers taken at four different temperatures. From the backscatter coefficients, estimates of the ESD and EAC were obtained. Figure 9.8 shows the changes in the ESD and EAC estimates for the rabbit and beef livers

Fig. 9.9 (*top and clockwise*) B-mode image of liver sample, EAC versus temperature, μ parameter versus temperature, k parameter versus temperature and ESD versus temperature

versus temperature. Significant increases in ESD and decreases in EAC of 20–40 % were observed in the samples over the range of temperatures examined. The results of this study suggest that the backscatter coefficient and spectral-based parameters can differentiate between livers elevated to different temperatures. The dependencies of the spectral-based parameters on the temperature elevation of tissues could provide a means to monitor HIFU lesion formation and temperature elevation during therapy. One advantage to using the spectral-based parameters is that they are absolute functions of the tissue state. Therefore, to obtain an estimate of the temperature, previous image frames are not needed. This means that techniques based on estimating the spectral-based parameters will minimize tissue motion artifacts.

In a related study, real time monitoring of HIFU induced heating was accomplished using spectral-based estimates of the scatterer property changes and using changes in estimates based on the envelope statistics (Hruska and Oelze 2009). In this study, fresh liver samples and tumors in live rats (MAT IIB) were imaged with a clinical system during heating with a HIFU transducer. The rise in temperature was monitored with a thermocouple. Estimates of the ESD, EAC, and two estimates from the envelope statistics were utilized. The envelope of the backscattered ultrasound was modeled using the homodyned K distribution (Hruska and Oelze 2009). From the homodyned K distribution, the k parameter and the μ parameter were estimated with each imaging frame. The k parameter is the ratio of coherent to incoherent signal energy and the μ parameter provides an estimate of the number of scatterers per resolution cell.

Fig. 9.10 (*top and clockwise*) B-mode image of rat tumor, EAC versus temperature, μ parameter versus temperature, k parameter versus temperature and ESD versus temperature

In the liver samples, the EAC was negatively correlated with the temperature elevation while the ESD was positively correlated with the temperature elevation. QUS images were constructed that mapped the changes in the QUS parameters versus time and temperature elevation. Figure 9.9 shows a B-mode image of the liver sample and the corresponding temperature profile and changes in the QUS parameters versus temperature. The different QUS parameters were observed to correlate (visually) to changes in temperature as recorded by the thermocouple.

In the case of the tumor exposed to HIFU, the EAC parameter were observed to track the changes in the temperature as monitored with the thermocouple. Figure 9.10 shows the B-mode image of the tumor and the corresponding temperature profile and QUS parameters versus temperature. The ESD and k parameters did not provide significant correlations with the elevation in temperature. These results suggest that QUS parameters have the potential to monitor the lesion formation induced by HIFU and to monitor the rise in temperature.

9.4 Conclusion

QUS techniques have demonstrated the ability to monitor and detect therapeutic response of cancer to radiation, chemotherapy, and thermal therapies. Changes in QUS parameter estimates following therapy have been correlated to changes in tissue microstructure assessed from histological images. These techniques appear to be sensitive to changes in tissue microstructure following various therapies. QUS techniques that are capable of detecting changes in tissue microstructure are

spectral based estimates (SS, SI, MBF, UIB, ESD, EAC), envelope statistics, estimates of attenuation, estimates of sound speed, elastographic imaging and techniques that examine changes in strain and stiffness of tissue following therapy.

Ultrasound imaging is a low-cost portable technique. The key advantage of this technique is that the image contrast is caused by changes in the physical properties of tissue following administration of various therapies. Therefore, the subject can be imaged before and multiple times during the treatment without the need of injecting specialized contrast agents as required for other techniques (e.g., PET, DCE-MRI). A technique capable of noninvasively monitoring the administration of therapy and rapidly assessing its effectiveness would be of great value to tailor treatments to individual patients and particularly promising in multistage interventions or combination treatments.

A penetration depth of 2–5 cm at the frequencies of 30 MHz down to 10 MHz allows the technique to be applicable to a variety of tumor types such as skin cancers, certain cancers of the breast and cancers that can be reached with endoscopic probes such as nasopharyngeal and gastro-intestinal cancers. Currently the ultrasound scanners used in clinical imaging use frequencies of 1–10 MHz and typically do not have RF capabilities to allow QUS analysis. Ongoing work in detecting cell death at lower ultrasound frequency of 5–10 MHz may extend the range of applications in the clinic and to other tumor sites seated deeper into the body. Finally, clinical ultrasound systems capable of providing raw RF signals for conducting QUS analysis have become largely available. Therefore, the potential for QUS techniques to play a role in monitoring and assessing therapy response in the future of cancer care is high.

References

Abolhassani MD, Norouzy A, Takavar A, Ghanaati H (2007) Noninvasive temperature estimation using sonographic digital images. J Ultrasound Med 26:215–222

Adams JB, Moore RG, Anderson JH, Strandberg JD, Marshall FF, Davoussi LR (1996) High-intensity focused ultrasound ablation of rabbit kidney tumors. J Endourol 10:71–75

Amini AN, Ebbini ES, Georgiou TT (2005) Noninvasive estimation of tissue temperature via high-resolution spectral analysis techniques. IEEE Trans Biomed Eng 52:221–228

Anand A, Savery D, Hall C (2007) Three-dimensional spatial and temporal temperature imaging in gel phantoms using backscattered ultrasound. IEEE Trans Ultrason Ferroelec Freq Contr 54:23–31

Arthur RM, Trobaugh JW, Straube WL, Moros EG (2005) Temperature dependence of ultrasonic backscattered energy in motion-compensated images. IEEE Trans Ultrason Ferroelect Freq Contr 52:1644–1652

Balter JM, Brock KK, Lam KL, Tatro D, Dawson LA, McShan DL, Ten Haken RK (2005) Evaluating the influence of setup uncertainties on treatment planning for focal liver tumors. Int J Radiat Oncol Biol Phys 63:610–614

Bamber JC, Hill CR (1979) Ultrasonic attenuation and propagation speed in mammalian tissues as a function of temperature. Ultrasound Med Biol 5:149–157

Bohris C, Schreiber WG, Jenne J, Simiantonakis I, Rastert R, Zabel HJ, Huber P, Bader R, Brix G (1999) Quantitative MR temperature monitoring of high-intensity focused ultrasound therapy. Magn Reson Imaging 17:603–610

Brindle K (2008) New approaches for imaging tumour responses to treatment. Nat Rev Cancer 8(2):94–107

Chaussy C, Thuroff S, Lacoste F, Gelet A (2002) HIFU and prostate cancer: the European experience. Proceedings 2nd international symposium on therapeutic ultrasound

Chung A, Hynynen K, Cline HE, Colucci V, Oshio H, Jolesz F (1996) Optimization of spoiled gradient-echo phase imaging for in vivo localization of focused ultrasound beam. Magnet Reson Med 36:745–752

Clement GT (2004) Perspectives in clinical uses of high-intensity focused ultrasound. Ultrasonics 42:1087–1093

Cline HE, Hynynen K, Watkins RD, Adams WJ, Schenck JF, Ettinger RH, Freund WR, Vetro JP, Jolesz FA (1995) Focused US system for MR imaging-guided tumor ablation. Radiology 194:731–737

Cobbold RSC (2007) Foundations of biomedical ultrasound. Oxford University Press, Inc, New York

Czarnota GJ, Kolios MC, Vaziri H, Benchimol S, Ottensmeyer FP, Sherar MD et al (1997) Ultrasonic biomicroscopy of viable, dead and apoptotic cells. Ultrasound Med Biol 23:961–965

Czarnota GJ, Kolios MC, Abraham J, Portnoy M, Ottensmeyer FP, Hunt JW et al (1999) Ultrasound imaging of apoptosis: high-resolution non-invasive monitoring of programmed cell death in vitro, in situ and in vivo. Br J Cancer 81:520–527

Daniels MJ, Varghese T, Madsen EL, Zagzebski JA (2007) Non-invasive ultrasound-based temperature imaging for monitoring radiofrequency heating-phantom results. Phys Med Biol 52:4827–4843

Daum DR, Smith NB, King R, Hynynen K (1999) In vivo demonstration of non-invasive thermal surgery of the liver using an ultrasonic phased array. Ultrasound Med Biol 25:1087–1098

Eisenhauer EA, Therasse P, Bogaerts J, Schwartz LH, Sargent D, Ford R, Dancey J, Arbuck S, Gwyther S, Mooney M et al (2009) New response evaluation criteria in solid tumours: revised RECIST guideline (version 1.1). Eur J Cancer 45:228–247

Foster RS, Bihrle R, Sanghvi NT, Fry FJ, Donohue JP (1993) High-intensity focused ultrasound in the treatment of prostatic disease. Eur Urol 23:29–33

Frizzell LA, Linke CA, Carstensen EL, Fridd CW (1977) Thresholds for focal ultrasonic lesions in rabbit kidney, liver, and testicle. IEEE Trans Biomed Eng BME 24:393–396

Fry WJ, Mosberg WH, Barnard JW, Fry FJ (1954) Production of focal destructive lesions in the central nervous system with ultrasound. J Neurosurg 11:471–478

Gelet A, Chapelon JY, Bouvier R, Souchon R, Pangaud C, Abdelrahim AF et al (1996) Treatment of prostate cancer with transrectal focused ultrasound: early clinical experience. Eur Urol 29:174–183

Gellermann J, Wlodarczyk W, Feussner A, Fahling H, Nadobny J, Hildebrandt B, Felix R, Wust P (2005) Methods and potentials of magnetic resonance imaging for monitoring radiofrequency hyperthermia in a hybrid system. Int J Hyperth 21:497–513

Ghoshal G, Luchies AC, Blue JP, Oelze ML (2011) Temperature dependent ultrasonic characterization of biological media. J Acoust Soc Am 130:2203–2211

Hazle JD, Stafford RJ, Price RE (2002) Magnetic resonance imaging-guided focused ultrasound thermal therapy in experimental animal models: correlation of ablation volumes with pathology in rabbit muscle and VX2 tumors. J Magnet Reson Imag 15:185–194

Hruska DP, Oelze ML (2009) Improved parameter estimates based on the homodyned K distribution. IEEE Tran Ultrason Ferroelect Freq Contr 56:2471–2481

Huber P, Stepanow B, Debus J, Joechle K, Mory M, Jenne J, Werner A, van Kaick G, Lorenz WJ (1994) Temperature monitoring of focused ultrasound therapy by MRI. Proceedings IEEE ultrasonics symposium, pp 1825–1828

Hynynen K, Jolesz FA (1998) Demonstration of potential non-invasive ultrasound brain therapy through an intact skull. Ultrasound Med Biol 24:275–283

Hynynen K, Freund WR, Cline HE, Chung AH, Watkins RD, Vetro JP, Jolesz FA (1996) A clinical noninvasive MRI monitored ultrasound surgery method. RadioGraphics 16:185–195

Hynynen K, McDannold N, Vykhodtseva NI, Jolesz FA (2001) Noninvasive MR image guided focal opening of the blood brain barrier. Radiology 220:640–646

Ian RPH, Tannock F, Bristow RG, Harrington L (2004) The basic science of oncology. McGraw-Hill Professional, New York

Insana MF, Wagner RF, Brown DG, Hall TJ (1990) Describing small-scale structure in random media using pulse-echo ultrasound. J Acoust Soc Am 87:179–192

Jaffe CC (2006) Measures of response: RECIST, WHO, and new alternatives. J Clin Oncol 24:3245–3251

Kemmerer JP, Oelze ML (2012) Ultrasonic assessment of thermal damage in rat liver. Ultrasound Med Biol 38: 2130-2137

Kemmerer J, Ghoshal G, Oelze ML (2010) Quantitative ultrasound assessment of HIFU induced lesions in rodent liver. Proceedings 2010 IEEE ultrasonics symposium, San Diego, pp 1404–1407

Kennedy JE, ter Haar GR, Cranston D (2003) High intensity focused ultrasound: surgery of the future? Brit J Rad 76:590–599

Kolios MC, Czarnota GJ (2009) Potential use of ultrasound for the detection of cell changes in cancer treatment. Future Oncol 5:1527–1532

Kolios MC, Czarnota GJ, Lee M, Hunt JW, Sherar MD (2002) Ultrasonic spectral parameter characterization of apoptosis. Ultrasound Med Biol 28:589–597

Kolios MC, Taggart L, Baddour RE, Foster FS, Hunt JW, Czarnota GJ et al (2003) An investigation of backscatter power spectra from cells, cell pellets and microspheres. Proceedings of 2003 IEEE ultrasonics symposium, pp 752–757

Konofagou E, Thierman J, Hynynen K (2003) The use of ultrasound-stimulated acoustic emission in the monitoring of modulus changes with temperature. Ultrasonics 41:337–345

Liu D, Ebbini ES (2010) Real-time 2-D temperature imaging using ultrasound. IEEE Trans Biomed Eng 57:12–16

Lizzi FL, Greenbaum M, Feleppa EJ, Elbaum M, Coleman DJ (1983) Theoretical framework for spectrum analysis in ultrasonic tissue characterization. J Acoust Soc Am 73:1366–1373

Lizzi FL, Coleman DJ, Driller J, Ostromogilsky M, Chang S, Greenall P (1984) Ultrasonic hyperthermia for ophthalmic therapy. IEEE Trans Son Ultrason 31:473–481

Lizzi FL, Muratore R, Deng CX, Ketterling JA, Alam SK, Mikaelian S, Kalisz A (2003) Radiation-force technique to monitor lesions during ultrasonic therapy. Ultrasound Med Biol 29:1593–1605

Maass-Moreno R, Damianou CA (1996) Noninvaisive temperature estimation in tissue via ultrasound echo-shifts. Part I. Analytical model. J Acoust Soc Am 100:2514–2521

Madersbacher S, Pedevillas M, Vingers L, Susani M, Marberger M (1995) Effect of high-intensity focused ultrasound on human prostate cancer in vivo. Cancer Res 55:3346–3351

Michaelis LC, Ratain MJ (2006) Measuring response in a post-RECIST world: from black and white to shades of grey. Nat Rev Cancer 6:409–414

Miller NR, Bamber JC, Meaney PM (2002) Fundamental limitations of noninvasive temperature imaging by means of ultrasound echo strain estimation. Ultrasound Med Biol 28:1319–1333

Oelze ML (2006) J. F. Zachary JF. Examination of cancer in mouse models using quantitative ultrasound. Ultrasound Med Biol 11:1639–1648

Pernot M, Tanter M, Bercoff J, Waters KR, Fink M (2004) Temperature estimation using ultrasonic spatial compound imaging. IEEE Trans Ultrason, Ferroelect, Freq Contr 51:606–615

Prat F, Centarti M, Sibille A, Abou el Fadil FA, Henry L, Chapelon JY et al (1995) Extracorporeal high-intensity focused ultrasound for VX2 liver tumors in the rabbit. Hepatology 21:832–836

Roberg K, Jonsson AC, Grenman R, Norberg-Spaak L (2007) Radiotherapy response in oral squamous carcinoma cell lines: evaluation of apoptotic proteins as prognostic factors. Head Neck 29:325–334

Sanghvi NT, Fry FJ, Bihrle R, Foster RS, Phillips MH, Syrus J et al (1996) Non-invasive surgery of prostate tissue by high-intensity focused ultrasound. IEEE Trans Ultrson Ferroelect Freq Contr 43:1099–1110

Seip R, Ebbini ES (1995) Noninvasive estimation of tissue temperature response to heating fields using diagnostic ultrasound. IEEE Trans Biomed Eng 42:828–839

Sibille A, Prat F, Chapelon JY, Abou el Fadil, Henry L, Theillere Y et al (1993) Characterization of extracorporeal ablation of normal and tumor-bearing liver tissue by high-intensity focused ultrasound. Ultrasound Med Biol 19:803–813

Silverman RH, Coleman DJ, Lizzi FL, Torpey JH, Driller J, Iwamoto T, Burgess SEP, Rosado A (1986) Ultrasonics tissue characterization and histopathology in tumor xenografts following ultrasonically induced hyperthermia. Ultrasound Med Biol 12:639–645

Silverman RH, Muratore R, Ketterling JA, Mamou J, Coleman DJ, Feleppa EJ (2006) Improved visualization of high-intensity focused ultrasound lesions. Ultrasound Med Biol 32:1743–1751

Simon C, VanBaren P, Ebbini ES (1998) Two-dimensional temperature estimation using diagnostic ultrasound. IEEE Trans Ultrason Ferroelect Freq Contr 45:1088–1099

Smith NB, Webb AG, Ellis DS, Wilmes LJ, O'Brien WD Jr (1995) Experimental verification of theoretical in vivo ultrasound heating using cobalt detected magnetic resonance. IEEE Trans, Ultrason, Ferroelectr Freq Contr 42:489–491

Spaepen K, Stroobants S, Dupont P, Van Steenweghen S, Thomas J, Vandenberghe P et al (2001) Prognostic value of positron emission tomography (PET) with fluorine-18 fluorodeoxyglucose ([18F]FDG) after first-line chemotherapy in non-hodgkin's lymphoma: is [18F]FDG-PET a valid alternative to conventional diagnostic methods? J Clin Oncol 19:414–419

Sun J, Hynynen K (1999) The potential of transskull ultrasound therapy and surgery using the maximum available skull surface area. J Acoust Soc Am 105:2519–2527

Symmans WF, Volm MD, Shapiro RL, Perkins AB, Kim AY, Demaria S et al (2000) Paclitaxel-induced apoptosis and mitotic arrest assessed by serial fine-needle aspiration: implications for early prediction of breast cancer response to neoadjuvant treatment. Clin Cancer Res 6:4610–4617

Tempany CMC, Stewart EA, McDannold N, Quade BJ, Jolesz FA, Hynynen K (2003) MR imaging-guided focused ultrasound surgery of uterine leiomyomas: A feasibility study. Radiology 226:897–905

ter Haar GR, Rivens IH, Chen L, Riddler S (1991) High-intensity focused ultrasound for the treatment of rat tumours. Phys Med Biol 36:1495–1501

Trobaugh JW, Artur RM, Straube WL, Moros EG (2008) A simulation model for ultrasonic temperature imaging using change in backscattered energy. Ultrasound Med Biol 34:289–298

Tunis AS, Baddour RE, Czarnota GJ, Giles A, Worthington AE, Sherar MD et al (2005) Using high frequency ultrasound envelope statistics to determine scatterer number density in dilute cell solutions. Proceedings of 2005 IEEE ultrasonic symposium, pp 878–881

Uchida T, Yokoyama E, Iwamura M, Koshiba K, Terai A, Terachi T et al (1995) High-intensity focused ultrasound for benign prostatic hyperplasia. Int J Urol 2:181–185

Varghese T, Zagzebski JA, Chen Q, Techavipoo U, Frank G, Johnson C, Wright A, Jr Lee FT (2002a) FT. Ultrasound monitoring of temperature change during radiofrequency ablation: Preliminary in vivo results. Ultrasound Med Biol 28:321–329

Varghese T, Zagzebski JA, Lee FT Jr (2002b) Elastographic imaging of thermal lesions in the liver in vivo following radiofrequency ablation: preliminary results. Ultrasound Med Biol 28:1467–1473

Vlad RM, Czarnota GJ, Giles A, Sherar MD, Hunt JW, Kolios MC (2005) High-frequency ultrasound for monitoring changes in liver tissue during preservation. Phys Med Biol 50:197–213

Vlad RM, Alajez NM, Giles A, Kolios MC, Czarnota GJ (2008) Quantitative ultrasound characterization of cancer radiotherapy effects in vitro. Int J Radiat Oncol Biol Phys 72:1236–1243

Vlad RM, Brand S, Giles A, Kolios MC, Czarnota GJ (2009) Quantitative ultrasound characterization of responses to radiotherapy in cancer mouse models. Clin Cancer Res 15:2067–2075

Vlad RM, Kolios MC, Moseley JL, Czarnota GJ, Brock KK (2010) Evaluating the extent of cell death in 3D high frequency ultrasound by registration with whole-mount tumor histopathology. Med Phys 37:4288–4297

Vlad RM, Kolios MC, Czarnota GJ (2011) Ultrasound imaging of apoptosis: spectroscopic detection of DNA-damage effects at high and low frequencies. Methods Mol Biol 682:165–187

Weber WA, Ott K, Becker K, Dittler HJ, Helmberger H, Avril NE et al (2001) Prediction of response to preoperative chemotherapy in adenocarcinomas of the esophagogastric junction by metabolic imaging. J Clin Oncol 19:3058–3065

Weber WA, Petersen V, Schmidt B, Tyndale-Hines L, Link T, Peschel C et al (2003) Positron emission tomography in non-small-cell lung cancer: prediction of response to chemotherapy by quantitative assessment of glucose use. J Clin Oncol 21:2651–2657

Weidensteiner C, Quesson B, Caire-Gana B, Kerioui N, Rullier A, Trillaud H, Moonen CTW (2003) Real-time MR temperature mapping of rabbit liver in vivo during thermal ablation. Magnet Reson Med 50:322–330

Yang R, Reilly CR, Rescorla FJ, Faught PR, Sanghvi NT, Fry FJ et al (1991) High-intensity focused ultrasound in the treatment of experimental liver tumors. Arch Surg 126:1002–1010

Yeh E, Slanetz P, Kopans DB et al (2005) Prospective comparison of mammography, sonography, and MRI in patients undergoing neoadjuvant chemotherapy for palpable breast cancer. Am J Roentgenol 184:868–877

Part II
Envelope Statistics

Chapter 10
Review of Envelope Statistics Models for Quantitative Ultrasound Imaging and Tissue Characterization

François Destrempes and Guy Cloutier

Abstract The homodyned K-distribution and the K-distribution, viewed as a special case, as well as the Rayleigh and the Rice distributions, viewed as limiting cases, are discussed in the context of quantitative ultrasound (QUS) imaging. The Nakagami distribution is presented as an approximation of the homodyned K-distribution. The main assumptions made are: (1) the absence of log-compression or application of non-linear filtering on the echo envelope of the radiofrequency signal; (2) the randomness and independence of the diffuse scatterers. We explain why other available models are less amenable to a physical interpretation of their parameters. We also present the main methods for the estimation of the statistical parameters of these distributions. We explain why we advocate the methods based on the *X*-statistics for the Rice and the Nakagami distributions, and the K-distribution. The limitations of the proposed models are presented. Several new results are included in the discussion sections, with proofs in the appendix.

Keywords Quantitative ultrasound (QUS) · Ultrasound tissue characterization · Ultrasound imaging · Echo envelope · Homodyned K-distribution · K-distribution · Rice distribution · Rayleigh distribution · Nakagami distribution · Parameters estimation · Moments · Log-moments

F. Destrempes · G. Cloutier (✉)
Laboratory of Biorheology and Medical Ultrasonics, University of Montreal Hospital Research Center (CRCHUM), Montréal, Québec H2L-2W5, Canada
e-mail: guy.cloutier@umontreal.ca

F. Destrempes
e-mail: francois.destrempes@crchum.qc.ca

G. Cloutier
The Department of Radiology, Radio-Oncology and Nuclear Medicine, University of Montreal, Montréal, Québec H3T-1J4, Canada

G. Cloutier
The Institute of Biomedical Engineering, University of Montreal, Montréal, Québec H3T-1J4, Canada

J. Mamou and M. L. Oelze (eds.), *Quantitative Ultrasound in Soft Tissues*, DOI: 10.1007/978-94-007-6952-6_10,

10.1 Introduction

The statistical distributions presented here appeared in the context of various applications in the past 130 years or so. The Rayleigh distribution was introduced in Rayleigh (1880) in the context of sound propagation. The Rice distribution appeared in Nakagami (1940), and in Rice (1945) as a model of wave propagation. The K-distribution was first introduced in Lord (1954) in the context of random walks and then in the context of sea echo (Jakeman and Pusey 1976). The homodyned K-distribution was introduced and studied in Jakeman (1980) and Jakeman and Tough (1987) as a model of weak scattering. The Nakagami distribution was defined in Nakagami (1943) in the field of wave propagation.

In ultrasound imaging, the Rayleigh distribution appeared as a model of the gray level (also called amplitude) in an unfiltered B-mode image, viewed as the envelope of the radiofrequency (RF) image, in the case of a high density of random scatterers with no coherent signal component (Burckhardt 1978; Wagner et al. 1983). The Rice distribution corresponds to a high density of random scatterers (the diffuse signal component), but combined with the presence of a coherent signal component (Insana et al. 1986). Non-Rayleigh distributions were considered in ultrasound imaging as early as the pioneer article of Burckhardt (1978). The K-distribution corresponds to a variable (effective) density α of random scatterers, with no coherent signal component and was introduced in ultrasound imaging by Shankar et al. (1993), and Molthen et al. (1993), Narayanan et al. (1994), Shankar (1995) and Molthen et al. (1995). The homodyned K-distribution corresponds to the general case of a variable effective density of random scatterers with or without a coherent signal component (Dutt and Greenleaf 1994). A simpler model consists in modeling the gray level of the speckle pattern in a B-mode image by a Nakagami distribution (Shankar 2000; Dumane and Shankar 2001). In the context of QUS, the estimated parameters of the statistical distribution of the echo envelope play the role of quantitative measures that give information about the underlying tissues of interest.

The Nakagami distribution has been the most frequently adopted model in the context of tissue characterization, probably due to its simplicity. As the pioneer work, let us mention Shankar et al. (2001) in the context of breast tumor classification. The Nakagami model was then systematically used in various medical ultrasound imaging fields, including: ophthalmology (Tsui et al. 2007); vascular flow applications (Huang et al. 2007; Huang and Wang 2007; Tsui et al. 2008a, 2009a, 2009b); and breast cancer (Tsui et al. 2008b, 2010a, 2010b, 2010c). The K-distribution was used in the context of breast cancer classification in the pioneer work of Shankar et al. (1993). More recently, the homodyned K-distribution was used for cardiac tissue characterization (Hao et al. 2002) and cancerous lesion classification (Oelze and O'Brien 2007; Hruska et al. 2009; Mamou et al. 2010, 2011), and a model of mixtures of Rayleigh distributions was adopted for liver fibrosis quantification (Yamaguchi et al. 2011).

Whereas at the time of Shankar et al. (1993) and Dutt and Greenleaf (1994), the estimation of the (homodyned) K-distribution was a problem, since then, several estimation methods have been published. In particular, the K-distribution can be estimated using the simple and reliable X-statistics (Blacknell and Tough 2001) (defined as the log-moment $E[I \log I]/E[I] - E[\log I]$, where I denotes the square of the echo envelope amplitude) and a method by Hruska and Oelze (2009) was proposed for the estimation of the homodyned K-distribution. Thus, the use of the Nakagami model does not seem justified anymore in the context of QUS, since it reduces the information carried by the homodyned K-distribution model.

10.2 Chapter Content

The remaining part of this chapter is organized as follows. Section 10.3 presents in details the various models mentioned in the introduction, as well as other available models. A physical underlying model is also presented to help with the interpretation of the various parameters. In Sect. 10.4, the most frequently used estimation methods for the main distributions are presented. Finally, Sect. 10.5 presents the limitations of the main models and hints to future work on that matter.

In Sect. 10.4.1, various estimation methods are explained: (1) the Maximum Likelihood Estimator (MLE) and the Maximum A Posteriori (MAP); (2) moments based methods; and (3) log-moments based methods. Then, in Sects. 10.4.2–10.4.6, we kept the same structure in the presentation of the estimation methods for each of the five distributions presented in Sects. 10.3.1 and 10.3.3 whenever possible (according to the literature).

In Sects. 10.3 and 10.4, various remarks and additional results are mentioned in the subsections entitled "discussion". As far as we know, most of these results are new (Theorems 8-12, 18-23, 25-26, Corollary 2, Lemmas 4 and 5), except probably Lemmas 1-3, although we did not find references. Theorem 28 was used explicitly in Destrempes et al. (2009, Table 1), but without proof. The proofs of the new results are postponed to the appendix. The purpose of these new results is to deepen the understanding of the published methods mentioned in this chapter.

Table 10.1 Main distributions discussed in this chapter and the relations among them

Distribution	Notation	Relation
Gamma	$\mathcal{G}(w\|\alpha, 1)$	
Rice	$P_{\mathrm{Ri}}(A\|\varepsilon, \sigma^2)$	
Rayleigh	$P_{\mathrm{Ra}}(A\|\sigma^2)$	$= P_{\mathrm{Ri}}(A\|0, \sigma^2)$
Homodyned K	$P_{\mathrm{HK}}(A\|\varepsilon, \sigma^2, \alpha)$	$= \int_0^\infty P_{\mathrm{Ri}}(A\|\varepsilon, \sigma^2 w)\mathcal{G}(w\|\alpha, 1)\, dw$
K	$P_{\mathrm{K}}(A\|\sigma^2, \alpha)$	$= \int_0^\infty P_{\mathrm{Ra}}(A\|\sigma^2 w)\mathcal{G}(w\|\alpha, 1)\, dw$
		$= P_{\mathrm{HK}}(A\|0, \sigma^2, \alpha)$
Rice	$P_{\mathrm{Ri}}(A\|\varepsilon, \sigma^2)$	$= \lim_{\alpha\to\infty} P_{\mathrm{HK}}(A\|\varepsilon, \sigma^2/\alpha, \alpha)$
Rayleigh	$P_{\mathrm{Ra}}(A\|\sigma^2)$	$= \lim_{\alpha\to\infty} P_{\mathrm{K}}(A\|\sigma^2/\alpha, \alpha)$
Nakagami	$\mathrm{N}(A\|m, \Omega)$	Approximation of the homodyned K-distribution

10.3 Statistical Models

We first present in Sect. 10.3.1 various models for the first-order statistics of the amplitude of the echo envelope. The most general of these models is the homodyned K-distribution that depends on three parameters $\varepsilon \geq 0$, $\sigma^2 > 0$ and $\alpha > 0$. The Rice distribution with parameter $\sigma^2 = \overline{a^2}/2$ is viewed as the limiting case of the homodyned K-distribution with parameter σ^2 of the form $\overline{a^2}/(2\alpha)$ when $\alpha \to \infty$. The K-distribution is a special case of the homodyned K-distribution with $\varepsilon = 0$, whereas the Rayleigh distribution is a special case of the Rice distribution with the same constraint. The parameter α is related to the homogeneity of the diffuse scattering medium and the density of the scatterers. It is called the *scatterer clustering parameter* (Dutt and Greenleaf 1994). In the context of the K-distribution, it is also called the *effective number of scatterers* (Narayanan et al. 1994). The parameter ε is called the *coherent component* and is related to the strength of the specular reflection or the periodic organization of the scatterers. The diffuse signal power can be viewed as $2\sigma^2\alpha$ for the homodyned K-distribution (and K-distribution), whereas ε^2 can be viewed as the coherent signal power. In Sect. 10.3.2, an underlying physical model is presented. In Sect. 10.3.3, the Nakagami distribution is described as an approximation of the homodyned K-distribution. Finally, in Sect. 10.3.4, the relevance of these distributions compared to other available models is discussed (see Destrempes and Cloutier (2010) for further reading on that topic). The reader may refer to Table 10.1 for a summarize of the main distributions discussed here and the relations among them.

10.3.1 The Homodyned K-Distribution and Related Distributions

10.3.1.1 The Rayleigh Distribution

The (2-dimensional) Rayleigh distribution (Rayleigh 1880) is defined by

$$P_{\mathrm{Ra}}(A \mid \sigma^2) = \frac{A}{\sigma^2} \exp\left(-\frac{A^2}{2\sigma^2}\right), \tag{10.1}$$

where A represents the amplitude of the signal. In Jakeman and Tough (1987), the distribution is expressed, in the context of n-dimensional random walks, in terms of the variable $\overline{a^2} = n\sigma^2$. The case $n = 2$ corresponds to Eq. (10.1). Equivalently, the intensity I, i.e. the square of the amplitude A, is distributed according to an exponential distribution.

10.3.1.2 The Rice Distribution

The (2-dimensional) Rice distribution is expressed as

$$P_{\mathrm{Ri}}(A \mid \varepsilon, \sigma^2) = \frac{A}{\sigma^2} I_0\left(\frac{\varepsilon}{\sigma^2} A\right) \exp\left(-\frac{(\varepsilon^2 + A^2)}{2\sigma^2}\right), \tag{10.2}$$

where $\sigma > 0$ and $\varepsilon \geq 0$ are real numbers and I_0 denotes the modified Bessel function of the first kind of order 0 (the intensity I should not be confused with the Bessel function I_0). See Jakeman and Tough (1987, Eq. 2.16) for a generalization in dimension $n \geq 2$. The special case where $\varepsilon \to 0$ yields the Rayleigh distribution. The case $n = 2$ corresponds to Nakagami (1940) and Rice (1945). In Nakagami (1960, p. 4, Eq. 5), the Rice distribution is called the "n-distribution" (Nakagami, 1940).

10.3.1.3 The K-Distribution

The (2-dimensional) K-distribution (Lord 1954; Jakeman and Pusey 1976) is defined by

$$P_{\mathrm{K}}(A \mid \sigma^2, \alpha) = \frac{4A^{\alpha}}{(2\sigma^2)^{(\alpha+1)/2}\Gamma(\alpha)} K_{\alpha-1}\left(\sqrt{\frac{2}{\sigma^2}} A\right), \tag{10.3}$$

where $\alpha > 0$, $\sigma^2 > 0$, Γ is the Euler gamma function, and K_p denotes the modified Bessel function of the second kind of order p. In Jakeman and Tough (1987, Eq. 2.11), the distribution is expressed in terms of the parameters α and $b = \sqrt{\frac{2}{\sigma^2}}$. In view of the compound representation presented below, we find the proposed parametrization more convenient.

Theorem 1 (Jakeman and Tough 1987). *The compound representation of the K-distribution is*

$$P_{\mathrm{K}}(A \mid \sigma^2, \alpha) = \int_0^{\infty} P_{\mathrm{Ra}}(A \mid \sigma^2 w) \mathcal{G}(w \mid \alpha, 1)\, dw, \tag{10.4}$$

where P_{Ra} denotes the Rayleigh distribution, and $\mathcal{G}(w \mid \alpha, 1)$ is the gamma distribution $w^{\alpha-1} \exp(-w)/\Gamma(\alpha)$ of mean and variance equal to α.

The compound representation is useful to simulate the K-distribution, and in the evaluation of its value. A K-distribution with parameters $\sigma^2 = \overline{a^2}/(2\alpha)$ and α yields the Rayleigh distribution with parameter "σ^2" $= \overline{a^2}/2$, as $\alpha \to \infty$. See Jakeman and Tough (1987, Eq. 2.12). Thus, the parameter "σ^2" of the limiting Rayleigh distribution is $\overline{a^2}/2$, and should not be confused with the parameter σ^2 of the K-distribution. The relation between these two quantities is "σ^2" $= \overline{a^2}/2 = \sigma^2\alpha$.

10.3.1.4 The Homodyned K-Distribution

The (2-dimensional) homodyned K-distribution (Jakeman 1980; Jakeman and Tough 1987) is defined by

$$P_{\mathrm{HK}}(A \mid \varepsilon, \sigma^2, \alpha) = A \int_0^\infty u J_0(u\varepsilon) J_0(uA) \Big(1 + \frac{u^2 \sigma^2}{2}\Big)^{-\alpha} du \tag{10.5}$$

where $\sigma^2 > 0$, $\alpha > 0$, $\varepsilon \geq 0$, and J_0 denotes the Bessel function of the first kind of order 0. In Jakeman and Tough (1987, Eq. 4.13), the homodyned K-distribution is expressed in terms of the parameters α, $\overline{a^2} = n\sigma^2\alpha$, and $a_0 = \varepsilon$, in the context of n-dimensional random walks.

Theorem 2 (Jakeman and Tough 1987). *The compound representation of the homodyned K-distribution is*

$$P_{\mathrm{HK}}(A \mid \varepsilon, \sigma^2, \alpha) = \int_0^\infty P_{\mathrm{Ri}}(A \mid \varepsilon, \sigma^2 w) \mathcal{G}(w \mid \alpha, 1) d\, w, \tag{10.6}$$

where P_{Ri} denotes the Rice distribution and $\mathcal{G}(w \mid \alpha, 1)$ is the gamma distribution with mean and variance equal to α.

The case $\varepsilon \to 0$ yields the K-distribution (with parameters σ^2, α). In particular, the compound representation of the homodyned K-distribution is consistent with Eq. (10.4), upon taking $\varepsilon \to 0$. A homodyned K-distribution with parameters ε, $\sigma^2 = \overline{a^2}/(2\alpha)$ and α yields the Rice distribution with parameters ε and "σ^2" $= \overline{a^2}/2$, as $\alpha \to \infty$. Thus, if in addition, $\varepsilon \to 0$, then one obtains the Rayleigh distribution with parameter "σ^2" $= \overline{a^2}/2$, as $\alpha \to \infty$. Figure 10.1 illustrates four representative examples of the homodyned K-distribution (including two examples of the K-distribution, as a special case).

Two functions of the three parameters of the homodyned K-distribution are invariant under scaling of the intensity (Dutt and Greenleaf 1994): (1) the parameter α; (2) the structure parameter $\kappa = \varepsilon^2/(2\sigma^2\alpha)$, i.e. the ratio of the coherent signal power ε^2 with the diffuse signal power $\overline{a^2} = 2\sigma^2\alpha$. Other parameters of the homodyned K-distribution were considered in the literature: the coherent to diffuse signal ratio $k = \sqrt{2\kappa} = \varepsilon/(\sigma\sqrt{\alpha})$ (Dutt and Greenleaf 1994; Dutt 1995; Hruska and Oelze 2009), and the parameter β equal to $1/\alpha$ (Dutt and Greenleaf 1994; Dutt 1995).

Considering $\sigma^2 = \overline{a^2}/(2\alpha)$ and letting α tend to infinity, one obtains a Rice distribution for which the diffuse signal power is also $\overline{a^2}$ and the structure parameter κ is also equal to $\varepsilon^2/\overline{a^2}$.

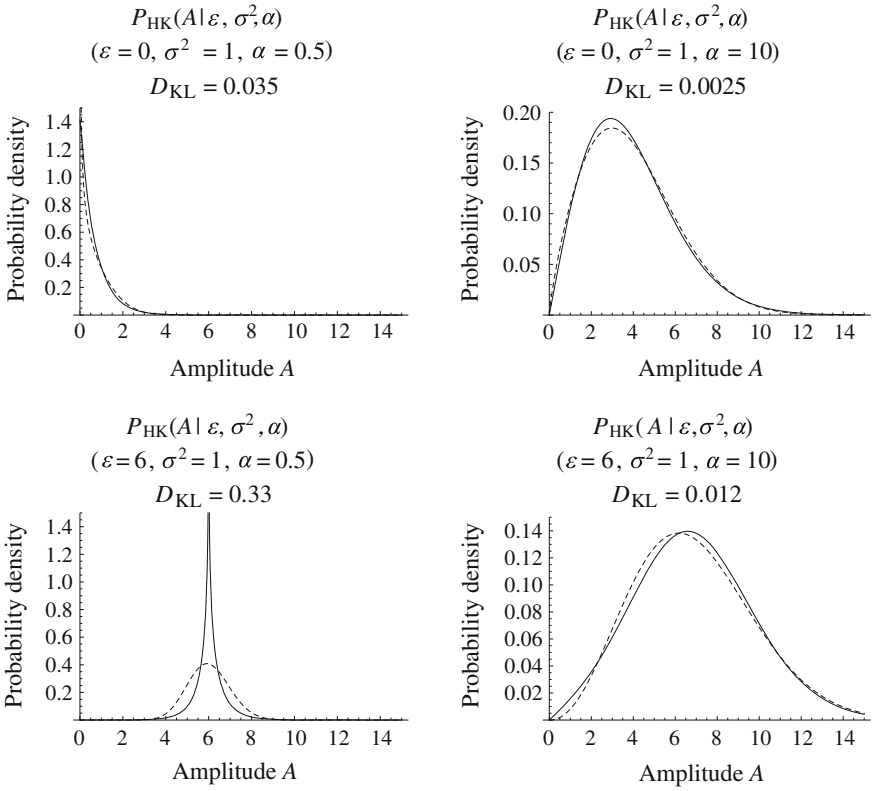

Fig. 10.1 Typical examples of the homodyned K-distribution. *Top row* K-distribution ($\varepsilon = 0$). *Bottom row* $\varepsilon > 0$. The *dashed curves* represent the approximating Nakagami distributions. The Kullback-Leibler distance values between the two distributions were: *top left* 0.035; *top right* 0.0025; *bottom left* 0.33 (with a coherent to diffuse signal ratio $k = \varepsilon/(\sigma\sqrt{\alpha})$ equal to 8.5); *bottom right* 0.012 (with $k \approx 1.9$)

10.3.2 Interpretation of the Distributions in the Context of Ultrasound Imaging

In Shankar et al. (1993), Molthen et al. (1993), Narayanan et al. (1994), Shankar (1995) and Molthen et al. (1995), one considers N_s scatterers lying in an ambient scattering medium within the resolution cell. Each scatterer corresponds to a phasor $a_j e^{i\phi_j}$ with two elements: (1) an amplitude a_j depending on the scattering properties (i.e., the scattering cross section) and the position of the scatterer with respect to the ultrasound beam, the instrumentation and the attenuation; (2) a phase ϕ_j that depends on the scatterer's position. One then postulates (Narayanan et al. 1994) a K-distribution with parameters σ^2 and α_s for each amplitude and considers uniformly distributed independent phases for each scatterer. The choice of the

K-distribution was motivated in Narayanan et al. (1994) by its good modeling properties of the first-order statistics of the echo envelope in the case where the Rayleigh distribution model (corresponding to infinitely many scatterers of identical cross-sections) breaks down, as explained in the next paragraph. Assuming weak scattering, the resulting complex signal is expressed as

$$\mathbf{A} = \sum_{j=1}^{N_s} a_j e^{i\phi_j}. \tag{10.7}$$

Then, its amplitude A is viewed as the norm of the complex signal.

Note that Eq. (10.7) can be viewed as a random walk in the Euclidean plane (corresponding to $n = 2$), since the complex number $e^{i\phi_j}$ corresponds to the vector $(\cos(\phi_j), \sin(\phi_j))$. Thus, the amplitude $A = \mathbf{A}$ corresponding to Eq. (10.7) follows a K-distribution with parameter $\alpha = \alpha_s N_s$. In that context, α is called the *effective number of scatterers*, because the number of scatterers N_s is multiplied by the parameter α_s. For instance, if N_s is large, but α_s is so small that $\alpha_s N_s \ll 10$, then the resulting distribution is a K-distribution rather than a Rayleigh distribution. For the same reason, even if N_s is small, but α_s is so large that $\alpha_s N_s \geq 10$, then one obtains a Rayleigh distribution. The parameter α_s is a parameter describing the lack of uniformity of the scattering cross sections in the range cell (c.f. Narayanan et al. 1994, Eq. (6)). A small value of α_s corresponds to a great variability, whereas a large value of α_s corresponds to a small variability. Thus, the parameter α_s is viewed as a measure of homogeneity of the scattering medium. The choice of the K-distribution is also consistent with the observation that the higher order moments of the intensity of the echo envelope may be larger than the ones predicted by the Rayleigh distribution model in the case of pathological tissues (Shankar et al. 1993). For instance, under the Rayleigh model, one would have $E[I^2]/E[I]^2 = 2$, whereas the K-distribution model yields $E[I^2]/E[I]^2 = 2(1 + 1/\alpha)$, which corresponds to observed values upon taking α sufficiently small. So, the statistics of the echo envelope depart from the Rayleigh model if the number of scatterers is small and α_s is not too large, or if the cross-sections are heterogeneous and N_s is not too large.

Adding a coherent component $\boldsymbol{\varepsilon}$, with constant amplitude ε and either a constant phase or a uniformly distributed phase, then yields a homodyned K-distribution with parameters ε, σ^2 and $\alpha = \alpha_s N_s$, for the amplitude $A = \|\boldsymbol{\varepsilon} + \mathbf{A}\|$. Since a coherent component may arise when the scatterers are organized periodically, the parameter α does not quite represent the effective number of scatterers in that context, but it may still be viewed as a scatterer clustering parameter. The coherent component may also be caused by specular reflection.

10.3.3 The Nakagami Distribution as an Approximation

The Nakagami distribution (Nakagami 1943, 1960) is defined by

$$\mathrm{N}\ (A \mid m, \Omega) = \frac{2m^m}{\Gamma(m)\Omega^m} A^{2m-1} e^{-mA^2/\Omega}, \tag{10.8}$$

where Γ is the Euler gamma function. The real numbers $m > 0$ and $\Omega > 0$ are called the shape parameter and the scaling parameter, respectively. Equivalently, the intensity $I = A^2$ follows a gamma distribution, with shape parameter m and scale parameter Ω/m.

The shape parameter m can be interpreted as the square of the intensity signal-to-noise ratio (SNR), i.e. $m = \frac{E[I]^2}{Var(I)}$ and Ω represents the mean intensity $E[I]$ (i.e., the total signal power). The intensity SNR should not be confused with the amplitude SNR. For instance, when $m = 1$, one retrieves the Rayleigh distribution. This observation can be found in Nakagami (1960, p. 17, Eqs. 50 and 51). In that case, the intensity SNR is equal to 1, whereas the amplitude SNR is about 1.91.

The Nakagami distribution can be viewed as an approximation of the homodyned K-distribution. First of all, we have the limiting case where $\alpha \to \infty$, which yields the Rice distribution and corresponds to the case $m \geq 1$.

Theorem 3 (Destrempes and Cloutier 2010). *Let* $m = \frac{(\varepsilon^2+2\sigma^2)^2}{4\sigma^2(\varepsilon^2+\sigma^2)}$ *and* $\Omega = \varepsilon^2 + 2\sigma^2$. *Then,*

$$\mathcal{D}_{KL}\Big(P_{\mathrm{Ri}}(\varepsilon, \sigma^2),\ \mathrm{N}\ (m, \Omega)\Big) \leq 0.02, \tag{10.9}$$

where $\mathcal{D}_{KL}$ *denotes the Kullback-Leibler distance* (Kullback and Leibler 1951) *between two distributions.*

Recall that the Kullback-Leibler distance (also called Kullback-Leibler divergence because it is non-symmetric) is a measure of the difference between two probability distribution functions (PDF) $f(x)$ and $g(x)$ in the continuous random variable x and is defined by $\int f(x) \log \frac{f(x)}{g(x)}\, dx$. It has the properties: (1) $\mathcal{D}_{\mathrm{KL}}(f, g) \geq 0$ for any PDFs f and g; and (2) $\mathcal{D}_{\mathrm{KL}}(f, g) = 0$ if and only if $f \equiv g$. However, it is a non-symmetric measure (i.e., $\mathcal{D}_{\mathrm{KL}}(f, g)$ is not necessarily equal to $\mathcal{D}_{\mathrm{KL}}(g,f)$). The choice of m and Ω in Theorem 3 is consistent with the identities $SNR^2 = \frac{(\varepsilon^2+2\sigma^2)^2}{4\sigma^2(\varepsilon^2+\sigma^2)}$ and $E[I] = \varepsilon^2 + 2\sigma^2$ valid for the Rice distribution. See also Nakagami (1960, p. 18, Eq. (55)).

We also have the following approximation result in the case of the K-distribution ($\varepsilon \to 0$), which corresponds to the case $m < 1$.

Theorem 4 (Destrempes and Cloutier 2010). *Let* $m = \frac{\alpha}{(\alpha+1)}$ *and* $\Omega = 2\sigma^2\alpha$. *Then,*

$$\mathcal{D}_{\mathrm{KL}}\Big(P_{\mathrm{K}}(\sigma^2,\alpha),\ \mathrm{N}\ (m,\Omega)\Big)\leq 0.0325. \tag{10.10}$$

For Theorem 4, the choice of m and Ω is consistent with the identities $E[I\log I]/E[I]-E[\log I]=1/m$ and $E[I\log I]/E[I]-E[\log I]=1+1/\alpha$ valid for the Nakagami distribution and the K-distribution, respectively (see Sects. 10.4.4.5 and 10.4.6.3).

10.3.4 Discussion

In this section, a new result on the Nakagami distribution as an approximation of the homodyned K-distribution is introduced (in greater generality than Theorems 3 and 4). We then discuss the consistency of the distributions presented in Sect. 10.3.1 in the limit case of a vanishing diffuse signal power, and we explain why other models available in the literature fail to have this feature (Destrempes and Cloutier 2010). Finally, as a new result, that property is shown to hold for the Nakagami distribution.

Considering the general case of a homodyned K-distribution with parameters ε, σ^2, and α, the $M^{(1)}$-statistics $E[A]/\sqrt{E[I]}$ is expressed explicitly in Theorem 24 as a function $M^{(1)}_{\mathrm{HK}}(\gamma,\alpha)$, where $\gamma=\kappa\alpha$. Using the identity $M^{(1)}_{\mathrm{Na}}(m)=\frac{\Gamma(1/2+m)}{\sqrt{m}\Gamma(m)}$ of Theorem 30, one then solves the equation $M^{(1)}_{\mathrm{Na}}(m)=M^{(1)}_{\mathrm{HK}}(\gamma,\alpha)$ in the variable m, using a binary search algorithm based on Theorem 31. This yields a function $m=m(\gamma,\alpha)$. Moreover, considering $E[I]$, one is led to the identity $\Omega=\varepsilon^2+2\sigma^2\alpha=\mu$ (the average value of the intensity). So, one is interested in the Kullback-Leibler distance

$$\mathcal{D}_{\mathrm{KL}}\Big(P_{\mathrm{HK}}(\varepsilon=\sqrt{\frac{\mu\gamma}{(\gamma+\alpha)}},\sigma^2=\frac{\mu}{2(\gamma+\alpha)},\alpha),\ \mathrm{N}\ (m=m(\gamma,\alpha),\Omega=\mu)\Big), \tag{10.11}$$

as a function of γ, α, and μ. It can be seen that this function is independent of the scaling factor μ (this is actually a general property of the Kullback-Leibler distance).

We computed Eq. (10.11) for $k=\varepsilon/(\sigma\sqrt{\alpha})=0.0,0.1,\ldots,2.0$, $\alpha=1,2,\ldots,20$, taking $\sigma^2=1/\alpha$. For each value of k and α, a sample set of size $N=1{,}000$ was simulated according to the corresponding homodyned K-distribution. The Kullback-Leibler distance was then estimated as the average over the simulated set of $\log\Big(P_{\mathrm{HK}}(A_i\,|\,\varepsilon=k,\sigma^2=1/\alpha,\alpha)/\ \mathrm{N}\ (A_i\,|\,m=m(\gamma,\alpha),\Omega=k^2+2)\Big)$. The maximal value was 0.072 (this result could be slightly improved upon considering the X-statistics instead of the $M^{(1)}$-statistics). So, the Nakagami pdf is a satisfying approximation in that range of the parameters k and α. See Fig. 10.1 for examples of

approximating Nakagami distributions. In that figure, we included an example of a value of k much larger than 2; in that case, the KL distance is quite large (0.33).

Theorem 2 states that the homodyned K-distribution corresponds to a model in which the diffuse signal power $2\sigma^2$ of a Rice distribution is modulated by a gamma distribution, but not its coherent signal component ε. As mentioned in Destrempes and Cloutier (2010), there are several more models for the first-order statistics of the echo envelope. One modeling possibility introduced in Barakat (1986) and further developed in Jakeman and Tough (1987) is equivalent to modulate both the coherent signal component ε and the diffuse signal power $2\sigma^2$ of the Rice distribution by a gamma distribution. This gives rise to the generalized K-distribution. Note that this distribution has not been used in ultrasound imaging as of now. However, in Eltoft (2005), the Rician inverse Gaussian distribution (RiIG) is introduced, and it corresponds to a model in which both the coherent signal component ε and the diffuse signal power $2\sigma^2$ of a Rice distribution are modulated by an inverse Gaussian (IG) distribution, instead of a gamma distribution. Thus, this model is related to the generalized K-distribution, as further discussed in Destrempes and Cloutier (2010).

Three other distributions were introduced in the context of ultrasound imaging. The first one is called the generalized Nakagami distribution (Shankar 2000), and is obtained from the Nakagami distribution by a change of variable of the form $y = A^{1/s}$, where s is a shape adjustment parameter and A is the amplitude of the signal. This distribution was also proposed in Raju and Srinivasan (2002) (in the equivalent form of a generalized gamma distribution). The second other distribution is called the Nakagami-gamma distribution (Shankar 2003). That distribution can be viewed as a model in which the Rice distribution is approximated by a Nakagami distribution, and in which its total signal power Ω is modulated by a gamma distribution. The third distribution is called the Nakagami-generalized inverse Gaussian (NGIG) distribution (Agrawal and Karmeshu 2006), and it corresponds to a model in which the (approximating) Nakagami distribution has its total signal power Ω modulated by a generalized inverse Gaussian (GIG) distribution instead of a gamma distribution.

As shown in Destrempes and Cloutier (2010), none of these five other models is compatible with the limit case of a vanishing diffuse signal power $2\sigma^2\alpha_s$. Indeed, in that case, one should obtain an infinite intensity SNR (if $\varepsilon > 0$). It turns out that only the homodyned K-distribution and its related distributions satisfy that property. In fact, keeping α_s (the scattering cross sections homogeneity) and N_s (the number of random scatterers within the resolution cell) constant (see 10.3.2), one must have $\sigma^2 \to 0$ if the diffuse signal power $2\sigma^2\alpha_s N_s$ vanishes. Then, as computed in Destrempes and Cloutier (2010), one obtains an infinite intensity SNR if $\varepsilon > 0$, either for the Rice distribution or the homodyned K-distribution. Moreover, it was shown in Destrempes and Cloutier (2010) that the total signal power depends only on the coherent component in that case, which is a desirable property. Since the other distributions do not have these two properties, it makes the interpretation of

their parameters more delicate, even if goodness-of-fit tests with data might be satisfying.

Finally, let us show that the Nakagami distribution also has these two properties. For that purpose, we consider a homodyned K-distribution with parameters ε, σ^2, and α, and its approximating Nakagami distribution with parameters $m = m(\varepsilon^2/(2\sigma^2), \alpha)$ and $\Omega = \varepsilon^2 + 2\sigma^2\alpha$ as at the beginning of this section. If $\varepsilon > 0$ and α are fixed and $\sigma^2 \to 0$, then, the parameter $\gamma = \varepsilon^2/(2\sigma^2) \to \infty$. From Theorem 26, part b), one has $\lim_{\gamma\to\infty} M^{(1)}_{\mathrm{HK}}(\gamma, \alpha) = 1$ (α being fixed). Thus, from Theorem 31, part b), one concludes that $m(\gamma, \alpha) \to \infty$. Therefore, one obtains $SNR = \sqrt{m(\gamma, \alpha)} \to \infty$. Moreover, if $\sigma^2 \to 0$, then $\Omega = \varepsilon^2 + 2\sigma^2\alpha \to \varepsilon^2$, which is independent of the diffuse signal parameters σ^2 and α. Therefore, the Nakagami, just as the Rice distribution and the homodyned K-distribution, is compatible with the limit case of a vanishing diffuse signal.

10.4 Parameter Estimation Methods

We discuss various known methods for the estimation of the parameters of the distributions presented in 10.3 based on an independent and identically distributed (i.i.d.) sample set $(A_1, \ldots, A_N)$ of positive real numbers (representing the amplitude).

10.4.1 Overview of a Few Estimation Methods

10.4.1.1 The MLE and the MAP

The MLE is defined as a critical point of the log-likelihood function (Edgeworth 1908, 1909; Fisher 1912, 1922, 1925) (the reader may also consult Pratt (1976))

$$L(\theta) = \sum_{i=1}^{N} \log P(A_i \mid \theta), \tag{10.12}$$

where θ represents the vector of parameters of the distribution and $\{A_1, \ldots, A_N\}$ is the sample data of size N. Actually, there might be multiple critical points and no global maximum (on the entire parameter domain). However, if the true value of the parameters is in the interior of a compact subset of the parameter domain, then the global maximum of the log-likelihood on that compact set converges to the true value of the parameters as the size of the sample tends to infinity (Redner 1981). Thus, one can define the MLE as the critical point with largest log-likelihood value (Redner and Walker 1984). A major difficulty lies in the analysis of the critical points: how many are there and which one coincides with the MLE? In fact, if the sample size is not sufficiently large, there might be no critical point of

the log-likelihood function. Thus, one needs to address this issue before applying any numerical method to find the MLE.

One may also wish to impose a prior $\pi(\theta)$ on the parameters of the distribution. In that case, one considers the critical points of the constrained log-likelihood function

$$L(\theta) + \log \pi(\theta), \tag{10.13}$$

where $\log \pi(\theta)$ is viewed as a regularizing term. The MAP can then be defined as the critical point with largest value of the constrained log-likelihood function.

10.4.1.2 Moments Based Methods

Moments' methods have the advantage, over the MLE, of providing simpler and faster algorithms. On the other hand, the resulting systems of equations do not always admit a solution.

The simplest of these methods is based on the first few moments of the intensity. The number of moments considered is then equal to the number of parameters in the estimated distribution: one for the Rayleigh distribution, two for the Rice distribution, the K-distribution or the Nakagami distribution, and three for the homodyned K-distribution. Thus, one solves the system of equations

$$E[I^v] = \overline{I^v}, \quad v = 1, \ldots, r \tag{10.14}$$

where r is the number of parameters of the distribution. In Eq. (10.14), the left-hand side $E[I^v]$ represents a function of the parameters of the distribution, whereas the right-hand side $\overline{I^v}$ is the empirical moment computed from the data.

A slightly more complex method is based on the first few moments of the amplitude. Thus, one solves the system of equations

$$E[A^v] = \overline{A^v}, \quad v = 1, \ldots, r. \tag{10.15}$$

Since the intensity is the square of the amplitude, such methods use lower orders of the intensity, and thus, are likely to be less sensitive to noise. On the other hand, the analytical expressions of those moments are typically more complex than integral order moments of the intensity.

One may also use arbitrary fractional order moments of the intensity. For later reference, we find convenient to introduce the $M^{(v)}$-statistics, defined as

$$M^{(v)} = \frac{\overline{A^v}}{(\overline{I})^{v/2}}, \tag{10.16}$$

where $v > 0$. This statistic is the fractional moment of order v of the amplitude normalized so that it becomes invariant under multiplication of the signal by a positive scaling constant.

Lemma 1 *For any non-constant random variable,* $0<M^{(v)}<1$, *if* $0<v<2$, *whereas* $M^{(v)}>1$, *if* $v>2$.

Proof If $v<2$, the function $I^{v/2}$ is convex. Therefore, by Jensen's inequality (Jensen 1906), we have $E[A^v]=E[I^{v/2}]<(E[I])^{v/2}$ since the random variable I is non-constant. If $v>2$, the function $I^{v/2}$ is concave and we obtain the reversed inequality. ■

If the number of parameters r is at least 2, the method based on the first few moments of the intensity is equivalent to solving the system

$$E[I]=\overline{I};\qquad \frac{E[A^v]}{(E[I])^{v/2}}=\frac{\overline{A^v}}{(\overline{I})^{v/2}},\quad v=4,6 \tag{10.17}$$

and thus amounts to working with the $M^{(4)}$ and $M^{(6)}$ statistics. Similarly, the method based on the first few moments of the amplitude is equivalent to solving the system

$$E[I]=\overline{I};\qquad \frac{E[A^v]}{(E[I])^{v/2}}=\frac{\overline{A^v}}{(\overline{I})^{v/2}},\quad v=1,3 \tag{10.18}$$

and thus amounts to working with the $M^{(1)}$ and $M^{(3)}$ statistics.

One may also combine various moments in the form of the SNR of a fractional order of the amplitude

$$R^{(v)}=\frac{\overline{A^v}}{(\overline{A^{2v}}-(\overline{A^v})^2)^{1/2}}, \tag{10.19}$$

or the skewness

$$S^{(v)}=\frac{\overline{A^{3v}}-3\overline{A^v}\,\overline{A^{2v}}+2(\overline{A^v})^3}{(\overline{A^{2v}}-(\overline{A^v})^2)^{3/2}}, \tag{10.20}$$

or the kurtosis

$$K^{(v)}=\frac{\overline{A^{4v}}-4\overline{A^v}\,\overline{A^{3v}}+6\overline{A^{2v}}\,(\overline{A^v})^2-3(\overline{A^v})^4}{(\overline{A^{2v}}-(\overline{A^v})^2)^2}. \tag{10.21}$$

Note that these three statistics can be expressed in terms of the family of $M^{(v)}$-statistics. For instance, we have $R^{(v)}=\frac{M^{(v)}}{(M^{(2v)}-(M^{(v)})^2)^{1/2}}$.

Considering more equations than the number of parameters of the distribution yields an overdetermined system of (non-linear) equations that may be solved in the sense of the least mean square (LMS). Thus, overall, all these methods amount to considering various combinations of the $M^{(v)}$-statistics.

10.4.1.3 Log-Moments Based Methods

One may also work with moments of functions of the intensity that involve its logarithm. Ideally, one would consider powers of the logarithm of the intensity. But powers greater than 1 appear to be intractable for the distributions considered in this chapter, because the resulting integrals are not known explicitly as far as we can tell. Moreover, one may want to obtain functions that are invariant under a change of the intensity by a scaling factor. Thus, one is led to the so-called U-statistics (Oliver 1993)

$$U = \overline{\log I} - \log \overline{I}, \tag{10.22}$$

and the X-statistics (Blacknell and Tough 2001)

$$X = \overline{I \log I}/\overline{I} - \overline{\log I}. \tag{10.23}$$

Lemma 2 *For any non-constant random variable,* $U < 0$.

Proof The function $\log I$ is convex. Therefore, from Jensen's inequality, we obtain $E[\log I] < \log E[I]$, since the random variable I is non-constant. ■

Lemma 3 *For any non-constant random variable,* $X > 0$.

Proof The function $I \log I$ is concave. Thus, $E[I \log I] > E[I] \log E[I]$. From Lemma 2, we conclude that $E[I \log I] > E[I]E[\log I]$. ■

10.4.2 Parameter Estimation Method for the Rayleigh Distribution

Since a Rayleigh distribution with parameter σ^2 on the amplitude A is equivalent to an exponential distribution with parameter $2\sigma^2$ on the intensity $I = A^2$, the MLE of the parameter σ^2 is equal to $\overline{I}/2$. Note that, in this special case, the MLE coincides with the estimator based on the first moment of the intensity.

10.4.3 Parameter Estimation Methods for the Rice Distribution

10.4.3.1 The MLE for the Rice Distribution

In Talukdar and Lawing (1991), the Rice distribution is estimated in the sense of the MLE, as follows.

Theorem 5 (Talukdar and Lawing 1991). *Let $A_1, \ldots, A_N$ be a finite sample set of positive numbers. Let $\varepsilon \geq 0$ and $\sigma^2 > 0$ be the parameters of the Rice distribution. Let $\mu = \varepsilon^2 + 2\sigma^2$, and $\kappa = \varepsilon^2/(2\sigma^2)$. Let $y_i = A_i/\sqrt{\overline{I}}$, where $\overline{I} = 1/N \sum_{i=1}^N A_i^2$. Then, the critical points of the log-likelihood function $L_{Ri}(\varepsilon, \sigma^2)$ of the Rice distribution are the points of the form*

$$\varepsilon = \sqrt{\mu\kappa/(\kappa+1)}; \quad \sigma^2 = \mu/(2(\kappa+1)), \tag{10.24}$$

where $\mu = \overline{I}$ *and* $\kappa \geq 0$ *is any root of the function $f(\kappa)$ defined by*

$$\frac{1}{(1+\kappa)} + \frac{(1+2\kappa)}{N\sqrt{\kappa(1+\kappa)}} \sum_{i=1}^{N} y_i \frac{I_1(2y_i\sqrt{\kappa(1+\kappa)})}{I_0(2y_i\sqrt{\kappa(1+\kappa)})} - 2. \tag{10.25}$$

Here, I_p denotes the modified Bessel function of the first kind of order p (the subscript avoids the confusion with the intensity I).

Theorem 5 gives useful information on the value of μ for the critical points of the log-likelihood function. It also introduces a one-variable function $f(\kappa)$. But the main drawback is the lack of information on the roots of f. Fortunately, a more recent result gives complete information about the critical points of the log-likelihood function of the Rice distribution in the following form.

Theorem 6 (Carrobi and Cati 2008). *Let $A_1, \ldots, A_N$ be a finite sample set of positive numbers. Let $\varepsilon \geq 0$ and $\sigma^2 > 0$ be the parameters of the Rice distribution. Let $\overline{I} = 1/N \sum_{i=1}^N A_i^2$. Assume that the elements A_i are not all identical. Then, the log-likelihood function $L_{\mathrm{Ri}}(\varepsilon, \sigma^2)$ of the Rice distribution has exactly two critical points: $(0, \overline{I}/2)$ and another one, denoted $(\hat{\varepsilon}, \hat{\sigma}^2)$, that satisfies $\hat{\varepsilon} > 0$ and $\hat{\sigma}^2 > 0$. Moreover, the MLE is the second one. In fact, the MLE is actually an absolute maximum of the log-likelihood function on its domain.*

Thus, the MLE $(\hat{\varepsilon}, \hat{\sigma}^2)$ consists of the unique critical point of the log-likelihood function $L_{\mathrm{Ri}}(\varepsilon, \sigma^2)$ for which both coordinates are positive.

10.4.3.2 Expression of Fractional Order Moments of the Amplitude

The $M^{(v)}$-statistics is explicitly known for the Rice distribution.

Theorem 7 (Rice 1954). *Assume that $A = \sqrt{I}$ is distributed according to the Rice distribution, with parameters $\varepsilon \geq 0$ and $\sigma^2 > 0$. Set $\kappa = \varepsilon^2/(2\sigma^2)$. Then, the $M^{(v)}$-statistics $E[A^v]/E[I]^{v/2}$ is equal to*

$$M_{\mathrm{Ri}}^{(v)}(\kappa) = \frac{\Gamma(v/2+1)}{(\kappa+1)^{v/2}} {}_1F_1(-v/2, 1, -\kappa), \tag{10.26}$$

where ${}_pF_q(a_1, ..., a_p; b_1, ..., b_q; z)$ *is the generalized hypergeometric series (here* $p = q = 1$*).*

10.4.3.3 Method Based on the Moments of the Amplitude

In Talukdar and Lawing (1991), an estimation method of the Rice distribution based on the first two moments of the amplitude is proposed as an alternative to the MLE. The method consists of solving the system of equations

$$E[A] = \overline{A}; \qquad E[A^2] = \overline{A^2}. \tag{10.27}$$

For that purpose, it is proposed to consider the equivalent system $E[I] = \overline{I}$ and $\frac{E[A]}{E[I]^{1/2}} = M^{(1)}$. The point of using this equivalent system is that the $M^{(1)}$-statistics for the Rice distribution depends only on the parameter κ. As a special case of Theorem 7, we have the $M^{(1)}$-statistics.

Corollary 1 Talukdar and Lawing (1991). *Assume that* $A = \sqrt{I}$ *is distributed according to the Rice distribution, with parameters* $\varepsilon \geq 0$ *and* $\sigma^2 > 0$*. Set* $\kappa = \varepsilon^2/(2\sigma^2)$*. Then, the* $M^{(1)}$*-statistics* $E[A]/E[I]^{1/2}$ *is equal to*

$$M_{\mathrm{Ri}}^{(1)}(\kappa) = \frac{\Gamma(3/2)}{\sqrt{\kappa + 1}} e^{-\kappa/2} \Big((1 + \kappa) I_0(\kappa/2) + \kappa I_1(\kappa/2) \Big), \tag{10.28}$$

where I_p *denotes the modified Bessel function of the first kind of order* p*.*

10.4.3.4 Discussion

In this section, we present a new result on the computation of the MLE of the Rice distribution. We show that the Talukdar-Lawing estimator of Sect. 10.4.3.3 can be computed with a binary search algorithm. We introduce two log-moments based methods for the Rice distribution. Finally, we compare these estimators on simulated data.

Concerning the MLE computation, a little more work allows to combine Theorems 5 and 6 into the following result. See Fig. 10.2 for an illustration of the function $f(\kappa)$.

Theorem 8 *Notation as in Theorem 5. Assume that the data elements* A_i *are not all identical. Then, the function* $f(\kappa)$ *of Eq. 10.25 has exactly two non-negative roots:* 0 *and a unique positive root, denoted* κ_**. The MLE is expressed as in Eq. (10.24), with* $\kappa = \kappa_*$ *(i.e. the unique positive root of the function* f*). Moreover,* $f(\kappa) > 0$ *on the interval* $(0, \kappa_*)$*, and* $f(\kappa) < 0$ *on the interval* (κ_*, ∞)*.*

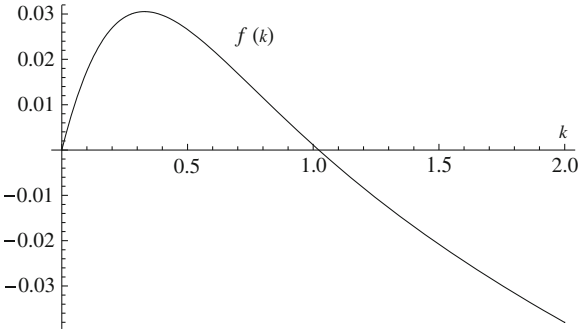

Fig. 10.2 Typical behavior of the function $f(\kappa)$ defined in Eq. (10.25), assuming that the data elements are not all identical. The function f has two non-negative roots (0 and $\kappa_* > 0$); $f(\kappa) > 0$ for $0 < \kappa < \kappa_*$, and $f(\kappa) < 0$ for $\kappa > \kappa_*$ (here, $N = 2$, $y_1 = 0.5$, $y_2 = \sqrt{2 - (0.5)^2}$, so that $\frac{1}{2}(y_1^2 + y_2^2) = 1$)

Theorem 8 implies that an efficient binary search algorithm can be used for the computation of the MLE of the Rice distribution.

Concerning the estimation method based on the $M^{(\nu)}$-statistics, in general, there is no closed form for a solution to the equation. $M_{\mathrm{Ri}}^{(\nu)}(\kappa) = M$, but one can use the following result, relevant for any $\nu \neq 2$. See Fig. 10.3, right column, for an illustration of the function $M_{\mathrm{Ri}}^{(\nu)}(\kappa)$.

Theorem 9 *Let* $\nu > 0$. *Then,*

(a) $\lim_{\kappa \to 0} M_{\mathrm{Ri}}^{(\nu)}(\kappa) = \Gamma(\nu/2 + 1)$;

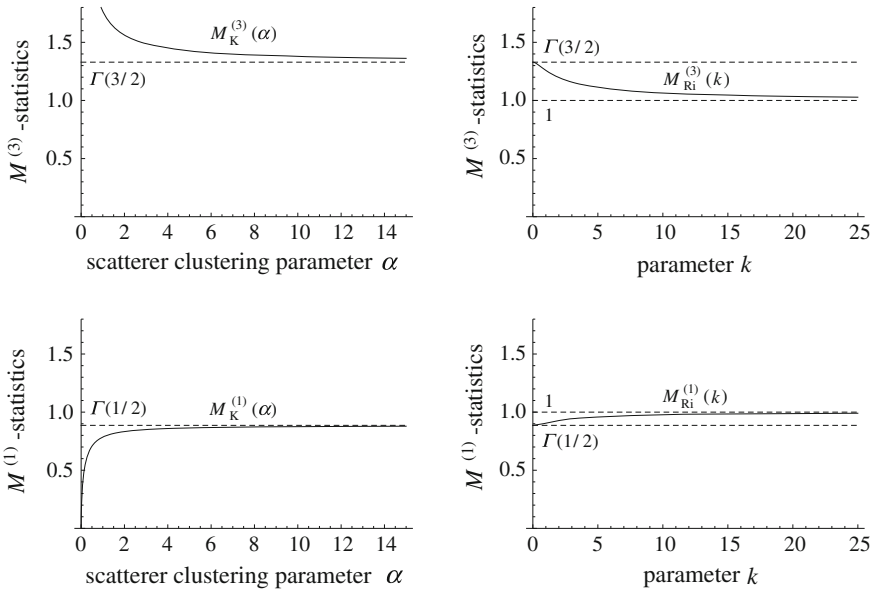

Fig. 10.3 Typical behavior of the $M^{(\nu)}$-statistics for the K-distribution (*left column*) and the Rice distribution (*right column*), when $\nu < 2$ (*bottom row*) and $\nu > 2$ (*top row*)

(b) $\lim_{\kappa\to\infty} M_{\mathrm{Ri}}^{(v)}(\kappa) = 1$;

(c) *if* $v<2$, *the function* $M_{\mathrm{Ri}}^{(v)}(\kappa)$ *is an increasing function; if* $v > 2$, *the function* $M_{\mathrm{Ri}}^{(v)}(\kappa)$ *is a decreasing function.*

Thus, let $M > 0$ be a real number (playing the role of the $M^{(v)}$-statistics). If $v<2$ and $\Gamma(v/2+1) \le M < 1$, then an efficient binary search algorithm yields the unique solution to the equation $M_{\mathrm{Ri}}^{(v)}(\kappa) = M$. Indeed, from Theorem 9, the function $M_{\mathrm{Ri}}^{(v)}(\kappa)$ is increasing in that case and its range is the interval $[\Gamma(v/2+1), 1)$. On the other hand, if $v<2$ and $M<\Gamma(v/2+1)$, then there is no solution to the equation $M_{\mathrm{Ri}}^{(v)}(\kappa) = M$. Nevertheless, in that case, the value $\kappa = 0$ minimizes the distance between $M_{\mathrm{Ri}}^{(v)}(\kappa)$ and M. Thus, it makes sense to take $\kappa = 0$. Similarly, if $v > 2$ and $1 < M \le \Gamma(v/2+1)$, then there is a unique solution to the equation $M_{\mathrm{Ri}}^{(v)}(\kappa) = M$, and this solution can be found efficiently with a binary search algorithm. On the other hand, if $v > 2$ and $M > \Gamma(v/2+1)$, one may take $\kappa = 0$. Thus, it makes sense to switch to the Rayleigh model (corresponding to $\kappa = 0$), whenever the equation $M_{\mathrm{Ri}}^{(v)}(\kappa) = M$ has no solution. This argument applies to the special case where $v = 1$, which corresponds to the Talukdar-Lawing method of Corollary 1. For later reference, we introduce here what we call the Rice conditions

$$v<2 \text{ and } \Gamma(v/2+1) \le M < 1, \text{ or } v > 2 \text{ and } 1 < M \le \Gamma(v/2+1). \quad (10.29)$$

Thus, as explained above, the equation $M_{\mathrm{Ri}}^{(v)}(\kappa) = M$ has a solution if and only if the Rice conditions are satisfied. Note that the U and X-statistics can be computed analytically for the Rice distribution.

Theorem 10 *Assume that* $A = \sqrt{I}$ *is distributed according to the Rice distribution, with parameters* $\varepsilon \ge 0$ *and* $\sigma^2 > 0$. *Set* $\kappa = \varepsilon^2/(2\sigma^2)$. *Then,*

(a) *the U-statistics* $E[\log I] - \log E[I]$ *is equal to*

$$U_{\mathrm{Ri}}(\kappa) = \Gamma(0,\kappa) + \log\frac{\kappa}{\kappa+1}, \quad (10.30)$$

where $\Gamma(0,x)$ *is the incomplete gamma function* $\int_x^\infty \frac{e^{-t}}{t}\,dt$;

(b) *the X-statistics* $E[I\log I]/E[I] - E[\log I]$ *is equal to*

$$X_{\mathrm{Ri}}(\kappa) = \frac{1}{\kappa+1}(2 - e^{-\kappa}). \quad (10.31)$$

Theorem 11 below shows that a binary search algorithm can be used to solve the equation $U_{\mathrm{Ri}} = U$ if and only if $U \ge -\gamma_E$, where γ_E is the Euler's constant. If ever $U < -\gamma_E$, one may switch to the Rayleigh model ($\kappa = 0$). Similarly, Theorem 12 shows that the equation $X_{\mathrm{Ri}} = X$ has a solution (which is then unique

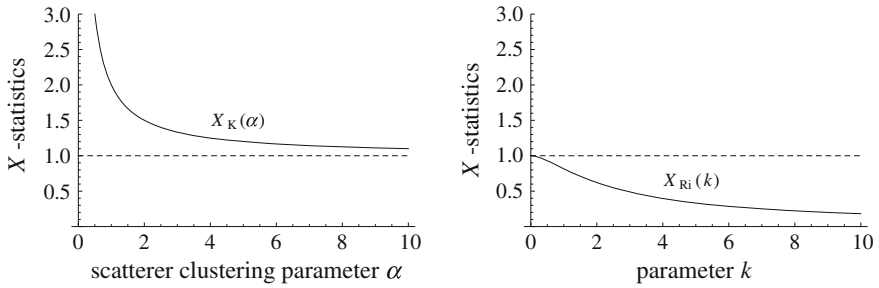

Fig. 10.4 Typical behavior of the X-statistics for the K-distribution (*left column*) and the Rice distribution (*right column*)

and can be found with a binary search algorithm) if and only if $X < 4$. If ever $X \geq 4$, one may switch to the Rayleigh model.

Theorem 11

(a) $\lim_{\kappa \to 0} U_{\mathrm{Ri}}(\kappa) = -\gamma_E$, *where* γ_E *is the Euler's constant;*
(b) $\lim_{\kappa \to \infty} U_{\mathrm{Ri}}(\kappa) = 0$;
(c) *the function* $U_{\mathrm{Ri}}(\kappa)$ *is an increasing function.*

Theorem 12

(a) $\lim_{\kappa \to 0} X_{\mathrm{Ri}}(\kappa) = 1$;
(b) $\lim_{\kappa \to \infty} X_{\mathrm{Ri}}(\kappa) = 0$;
(c) *the function* $X_{\mathrm{Ri}}(\kappa)$ *is a decreasing function.*

See Fig. 10.4, right column, for an illustration of the X-statistics for the Rice distribution.

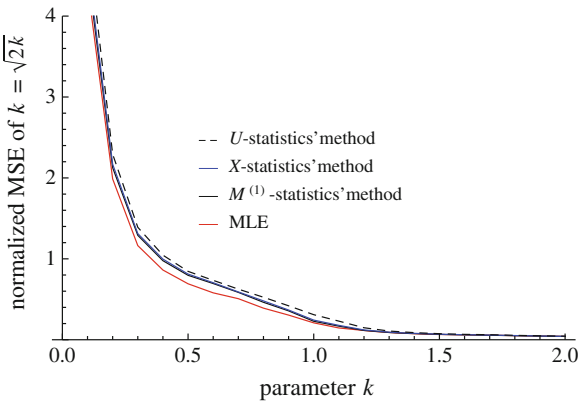

Fig. 10.5 Comparison of the normalized MSE $\sqrt{E[(\hat{k}-k)^2]}/k$, where $k = \varepsilon/\sigma$, for the estimators based on the MLE (*red solid line*), the $M^{(1)}$-statistics (*black solid line*), the X-statistics (*blue solid line*) and the U-statistics (*dashed line*) in the case of the Rice distribution. The sample size is $N = 1,000$

In order to compare these four estimators, we considered the parameter $k = \sqrt{2\kappa} = \varepsilon/\sigma$ with values in the set $\{0.1, 0.2, \ldots, 2.0\}$. For each value of k, 1,000 datasets of $N = 1,000$ elements each were simulated according to the corresponding Rice distribution. Thus, we could estimate the normalized mean squared error (MSE) of the estimator $\hat{k}$ as $\sqrt{E[(\hat{k}-k)^2]}/k$. The resulting normalized MSE curves are presented in Fig. 10.5. As one can see, the MLE is slightly better than the estimators based on the $M^{(1)}$ or the X-statistics. The method based on the U-statistics is slightly worse than the other estimators. The two estimators based on the $M^{(1)}$ and the X-statistics are practically equivalent.

10.4.4 Parameter Estimation Methods for the K-Distribution

10.4.4.1 The MLE for the K-Distribution

The partial derivatives of the log-likelihood function of the K-distribution with respect to α and σ^2 are equal to

$$\frac{\partial}{\partial\alpha}L_{\mathrm{K}}(\sigma^2,\alpha) = -N\psi(\alpha) + \sum_{i=1}^{N}\log\left(\frac{1}{\sqrt{2\sigma^2}}A_i\right) + \frac{\frac{\partial}{\partial\alpha}K_{\alpha-1}\left(\sqrt{\frac{2}{\sigma^2}}A_i\right)}{K_{\alpha-1}\left(\sqrt{\frac{2}{\sigma^2}}A_i\right)}; \tag{10.32}$$

$$\frac{\partial}{\partial\sigma^2}L_{\mathrm{K}}(\sigma^2,\alpha) = -\frac{N\alpha}{\sigma^2} + \sum_{i=1}^{N}\frac{1}{\sigma^2}\left(\frac{1}{\sqrt{2\sigma^2}}A_i\right)\frac{K_{\alpha}\left(\sqrt{\frac{2}{\sigma^2}}A_i\right)}{K_{\alpha-1}\left(\sqrt{\frac{2}{\sigma^2}}A_i\right)}. \tag{10.33}$$

Solutions to this system of two non-linear equations are found numerically in Joughin et al. (1993). In Roberts and Furui (2000), an Expectation-Maximization (EM) algorithm is proposed for finding the MLE. In that context, the variable w of Eq. (10.4) is viewed as the latent variable. A variant of the EM algorithm is used in Chung et al. (2005) in place of the standard EM algorithm.

However, none of the methods (Joughin et al. 1993; Roberts and Furui 2000; Chung et al. 2005) can be used in full generality, because the MLE is not always well-defined for the K-distribution. See Sect. 10.4.4.6 for a discussion on that issue.

10.4.4.2 Expression of Fractional Order Moments of the Amplitude

The $M^{(v)}$-statistics is explicitly known for the K-distribution.

Theorem 13 (Dutt and Greenleaf 1995). *Assume that* $A = \sqrt{I}$ *is distributed according to the K-distribution, with parameters* $\sigma^2 > 0$ and $\alpha > 0$. *Then, the* $M^{(v)}$*-statistics* $E[A^v]/E[I]^{v/2}$ *is equal to*

$$M_{\mathrm{K}}^{(v)}(\alpha) = \Gamma(v/2+1)\frac{\Gamma(v/2+\alpha)}{\alpha^{v/2}\Gamma(\alpha)}. \tag{10.34}$$

10.4.4.3 A Method Based on the Moments of the Intensity

The simplest moments method consists in solving the system of equations

$$E[I] = \overline{I}; \qquad E[I^2] = \overline{I^2}. \tag{10.35}$$

Equivalently, that method is based on the mean intensity and the $M^{(4)}$-statistics (that statistics is called the V-statistics in Blacknell and Tough (2001)). One computes for the K-distribution $V_{\mathrm{K}}(\alpha) = E[I^2]/E[I]^2 = 2\left(1+\frac{1}{\alpha}\right)$. Thus, there is a solution to the system (10.35) if and only if $V > 2$, in which case the solution is equal to $\alpha = 2/(V-2)$.

10.4.4.4 Two Methods Based on Fractional Order Moments of the Amplitude

In Dutt and Greenleaf (1995), the authors suggest to use the SNR based on fractional order moments in the form of the $R^{(v)}$-statistics, where $v > 0$. In that study, it is shown that a value of $v = 1/4$ yields a reliable estimator. We have the following result (note that there is a typographical error in Dutt and Greenleaf (1995, Eq. (6), p. 253)).

Theorem 14 (Dutt and Greenleaf 1995). *Assume that* A *is distributed according to the K-distribution, with parameters* $\sigma^2 > 0$ and $\alpha > 0$. *Then, the* $R^{(v)}$*-statistics* $\frac{E[A^v]}{\sqrt{E[A^{2v}]-E[A^v]^2}}$ *is expressed as*

$$R_{\mathrm{K}}^{(v)}(\alpha) = \frac{\Gamma(v/2+1)\Gamma(v/2+\alpha)}{\sqrt{\Gamma(v+1)\Gamma(v+\alpha)\Gamma(\alpha) - \Gamma^2(v/2+1)\Gamma^2(v/2+\alpha)}}. \tag{10.36}$$

In Iskander and Zoubir (1999), the authors suggest the use of fractional order moments in the form of the Y-statistics $\frac{E[A^{2r+2s}]}{E[A^{2r}]E[A^{2s}]}$, where $s > 0$, and $r \in \mathbb{N}$. It is

shown that a value of $s<2$ yields lower variance of the resulting estimator, taking $r=1$. The following result holds.

Theorem 15 (Iskander and Zoubir 1999). *Assume that A is distributed according to the K-distribution, with parameters* $\sigma^2>0$ *and* $\alpha>0$. *Then, the Y-statistics* $\frac{E[A^{2+2s}]}{E[A^2]E[A^{2s}]}$ *is expressed as*

$$Y_{\mathrm{K}}(\alpha)=(1+s)(1+\frac{s}{\alpha}). \tag{10.37}$$

Using Theorem 15, there is a solution to the equation $Y_{\mathrm{K}}(\alpha)=Y$ if and only if $Y>1+s$. In that case, $\alpha=\frac{s(1+s)}{Y-(1+s)}$ is the unique solution. Note that the V-statistics corresponds to the special case where $s=1$.

10.4.4.5 Two Log-Moments Methods

In the case of the K-distribution, it has been proposed (Oliver 1993) to use the U-statistics in order to estimate α.

Theorem 16 (Oliver 1993). *Assume that* $\sqrt{I}$ *is distributed according to the K-distribution, with parameters* $\sigma^2>0$ and $\alpha>0$. *Then, the U-statistics* $E[\log I]-\log E[I]$ *is expressed as*

$$U_{\mathrm{K}}(\alpha)=-\gamma_E+\psi(\alpha)-\log\alpha, \tag{10.38}$$

where γ_E *is the Euler's constant and* $\psi(z)=d[\log\Gamma(z)]/dz$ *is the digamma function* (Abramowitz and Stegun 1972, (6.3.1)).

There is also a method (Blacknell and Tough 2001) based on the X-statistics.

Theorem 17 (Blacknell and Tough 2001). *Assume that* $\sqrt{I}$ *is distributed according to the K-distribution, with parameters* $\sigma^2>0$ and $\alpha>0$. *Then, the X-statistics* $E[I\log I]/E[I]-E[\log I]$ *is expressed as*

$$X_{\mathrm{K}}(\alpha)=1+\frac{1}{\alpha}. \tag{10.39}$$

Lemma 3 guarantees that X is non-negative. Thus, there is a solution to the equation $X_{\mathrm{K}}(\alpha)=X$ if and only if $X>1$, in which case the unique solution is equal to $\alpha=1/(X-1)$. See Fig. 10.4, left column, for an illustration of the X-statistics for the K-distribution.

10.4.4.6 Discussion

In this section, we present further results on the MLE and the MAP of the K-distribution. We then show that the methods introduced in Sects. 10.4.4.3 to 10.4.4.5 can be solved with a binary search algorithm. Finally, we present a comparison of these estimators on simulated data.

Arguing that the existing methods for computing the MLE are time consuming and that moments based methods do not always lead to a solution of the resulting equations, a Bayesian estimation method of the SNR (denoted D and called the detection index) was proposed in Abraham and Lyons (2010).

To clarify the notion of MLE for the K-distribution, we present the following two results.

Theorem 18 *Let $\alpha > 0$ be fixed. Then, there exists a root $\sigma^2(\alpha, \tilde{A}) > 0$ of $\frac{\partial}{\partial \sigma^2} L_K(\sigma^2, \alpha)$.*

Theorem 19 *Let $N \geq 1$ be the sample size and $\sigma^2(\alpha, \tilde{A})$ denote any root of $\frac{\partial}{\partial \sigma^2} L_K(\sigma^2, \alpha)$. Then,*

(a) $\lim_{\alpha \to 0} \alpha \frac{\partial}{\partial \alpha} L_K(\sigma^2(\alpha, \tilde{A}), \alpha) \geq N$.
(b) $\lim_{\alpha \to \infty} \alpha \frac{\partial}{\partial \alpha} L_K(\sigma^2(\alpha, \tilde{A}), \alpha) = 0$.

Thus, if ever the function $\frac{\partial}{\partial \alpha} L_K(\sigma^2(\alpha, \tilde{A}), \alpha)$ is decreasing for some sample set, then there is no MLE. This is the case, for instance, if $\{A_1, A_2\} = \{\frac{1}{2}, \frac{\sqrt{7}}{2}\}$ (see Fig. 10.6). So, the point in considering other estimators than the MLE is not so much that its computation is time consuming, but rather that it is not always well-defined for the K-distribution.

However, one may set a prior on the parameters σ^2 and α and see if the maximum a posteriori (MAP) is well-defined. For the K-distribution, let us consider the prior $\pi(\alpha) = 1/\alpha$ (so, this prior does not depend on σ^2 for simplicity of technical considerations). This amounts to setting the Jeffreys non-informative prior (Jeffreys 1946) on the parameter α. Recall that the Jeffreys prior is defined as

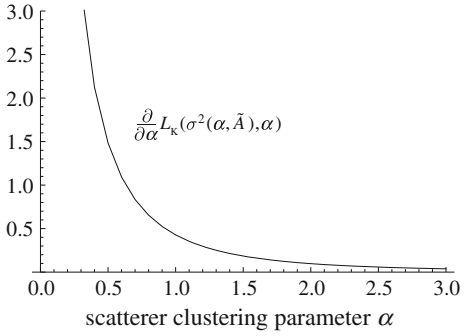

Fig. 10.6 Behavior of the function $\frac{\partial}{\partial \alpha} L_K(\sigma^2(\alpha, \tilde{A}), \alpha)$ for the K-distribution in the case where $\tilde{A} = \{\frac{1}{2}, \frac{\sqrt{7}}{2}\}$. The MLE is not defined in this case

$\pi(\alpha) = \big(I_F(\alpha)\big)^{1/2}$, where $I_F(\alpha)$ denotes the Fisher information (Fisher 1956), namely $I_F(\alpha) = -E[\frac{\partial^2}{\partial^2 \alpha} \log P(A \mid \sigma^2, \alpha)] = E[\big(\frac{\partial}{\partial \alpha} \log P(A \mid \sigma^2, \alpha)\big)^2]$. In Abraham and Lyons (2010), it is shown that $\pi(\alpha) \sim 1/\alpha$ for large values of α. Then, the MAP corresponds to a solution to the system of equations

$$\frac{\partial}{\partial \alpha} L_{\mathrm{K}}(\sigma^2, \alpha) + \frac{\partial}{\partial \alpha} \log \pi(\alpha) = 0; \tag{10.40}$$

$$\frac{\partial}{\partial \sigma^2} L_{\mathrm{K}}(\sigma^2, \alpha) = 0. \tag{10.41}$$

Now, with the proposed prior, we obtain $\frac{\partial}{\partial \alpha} \log \pi(\alpha) = -1/\alpha$. Then, from Theorem 19, we know that $\frac{\partial}{\partial \sigma^2} L_{\mathrm{K}}(\sigma^2(\alpha, \tilde{A}), \alpha) - 1/\alpha \geq (N-1)/\alpha > 0$, for α sufficiently small and $N > 1$, and that $\frac{\partial}{\partial \alpha} L_{\mathrm{K}}(\sigma^2(\alpha, \tilde{A}), \alpha) - 1/\alpha < 0$ for α sufficiently large. Therefore, the Intermediate Value Theorem implies that there is $\alpha > 0$ for which $\frac{\partial}{\partial \alpha} L_{\mathrm{K}}(\sigma^2(\alpha, \tilde{A}), \alpha) - 1/\alpha = 0$. Thus, this MAP estimator is well-defined for the K-distribution. Furthermore, its computation is amenable to a binary search algorithm. Note that one may have chosen the prior $\pi(\sigma^2, \alpha) = \frac{1}{\sigma}$ because it is *scale-invariant* (i.e., $P_K(A \mid \sigma^2, \alpha) = \frac{1}{\sigma} P_K(\frac{A}{\sigma} \mid 1, \alpha)$). However, with that choice of prior, one may have an undefined MAP estimator. Other priors are possible, but we have not explored that avenue here.

Note that in Abraham and Lyons (2010), it is advocated to take the non-informative prior $1/\alpha^2$ instead of the Jeffreys prior $1/\alpha$, in order to obtain a posterior distribution with a well-defined mean, i.e. such that $\int_0^\infty \alpha P(\alpha \mid \tilde{A})\, d\alpha < \infty$. But, there is no need to require a finite posterior mean to define the MAP. The only requirement is a finite sum for the posterior distribution (i.e., $\int_0^\infty P(\alpha \mid \tilde{A})\, d\alpha < \infty$. Now, taking the prior $1/\alpha^2$ (Abraham and Lyons 2010), the first statement is equivalent to $\int_0^\infty \alpha \prod_{i=1}^N P(A_i \mid \sigma^2 \alpha) \frac{1}{\alpha^2}\, d\alpha < \infty$. On the other hand, taking the Jeffreys prior $1/\alpha$, the second statement is equivalent to $\int_0^\infty \prod_{i=1}^N P(A_i \mid \sigma^2 \alpha) \frac{1}{\alpha}\, d\alpha < \infty$. Thus, as one can see, the two statements are equivalent (because, two different priors are considered).

One may wish to simplify the above MAP estimator by considering a hybrid MAP. Namely, the first moment of the intensity yields the identity $\sigma^2 = \overline{I}/(2\alpha)$. Substituting this expression into the difference of Eq. (10.40) with Eq. (10.41) yields the equation

$$\left\{ \alpha \frac{\partial}{\partial \alpha} L_{\mathrm{K}}(\sigma^2, \alpha) - \sigma^2 \frac{\partial}{\partial \sigma^2} L_{\mathrm{K}}(\sigma^2, \alpha) \right\} \Big|_{\sigma^2 = \overline{I}/(2\alpha)} - 1 = 0. \tag{10.42}$$

The following result implies that a solution to Eq. (10.42) can be found with a binary search algorithm, provided that the sample size N is greater than 1.

Theorem 20 *Let $N \geq 1$ be the sample size. Then,*

a) $\lim_{\alpha\to 0}\left\{\alpha \frac{\partial}{\partial\alpha} L_K(\sigma^2,\alpha) - \sigma^2 \frac{\partial}{\partial\sigma^2} L_K(\sigma^2,\alpha)\right\}\Big|_{\sigma^2=\overline{I}/(2\alpha)} = N.$

b) $\lim_{\alpha\to\infty}\left\{\alpha \frac{\partial}{\partial\alpha} L_K(\sigma^2,\alpha) - \sigma^2 \frac{\partial}{\partial\sigma^2} L_K(\sigma^2,\alpha)\right\}\Big|_{\sigma^2=\overline{I}/(2\alpha)} = 0.$

Concerning the estimation method based on the $M^{(v)}$-statistics, in general, there is no closed form for a solution to the equation $M_K^{(v)}(\alpha) = M$, but one can use the following result, relevant for any $v \neq 2$. See Fig. 10.3, left column, for an illustration of the function $M_K^{(v)}(\alpha)$.

Theorem 21 *We have the following properties*

(a) *if* $v<2$, then $\lim_{\alpha\to 0} M_K^{(v)}(\alpha) = 0$; *if* $v > 2$, *then* $\lim_{\alpha\to 0} M_K^{(v)}(\alpha) = \infty$;
(b) $\lim_{\alpha\to\infty} M_K^{(v)}(\alpha) = \Gamma(v/2+1)$;
(c) *if* $v<2$, then $M_K^{(v)}(\alpha)$ *is strictly increasing on its domain* $(0,\infty)$; *if* $v > 2$, *then* $M_K^{(v)}(\alpha)$ *is strictly decreasing on its domain* $(0,\infty)$.

So, let $M > 0$ be a real number (playing the role of the $M^{(v)}$-statistics). If $v<2$ and $0<M<\Gamma(v/2+1)$, then an efficient binary search algorithm yields the unique solution to the equation $M_K^{(v)}(\alpha) = M$. Indeed, from Theorem 21, the function $M_K^{(v)}(\alpha)$ is increasing in that case and its range is the interval $(0,\Gamma(v/2+1))$. On the other hand, if $v<2$ and $\Gamma(v/2+1) \leq M < 1$, then there is no solution to the equation $M_K^{(v)}(\alpha) = M$. However, in that case, the distance between $M_K^{(v)}(\alpha)$ and M is minimal as $\alpha \to \infty$. Thus, it makes sense to take the Rayleigh distribution. Similarly, if $v > 2$ and $M > \Gamma(v/2+1)$, then there is a unique solution to the equation $M_K^{(v)}(\alpha) = M$, and this solution can be found efficiently with a binary search algorithm. On the other hand, if $v > 2$ and $1<M<\Gamma(v/2+1)$, one may take $\alpha \to \infty$. For later reference, we introduce here what we call the K-distribution conditions

$$v<2 \text{ and } 0<M<\Gamma(v/2+1), \text{ or } v>2 \text{ and } \Gamma(v/2+1)<M. \tag{10.43}$$

Thus, the equation $M_K^{(v)}(\alpha) = M$ has a solution if and only if the K-distribution conditions are satisfied. Note that the Rice conditions (10.29) and the K-distribution conditions (10.43) are mutually exclusive and they are exhaustive (that it is to say, with the understanding that M plays the role of the $M^{(v)}$-statistics).

Concerning the parameter estimation method (Dutt and Greenleaf 1995), the following result shows that the equation $R_K^{(v)}(\alpha) = R$, where $R > 0$ plays the role of the $R^{(v)}$-statistics, has a solution if and only if $R < \frac{\Gamma(v/2+1)}{\sqrt{\Gamma(v+1)-\Gamma^2(v/2+1)}}$, and that there is at most one solution. Moreover, it shows that an efficient binary search algorithm can be used to find the solution, whenever it exists. Finally, one sees that the

solution $\alpha = \infty$ is the one that minimizes the distance between $R_{\mathrm{K}}^{(\nu)}(\alpha)$ and R, whenever the equation $R_{\mathrm{K}}^{(\nu)}(\alpha) = R$ has no solution. This amounts to switch to the Rayleigh model, with parameter $a^2 = \lim_{\alpha\to\infty} \sigma^2\alpha = \overline{I}$.

Theorem 22 *The following properties hold*

(a) $\lim_{\alpha\to 0} R_{\mathrm{K}}^{(\nu)}(\alpha) = 0$;
(b) $\lim_{\alpha\to\infty} R_{\mathrm{K}}^{(\nu)}(\alpha) = \frac{\Gamma(\nu/2+1)}{\sqrt{\Gamma(\nu+1)-\Gamma^2(\nu/2+1)}}$;
(c) $R_{\mathrm{K}}^{(\nu)}(\alpha)$ *is strictly increasing on its domain* $(0,\infty)$.

Concerning the method of Oliver (1993), the following result shows that an efficient binary search algorithm can be used in order to find the unique solution to the equation $U_{\mathrm{K}}(\alpha) = U$, whenever $U < -\gamma_E$. If ever $U \geq -\gamma_E$, Theorem 23 shows that it makes sense to adopt the Rayleigh model.

Theorem 23 *We have the following properties*

(a) $\lim_{\alpha\to 0} U_{\mathrm{K}}(\alpha) = -\infty$;
(b) $\lim_{\alpha\to\infty} U_{\mathrm{K}}(\alpha) = -\gamma_E$;
(c) $U_{\mathrm{K}}(\alpha)$ *is strictly increasing on its domain* $(0,\infty)$.

Similarly, one may switch to the Rayleigh distribution, whenever $V \leq 2$ (c.f. Sect. 10.4.4.3), or $Y \leq 1+s$ (c.f. Sect. 10.4.4.4), or $X \leq 1$ (c.f. Sect. 10.4.4.5). Theorems 22 and 23 are illustrated in Fig. 10.7.

In order to compare the various estimators, we considered the parameter α with values in the set $\{1, 2, \ldots, 20\}$. For each value of α, 1,000 datasets of $N = 1,000$ elements each were simulated according to the corresponding K-distribution. As in Dutt and Greenleaf (1994), one may consider the estimation of the parameter $\beta = 1/\alpha$ instead of α itself. In that case, one does not need to discard values of $1/\alpha$, because whenever the method has no solution, one may switch to the Rayleigh model ($\alpha = \infty$), which corresponds to $1/\alpha = 0$. Thus, we could estimate the

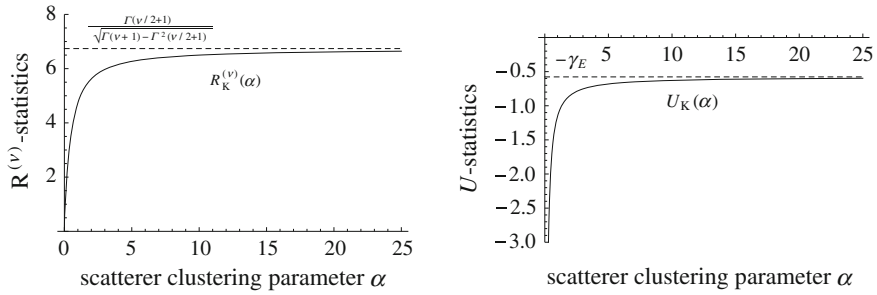

Fig. 10.7 Typical behavior of the $R^{(\nu)}$-statistics (*left image*) and of the U-statistics (*right image*) for the K-distribution. Here, $\nu = 1/4$

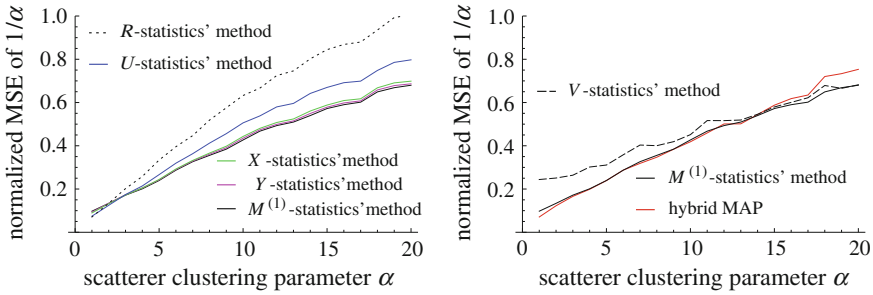

Fig. 10.8 *Left*: Comparison between the normalized MSE $\sqrt{E[(\hat{\beta}-\beta)^2]}/\beta$, where $\beta = 1/\alpha$, of the estimators based on the $M^{(1)}$-statistics (*black solid line*), the Y-statistics (*magenta solid line*), the X-statistics (*green solid line*), the U-statistics (*blue solid line*), and the R-statistics (*dotted line*), for the K-distribution. *Right*: Comparison between the normalized MSE of the estimators based on the $M^{(1)}$-statistics (*black solid line*), the V-statistics (*dashed line*), and the hybrid MAP (*red solid line*). The sample size is $N = 1,000$

normalized mean squared error (MSE) of the estimator $\hat{\beta}$ as $\sqrt{E[(\hat{\beta}-\beta)^2]}/\beta$. The resulting normalized MSE curves are presented in Fig. 10.8. As one can see, the estimators based on the $M^{(1)}$, Y, or X statistics and the hybrid MAP are practically equivalent and are better than the estimators based on the U or the R statistics.

10.4.5 Parameter Estimation Methods for the Homodyned K-Distribution

10.4.5.1 Expression of Fractional Order Moments of the Amplitude

Theorem 24 *Assume that $A = \sqrt{I}$ is distributed according to the homodyned K-distribution, with parameters $\varepsilon \geq 0$, $\sigma^2 > 0$ and $\alpha > 0$. Let $\gamma = \varepsilon^2/(2\sigma^2)$. Then,*

(a) (Prager et al. 2002) *if $\gamma \geq 0$, the $M^{(v)}$-statistics $E[A^v]/E[I]^{v/2}$ can be expressed in the following form*

$$M_{\mathrm{HK}}^{(v)}(\gamma,\alpha) = \frac{\Gamma(v/2+1)}{(\gamma+\alpha)^{v/2}} \int_0^\infty w^{v/2}\, {}_1F_1(-v/2,1,-\frac{\gamma}{w})\mathcal{G}(w\,|\,\alpha,1)\,dw, \qquad (10.44)$$

where ${}_pF_q$ denotes the hypergeometric series (here, $p = q = 1$).

(b) (Dutt and Greenleaf 1995) *if $\gamma = 0$, the $M^{(v)}$-statistics is equal to*

$$M_{\mathrm{HK}}^{(v)}(0,\alpha) = \Gamma(v/2+1)\frac{\Gamma(v/2+\alpha)}{\alpha^{v/2}\Gamma(\alpha)}. \qquad (10.45)$$

(c) (Hruska and Oelze 2009) *if* $\nu/2+\alpha$ *is not an integer and* $\gamma \geq 0$, *the* $M^{(\nu)}$*-statistics can be expressed as*

$$M_{\mathrm{HK}}^{(\nu)}(\gamma,\alpha) = \frac{\Gamma(\nu/2+1)}{(\gamma+\alpha)^{\nu/2}}\left\{\frac{\Gamma(\nu/2+\alpha)}{\Gamma(\alpha)}\,{}_1F_2(-\nu/2;1,1-\nu/2-\alpha;\gamma)\right.$$
$$\left. + \frac{\Gamma(\nu/2+1)\sin(\pi\nu/2)}{\Gamma^2(1+\nu/2+\alpha)\sin(\pi(\nu/2+\alpha))}\,\gamma^{\nu/2+\alpha}\,{}_1F_2(\alpha;1+\nu/2+\alpha,1+\nu/2+\alpha;\gamma)\right\}. \tag{10.46}$$

(d) (Jakeman and Tough 1987) *if* $\nu/2 > 2$ *is an integer and* $\gamma \geq 0$, *then the* $M^{(\nu)}$*-statistics is equal to*

$$M_{\mathrm{HK}}^{(\nu)}(\gamma,\alpha) = \frac{(\nu/2)!(\nu/2)!}{(\gamma+\alpha)^{\nu/2}\Gamma(\alpha)}\sum_{i=0}^{\nu/2}\frac{\Gamma(\nu/2-i+\alpha)}{i!i!(\nu/2-i)!}\gamma^i. \tag{10.47}$$

10.4.5.2 A Method Based on the Moments of the Intensity

A moments' method for the estimation of the homodyned K-distribution was proposed in Dutt and Greenleaf (1994). Namely, one solves the system of equations

$$E[I] = \overline{I}; \qquad E[I^2] = \overline{I^2}; \qquad E[I^3] = \overline{I^3} \tag{10.48}$$

in order to estimate $(\varepsilon, \sigma^2, \alpha)$, where $I = A^2$ is the intensity. In Prager et al. (2003), the three moments $E[I]$, $E[I^2]$, and $E[I^3]$ are expressed analytically as functions of $\tau^2 = \sigma^2\alpha$ (denoted σ^2 in that reference), $k = \varepsilon/(\sigma\sqrt{\alpha})$, and $\beta = 1/\alpha$, as follows

$$\begin{aligned} E[I] &= \tau^2[k^2+2];\\ E[I^2] &= \tau^4[8(1+\beta)+8k^2+k^4];\\ E[I^3] &= \tau^6[48(1+3\beta+2\beta^2)+72k^2(1+\beta)+18k^4+k^6]. \end{aligned} \tag{10.49}$$

In Prager et al. (2003, Appendix C, p. 712), an algebraic method is presented to solve the system (10.49) for τ^2, k, and β, rejecting negative or imaginary values.

Observe that Eq. (10.48) is equivalent to the system of equations

$$\mu = \overline{I}; \qquad M_{\mathrm{HK}}^{(4)}(\gamma,\alpha) = \overline{I^2}/\overline{I}^2; \qquad M_{\mathrm{HK}}^{(6)}(\gamma,\alpha) = \overline{I^3}/\overline{I}^3, \tag{10.50}$$

where $\mu = \varepsilon^2 + 2\sigma^2\alpha = E[I]$. Moreover, the values of ε and σ^2 can be recovered from γ, α and μ with the change of variables

$$\varepsilon = \sqrt{\mu \frac{\gamma}{(\gamma+\alpha)}}; \qquad \sigma^2 = \mu \frac{1}{2(\gamma+\alpha)}. \tag{10.51}$$

10.4.5.3 A Method Based on the Moments of the Amplitude

In Dutt (1995, Sect. 9.2.2, p. 116), it was suggested to use the first three moments of the amplitude to estimate the homodyned K-distribution, namely, to solve the system of equations

$$E[A] = \overline{A}; \qquad E[A^2] = \overline{A^2}; \qquad E[A^3] = \overline{A^3}. \tag{10.52}$$

However, at that time, the authors could not find a closed form expression of the moments of the amplitude. So, approximate expressions were used instead. As noted in Dutt (1995, p. 117), the parameter estimation might break down for small values of α and large values of k, due to the weakness of the approximations.

Note that an explicit expression of an arbitrary moment of the amplitude was given in Hruska and Oelze (2009, Eq. (8), p. 2473). Thus, the estimation method based on the first three moments of the amplitude would likely need to be tested again with the exact expressions of those moments.

Observe that Eq. (10.52) is equivalent to the system of equations

$$\mu = \overline{I}; \qquad M_{\mathrm{HK}}^{(1)}(\gamma,\alpha) = \overline{A}/\overline{I}^{1/2}; \qquad M_{\mathrm{HK}}^{(3)}(\gamma,\alpha) = \overline{A^3}/\overline{I}^{3/2}. \tag{10.53}$$

10.4.5.4 Methods Based on the SNR of Fractional Order Moments of the Amplitude

In Dutt (1995, Sect. 9.2.4, p. 117), it was proposed to use the SNR R of the amplitude and of the intensity. It is reported in Dutt (1995, Sect. 9.5, p. 142) that the method based on SNRs gave better results than the three methods presented in Sects. 10.4.5.2, 10.4.5.3 and 10.4.5.5. But then, the exact expression of Eq. (10.46) was not used, so that this conclusion is not necessarily valid.

In Martin-Fernandez and Alberola-Lopez (2007), the authors suggested to use the statistics R for two distinct values of ν (or more), using an exact expression of that statistics. In fact, the authors suggested the values 0.01, 0.03, 0.05, 0.075, 0.1, 0.25, 0.4, 0.5, 0.75, and 1. A solution is then found by inspection of the SNR level curves. Namely, for each value of the fractional order ν, the statistics R is expressed analytically as a function of $k = \varepsilon/(\sigma\sqrt{\alpha})$, and α (denoted μ in that reference). One then considers the point (k,α) that is closest to all the corresponding SNR level curves, in the sense of the least mean squares (LMS). Thus, this method is an extension of the method based on the SNRs of Dutt (1995, Sect. 9.2.4).

10.4.5.5 A Method Based on the SNR and Skewness of the Amplitude

In Dutt (1995, Sect. 9.2.4, p. 117), it was proposed to use the SNR $R = \frac{E[A]}{(E[A^2]-E^2[A])^{1/2}}$ and the skewness $S = \frac{E[(A-E[A])^3]}{(E[A^2]-E^2[A])^{3/2}}$ of the amplitude for the estimation of the homodyned K-distribution. Again, that method should be tested with the exact expression of Eq. (10.46).

10.4.5.6 A Method Based on the SNR, Skewness and Kurtosis of Fractional Order Moments of the Amplitude

In Hruska and Oelze (2009), the authors suggested the use of the SNR R, the skewness S, and the kurtosis $K = \frac{E[(A^\nu-E[A^\nu])^4]}{(E[A^{2\nu}]-E^2[A^\nu])^2}$, for two values of ν, namely 0.72 and 0.88. These statistics were expressed analytically as a function of $k = \varepsilon/(\sigma\sqrt{\alpha})$, and α (denoted μ in that reference). One then considers the point (k, α) that is closest to the six corresponding SNR, skewness, and kurtosis level curves in the sense of the LMS. In order to do so, the (k, α)-space was sampled at the points of the form $(i \times 0.01, 10^{-3+j\times 0.01})$, with $0 \leq i, j \leq 500$. The two methods (Martin-Fernandez and Alberola-Lopez 2007; Hruska and Oelze 2009) were not compared in Hruska and Oelze (2009). However, the choice of the fractional orders 0.72 and 0.88 was validated empirically in Hruska and Oelze (2009) (as opposed to taking the numerous fractional orders $0.01, \ldots, 1$ in Martin-Fernandez and Alberola-Lopez (2007)).

10.4.5.7 Discussion

In this section, we present new results on the $M^{(\nu)}$-statistics and the MLE for the homodyned K-distribution.

Concerning Theorem 24, the case where $\nu/2 + \alpha$ is not integer (with no restriction on γ) is covered by part c), whereas part b) covers the case where $\nu/2 + \alpha$ is an integer, but with the restriction $\gamma = 0$. So, what about the case where $\gamma > 0$ and $\nu/2 + \alpha$ is an integer. The following result answers that question. However, in practice, one may use linear interpolation to approximate the $M^{(\nu)}$-statistics whenever $\nu/2 + \alpha$ is close to an integer (as done in Hruska and Oelze (2009)).

Theorem 25 *Assume that* $A = \sqrt{I}$ *is distributed according to the homodyned K-distribution, with parameters* $\varepsilon \geq 0$, $\sigma^2 > 0$ and $\alpha > 0$. *Let* $\gamma = \varepsilon^2/(2\sigma^2)$. *Then, if* $\gamma > 0$, *the* $M^{(\nu)}$*-statistics is expressed as*

$$M_{\mathrm{HK}}^{(\nu)}(\gamma,\alpha)=\frac{2}{(\gamma+\alpha)^{\nu/2}}\frac{\Gamma(\nu/2+1)}{\Gamma(\alpha)}\sum_{n=0}^{\infty}\frac{(1+\nu/2)_n}{n!n!}\sqrt{\gamma}^{\nu/2+\alpha+n}K_{\nu/2+\alpha-n}(2\sqrt{\gamma}). \tag{10.54}$$

where $(1+\nu/2)_n$ *denotes the rising factorial* $\Gamma(1+\nu/2+n)/\Gamma(1+\nu/2)$.

Theorems 9 and 21 on the behavior of the functions $M_{\mathrm{Ri}}^{(\nu)}(\kappa)$ and $M_{\mathrm{K}}^{(\nu)}(\alpha)$, respectively, can be extended to the following theorem.

Theorem 26 *Assume that* $A=\sqrt{I}$ *is distributed according to the homodyned K-distribution, with parameters* $\varepsilon\geq 0$, $\sigma^2>0$ *and* $\alpha>0$. *Let* $\gamma=\varepsilon^2/(2\sigma^2)$. *Then,*

(a) $\lim_{\gamma\to 0}M_{HK}^{(\nu)}(\gamma,\alpha)=M_K^{(\nu)}(\alpha)$ (*the function introduced in Theorem* 13).
(b) $\lim_{\gamma\to\infty}M_{\mathrm{HK}}^{(\nu)}(\gamma,\alpha)=1$.
(c) For any $\alpha>0$ *and* $\gamma>0$, *the function* $M_{HK}^{(\nu)}(\gamma,\alpha)$ *is increasing in the variable* γ, *if* $\nu<2$, *whereas it is decreasing in the variable* γ, *if* $\nu>2$.

See Fig. 10.9 for an illustration of Theorem 26. Theorem 26 implies that the equation $M_{\mathrm{HK}}^{(\nu)}(\gamma,\alpha)=M$, α being known, has at most one solution, and moreover, it gives sufficient and necessary conditions for a solution to exist, as expressed in the following Corollary.

Corollary 2 *Let* $M>0$ *be a real number (playing the role of* $M^{(\nu)}$*). There exists at most one non-negative solution* $\gamma=\gamma_M^{(\nu)}(\alpha)$ *to the equation* $M_{\mathrm{HK}}^{(\nu)}(\gamma,\alpha)=M$, α *being known.*

(a) *If the Rice conditions* (10.29) *are satisfied, then there exists a non-negative solution for any* $\alpha>0$.
(b) *If the K-distribution conditions* (10.43) *are satisfied, then there exists a non-negative solution if and only if* $\alpha\leq\alpha_0=(M_{\mathrm{K}}^{(\nu)})^{-1}(M)$.

So, given $\alpha>0$, $\overline{I}$ and $\overline{A}$, one can recover ε and σ^2 as follows. First of all, we take $\gamma=\gamma_M^{(\nu)}(\alpha)$, where $M=\overline{A}/(\overline{I})^{1/2}$. Then, one uses Eq. (10.51), with $\mu=\overline{I}$ and $\gamma=\gamma_M^{(\nu)}(\alpha)$. In this manner, well-defined functions can be obtained

$$\varepsilon(\alpha,\overline{I},\overline{A});\qquad \sigma^2(\alpha,\overline{I},\overline{A}), \tag{10.55}$$

We now discuss briefly the MLE for the homodyned K-distribution. The following result is useful for the computation of the partial derivatives of that distribution.

Lemma 4 *Let* $\varepsilon\geq 0$, $\sigma^2>0$ *and* $\alpha>0$.

(a) *The homodyned K-distribution* $P_{\mathrm{HK}}(A\,|\,\varepsilon,\sigma^2,\alpha)$ *can be expressed as*

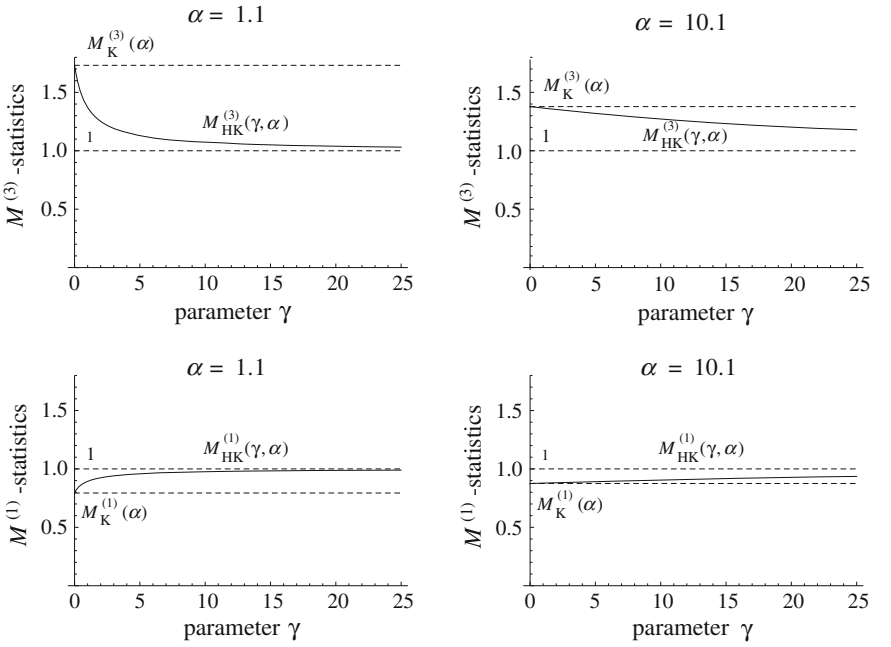

Fig. 10.9 Typical behavior of the $M^{(\nu)}$-statistics for the homodyned K-distribution, α being fixed, when $\nu < 2$ (*bottom row*) and $\nu > 2$ (*top row*). In fact, we took here $\nu = 1$ (*bottom row*) and $\nu = 3$ (*top row*), as well as $\alpha = 1.1$ (*left column*) and $\alpha = 10.1$ (*right column*)

$$\frac{1}{\pi}\int_0^{\pi}\frac{2A}{\sigma^2\Gamma(\alpha)}\left(\frac{X(\theta)}{2}\right)^{\alpha-1}K_{\alpha-1}\big(X(\theta)\big)d\ \theta, \tag{10.56}$$

where $X(\theta) = \sqrt{\frac{2}{\sigma^2}}\sqrt{A^2+\varepsilon^2-2A\varepsilon\cos\theta}$.

(b) *The partial derivative* $\frac{\partial}{\partial\varepsilon}P_{\mathrm{HK}}(A\,|\,\varepsilon,\sigma^2,\alpha)$ *can be expressed as*

$$\frac{1}{\pi}\int_0^{\pi}\frac{2A}{\sigma^4\Gamma(\alpha)}(A\cos\theta-\varepsilon)\left(\frac{X(\theta)}{2}\right)^{\alpha-2}K_{\alpha-2}\big(X(\theta)\big)d\ \theta. \tag{10.57}$$

(c) *The partial derivative* $\frac{\partial}{\partial\sigma^2}P_{\mathrm{HK}}(A\,|\,\varepsilon,\sigma^2,\alpha)$ *can be expressed as*

$$\begin{aligned}&-\frac{\alpha}{\sigma^2}\frac{1}{\pi}\int_0^{\pi}\frac{2A}{\sigma^2\Gamma(\alpha)}\left(\frac{X(\theta)}{2}\right)^{\alpha-1}K_{\alpha-1}\big(X(\theta)\big)d\ \theta\\&+\frac{1}{\sigma^2}\frac{1}{\pi}\int_0^{\pi}\frac{2A}{\sigma^2\Gamma(\alpha)}\left(\frac{X(\theta)}{2}\right)^{\alpha}K_{\alpha}\big(X(\theta)\big)d\ \theta.\end{aligned} \tag{10.58}$$

(d) *The partial derivative* $\frac{\partial}{\partial\alpha}P_{\mathrm{HK}}(A\,|\,\varepsilon,\sigma^2,\alpha)$ *can be expressed as*

$$\frac{1}{\pi}\int_0^{\pi}\frac{2A}{\sigma^2\Gamma(\alpha)}\left(\frac{X(\theta)}{2}\right)^{\alpha-1}K_{\alpha-1}\Big(X(\theta)\Big)\\ \times\left\{-\psi(\alpha)+\log\left(\frac{X(\theta)}{2}\right)+\frac{\frac{\partial}{\partial\alpha}K_{\alpha-1}\Big(X(\theta)\Big)}{K_{\alpha-1}\Big(X(\theta)\Big)}\right\}d\theta, \tag{10.59}$$

where ψ denotes the digamma function.

One could then extend Theorems 18 and 19 in the context of the homodyned K-distribution. In fact, we suspect that the MLE is not always well-defined for the homodyned K-distribution. Thus, one would have to consider a MAP estimator. Since such an estimator results in a time-consuming algorithm, we will not develop further that topic here.

10.4.6 Parameter Estimation Methods for the Nakagami Distribution

10.4.6.1 The MLE for the Nakagami Distribution

Since a Nakagami distribution on the amplitude A is equivalent to a gamma distribution on the intensity $I = A^2$, the estimation of the Nakagami distribution parameters amounts to the well-known estimation problem of the gamma distribution. In particular, the MLE is the unique solution to the equation

$$\Omega = \overline{I}; \qquad \psi(m) - \log m = \overline{\log I} - \log \overline{I}, \tag{10.60}$$

where ψ denotes the digamma function.

10.4.6.2 A Method Based on the First Two Moments of the Intensity

The most frequently used method for the parameter estimation of the Nakagami distribution is based on the first two moments of the intensity in the following form

$$\Omega = \overline{I}; \qquad m = \frac{\overline{I}^2}{\overline{I^2} - \overline{I}^2}. \tag{10.61}$$

Note that the term $\frac{\overline{I}^2}{\overline{I^2}-\overline{I}^2}$ is the square of the SNR of the intensity. This method is equivalent to the V-statistics' method (i.e., based on the $M^{(4)}$-statistics $\overline{I^2}/\overline{I}^2$).

10.4.6.3 Discussion

We first mention a relation between the MLE and the U-statistics for the Nakagami distribution. Then, new results on moments and log-moments based methods are presented. Finally, a comparison of these estimators on simulated data is reported.

Concerning the MLE of the Nakagami distribution, note that the term $\overline{\log I} - \log \bar{I}$ is the U-statistics. Thus, it is negative unless all terms I_i are identical. Also, the term $\psi(m) - \log m$ is the analytical expression of the U-statistics for the Nakagami distribution, as stated in the following result.

Theorem 27 *Let A be distributed according to the Nakagami distribution with parameters m and Ω. Then, the U-statistics $E[\log I] - \log E[I]$ is expressed as $U_{\mathrm{Na}}(m) = \psi(m) - \log m$.*

Thus, the MLE turns out to correspond to the U-statistics' method. But unlike the K-distribution, the equation $\psi(m) - \log m = U$ admits a solution for any $U < 0$. Indeed, the following result shows that a binary search can be used to compute the unique solution to that equation.

Theorem 28 (Destrempes et al. 2009). *The following properties hold*

a) $\lim_{m\to 0} \psi(m) - \log m = -\infty$;
b) $\lim_{m\to\infty} \psi(m) - \log m = 0$;
c) the function $\psi(m) - \log m$ *is strictly increasing on its domain* $(0, \infty)$.

Proof

a) We have the identity described in Abramowitz and Stegun (1972, p. 259, (6.3.21)) $\psi(m) = \log(m) - \frac{1}{2m} - 2\int_0^\infty \frac{t}{(t^2+m^2)(e^{2\pi t}-1)}$, for $m > 0$. This yields $-\log(m) + \psi(m) \leq -\frac{1}{2m}$, and hence $\lim_{m\to 0} -\log(m) + \psi(m) = -\infty$.
b) The same identity as above yields the computation $\lim_{m\to\infty} -\log(m) + \psi(m) = -2\lim_{m\to\infty} \int_0^\infty \frac{t}{(t^2+m^2)(e^{2\pi t}-1)}\, dt = 0$.
c) We have $\frac{\partial}{\partial m} U_{\mathrm{Na}}(m) = -\frac{1}{m} + \psi^{(1)}(m)$. But from Abramowitz and Stegun (1972, p. 260, (6.4.1)), we have $\psi^{(1)}(m) = \int_0^\infty \frac{te^{-mt}}{1-e^{-t}}\, dt$. Now, $\frac{te^{-\pi t}}{1-e^{-t}} > e^{-mt}$, since $e^{-t} > 1 - t$, for $t > 0$. Therefore, $\psi^{(1)}(m) > \int_0^\infty e^{-mt}\, dt = \frac{1}{m}$, and we are done. ■

One can also show that the X-statistics is equal to $1/m$ for the Nakagami distribution.

Theorem 29 *Let A be distributed according to the Nakagami distribution with parameters m and Ω. Then, the X-statistic $E[I \log I]/E[I] - \log E[I]$ is expressed as $X_{\mathrm{Na}}(m) = \frac{1}{m}$.*

Thus, the shape parameter of the Nakagami distribution can be estimated directly with the equation $m = 1/X$, where $X = \overline{I \log I}/\overline{I} - \overline{\log I}$.

Finally, one can compute explicitly the $M^{(1)}$-statistics for the Nakagami distribution.

Theorem 30 *Let A be distributed according to the Nakagami distribution with parameters m and Ω. Then, the $M^{(1)}$-statistic $E[A]/\sqrt{E[I]}$ is expressed as $M^{(1)}_{\mathrm{Na}}(m) = \frac{\Gamma(1/2+m)}{\sqrt{m}\Gamma(m)}$.*

The equation $M^{(1)}_{\mathrm{Na}}(m) = M$ can be estimated with a binary search algorithm, for any $0 < M < 1$.

Theorem 31 *The following properties hold*

a) $\lim_{m\to 0} \frac{\Gamma(1/2+m)}{\sqrt{m}\Gamma(m)} = 0$;
b) $\lim_{m\to\infty} \frac{\Gamma(1/2+m)}{\sqrt{m}\Gamma(m)} = 1$;
c) the function $\frac{\Gamma(1/2+m)}{\sqrt{m}\Gamma(m)}$ is strictly increasing on its domain $(0, \infty)$.

Theorems 27, 29, 30 and 31 can be checked directly using the software Mathematica (Wolfram Research, Inc., Champaign, IL, USA, version 7.0).

In order to compare these four estimators, we considered the parameter m with values in the set $\{0.1, 0.2, \ldots, 2.0\}$. For each value of m, 1,000 datasets of $N = 1,000$ elements each were simulated according to the corresponding Nakagami distribution. We could estimate the normalized MSE of the estimator $\hat{m}$ as $\sqrt{E[(\hat{m} - m)^2]}/m$. The resulting normalized MSE curves are presented in Fig. 10.10. As one can see, the estimators based on the MLE (i.e., the U-statistics, in this case) or the X-statistics are practically equivalent. They are better than the estimator based on the $M^{(1)}$-statistics, especially on the interval $m \in [0.0, 0.5]$. These three estimators are systematically better than the estimator based on the V-statistics.

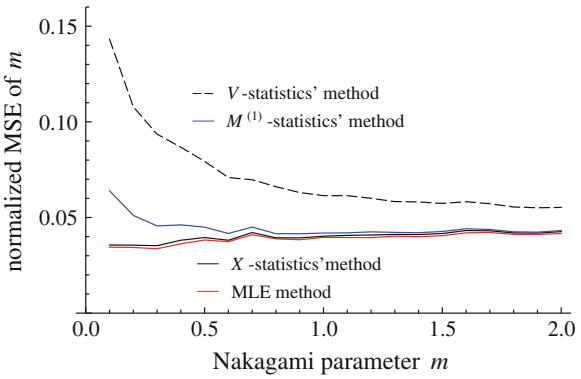

Fig. 10.10 Comparison between the normalized MSE $\sqrt{E[(\hat{m} - m)^2]}/m$ of the estimators based on the MLE (*red solid line*), the X-statistics (*black solid line*), the $M^{(1)}$-statistics (*blue solid line*), and the V-statistics (*dashed line*), for the Nakagami distribution. The sample size is $N = 1,000$

10.5 Conclusion

We conclude with the following issues.

1. It was argued that the homodyned K-distribution is a sound model for the first-order statistics of the echo envelope of the RF ultrasound signal, in the context where the backscattered echo signal received at the transducer of an ultrasound device is assumed to be the vector sum of the individual signals produced by the scatterers distributed in the medium (Wagner et al. 1983, 1987). The K-distribution is a special case where there is no coherent component (due to the absence of specular reflection). The Rice and the Rayleigh distributions are limit cases of the homodyned K-distribution or the K-distribution, respectively, corresponding to an infinite homogeneity of the diffuse scattering medium. The Nakagami is an approximation of the homodyned K-distribution. All these five distributions share two desirable properties: (1) the total signal power depends only on the coherent component in the case of a vanishing diffuse signal; and (2) the intensity SNR is infinite in that case. The other models presented in Jakeman and Tough (1987), Shankar (2000, 2003), Barakat (1986), Eltoft (2005), Raju and Srinivasan (2002), Agrawal and Karmeshu (2006) do not have these two properties. Thus, we recommend the homodyned K-distribution (or its related distributions, in special cases) as a model for the ultrasound echo envelope in that context, as was done in Dutt and Greenleaf (1994), Hruska and Oelze (2009) and Destrempes and Cloutier (2010).
2. It was shown that the methods based on the X-statistics and the mean intensity are practically as good as the MLE for the Rice and the Nakagami distributions, or the proposed hybrid MAP for the K-distribution. For the homodyned K-distribution, one may use a method based on the SNR, skewness and kurtosis of fractional orders of the amplitude (Hruska and Oelze 2009).
3. A homodyned K-distribution with parameters (k, α) in the range $[0, 2] \times [1, 20]$ can be approximated by a Nakagami distribution with KL distance less than 0.072 (but for much larger values of k, the KL distance might be much larger). However, although one may express the two parameters Ω and m of the Nakagami distribution in terms of the three parameters ε, σ^2 and α of the homodyned K-distribution in the form $\Omega = \varepsilon^2 + 2\sigma^2\alpha$ and $m = \frac{(\varepsilon^2+2\sigma^2\alpha)^2}{4\sigma^2\alpha(\varepsilon^2+\sigma^2(2+\alpha))}$, as follows from Destrempes and Cloutier (2010, Eq. (23) and Tables 3 and 4), the converse statement is not true. Thus, the Nakagami distribution gives less information on the statistical properties of the echo envelope than the homodyned K-distribution. In particular, one may not retrieve the coherent or diffuse signal power from the parameters of the Nakagami distribution. For this reason, we recommend the use of the homodyned K-distribution, rather than the Nakagami distribution, in the context of tissue characterization. On the other hand, the Nakagami distribution may be used in the context of image segmentation, since in that application, the main property is a good fit of the

distribution with the data. This was the point of view adopted in Destrempes et al. (2009, 2011) and Bouhlel and Sevestre-Ghalila (2009).

4. When the product of the wave number with the mean size of the scatterers is much smaller than the wavelength, and acoustic impedance of the scatterers is close to the impedance of the embedding medium, a high density of scatterers results in a packing organization that implies constructive and destructive wave interferences and a correlation between the individual signals produced by the scatterers (Hayley et al. 1967; Twersky 1975, 1978, 1987, 1988; Lucas and Twersky 1987; Berger et al. 1991). In such a case, the assumption made here on the randomness of the scatterer positions (or phase) might not be valid. The resulting first-order statistics might still be characterized with the proposed models, but the physical interpretation of the parameters should be done with caution in that case and should be further studied. See Wagner et al. (1987), Weng et al. (1990, 1992) and Narayanan et al. (1997) for further reading on that issue.
5. The distributions mentioned here concern the envelope of the RF signal. When a log-compression or other (nonlinear or linear) operators are applied to the envelope, the distribution of the gray levels no longer follows the distributions computed on the RF echo envelope. In the case of log-compression, the resulting distribution has been modeled in Dutt and Greenleaf (1996), assuming the K-distribution for the envelope. In Prager et al. (2003), a decompression algorithm is proposed, assuming the homodyned K-distribution for the envelope. As mentioned before, operators other than log-compression can be applied on the envelope. In Nillesen et al. (2008), a linear filter was applied to the RF data before computing the envelope. Five distributions were tested to fit the data: the Rayleigh distribution, the K-distribution, the Nakagami distribution, the inverse Gaussian distribution and the gamma distribution. The authors showed, based on empirical tests, that, overall, the gamma distribution best fits the data. See also Tao et al. (2002, 2006) and Shankar et al. (2003) for further reading on the gamma distribution model in ultrasound imaging. See also Keyes and Tucker (1999) for a comparison of the K-distribution with a few other models as well as Tsui et al. (2005, 2009c), Tsui and Wang (2004), Tsui and Chang (2007) for the effect of log-compression or transducer characteristics on the parameters of the Nakagami distribution. Here, we were concerned with the statistical distributions of the amplitude of the unfiltered envelope of the RF image, and therefore we did not study such distributions.
6. The parameters of the homodyned K-distribution reveal the scattering properties of the underlying tissue, but they are also instrumentation and depth dependent. In particular, the transducer center frequency, the point spread function (PSF) and the attenuation of the signal within the tissue play a role. A challenge consists in removing these dependencies. See Hruska (2009) for further reading on that matter.
7. The estimation problem is important, since the use of poor estimators might wash down the performance of a method, otherwise fine. However, the mere study of the bias and variance of an estimator is not sufficient, since it assumes

data distributed according to the distribution. Moreover, in the context of ultrasound imaging, various factors intervene, such as the presence of noise, the efficiency of the algorithm (in view of clinical applications, where the speed of execution of an algorithm is relevant). Thus, ideally, the study of an estimation method should include simulations of ultrasound data, as well as in vitro and in vivo experimental tests.

10.5.1 Perspective

In the future, it would be interesting to see a study of log-moments methods for the homodyned K-distribution. We believe that it would be instructive to establish relations between echo envelope statistics and spectral quantitative measures. See Oelze and O'Brien (2007) for an example of quantitative ultrasound assessment in the context of breast cancer that used the parameters of the homodyned K-distribution combined with an analysis of the normalized backscattered power spectrum. In the articles by Shankar et al. (1993), Molthen et al. (1993), Narayanan et al. (1994), Shankar (1995) and Molthen et al. (1995), an underlying physical model for the K-distribution was introduced. In the more recent article by Saha and Kolios (2011), the Nakagami distribution was estimated on simulated tissues based on a scattering model. A challenge consists in deepening the understanding of an underlying physical model for the homodyned K-distribution. Finally, it would be desirable to take into account the effect of instrumentation and attenuation on the echo envelope statistics. Thus, there remains several challenging problems in that area of QUS imaging, that we believe will turn out to be useful in a clinical context.

Acknowledgments The authors acknowledge the continuous financial support of the Canadian Institutes of Health Research and Natural Sciences and Engineering Research Council of Canada.

Appendix: Proofs of the New Results

Proof of Theorem 8 From Theorem 6, there is exactly one critical point of $L(\varepsilon, \sigma^2)$ for which $\varepsilon > 0$, and it is the MLE (here, for L denotes L_{Ri}). Therefore (using Theorem 5), the function $f(\kappa)$ has exactly one positive root κ_* and it corresponds to the MLE. Moreover, one can check that $\kappa = 0$ is also a root of the function f. Namely, we have $\lim_{\kappa\to 0} f(\kappa) = -1 + \frac{1}{N}\sum_{i=1}^{N} y_i^2$, and by construction, $\frac{1}{N}\sum_{i=1}^{N} y_i^2 = 1$.

We have $\lim_{\kappa\to\infty} f(\kappa) = 2(-1 + \frac{1}{N}\sum_{i=1}^{N} y_i) = 2(-1 + \overline{\sqrt{I}}/\sqrt{\bar{I}})$. A direct application of Cauchy-Schwartz' inequality ensures that $\overline{\sqrt{I}}/\sqrt{\bar{I}} < 1$, so that

$\lim_{\kappa\to\infty} f(\kappa) < 0$. In view of the Intermediate Value Theorem for continuous functions, it follows that $f(\kappa) < 0$, if $\kappa > \kappa_*$.

Next, we want to show that $f(\kappa) > 0$ for $\kappa \in (0, \kappa_*)$. Since κ_* is the only positive root of f, and since $f(\kappa) < 0$ on (κ_*, ∞), it is enough to show that $\frac{\partial f}{\partial \kappa} < 0$ at κ_*; for then, $f(\kappa) > 0$ if $\kappa < \kappa_*$ is sufficiently near κ_*, and hence, $f(\kappa) > 0$ on $(0, \kappa_*)$ using the Intermediate Value Theorem.

First of all, we claim that $\frac{\partial f}{\partial \kappa} = \frac{1}{N}\frac{\partial^2 L}{\partial \kappa^2}$ at a critical point of $L(\varepsilon, \sigma^2) = \sum_{i=1}^N \log P_{\mathrm{Ri}}(A_i \,|\, \varepsilon, \sigma^2)$, whenever $\varepsilon > 0$ (i.e. $\kappa > 0$). Indeed, with the change of variable $\varepsilon = \sqrt{\frac{\mu\kappa}{(\kappa+1)}}$ and $\sigma^2 = \frac{\mu}{2(\kappa+1)}$, we obtain directly from Eq. (10.2)

$$\begin{aligned}\frac{1}{N}L(\mu,\kappa) = &\frac{1}{N}\sum_{i=1}^N \log A_i - \log\mu + \log 2 + \log(\kappa+1)\\ &- \frac{(\kappa+1)}{\mu}\frac{1}{N}\sum_{i=1}^N A_i^2 - \kappa + \frac{1}{N}\sum_{i=1}^N \log I_0\Big(\frac{2A_i}{\sqrt{\mu}}\sqrt{\kappa(\kappa+1)}\Big).\end{aligned} \tag{10.62}$$

Next, the derivative of $\frac{1}{N}L(\mu,\kappa)$ with respect to κ is equal to

$$\frac{1}{(\kappa+1)} - \frac{1}{\mu}\frac{1}{N}\sum_{i=1}^N A_i^2 - 1 + \frac{(2\kappa+1)}{\sqrt{\kappa(\kappa+1)}}\frac{1}{N}\sum_{i=1}^N \frac{A_i}{\sqrt{\mu}}\frac{I_1(\frac{2A_i}{\sqrt{\mu}}\sqrt{\kappa(\kappa+1)})}{I_0(\frac{2A_i}{\sqrt{\mu}}\sqrt{\kappa(\kappa+1)})}. \tag{10.63}$$

But, from Talukdar and Lawing (1991), we have $\mu = \overline{I} = \frac{1}{N}\sum_{i=1}^N A_i^2$ at a critical point (ε, a^2) of L_{Ri}. Therefore, we obtain that $\frac{1}{N}\frac{\partial L}{\partial \kappa} = f(\kappa)$ at such a critical point (because $A_i/\sqrt{\mu}$ is then equal to $y_i = A_i/\sqrt{\overline{I}}$). Taking the partial derivative of Eq. (10.63) with respect to κ, we also see that $\frac{\partial f}{\partial \kappa} = \frac{1}{N}\frac{\partial^2 L}{\partial \kappa^2}$ at a critical point (ε, σ^2) of L.

Now, recall that if $u = u(x,y)$ and $v = v(x,y)$ is a change of variable, then

$$\begin{aligned}\frac{\partial^2 L}{\partial u \partial v} = &\frac{\partial L}{\partial x}\frac{\partial^2 x}{\partial u \partial v} + \frac{\partial L}{\partial y}\frac{\partial^2 y}{\partial u \partial v}\\ &+ \frac{\partial^2 L}{\partial x^2}\frac{\partial x}{\partial u}\frac{\partial x}{\partial v} + \frac{\partial^2 L}{\partial y \partial x}\frac{\partial y}{\partial u}\frac{\partial x}{\partial v} + \frac{\partial^2 L}{\partial x \partial y}\frac{\partial x}{\partial u}\frac{\partial y}{\partial v} + \frac{\partial^2 L}{\partial y^2}\frac{\partial y}{\partial u}\frac{\partial y}{\partial v};\\ \frac{\partial^2 L}{\partial u^2} = &\frac{\partial L}{\partial x}\frac{\partial^2 x}{\partial u^2} + \frac{\partial L}{\partial y}\frac{\partial^2 y}{\partial u^2}\\ &+ \frac{\partial^2 L}{\partial x^2}\Big(\frac{\partial x}{\partial u}\Big)^2 + 2\frac{\partial^2 L}{\partial x \partial y}\frac{\partial x}{\partial u}\frac{\partial y}{\partial u} + \frac{\partial^2 L}{\partial y^2}\Big(\frac{\partial y}{\partial u}\Big)^2.\end{aligned} \tag{10.64}$$

At this point, we find convenient to use the change of variable $\varepsilon^2 = \mu\kappa/(1+\kappa)$ and $\sigma^2 = \mu/(2(1+\kappa))$. We develop $\frac{\partial^2}{\partial \kappa^2}L = \Big(G_{11} - G_{12} + \frac{1}{4}G_{22}\Big)\frac{\mu^2}{(\kappa+1)^4}$ at a critical point of L, where $G_{11} = \frac{\partial^2 L}{\partial \varepsilon^2 \partial \varepsilon^2}$, $G_{12} = \frac{\partial^2 L}{\partial \varepsilon^2 \partial \sigma^2}$, and $G_{22} = \frac{\partial^2 L}{\partial \sigma^2 \partial \sigma^2}$ (we make use of the fact

that $\frac{\partial L}{\partial \varepsilon^2} = 0 = \frac{\partial L}{\partial \sigma^2}$ at the critical point). Now, from Carrobi and Cati (2008, Appendix A, p. 686-687), we have $H_{11}H_{22} - H_{12}^2 > 0$ and $H_{11} < 0$ at the critical point of interest, where $H_{11} = \frac{\partial^2 L}{\partial \varepsilon \partial \varepsilon}$, $H_{12} = \frac{\partial^2 L}{\partial \varepsilon \partial \sigma^2}$, and $H_{22} = \frac{\partial^2 L}{\partial \sigma^2 \partial \sigma^2}$ (σ^2 is viewed as a variable). From there, if one uses the change of variable $\varepsilon = \sqrt{\varepsilon^2}$ (and $\sigma^2 = \sigma^2$), one concludes that $G_{11}G_{22} - G_{12}^2 = \left(H_{11}H_{22} - H_{12}^2\right)\frac{1}{4\varepsilon^2} > 0$ and $G_{11} = H_{11}\frac{1}{4\varepsilon^2} < 0$, at that critical point. Thus, we obtain the upper bound $G_{22} < G_{12}^2/G_{11}$ (because $G_{11} < 0$), and therefore $\frac{\partial^2 L}{\partial \kappa^2} < \left(G_{11} - \quad G_{12} + \frac{1}{4}G_{12}^2/G_{11}\right)\frac{\mu^2}{(\kappa+1)^4}$. But this is equal to $\frac{1}{G_{11}}\frac{\mu^2}{(\kappa+1)^4}\left(G_{11} - \frac{1}{2}G_{12}\right)^2$, and it is non-positive since $G_{11} < 0$. Therefore, $\frac{\partial f}{\partial \kappa} = \frac{1}{N}\frac{\partial^2 L}{\partial \kappa^2} < 0$ at the point $\kappa = \kappa_*$ (with $\mu = \overline{I}$). This completes the proof of Theorem 8. ■

Proof of Theorem 9 (a) Setting $\kappa = 0$ in Theorem 7, we obtain directly $M_{\text{Ri}}^{(v)}(0) = \Gamma(v/2+1)$.

(b) From Luke (1962, pp.7–8), we have the following asymptotic behavior

$$ {}_1F_1(a_1; b_1; z) \propto \frac{\Gamma(b_1)}{\Gamma(a_1)} z^{\chi} e^{z}\Big(1 + \mathcal{O}(1/z)\Big), \tag{10.65} $$

where $\chi = a_1 - b_1$, valid for $|\arg z| < \pi$ and $|z| \to \infty$. Therefore, we have

$$ {}_1F_1(v/2+1; 1; \kappa) \propto \frac{1}{\Gamma(v/2+1)} \kappa^{v/2} e^{\kappa}\Big(1 + \mathcal{O}(1/\kappa)\Big). \tag{10.66} $$

We conclude that $\lim_{\kappa\to\infty} M_{\text{Ri}}^{(v)}(\kappa) = \lim_{\kappa\to\infty} \frac{\Gamma(v/2+1)e^{-\kappa}}{(\kappa+1)^{v/2}} \times \frac{1}{\Gamma(v/2+1)} \kappa^{v/2} e^{\kappa} = 1$.

(c) From the definition $M_{\text{Ri}}^{(v)}(\kappa) = \Gamma(v/2+1)\frac{{}_1F_1(1+v/2,1,\kappa)}{e^{\kappa}(\kappa+1)^{v/2}}$, we obtain after algebraic simplifications

$$ \frac{d}{d\,\kappa} M_{\text{Ri}}^{(v)} = \Gamma(v/2+1) \frac{\frac{d}{d\,\kappa}{}_1F_1(1+v/2,1,\kappa) - {}_1F_1(1+v/2,1,\kappa)\left(1 + \frac{v}{2}(\kappa+1)^{-1}\right)}{e^{\kappa}(\kappa+1)^{v/2}}. \tag{10.67} $$

Now, from Gradshteyn and Ryshik (1994, 9.213, p.1086) and Gradshteyn and Ryshik (1994, 9.212(3), p.1086), we have $\frac{d}{d\,\kappa}{}_1F_1(1+v/2,1,\kappa) = (1+v/2)\,{}_1F_1(2+v/2,2,\kappa) = \frac{v}{2}{}_1F_1(1+v/2,2,\kappa) + {}_1F_1(1+v/2,1,\kappa)$. So, omitting the positive factor $\Gamma(v/2+1)e^{-\kappa}(\kappa+1)^{-v/2}$, we obtain

$$ \frac{v}{2}{}_1F_1(1+v/2,2,\kappa) - \frac{v}{2}{}_1F_1(1+v/2,1,\kappa)(\kappa+1)^{-1}. \tag{10.68} $$

Multiplying by $(\kappa+1)$ and dividing by $v/2$ (both are positive numbers), we obtain

$$ {}_1F_1(1+v/2,2,\kappa)(\kappa+1) - {}_1F_1(1+v/2,1,\kappa). \tag{10.69} $$

Using (Gradshteyn and Ryshik 1994, 9.212(2), p.1086), we have $\kappa\, {}_1F_1(1+v/2,2,\kappa) - {}_1F_1(1+v/2,1,\kappa) = -{}_1F_1(v/2,1,\kappa)$. Therefore, we finally obtain (up to a positive constant)

$$ {}_1F_1(1+v/2,2,\kappa) - {}_1F_1(v/2,1,\kappa). \tag{10.70}$$

Now, by definition, the hypergeometric function ${}_1F_1(a,b,z)$ is equal to $\sum_{n=0}^{\infty} \frac{(a)_n}{(b)_n}\frac{z^n}{n!}$, where $(a)_n = a(a+1)...(a+n-1)$ is the rising factorial. If $v/2<1$, then $\frac{(1+v/2)_n}{(2)_n} > \frac{(v/2)_n}{(1)_n}$ and hence ${}_1F_1(1+v/2,2,\gamma) - {}_1F_1(v/2,1,\gamma) > 0$, On the other hand, if $v/2>1$, then $\frac{(1+v/2)_n}{(2)_n} < \frac{(v/2)_n}{(1)_n}$ and hence ${}_1F_1(1+v/2, 2,\kappa) - {}_1F_1(v/2,1,\kappa) < 0$. This completes the proof of the theorem. ■

Proof of Theorem 10 (a) First of all, using the change of variable $I = A^2$, one computes

$$\int_0^\infty \log A^2 P_{\mathrm{Ri}}(A \mid \varepsilon,\sigma^2)\, dA = \int_0^\infty \log I \frac{1}{2\sigma^2} I_0\Big(\frac{\varepsilon}{\sigma^2}\sqrt{I}\Big) e^{-\varepsilon^2/(2\sigma^2)} e^{-I/(2\sigma^2)}\, dI, \tag{10.71}$$

which is a Laplace transform equal to $\Gamma(0,\frac{\varepsilon^2}{2\sigma^2}) + \log\varepsilon^2$, where $\Gamma(0,x)$ is the incomplete gamma function $\int_x^\infty \frac{e^{-t}}{t}\, dt$. Then, after subtraction by the term $\log(\varepsilon^2+2\sigma^2)$, one obtains $\Gamma(0,\frac{\varepsilon^2}{2\sigma^2}) + \log(\frac{\varepsilon^2}{\varepsilon^2+2\sigma^2})$, which is equal to $\Gamma(0,\kappa) + \log(\frac{\kappa}{\kappa+1})$ (where $\kappa = \varepsilon^2/(2\sigma^2)$).

(b) Again, using the change of variable $I = A^2$, we compute

$$\begin{aligned} &\int_0^\infty A^2 \log A^2 P_{\mathrm{Ri}}(A \mid \varepsilon,\sigma^2)\, dA \\ &= \int_0^\infty I \log I \frac{1}{2\sigma^2} I_0\Big(\frac{\varepsilon}{\sigma^2}\sqrt{I}\Big) e^{-\varepsilon^2/(2\sigma^2)} e^{-I/(2\sigma^2)}\, dI. \end{aligned} \tag{10.72}$$

This Laplace transform is equal to $4\sigma^2 - 2e^{-\frac{\varepsilon^2}{2\sigma^2}}\sigma^2 + (\varepsilon^2+2\sigma^2)\big(\Gamma(0,\frac{\varepsilon^2}{2\sigma^2}) + \log\varepsilon^2\big)$. Dividing by $\varepsilon^2+2\sigma^2$ and subtracting $E[\log I] = \Gamma(0,\frac{\varepsilon^2}{2\sigma^2}) + \log\varepsilon^2$ (from the proof of part a)), one obtains $(4\sigma^2 - 2e^{-\frac{\varepsilon^2}{2\sigma^2}}\sigma^2) \div (\varepsilon^2+2\sigma^2)$, which is equal to $\frac{1}{\kappa+1}(2-e^{-\kappa})$, after algebraic simplifications. ■

Proof of Theorem 11 (a) From Abramowitz and Stegun (1972, (6.5.15), p. 262), we have $\Gamma(0,\kappa) = E_1(\kappa)$ (the exponential integral). Moreover, from Abramowitz and Stegun (1972, (5.1.11), p. 229), $E_1(\kappa) = -\gamma_E - \log\kappa + \sum_{n=1}^\infty \frac{(-1)^n\kappa^n}{nn!}$. We conclude that $U_{\mathrm{Ri}}(\kappa) = -\gamma_E - \log(1+\kappa) + \sum_{n=1}^\infty \frac{(-1)^n\kappa^n}{nn!}$. Henceforth, $\lim_{\kappa\to 0} U_{\mathrm{Ri}}(\kappa) = -\gamma_E$.

(b) Since $\Gamma(0,\kappa) = \int_\kappa^\infty \frac{e^{-t}}{t}\, dt$, it follows that $\lim_{\kappa\to\infty}\Gamma(0,\kappa) = 0$. Moreover, $\lim_{\kappa\to\infty}\log\frac{\kappa}{\kappa+1} = 0$.

(c) We compute $\frac{d}{d\kappa}U_{\mathrm{Ri}}(\kappa) = -\frac{e^{-\kappa}}{\kappa} + \frac{1}{\kappa} - \frac{1}{\kappa+1}$. This is positive because $e^{\kappa} > 1 + \kappa$, for $\kappa > 0$. ■

Proof of Theorem 12 Parts (a) and (b) follow from basic Calculus.

(c) We compute $\frac{d}{d\kappa}X_{\mathrm{Ri}}(\kappa) = \frac{e^{-\kappa}(\kappa+1)-(2-e^{-\kappa})}{(\kappa+1)^2}$. Ignoring the positive factor $1/(\kappa+1)^2$, we obtain $e^{-\kappa}(2+\kappa) - 2$. This is negative since $e^{\kappa} > 1 + \kappa/2$, for $\kappa > 0$. ■

Lemma 5 *Let $\alpha > 0$ be fixed. Denote any root of $\frac{\partial}{\partial\sigma^2}L(\sigma^2, \alpha)$ by $\sigma^2(\alpha, \tilde{A})$, where $\tilde{A} = \{A_1, A_2, ..., A_N\}$.*

(a) *If $0 < \alpha \leq 1/2$, then $\sigma^2(\alpha, \tilde{A}) \geq \frac{\alpha+\alpha^2+\sqrt{2\alpha^3+\alpha^4}}{\alpha^2}\left(\overline{A}\right)^2$.*

(b) *If $1/2 < \alpha \leq 3$, then $\sigma^2(\alpha, \tilde{A}) \geq \frac{1}{2\alpha^2}\left(\overline{A}\right)^2$.*

(c) *If $\alpha > 3$, then $\sigma^2(\alpha, \tilde{A}) \geq \frac{2\alpha-3+\sqrt{4\alpha-7}}{4(\alpha-2)^2}\left(\overline{A}\right)^2$.*

(d) *If $0 < \alpha \leq 1/2$, then $\sigma^2(\alpha, \tilde{A}) \leq \frac{1}{2\alpha^2}\left(\overline{A}\right)^2$.*

(e) *If $1/2 < \alpha \leq 3/2$, then $\sigma^2(\alpha, \tilde{A}) \leq \frac{1}{2(\alpha/2+1/4)^2}\left(\overline{A}\right)^2$.*

(f) *If $3/2 < \alpha \leq 3$, then $\sigma^2(\alpha, \tilde{A}) \leq \frac{1}{2}\left(\overline{A}\right)^2$.*

(g) *If $\alpha > 3$, then $\sigma^2(\alpha, \tilde{A}) \leq \frac{1}{2(\alpha-2)}\overline{A^2}$.*

(h) *The function $\frac{\partial}{\partial\sigma^2}L(\sigma^2, \alpha)$ is positive at the lower bounds mentioned in parts (a) to (c), whereas it is negative at the upper bounds of parts (d) to (g).*

Proof We compute

$$\sigma^2 \frac{\frac{\partial}{\partial\sigma^2}P_{\mathrm{K}}(A \mid \sigma^2, \alpha)}{P_{\mathrm{K}}(A \mid \sigma^2, \alpha)} = -\alpha + \left(\frac{1}{\sqrt{2\sigma^2}}A\right)\frac{K_{\alpha}\left(\sqrt{\frac{2}{\sigma^2}}A\right)}{K_{\alpha-1}\left(\sqrt{\frac{2}{\sigma^2}}A\right)}. \tag{10.73}$$

Part a). If $0 < \alpha \leq 1/2$, then $K_{\alpha-1}(x) = K_{1-\alpha}(x) < K_1(x)$ and $K_{\alpha}(x) > K_0(x)$ for any $x > 0$. Also, the inequality $K_0(x)/K_1(x) > 1 - \frac{1}{(x+1)}$ holds for any $x > 0$. Therefore, from Eq. (10.73), we obtain $\sigma^2 \frac{\frac{\partial}{\partial\sigma^2}P_{\mathrm{HK}}(A \mid \sigma^2, \alpha)}{P_{\mathrm{HK}}(A \mid \sigma^2, \alpha)} > -\alpha + \frac{1}{2}f(\sqrt{\frac{2}{\sigma^2}}A)$, where $f(x) = x(1 - \frac{1}{(x+1)})$. Thus, we obtain that

$$\sigma^2 \frac{\partial}{\partial\sigma^2}L(\sigma^2, \alpha) > -N\alpha + \frac{1}{2}\sum_{i=1}^{N} f(\sqrt{\frac{2}{\sigma^2}}A_i). \tag{10.74}$$

Here, L denotes L_{K}. Now, the function $f(x)$ is convex. Therefore, from Jensen's inequality (Jensen 1906), we conclude that

$$\sigma^2 \frac{\partial}{\partial\sigma^2}L(\sigma^2, \alpha) > -N\alpha + \frac{N}{2}f(\sqrt{\frac{2}{\sigma^2}}\overline{A}). \tag{10.75}$$

But the right-hand side of Eq. (10.75) is positive if $\sigma^2 < \frac{\alpha+\alpha^2+\sqrt{2\alpha^3+\alpha^4}}{\alpha^2}\left(\overline{A}\right)^2$. This proves part a).

Part b). If $\alpha > 1/2$, then $K_\alpha(x) > K_{\alpha-1}(x)$ for any $x > 0$. Therefore, from Eq. (10.73), we obtain $\sigma^2 \frac{\frac{\partial}{\partial\sigma^2}P_K(A\,|\,\sigma^2,\alpha)}{P_K(A\,|\,\sigma^2,\alpha)} > -\alpha + \frac{1}{\sqrt{2\sigma^2}}A$. Thus, we conclude that

$$\sigma^2 \frac{\partial}{\partial\sigma^2}L(\sigma^2,\alpha) > -N\alpha + \frac{1}{\sqrt{2\sigma^2}}\sum_{i=1}^N A_i. \tag{10.76}$$

But the right-hand side of Eq. (10.76) is positive if $\sigma^2 < \frac{1}{2\alpha^2}\left(\overline{A}\right)^2$. This proves part b).

Part c). If $\alpha > 3$, then $\frac{x}{2}\frac{K_\alpha(x)}{K_{\alpha-1}(x)} > \frac{x}{2} \times \left(\frac{2(\alpha-1)}{x} + \frac{1}{\frac{2(\alpha-2)}{x}+1}\right)$. Thus, $\sigma^2 \frac{\frac{\partial}{\partial\sigma^2}P_K(A\,|\,\sigma^2,\alpha)}{P_K(A\,|\,\sigma^2,\alpha)}$ has lower bound $-1 + f\left(\frac{A}{\sqrt{2\sigma^2}}\right)$, where $f(x) = \left(\frac{(\alpha-2)}{x^2} + \frac{1}{x}\right)^{-1}$. Thus, we conclude that

$$\sigma^2 \frac{\partial}{\partial\sigma^2}L(\sigma^2,\alpha) > -N + \sum_{i=1}^N \frac{1}{\frac{2\sigma^2(\alpha-2)}{A_i^2} + \frac{\sqrt{2\sigma^2}}{A_i}}. \tag{10.77}$$

From Jensen's inequality, we then obtain

$$\sigma^2 \frac{\partial}{\partial\sigma^2}L(\sigma^2,\alpha) > -N + N\frac{1}{\frac{2\sigma^2(\alpha-2)}{\overline{A}^2} + \frac{\sqrt{2\sigma^2}}{\overline{A}}}, \tag{10.78}$$

because the function $f(x)$ above is convex. But the right-hand side of Eq. (10.78) is positive if $\sigma^2 < \frac{2\alpha-3+\sqrt{4\alpha-7}}{4(\alpha-2)^2}\left(\overline{A}\right)^2$. This proves part c).

Part d). If $0 < \alpha \leq 1/2$, then $K_\alpha(x) < K_{\alpha-1}(x)$ for any $x > 0$. Therefore, from Eq. (10.73), we obtain $\sigma^2 \frac{\frac{\partial}{\partial\sigma^2}P_K(A\,|\,\sigma^2,\alpha)}{P_K(A\,|\,\sigma^2,\alpha)} < -\alpha + \frac{1}{\sqrt{2\sigma^2}}A$. This yields the inequality

$$\sigma^2 \frac{\partial}{\partial\sigma^2}L(\sigma^2,\alpha) < -N\alpha + \frac{1}{\sqrt{2\sigma^2}}\sum_{i=1}^N A_i. \tag{10.79}$$

But the right-hand side of Eq. (10.79) is negative if $\sigma^2 > \frac{1}{2\alpha^2}\left(\overline{A}\right)^2$. This proves part d).

Part e). If $1/2 < \alpha \leq 3/2$, then $\frac{K_\alpha(x)}{K_{\alpha-1}(x)} < 1 + \frac{(\alpha-1/2)}{x}$ for any $x > 0$. Therefore, we have $\sigma^2 \frac{\frac{\partial}{\partial\sigma^2}P_K(A\,|\,\sigma^2,\alpha)}{P_K(A\,|\,\sigma^2,\alpha)} < -\frac{\alpha}{2} - \frac{1}{4} + \frac{1}{\sqrt{2\sigma^2}}A$. It follows that

$$\sigma^2 \frac{\partial}{\partial\sigma^2}L(\sigma^2,\alpha) < -N(\alpha/2 + 1/4) + \frac{1}{\sqrt{2\sigma^2}}\sum_{i=1}^N A_i. \tag{10.80}$$

But the right-hand side of Eq. (10.80) is negative if $\sigma^2 > \frac{1}{2(\alpha/2+1/4)^2}\left(\overline{A}\right)^2$. This proves part e).

Part f). If $3/2<\alpha\leq 3$, then $\frac{K_\alpha(x)}{K_{\alpha-1}(x)}<1+\frac{2(\alpha-1)}{x}$ for any $x>0$. Thus, we obtain $\sigma^2\frac{\partial}{\partial\sigma^2}P_{\mathrm{K}}(A\,|\,\sigma^2,\alpha)}{P_{\mathrm{K}}(A\,|\,\sigma^2,\alpha)}<-\alpha+(\alpha-1)+\frac{1}{\sqrt{2\sigma^2}}A$. From there, we conclude that

$$\sigma^2\frac{\partial}{\partial\sigma^2}L(\sigma^2,\alpha)<-N+\frac{1}{\sqrt{2\sigma^2}}\sum_{i=1}^{N}A_i. \tag{10.81}$$

But the right-hand side of Eq. (10.81) is negative if $\sigma^2>\frac{1}{2}\left(\overline{A}\right)^2$. Hence, part f) of the Theorem.

Part g). If $3<\alpha$, then $\frac{x}{2}\frac{K_\alpha(x)}{K_{\alpha-1}(x)}<(\alpha-1)+\frac{x^2}{4(\alpha-2)}$ for any $x>0$. Therefore, we obtain

$$\sigma^2\frac{\partial}{\partial\sigma^2}L(\sigma^2,\alpha)<-N+\frac{1}{2\sigma^2(\alpha-2)}\sum_{i=1}^{N}A_i^2. \tag{10.82}$$

But the right-hand side of Eq. (10.82) is negative if $\sigma^2>\frac{1}{2(\alpha-2)}\overline{A^2}$. Hence, part g) of the Theorem.

Finally, part h) follows from the proof of parts a) to g). ■

Proof of Theorem 18 From Lemma 5, for any $\alpha>0$, there exist two values $0<\sigma_1^2<\sigma_2^2$ for which $\frac{\partial}{\partial\sigma^2}L(\sigma_1^2,\alpha)>0$ and $\frac{\partial}{\partial\sigma^2}L(\sigma_2^2,\alpha)<0$, where L denotes L_{K}. Thus, by the Intermediate Value Theorem, there exists $\sigma^2=\sigma^2(\alpha,\tilde{A})$ such that $\frac{\partial}{\partial\sigma^2}L(\sigma^2,\alpha)=0$. ■

Proof of Theorem 19 Part a). Let $0<\alpha<1/2$. In Eq. (10.32), the term $-\psi(\alpha)+\log\left(\frac{x}{2}\right)-\frac{\frac{\partial}{\partial\alpha}K_{1-\alpha}(x)}{K_{1-\alpha}(x)}$ is an increasing function of $x>0$. Also, from Lemma 5 part d), we have $\sigma^2(\alpha,\tilde{A})\leq\frac{1}{2\alpha^2}\left(\overline{A}\right)^2$. Therefore, we obtain $\sqrt{\frac{2}{\sigma^2}}A_i\geq 2\alpha\frac{A_i}{\overline{A}}$. It follows that $LB(\alpha)=-\psi(\alpha)+\log\left(\alpha\frac{A_i}{\overline{A}}\right)-\frac{\frac{\partial}{\partial\alpha}K_{1-\alpha}\left(2\alpha\frac{A_i}{\overline{A}}\right)}{K_{1-\alpha}\left(2\alpha\frac{A_i}{\overline{A}}\right)}$ is a lower bound for that term. Now, from Abramowitz and Stegun (1972, Eq. (9.6.45), p. 377), we have $\frac{\frac{\partial}{\partial\alpha}K_{1-\alpha}(x)}{K_{1-\alpha}(x)}\approx\frac{\frac{\partial}{\partial\alpha}K_1(x)}{K_1(x)}=\frac{K_0(x)}{xK_1(x)}$ as $\alpha\to 0$. Moreover, from Abramowitz and Stegun (1972, Eqs. (9.6.8) and (9.6.9), p. 375), we have $\frac{K_0(x)}{xK_1(x)}\sim-\log x$ for small values of $x>0$. But $x=2\alpha\frac{A_i}{\overline{A}}$ has small values for $\alpha\to 0$. Thus, we obtain $\lim_{\alpha\to 0}\alpha LB(\alpha)=\lim_{\alpha\to 0}\alpha\left\{-\psi(\alpha)+\log\left(\alpha\frac{A_i}{\overline{A}}\right)+\log\left(2\alpha\frac{A_i}{\overline{A}}\right)\right\}=1$. This proves part a).

Part b). First of all, we observe that there exist constants $0<C_1<C_2$, such that $\frac{1}{C_2}\leq\liminf_{\alpha\to\infty}\frac{\sigma^2(\alpha,\tilde{A})}{1/\alpha}\leq\limsup_{\alpha\to\infty}\frac{\sigma^2(\alpha,\tilde{A})}{1/\alpha}\leq\frac{1}{C_1}$. The first inequality follows from Lemma 5 part c), whereas the third inequality follows from Lemma 5 part g).

Let L denote L_K. Since by definition $\frac{\partial}{\partial\sigma^2}L(\sigma^2,\alpha)|_{\sigma^2(\alpha,\bar{A})}=0$, we might as well consider the expression $\alpha\frac{\partial}{\partial\alpha}L(\sigma^2,\alpha)-\sigma^2\frac{\partial}{\partial\sigma^2}L(\sigma^2,\alpha)$. From Eqs. (10.32) and (10.33), each term of that expression is equal to

$$\begin{aligned}&-\alpha\psi(\alpha)+\alpha\log\Big(\frac{1}{\sqrt{2\sigma^2}}A_i\Big)+\alpha\frac{\frac{\partial}{\partial\alpha}K_{\alpha-1}\Big(\sqrt{\frac{2}{\sigma^2}}A_i\Big)}{K_{\alpha-1}\Big(\sqrt{\frac{2}{\sigma^2}}A_i\Big)}\\&+\alpha-\Big(\frac{1}{\sqrt{2\sigma^2}}A_i\Big)\frac{K_\alpha\Big(\sqrt{\frac{2}{\sigma^2}}A_i\Big)}{K_{\alpha-1}\Big(\sqrt{\frac{2}{\sigma^2}}A_i\Big)}.\end{aligned}\tag{10.83}$$

From Abraham and Lyons (2002, Eq. (46)), we have $\frac{\frac{\partial}{\partial\alpha}K_{\alpha-1}(x)}{K_{\alpha-1}(x)}\sim\psi(\alpha-1)-\log(x/2)+\frac{x^2}{4\alpha^2}$ for large values of α. Also, from Abraham and Lyons (2002, Eq. (45)), we have $K_\alpha(x)\sim\frac{\Gamma(\alpha)}{2(x/2)^\alpha}\Big(1-\frac{(x/2)^2}{(\alpha-1)(\alpha-2)}\Big)^{\alpha-2}$ for large values of α. Therefore, taking $\sigma^2=1/(C\alpha)$, we obtain the asymptotic expression

$$-\alpha\psi(\alpha)+\alpha\psi(\alpha-1)+\frac{CA_i^2}{2}+\alpha-(\alpha-1)\frac{\Big(1-\frac{C\alpha A_i^2}{2(\alpha-1)(\alpha-2)}\Big)^{\alpha-2}}{\Big(1-\frac{C\alpha A_i^2}{2(\alpha-2)(\alpha-3)}\Big)^{\alpha-3}}.\tag{10.84}$$

Finally, Eq. (10.84) tends to 0 as α tends to infinity. This proves part b). ■

Proof of Theorem 20 Part a). Let $0<\alpha<1$. We consider again Eq. (10.83). Using the asymptotic forms (for small values of x and of α) $\frac{\frac{\partial}{\partial\alpha}K_{1-\alpha}(x)}{K_{1-\alpha}(x)}\approx\frac{K_0(x)}{xK_1(x)}$, $\frac{K_0(x)}{xK_1(x)}\sim-\log x$ and $(\frac{x}{2})\frac{K_0(x)}{K_1(x)}\sim-\frac{x^2}{2}\log x$, and setting $x=\sqrt{\frac{2}{\sigma^2}}A_i$ with $\sigma^2=1/(C\alpha)$ and $C=2/\overline{I}$, we obtain the asymptotic expression

$$-\alpha\psi(\alpha)+\alpha\log\big(\frac{1}{2}\sqrt{\alpha}\sqrt{C}A_i\big)+\alpha\log\big(\sqrt{\alpha}\sqrt{C}A_i\big)+\alpha+\alpha^2CA_i^2\log\big(\sqrt{\alpha}\sqrt{C}A_i\big).\tag{10.85}$$

Part a) then follows by taking the limit of Eq. (10.85) as $\alpha\to0$.

Part b). Taking $\sigma^2=1/(C\alpha)$, where $C=2/\overline{I}$, into Eq. (10.84), we obtain the limit 0 as $\to\infty$. This proves part b). ■

Proof of Theorem 21 a) At $\alpha=0$, we have $\Gamma(\alpha+v/2)=\Gamma(v/2)$. Also, $\Gamma(\alpha)$ has a simple pole with residue 1 at $\alpha=0$. Therefore, $\frac{\Gamma(\alpha+1/2)}{\alpha^{v/2}\Gamma(\alpha)}\sim\Gamma(v/2)\alpha^{1-v/2}$ at $\alpha\approx0$, which shows part a).

b) Using Sterling's formula, we have $\frac{\Gamma(\alpha+v/2)}{\alpha^{v/2}\Gamma(\alpha)}\sim\frac{e^{-\alpha-v/2}(\alpha+v/2)^{\alpha+v/2-1/2}}{\alpha^{v/2}e^{-\alpha}\alpha^{\alpha-1/2}}$, which is equal to $e^{-v/2}\Big(1+\frac{v/2}{\alpha}\Big)^\alpha\Big(1+\frac{v/2}{\alpha}\Big)^{v/2-1/2}$. Therefore, $\lim_{\alpha\to\infty}\frac{\Gamma(\alpha+v/2)}{\alpha^{v/2}\Gamma(\alpha)}=1$, and we are done.

c) Using the logarithmic derivative, we have $\frac{d}{d\alpha}M_{\mathrm{K}}^{(\nu)}(\alpha) = M_{\mathrm{K}}^{(\nu)}(\alpha)\Big(\psi(\alpha+\nu/2) - \psi(\alpha) - \frac{\nu}{2\alpha}\Big)$. Now, we have $M_{\mathrm{K}}^{(\nu)}(\alpha) > 0$. Also, $\frac{1}{\alpha} = \psi(\alpha+1) - \psi(\alpha)$, and hence $\psi(\alpha+\nu/2) - \psi(\alpha) - \frac{\nu}{2\alpha} = \psi(\alpha+\nu/2) - \Big(\frac{\nu}{2}\psi(\alpha+1) + (1-\frac{\nu}{2})\psi(\alpha)\Big)$. Since the function ψ is convex, we conclude that $\psi(\alpha+\nu/2) - \Big(\frac{\nu}{2}\psi(\alpha+1) + (1-\frac{\nu}{2})\psi(\alpha)\Big) > 0$, if $\nu/2 < 1$, whereas it is negative if $\nu/2 > 1$. ■

Proof of Theorem 22 a) We consider the function $f(\alpha) = \frac{\Gamma(\nu+1)\Gamma(\nu+\alpha)\Gamma(\alpha)}{\Gamma^2(\nu/2+1)\Gamma^2(\nu/2+\alpha)}$, noting that $R_{\mathrm{K}}^{(\nu)} = \big(f(\alpha)-1\big)^{-1/2}$. Now, as $\alpha \to 0$, we have $\Gamma(\alpha) \to \infty$, whereas $\frac{\Gamma(\nu+1)\Gamma(\nu+\alpha)}{\Gamma^2(\nu/2+1)\Gamma^2(\nu/2+\alpha)} \to \frac{\Gamma(\nu+1)\Gamma(\nu)}{\Gamma^2(\nu/2+1)\Gamma^2(\nu/2)} > 0$. This proves part a).

b) Next, using directly Sterling's formula for $\Gamma(\nu+\alpha)$, $\Gamma(\alpha)$ and $\Gamma(\nu/2+\alpha)$, one finds that $\lim_{\alpha\to\infty} f(\alpha) = \frac{\Gamma(\nu+1)}{\Gamma^2(\nu/2+1)}$, which proves part b).

c) Finally, taking the logarithmic derivative of $f(\alpha)$ yields $\frac{df}{d\alpha} = f(\alpha)\big(\psi(\nu+\alpha) + \psi(\alpha) - 2\psi(\nu/2+\alpha)\big)$. This is negative, since $f(\alpha) > 0$ and $\psi(\nu/2+\alpha) > \frac{1}{2}(\psi(\nu+\alpha) + \psi(\alpha))$ (because ψ is a convex function). It follows that $f(\alpha) > \lim_{\alpha\to\infty} f(\alpha) = \frac{\Gamma(\nu+1)}{\Gamma^2(\nu/2+1)}$. We claim that $g(\nu) = \frac{\Gamma(\nu+1)}{\Gamma^2(\nu/2+1)} > 1$, for any $\nu > 0$. In fact, the function $g(\nu)$ is increasing (its derivative is equal to $g(\nu)(\psi(\nu+1) - \psi(\nu/2+1))$) and $g(0) = 1$. Therefore, $f(\alpha) > 1$, and it follows that $\big(f(\alpha)-1\big)^{-1/2}$ is an increasing function. This completes the proof of part c). ■

Proof of Theorem 23 This is an immediate consequence of Theorem 28. ■

Proof of Theorem 24 Starting with Eq. (10.44), we compute

$$\begin{aligned} M_{\mathrm{HK}}^{(\nu)}(\gamma,\alpha) &= \frac{\Gamma(\nu/2+1)}{(\gamma+\alpha)^{\nu/2}} \int_0^\infty w^{\nu/2}\, {}_1F_1(-\nu/2, 1, -\frac{\gamma}{w}) \mathcal{G}(w \mid \alpha, 1)\, dw \\ &= \frac{\Gamma(\nu/2+1)}{(\gamma+\alpha)^{\nu/2}} \int_0^\infty w^{\nu/2} e^{-\gamma/w}\, {}_1F_1(1+\nu/2, 1, \frac{\gamma}{w}) \mathcal{G}(w \mid \alpha, 1)\, dw \\ &= \frac{1}{(\gamma+\alpha)^{\nu/2}} \frac{\Gamma(\nu/2+1)}{\Gamma(\alpha)} \sum_{n=0}^\infty \frac{(1+\nu/2)_n}{n!n!} \gamma^n \int_0^\infty w^{\nu/2+\alpha-n-1} e^{-\gamma/w} e^{-w}\, dw. \end{aligned} \tag{10.86}$$

Using (Erdélyi 1954, I, p. 146, (29)), this is equal to

$$\begin{aligned} &\frac{1}{(\gamma+\alpha)^{\nu/2}} \frac{\Gamma(\nu/2+1)}{\Gamma(\alpha)} \sum_{n=0}^\infty \frac{(1+\nu/2)_n}{n!n!} \gamma^n 2(\sqrt{\gamma})^{\nu/2+\alpha-n} K_{\nu/2+\alpha-n}(2\sqrt{\gamma}) \\ &= \frac{2}{(\gamma+\alpha)^{\nu/2}} \frac{\Gamma(\nu/2+1)}{\Gamma(\alpha)} \sum_{n=0}^\infty \frac{(1+\nu/2)_n}{n!n!} (\sqrt{\gamma})^{\nu/2+\alpha+n} K_{\nu/2+\alpha-n}(2\sqrt{\gamma}). \end{aligned} \tag{10.87}$$

This completes the proof of Theorem 25. ■

Proof of Theorem 26 a) This follows from Theorem 24, part b), and Theorem 13.

b) From Theorem 24, part a), we know that $M_{\text{HK}}^{(v)}(\gamma,\alpha)$ is equal to $\frac{\Gamma(v/2+1)}{(\gamma+\alpha)^{v/2}}\int_0^\infty w^{v/2}\,{}_1F_1(-v/2,1,-\gamma/w)\mathcal{G}(w\,|\,\alpha,1)\,dw$. From Luke (1962, pp. 7–8), we have $\Gamma(v/2+1)\,{}_1F_1(-v/2,1,-z)=\Gamma(v/2+1)e^{-z}\,{}_1F_1(1+v/2,1,z)=z^{v/2}(1+O(1/z))$, for large values of z. Let $\eta>0$ be a real number (arbitrarily small). Take z_0 sufficiently large so that $(1-\eta)z^{v/2}\le\Gamma(v/2+1)\,{}_1F_1(-v/2,1,-z)\le(1+\eta)z^{v/2}$, for any $z\ge z_0$. Then, if $\gamma/w\ge z_0$, i.e. $w\le\gamma/z_0$, we have $(1-\eta)\gamma^{v/2}\le\Gamma(v/2+1)w^{v/2}\,{}_1F_1(-v/2,1,-\gamma/w)\le(1+\eta)\gamma^{v/2}$. Therefore, the integral $\frac{\Gamma(v/2+1)}{(\gamma+\alpha)^{v/2}}\int_0^{\gamma/z_0} w^{v/2}\,{}_1F_1(-v/2,1,-\gamma/w)\mathcal{G}(w\,|\,\alpha,1)\,dw$ has lower bound $(1-\eta)\frac{\gamma^{v/2}}{(\gamma+\alpha)^{v/2}}Pr(w\le\gamma/z_0)$ and upper bound $(1+\eta)\frac{\gamma^{v/2}}{(\gamma+\alpha)^{v/2}}Pr(w\le\gamma/z_0)$. On the other hand, the function ${}_1F_1(-v/2,1,-z)$ equals 1 at $z=0$, and hence there is a real number $C>0$ such that $0<{}_1F_1(-v/2,1,-\gamma/w)\le C$ for any $w>\gamma/z_0$. Thus, the integral $\frac{\Gamma(v/2+1)}{(\gamma+\alpha)^{v/2}}\int_{\gamma/z_0}^\infty w^{v/2}\,{}_1F_1(-v/2,1,-\gamma/w)\mathcal{G}(w\,|\,\alpha,1)\,dw$ has lower bound 0 and upper bound $\frac{\Gamma(v/2+1)}{(\gamma+\alpha)^{v/2}}C\frac{\Gamma(v/2+\alpha)}{\Gamma(\alpha)}$. But now, $\lim_{\gamma\to\infty}\frac{\gamma^{v/2}}{(\gamma+\alpha)^{v/2}}=1$, $\lim_{\gamma\to\infty}Pr(w\le\gamma/z_0)=1$, and $\lim_{\gamma\to\infty}\frac{1}{(\gamma+\alpha)^{v/2}}=0$. Therefore, we obtain $\liminf_{\gamma\to\infty}M_{\text{HK}}^{(v)}(\gamma,\alpha)\ge1-\eta$ and $\limsup_{\gamma\to\infty}M_{\text{HK}}^{(v)}(\gamma,\alpha)\le1+\eta$. Since η is arbitrarily small, we conclude that $\lim_{\gamma\to\infty}M_{\text{HK}}^{(v)}(\gamma,\alpha)=1$.

c) We consider the function $f(\gamma,w)=\frac{{}_1F_1(1+v/2,1,\gamma/w)}{e^{\gamma/w}(\gamma+\alpha)^{v/2}}$. From Theorem 24, part a), we have $M_{\text{HK}}^{(v)}(\gamma,\alpha)=\Gamma(v/2+1)\int_0^\infty w^{v/2}f(\gamma,w)\mathcal{G}(w\,|\,\alpha,1)\,dw$. Thus, we obtain $\frac{\partial}{\partial\gamma}M_{\text{HK}}^{(v)}(\gamma,\alpha)=\Gamma(v/2+1)\int_0^\infty w^{v/2}\frac{\partial}{\partial\gamma}f(\gamma,w)\mathcal{G}(w\,|\,\alpha,1)\,dw$.

We compute the value of $\frac{\partial}{\partial\gamma}f(\gamma,w)$ as

$$\frac{\frac{d}{dz}{}_1F_1(1+v/2,1,\gamma/w)w^{-1}-{}_1F_1(1+v/2,1,\gamma/w)\left(w^{-1}+\frac{v}{2}(\gamma+\alpha)^{-1}\right)}{e^{\gamma/w}(\gamma+\alpha)^{v/2}}. \tag{10.88}$$

Using (Gradshteyn and Ryshik 1994, 9.213, p. 1086) and (Gradshteyn and Ryshik 1994, 9.212(3), p. 1086), we have $\frac{d}{dz}{}_1F_1(1+v/2,1,\gamma/w)=(1+v/2)\,{}_1F_1(2+v/2,2,\gamma/w)=\frac{v}{2}\,{}_1F_1(1+v/2,2,\gamma/w)+{}_1F_1(1+v/2,1,\gamma/w)$. So, we obtain after algebraic simplifications

$$\frac{v/2}{e^{\gamma/w}(\gamma+\alpha)^{v/2+1}}\left\{{}_1F_1(1+v/2,2,\gamma/w)\left(\frac{\gamma}{w}+\frac{\alpha}{w}\right)-{}_1F_1(1+v/2,1,\gamma/w)\right\}. \tag{10.89}$$

Using (Gradshteyn and Ryshik 1994, 9.212(2), p. 1086), we have $\frac{\gamma}{w}{}_1F_1(1+v/2,2,\gamma/w) - {}_1F_1(1+v/2,1,\gamma/w) = -{}_1F_1(v/2,1,\gamma/w)$. Therefore, we finally obtain

$$\frac{\alpha v/2}{e^{\gamma/w}(\gamma+\alpha)^{v/2+1}w}\left\{{}_1F_1(1+v/2,2,\gamma/w) - \frac{w}{\alpha}{}_1F_1(v/2,1,\gamma/w)\right\}. \tag{10.90}$$

Now, let $v/2<1$. Then, we obtain the strict lower bound for $\frac{\partial}{\partial\gamma}f(\gamma,w)$

$$\frac{\alpha v/2}{e^{\gamma/w}(\gamma+\alpha)^{v/2+1}w}\left\{{}_1F_1(1+v/2,2,\gamma/w) - \frac{w}{\alpha}{}_1F_1(1+v/2,2,\gamma/w)\right\}. \tag{10.91}$$

Consider the function $g(\gamma,w) = \Gamma(v/2+1)w^{v/2}\frac{\alpha v/2}{e^{\gamma/w}(\gamma+\alpha)^{v/2+1}w}{}_1F_1(1+v/2,2,\gamma/w)$. We have shown that

$$\frac{\partial}{\partial\gamma}M_{\mathrm{HK}}^{(v)}(\gamma,\alpha) > \int_0^\infty g(\gamma,w)\mathcal{G}(w\,|\,\alpha,1)\,dw - \int_0^\infty \frac{w}{\alpha}g(\gamma,w)\mathcal{G}(w\,|\,\alpha,1)\,dw. \tag{10.92}$$

But, $\frac{w}{\alpha}\mathcal{G}(w\,|\,\alpha,1) = \mathcal{G}(w\,|\,\alpha+1,1)$. So, we obtain

$$\frac{\partial}{\partial\gamma}M_{\mathrm{HK}}^{(v)}(\gamma,\alpha) > \int_0^\infty g(\gamma,w)\mathcal{G}(w\,|\,\alpha,1)\,dw - \int_0^\infty g(\gamma,w)\mathcal{G}(w\,|\,\alpha+1,1)\,dw. \tag{10.93}$$

Thus, we want to show that $\int_0^\infty g(\gamma,w)\mathcal{G}(w\,|\,\alpha,1)\,dw - \int_0^\infty g(\gamma,w)\mathcal{G}(w\,|\,\alpha+1,1)\,dw \geq 0$. Ignoring the positive factor $\Gamma(v/2+1)\frac{\alpha v/2}{(\gamma+\alpha)^{v/2+1}}$, we are thus lead to the function $h(\gamma,w) = \frac{w^{v/2-1}{}_1F_1(1+v/2,2,\gamma/w)}{e^{\gamma/w}}$, and we show that $\int_0^\infty h(\gamma,w)\mathcal{G}(w\,|\,\alpha,1)\,dw - \int_0^\infty h(\gamma,w)\mathcal{G}(w\,|\,\alpha+1,1)\,dw \geq 0$ as follows. In Lemma 6, we show that $h(\gamma,w)$ is decreasing in the variable w, if $v/2<1$. Then, in Lemma 7, we show that for any decreasing positive function $H(w)$, we have $\int_0^\infty H(w)\mathcal{G}(w\,|\,\alpha,1)\,dw - \int_0^\infty H(w)\mathcal{G}(w\,|\,\alpha+1,1)\,dw \geq 0$.

Next, let $v/2>1$. Then, we obtain the strict upper bound for $\frac{\partial}{\partial\gamma}f(\gamma,w)$

$$\frac{\alpha v/2}{e^{\gamma/w}(\gamma+\alpha)^{v/2+1}w}\left\{{}_1F_1(1+v/2,2,\gamma/w) - \frac{w}{\alpha}{}_1F_1(1+v/2,2,\gamma/w)\right\}. \tag{10.94}$$

The same argument as above (but with reversed inequalities) leads to

$$\frac{\partial}{\partial\gamma}M_{\mathrm{HK}}^{(v)}(\gamma,\alpha) < \int_0^\infty g(\gamma,w)\mathcal{G}(w\,|\,\alpha,1)\,dw - \int_0^\infty g(\gamma,w)\mathcal{G}(w\,|\,\alpha+1,1)\,dw, \tag{10.95}$$

where the function $g(\gamma, w)$ is defined as above. So, in this case, we want to show that $\int_0^\infty h(\gamma, w)\mathcal{G}(w \mid \alpha, 1)\, dw - \int_0^\infty h(\gamma, w)\mathcal{G}(w \mid \alpha + 1, 1)\, dw \leq 0$, where $h(\gamma, w)$ is defined as above. But, this is implied by Lemmas 6 and 7 (case $v/2 > 1$). This completes the proof of the theorem. ■

Lemma 6*a) If $v/2 < 1$, the function $h(\gamma, w) = \frac{w^{v/2-1}\, {}_1F_1(1+v/2,2,\gamma/w)}{e^{\gamma/w}}$ is decreasing in the variable w.*

b) If $v/2 > 1$, the function $h(\gamma, w)$ is increasing in the variable w.

Proof Using the change of variable $x = \gamma/w$, we consider the function $F(x) = \frac{{}_1F_1(1+v/2,2,x)}{e^x x^{v/2-1}}$. So, we want to show that $F(x)$ is increasing if $v/2 < 1$ and $F(x)$ is decreasing if $v/2 > 1$ (the function $x = \gamma/w$ is decreasing in the variable w).

We compute

$$\frac{d}{dx} F(x) = \frac{\frac{d}{dz}{}_1F_1(1 + v/2, 2, x) - {}_1F_1(1 + v/2, 2, x)\left(1 + (\frac{v}{2} - 1)x^{-1}\right)}{e^x x^{v/2-1}}. \quad (10.96)$$

Using (Gradshteyn and Ryshik 1994, 9.213, p. 1086) and (Gradshteyn and Ryshik 1994, 9.212(3), p. 1086), we have $\frac{d}{dz}{}_1F_1(1 + v/2, 2, x) = \frac{(1+v/2)}{2}{}_1F_1(2 + v/2, 3, x) = \frac{(v/2-1)}{2}{}_1F_1(1 + v/2, 3, x) + \frac{2}{2}{}_1F_1(1 + v/2, 2, x)$.

So, we obtain after algebraic simplifications

$$\frac{(v/2 - 1)}{e^x x^{v/2}} \left\{ \frac{x}{2}{}_1F_1(1 + v/2, 3, x) - {}_1F_1(1 + v/2, 2, x) \right\}. \quad (10.97)$$

Using (Gradshteyn and Ryshik 1994, 9.212(2), p. 1086), we finally obtain

$$-\frac{(v/2 - 1)}{e^x x^{v/2}}{}_1F_1(1 + v/2, 1, x). \quad (10.98)$$

The result is now clear. ■

Lemma 7 *a) Let $H(w)$ be a decreasing positive function. Then, one has $\int_0^\infty H(w)\mathcal{G}(w \mid \alpha, 1)\, dw - \int_0^\infty H(w)\mathcal{G}(w \mid \alpha + 1, 1)\, dw \geq 0$.*

b) Let $H(w)$ be an increasing positive function. Then, one has $\int_0^\infty H(w)\mathcal{G}(w \mid \alpha, 1)\, dw - \int_0^\infty H(w)\mathcal{G}(w \mid \alpha + 1, 1)\, dw \leq 0$.

Proof a) Since $H(w)$ is a positive decreasing function, we can approximate it by functions of the form $\sum_{n=1}^N a_n B(b_n, w)$, where $a_n \geq 0$, $b_n > 0$, and $B(b, w)$ is equal to 1 if $w \in [0, b]$, and $B(b, w) = 0$, if $w > b$. Now, $\int_0^\infty B(b, w)\mathcal{G}(w \mid \alpha, 1)\, dw = \int_0^b \mathcal{G}(w \mid \alpha, 1)\, dw = 1 - \frac{\Gamma(\alpha,b)}{\Gamma(\alpha)}$, where $\Gamma(\alpha, b)$ is the incomplete Euler gamma function. But the function $1 - \frac{\Gamma(\alpha,b)}{\Gamma(\alpha)}$ is decreasing. Therefore, $\int_0^\infty B(b, w)\mathcal{G}(w \mid \alpha, 1)\, dw > \int_0^\infty B(b, w)\mathcal{G}(w \mid \alpha + 1, 1)\, dw$, and we are done.

b) Since $H(w)$ is a positive increasing function,, we can approximate $H(w)$ by functions of the form $\sum_{n=1}^{N} a_n\,(1 - B(b_n, w))$, where $a_n \geq 0$, $b_n > 0$. Now, $\int_0^\infty (1 - B(b, w))\mathcal{G}(w \mid \alpha, 1)\, dw = \frac{\Gamma(\alpha,b)}{\Gamma(\alpha)}$, and we are done. ■

Proof of Corollary 2. Let $\nu/2 < 1$. Since $0 < M < 1$, we conclude from Theorem 26, using the Intermediate Value Theorem, that for any $\alpha > 0$ such that $M_K(\alpha) \leq M$, there is a unique value of $\gamma \geq 0$ for which $M_{HK}^{(\nu)}(\gamma, \alpha) = M$. Thus, if $M \geq \Gamma(\nu/2 + 1)$, α has no restrictions, because $M_K^{(\nu)}(\alpha) < \Gamma(\nu/2 + 1)$ for any $\alpha > 0$ (Theorem 21). On the other hand, if $M_K(\alpha) < M$, let α_0 be the unique solution to the equation $M_K^{(\nu)}(\alpha_0) = M$ (Theorem 21). Then, using once more Theorem 21, we obtain that $M_K^{(\nu)}(\alpha) < M$ if and only if $\alpha \leq \alpha_0$. Henceforth, if $M_K^{(\nu)}(\alpha) < M$, the domain of the function $\gamma_M^{(\nu)}(\alpha)$ is the interval $(0, \alpha_0]$

The case $\nu/2 > 1$ is handled similarly, but with reversed inequalities. ■

Proof of Lemma 4. Part a). From the definition in Eq. (10.6), the distribution $P_{\mathrm{HK}}(A \mid \varepsilon, \sigma^2, \alpha)$ is equal to $\int_0^\infty P_{\mathrm{Ri}}(A \mid \varepsilon, \sigma^2 w)\mathcal{G}(w \mid \alpha, 1) d\, w$. Using the identity $I_0(z) = \frac{1}{\pi}\int_0^\pi e^{z\cos\theta} d\,\theta$ from Abramowitz and Stegun (1972, Eq. (9.6.16), p. 376) and the definition of the Rice distribution (10.2) , we can express $P_{\mathrm{Ri}}(A \mid \varepsilon, \sigma^2 w)$ in the form $\frac{1}{\pi}\int_0^\pi \frac{A}{\sigma^2 w}\exp\left(\frac{\varepsilon}{\sigma^2 w} A\cos\theta\right)\exp\left(-\frac{(\varepsilon^2 + A^2)}{2\sigma^2 w}\right) d\,\theta$. It follows that $P_{\mathrm{HK}}(A \mid \varepsilon, \sigma^2, \alpha)$ can be written as

$$\frac{1}{\pi}\int_0^\pi \left\{\int_0^\infty \frac{A}{\sigma^2 w}\exp\left(\frac{\varepsilon}{\sigma^2 w} A\cos\theta\right)\exp\left(-\frac{(\varepsilon^2 + A^2)}{2\sigma^2 w}\right)\mathcal{G}(w \mid \alpha, 1) d\, w\right\} d\ \theta, \tag{10.99}$$

which yields Eq. (10.56) after evaluation of the inner integral.

Part b). Using Eq. (10.56), the partial derivative of the homodyned K-distribution with respect to ε is equal to

$$\begin{aligned}
&\frac{1}{\pi}\int_0^\pi \frac{2A}{\sigma^2\Gamma(\alpha)}\frac{\partial}{\partial\varepsilon}\left\{\left(\frac{X(\theta)}{2}\right)^{\alpha-1} K_{\alpha-1}\big(X(\theta)\big)\right\} d\ \theta \\
&= \frac{1}{\pi}\int_0^\pi \frac{2A}{\sigma^2\Gamma(\alpha)}\left\{\frac{(\alpha-1)}{2}\left(\frac{X(\theta)}{2}\right)^{\alpha-2} K_{\alpha-1}\big(X(\theta)\big)\right. \\
&\qquad \left. + \left(\frac{X(\theta)}{2}\right)^{\alpha-1}\frac{d}{d\,z} K_{\alpha-1}\big(X(\theta)\big)\right\}\frac{\partial}{\partial\varepsilon} X(\theta) d\ \theta \\
&= -\frac{1}{\pi}\int_0^\pi \frac{2A}{\sigma^2\Gamma(\alpha)}\left(\frac{X(\theta)}{2}\right)^{\alpha-1} K_{\alpha-2}\big(X(\theta)\big) 2\frac{(\varepsilon - A\cos\theta)}{\sigma^2 X(\theta)} d\ \theta.
\end{aligned} \tag{10.100}$$

Here, we have used the identity $z\frac{d}{dz}K_{\alpha-1}(z) + (\alpha - 1)K_{\alpha-1}(z) = -z\,K_{\alpha-2}(z)$ (Abramowitz and Stegun 1972, Eq. (9.6.26), 2nd identity, p. 376) and algebraic simplifications.

Part c). Using Eq. (10.56), the partial derivative of the homodyned K-distribution with respect to σ^2 is equal to

$$\begin{aligned}
&\frac{1}{\pi}\int_0^\pi \frac{2A}{\Gamma(\alpha)}\frac{\partial}{\partial\sigma^2}\left\{\frac{1}{\sigma^2}\left(\frac{X(\theta)}{2}\right)^{\alpha-1}K_{\alpha-1}\big(X(\theta)\big)\right\}d\ \theta\\
&=-\frac{1}{\sigma^2}\frac{1}{\pi}\int_0^\pi \frac{2A}{\sigma^2\Gamma(\alpha)}\left(\frac{X(\theta)}{2}\right)^{\alpha-1}K_{\alpha-1}\big(X(\theta)\big)d\ \theta\\
&\quad+\frac{1}{\pi}\int_0^\pi \frac{2A}{\sigma^2\Gamma(\alpha)}\left\{\frac{(\alpha-1)}{2}\left(\frac{X(\theta)}{2}\right)^{\alpha-2}K_{\alpha-1}\big(X(\theta)\big)\right.\\
&\quad\left.+\left(\frac{X(\theta)}{2}\right)^{\alpha-1}\frac{d}{dz}K_{\alpha-1}\big(X(\theta)\big)\right\}\frac{\partial}{\partial\sigma^2}X(\theta)d\ \theta\\
&=-\frac{1}{\sigma^2}\frac{1}{\pi}\int_0^\pi \frac{2A}{\sigma^2\Gamma(\alpha)}\left(\frac{X(\theta)}{2}\right)^{\alpha-1}K_{\alpha-1}\big(X(\theta)\big)d\ \theta\\
&\quad-\frac{1}{\sigma^2}\frac{1}{\pi}\int_0^\pi \frac{2A}{\sigma^2\Gamma(\alpha)}\left\{(\alpha-1)\left(\frac{X(\theta)}{2}\right)^{\alpha-2}K_{\alpha-1}\big(X(\theta)\big)\right.\\
&\quad\left.-\left(\frac{X(\theta)}{2}\right)^{\alpha-1}K_{\alpha}\big(X(\theta)\big)\right\}\left(\frac{X(\theta)}{2}\right)d\ \theta\\
&=-\frac{\alpha}{\sigma^2}\frac{1}{\pi}\int_0^\pi \frac{2A}{\sigma^2\Gamma(\alpha)}\left(\frac{X(\theta)}{2}\right)^{\alpha-1}K_{\alpha-1}\big(X(\theta)\big)d\ \theta\\
&\quad+\frac{1}{\sigma^2}\frac{1}{\pi}\int_0^\pi \frac{2A}{\sigma^2\Gamma(\alpha)}\left(\frac{X(\theta)}{2}\right)^{\alpha}K_{\alpha}\big(X(\theta)\big)d\ \theta.
\end{aligned}\tag{10.101}$$

Here, we have used the identity $\frac{z}{2}\frac{d}{dz}K_{\alpha-1}(z)=-\frac{z}{2}K_\alpha(z)+\frac{(\alpha-1)}{2}K_{\alpha-1}(z)$ (Abramowitz and Stegun 1972, Eq. (9.6.26), 4th identity, p. 376) and algebraic simplifications.

Part d). Eq. (10.59) follows from part a) upon taking the logarithmic derivative of the integrand in Eq. (10.56). ■

References

Abraham DA, Lyons AP (2002) Novel physical interpretation of K-distributed reverberation. IEEE J Oceanic Eng 27(4):800–813

Abraham DA, Lyons AP (2010) Reliable methods for estimating the K-distribution shape parameter. IEEE J Oceanic Eng 35(2):288–302

Abramowitz M, Stegun IA (eds) (1972) Handbook of mathematical functions with formulas, graphs, and mathematical tables. Dover, New York

Agrawal R, Karmeshu (2006) Ultrasonic basckscattering in tissue: characterization through Nakagami-generalized inverse Gaussian distribution. Comp Biol Med 37:166–172

Barakat R (1986) Weak-scatterer generalizations of the K-density function with application to laser in atmospheric turbulence. J Opt Soc Am A 3:401–409

Berger NE, Lucas RJ, Twersky V (1991) Polydisperse scattering theory and comparisons with data for red blood cells. J Acoust Soc Am 89(3):1394–1401

Blacknell D, Tough RJA (2001) Parameter estimation for the k-distributed based on [z log (z)]. IEE Proc Radar Sonar Navig 148(6):309–312

Bouhlel N, Sevestre-Ghalila S (2009) Nakagami Markov random field as texture model for ultrasound RF envelope image. Computers Biol Med 39:535–544

Burckhardt CB (1978) Speckle in ultrasound b-mode scans. IEEE Trans Son Ultrason SU-25(1):1–6

Carrobi CFM, Cati M (2008) The absolute maximum of the likelihood function of the Rice distribution: existence and uniqueness. IEEE Trans Instrum Measur 57(4):682–689

Chung P-J, Roberts WJJ, Bohme JF (2005) Recursive K-distribution parameter estimation. IEEE Trans Signal Processing 53(2):397–402

Destrempes F, Meunier J, Giroux M-F, Soulez G, Cloutier G (2009) Segmentation in ultrasonic B-mode images of healthy carotid arteries using mixtures of Nakagami distributions and stochastic optimization. IEEE Trans Med Imag 28(2):215–229

Destrempes F, Cloutier G (2010) A critical review and uniformized representation of statistical distributions modeling the ultrasound echo envelope. Ultrasound Med Biol 36(7):1037–1051

Destrempes F, Meunier J, Giroux M-F, Soulez G, Cloutier G (2011) Segmentation of plaques in sequences of ultrasonic B-mode images of carotid arteries based on motion estimation and a Bayesian model. IEEE Trans Biomed Eng 58(8):2202–2211

Dumane VA, Shankar PM (2001) Use of frequency diversity and Nakagami statistics in ultrasonic tissue characterization. IEEE Trans Ultrason Ferroelectr Freq Control 48(5):1139–1146

Dutt V (1995) Statistical analysis of ultrasound echo envelope. PhD Thesis, Mayo Graduate School, August

Dutt V, Greenleaf JF (1994) Ultrasound echo envelope analysis using a homodyned K distribution signal model. Ultrasonic Imaging 16:265–287

Dutt V, Greenleaf JF (1995) Speckle analysis using signal to noise ratios based on fractional order moments. Ultrasonic Imaging 17:251–268

Dutt V, Greenleaf JF (1996) Statistics of the log-compressed echo envelope. J Acoust Soc Am 99(6):265–287

Edgeworth FY (1908) On the probable errors of frequency-constants I, II, III. J Roy Statist Soc 71:381–397, 499–512, 651–678

Edgeworth FY (1909) On the probable errors of frequency-constants. Addendum. J Roy Statist Soc 72:81–90

Eltoft T (2005) The rician inverse Gaussian distribution: a new model for non-rayleigh signal amplitude statistics. IEEE Trans Image Proces 14:1722–1735

Erdélyi A (1954) Tables of integral transforms. McGraw-Hill Book Co., Inc., New York

Fisher RA (1912) On an absolute criterion for fitting frequency curves. Messenger Math 41:155–160

Fisher RA (1922) On the mathematical foundations of theoretical statistics. Philos Trans Roy London Ser A 222:309–368

Fisher RA (1925) Theory of statistical estimation. In: Proceedings of the cambridge philosophical society, vol 22, pp 700–725

Fisher RA (1956) Statistical methods and scientific inference. Oliver and Boyd, Edinburgh

Gradshteyn IS, Ryshik IM (eds) (1994) Table of integrals, series, and products. Academic Press

Hao X, Bruce CJ, Pislaru C, Greenleaf JF (2002) Characterization of reperfused infarcted myocardium from high-frequency intracardiac ultrasound imaging using homodyned K distribution. IEEE Trans Ultrason Ferroelectr Freq Control 49(11):1530–1542

Hayley SW, Kays TH, Twersky V (1967) Comparison of distribution functions from scattering data on different sets of spheres. IEEE Trans Antennas Propag AP-15(1):118–135

Hruska DP (2009) Improved techniques for statistical analysis of the envelope of backscattered ultrasound using the homodyned K distribution. M.Sc. Thesis, University of Illinois at Urbana-Champaign

Hruska DP, Sanchez J, Oelze ML (2009) Improved diagnostics through quantitative ultrasound imaging. In: International Conference of the IEEE Engineering in Medicine and Biology Society, pp 1956–1959

Hruska DP, Oelze ML (2009) Improved parameter estimates based on the homodyned K distribution. IEEE Trans Ultrason Ferroelectr Freq Control 56(11):2471–2481

Huang C-C, Tsui P-H, Wang S-H (2007) Detection of coagulating blood under steady flow by statistical analysis of backscattered signals. IEEE Trans Ultrason Ferroelectr Freq Control 54(2):435–442

Huang C-C, Wang S-H (2007) Statistical variations of ultrasound signals backscattered from flowing blood. Ultrasound Med Biol 33(12):1943–1954

Insana MF, Wagner RF, Garra BS, Brown DG, Shawker TH (1986) Analysis of ultrasound image texture via generalized Rician statistics. Opt Eng 25(6):743–748

Iskander DR, Zoubir AM (1999) Estimation of the parameters of the K-distribution using higher order and fractional moments. IEEE Trans Aerosp Electron Syst 35(4):1453–1457

Jakeman E, Pusey PN (1976) A model for non-Rayleigh sea echo. IEEE Trans Antennas Propag 24:806–814

Jakeman E (1980) On the statistics of K-distributed noise. J Phys A 13:31–48

Jakeman E, Tough RJA (1987) Generalized *k* distribution: a statistical model for weak scattering. J Opt Soc Am A 4:1764–1772

Jeffreys H (1946) An invariant form for the prior probability in estimation problems. In: Proc. Roy. Soc. London (Ser. A), vol 186, pp 453–461

Jensen J (1906) Sur les fonctions convexes et les inégalités entre les valeurs moyennes. Acta Mathematica 30:175–193

Joughin IR, Percival DB, Winebrenner DP (1993) Maximum likelihood estimation of K distribution parameters for SAR data. IEEE Trans Geosci Remote Sens 31(5):989–999

Keyes TK, Tucker WT (1999) The K-distribution for modeling the envelope amplitude of a backscattered signal. IEEE Trans Ultrason Ferroelectr Freq Control 46(4):883–887

Kullback S, Leibler RA (1951) On information and sufficiency. Ann Math Stat 22:79–86

Lord RD (1954) The use of the Hankel transform in statistics. I. Biometrika 41:44–55

Lucas RJ, Twersky V (1987) Inversion of ultrasonic scattering data for red blood cell suspension under different flow conditions. J Acoust Soc Am 82(3):794–799

Luke YL (1962) Integrals of Bessel functions. McGraw-Hill Book Company, Inc.

Mamou J, Coron A, Oelze ML, Saegusa-Beecroft E, Hata M, Lee P, Machi J, Yanagihara E, Laugier P, Feleppa EJ (2010) Three-dimensional high-frequency spectral and envelope quantification of excised human lymph nodes. In: IEEE ultrasonics, symposium, pp 604–607

Mamou J, Coron A, Oelze ML, Saegusa-Beecroft E, Hata M, Lee P, Machi J, Yanagihara E, Laugier P, Feleppa EJ (2011) Three-dimensional high-frequency backscatter and envelope quantification of cancerous human lymph nodes. Ultrasound Med Biol 37(3):2055–2068

Martin-Fernandez M, Alberola-Lopez C (2007) Parameter estimation of the homodyned K distribution based on signal to noise ratio. In: IEEE utrasound, symposium, pp 158–161

Molthen RC, Narayanan VM, Shankar PM, Reid JM, Genis V, Vergara-Dominguez L (1993) Ultrasound echo evaluation by K-distribution. In: IEEE ultrasonics, symposium, pp. 957–960

Molthen RC, Shankar PM, Reid JM (1995) Characterization of ultrasonic B-scans using non-Rayleigh statistics. Ultrasound Med Biol 21:161–170

Nakagami M (1940) Study of the resultant amplitude of many vibrations whose phases and amplitudes are at random. J Inst Elec Commun Eng Japan 24(202):17–26

Nakagami M (1943) Statistical character of short-wave fading. J Inst Elec Commun Eng Japan 27:145–150

Nakagami M (1960) The m distribution—a general formula of intensity distribution in rapid fading. In: Hoffman WC (ed) Stat Methods Radio Wave Propag. Pergamon Press, New York, pp 3–36

Narayanan VM, Shankar PM, Reid JM (1994) Non-Rayleigh statistics of ultrasonic backscattered signals. IEEE Trans Ultrason Ferroelectr Freq Control 41(6):845–852

Narayanan VM, Molthen RC, Shankar PM, Vergara L, Reid JM (1997) Studies on ultrasonic scattering from quasi-periodic structures. IEEE Trans Ultrason Ferroelectr Freq Control 44(1):114–124

Nillesen MM, Lopata RGP, Gerrits IH, Kapusta L, Thussen JM, de Korte CL (2008) Modeling envelope statistics of blood and myocardium for segmentation of echocardiographic images. Ultrasound Med Biol 34(4):674–680

Oelze ML, O'Brien WD Jr (2007) Quantitative ultrasound assessment of breast cancer using a multiparameter approach. In: IEEE utrasound symposium, pp 981–984

Oliver CJ (1993) Optimum texture estimators for SAR clutter. J Phys D Appl Phys 26(11):1824–1835

Prager RW, Gee AH, Treece GM, Berman LH (2002) Analysis of speckle in ultrasound images using fractional order statistics and the homodyned K-distribution. Ultrasonics 40:133–137

Prager RW, Gee AH, Treece GM, Berman LH (2003) Decompression and speckle detection for ultrasound images using the homodyned K-distribution. Pattern Recogn Let 24(4–5):705–713

Pratt JW (1976) FY Edgeworth and RA Fisher on the efficiency of maximum likelihood estimation. Ann Stat 4:501–514

Raju BI, Srinivasan MA (2002) Statistics of envelope of high-frequency ultrasonic backscatter from human skin in vivo. IEEE Trans Ultrason Ferroelect Freq Contr 49(7):871–882

Rayleigh L (1880) On the resultant of a large number of vibrations of the same pitch and of arbitrary phase. Phil Mag 10:73

Redner R (1981) Note on the consistency of the maximum likelihood estimate for nonidentifiable distributions. Ann Stat 9(1):225–228

Redner RA, Walker HF (1984) Mixture densities, maximum likelihood and the EM algorithm. SIAM Rev 26(2):195–239

Rice SO (1945) Mathematical analysis of random noise. Bell Sys Tech J 24:46–156

Rice SO (1954) Mathematical analysis of random noise. In: Wax N (ed) Selected papers on noise and stochastic processes. Dover, New York, pp 133–294

Roberts WJJ, Furui S (2000) Maximum likelihood estimation of K-distribution parameters via the expectation-maximization algorithm. IEEE Trans Signal Proces 48(12):3303–3306

Saha RK, Kolios MC (2011) Effects of cell spatial organization and size distribution on ultrasound backscattering. IEEE Trans Ultrason Ferroelectr Freq Control 58(10):2118–2131

Shankar PM, Reid JM, Ortega H, Piccoli CW, Goldberg BB (1993) Use of non-Rayleigh statistics for the identification of tumors in ultrasonic B-scans of the breast. IEEE Trans Med Imag 12(4):687–692

Shankar PM (1995) A model for ultrasonic scattering from tissues based on the K distribution. Phys Med Biol 40:1633–1649

Shankar PM (2000) A general statistical model for ultrasonic backscattering from tissues. IEEE Trans Ultrason Ferroelectr Freq Control 47(3):727–736

Shankar PM, Dumane VA, Reid JM, Genis V, Forsberg F, Piccoli CW, Goldberg BB (2001) Classification of ultrasonic B-mode images of breast masses using Nakagami distribution. IEEE Trans Ultrason Ferroelectr Freq Control 48(2):569–580

Shankar PM, Forsberg F, Lown L (2003) Statistical modeling of atherosclerotic plaque in carotid B mode images—a feasibility study. Ultrasound Med Biol 29(9):1305–1309

Shankar PM (2003) A compound scattering pdf for the ultrasonic echo envelope and its relationship to K and Nakagami distributions. IEEE Trans Ultrason Ferroelect Freq Contr 50(3):339–343

Talukdar KK, Lawing WD (1991) Estimation of the parameters of the Rice distribution. J Acoust Soc Am 89(3):1193–1197

Tao Z, Beaty J, Jaffe CC, Tagare HD (2002) Gray level models for segmenting myocaridum and blood in cardiac ultrasound images. In: IEEE international symposium on biomedical, imaging, pp 265–268

Tao Z, Tagare HD, Beaty JD (2006) Evaluation of four probability distribution models for speckle in clinical cardiac ultrasound images. IEEE Trans Med Imag 25(11):1483–1491

Tsui P-H, Wang S-H (2004) The effect of transducer characteristics on the estimation of nakagami paramater as a function of scatterer concentration. Ultrasound Med Biol 30(10):1345–1353

Tsui P-H, Wang S-H, Huang C-C (2005) The effect of logarithmic compression on estimation of the nakagami parameter for ultrasonic tissue characterization: a simulation study. Phys Med Biol 50(14):3235–3244

Tsui P-H, Huang C-C, Chang C-C, Wang S-H, Shung K-K (2007) Feasibility study of using high-frequency ultrasonic Nakagami imaging for characterizing the cataract lens in vitro. Phys Med Biol 52(21):6413–6425

Tsui P-H, Chang C-C (2007) Imaging local scatterer concentrations by the nakagami statistical model. Ultrasound Med Biol 33(4):608–619

Tsui P-H, Yeh C-K, Chang C-C (2008a) Feasibility exploration of blood flow estimation by contrast-assisted Nakagami imaging. Ultrason Imaging 30(3):133–150

Tsui P-H, Yeh C-K, Chang C-C, Liao Y-Y (2008b) Classification of breast masses by ultrasonic Nakagami imaging: a feasibility study. Phys Med Biol 53:6027–6044

Tsui P-H, Yeh C-K, Chang C-C (2009a) Microvascular flow estimation by contrast-assisted ultrasound B-scan and statistical parametric images. IEEE Trans Inf Technol Biomed 13(3):360–369

Tsui P-H, Yeh C-K, Chang C-C (2009b) Microvascular flow estimation by microbubble-assisted nakagami imaging. Ultrasound Med Biol 35(4):653–671

Tsui P-H, Chang C-C, Ho M-C, Lee Y-H, Chen Y-S, Chang C-C, Huang N-E, Wu Z-H, Chang K-J (2009c) Use of Nakagami statistics and empirical mode decomposition for ultrasound tissue characterization by a nonfocused transducer. Ultrasound Med Biol 35(12):2055–2068

Tsui P-H, Hsu C-W, Ho M-C, Chen Y-S, Lin J-J, Chang C-C, Chu C-C (2010a) Three-dimensional ultrasonic Nakagami imaging for tissue characterization. Phys Med Biol 55(19):5849–5866

Tsui P-H, Liao Y-Y, Chang C-C, Kuo W-H, Chang K-J, Yeh C-K (2010b) Classification of benign and malignant breast tumors by 2-d analysis based on contour description and scatterer characterization. IEEE Trans Med Imag 29(2):513–522

Tsui P-H, Yeh C-K, Liao Y-Y, Chang C-C, Kuo W-H, Chang K-J, Chen C-N (2010c) Ultrasonic Nakagami imaging: a strategy to visualize the scatterer properties of benign and malignant breast tumors. Ultrasound Med Biol 36(2):209–217

Twersky V (1975) Transparency of pair-correlated random distributions of small scatterers with applications to the cornea. J Opt Soc Am 65(5):524–530

Twersky V (1978) Acoustic bulk parameters in distributions of pair-correlated scatterers. J Opt Soc Am 64:1710–1719

Twersky V (1987) Low-frequency scattering by correlated distributions of randomly oriented particles. J Acoust Soc Am 81(7):1609–1618

Twersky V (1988) Low-frequency scattering by mixtures of correlated nonspherical particles. J Acoust Soc Am 84(1):409–415

Wagner RF, Smith SW, Sandrick JM, Lopez H (1983) Statistics of speckle in ultrasound B-scans. IEEE Trans Sonics Ultras 30(3):156–163

Wagner RF, Insana MF, Brown DG (1987) Statistical properties of radio-frequency and envelope-detected signals with applications to medical ultrasound. J Opt Soc Am A 4(5):910–922

Weng L, Reid J, Shankar P, Soetanto K (1990) Non-uniform ultrasound speckle phase distribution applied to scatterer spacing estimation. In: IEEE ultrasonics, symposium, pp 1593–1596

Weng L, Reid JM, Shankar PM, Soetanto K, Lu X-M (1992) Nonuniform phase distribution in ultrasound speckle analysis-Part I: background and experimental demonstration. IEEE Trans Ultrason Ferroelectr Freq Control 39(3):352–359

Yamaguchi T, Zenbutsu S, Igarashi Y, Kamiyama N, Mamou J, Hachiya H (2011) Echo envelope analysis method for quantifying heterogeneity of scatterer distribution for tissue characterization of liver fibrosis. In: IEEE ultrasonics, symposium, pp 1412–1415

Chapter 11
The Quantitative Ultrasound Diagnosis of Liver Fibrosis Using Statistical Analysis of the Echo Envelope

Tadashi Yamaguchi

Abstract The development of a quantitative diagnostic method for liver fibrosis using ultrasound would be highly medically significant. Detection and classification of tissue disease using the characteristics of the ultrasound echo signal, such as power spectrum, texture parameters, local attenuation and statistical characteristics, requires an understanding of the relationship between complicated scatterer structures and the echo signal. In this chapter, a quantitative ultrasound (QUS) method for detecting and classifying liver fibrosis on the basis of the estimation of scatterer density from the statistical analysis of echo envelopes is introduced. Fibrotic tissue is inhomogeneous; therefore, its envelope probability density function (PDF) cannot be accurately modeled by a single PDF. Additionally, some regions have variable scatterer densities. In order to detect and characterize the fibrotic liver quantitatively, the relationship between the scatterer distribution and the PDF of echo envelopes of inhomogeneous scattering media using computer simulations was examined. Based on these simulations, the analysis parameters in the simulated fibrotic tissue were successfully used to characterize liver fibrosis in clinical data sets.

Keywords Liver fibrosis · Envelope statistics

11.1 Introduction

Ultrasound imaging is highly sensitive to changes in the acoustic properties of tissues, and abnormalities are often diagnosed on the basis of recognition not only of the shapes of important structures but also of subtle changes in tissue texture. In ultrasound tissue characterization based on the characteristics of the echo signals,

T. Yamaguchi (✉)
Research Center for Frontier Medical Engineering, Chiba University,
1-33 Yayoicho, Inage, Chiba 263-8522, Japan
e-mail: yamaguchi@faculty.chiba-u.jp

J. Mamou and M. L. Oelze (eds.), *Quantitative Ultrasound in Soft Tissues*, DOI: 10.1007/978-94-007-6952-6_11,

such as power spectrum, texture parameters, local attenuation and statistical characteristics, it is assumed that changes in tissue properties such as attenuation and elasticity are uniform in the liver, and therefore, a single evaluation index is used in many methods (Valckx and Thijssen 1997; Shankar 2000; Oelze et al. 2002; Ito et al. 2007; Oosterveld et al. 1993; Kikuchi et al. 1995; Bleck et al. 1996; Yamaguchi and Hachiya 1998; Fukuda et al. 1998; Badawi et al. 1999; Yamaguchi et al. 2001; Wang et al. 2002; Yeh et al. 2002, 2003; Sandrin et al. 2003; Fujii et al. 2004; Yamada et al. 2006; Toyoda et al. 2009).

Ultrasound images include granular patterns known as speckle. The speckle in ultrasound images is not just a function of the scattering of structures in tissues but is also the result of coherent accumulation of random scattering from within the resolution cell of the imaging system (Burckhardt 1978; Wargner et al. 1983; Tuthill et al. 1983). The probability density function (PDF) of the ultrasound echo amplitude from many identical scatterers from random spatial locations is characterized by the Rayleigh distribution (Toyoda et al. 2009; Burckhardt 1978). However, because the spatial scatterer distribution in an actual tissue is not absolutely random and may not come from identical scatterers, the Rayleigh distribution may not approximate the statistical characteristics of echo envelope. Therefore, various statistical distributions have been proposed to model the first-order statistics of the amplitude of the echo envelope (Narayanan and Shankar 1991; Shankar et al. 1993; Dutt V Greenleaf 1996; Cramblitt and Parker 1999; Shankar 2001).

In this chapter, the relationships of these statistical distributions are briefly presented. Next, a procedure for approximating the complicated scattering structures in tissue by a simple mathematical model is examined. These models are then applied to actual clinical diagnosis. Specifically, clinical data using diagnostic ultrasound equipment will be used with the envelope statistics approaches to diagnose liver fibrosis.

11.2 Relationship Between Statistical Models and Scatterer Distributions

Theoretically, the PDF of the echo amplitude envelope when many identical scatterers per resolution cell are present with random spatial locations, e.g., like in normal liver tissue, is the Rayleigh distribution (Burckhardt 1978; Wargner et al. 1983; Tuthill et al. 1983). However, the PDF of the echo amplitude envelope can become non-Rayleigh under different experimental conditions in heterogenous media. In this case, the PDF might be better approximated by the *k*-distribution, the Nakagami model or modified statistical models such as the homodyned *k*-distribution and the generalized Nakagami model (Narayanan and Shankar 1991; Shankar et al. 1993; Dutt V Greenleaf 1996; Cramblitt and Parker 1999; Shankar 2001). These standard PDFs can represent more scattering conditions then the simple model of the Rayleigh distribution (Fig. 11.1), and they contain two or more parameters that can be useful for tissue characterization. Therefore, the

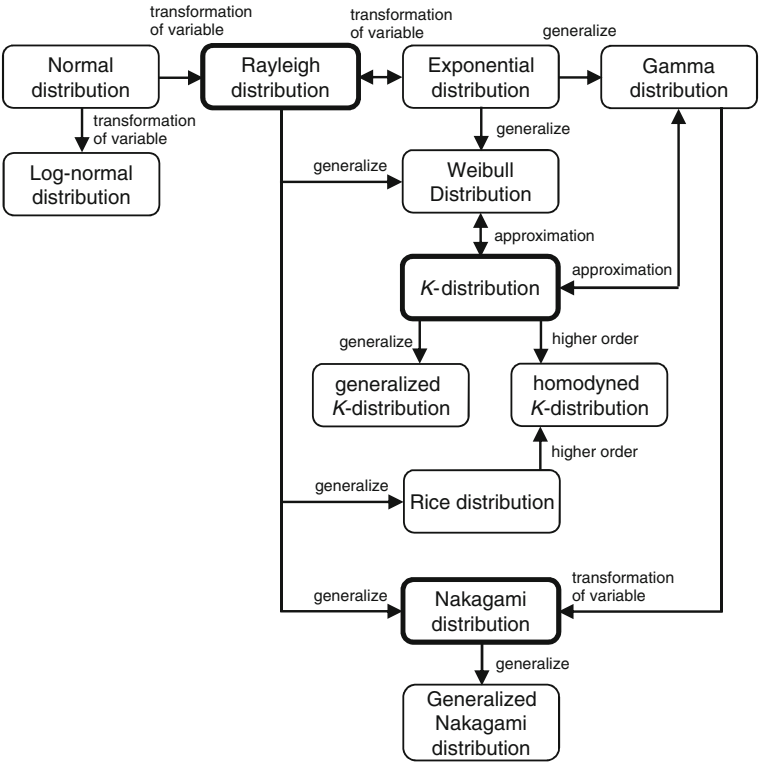

Fig. 11.1 Relationship between statistical models of the echo envelope

ability of these more general PDFs to fit experimental data is usually better than with the Rayleigh PDF that depends on a single parameter. Notionally, the relationship between each statistical model and different scattering conditions is illustrated in Fig. 11.2. Nevertheless, little is known about how to correctly model the echo amplitude envelope in heterogeneous media, which is the case for almost

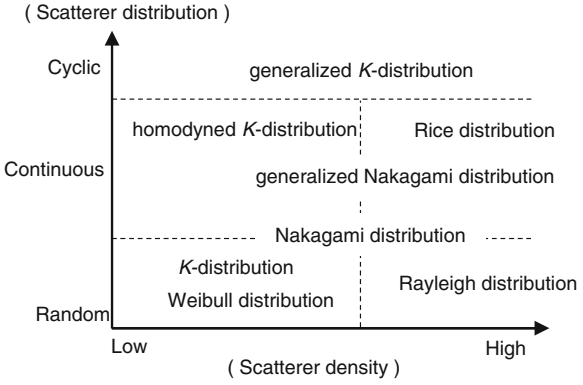

Fig. 11.2 Relationship between each statistical model and different scattering conditions

all living tissues. Therefore, an analysis method for associating a tissue structure to a simple mathematical statistics model was proposed. The basics and details are explained in the following sections.

11.3 Basics of Echo Envelope Statistical Analysis for Liver Fibrosis

11.3.1 The Histologic Characteristics of Liver Fibrosis

Ideally, the human liver is composed of small hexagonal structures termed liver lobules. The size of each liver lobule is about 1 mm in diameter and 1 mm in height, and they contain over 500 thousand liver cells, a central vein at the center and hepatic portal veins at the apex. These structures are smaller than the wavelength of the typical ultrasound pulse used in clinical examinations and can serve as scatterers of ultrasound. A fiber will be generated in the portal vein region in liver lobule if fibrosis (i.e. hepatitis) develops. The changes in the liver that lead from the onset of fibrosis to cirrhosis are gradual. Cirrhosis, an irreversible and the final condition of liver fibrosis, destroys a large number of liver lobules and replaces them with a permanent type of connective tissue called regenerative nodules. These nodules cannot perform the various functions of the liver.

As a matter of course, fibrotic liver is a heterogeneous medium with different types of tissues intermingled. It is important to parameterize the amount of mixture of fiber tissues in the heterogeneous liver in order to diagnose the advance of fibrosis. As compared with normal liver, the density of tissue fiber structure is high. Moreover, according to the kind of fibrosis generated and specific generation process, the variation of density liver tissue can be large. The difference in the density of the liver appears in an echo image as a difference in brightness or textures, because the nodules and collection of fibrous structures that develop are larger than the ultrasound wavelength and/or the scatterer density of fibers is larger than that of a normal liver. Furthermore, normal liver also consists of different types of tissues, i.e., the main cellular structure of liver, and various kinds of blood vessels or bile ducts. The density of tissue inside a blood vessel or bile duct is very low compared to the liver parenchyma. The changes in the densities of liver tissues affect the ultrasound echo image, i.e., as is the case for liver fibrosis.

11.3.2 Basic Analysis Method of Characteristics of Echo Signals

In a homogeneous medium with high scatterer density of identical scatterers with random spatial locations, the PDF, $p(x)$, of demodulated echo amplitude x can be approximated by the Rayleigh distribution given by

$$p(x) = \frac{2x}{\sigma^2} e^{-(x^2/\sigma^2)}, \tag{11.1}$$

where σ is a scale parameter representing the variance of the echo amplitude envelope.

One method to quantify the PDF of the characteristics of the echo amplitude envelope is through quantile–quantile probability plots (Q–Q plots). A Q–Q plot is used to compare distributions. To form the Q–Q plot for the Rayleigh distribution, the accumulative distribution function, $F(x)$, is used

$$F(x) = \int_0^x p(x)dx \quad = 1 - e^{-(x/\sigma)^2}. \tag{11.2}$$

Using a logarithmic transform, Eq. (11.2) can be rewritten as

$$\ln[-\ln\{1 - F(x)\}] = 2\{\ln(x) - \ln(\sigma)\}. \tag{11.3}$$

Typically, in the Q–Q plot of the Rayleigh distribution, the horizontal axis is the log-compressed amplitude $X = \ln(x)$, the vertical axis $Y = \ln(-\ln(1-F(x)))$ and the Y-intercept is determined by $-2\ln(\sigma)$. If perfect approximation of the simulated echo signal by the Rayleigh distribution is possible, then the resulting Q–Q would be a straight line with a slope of two and a zero intercept, because $\sigma^2 = 1$ in the normalized Rayleigh distribution described by Eq. (11.1). However, the shape of the Q–Q plots from the echo signals from a heterogeneous medium has different characteristics. The characteristics are explained below using a computation simulation in the next section.

11.3.3 Computer Simulation Models of Heterogeneous Medium

Computer simulations were performed using Field II (Jensen 1991, 1999; Jensen and Svendsen 1992) and MATLAB (The MathWorks Inc., MA, United States) in a two-dimensional (2D) space. A linear-array probe with 128 elements was simulated, and the size and the kerf of each element were 5.00 × 0.385 mm and 0.05 mm, respectively. The center frequency of the probe was set to 6.0 MHz and the sampling frequency was 50 MHz using 16-bit accuracy. The focal length was 40 mm, and the speed of sound was 1,540 m/s. The size of the scattering domain was 60 × 60 mm, and scatterers were placed inside this domain with random spatial locations. An ultrasonic wave was used to radiate each of six computer-simulated domains having media with different scattering properties.

The 2D heterogeneous-medium models were simulated by embedding a circular scattering region in the computational domain with a number density different from that of the base medium. The base medium, which simulated normal liver tissue, was homogeneous with a uniform density of 10 scatterers per resolution cell (sc/rc). The base medium was termed “surrounding medium” in order to

Fig. 11.3 Heterogeneous scatterer medium models that imitated a blood vessel or bile duct. A circular scatterer medium of 1 sc/rc is embedded in a surrounding scatterer medium of 10 sc/rc

Fig. 11.4 Heterogeneous scatterer medium models that imitated fiber. A circular scatterer medium of 60 sc/rc is embedded in a surrounding scatterer medium of 10 sc/rc

distinguish it from the circular region. For instance, to model a blood vessel or a bile duct, a circular region containing 1 sc/rc was embedded into the base medium, which contained 10 sc/rc. Similarly, a circular region with 60 sc/rc was embedded into the base medium to model fibrosis. The circular region was also a homogeneous medium. When the circular region was embedded in the base medium, the resulting heterogeneous medium contained two different scattering media. In actual living tissues like liver, two or more regions having different scatterer densities can have various mixed scattering properties. The mixing properties correspond to the amount of diseased tissue in the liver. Therefore, we created several kinds of heterogeneous-medium models by changing the size of the circular regions embedded inside the base medium. In every case, the scatterer density of the circular region was different from that of the base medium. Six different models were created by varying the mixing properties of the circular region. The six heterogeneous scatterer models are shown in Figs. 11.3 and 11.4. In Figs. 11.3 and 11.4a–f, the fraction of the circular regions within field of view in each simulation model is 8, 12, 18, 24, 30 and 40 %, respectively (Yamaguchi et al. 2010; Yamaguchi and Hachiya 2010).

11.3.4 Basic Characteristics of Echo Signals in the Simulation Model

The statistical characteristics of the simulated echo-signal envelope from the same region of interest (ROI) in each simulated domain were analyzed. The size of the ROI was 25 mm in depth $\times$ 40 mm in the lateral direction. The ROI dimensions are about 8 times greater than the resolution-cell dimensions of the simulated imaging system. (The resolution cell is defined as the product of the -3 dB beam width and the -3 dB pulse length.)

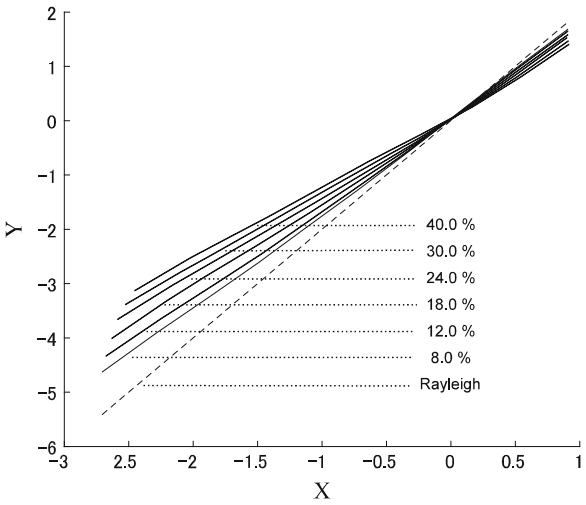

Fig. 11.5 The result of Q–Q plot of each heterogeneous model (Fig. 11.1) which imitated a blood vessel or a bile duct

Figure 11.5 displays the Q–Q plots of each heterogeneous model shown in Fig. 11.3. This figure shows that the mixing properties and the value of the Q–Q plot slope (differential coefficient) are almost linearly related. This result demonstrates that the relevant properties of echo signals can be approximated successfully with only one PDF such as Weibull or *k*-distribution (Narayanan and Shankar 1991; Cramblitt and Parker 1999; Jensen and Svendsen 1992). Another feature of the Q–Q plots is that the line always goes through the origin (i.e., $X = Y = 0$). These features can be quantified by using advanced models like the Weibull or Nakagami distribution, which are easily related to the Rayleigh distribution.

Figure 11.6 shows the Q–Q plots of each heterogeneous model from Fig. 11.4. All the Q–Q plot lines are curved, and the curvature increases with increasing inclusion size. However, each plotted whole line is not necessarily a curve. The plot is usually straight until it bends around the average value of normalized amplitude in the comparison Rayleigh distribution (i.e., near X equals 0). Note that the slope of the portion whose amplitude is smaller than the root mean square takes a value of approximately 2, independent of the inclusion size. These phenomena can be understood by investigating the relationships between the probability distribution of the echo-signal envelope and the scatterer distribution.

11.4 Q–Q Plot Based Estimation Method of Scatterer Density Applied to Liver Fibrosis Data

11.4.1 Basics of Applied Estimation Method

From the observations of the previous sections, liver-fibrosis characterization can be successful if the high-amplitude and the low-amplitude regions of the envelope

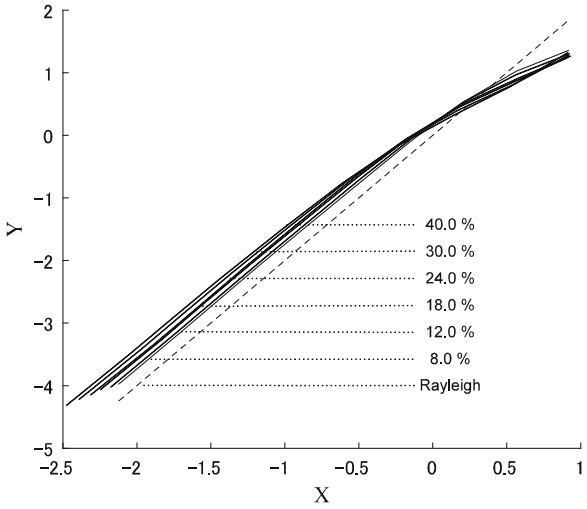

Fig. 11.6 The result of Q–Q plot of each heterogeneous model (Fig. 11.4) which imitated liver fibrosis

can be quantified effectively. Therefore, an applied signal-analysis method was proposed.

In heterogeneous scatterer medium models that imitated fibrotic liver, the PDF of echo envelope amplitude of the circular scatterer medium of 10 sc/rc was approximated by the Rayleigh distribution, and the PDF of echo envelope amplitude of surrounding scatterer medium of 1 sc/rc was also approximated by the Rayleigh distribution. However, dispersion of these two Rayleigh distributions differed. In the Q–Q plot based estimation method of scatterer density, the PDF of echo data from the fibrotic tissue can be assumed to be a composite function of two Rayleigh distributions with different σ values. If the mixing ratio of diseased tissue in the liver is defined as α, then the PDF of the echo envelope of fibrotic liver can be expressed by

$$p_{\mathrm{mix}}(x) = (1-\alpha)p_{\mathrm{nor}}(x) + \alpha p_{\mathrm{dis}}(x). \tag{11.4}$$

In Eq. (11.4), p_{nor} and p_{dis} are the Rayleigh distributions of normal liver and diseased tissue (or blood vessel and/or bile), and the variances of the echo envelopes are σ^2_{nor} and σ^2_{dis}, respectively. The variance ratio $r_\sigma = \sigma^2_{\mathrm{dis}}/\sigma^2_{\mathrm{nor}}$, which corresponds to the degree of diseased tissue, and therefore, the ratio of scatterer density and the mixing ratio α, which corresponds to the amount of diseased tissue, are parameters of the echo amplitude envelope distribution of simulation model.

Figure 11.7 illustrates the Q–Q plot based estimation method for characterizing liver fibrosis. The Q–Q plot of the echo signal in an ROI is approximated by two straight lines. These two straight lines are derived by minimizing the sum of the Kullback–Leibler (K-L) divergence D_{KL} between the Q–Q plot result and the two straight lines. D_{KL} is evaluated by

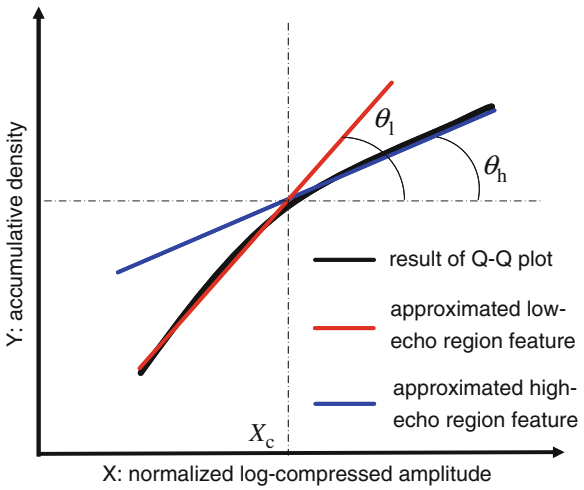

Fig. 11.7 Illustration of the estimation method for liver fibrosis

$$D_{KL}(p||q) = \sum_{x=0}^{\infty} p(x) \log \frac{p(x)}{q(x)}, \tag{11.5}$$

where the PDF of the simulated echo-signal envelope is $p(x)$ and that of the Rayleigh distribution function is $q(x)$.

The parameters used for fibrosis characterization are $S_h = \tan\theta_h$, $S_l = \tan\theta_l$ and X_c, which is the X value where the two straight lines intersect. In the case of low scatter densities, such as blood vessels or bile ducts, the characteristics of the echo-signal envelope predominantly appear in the straight line with a slope value S_l, but in the case of high scatterer density, such as fibrotic regions, the characteristics predominantly appear in the straight line with a slope value S_h. If a small amount of signal from fibrotic liver is contained in the analysis ROI filled with the speckle presumably from a normal liver, then S_h has lower value than S_l and would follow curves produced in Fig. 11.6.

The differences among characteristics of the PDFs for different degrees of liver fibrosis depend on the mixing ratio of diseased tissue r_α as shown in Figs. 11.5 and 11.6. The ratio of scatterer density $r_\sigma = {\sigma_{\mathrm{dis}}}^2/{\sigma_{\mathrm{nor}}}^2$ also is an important parameter for estimating the degree of fibrosis because the stiffness of tissue is correlated with scatterer density. We also examined the influence of the difference in the scatterer density of the mixing medium compared to the surrounding medium, i.e., the homogeneous base medium.

In the heterogeneous-medium simulations, the mixing ratio of the circular region in the ROI was fixed at 30 %, and the scatterer density was varied. Specifically, the scatterer density of the surrounding medium was 10 sc/rc, and the scatterer densities of the circular region were varied from 1 to 60 sc/rc. When the scatterer density of the circular region was 10 sc/rc, the scatterer density of the circular region became equal to the scatterer density of the surrounding medium, i.e., it was a pure homogeneous scattering medium. The properties of the

Fig. 11.8 A heterogeneous scattering medium in which the scatterer densities of the circular region vary

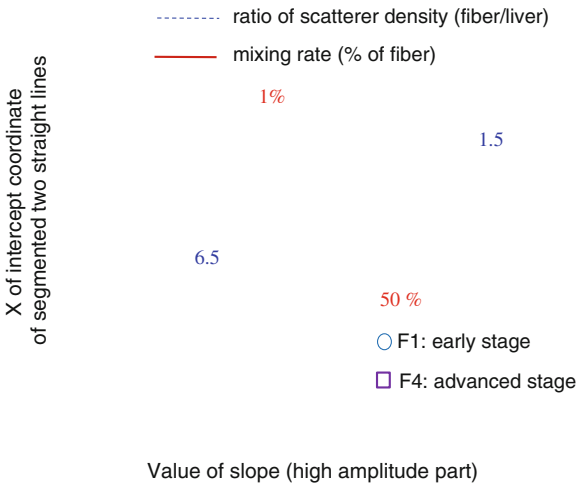

Fig. 11.9 Evaluation chart for estimating the ratio of scatterer density and the mixing ratio of fibrotic liver and normal liver

heterogeneous scattering models are shown in Fig. 11.8. In Fig. 11.8a–f, the scatterer density of the circular region is 1, 3, 5, 20, 40, or 60 sc/rc, respectively.

The values of slope in high echo amplitude part S_h and low echo amplitude part S_l and the parameter X_c of the position at which two straight lines intersect can be calculated from the mixing ratio α and the ratio of scatterer density r_σ from Eq. (11.4) and simulation models as shown in Figs. 11.3, 11.4 and 11.8. Figure 11.9 shows an example of an evaluation chart which uses the ratio of scatterer density and mixing ratio evaluated from S_h and X_c. This chart shows the values which S_h and X_c can take when α and/or each dispersion of P_{nor} and P_{dis} in Eq. (11.4) are changed. The calculated ranges of the ratio of scatterer density and the mixing ratio for the evaluation chart are 1–10 and 0–50 %, respectively. Solid lines are level lines on which the mixing ratio is constant and dotted lines are level lines on which the ratio of scatterer density is constant. When the ratio of scatterer density is unity, the PDF becomes a Rayleigh distribution, which corresponds to normal liver. The distribution deviates from the Rayleigh distribution when the ratio of scatterer density and the mixing ratio increase. This increase was observed to be associated with liver fibrosis progression.

Using clinical data, S_h and X_c easily can be calculated from the Q–Q plot of the observed PDF. Next, the ratio of scatterer density and the mixing ratio that

correspond to the degree of degeneration and the amount of fibrous tissue can be obtained using Fig. 11.9. In summary, using this method with clinical data, the fibrosis stage can be quantified using an inverse approach based on the model described in Eq. (11.4).

Figure 11.9 also illustrates how the ratio of scatterer density and mixture ratio can be estimated clinically. Additionally, in vivo clinical data obtained from patients with early (F1, i.e., portal fibrotic widening) and advanced (F4, i.e., cirrhosis) fibrosis indicated that advanced cases have a higher scatterer density. Additionally, the relationship between S_h and S_l can be used to estimate the degree of vascularization or bile duct presence. When the value of S_h and S_l is comparable, and they are smaller than 2 as shown in Fig. 11.5, it is assumed that the echo from a vascularization or a bile duct is included in the analyzed echo data.

11.4.2 Example of Clinical Data Experiment

The Q–Q plot based estimation method was applied to clinical data obtained from patients, and parameter values were displayed as pixel values in parametric images permitting quantitative evaluation of liver fibrosis. The clinical data sets were acquired from one healthy adult volunteer and four adult patients with chronic hepatitis C who underwent liver biopsy at Ogaki Municipal Hospital (Toyoda et al. 2009; Yamaguchi et al. 2010; Yamaguchi and Hachiya 2010). The data from the four patients were classified between F1 and F4 according to the new Inuyama classification using the biopsy results. The amplitudes of the received echo signals in each B-mode scan line were obtained using a prototype system based on a commercially available diagnostic ultrasound system (SSA-770A, Toshiba Medical Systems Co., Otawara, Japan) with a convex transducer. In harmonic mode, the transmission and reception frequencies of the ultrasound system were 3.5 and 7.0 MHz respectively with a 40 MHz sampling frequency. The amplitude data used for analysis were anti-logged data calculated from 15-bit logged data. The scan-line density was 380 lines per 90 degrees, and the amplitude data in each scan line (15 bit) were decimated at 100 samples/mm.

The analysis was carried out for each of the five clinical data sets using ROIs covering the entire liver as observed on the ultrasound image. Each ROI had a size of 5 × 5 mm, and overlapping ROIs were used to cover the entire liver. The parameters S_l, S_h, and X_c in the samples in the liver area were calculated in each ROI for each clinical data set. Figure 11.10 displays the resulting parametric images using all three parameters (S_l, S_h, and X_c.). If $1.5 \leq S_l < 2.0$, $0.5 \leq S_h < 1.3$, and $0.2 \leq X_c < 0.7$, then the central pixel of the ROI was assumed to be fibrotic. These classification criteria were determined from the results of the computer simulations. In Fig. 11.10, only the walls of the thick blood vessels appear red in F0, and few liver regions are designated as fibrotic in F1. This suggests a reduction in false-positive determinations was achieved by introducing the new parameters.

Fig. 11.10 Results of parametric imaging on the basis of the three parameters S_l, S_h, and X_c. **a** F0, **b** F1, **c** F2, **d** F3 and **e** F4

Fig. 11.11 Azan staining histology. Fibrous tissue is dyed with blue stain. The length of the short axis of each pathology specimen is 700–800 μm. **a** F0, **b** F1, **c** F2, **d** F3 and **e** F4

Overall, the red regions in Fig. 11.10 (i.e., the fibrotic regions) spread in proportion to the degree of pathological change. These results were consistent with the histological features of fibrosis in each liver sample as observed in Azan stained histology shown in Fig. 11.11.

11.5 Conclusion

In this chapter, the PDFs of the echo amplitude envelope in heterogeneous media using basic and applied distribution functions were examined. The results of the analysis in the media with variable scatterer densities indicated that the tissue structural changes could be divided into different conditions. By estimating three parameters, these different conditions were divided adequately and it became possible to detect and potentially grade liver fibrosis.

Additionally, ultrasound-derived results were consistent with histological features of clinical data sets. The scatterer density and the degree of fibrosis (fractional amount of fibrotic tissue) can be estimated by plotting echo-signal envelope statistical parameters. Therefore, the proposed method of envelope analysis potentially can provide invaluable information for non-invasive detection and characterization of liver fibrosis.

This method can further be applied to other diseases when the relationship of each parameter, scatterer density, and tissue structure is investigated for the case of each disease.

References

Badawi M, Derbala AS, Youssef ABM (1999) Fuzzy logic algorithm for quantitative tissue characterization of diffuse liver diseases from ultrasound images. Int J Med Inform 55(2):135–147

Bleck JS, Ranft U, Gebel M et al (1996) Random field models in the textural analysis of ultrasound images of the liver. IEEE Trans Med Imaging 15(6):796–801

Burckhardt CB (1978) Speckle in ultrasound B-mode scans. IEEE Trans Sonic Ultrason 25(1):1–6

Cramblitt RM, Parker KJ (1999) Generation of non-Rayleigh speckle distribution using marked regularity models. IEEE Trans Ultrason Ferroelec Freq Contr 46(4):867–874

Dutt V Greenleaf JF (1996) Adaptec speckle reduction filter for log-compressed B-scan images. IEEE Trans Med Imaging 15(6):802–813

Fujii Y, Taniguchi N, Takano R et al (2004) Texture analysis with a new method in which the region of interest is segmented into multiple layers for radiofrequency amplitude histogram analysis of fibrous rat livers. J Med Ultrason 31(1):13–20

Fukuda H, Ebara M, Kobayashi A et al (1998) An image analyzing system using an artificial neural network for evaluating the parenchymal echo pattern of cirrhotic liver and chronic hepatitis. IEEE Trans Biomed Eng 45(3):396–400

Ito T, Ishihara K, Deura I et al (2007) Tissue characterization of uterine myometrium using the ultrasound gray-level histogram width. J Med Ultrason 34(4):189–192

Jensen JA (1991) A model for the propagation and scattering of ultrasound in tissue. J Acoust Soc Am 89(1):182–191

Jensen JA (1999) Linear description of ultrasound imaging systems, Notes for the International Summer School on Advanced Ultrasound Imaging. Technical University of Denmark, 5–9 July

Jensen JA, Svendsen NB (1992) Calculation of pressure fields from arbitrarily shaped, apodized, and excited ultrasound transducers. IEEE Trans Ultrason Ferroelec Freq Contr 39(2):262–267

Kikuchi T, Nakazawa T, Fukuzawa T (1995) Quantitative estimation of the amount of fibrous in the rat liver using fractal dimension of the shape of power spectrum. Jpn J Appl Phys 34(5):2831–2834

Narayanan MV, Shankar PM (1991) Non-rayleigh statistics of ultrasonic backscattered signals. IEEE Trans Ultrason Ferroelect Freq Contr 41(4):845–852

Oelze ML, Zachary JF, O'Brien WD Jr (2002) Characterization of tissue microstructure using ultrasonic backscatter: theory and technique for optimization using a Gaussian form factor. J Acoust Soc Am 112(9):1202–1211

Oosterveld BJ, Thijssen JM, Hartman PC et al (1993) Detection of diffuse liver disease by quantitative echography: dependence on a priori choice of parameters. Ultrasound Med Biol 19(1):21–25

Sandrin L, Fourquet B, Hasquenoph JM et al (2003) Transient elastography: a new noninvasive method for assessment of hepatic fibrosis. Ultrasound Med Biol 29(12):1705–1713

Shankar PM (2000) A general statistical model for ultrasonic backscattering from tissue. IEEE Trans Ultrason Ferroelect Freq Contr 47(3):727–736

Shankar PM (2001) Ultrasonic tissue characterization using a generalized Nakagami model. IEEE Trans Ultrason Ferroelec Freq Contr 48(6):1716–1720

Shankar PM, Reid JM, Ortega H et al (1993) Use of non-rayleigh statistics for the identification of tumors in ultrasonic B-scans of the breast. IEEE Trans Med Imaging 12(4):687–692

Toyoda H, Kumada T, Yamaguchi T, Kamiyama N, Hachiya H et al (2009) Evaluation of liver fibrosis in patients with chronic hepatitis c on b-mode images using an algorithm based on statistical analysis of ultrasound signals. Am J Roentgenol 193(4):1037–1043

Tuthill TA, Sperry RH, Parker KJ (1983) Deviations from rayleigh statistics in ultrasonic speckles. Ultrason Imaging 10(2):81–89

Valckx FMJ, Thijssen JM (1997) Characterization of echographic image texture by cooccurrence matrix parameter. Ultrasound Med Biol 23(4):559–571

Wang Y, Itou K, Taniguchi N et al (2002) Studies on tissue characterization by texture analysis with co-occurrence matrix method using ultrasonography and CT imaging. J Med Ultrason 29(4):211–223

Wargner RF, Smith SW, Sandrik JM, Lopez H (1983) Statistics of speckle in ultrasound Bscans. IEEE Trans Sonic Ultrason 30(3):156–163

Yamada H, Yamagici T, Hachiya H, Ebara M et al (2006) A piot approach for quantitative assessment of liver fibrosis using ultrasound: preliminary result in 79 cases. J Hepatol 44(1):68–75

Yamaguchi T, Hachiya H (1998) Estimation of the scatterer distribution of the cirrhotic liver using ultrasonic image. Jpn J Appl Phys 37(5):3093–3096

Yamaguchi T, Hachiya H (2010) Proposal of a parametric imaging method for quantitative diagnosis of liver fibrosis. J Med Ultrason 37(4):155–166

Yamaguchi T, Hachiya H, Kamiyama N et al (2001) Estimation of characteristics of echo envelope using RF echo signal from the liver. Jpn J Appl Phys 40(5):3900–3904

Yamaguchi T, Mamou J, Hachiya H et al (2010) Echo envelope analysis method for quantifying heterogeneity of scatterer distribution for tissue characterization of liver fibrosis. In: Proceedings of IEEE ultrasonics symposium, pp 1412–1415

Yeh WC, Li PC, Jeng YM et al (2002) Elastic modulus measurements of human liver and correlation with pathology. Ultrasound Med Biol 28(4):467–474

Yeh WC, Huang SW, Li PC (2003) Liver fibrosis grade classification with B-mode ultrasound. Ultrasound Med Biol 29(9):1229–1235

Part III
Scanning Acoustic Microscopy

Chapter 12
Recent Applications of Acoustic Microscopy for Quantitative Measurement of Acoustic Properties of Soft Tissues

Yoshifumi Saijo

Abstract High resolution biomedical imaging using high frequency ultrasound is possible because both wavelength and beamwidth are inversely proportional to ultrasonic frequency. Scanning acoustic microscopy (SAM) uses 100 MHz or higher frequency ultrasound. The spatial resolution achieved by a 100 MHz and 1 GHz ultrasound SAM are 15 and 1.5 μm, respectively. This level of detail enables cellular imaging. There are three unique features of SAM compared with other microscopy modalities such as optical, electron and atomic force microscopy. First, SAM can be applied for easy and simple histopathological examinations because it does not require special staining techniques. The contrast observed in SAM images depends on the acoustic properties (i.e., density, stiffness, and attenuation) and on the topographic contour of the tissue. Second, microscopic acoustic properties obtained with high frequency ultrasound can be used for assessing echo intensity and texture in clinical echography with lower frequency ultrasound. Third, SAM data can provide the basic data for assessing biomechanics of tissues and cells. Ultrasound is transmitted through a coupling medium and focused on the surface of the substrate. Transmitted ultrasound is reflected at both the surface of the biological material and the interface between the biological material and the substrate. The transducer receives the sum of these two reflections. The interference of these two reflections is determined by acoustic properties of the biological material. The interference signal as a function of the frequency depends on the thickness and sound speed of the sample. The interference signal as a function of the intensity depends on the amplitude of the surface reflection and attenuation of ultrasound propagating through the tissue. For bone, cartilage, tendon and cardiovascular tissues, microacoustic properties can provide important information on biomechanical properties. Biomechanic evaluation of these tissues is especially important for assessing the pathophysiology. Cells are considered to consist of viscoelastic materials and SAM has provided information on viscosity

Y. Saijo (✉)
Biomedical Imaging Laboratory, Graduate School of Biomedical Engineering, Tohoku University, 4-1 Seiryomachi, Aoba-ku, Sendai 980-8575, Japan
e-mail: saijo@idac.tohoku.ac.jp

J. Mamou and M. L. Oelze (eds.), *Quantitative Ultrasound in Soft Tissues*, DOI: 10.1007/978-94-007-6952-6_12,

by ultrasonic attenuation estimates and information on elasticity by sound speed estimates. Instead of stretching cells or using atomic force microscopy for measuring biomechanical properties, SAM can be used to measure precise mechanical property distributions without contact to the cells. Thus, SAM provides a new paradigm of pathology that is based on the mechanical properties of is the object being imaged. Recent developments such as ultrasound speed microscopy, 3D ultrasound microscopy and high frequency array transducers may provide a clinically applicable SAM in the near future.

12.1 Introduction

High resolution biomedical imaging using high frequency ultrasound is possible because both wavelength and beam width are inversely proportional to ultrasonic frequency. Routine echography in clinical applications uses ultrasound in the frequency ranges between 1 and 15 MHz with corresponding spatial resolution approximately a few hundred micrometers to several millimeters. Scanning acoustic microscopy (SAM) uses 100 MHz or higher frequency ultrasound (1 GHz). The spatial resolution achieved by a 100 MHz (1 GHz) ultrasound SAM are 15 (1.5 μm), respectively; this level of detail enables cellular imaging. SAM provides a source of contrast different from conventional echography that is based on the mechanical properties of object being imaged. There are three unique features of SAM compared with other microscopy modalities such as optical, electron and atomic force microscopy. First, SAM can be applied for easy and simple histopathological examinations because it does not require special staining techniques because the contrast observed in SAM images depends on the acoustic properties (i.e., density, stiffness, and attenuation) and on the topographic contour of the tissue.

Second, microscopic acoustic properties obtained with high frequency ultrasound can be used for assessing echo intensity and texture in clinical echography with lower frequency ultrasound. Density $\boldsymbol{\rho}$ and sound speed $\boldsymbol{c}$ determine the characteristic acoustic impedance $\boldsymbol{Z}$ of the material as

$$\boldsymbol{Z} = \boldsymbol{\rho}\,\boldsymbol{c} \tag{12.1}$$

Assuming that the interface between two fluid-like media is infinite and plane, the relative reflected sound power, in dB, can be determined from the specific acoustic impedance of each medium if the material is approximately isotropic.

$$\boldsymbol{dB} = 10\ \log_{10}\frac{P_r}{P_i} = 10\ \log_{10}\frac{(Z_a - Z_b)^2}{(Z_a + Z_b)^2} \tag{12.2}$$

where P_r is the sound power reflected at interface, P_i is the incident sound power, Z_a is the acoustic impedance of medium a, Z_b is the acoustic impedance of medium b.

Third, SAM data can provide the basic data for assessing biomechanics of tissues and cells. Furthermore, SAM can microscopically target materials where direct mechanical measurements cannot be applied. In its simplest form, the relationship between the sound speed and the elastic bulk modulus of a fluid media is

$$c = \sqrt{\frac{K}{\rho}} \tag{12.3}$$

where c is the sound speed, K is the elastic bulk modulus, and ρ is the density.

Because biological soft tissue may be considered as a fluid, the sound speed and impedance can be used to estimate elastic properties of the tissue. Recent biomechanical studies have suggested that the mechanical properties of tissues may not be sufficiently similar to fluids and should be treated as soft solid materials. However, the acoustical relationships of solid materials can also be described by the following equation.

$$c = \sqrt{\frac{E(1-\sigma)}{\rho(1+\sigma)(1-2\sigma)}} \tag{12.4}$$

where c is the sound speed, E is the Young's modulus, σ is the Poisson's ratio, and ρ is the density. This equation indicates that the Young's modulus of tissue and the sound speed are closely related.

Soft materials are sometimes considered to be viscoelastic materials. In these cases, viscosity is also derived from acoustic properties, although it is a complicated procedure (Mikhailov et al. 1964). The tissue absorption is given by

$$\alpha = \frac{2f^2\pi^2}{3\rho c^3}\left(\eta v + \frac{4}{3}\eta_s\right) \tag{12.5}$$

where α is the absorption, f is the frequency, η_v is the volumetric viscosity, η_s is the shear viscosity, ρ_0 is the density, and c is the speed of sound.

12.2 Principles of Acoustic Microscopy

Figure 12.1 shows a schematic illustration of ultrasonic reflections from a tissue surface and from the interface between tissue and substrate in acoustic microscopy. The soft biological material is attached to a substrate. A normal glass slide or high-molecular polymer materials used in dishes for cell culture can be used as the substrates. The biological material is sectioned as an appropriate thickness to separate the reflections from the tissue surface and from the interface between

Fig. 12.1 Schematic illustration of ultrasonic reflections from a tissue surface and from the interface between tissue and substrate in acoustic microscopy

tissue and substrate. Single-layered cultured cells are also appropriate objects for SAM.

The ultrasound is transmitted through a coupling medium and focused on the surface of the substrate. Transmitted ultrasound is reflected at both the surface of the biological material (S_s) and the interface between the biological material and the substrate (S_d). The transducer receives the sum of these two reflections. The interference of these two reflections is determined by acoustic properties of the biological material. The interference signal as a function of the frequency depends on the thickness and sound speed of the sample. The interference signal as a function of the intensity depends on the amplitude of the surface reflection and attenuation of ultrasound propagating through the tissue. The speed of sound can be estimated through analysis of the frequency-dependent characteristics of the interference signal. In our previous SAM system, the frequency-dependent characteristics were obtained from serial measurements with varying frequencies from 100 to 200 MHz with 10 MHz steps between scans. The newly proposed ultrasound microscope obtains the frequency-dependent characteristics by fast Fourier transform of a single broad-band pulse.

12.3 Application to Cellular Imaging

Application of SAM for cellular imaging began at the very early stages of SAM development (Lemons and Quate 1975). Johnston et al. (1979) used SAM for the analysis of subcellular components. They could detect such features as nuclei and nucleoli, mitochondria, and actin cables of fixed cells. Hildebrand et al. (1981) applied SAM for the observation of living cells. Their analysis of acoustic images of actively motile cells indicated that leading lamella were less dense or stiff than the quiescent trailing processes of the cells.

Following the Stanford group, Bereiter-Hahn (1985) at Frankfurt performed series of studies on the biomechanics of living cells by observations with SAM. He proposed a hypothesis that the shape and locomotion of tissue cells depended on the interaction of elements of the cytoskeleton, adhesion to the substrate and an intracellular hydrostatic pressure. His group also found that higher values of impedance and attenuation coefficients were found in the cell periphery than in the central part of the cell. The phenomenon was suggested to be due to the different

organization of cytoskeletal elements (Litniewski and Bereiter-Hahn 1990). Veselý et al. (1994) developed subtraction of the SAM images (SubSAM) of live cells as a method for investigating minimal changes in cellular topography and elasticity. SubSAM opened an approach to a characterization of cell motility in vitro and to an understanding of early cellular reactions to various stimuli. They assumed that migration was due to an extension of the cell into the direction of minimum stiffness, and they were consistent with the hypothesis that local release of hydrostatic pressure provided the driving force for the flux of cytoplasm (Bereiter-Hahn and Lüers 1998).

Briggs and coworkers at Oxford University are also pioneers of acoustic microscopy. They utilized short ultrasonic pulses to derive the thickness of the cell. From these measurements, they calculated the acoustic velocity, impedance and attenuation by analyzing two separate signals reflected from the top and the bottom of the cell (Briggs et al. 1993).

Recently, time-resolved acoustic microscopy with GHz frequency ultrasound has been developed for cellular imaging. Weiss et al. (2007) compared the acoustical images of chicken heart muscle cells and fluorescence optical images of the same cells after staining showed that the actin fibers ended inside the dark streaks in the acoustical images and thus represented the focal contacts (FCs). Figure 12.2 shows optical and acoustical images of embryonic chicken heart muscle cells taken at room temperature. The acoustical images have dimensions of 65×65 μm and were taken with a center frequency of 860 MHz at the focus ($z = 0$). They also estimated quantitative acoustical properties of a single HeLa cell in vivo and to derive elastic parameters of subcellular structures. The value of the sound velocity inside the cell ($1{,}534.5 \pm 33.6$ m/s) was only slightly higher than that of the cell medium (1,501 m/s) (Weiss et al. 2007).

A research group from Toronto has also been investigating ultrasound backscatter from leukemia cells, but for the purposes of monitoring treatment. After the treatment, backscatter increased by 400 % compared with estimates obtained from the control samples. Changes in spectral parameters were hypothesized to be linked to structural cell changes during apoptosis (Taggart et al. 2007). They clarified the mechanism of backscatter change by comparing high frequency

Fig. 12.2 Optical and acoustical images of embryonic chicken heart muscle cells taken at room temperature

ultrasound spectroscopy (10–60 MHz) and SAM (0.9 GHz) on HeLa cells that were exposed to the chemotherapeutic agent cisplatin (Brand et al. 2008).

We have also applied SAM for cellular imaging in human pulmonary arterial endothelial cells. Cold preservation is the most practical method to maintain the viability of isolated lungs in clinical lung transplantation. However, rapid cooling may affect pulmonary endothelial function. Human pulmonary arterial endothelial cells were incubated at 4 °C for 2 h. Microtubules were visualized using immunocytochemical techniques. Ultrasonic attenuation was estimated with scanning acoustic microscopy. Endothelial barrier integrity was estimated as transendothelial electric resistance. Low temperature caused a reversible microtubule disassembly (Suzuki et al. 2004). Figure 12.3 shows the ultrasonic attenuation, endothelial electric resistance and microtubule formation during and after rapid cooling of pulmonary endothelial cells.

A two-dimensional distribution of the ultrasonic intensity, which is closely related to the mechanical properties of the cells, was visualized to analyze cell organs, such as the nucleus at the center part of the cell and the cytoskeleton at the peripheral zone. TGF-beta 1 induces fibroblasts to synthesize and contract extracellular matrix (ECM) components and connective tissue growth factor (CTGF). After stimulation with TGF-beta1, the ultrasonic intensity at the actin zone was significantly increased compared with the control (Hagiwara et al. 2009). Figure 12.4 shows the ultrasonic intensity image obtained with 300 MHz SAM before (left) and after (right) the stimulation by TGF-beta1.

Figure 12.5 shows 1.2 GHz SAM image of a cultured smooth muscle cell of the renal artery. The fringe shift indicates the difference of the cellular thickness.

Fig. 12.3 Ultrasonic attenuation, endothelial electric resistance and microtubule formation during and after rapid cooling of pulmonary endothelial cell

Fig. 12.4 Ultrasonic intensity image obtained with 300 MHz SAM before (*left*) and after (*right*) the stimulation by TGF-beta1

Fig. 12.5 1.2 GHz SAM image of a cultured smooth muscle cell of the renal artery

12.4 Conventional SAM Images

As described previously, soft tissues should be sliced thinly so that ultrasound can penetrate through the tissue and be reflected at the interface between tissue and substrate. From our experiences, approximately 10 micron thick specimens were appropriate for a 100 MHz SAM system because of signal amplitude and image quality. If the speed of sound is 1,500 m/s in the specimen, the wavelength of the 100 MHz ultrasound is approximately 15 μm. Thus, time-of-flight methods cannot

Fig. 12.6 Optical (*left*), ultrasonic attenuation (*center*) and sound speed (*right*) images of a papillary adenocarcinoma. *Scale bar* 1.0 mm

be applied for the thickness measurement of such thin materials. Our group proposed an unique method for calculating thickness and sound speed of thinly sliced tissues using the interference between surface and bottom reflections (Saijo et al. 1991, 1997). Results of these techniques are discussed in the following subsections.

12.4.1 Gastric Cancer (Saijo et al. 1991)

Gastric cancer tissues were classified into five groups according to their pathological findings; papillary adenocarcinoma, well-differentiated tubular adenocarcinoma, moderately differentiated tubular adenocarcinoma, poorly differentiated adenocarcinoma, and signet-ring cell carcinoma. Figure 12.6 shows an example of optical and acoustical images of a papillary adenocarcinoma. Figure 12.7 shows the bar graph providing sound speed estimates for normal mucosa and five kinds of cancer tissues.

Fig. 12.7 Bar graph showing sound speed in normal mucosa and five kinds of cancer tissues. (*Norm* normal mucosa, *Pap* papillary adenocarcinoma, *Well* well-differentiated tubular adenocarcinoma, *Mod* moderately-differentiated tubular adenocarcinoma, *Poor* poorly-differentiated adenocarcinoma, *Sig* signet-ring cell carcinoma)

The values of the sound speed increased as the cellular differentiation proceeded through the three kinds of tubular adenocarcinoma. As the density of the biological soft tissues can be assumed to be nearly constant, increased sound speed can thus be interpreted to mean that tubular adenocarcinoma tissues become acoustically stiffer as the differentiation of the tissue proceeds. Electron microscopy has shown that the number of desmosomes, which are considered to attach cell-to-cell, is significantly decreased in poorly differentiated adenocarcinomas. Well-differentiated tubular adenocarcinoma specimens exhibit nearly the same number of desmosomes as in normal mucosal tissue. This increasing trend was thus regarded as the result of tightening of the intercellular attachment. Both the ultrasonic attenuation and the sound speed were significantly lower in the signet-ring cell carcinoma than in the adenocarcinoma. The intracellular component of the signet-ring cell carcinoma is the periodic acid, Schiff stain (PAS) positive substrate. The lower values of the ultrasonic attenuation and sound speed may be attributed to the intracellular chemical components of the tumor tissues. These images of the gastric cancer tumors clearly indicate that the SAM system can be used to classify the types of cancer tissues, as revealed by estimates of the acoustic parameters associated with the pathologies.

12.4.2 Myocardial Infarction

Because cardiac B-scan was developed at Tohoku University in early 1960s (Tanaka et al. 1971), the origin of the strong echo in myocardium has been investigated by various methods. The "Sensitivity Varying Method" in which relative echo intensity of the myocardium tissue was compared with those of left ventricular cavity (defined as zero) and pericardium (defined as the strongest) was used for semiquantitative analysis of the echo intensity of myocardium. The echo intensity of myocardium and histopathology were compared in hypertrophic cardiomyopathy. The study demonstrated a relationship between the strong echo portion and collagen fiber distribution (Tanaka et al. 1985). However, there have been several reports that collagen content and myocardial echo amplitude were only weakly correlated (Lythall et al. 1993).

The discrepancy may be caused from difference of optical histology and acoustic properties; thus, acoustic microscopy was equipped for quantitative measurement of acoustic properties of myocardial tissue components at the microscopic level. Acoustic properties of the tissue elements in myocardial infarction were estimated and the elastic bulk modulus of the normal and pathological myocardium was assessed from the acoustic parameters. Four kinds of tissue elements: normal myocardium, degenerated myocardium, granulation and fibrosis, were observed in the specimens. Figure 12.8 is the acoustic image of the myocardial infarction tissue. Fibrotic lesion corresponds to high attenuation in this image. The average sound speeds were 1,620 m/s in the normal myocardium,

Fig. 12.8 Optical (*left*), ultrasonic attenuation (*center*) and sound speed (*right*) images of acute myocardial infarction. *Scale bar* 1.0 mm

1,572 m/s in the degenerated myocardium, and 1,690 m/s in the fibrosis, respectively (Fig. 12.9).

The density of each tissue element was measured by the graded $CuSO_4$ solution method, and the specific acoustic impedance was calculated by the sound speed and the density of each tissue element. The values were 1.75×10^6 Ns/m^3 in the normal myocardium, 1.69×10^6 Ns/m^3 in the degenerated myocardium, and 1.85×10^6 Ns/m^3 in the fibrosis, respectively. The relative reflected sound power (in dB) was calculated on the assumption that the interface between the two kinds of tissue elements was infinite and plane. The level at the interface between degenerated myocardium and fibrosis was calculated as 15.4 dB. The clinical echocardiography literature indicated that the strong echo of 15 dB was observed at the area of the scar in myocardial infarction. The origin of the strong echo was clarified by the acoustic microscopy measurements (Saijo et al. 1997).

Chandraratna et al. (1997) also assessed the bright echo area in myocardium by using a 600 MHz SAM system. They also showed that the echo intensity was affected by collagen fiber morphology (Tabel et al. 2006).

Because the biological tissues are modeled as fluid, the values of bulk modulus also can be calculated from the values of sound speed and density. The average estimated value of bulk modulus was 2.84×10^9 N/m^2 for the normal myocardium, 2.65×10^9 N/m^2 for the degenerated myocardium, 3.12×10^9 N/m^2 for the fibrosis, respectively. One of the roles of collagen fibers in acute myocardial infarction is to prevent the expansion of the infarction, and the frequency of left

Fig. 12.9 Bar graph showing sound speed in four kinds of tissue elements observed in acute myocardial infarction

ventricular rupture has been reported higher in the group which exhibits no remarkable increment of the scar in myocardium (Uusimaa et al. 1997). From the estimates, the bulk modulus of fibrosis was highest in the tissue components in myocardial infarction. This suggested that the fibrosis formation soon after myocardial infarction may prevent the infarct expansion and the cardiac rupture.

12.4.3 Kidney

SAM investigation of kidney was first initiated by Kessler et al. (1974) in the dawn of acoustic microscopy. However, the quantitative data on kidney tissues were only presented 20 years later when our group re-started investigations of kidney. Regarding renal cell carcinoma, the values of ultrasonic attenuation and sound speed were lower in both kinds of cancer cells than in normal kidney, although a significant difference was not found between the clear cell and granular cell. Also, both acoustic parameters for the cancer cells were significantly lower than those in hemorrhage and fibrosis. These data suggest that the elasticity of renal cell carcinoma tissue may be lower than that of normal kidney. Moreover, the high intensity echo in clinical echography may be related to the heterogeneity of the microscopic features of the acoustic field in the carcinoma tissue (Sasaki et al. 1996). We also applied SAM to measure acoustic properties of renal angiomyolipoma. The results suggested the difference of the clinical echographic features of renal cell carcinoma and angiomyolipoma (Sasaki et al. 1997).

For the acoustic properties of dialysed kidney, the attenuation constant for inflammatory granulation tissue was significantly higher than that for hyaline degeneration tissue ($P < 0.001$). Sound speed was high for granulation tissue, but tended to diminish gradually for hyaline degeneration. Sound speed increased again with progression to cystic degeneration ($P < 0.001$), but the ultrasonic attenuation remained low. When a cystic kidney contained a malignant lesion, the previously low ultrasonic attenuation increased at that site ($P < 0.001$), and the previously high sound speed was diminished ($P < 0.001$). Our data suggest that the physical properties of dialysed kidneys at different stages of pathology can be classified by their acoustic properties (Sasaki et al. 1997).

12.4.4 Atherosclerosis

The normal coronary artery consists of three parts and the structure is represented in the optical microscopic images. The intima is comprised of the endothelium, the inner elastic membrane, and thin collagen fibers. The media is comprised of the elastic fibers and the smooth muscle. The adventitia is comprised of the collagen fibers. The atherosclerotic intima consists of the thick collagen fibers, calcification, and lipid pool. In the present study, the acoustic properties of five kinds of tissue

Fig. 12.10 Optical (*left*), ultrasonic attenuation (*center*) and sound speed (*right*) images of coronary artery. *Scale bar* 1.0 mm

elements, viz., the intimal collagen fiber, calcification, normal media, adventitia, and fatty plaque were estimated. The cross-sectional images of coronary arteries were observed by both optical and acoustic microscopy (Saijo et al. 2007). Figure 12.10 shows an example of coronary artery images.

Based on the sound speed distribution, regions with different elastic parameters were divided. Geometric and compositional information of each acoustic image was digitized using NIH Image 1.60 software (free software from NIH) on a personal computer (Power Macintosh 9600/233). Finite element meshes were generated using ANSYS 5.5 (SAS IP, Inc., PA) software on a workstation (Ultra10, Sun Microsystems, CA). The finite element models were solved for an intraluminal pressure load of 110 mm Hg–14.6 kPa. In the calculation process, the region in the images was considered as a part of the circumferential vessel wall and the central angle was 30°. The sound speed distribution was inhomogeneous and the discontinuity of the elastic property in the fibrous cap was observed in the atherosclerotic coronary artery. Then, the fibrotic region was divided into four regions according to the elasticity distribution. The first principle stress distribution of the normal coronary artery showed that the stress was dominant in intima but the stress distribution in the intima was uniform. The stress distribution in the atherosclerotic plaque showed that the mean value of the stress was smaller than that found in the intima of the normal coronary artery, but the peak stress was very high and concentrated into the crack-like structure of the fibrous cap (Fig. 12.11a–d). The results indicated the pathophysiology of coronary plaque rupture was strongly correlated with biomechanical properties of the tissue components in coronary artery (Saijo et al. 2001).

Figure 12.12 shows the optical (a), 200 MHz (b) and 1.1 GHz (c) acoustic microscopy images of normal human coronary artery. The image quality is better in the 1.1 GHz image due to improved spatial resolution. For example, each elastic fiber in the media can be observed in the 1.1 GHz image while the media is almost homogeneous in the 200 MHz image. However, the three-layered appearance of coronary artery is more obvious in the 200 MHz image. The intima and adventitia had higher ultrasonic attenuation than that of the media.

Fig. 12.11 SAM data applied to FEM simulation. **a** Optical microscope, **b** acoustic microscope (sound speed), **c** FEM model, **d** stress distribution of atherosclerotic coronary artery

Fig. 12.12 Comparison of the spatial resolution according to the ultrasonic frequency. **a** Optical, **b** 200 MHz SAM, **c** 1.1 GHz SAM images of normal human coronary artery. *Scale bar* 0.2 mm

For the assessment of plaque rupture occurring in a vulnerable plaque, SAM investigations on atherosclerosis-prone mice were performed. The acoustic properties of the normal vessel wall and plaques, particularly fibrous caps of lipid-rich plaques, were evaluated in the aortic roots of six normal C57BL mice and 12 atherosclerosis-prone apoE-deficient (apoE(-/-)) mice by SAM. After processing, the attenuation of high-frequency (1.1 GHz) focused ultrasound was measured in unstained tissue sections by SAM followed by quantification of the amount and type of collagen in picrosirius red stained sections by means of polarized light microscopy (PLM). Collagen appeared green in thin fibrous caps and bright orange in thick caps by PLM. The attenuation of ultrasound was significantly higher in the collagen fibers with orange color compared to those with green color (17.2 vs. 6.6×10^3 dB/mm) (Saijo et al. 2001).

Human carotid atherosclerotic lesions were imaged by a GHz-range SAM system. The atherosclerotic lesions were characterized by either thickened fibrosis with dense collagen fibers or lipid accumulation with sparse collagen network by optical microscopy. SAM revealed that the fibrosis was classified into type I and type III collagen by attenuation of ultrasound and that the sound field of lipid accumulation lesions became inhomogeneous. The results could provide the scientific basis for imaging of vulnerable plaques using diagnostic ultrasound (Saijo et al. 2002).

Comparison of an in vivo intravascular ultrasound (IVUS) image and in vitro excised tissue demonstrated the importance of SAM for understanding a lower frequency ultrasound image. Figure 12.13 shows the comparison of a: optical (Elastica-Masson staining), b: SAM (attenuation) c: SAM (sound speed) and d: IVUS of thrombus in acute coronary syndrome. The tissue was obtained by an aspiration catheter (PercuSerge, Medtronic, Minneapolis, MN, USA) in a clinical setting. The white square in the IVUS image corresponds to microscopy images.

12.5 Ultrasound Speed Microscopy

A single ultrasound pulse with a pulse width of 2 ns was emitted and received by the same transducer above the specimen. Saline was used as the coupling medium between the transducer and the specimen. The reflections from the tissue surface and those from the interface between the tissue and glass were received by the transducer and were introduced into a Windows-based PC with a fast digitizer card (Acqiris DP210, 2GSa/s, 8-bit, onboard memory 16 MB, Geneve, Switzerland). The frequency range was 500 MHz, and the sampling rate was 2 GS/s. Eight consecutive values of the signal taken for a pulse response were averaged in order to reduce random noise.

The transducer was mounted on an X–Y stage with a microcomputer board that was driven by the PC through RS232C. Both X-scan and Y-scan directions were driven by linear servo motors and the position was detected by an encoder. The scan was controlled to reduce the effects of acceleration at the start and

Fig. 12.13 Comparison of SAM and IVUS images. **a** Optical (Elastica-Masson staining), **b** SAM (attenuation), **c** SAM (sound speed) and **d** IVUS of thrombus in acute coronary syndrome

deceleration at the end of the X-scan. Finally, two-dimensional distributions of ultrasonic intensity, sound speed, attenuation coefficient and thickness of a specimen measuring 2.4 × 2.4 mm were visualized using 300 × 300 pixels. The total scanning time was 63 s.

Denoting the standardized phase of the reflection wave at the tissue surface as ϕ_{front}, the standardized phase at the interference between the tissue and the substrate as ϕ_{rear} then,

$$2\pi f \times \frac{2d}{c_o} = \phi_{front} \tag{12.6}$$

$$2\pi f \times 2d\left(\frac{1}{c_o} - \frac{1}{c}\right) = \phi_{rear} \tag{12.7}$$

where d is the tissue thickness, c_o is the sound speed in coupling medium and c is the sound speed in the tissue. Thickness is obtained as

$$d = \frac{c_o}{4\pi f}\phi_{front} \tag{12.8}$$

Fig. 12.14 USM images (*left* ultrasonic attenuation, *right* sound speed) of an adenocarcinoma of the lung. *Scale bar* 0.5 mm

Finally, sound speed is calculated as

$$c = \left(\frac{1}{c_o} - \frac{\phi_{rear}}{4\pi f d} \right)^{-1} \tag{12.9}$$

After determination of the thickness, attenuation of ultrasound was then calculated by dividing the reflected amplitude by the thickness and frequency.

12.5.1 Examples of USM Images

Figure 12.14 shows the ultrasound speed microscope images of an adenocarcinoma of the lung. The acoustic properties of the adenocarcinoma lesion are homogeneous and the sound speed is approximately 1,600 m/s. Indentation of pleura and vessels were observed in this sample and the sound speed of these parts were estimated at up to 1,750 m/s.

Figure 12.15 is an image of pulmonary tuberculosis. The histology is characterized by formation of granuloma, which is specially called as tubercle. A Langhans's cell is formed by fusion of some epithelioid cells. Non-structured hyalinized tissue is surrounded by a granuloma with Langhans's cells. Ultrasonic attenuation and sound speed of the granuloma was observed to be high.

Figure 12.16 is an image of a squamous cell carcinoma of the esophagus. The cancer cells differentiate to stratified squamous epithelium. This type of cell occupies 90 % of esophageal cancer. Keritinization and inter-cellular bridge formation are the typical findings of the differentiation. The ultrasonic attenuation and sound speed were observed to be higher than those of normal mucosa.

Figure 12.17 is an image of a well-differentiated tubular adenocarcinoma of the stomach. The adenocarcinoma image shows clear tubular structure. The tubular

Fig. 12.15 USM images (*left* ultrasonic attenuation, *right* sound speed) of pulmonary tuberculosis. *Scale bar* 0.5 mm

Fig. 12.16 USM images (*left* ultrasonic attenuation, *right* sound speed) of a squamous cell carcinoma of the esophagus. *Scale bar* 0.5 mm

Fig. 12.17 USM images (*left* ultrasonic attenuation, *right* sound speed) of a well-differentiated tubular adenocarcinoma of the stomach. *Scale bar* 0.5 mm

Fig. 12.18 USM images (*left* ultrasonic attenuation, *right* sound speed) of a moderately differentiated adenocarcinoma of the colon. *Scale bar* 0.5 mm

structure had higher ultrasonic attenuation and sound speed than the surrounding zone. The sound speed values were similar to our previous estimates (Sasaki et al. 1997).

Figure 12.18 is an image of a moderately differentiated adenocarcinoma of the colon. A adenocarcinoma with desmoplasia (fibrosis) is typical for this cancer. The case shown here was classified as early stage because the tumor was localized in submucosal layer. A part of the cancer tissue contained rich fibrosis and the lesion had high ultrasonic attenuation and sound speed.

12.5.2 Articular Tissues

As described before, SAM data can be used as the basic data for assessing biomechanics of tissues and cells. Research on biomechanics is widely performed in the field of orthopedic surgery. The acoustic properties of rabbit supraspinatus tendon insertions were estimated using a SAM system. In the tendon proper and the non-mineralized fibrocartilage, the sound speed and ultrasonic attenuation gradually decreased as the predominant collagen type changed from I to II. In the mineralized fibrocartilage, the acoustic properties increased markedly with the mineralization of the fibrocartilaginous tissue. These results indicate that the non-mineralized fibrocartilage has the lowest elastic modulus among four zones at the insertion site, which could be interpreted as an adaptation to various types of biomechanical stress (Sano et al. 2006).

Our group also attempted to quantify changes of articular cartilage of the knee joint during immobilization in a rat model. The knee joints of adult male rats were immobilized at 150° of flexion using an internal fixator for 3 days, and 1, 2, 4, 8, and 16 weeks. The articular cartilage from the medial midcondylar region of the knee was obtained, divided into three areas (non-contact area, transitional area,

Fig. 12.19 Gradation color images and sound speed changes of articular cartilage assessed by scanning acoustic microscopy (*SAM*). The *upper row* (**A** and **B**) shows gradation color images of the tibial articular cartilage at 16 weeks; the *second row* (**C** and **D**) shows each corresponding area to each *upper row* with hematoxylin and eosin staining, respectively. (**A** and **C**): the immobilized group, (**B** and **D**): the control group, (**E**): gradation color scale bar. The low sound speed area gradually expanded from the surface of the articular cartilage in the immobilized group. The *third row* (**F** and **G**) shows the femoral cartilage; the *lower row* (**H** and **I**) shows the tibial cartilage of the sound speed. (**F** and **H**): the transitional area, (**G** and **I**): the noncontact area

contact area), and in each area, a degree of degeneration was evaluated by gross observation, histomorphometric grading, and measurements of thickness and number of chondrocytes. Figure 12.19 shows the results.

Degeneration of the articular cartilage was mainly observed in the contact and transitional areas. Matrix staining intensity by safranin-O and number of chondrocytes were decreased in these two areas. The thickness of the articular cartilage in the non-contact and contact areas was unchanged, but it was increased in the transitional area. Decrease in sound speed was observed in the transitional area of both the femoral and tibial cartilage, indicating the softening of the articular cartilage. The changes of articular cartilage became obvious as early as one week after immobilization. These changes may be due to a lack of mechanical stress or a lack of joint fluid circulation during immobilization (Hagiwara et al. 2009; Ando et al. 2011).

Fig. 12.20 Schematic illustration of reflections in acoustic impedance mode

12.6 Ultrasound Impedance Microscope

Figure 12.20 shows the schematic illustration of reflections in acoustic impedance mode. In this mode, reflection from the interface between the thin plastic plate and tissue was visualized. Thus, thin-slicing of the tissue is not required in this mode.

The target signal is compared with the reference signal and interpreted into acoustic impedance as

$$Z_{target} = \frac{1 - \frac{S_{target}}{S_0}}{1 + \frac{S_{target}}{S_0}} Z_{sub} = \frac{1 - \frac{S_{target}}{S_{ref}} \cdot \frac{Z_{sub} - Z_{ref}}{Z_{sub} + Z_{ref}}}{1 + \frac{S_{target}}{S_{ref}} \cdot \frac{Z_{sub} - Z_{ref}}{Z_{sub} + Z_{ref}}} Z_{sub} \tag{12.10}$$

where $\boldsymbol{S}_0$ is the transmitted signal, $\boldsymbol{S_{target}}$ and $\boldsymbol{S_{ref}}$ are reflections from the target and reference, and $\boldsymbol{Z_{target}}$, $\boldsymbol{Z_{ref}}$ and $\boldsymbol{Z_{sub}}$ are the acoustic impedances of the target, reference and substrate, respectively (Saijo 2009).

Acoustic impedance was assumed to be 1.5×10^6 Ns/m^3 when water was used as a reference. When silicon rubber was used, its acoustic impedance was calibrated with water as the standard reference material. In our analysis, 0.965×10^6 Ns/m^3 was used. The acoustic impedance of the substrate was calculated to be 3.22×10^6 Ns/m^3, considering its sound speed and density.

Figure 12.21 shows the ultrasound impedance image of a rat brain. This image was obtained by placing fresh brain tissue on the plastic plate. Each layer of the brain was clearly observed due to acoustic impedance differences.

12.7 Summary of This Chapter

The principle and brief history of scanning acoustic microscopy (SAM) for medicine and biology were described here. SAM was able to visualize high quality microscopy images of tissues and cells suitable for histopathological examinations.

For bone, cartilage, tendon and cardiovascular tissues, micro-acoustic properties provided important information on biomechanical properties. Biomechanics of these tissues are especially important for assessing the pathophysiology.

Cells are considered to consist of visco-elastic materials and SAM has provided information on viscosity by ultrasonic attenuation estimates and information on

Fig. 12.21 Ultrasound impedance image of rat brain. *Scale bar* 0.5 mm

elasticity by sound speed estimates. Instead of stretching cells or using atomic force microscopy for measuring biomechanical properties, SAM can be used to measure precise mechanical property distributions without contact to the cells.

Thus, SAM introduced a new concept of pathology that is based on the mechanical properties of is the object being imaged. Recent developments such as ultrasound speed microscopy, 3D ultrasound microscopy and high frequency array transducers may provide a clinically applicable SAM in the near future.

References

Ando A, Suda H, Hagiwara Y, Onoda Y, Chimoto E, Saijo Y, Itoi E (2011) Reversibility of immobilization-induced articular cartilage degeneration after remobilization in rat knee joints. Tohoku J Exp Med 224(2):77–85

Bereiter-Hahn J (1985) Architecture of tissue cells. The structural basis which determines shape and locomotion of cells. Acta Biotheor 34(2–4):139–148

Bereiter-Hahn J, Lüers H (1998) Subcellular tension fields and mechanical resistance of the lamella front related to the direction of locomotion. Cell Biochem Biophys 29(3):243–262

Brand S, Weiss EC, Lemor RM, Kolios MC (2008) High frequency ultrasound tissue characterization and acoustic microscopy of intracellular changes. Ultrasound Med Biol 34(9):1396–1407

Briggs GA, Wang J, Gundle R (1993) Quantitative acoustic microscopy of individual living human cells. J Microsc 172(Pt 1):3–12

Chandraratna PA, Whittaker P, Chandraratna PM, Gallet J, Kloner RA, Hla A (1997) Characterization of collagen by high-frequency ultrasound: evidence for different acoustic properties based on collagen fiber morphologic characteristics. Am Heart J 133(3):364–368

Hagiwara Y, Saijo Y, Ando A, Chimoto E, Suda H, Onoda Y, Itoi E (2009a) Ultrasonic intensity microscopy for imaging of living cells. Ultrasonics 49(3):386–388

Hagiwara Y, Ando A, Chimoto E, Saijo Y, Ohmori-Matsuda K, Itoi E (2009b) Changes of articular cartilage after immobilization in a rat knee contracture model. J Orthop Res 27(2):236–242

Hildebrand JA, Rugar D, Johnston RN, Quate CF (1981) Acoustic microscopy of living cells. Proc Natl Acad Sci USA 78(3):1656–1660

Johnston RN, Atalar A, Heiserman J, Jipson V, Quate CF (1979) Acoustic microscopy: resolution of subcellular detail. Proc Natl Acad Sci USA 76(7):3325–3329

Kessler LW, Fields SI, Dunn F (1974) Acoustic microscopy of mammalian kidney. J Clin Ultrasound 2(4):317–320

Lemons RA, Quate CF (1975) Acoustic microscopy: biomedical applications. Science 188(4191):905–911

Litniewski J, Bereiter-Hahn J (1990) Measurements of cells in culture by scanning acoustic microscopy. J Microsc 158(Pt 1):95–107

Lythall DA, Bishop J, Greenbaum RA, Ilsley CJ, Mitchell AG, Gibson DG, Yacoub MH (1993) Relationship between myocardial collagen and echo amplitude in non-fibrotic hearts. Eur Heart J 14(3):344–350

Mikhailov IG, Soloviev VA, Syrnikov YP (1964) Basics of molecular acoustics. Khimia Publications, Moscow

Saijo Y (2009) Acoustic microscopy: latest developments and applications. Imaging Med 1(1):47–63

Saijo Y, Tanaka M, Okawai H, Dunn F (1991) The ultrasonic properties of gastric cancer tissues obtained with a scanning acoustic microscope system. Ultrasound Med Biol 17(7):709–714

Saijo Y, Tanaka M, Okawai H, Sasaki H, Nitta SI, Dunn F (1997) Ultrasonic tissue characterization of infarcted myocardium by scanning acoustic microscopy. Ultrasound Med Biol 23(1):77–85

Saijo Y, Ohashi T, Sasaki H, Sato M, Jorgensen CS, Nitta S (2001a) Application of scanning acoustic microscopy for assessing stress distribution in atherosclerotic plaque. Ann Biomed Eng 29(12):1048–1053

Saijo Y, Jørgensen CS, Falk E (2001b) Ultrasonic tissue characterization of collagen in lipid-rich plaques in apoE-deficient mice. Atherosclerosis 158(2):289–295

Saijo Y, Jørgensen CS, Mondek P, Sefránek V, Paaske W (2002) Acoustic inhomogeneity of carotid arterial plaques determined by GHz frequency range acoustic microscopy. Ultrasound Med Biol 28(7):933–937

Saijo Y, Santos Filho E, Sasaki H, Yambe T, Tanaka M, Hozumi N, Kobayashi K, Okada N (2007) Ultrasonic tissue characterization of atherosclerosis by a speed-of-sound microscanning system. IEEE Trans Ultrasound Ferroelectr Freq Control 54(8):1571–1577

Sano H, Saijo Y, Kokubun S (2006) Non-mineralized fibrocartilage shows the lowest elastic modulus in the rabbit supraspinatus tendon insertion: measurement with scanning acoustic microscopy. J Shoulder Elbow Surg 15(6):743–749

Sasaki H, Tanaka M, Saijo Y, Okawai H, Terasawa Y, Nitta S, Suzuki K (1996) Ultrasonic tissue characterization of renal cell carcinoma tissue. Nephron 74(1):125–130

Sasaki H, Saijo Y, Tanaka M, Nitta S, Yambe T, Terasawa Y (1997a) Characterization of renal angiomyolipoma by scanning acoustic microscopy. J Pathol 181(4):455–461

Sasaki H, Saijo Y, Tanaka M, Nitta S, Terasawa Y, Yambe T, Taguma Y (1997b) Acoustic properties of dialysed kidney by scanning acoustic microscopy. Nephrol Dial Transplant 12(10):2151–2154

Suzuki S, Bing H, Sugawara T, Matsuda Y, Tabata T, Hoshikawa Y, Saijo Y, Kondo T (2004) Paclitaxel prevents loss of pulmonary endothelial barrier integrity during cold preservation. Transplantation 78(4):524–529

Tabel GM, Whittaker P, Vlachonassios K, Sonawala M, Chandraratna PA (2006) Collagen fiber morphology determines echogenicity of myocardial scar: implications for image interpretation. Echocardiography 23(2):103–107

Taggart LR, Baddour RE, Giles A, Czarnota GJ, Kolios MC (2007) Ultrasonic characterization of whole cells and isolated nuclei. Ultrasound Med Biol 33(3):389–401

Tanaka M, Neyazaki T, Kosaka S, Sugi H, Oka S, Ebina T, Terasawa Y, Unno K, Nitta K (1971) Ultrasonic evaluation of anatomical abnormalities of heart in congenital and acquired heart diseases. Br Heart J 33(5):686–698

Tanaka M, Nitta S, Nitta K, Sogo Y, Yamamoto A, Katahira Y, Sato N, Ohkawai H, Tezuka F (1985) Non-invasive estimation by cross sectional echocardiography of myocardial damage in cardiomyopathy. Br Heart J 53(2):137–152

Uusimaa P, Risteli J, Niemelä M, Lumme J, Ikäheimo M, Jounela A, Peuhkurinen K (1997) Collagen scar formation after acute myocardial infarction: relationships to infarct size, left ventricular function, and coronary artery patency. Circulation 96(8):2565–2572

Veselý P, Lücers H, Riehle M, Bereiter-Hahn J (1994) Subtraction scanning acoustic microscopy reveals motility domains in cells in vitro. Cell Motil Cytoskelet 29(3):231–240

Weiss EC, Lemor RM, Pilarczyk G, Anastasiadis P, Zinin PV (2007a) Imaging of focal contacts of chicken heart muscle cells by high-frequency acoustic microscopy. Ultrasound Med Biol 33(8):1320–1326

Weiss EC, Anastasiadis P, Pilarczyk G, Lemor RM, Zinin PV (2007b) Mechanical properties of single cells by high-frequency time-resolved acoustic microscopy. IEEE Trans Ultrason Ferroelectr Freq Control 54(11):2257–2271

Chapter 13
Acoustic Microscopy of Cells

Michael C. Kolios, Eric M. Strohm and Gregory J. Czarnota

Abstract Acoustic microscopy has proven to be a versatile biological tool since it was first developed nearly 40 years ago. It can be used to create ultrasound images with a resolution that approach conventional optical microscopy, or provide quantitative data about the mechanical properties of the material being investigated. This chapter focuses on acoustic microscopy methods to investigate how single cells change during biological processes such as mitosis and chemotherapy-induced apoptosis. Using ultrasound frequencies at 375 MHz, various properties of cells (such as the thickness, sound speed, acoustic impedance, density, bulk modulus and attenuation) were calculated during these biological processes. Significant differences in these properties were observed between cells in their normal resting state and late-stage apoptosis. C-scan and B-scan imaging of apoptotic cells using 375 and 1,000 MHz provided information that could not be obtained using other scanning methods. Variations in the ultrasound backscatter were observed over time, which suggests that rapid changes in the ultrasound scattering structures occur within seconds. In contrast, non-apoptotic cells did not show the same activity. Finally, high resolution attenuation imaging of cells using frequencies up to 1.2 GHz clearly showed organelles such as the nucleus, nucleolus and vacuoles. During apoptosis, the nucleus became highly attenuating and was several times more attenuating than the surrounding cytoplasm. In summary, this chapter describes acoustic microscopy methods and techniques for a qualitative and quantitative analysis of biological material.

M. C. Kolios (✉) · E. M. Strohm
Department of Physics, Ryerson University, 350 Victoria Street, Toronto, ON M5B 2K3, Canada
e-mail: mkolios@ryerson.ca

G. J. Czarnota
Department of Radiation Oncology, Odette Cancer Centre and Imaging Research, Sunnybrook Research Institute, Sunnybrook Health Sciences Centre, 2075 Bayview Avenue, Toronto, ON M4N 3M5, Canada

J. Mamou and M. L. Oelze (eds.), *Quantitative Ultrasound in Soft Tissues*, DOI: 10.1007/978-94-007-6952-6_13,

13.1 Introduction

The concept of using high frequency acoustic waves for imaging was first proposed in 1929 by Sokolov (Sokolov 1929). The first high frequency ultrasound imaging device was then patented and created by Sokolov to detect subsurface flaws in materials in 1937 (Sokolov 1939), but the device suffered from technical limitations and was not practical at the 3 GHz operating frequency. Throughout the next few decades advances were made in acoustic microscopy, including a scanning laser acoustic microscope in 1972 that operated up to 100 MHz (Kessler et al. 1972). In 1974 the first sub-micron resolution scanning acoustic microscope was created by Lemons and Quate (Lemons and Quate 1974). Two practical applications were readily apparent: subsurface material imaging and flaw detection (used extensively in nondestructive testing, NDT) and probing small biological specimens. Readers are encouraged to review the numerous excellent references on the use of acoustic microscopy for NDT for further information on that subject (Kundu 2004; Shull 2002; Hellier 2001; Rose 2004). This chapter will focus on the examination of biological media using acoustic microscopy methods.

Biological cells and tissue have poor inherent optical contrast when viewed using optical microscopes. Techniques such as phase contrast, dark field and differential interference contrast can help improve optical imaging of cells (Spector and Goldman 2006). Fluorescent staining can improve identification of specific cellular structures, but requires the addition of dyes that may alter the natural state of a living cell and can only be used for a finite time after administration. While unstained cells have poor optical contrast, they have greater acoustic contrast due to the variations in mechanical properties throughout the cell. Moreover, acoustic waves are penetrating, and can be used to visualize the internal structure of cells and thin tissue samples. Acoustic microscopy is not limited to imaging; it can also be used to determine quantitative information about the specimen.

There are many publications that describe how acoustic microscopy can be used for imaging and quantifying cellular properties. Images of various types of living and fixed cells and tissue were first published in 1975 using frequencies up to 900 MHz (Lemons and Quate 1975), and spatial resolutions comparable to optical microscopes were demonstrated in 1978 (Jipson and Quate 1978). This work was followed up by high quality sub-micron resolution measurements of fixed cells (Johnston et al. 1979) and red blood cells (Wickramasinghe 1979) in 1979, then live cells in 1981 (Hildebrand et al. 1981). Individual chromosomes extracted from cultured peripheral blood leukocytes were imaged using low temperature acoustic microscopy using 1.8 GHz with resolution of 0.38 μm in 1980 (Rugar et al. 1980). Another resolution milestone was reached when individual bacteria were imaged using 8 GHz ultrasound and liquid helium, reaching a resolution of 20 nm (Hadimioglu and Foster 1984). These initial studies showcased the ability of ultrahigh frequency acoustic imaging to resolve detail at the sub-micron level in live

cells without any stains. Following these seminal publications, numerous studies have reported high resolution imaging of individual cells and cellular structures.

Acoustic microscopy has also been used to determine quantitative information about the cell itself. The thickness, acoustic impedance and attenuation of single living cells can be estimated from the interference fringes caused by reflections from the substrate and cell surface (Hildebrand and Rugar 1984; Litniewski and Bereiter-Hahn 1990; Lüers et al. 1991), but requires thin samples and prior knowledge of the sound speed and density distribution within the cell. Measurements of the reflected signal as a function of transducer position above the sample are called $v(z)$ curves (Atalar et al. 1977). The incident acoustic wave can undergo mode conversion to a surface acoustic wave at specific angles of incidence and transducer positions. The surface wave is then reemitted back towards the transducer, which cause variations in the $v(z)$ signal as a function of position. These variations can be used to determine several properties of cells such as the thickness, sound speed, density elasticity and attenuation (Kundu et al. 1991). Variations of the signal as a function of frequency, known as a $v(f)$ curve, can also be used to measure the thickness, sound speed and attenuation of cells (Kundu et al. 2000). Time resolved methods require resolving the echoes from the cell surface and substrate. The difference in time and amplitude of these echoes can be used to determine the thickness, sound speed, acoustic impedance and attenuation of a cell (Briggs et al. 1993; Daft et al. 1989; Weiss et al. 2007).

Acoustic microscopy methods can be applied to living cells to image changes in cellular structure over time. Examples include probing cells during mitosis (Linder et al. 1992; Strohm et al. 2010), apoptosis (Strohm et al. 2010), measuring cell volume (Weiss et al. 2007), cell motility (Veselý et al. 1994; Zoller et al. 1997) and cell adhesion to substrates (Tittmann et al. 2007; Hildebrand 1985). Moreover, quantitative information about cellular properties can be extracted and related to the cellular structure. Excellent comprehensive reviews of the history, lens design theory, wave theory, spatial resolution limitations, and applications are given elsewhere (Kundu 2004; Briggs and Kolosov 2009; Maev 2008).

13.2 History of Advances

The first generation acoustic microscopes did not have the ability to optically view samples during acoustic measurements. Optical imaging was performed either before or after the acoustic measurements. Difficulties arose in aligning the optical and acoustic measurements over the same sample region, particularly for live cell imaging where cells can move or change shape over time. Cell motility made it difficult to ensure the appropriate viable cells or even a specific cell was being interrogated. Methods were developed to integrate optical imaging directly into the transducer (Faridian and Wickramasinghe 1983) using rapid sequential optical and acoustic imaging (Nakamura et al. 1986), and more recently by combining the acoustic lens with an inverted optical microscope for simultaneous optical and

Fig. 13.1 The SASAM 1000 acoustic microscope (Kibero GmbH, Germany). *Left* (*A*) Climate controlled chamber, (*B*) Olympus inverted microscope and transducer module, (*C*) Computer controller, (*D*) Climate controller module, (*E*) Electronics systems. *Right* A close up of the sample holder, with the transducer positioned above and the optical objective underneath. (*A*) Transducer, (*B*) Sample holder, (*C*) Thermocouple

acoustic imaging (Kanngiesser and Anliker 1992; Lemor et al. 2003; Weiss et al. 2007). An example of a combined optical-acoustic microscope called the SASAM recently developed by Kibero GmbH is shown in Fig. 13.1. The acoustic lens is built on top of an inverted optical microscope (IX-81, Olympus, Japan) and acoustic measurements are made from the top of the sample, while optical imaging is performed through the optical objectives underneath the sample (Fig. 13.1). The incandescent lamp used for optical imaging can be replaced with a xenon arc lamp for fluorescent imaging. The optical and acoustic systems can be separately controlled entirely via external hardware and a computer. A rotating module above the sample houses the acoustic lens and an optical condenser. The condenser can be rotated in place to make high quality transmission optical measurements with optional phase contrast enhancement, however only reflection-mode optical images are possible when the transducer is positioned over the sample. The entire acoustic microscope is housed in an environmentally controlled chamber to maintain constant temperature during measurements, which is particularly important for longitudinal cellular measurements over time.

One of the most important elements of the instrument is the ultrasound transducer, which converts the electrical signal into pressure waves and vice versa. Various single element transducers can be used with this system. An example of three different transducers with center frequencies of 200, 375 and 1,200 MHz is shown in Fig. 13.2a. A schematic of transducer operation typically used in acoustic microscopy is shown in Fig. 13.2b. The bulk of the transducer consists of a sapphire buffer rod (typically 4–6 mm in length, 2–4 mm in diameter) with a spherical cavity ground at the bottom, and a piezoelectric material (typically zinc oxide (ZnO) for ultrahigh frequency applications) at the top. Pressure waves created by the ZnO travel through the lens and are focused by the cavity onto the sample. Reflected echoes travel back through the lens, are converted to a voltage by the ZnO

Fig. 13.2 *Left* Three transducers used in the SASAM acoustic microscope. From left to right are 200, 375 and 1,200 MHz transducers. *Right* A diagram showing the typical construction and use of a transducer with focus within the cell

piezoelectric and then the analog signals are digitized by a computer. The cavity aperture and angle, along with buffer rod dimensions are calculated depending on the application and frequency used. An excellent thorough review of acoustic microscopy lens design and theory is discussed in Briggs and Kolosov (2009).

Combining optical and acoustical imaging ensures that cells can be observed optically during the acoustic measurements and allows for precise acoustic targeting to cells or cell regions of interest as the transducer is visible in the optical images. Figure 13.3 shows a 375 MHz transducer positioned above cells on a cell culture dish. The 300 μm transducer diameter cavity and several live cells are visible within the optical field of view. The transducer appears blurred as it 300 μm above the sample and beyond the focal range of the 10x optical objective. The cells directly under the transducer cavity appear dark with poor contrast (region B), whereas the cells around the flat transducer rim appear brighter with better contrast (region C). This is because the transducer rim is flat and perpendicular to the sample; the light from the objective travels through the sample and is reflected by the rim back through the sample. This causes slightly better contrast for cells under the rim than the cavity. Higher frequency transducers have a smaller aperture (50–100 μm for GHz frequencies), and therefore are easier to position with respect to the sample.

Maintaining constant temperature during acoustic measurements is crucial for ultra-high frequency acoustic imaging. Temperature fluctuations can have a strong effect on transducer sensitivity, where a shift of only 0.1 °C is enough to cause a measurable change in focus when using a GHz transducer. This can affect the imaging sensitivity and increase errors during quantitative measurements of cell properties. The environmental control system used with the Kibero SASAM acoustic microscope can maintain temperature stability of 37 °C ± 0.05 °C. If samples are left undisturbed in the system over prolonged periods of time, temperature stability has approached ±0.02 °C. The substrates and samples should be at the target temperature within the environmental chamber before starting measurements. When a substrate at room temperature is placed in the heated chamber,

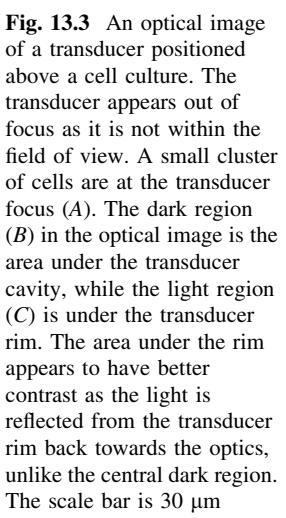

Fig. 13.3 An optical image of a transducer positioned above a cell culture. The transducer appears out of focus as it is not within the field of view. A small cluster of cells are at the transducer focus (*A*). The dark region (*B*) in the optical image is the area under the transducer cavity, while the light region (*C*) is under the transducer rim. The area under the rim appears to have better contrast as the light is reflected from the transducer rim back towards the optics, unlike the central dark region. The scale bar is 30 μm

it will expand as it acclimatizes. This effectively moves the sample towards the transducer, causing deviations in focus over time.

Cells present an additional difficulty over static or fixed samples in that they are alive; they must be kept in proper conditions to ensure they are viable and in their natural state. This generally requires temperatures around 37 °C with specific humidity and carbon dioxide levels, and a growth medium with the appropriate nutrients (the exact conditions depend on the cell type used). If cells are kept under non-optimum conditions, they can become stressed and deviate from their natural state. Extreme conditions can result in cell degradation which results in cell rounding, poor adhesion and even death.

The hardware used for ultra-high frequency acoustic microscopy must be optimized for high speed/high frequency data transfer (8 GHz sampling rates when using frequencies over 1 GHz) if the radiofrequency (RF) data are to be acquired for further analysis. Technological advancements in electronics and computers have enabled offline analysis of the RF data generated during acoustic measurements, where post-processing methods can be used to improve the signal. In addition, low-noise and low-attenuation cables should be used to reduce transmission losses.

13.3 Single Cell Imaging

One of the first applications of the acoustic microscope was to image biological material, specifically single cells. The resolution approaches 1 μm at 1 GHz, which is suitable for imaging single cells which are typically 15–30 μm in diameter. Acoustic microscopes use a single element transducer. To create a 2D

image, the transducer must be scanned over the sample to record the signal at each position. Acquisition times for a 50 × 50 μm area can range from several seconds to several minutes, depending on the step size of the raster scan and temporal averaging of the RF signals. Smaller step sizes increase resolution and higher temporal averaging increase the signal to noise ratio (SNR) resulting in a better image, but comes at the cost of acquisition time. Imaging live cells presents some difficulties, as they can move during acquisition. Some cells are known to move up to several microns per minute (Kay et al. 2008) and cell activity increases dramatically during biological processes such as mitosis and apoptosis. Therefore, it is challenging to reduce acquisition time while maintaining image quality.

Typically two types of images are generated using acoustic microscopy: attenuation images and backscatter images, both of which can give valuable information about the cell structure. During a scan, ultrasound echoes are recorded from the cell surface, cell interior and substrate. As the ultrasound pulse propagates, it is attenuated as it travels through the cell and back to the transducer. In a backscatter image, the echo from the substrate is gated out of the image, and only the scattered ultrasound from within the cell is used to create the image. This gives a map of the scattering regions within a cell above the substrate. An attenuation image maps the total attenuation of the ultrasound pulse as it travels through the specimen. The attenuation varies through different parts of the cell depending on the cell thickness and the cell composition at the measurement location (such as cytoplasm or the nucleus). The attenuation image can be generated by using the gated signal from the substrate echo only (ignoring any backscatter from within the cell), and gives a map of the attenuation throughout cell.

The combined optical-acoustic microscope is ideal for imaging live cells over time to monitor various biological processes. One such process important to cancer therapy is apoptosis, where cells undergo significant biological and morphological changes over a period of time of up to several hours (Kerr et al. 1972; Taylor et al. 2008). Figure 13.4 illustrates the apoptotic process. During the initial stages of apoptosis, small protrusions in the membrane called blebs can be observed. Eventually the cell morphs into a spherical shape due to the digestion of the structural proteins that help maintain the normal cellular shape. Blebbing increases and nuclear condensation occurs. Over time, the intracellular contents are internalized into smaller apoptotic bodies, which are then eventually engulfed by phagocytes in vivo. Significant insight into the changes a cell undergoes during apoptosis has been observed using various optical imaging methods including confocal microscopy (Pelling et al. 2009). Ultrasound is based on a different type of contrast mechanism, mechanical contrast, and can be used to complement optical studies and help understand the mechanical changes that occur during the apoptotic process.

Our research group has studied the apoptotic process using breast cancer (MCF7) cells. These are mammary cancer cells derived from an invasive breast ductal carcinoma that have been used extensively in cancer studies since the early 1970s (Lacroix and Leclercq 2004). Paclitaxel was added to the MCF7 cell culture 24 h prior to imaging to induce apoptosis; specific experimental details can be found in Strohm et al. (2010). The cells used in this study are adherent.

Fig. 13.4 A schematic diagram of the apoptotic process. A cell (**a**) will lose structural integrity due to the digestion of structural proteins, resulting in morphological changes into a spherical shape (**b**). The internal components are compartmentalized into smaller apoptotic bodies (**c**), which can then be removed by the immune system (**d**). Blebbing or small protrusions in membrane can be observed from early stages

When adherent cells undergo apoptosis, they round up, enabling easy identification optically due to their morphological shape change. However optical identification of apoptotic cells can be inconclusive, therefore fluorescent stains are used to help identify apoptosis, particularly the stage of apoptosis. Hoechst 33342 stain labels the DNA in all cells and fluoresces blue. It enables accurate delineation of the nuclear membrane, which is important for identifying viable cells. Two stains are commonly used simultaneously to detect apoptosis: Annexin-V (which fluoresces green) and propidium iodide (which fluoresces red). Annexin-V binds to phosphatidylserine, a phospholipid usually present only in the cellular interior. During the very early stages of apoptosis, phosphatidylserine becomes exposed on the cellular membrane exterior to which Annexin-V can then bind. Propidium iodide labels DNA but cannot pass through the membrane of a healthy viable cell. Hoechst 33342 and propidium iodide both stain DNA, but only Hoechst 33342 can penetrate and stain cells at any stage of the cell cycle while propidium iodide can only penetrate into cells that have lost membrane integrity. Membrane integrity is lost during the later stages of apoptosis. Therefore Annexin-V and propidium iodide can be used in combination to identify the stage of apoptosis. Cells that stain Annexin-V positive and propidium iodide negative indicate a cell in an early stage of apoptosis, while both Annexin-V and propidium iodide positive indicate a cell in the later stage of apoptosis. Figure 13.5 shows cells identified in various stages of apoptosis due to the presence or absence of these stains. The stained cells can then be selected for acoustical imaging and quantitative measurements at different stages of apoptosis.

In the 1990s, measurements of the ultrasound backscatter (20–60 MHz) on cells centrifuged into a tumor-mimicking cell pellet showed an increase in the backscatter intensity for cells undergoing apoptosis (Czarnota et al. 1997, 1999; Kolios et al. 2002) compared to non-apoptotic cells. Individual cells cannot be resolved at these frequencies, so acoustic microscopy must be used to examine changes on the single cell level. Acoustic backscatter and attenuation images of MCF7 cells before and during apoptosis are shown in Fig. 13.6 (using 375 MHz) and Fig. 13.7 (using 1000 MHz). Optical images taken a short time after the acoustic measurements are shown for comparison. All measurements used a 0.5 μm step size

Fig. 13.5 Cells stained for apoptosis and viewed under fluorescence. The regions labeled "*A*" are cells stained blue (Hoechst 33342), and are normal viable cells in the interphase of the cell cycle. Cells labeled "*B*" are in early stage apoptosis, and are stained blue and green (Annexin-V). Cells labeled "*C*" are in late stage apoptosis, and are stained blue, green and red (propidium iodide). In some cases, the blue and red stains overlap creating a purple color. Cells labeled "*D*" are stained red only, without any green. These may be cells in advanced stages of apoptosis, or may be other cellular DNA debris. For these cells, it is unknown if cell death was apoptotic or through another process of cell death. The scale bar is 30 μm

Fig. 13.6 MCF7 cells before apoptosis (*top*) and after (*bottom*). From *left* to *right*: optical image, acoustic backscatter image and acoustic attenuation image. The acoustic images were made using a 375 MHz transducer. The images are of two different cells in the same cell culture. The scale is 15 μm. (Figure reproduced from Strohm et al. (2010), © 2010 IEEE)

with 100 point averaging at 375 MHz and 1,000 point averaging at 1,000 MHz. Key differences in the images before and after apoptosis were observed. For the cells imaged using 375 MHz ultrasound (Fig. 13.6), the optical image shows a dramatic difference in the cell morphology before and after apoptosis. Before apoptosis, the cell is adherent to the substrate and some surface blebs are visible around the outer membrane. Major cellular organelles such as the nucleus and nucleolus are visible. During apoptosis, the cell has detached from the substrate and appears rounded, and cell organelles are no longer visible. Similar changes are observed in the ultrasound attenuation images. In the backscatter images, the backscatter occurs mainly around the nucleus for the non-apoptotic cell, while backscatter occurs throughout the entire cell during apoptosis. Increased detail is observed for cells imaged using 1,000 MHz ultrasound (Fig. 13.7). In the attenuation image, the nuclear membrane, the nucleolus and smaller cell organelles (possibly vacuoles) are clearly visible; similar features are observed in both the attenuation and optical image. The cell membrane shape is slightly different than the optical image due to the time delay between the acquisition of the optical and acoustic measurements. Fringes are observed in the acoustic backscatter image, and are caused by the constructive and destructive interference of the signal between the cell surface and substrate as the cell thickness is comparable to the ultrasound wavelength. The ultrasound backscatter images of the cells undergoing apoptosis conveys information not found in the optical image (Figs. 13.6 and 13.7). Ultrasound backscatter is observed throughout the entire cell at both 375 and

Fig. 13.7 MCF7 cells before apoptosis (*top*) and after (*bottom*). From *left* to *right*: optical image, acoustic backscatter image and acoustic attenuation image. The acoustic images were made using a 1,000 MHz transducer. The images are of two different cells in the same cell culture. The scale is 15 μm. (Figure reproduced from Strohm et al. (2010), © 2010 IEEE)

Fig. 13.8 A cell in early stage apoptosis was stained with Hoechst 33342 to identify the nucleus prior to acoustic measurements made at 1,000 MHz. The attenuation image shows a highly attenuating central region of the cell (*left*), which coincides with the stained nucleus (*middle*). An optical image of the cell is shown to the *right*. The scale bar is 15 μm

1,000 MHz. The backscatter pattern observed in the apoptotic cells at both frequencies is suggestive of speckle. In these images, the nature of the dominant ultrasonic scattering structure changes due to the smaller wavelength (Kolios 2009). The attenuation image of the apoptotic cell (Fig. 13.7) shows detail not observed optically (or even acoustically at 375 MHz). The nucleus is clearly delineated, and is 2–3 times more attenuating than the surrounding cytoplasm. Small protrusions from the cell are visible, which are also observed in the optical image. Figure 13.8 shows an apoptotic cell imaged at 1,000 MHz along with two optical images: a bright field image and a fluorescence image where the cell has been stained with Hoechst 33342 to label the nucleus. The stained nucleus in the optical image and the highly attenuating center in the ultrasound image spatially overlap, indicating the attenuating area observed in the attenuation image is the nucleus. Further details are observed in two apoptotic cells imaged at 1,200 MHz (Fig. 13.9). The attenuation through the nucleus was 2.5 times higher through the

Fig. 13.9 Attenuation images of two different MCF7 cells in early stage apoptosis measured at 1,200 MHz. The highly attenuating nucleus is clearly visible, separate from the surrounding cytoplasm. In both images, protrusions from the nucleus into the cytoplasm and out of the cell are visible. The scale bar is 15 μm

Fig. 13.10 Ultrasound B-scans of cells at 375 (**a**, **b**) and 1,000 MHz (**c**, **d**, **e**). The same cell is shown in (**d**) and (**e**) but with the transducer focus at different positions (indicated by the *arrow*) to show that speckle occurs throughout the entire cell. The scale is 15 μm. (Figure reproduced from Strohm et al. (2010), © 2010 IEEE)

nucleus than the cytoplasm, and protrusions from the nucleus into the surrounding cytoplasm and towards the cell exterior were observed.

Due to the penetrating nature of ultrasound, it can be used to visualize structures inside of cells and create cross-sectional images known as B-scans. This image format is what is typically presented in clinical ultrasound images. B-scans were made of apoptotic and non-apoptotic cells at 375 MHz and 1,000 MHz (Fig. 13.10). At 375 MHz, the transducer was able to resolve parts of the cell membrane of the non-apoptotic cell (Fig. 13.10a), losing detail around the cell periphery where the membrane was close to the substrate. During apoptosis (Fig. 13.10b), backscatter occurred throughout the cell in a pattern that resembled a speckle pattern. The diffuse nature of the backscatter was possibly due to the relatively low lateral and axial resolution (approximately 4 μm each) of the 375 MHz transducer in comparison to the cell size. At 1,000 MHz, the cell membrane was clearly visible (Fig. 13.10c). Relatively little backscatter occurred from within the cell. In contrast, the apoptotic cell showed extensive scattering throughout the cell (Fig. 13.10d, e). Figure 13.10d was acquired with the ultrasound transducer focus approximately two-thirds below the cell surface the cell, while Fig. 13.10e was acquired with the ultrasound transducer focus near the top of the cell. Here the observed backscatter was clearly speckle, which is the well-known interference pattern generated by sub-resolution scatters that is typical of clinical ultrasound images at much lower frequencies. The speckle dimensions appeared to be oval shaped, with the axial length twice the lateral length. The axial and lateral resolutions of the 1,000 MHz transducer are approximately 2.1 and 1.2 μm, which agree with the speckle dimensions, further suggesting the backscatter observed within the cell was speckle (Foster et al. 1983). The transducer depth of field was approximately 10 μm. With the focus near the top of the cell (18 μm above the substrate), speckle near the bottom half of the cell could not be resolved due poor sensitivity of the transducer outside of the transducer depth of field. Additionally, the scattering that occurred from the top half of the cell attenuated the ultrasound focused at the bottom of the cell. The amount of speckle present in non-apoptotic cells was less than in an apoptotic cell. This indicates

extensive activity and structural changes were occurring within the cell during apoptosis, as the presence of speckle suggests many sub-resolution scattering sources within the apoptotic cell.

13.4 Temporal Imaging

Apoptosis is a biological process in which the cell undergoes specific structural and morphological changes in a highly controlled time sequence to reach an end goal: cell death with minimal disruption to surrounding tissue. To examine how the ultrasound echoes change in time from an apoptotic cell, optical and acoustic methods were used to image an apoptotic cell every 60 s (Fig. 13.11a). A step size of 1.0 μm with 100 point averaging was used with a 375 MHz transducer. The optical image was recorded with the transducer above the cell (as shown in Fig. 13.3) which resulted in poor contrast and detail due to poor optical illumination. The ultrasound attenuation image of the apoptotic cell did not change over time, while variations in the backscatter pattern (speckle) were observed between images. The bulk composition of the cell affects the ultrasound attenuation; because negligible changes were occurring in the attenuation images over time, it can be inferred that the bulk properties of the cell were not changing over the short timescales of these measurements. However, the variations in backscatter observed between images were indicative of rapid structural changes occurring within the cell. In comparison, the optical, ultrasound backscatter and ultrasound attenuation measurements of a non-apoptotic cell showed minimal variation when measured 20 min apart (Fig. 13.11b). In particular, the ultrasound backscatter occurred mainly from the nuclear area of the cell, whereas the backscatter occurred throughout the entire apoptotic cell.

A method was developed to quantify the variations in ultrasound backscatter observed during apoptosis using the cross correlation of RF signals. The normalized cross correlation R between two discrete signals x and y is given by

$$R_{xy}(m) = \frac{\sum_{k}^{N} y(k)x(k+m)}{N\sqrt{\sigma_x^2 \sigma_y^2}}, \tag{13.1}$$

where N is the length of the signal, σ is the variance and m is the lag (Ratner and Bankman 2009). The correlation is equal to one if two signals are identical, and equal to zero if there is no correlation. The 375 MHz transducer was positioned above the center of the cell and the backscattered signal was recorded every 10 s for 900 s (90 measurements). This was done for eight cells: four apoptotic and four non-apoptotic. Figure 13.12 shows the signal measured at one specific time point showing the echo from both the cell and substrate. The signal used in the calculations was gated to include the backscattered signal from the cell (between 1,500 and 1,520 ns in Fig. 13.12, 160 data points). Then for each cell, the correlation

Fig. 13.11 Optical and ultrasound images of an apoptotic cell measured 1 min apart (**a**) and a non-apoptotic cell measured 20 min apart (**b**). *Top row* optical images, *middle row* ultrasound backscatter images, *bottom row* ultrasound attenuation images. Optical image quality and contrast are poor as the images were recorded during acoustic scans. The scale bar is 15 μm. The scale bar and ultrasound intensity scale are equal in both images. (Figure **a** reproduced from Strohm et al. (2010), © 2010 IEEE)

Fig. 13.12 The ultrasound RF signals and envelope from the cell (at 1510 ns) and substrate (at 1526 ns). The echo from the cell was approximately 18 mV (inset), much smaller than the 0.6 V signal from the glass substrate. (Figure reproduced from Strohm et al. (2010), © 2010 IEEE)

was calculated by comparing the first signal measured (at $t = 0$) to each subsequent signal. If there was no change in the signal over time, the correlation would be equal to one for all measurements. Conversely if the signal changed with time, the correlation would vary depending on how different the two signals were.

The normalized cross correlation for the four non-apoptotic and four apoptotic cells are shown in Fig. 13.13a and b, respectively. Over the 90 measurements, the average correlation for the four non-apoptotic cells was 0.93 ± 0.05. Conversely, the average correlation of the apoptotic cells was 0.68 ± 0.17, with variations occurring on a timescale on the order of seconds for all cells over the entire measurement period. These calculations indicate the signal from the non-apoptotic cells were stable over time with minimal variations, in contrast to the rapidly varying signals observed with apoptotic cells. These results correlate well with the changes in speckle pattern observed from the images measured from apoptotic

Fig. 13.13 The average normalized cross correlation measured for four non-apoptotic cells (**a**) and four apoptotic cells (**b**). The correlation of the non-apoptotic cells was close to unity, indicating that minimal changes in the signal occurred over time. In contrast, the correlation for the apoptotic cells rapidly changed with time, indicating extensive signal variations over time. (Figure reproduced from Strohm et al. (2010), © 2010 IEEE)

cells one minute apart (Fig. 13.11a). Based on these results, we can conclude that intracellular variations occur over a time period of seconds during apoptosis.

13.5 Quantitative Measurements

Several studies have measured the properties of individual cells using various acoustic microscopy methods; however, it is difficult to compare the results between different measurement systems or techniques. It is even more difficult to compare the results from one cell line to another due to differences in cell types, environmental settings and growth conditions. Additionally, systematic issues may arise that prevent accurate absolute measurements. However, quantitative measurement techniques have been developed to mechanical properties of cells using time resolved or $v(z)$ measurements. These methods have been used previously to determine properties of cells such as the thickness, sound speed, acoustic impedance, density, bulk modulus and attenuation as discussed above.

The time resolved method is used to determine the cell thickness and sound speed. Echoes from the cell surface (t_1), cell substrate interface (t_2) and a reference measurement on the substrate beside the cell (t_0) must be resolved (Fig. 13.14). The cell thickness d can be calculated using the echoes from the cell surface and the reference measurement using

$$d = \frac{c_0}{2}(t_0 - t_1), \tag{13.2}$$

where c_0 is the sound speed in the coupling fluid. For live cell measurements, coupling is achieved by using the cell medium or phosphate buffered saline (PBS) to ensure cell viability during the experiments. In many situations, the sound speed of the coupling medium is unknown at the high frequencies used and acoustic microscopy methods can be used determine the sound speed and dispersion of the

Fig. 13.14 A diagram showing the transducer positioned above a single cell for time resolved measurements. The time of flight of the ultrasound echoes from the cell surface (t_2), cell-substrate interface (t_1) and a reference measurement from the substrate beside the cell (t_0) are used to calculate the thickness and sound speed of the cell

medium (Strohm and Kolios 2011). The sound speed within the cell can be calculated from the three echoes using

$$c = c_0 \frac{t_0 - t_1}{t_2 - t_1}. \tag{13.3}$$

The thickness and sound speed of cells are straightforward to acquire and have been reported in literature for a variety of cell types using different methods, including time resolved methods. To obtain the other cell properties, the acoustic impedance must be calculated using the echo amplitude from the cell surface, cell-substrate interface and the substrate reference measurement. The amplitudes vary as a function of transducer position, and the focus position of the cell surface, substrate and reference will all be different. The maximum amplitude from each surface must be found by measuring the signal as a function of transducer position above the cell (a $v(z)$ curve). A $v(z)$ curve showing the signal from the three interfaces of a 11 μm thick cell adhered to a glass substrateusing a 375 MHz transducer is shown in Fig. 13.15 (note the amplitude from the cell membrane, A_2, has been scaled by a factor of 10); from this plot, the maximum amplitude from each surface is determined (A_1, A_2 and A_3). The amplitude maxima A_2 and A_3 occur closer together for a cell as the sound speed within the cell and coupling fluid are comparable. These amplitudes are used to determine the acoustic impedance of the cell. Before this is done, the reference amplitude from the substrate (A_3) must be corrected. The acoustic impedance calculations assume perfect reflection from the substrate. While most of the ultrasound energy is reflected from the glass back towards the transducer, some will be transmitted through the glass. In addition, ultrasound incident on the substrate at specific angles will be converted to other transmission modes such as surface acoustic

Fig. 13.15 $V(z)$ curves from a 11 μm thick cell in interphase on top of a glass substrate. The signal amplitude is measured as a function of transducer position axially through the sample. A_2 is from the top of the cell and A_1 is from the cell-substrate interface. The reference measurement A_3 is done on the glass beside the cell. The cell membrane measurement A_2 is scaled up by a factor of 10

waves (Briggs and Kolosov 2009). A_0 is the corrected amplitude assuming perfect reflectance from the substrate, and can be calculated using

$$A_0 = A_3 \frac{Z_s - Z_0}{Z_s + Z_0}, \tag{13.4}$$

where Z_0 is the known acoustic impedance of the coupling fluid. With the maximum amplitudes from the cell surface (A_1) and reference measurement (A_0) known, the acoustic impedance within the cell Z_c can be calculated using

$$Z_c = Z_0 \frac{A_0 + A_1}{A_0 - A_1}. \tag{13.5}$$

The results from the time resolved method (cell thickness and sound speed) and $v(z)$ method (cell acoustic impedance) can be used to calculate the density and bulk modulus of the cell. The cell density is calculated using

$$\rho = \frac{Z_c}{c}, \tag{13.6}$$

and the bulk modulus is calculated using

$$K = cZ_c = \rho c^2, \tag{13.7}$$

where c was found using time resolved methods and Z_c using the $v(z)$ curve. Using the combined methods from the time resolved measurements and $v(z)$ curves, the thickness, sound speed, acoustic impedance, density and bulk modulus of a cell can been estimated.

The attenuation in the cell can be found by measuring the difference in the echo amplitude between the substrate under the cell (A_2) and the reference amplitude beside the cell (A_3) while the transducer remains at a fixed position above the cell. The acoustic impedance of the substrate (Z_s), coupling fluid (Z_0) and the cell (Z_c) must be known to correct the amplitude echoes from the cell surface and substrate. In addition, the cell thickness d at the measurement position must be known. If these variables are known, then the attenuation within the cell can be calculated using

$$\alpha = \alpha_c + \frac{1}{2d} \ln \left[\frac{A_0}{A_2} \frac{Z_s - Z_c}{Z_s + Z_c} \frac{4Z_c Z_0}{(Z_c + Z_0)^2} \frac{Z_s + Z_0}{Z_s - Z_0} \right] \tag{13.8}$$

where α_c is the attenuation in the coupling fluid through a distance $2d$. The units from this equation are given in Np/cm, and can be converted to dB/cm by multiplying by 8.686. Attenuation is frequency dependent that generally follows a power law of the form

$$\alpha = \alpha_0 f^n, \tag{13.9}$$

where α_0 is the attenuation coefficient and n is the exponent of the frequency dependent attenuation power law (Szabo 1995). The frequency dependence of bulk tissue (a_0 and n) has been reported using clinical frequency ranges of approximately 1–10 MHz (Duck 1990; Hill et al. 2004), and n typically has values between 1 and 1.5. For liquids, the attenuation frequency dependence is generally between 1.5 and 2, with water equal to 2 (Davidovich et al. 1972). While cells are composed mostly of water they have significant intracellular materials such as protein and therefore it is unknown how the attenuation varies with frequency. Several attempts have been made to measure the frequency dependent attenuation of individual cells (Daft et al. 1989), however those results are limited in that they cover only a small number of frequencies and use limited cell types. A comprehensive examination of how the attenuation of different cell types vary with frequency does not exist, which makes it difficult to compare the attenuation coefficient from single cells to that of bulk tissue.

Over the past 30 years, various methods including the time resolved measurements and $v(z)$ curves have been used to determine cellular properties. Most studies were done with a small sample size and lacked rigorous methodology verification. Variations can exist from cell to cell therefore a large sample size is essential to obtain representative and reproducible values. This is even more crucial when examining cells of different types or changes in cells during various biological processes.

A method to verify the combined time resolved and $v(z)$ curve method was presented in Strohm et al. (2010) where the properties of a 9 μm thick PVDF polymer were calculated. The thickness, sound speed, acoustic impedance, density and bulk modulus agreed to within 5 % of those supplied from the manufacturer. The attenuation could not be compared as it was unknown what the attenuation through the PVDF was at the frequencies used.

To help understand how the properties of cells change during apoptosis, single MCF7 cells were measured using ultra-high frequency ultrasound using the time resolved and $v(z)$ methods before and during apoptosis. Cells were prepared and stained with Hoechst 33342, Annexin-V and propidium iodide to identify the cell state. Cells with no more than three neighboring cells were selected for measurements. Cells in confluence were avoided due to the difficulty identifying cell borders (both acoustically and optically). Moreover, the pressures exerted on a measured cell by its neighbors are unknown and could vary from cell to cell, and even for the same cell as a function of time. Therefore, for consistency, isolated cells were selected. Cells in the metaphase state of mitosis were also chosen for quantitative measurements. During metaphase, the cell has a rounded appearance and the chromosomes line up along the center of the cell. The increased chromosome density within the measurement region may alter the cellular properties. The cell state can be identified optically or using a DNA-labeling stain such as Hoechst 33342. Optical and fluorescence images of cells in various states of mitosis are shown in Fig. 13.16. Fluorescent images of cells in the early and late stages of apoptosis are shown in Fig. 13.5.

Fig. 13.16 Fluorescence (*top*) and optical (*bottom*) images of cells during mitosis. The cells were stained with Hoechst 33342 to identify the DNA during fluorescence. The cells undergo specific morphological changes during each phase of mitosis, enabling easy optical identification. The scale bar is 10 μm

The cellular properties (thickness, sound speed, acoustic impedance, density, bulk modulus and attenuation) were calculated using both time resolved and $v(z)$ methods as discussed above. A 375 MHz transducer (60° aperture, 42 % − 6 dB bandwidth) centered on the cell nucleus was used for all measurements. $V(z)$ curves were made approximately ±25 μm around the transducer focus on the substrate with a 1 μm step size. Cells were selected based on the optical and fluorescence images. Further details regarding the acoustic microscope and measurement method are described in Strohm et al. (2010). A total of 159 cells were measured: 69 in interphase (normal cellular state), 31 in early apoptosis, 28 in late apoptosis and 31 in the metaphase stage of mitosis. The thickness, sound speed, acoustic impedance, density and bulk modulus for the four cell types measured are shown in Table 13.1. Histograms showing the distribution for each parameter are shown in Fig. 13.17. Table 13.2 summarizes the attenuation (dB/cm) and the

Table 13.1 The thickness, sound speed, acoustic impedance, density and bulk modulus of MCF7 cells in interphase, early stage apoptosis, late stage apoptosis, and the metaphase stage of mitosis. The amplitude and time of flight of the ultrasound echoes from the cells using a 375 MHz transducer were used with Eqs. 13.2–13.7 to calculate the properties. The standard deviation is given as the error. Values that were statistically different from the interphase state ($p < 0.01$) are marked with an asterisk

Cell Cycle	Number of cells	Thickness (μm)	Sound Speed (m/s)	Acoustic Impedance (MRayls)	Density (kg/m^3)	Bulk Modulus (GPa)
Interphase	69	11.1 ± 1.9	1575 ± 25	1.559 ± 0.015	990 ± 18	2.46 ± 0.05
Early apoptosis	31	15.2 ± 2.3*	1586 ± 22	1.556 ± 0.021	981 ± 17	2.47 ± 0.05
Late apoptosis	28	12.6 ± 2.3*	1557 ± 13*	1.539 ± 0.012*	988 ± 8	2.40 ± 0.03*
Metaphase	31	18.6 ± 1.5*	1567 ± 12	1.554 ± 0.014	992 ± 9	2.44 ± 0.03*
Water			1521.7	1.512	993.5	2.30

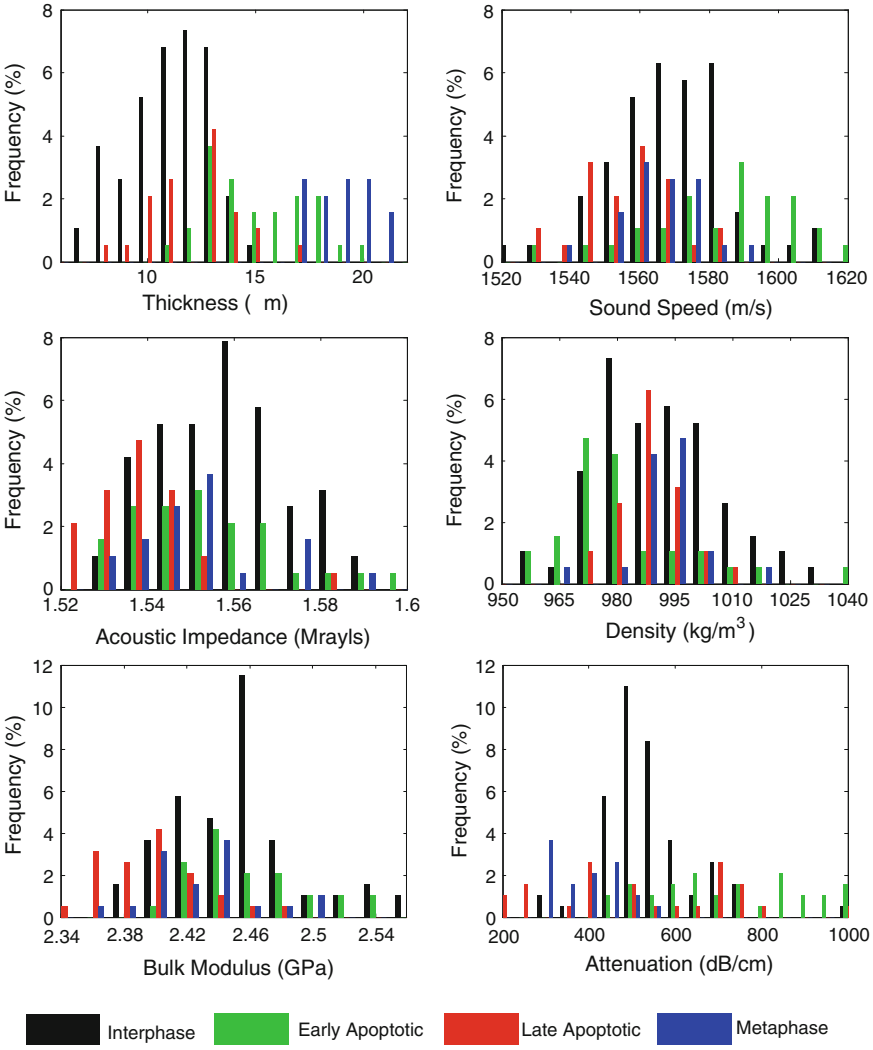

Fig. 13.17 Histograms of the thickness, sound speed, acoustic impedance, density, bulk modulus and attenuation for the MCF7 cells in interphase, early and late stage apoptosis and the metaphase state of mitosis. In most cases a normal distribution is observed, with the exception of the attenuation. Early and late stage attenuation calculations appeared to deviate from a normal distribution throughout the histogram

attenuation coefficient (dB/cm/MHz^n), where the attenuation coefficient was calculated from Eq. 13.9 using $n = 1$, 1.5 and 2. Three attenuation coefficients are reported using different power law factors as the frequency dependent attenuation at these frequencies is unknown. Finally, a student t-test was used to determine if there was a statistically significant difference between the interphase state and the early apoptosis, late apoptosis, and metaphase (single sided one tail, unequal

Table 13.2 The attenuation of MCF7 cells in interphase, early stage apoptosis, late stage apoptosis, and the metaphase stage of mitosis measured using a 375 MHz transducer. The attenuation calculated using Eq. 13.8 is shown with dB/cm units, along with the attenuation coefficient calculated using Eq. 13.9 with frequency to the power of 1.0, 1.5 and 2.0. The attenuation of cells in early apoptosis and metaphase states were statistically different than the interphase attenuation ($p < 0.01$)

Cell Cycle	Number of cells	Attenuation (dB/cm)	Attenuation ($dB/cm/MHz^{1.0}$)	Attenuation ($dB/cm/MHz^{1.5}$)	Attenuation ($dB/cm/MHz^{2.0}$)
Interphase	69	553 ± 132	1.47 ± 0.35	0.076 ± 0.018	0.0039 ± 0.0009
Early apoptosis	31	761 ± 207*	2.03 ± 0.55	0.105 ± 0.029	0.0054 ± 0.0015
Late apoptosis	28	539 ± 240	1.44 ± 0.64	0.074 ± 0.033	0.0038 ± 0.0017
Metaphase	31	400 ± 86*	1.07 ± 0.23	0.055 ± 0.012	0.0028 ± 0.0006

variance, unequal sample size, $p < 0.01$). Parameters that were statistically different from the interphase state are marked with an asterisk in Tables 13.1 and 13.2.

During apoptosis, the cell height increased from 11.1 μm for a cell in interphase to 15.2 μm for early stage apoptosis. The cell rounds to a spherical shape while losing some adhesion to the substrate during apoptosis. The cell volume doesn't change appreciably during this initial stage, the cell only changes shape which accounts for the increased thickness. By late stage apoptosis, the cell thickness decreased to 12.6 μm, which could be due to a decrease in cell volume as a result of loss of cellular material. A statistically significant decrease in the sound speed from 1586 to 1557 m/s was found from early to late stage apoptosis. From early to late stage apoptosis, statistically significant decreases in the acoustic impedance from 1.559 to 1.539 MRayls and the bulk modulus from 2.46 to 2.40 GPa were observed. In general, most parameters did not change from interphase to early stage apoptosis. This indicates that while the cell shape initially changed from a flat adherent to a rounded morphology, significant internal structural changes may be absent during the early stages of apoptosis. However, nearly all the cell properties changed from early to late stage apoptosis, which is likely related to the significant structural changes that occur within the cell. The acoustic measurements were made over the central region of the cell containing the nucleus. During apoptosis, it is known that the nucleus condenses and fragments. It is possible that the changes in cell parameters are due to changes in the nuclear structure as the cell nucleus undergoes chromatin condensation and nuclear fragmentation (Dini et al. 1996). These large structural changes are expected to produce changes both in the bulk material properties and in the scattering structures.

From the interphase cell state to the metaphase stage of mitosis, the thickness increased from 11.1 to 19.0 μm, which is due to the rounding shape of the cell. The other parameters (sound speed, density and acoustic impedance) did not change. The bulk modulus decreased from 2.46 to 2.44 GPa but with a p-value near the limits of statistical significance. We can conclude that despite a change in cell shape, the mechanical properties of cells undergo negligible changes from interphase to the metaphase stage of mitosis. This is similar to what was observed

during early stage apoptosis, where negligible differences in the cell properties were observed (aside from thickness).

Statistically significant differences in the attenuation between interphase to early apoptosis (545–740 dB/cm), then from early to late stage apoptosis (740–519 dB/cm) were observed. A decrease in the attenuation was also observed between cells in interphase and metaphase (545–399 dB/cm). Figure 13.17 shows the histogram of the measured attenuation values in all the experiments; a normal distribution was observed for the cells in the interphase and metaphase stage of mitosis, but not for cells in the early and late stage of apoptosis. The attenuation values were spread nearly evenly throughout the range of measured values. The average attenuation from these cells also had a high standard deviation, where it was nearly double that of the interphase and metaphase cells (Table 13.2). The large attenuation range for the apoptotic cells is likely due to the biological process itself. Apoptotic cells undergo significant changes over a rapid timescale as shown in Fig. 13.11. During this process, the internal organelles, proteins and other components are displaced within the cell. It is possible that the position of these structures influence the measurements by increasing the attenuation when within the ultrasound beamwidth, or decreasing the attenuation when absent. In contrast, metaphase is a controlled process lacking the turbulent nature observed in apoptosis. Therefore, it is not surprising to see a wide range of attenuation measurements from apoptotic cells.

13.6 Quantitative Measurement Sources of Errors

There are several sources of error when calculating the cellular properties discussed in the previous section. All calculations assumed water as the coupling fluid (1,521 m/s sound speed and 993.5 kg/m^3 density) and borosilicate glass as the substrate (12.577 MRayls acoustic impedance). Growth medium was used as the coupling fluid instead of water, which contains a small concentration of various salts and nutrients to ensure cell viability. The salts may increase the density and sound speed slightly, while it is unknown how the other ingredients will affect the sound speed and density. The cellular sound speed, acoustic impedance and bulk modulus are directly proportional to the coupling fluid sound speed; therefore, any differences in the coupling fluid sound speed will have a direct effect on the absolute sound speed, acoustic impedance and bulk modulus of the cell. The density reported for all cells is less than that of water. Most studies have reported cell densities higher than water and some errors in the density measurement could have occurred. The density is calculated from the acoustic impedance (Eq. 13.6), where the acoustic impedance calculation relies on accurate amplitude measurements of the ultrasound echoes (Eqs. 13.4 and 13.5). The amplitude A_3 is corrected for losses due to ultrasound transmission through the substrate only. Other uncorrected changes in the signal (e.g. due to mode conversion) would affect the incident amplitude A_0, which ultimately affect the density and bulk modulus

calculations as they are calculated from the acoustic impedance. While these issues may affect the accuracy of the cellular property estimates, these measurements provide an excellent relative estimate, where differences in the cellular properties were found between cells in different states.

The student t-test was used to determine if two properties were statistically different between different cell types and/or cell states. The t-test assumes a normal distribution and an appropriate sample size, and statistically significant results can erroneously result if these conditions are not met. Generally a p-value of 0.05 (95 % confidence) is used to ascertain if two results are statistically different; however, in the case of these measurements, some results did not follow a normal distribution (e.g. late stage apoptosis attenuation) or sample sizes were relatively low. Therefore, a stringent p-value of 0.01 (99 % confidence) was used to correct for any errors that may exist due to anomalies in the statistical mathematics.

13.7 Future Work

The methods presented in this chapter can be used to measure the cellular properties of cells during any biological process, to differentiate between malignant and benign cells, or even different cell lines and types. Future work will concentrate on improving the sample size of the early/late stage apoptosis measurements to increase accuracy, and examining if the properties of malignant and benign cells are different. These results provide an understanding of how changes on a single cell level affect the ultrasound signals from tumors during chemotherapy treatment using clinical frequency (1–15 MHz) and high frequency (20–60 MHz) ultrasound (Kolios and Czarnota 2009; Czarnota and Kolios 2010). Due to the complementary nature of ultrasound and photoacoustics, the SASAM acoustic microscope described in this chapter was modified to enable both acoustic and photoacoustic measurements. The optical absorption contrast mechanism is different than ultrasound, and using these probing methods in tandem can provide more information about micro-sized materials. Applications include measuring biological material with endogenous contrast such as melanoma cells (Rui et al. 2010) and red blood cells (Strohm et al. 2013; Rui et al. 2010), visualizing cellular DNA (Yao et al. 2010), determining vaporization thresholds (Strohm et al. 2011) and spectral characterization (Strohm et al. 2012) of perfluorocarbon emulsions.

Acknowledgments The authors would like to thank Maurice Pasternak for his help in data acquisition and signal processing and Arthur Worthington for his help in general laboratory issues. Support and scientific discussions with Drs. Eike Weiss, Robert Lemor and Sebastian Brand are gratefully acknowledged.

References

Atalar A, Quate CF, Wickramasinghe HK (1977) Phase imaging in reflection with the acoustic microscope. Appl Phys Lett 31(12):791–793

Briggs A, Kolosov O (2009) Acoustic microscopy. Oxford University Press, USA

Briggs GAD, Wang J, Gundle R (1993) Quantitative acoustic microscopy of individual living human cells. J Microsc 172(1):3–12

Czarnota GJ, Kolios MC (2010) Ultrasound detection of cell death. Imaging Med 2(1):17–28

Czarnota G, Kolios M, Vaziri H, Benchimol S (1997) Ultrasonic biomicroscopy of viable, dead and apoptotic cells. Ultrasound med 23(6):961–965

Czarnota GJ, Kolios MC, Abraham J, Portnoy M, Ottensmeyer FP, Hunt JW, Sherar MD (1999) Ultrasound imaging of apoptosis: high-resolution non-invasive monitoring of programmed cell death in vitro, in situ and in vivo. Br J Cancer 81(3):520–527

Daft CM, Briggs GA, O'Brien WD (1989) Frequency dependence of tissue attenuation measured by acoustic microscopy. J Acoust Soc Am 85(5):2194–2201

Davidovich L, Makhkamov S, Pulatova L, Khabibullaev PK, Khaliulin MG (1972) Acoustical properties of certain organic liquids at frequencies from 0.3. Sov Phys Acoust 18(2):264

Dini L, Coppola S, Ruzittu MT, Ghibelli L (1996) Multiple pathways for apoptotic nuclear fragmentation. Exp Cell Res 223(2):340–347

Duck FA (1990) Physical properties of tissue: a comprehensive reference book. Academic Press, San Diego

Faridian F, Wickramasinghe HK (1983) Simultaneous scanning optical and acoustic microscopy. Electron Lett 19(5):159–160

Foster DR, Arditi M, Foster FS, Patterson MS, Hunt JW (1983) Computer simulations of speckle in B-scan images. Ultrason Imaging 5(4):308–330

Hadimioglu B, Foster JS (1984) Advances in superfluid helium acoustic microscopy. J Appl Phys 56(7):1976–1980

Hellier C (2001) Handbook of nondestructive evaluation. McGraw-Hill Professional, New York

Hildebrand JA (1985) Observation of cell-substrate attachment with the acoustic microscope. IEEE Trans Sonics Ultrason 32(2):332–340

Hildebrand JA, Rugar D (1984) Measurement of cellular elastic properties by acoustic microscopy. J Microsc 134(3):245–260

Hildebrand JA, Rugar D, Johnston RN, Quate CF (1981) Acoustic microscopy of living cells. Proc Natl Acad Sci 78(3):1656–1660

Hill CR, Bamber JC, Haar G (2004) Physical principles of medical ultrasonics. Wiley, Hoboken

Jipson V, Quate CF (1978) Acoustic microscopy at optical wavelengths. Appl Phys Lett 32(12):789–791

Johnston RN, Atalar A, Heiserman J, Jipson V, Quate CF (1979) Acoustic microscopy: resolution of subcellular detail. Proc Natl Acad Sci 76(7):3325–3329

Kanngiesser H, Anliker M (1992) Ultrasound microscopy of biological structures with weak reflecting properties. In: Ermert H, Harjes HP (eds) Acoustical Imaging, vol 19, Plenum Press, New York, p 517–22

Kay RR, Langridge P, Traynor D, Hoeller O (2008) Changing directions in the study of chemotaxis. Nat Rev Mol Cell Biol 9(6):455–463

Kerr JFR, Wyllie AH, Currie AR (1972) Apoptosis: a basic biological phenomenon with wide-ranging implications in tissue kinetics. Br J Cancer 26(4):239

Kessler LW, Korpel A, Palermo PR (1972) Simultaneous acoustic and optical microscopy of biological specimens. Nature 239(5367):111–112

Kolios M (2009) Biomedical ultrasound imaging: from 1 to 1,000 mhz. Canadian Acoustics-Acoustique Canadienne 37(3):35–43

Kolios MC, Czarnota GJ (2009) Potential use of ultrasound for the detection of cell changes in cancer treatment. Future Oncol 5(10):1527–1532

Kolios MC, Czarnota GJ, Lee M, Hunt JW, Sherar MD (2002) Ultrasonic spectral parameter characterization of apoptosis. Ultrasound Med Biol 28(5):589–597

Kundu T (2004) Ultrasonic nondestructive evaluation: engineering and biological material characterization. CRC Press, Boca Raton

Kundu T, Bereiter-Hahn J, Hillmann K (1991) Measuring elastic properties of cells by evaluation of scanning acoustic microscopy V(Z) values using simplex algorithm. Biophys J 59(6):1194–1207

Kundu T, Bereiter-Hahn J, Karl I (2000) Cell property determination from the acoustic microscope generated voltage versus frequency curves. Biophys J 78(5):2270–2279

Lacroix M, Leclercq G (2004) Relevance of Breast Cancer Cell Lines as Models for Breast Tumours: an Update. Breast Cancer Res Treat 83(3):249–289

Lemons RA, Quate CF (1974) Acoustic microscope—scanning version. Appl Phys Lett 24(4):163

Lemons R, Quate C (1975) Acoustic microscopy: biomedical applications. Science 188(4191):905–911

Lemor RM, Weiss EC, Pilarczyk G, Zinin PV (2003) Measurements of elastic properties of cells using high-frequency time-resolved acoustic microscopy. In: IEEE Ultrasonics Symposium, vol 1, p 762–765 2003

Linder A, Winkelhaus S, Hauser M (1992) Acoustic imaging of the mitotic spindle in dividing XTH2-cells. In: Ermert H, Harjes HP (eds) Acoustical Imaging, vol 19, Plenum Press, New York, p 523–28

Litniewski J, Bereiter-Hahn J (1990) Measurements of cells in culture by scanning acoustic microscopy. J Microsc 158(1):95–107

Lüers H, Hillmann K, Litniewski J, Bereiter-Hahn J (1991) Acoustic microscopy of cultured cells. Cell Biochem Biophys 18(3):279–293

Maev RG (2008) Acoustic microscopy: fundamentals and applications. Wiley, Weinheim

Nakamura Y, Yamamoto S, Sakai M, Uchino F (1986) Ultrasonic microscope. US Patent 462153111,Nov 1986

Pelling AE, Veraitch FS, Chu CP-K, Mason C, Horton MA (2009) Mechanical dynamics of single cells during early apoptosis. Cell motil cytoskelet 66(7):409–422

Ratner BD, Bankman I (2009) Biomedical Engineering Desk Reference. Academic Press, Oxford

Rose JL (2004) Ultrasonic waves in solid media. Cambridge University Press, New York

Rugar D, Heiserman J, Minden S, Quate CF (1980) Acoustic microscopy of human metaphase chromosomes. J Microsc 120(2):193–199

Rui M, Narashimhan S, Bost W, Stracke F, Weiss E, Lemor R, Kolios MC (2010) Gigahertz optoacoustic imaging for cellular imaging. In: SPIE, vol. 7564, pp 756411–756411-6 2010

Rui M, Bost W, Weiss EC, Lemor R, Kolios MC (2010) Photoacoustic microscopy and spectroscopy of Individual red blood cells. OSA - Optics and Photonics Congress BIOMED/DH, pp 3–5

Shull PJ (2002) Nondestructive evaluation: theory, techniques, and applications. CRC Press, New York

Sokolov S (1929) On the problem of the propagation of ultrasonic oscillations in various bodies. Elek Nachr Tech 6:454–460

Sokolov S (1939) Means for indicating flaws in materials. US Patent 216412527, Jun 1939

Spector DL, Goldman RD (2006) Basic methods in microscopy: protocols and concepts from Cells: a laboratory manual. CSHL Press, New York

Strohm EM, Kolios MC (2011) Sound velocity and attenuation measurements of perfluorocarbon liquids using photoacoustic methods. In: IEEE International Ultrasonics Symposium, p 2368–2371 2011

Strohm EM, Pasternak M, Mercado M, Rui M, Kolios MC, Czarnota GJ (2010) A comparison of cellular ultrasonic properties during apoptosis and mitosis using acoustic microscopy. In: IEEE International Ultrasonics Symposium, 608–611 2010

Strohm EM, Czarnota GJ, Kolios MC (2010b) Quantitative measurements of apoptotic cell properties using acoustic microscopy. IEEE Trans Ultrason, Ferroelectr, Freq Control 57(10):2293–2304

Strohm EM, Rui M, Gorelikov I, Matsuura N, Kolios M (2011) Vaporization of perfluorocarbon droplets using optical irradiation. Biomed Opt Express 2(6):1432–1442

Strohm E, Gorelikov I, Matsuura N, Kolios M (2012) Photoacoustic spectral characterization of perfluorocarbon droplets In: Proceedings of SPIE, vol 8223, pp 82232F–82232F-8 2012

Strohm EM, Berndl E, Kolios MC (2013) Probing red blood cell morphology using high frequency Photoacoustics. Biophysical Journal 105(1) (In Press)

Szabo TL (1995) Causal theories and data for acoustic attenuation obeying a frequency power law. J Acoustical Soc Am 97(1):14

Taylor RC, Cullen SP, Martin SJ (2008) Apoptosis: controlled demolition at the cellular level. Nat Rev Mol Cell Biol 9(3):231–241

Tittmann BR, Miyasaka C, Mastro AM, Mercer RR (2007) Study of cellular adhesion with scanning acoustic microscopy. IEEE Trans Ultrason Ferroelectr Freq Control 54(8): 1502–1513

Veselý P, Lüers H, Riehle M, Bereiter-Hahn J (1994) Subtraction scanning acoustic microscopy reveals motility domains in cells in vitro. Cell Motil Cytoskelet 29(3):231–240

Weiss EC, Anastasiadis P, Pilarczyk G, Lernor RM, Zinin PV (2007a) Mechanical properties of single cells by high-frequency time-resolved acoustic microscopy. IEEE Trans Ultrason Ferroelectr Freq Control 54(11):2257–2271

Weiss EC, Wehner F, Lemor RM (2007) Measuring Cell Volume Regulation with Time Resolved Acoustic Microscopy. In: Andre MP (ed) Acoustical Imaging, vol 28, Springer, Dordrecht, Netherlands, p 73–80

Weiss EC, Lemor RM, Pilarczyk G, Anastasiadis P, Zinin PV (2007c) Imaging of focal contacts of chicken heart muscle cells by high-frequency acoustic microscopy. Ultrasound Med Biol 33(8):1320–1326

Wickramasinghe HK (1979) Contrast and imaging performance in the scanning acoustic microscope. J Appl Phys 50(2):664

Yao D-K, Maslov K, Shung KK, Zhou Q, Wang LV (2010) In vivo label-free photoacoustic microscopy of cell nuclei by excitation of DNA and RNA. Opt Lett 35(24):4139–4141

Zoller J, Brandle K, Bereiter-Hahn J (1997) Cellular motility in vitro as revealed by scanning acoustic microscopy depends on cell-cell contacts. Cell Tissue Res 290(1):43–50

Part IV
Ultrasound Computer Tomography

Chapter 14
Methods for Forward and Inverse Scattering in Ultrasound Tomography

Roberto J. Lavarello and Andrew J. Hesford

Abstract Ultrasonic computed tomography (UCT) is a potentially useful technique that has been explored for decades in the context of medical imaging. UCT can provide quantitative images of acoustical parameters such as speed of sound, attenuation, and density from measurements of pressure fields. Throughout the years, several algorithms that rely on different wave propagation models have been developed. In this chapter, the fundamentals of forward and inverse solvers for ultrasonic tomography will be described.

Keywords Ultrasonic tomography · Ray-based tomography · Diffraction tomography · Inverse scattering

14.1 Ultrasonic Tomography and the Wave Equation

Ultrasound imaging is widely used as a tool for medical diagnosis. The most commonly used ultrasonic imaging method is sonography or B-mode imaging. B-mode imaging uses data in reflection mode to produce anatomical greyscale images. The brightness of each pixel is proportional to the amplitude of the logarithmically compressed envelope of the echoes produced by tissues. Spatial localization is performed using the pulse-echo principle.

However, the propagation of acoustic waves is a much richer phenomenon than simple reflections of acoustic echoes. Attempts were conducted in the early 1970s

R. J. Lavarello (✉)
Departamento de Ingeniería, Pontificia Universidad Católica del Perú,
Av. Universitaria 1801, San Miguel Lima 32, Lima, Perú
e-mail: lavarello.rj@pucp.edu.pe

A. J. Hesford
Department of Electrical and Computer Engineering, University of Rochester,
601 Elmwood Avenue, UR Medical Center, Box 648, Rochester, NY 14642-8648, USA

J. Mamou and M. L. Oelze (eds.), *Quantitative Ultrasound in Soft Tissues*, DOI: 10.1007/978-94-007-6952-6_14,

to produce ultrasonic images in transmission mode that were more similar to projective images formed with other modalities such as radiography and scintigraphy. These transmission-mode ultrasonic images were constructed by placing a transmitter and a receiver transducer to face each other. By raster scanning a sample placed in between the transducer pair, images of quantities such as transmitted amplitude (Green et al. 1974; Marich et al. 1975) and time-of-flight delays (Heyser and Croissette 1973, 1974) were produced. Advantages of using ultrasound for projective imagings included the use of non-ionizing radiation and the potential to exploit new sources of contrast for diagnostic imaging.

It was also in the early 1970s that the feasibility of applying the theory of transmission tomography for clinical practice was demonstrated. In particular, Hounsfield developed the first X-ray computed tomography device that allowed production of two-dimensional cross-sectional images of X-ray attenuation coefficients from a set of projection data at different orientation angles (Hounsfield 1973). This is not the only tomographic imaging modality used in clinical practice. The concept of emission tomography using SPECT actually predates X-ray tomography, having been demonstrated by Kuhl and Edwards in the 1960s (1963). Emission tomography of humans using PET was reported in the mid 1970s (Phelps et al. 1976). It was also by the mid 1970s that live animal imaging using magnetic resonance principles was demonstrated (Damadian 1971; Lauterbur 1974). The advantages of tomographic imaging compared to projective imaging were quickly appreciated by the medical community. It is therefore not surprising that researchers in the field of ultrasonic imaging also attempted to construct tomograms from ultrasound projective data.

Acoustic tomography encompasses a set of techniques that aim to reconstruct images of acoustic parameters from measurements of scattered pressure fields at different spatial locations and frequencies. Considering the case of an incident monochromatic field of angular frequency ω propagating in fluid media, the wave equation can be written as

$$\begin{aligned} \rho(\mathbf{r})\nabla^2\rho(\mathbf{r})^{-1}p(\mathbf{r}) + k^2(\mathbf{r})p(\mathbf{r}) &= -\phi^{\text{inc}}(\mathbf{r}), \\ k(\mathbf{r}) &= \omega/c(\mathbf{r}) - \mathbf{i}\alpha_\omega(\mathbf{r}), \end{aligned} \tag{14.1}$$

where $p(\mathbf{r})$ is the acoustical pressure, $\phi^{\text{inc}}(\mathbf{r})$ are the acoustical sources, $k(\mathbf{r})$ is the complex wave number, and $\rho(\mathbf{r})$, $c(\mathbf{r})$ and $\alpha_\omega(\mathbf{r})$ are the density, sound speed, and acoustic attenuation (at frequency ω) of the medium, respectively.

Equation (14.1) explicitly shows the relationship between parameters of the medium and the complex scattered pressure field. Therefore, by inverting the wave equation one can potentially create images of these parameters. Towards this end, several approaches have been pursued throughout the decades in order to obtain quantitative two- and three-dimensional tomographic ultrasonic images.

14.2 Ray-Based Acoustic Tomography

The first experimental demonstrations of ultrasonic tomography were performed in the early 1970s. Given the limited power of computer resources at that time, it is not surprising that initial attempts at ultrasonic tomography were based on simplifications of the wave equation. If density is assumed to be constant, the wave equation (14.1) in the absence of a source can be written as

$$\nabla^2 p(\mathbf{r}) + k^2(\mathbf{r}) p(\mathbf{r}) = 0. \tag{14.2}$$

If we let $p = p_0 \exp(-ik_0\tau(\mathbf{r}))$, with the wave number k_0 corresponding to a homogeneous background of sound speed c_0, then the wave equation can be rewritten in terms of the acoustic wavefront $\tau(\mathbf{r})$ as

$$\left(\frac{k(\mathbf{r})}{k_0}\right)^2 - (\nabla\tau(\mathbf{r}) \cdot \nabla\tau(\mathbf{r})) - \frac{i\lambda_0}{2\pi}\nabla^2\tau(\mathbf{r}) = 0. \tag{14.3}$$

Furthermore, if the medium is assumed lossless and the wavelength $\lambda_0 \to 0$, the equation above can be written as

$$|\nabla\tau(\mathbf{r}, c)|^2 = n^2(\mathbf{r}), \tag{14.4}$$

where $n(\mathbf{r}) = c_0/c(\mathbf{r})$ is the acoustic index of refraction. Equation (14.4) is known as the eikonal equation, and is a fundamental result in geometrical acoustics (Pierce 1989). The eikonal equation dictates how the acoustic wave front changes due to variations of the acoustic wave number. The eikonal equation can alternatively be written as

$$|\nabla T(\mathbf{r}, s)|^2 = s^2(\mathbf{r}), \tag{14.5}$$

where $s(\mathbf{r}) = 1/c(\mathbf{r})$ is the slowness and $T(\mathbf{r}, s) = \tau(\mathbf{r}, c)/c_0$ is the time of flight required for the wave to reach point $\mathbf{r}$.

14.2.1 Straight-Ray Propagation

A very significant implication of Eq. (14.4) is that if variations of $s(\mathbf{r})$ are assumed to be negligible, i.e., $s(\mathbf{r}) \approx 1/c_0$, then $|\nabla T(\mathbf{r})|$ is a constant. Therefore, the minimum-time arrival path between a transmitter and a receiver is a straight line. Although some researchers attempted to perform acoustic tomography through bone (Carson et al. 1977; Dines et al. 1981), a more favorable condition is met when imaging soft tissues for which expected refraction index changes are typically less than 10 % (Goss et al. 1978, 1980). Therefore, at least in principle it was reasonable to assume a straight ray propagation between a transmitter and a receiver when imaging regions of the body composed exclusively of soft tissues. A particular but important case that satisfied this requirement was breast imaging,

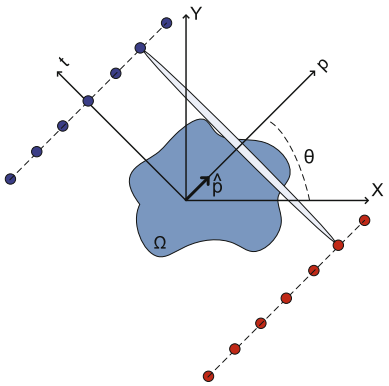

Fig. 14.1 Straight-ray acoustic tomography. Transducers with a narrow beam width are arranged in a line of transmitters (*red*) and a line of receivers (*blue*), and measurements of time-of-flight are collected. The scattering object occupies the region of space Ω

which to this day remains the most widely studied medical application of acoustic tomography.

Time-of-flight tomography creates tomograms of sound speed using measurements of $\Delta T(\mathbf{r}_t, \mathbf{r}_r) = T(\mathbf{r}_r - \mathbf{r}_t, s) - T(\mathbf{r_r} - \mathbf{r_t}, \mathbf{s_0})$, i.e., the difference in times of arrival between a transmitter at $\mathbf{r}_t$ and a receiver at $\mathbf{r}_r$ with and without the sample in between the transducers. If straight-ray propagation is assumed, $\Delta T(\mathbf{r}_t, \mathbf{r}_r)$ can be related to the slowness using

$$\Delta T(\mathbf{r}_t, \mathbf{r}_r) = \int_0^1 dl\, \Delta s\, \delta(\mathbf{r} - [\mathbf{r}_t + l \times (\mathbf{r}_r - \mathbf{r}_t)]), \tag{14.6}$$

where $\Delta s = (s(\mathbf{r}) - s_0)$. Consider the case of transmitters and receivers distributed in straight lines as shown in Figure 14.1. Equation (14.6) can then be rewritten as

$$\Delta T(p, \theta) = \int \int_{-\infty}^{\infty} d\mathbf{r} \Delta s(\mathbf{r})\, \delta(x \cos\theta + y \sin\theta - p). \tag{14.7}$$

With this configuration, the same theory extensively used for other tomographic medical imaging modalities can be used to create index of refraction tomograms (Greenleaf et al. 1975). In particular, and using the notation in Fig. 14.1, the Fourier slice theorem (Bracewell 1956) states that

$$\int_{-\infty}^{\infty} dp \Delta T(p, \theta) \mathrm{e}^{-j\kappa p} = \int \int_{-\infty}^{\infty} d\mathbf{r} \Delta s(\mathbf{r}) \mathrm{e}^{-j\kappa \hat{p} \cdot \mathbf{r}}, \tag{14.8}$$

i.e., the values of the 1D Fourier transform of the measured data $\Delta T(p, \theta)$ correspond to samples of the 2D Fourier transform of $\Delta s(\mathbf{r})$ over a line at θ degrees passing through the origin of k-space. A widely used method for the solution of Eq. (14.6) is the filtered backprojection algorithm (Bracewell and Riddle 1967; Ramachandran and Lakshminarayanan 1971; Shepp and Logan 1971). The algorithm is based on rewriting (14.8) in polar coordinates, which results in

$$\Delta s(\mathbf{r}) = \int_0^{\pi} d\theta \int_{-\infty}^{\infty} d\kappa |\kappa| \Delta \bar{T}(\kappa, \theta) \mathrm{e}^{j\kappa(\hat{p} \cdot \mathbf{r})}, \tag{14.9}$$

where $\Delta\bar{T}(\kappa,\theta)$ is the 1D Fourier transform of $\Delta T(p,\theta)$. The second integral in Eq. (14.9) is the convolution of $\Delta T(p,\theta)$ with a filter $h(p)$ whose Fourier transform is equal to $|\kappa|$. Therefore, Eq. (14.9) can be rewritten as

$$\Delta s(\mathbf{r}) = \int_0^{\pi} \Delta T_h(\hat{p}\cdot\mathbf{r},\theta), \tag{14.10}$$

where $\Delta T_h(p,\theta) = \Delta T(p,\theta) \underset{p}{*} h(p)$ and $\underset{p}{*}$ represents the convolution with respect to p. Algebraic methods were also developed for the inversion of Eq. (14.6) such as the simultaneous algebraic reconstruction technique (SART) (Andersen and Kak 1984). Reconstruction methods for fan-beam tomography were also explored for UCT under straight ray propagation assumptions (Glover 1978).

Creating tomograms of acoustic attenuation proved to be slightly more complicated. It was initially postulated that projections could be constructed from either transmitted signal amplitude or integrated intensity measurements (Greenleaf et al. 1974). However, these measurements were found to be sensitive to effects such as out-of-plane signal propagation, signal loss due to reflection, and phase cancellation across the receiver. Therefore, some researchers suggested extracting projection data from the power spectrum of the received data instead (Dines and Kak 1979; Klepper et al. 1981). After proper measurement of projection data, the reconstruction process was carried out using the same methods described for time-of-flight tomography.

14.2.2 Refraction-Corrected Tomography

However, the simple straight-ray model was quickly found to be inappropriate for tomography based on acoustic waves. In spite of the low variations of refraction index, ultrasonic waves may undergo a non-negligible amount of refraction when propagating through soft tissues. This is not the case for X-ray imaging, for which refraction effects can be safely neglected. This limitation was acknowledged even in the early days of acoustic tomography as a mechanism with potential to reduce the visualization of small structures when using UCT (Greenleaf et al. 1975, 1978). An illustration of the effects of refraction is presented in Fig. 14.2, where significant deviations from straight-ray path are shown when propagating through an object with only 10 % speed-of-sound contrast.

As a result, efforts were conducted in order to incorporate refraction effects in ray-based acoustic tomography. If the wavelength can be considered small compared to the size of the scatterer, the wavefront refraction can be explained using the eikonal equation in (14.4). Ray tracing methods allow for estimating the refracted paths that replace the straight lines assumed in Eq. (14.6).

Using the method of characteristics (Jakowatz and Kak 1976), the eikonal equation in Eq. (14.4) can be rewritten as a set of five ordinary differential equations given by

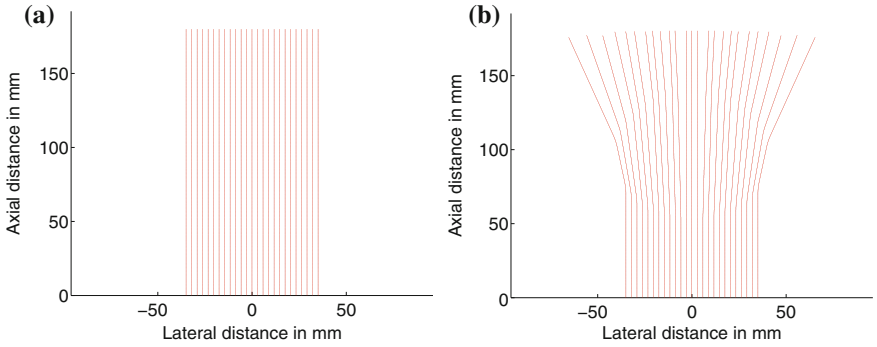

Fig. 14.2 Refraction effects on wave front propagation through a cylinder with index of refraction $n = 1/1.1$. **a** Homogeneous medium **b** Cylinder, index of refraction $n = 1/1.1$

$$\frac{dx}{ds} = \frac{p}{n}, \quad \frac{dy}{ds} = \frac{q}{n}, \quad \frac{dp}{ds} = \frac{\partial n}{\partial x}, \quad \frac{dq}{ds} = \frac{\partial n}{\partial y}, \quad \frac{d\tau}{ds} = n, \tag{14.11}$$

where $p = \partial\tau/\partial x$, $q = \partial\tau/\partial y$, and s is an auxiliary curve parameter. Only the first four equations in (14.11) are needed to obtain the ray path $(x(s), y(s))$ corresponding to transmitter location (x_0, y_0) and starting ray direction (p_0, q_0). Other approaches for ray tracing may be derived from different forms of the eikonal equation. For example, Johnson et al. (1975) performed ray tracing by solving the second-order differential form of the eikonal equation

$$\frac{d}{ds}\left(n\frac{d\mathbf{r}}{ds}\right) = \nabla n. \tag{14.12}$$

Numerical recipes for the solution of Eqs. (14.11) and (14.12) can be found in (Andersen and Kak 1982; Andersen 1986).

For the problem of refraction-corrected tomography one is concerned with finding the actual bent path that connects a transmitter with a receiver, i.e., the ray linking problem (Andersen and Kak 1982; Norton 1987). Ray linking in the geophysical imaging community was traditionally performed using ray shooting and ray bending methods (Julian and Gubbins 1977), with the former being one of the earliest methods proposed for refraction-corrected tomography (Schomberg 1978; Lytle and Dines 1980). Ray shooting consists of solving the eikonal equation for a fixed transmitter position (x_0, y_0) and different values of (p_0, q_0) to find all rays that pass through the receiver location. If more than one ray is found, the solution is taken to be equal to the ray of minimum travel time between transmitter and receiver. Ray bending is based on Fermat's principle,[1] which states that the ray

[1] The eikonal equation can alternatively be derived from Fermat's principle, and therefore this principle can also be used for ray tracing. The interested reader can refer to acoustics textbooks such as Pierce (1989).

that connects two points is the path of minimum travel time. Ray bending consists of perturbing an initial ray path joining the transmitter and receiver until a minimum time-of-flight criterion is met.

Ray linking approaches can be computationally expensive due to the need to calculate many ray paths for different transmitter/receiver pairs. Therefore, researchers sought alternative methods more efficient than classical ray linking (Andersen 1987). A particularly interesting class of algorithms consists of using graph theory methods to find the path of minimum travel time connecting transmitter/receiver pairs. Not only is this approach computationally efficient, but it also provides a global optimum solution and therefore avoids convergence problems of the shooting and bending methods (Moser 1991; Klimes and Kvasnicka 1994; Song and Zhang 1998; Li et al. 2010).

The main difficulty with reconstructing refraction-corrected acoustic tomograms is that in order to calculate the ray paths one has to know the spatial distribution of the index of refraction, which is the quantity that needs to be estimated. Therefore, the imaging problem becomes nonlinear with respect to the speed of sound distribution and more sophisticated methods than simple inverse Radon transforms need to be applied. Refraction-corrected approaches were applied since the early days of acoustic tomography by iteratively refining propagation paths based on the current estimate of the speed of sound distribution and the eikonal equation (Johnson et al. 1975; Schomberg 1978; Denis et al. 1995). Other researchers proposed methods based on modifying the measured data rather than the propagation paths (Norton and Linzer , 1982). Refraction-corrected paths were also proposed to reduce artifacts in acoustic attenuation reconstruction (Farrell 1981; Pan and Liu 1981).

14.2.3 Reflection Mode Tomography

Another variation of UCT is reflection mode tomography, which is based on using data collected in pulse-echo mode. Pulse-echo data $p(t, \mathbf{r}_{tr})$ collected with the transducer at location $\mathbf{r}_{tr}$ can be modeled as (Jensen 1990)

$$p(t, \mathbf{r}_{tr}) = v_{pe}(t) \underset{t}{*} \int d\mathbf{r} f_m(\mathbf{r}) h_{pe}(\mathbf{r}_{tr}, \mathbf{r}, t), \tag{14.13}$$

where $v_{pe}(t)$ is related to the pulse-echo wavelet generated by the transducer, $h_{pe}(\mathbf{r}_{tr}, \mathbf{r}, t)$ is the pulse-echo spatial impulse response of the transducer and $f_m(\mathbf{r})$ is the spatially varying reflectivity of the medium.[2]

[2] Equation 14.13 can actually be derived from direct first-order simplifications of the wave equation which are not presented here for brevity. The interested reader may refer to Jensen (1990).

For point-like transducers and at large measurement distances such that $|\mathbf{r}_{tr}| \gg |\mathbf{r}|$, $h_{pe}(\mathbf{r}_{tr}, \mathbf{r}, t) \propto \delta(t - 2|\mathbf{r}_{tr} - \mathbf{r}|/c_0)$. This allows Eq. (14.13) to be written as

$$p(t, \mathbf{r}_{tr}) \propto \int d\mathbf{r} f_m(\mathbf{r}) v_{pe}(t - 2|\mathbf{r}_{tr} - \mathbf{r}|/c_0). \tag{14.14}$$

Norton and Linzer (Norton and Linzer 1979a, b) proposed to collect pulse echo data in a circle of radius R, i.e., $\mathbf{r}_{tr} = (R\cos\theta, R\sin\theta)$ with $\theta \in [0, 2\pi]$. It was proposed that images of $f_m(\mathbf{r})$ could be generated by using the backpropagation operation[3]

$$\hat{f}(\mathbf{r}) = \int_0^{2\pi} d\theta p(2|\mathbf{r}_{tr} - \mathbf{r}|/c_0, \mathbf{r}_{tr}). \tag{14.15}$$

The formulation by Norton and Linzer assumes that propagation paths are straight lines. As discussed in Sect. 14.2.2, this will not be the case when propagating in inhomogeneous media. Bent ray paths derived from sound speed tomograms have been proposed to improve the backpropagation operation in Eq. (14.15) (Ashfaq and Ermert 2007; Schmidt et al. 2011; Koch et al. 2012).

14.2.4 Results and Limitations

Experimental imaging systems that utilize ray-based approaches to construct acoustic tomograms of sound speed and acoustic attenuation from tissues have been built over the decades. Several systems were built in the late 1970s and early 1980s to obtain clinical acoustic tomograms of human breasts (Glover 1977; Carson et al. 1981; Greenleaf and Bahn 1981; Schreiman et al. 1984). One example of a currently available system is CURE, developed at the Karmanos Cancer Institute (Duric et al. 2005). Both straight-ray (Duric et al. 2007) and refraction-corrected (Li et al. 2009) acoustic tomography have been implemented in this system. The CURE system provides images of speed of sound, attenuation, and reflectivity. Another example is the HUTT system, developed by researchers from the University of Southern California (Jeong et al. 2005, 2008, 2009). This system uses ray-based tomography to reconstruct images of attenuation coefficients at different frequencies. Image fusion methods are used to combine the different tomograms into 3D volumes for improved diagnostic capabilities. In laboratory environments, the 3D-USCT systems developed at the Karlsruhe Institute of Technology use transducers arranged in a 2D cylindrical aperture.

[3] This approach is in fact a synthetic aperture reconstruction method (Soumekh 1999) equivalent to the delay-and-sum algorithm. A commonly used variation is to perform the backpropagation operation using envelope-detected data, which results in a spatial compounding reconstruction method (Trahey et al. 1986).

Using ray-based theory, tomograms of sound speed and reflectivity have been constructed (Gemmeke and Ruiter 2007; Jiřík et al. 2012).

Ray-based tomography has also been proposed to reconstruct images of parameters other than sound speed, acoustic attenuation and reflectivity. For example, Zhang et al. proposed to reconstruct tomograms of the acoustic nonlinear parameter from measurements of second harmonic amplitude (Zhang and Gong 1999) and nonlinear interaction of waves at two different frequencies (Zhang et al. 2001).

Despite its successful experimental implementation, ray-based ultrasonic tomography has usually been met with partial skepticism due to the simplified physical model used to reconstruct the acoustic tomograms. Refraction is a dominant mechanism when imaging large objects compared to the wavelength, but diffraction needs to be considered when the size of scattering structures are on the order of the wavelength. Simulation studies suggest that even after refraction correction, ray-based tomography can only produce quantitatively accurate reconstructions of structures that are larger than a few wavelengths (i.e., 2–5 wavelengths) (Quan and Huang 2007). This limitation has also been observed with experimental data (Leach Jr. et al. 2002). Therefore, attention shifted in the early 1980s to methods that provide sub-wavelength resolution by taking diffraction into account.

14.3 Diffraction Tomography

Although diffraction tomography was formally introduced to the acoustic imaging community by Mueller et al. in the late 1970s (Mueller et al. 1979, Mueller 1980), the theoretical foundation for diffraction tomography was available in the literature prior to the development of ray-based acoustic tomography. In his seminal work on optical imaging back in 1969 (Wolf 1969), Emil Wolf outlined a method to reconstruct three-dimensional distributions of refractive index using measurements of scattered data. For the case of constant density, the wave equation in (14.1) can be written as

$$\nabla^2 p(\mathbf{r}) + k_0^2 p(\mathbf{r}) = -\phi^{\text{inc}}(\mathbf{r}) - O(k, \mathbf{r}) p(\mathbf{r}), \tag{14.16}$$

where $O(k, \mathbf{r}) = (k^2 - k_0^2)$ is the scattering potential function. Equation (14.16) can be written in terms of the Green's function $G_0(\mathbf{r})$ corresponding to k_0 as

$$p^{\text{sc}}(\mathbf{r}) = p(\mathbf{r}) - p^{\text{inc}}(\mathbf{r}) = \int_{\Omega} d\mathbf{r}' O(k, \mathbf{r}') p(\mathbf{r}') G_0(\mathbf{r}, \mathbf{r}'), \tag{14.17}$$

where $p^{\text{sc}}(\mathbf{r})$ is the scattered pressure field, $p^{\text{inc}}(\mathbf{r})$ is the incident pressure field caused by the sources $\phi^{\text{inc}}(\mathbf{r})$, and Ω is the region occupied by the object to be imaged.

14.3.1 The First-Order Born Approximation and the Fourier Diffraction Theorem

As in the case of refraction-corrected tomography, (14.17) is a nonlinear equation of the function $O(k, \mathbf{r})$ to be imaged because $p(\mathbf{r}')$ depends on the scattering potential function. In order to obtain a closed-form, tractable solution, Wolf (1969) invoked the first-order Born approximation to write Eq. (14.17) as

$$p^{\text{sc}}_{\text{Born}}(\mathbf{r}) = \int_{\Omega} d\mathbf{r}' O(k, \mathbf{r}') p^{\text{inc}}(\mathbf{r}') G_0(\mathbf{r}, \mathbf{r}'). \tag{14.18}$$

The results in Wolf (1969) were developed by Wolf using plane wave illumination and the plane wave decomposition of the 3D Green's function. The derivation provided here corresponds to the 2D case depicted in Fig. 14.3 and is presented with more details in Kak and Slaney (2001). The plane wave travels in the direction of the unit vector $\hat{s}_0$. The receivers are placed at locations $\mathbf{r}_r$ over a line $\eta = l_0$ perpendicular to $\hat{s}_0$. Under the first order Born approximation, the scattered field at locations $\mathbf{r}_r$ can be written as

$$p^{\text{sc}}_{\text{Born}}(\mathbf{r}_r) = \int_{\Omega} d\mathbf{r}' O(k, \mathbf{r}') e^{jk_0 \hat{s}_0 \cdot \mathbf{r}'} \frac{j}{4} H_0^{(1)}(k_0 |\mathbf{r} - \mathbf{r}'|) \tag{14.19}$$

where $H_0^{(1)}(\cdot)$ is the zero-order Hankel function of the first kind. Using the plane wave decomposition of the Hankel function (Chew 1995) results in

$$p^{\text{sc}}_{\text{Born}}(\xi, \phi_0) = \int_{\Omega} d\mathbf{r}' O(k, \mathbf{r}') e^{jk_0 \eta'} \frac{j}{4\pi} \int_{-\infty}^{\infty} d\alpha \frac{1}{\beta} e^{j[\alpha(\xi - \xi') + \beta |l_0 - \eta'|]}, \tag{14.20}$$

where $\beta = \sqrt{k_0^2 - \alpha^2}$. Rearranging terms and using the fact that $l_0 > \eta'$, $\forall \mathbf{r}' \in \Omega$ results in

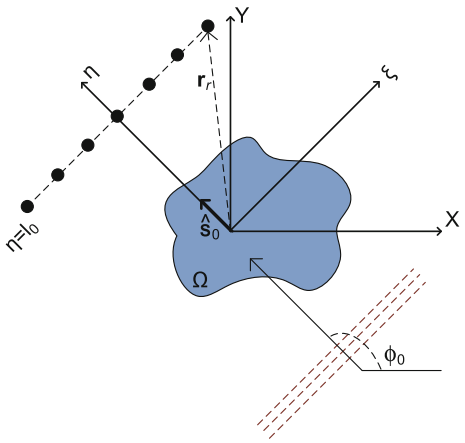

Fig. 14.3 Diffraction tomography using plane wave illumination and point receivers. The plane wave travels in the direction of the unit vector $\hat{s}_0$. The receivers are placed at locations $\mathbf{r}_r$ over a line $\eta = l_0$ perpendicular to $\hat{s}_0$. The scattering object occupies the region of space Ω

$$p^{\text{sc}}_{\text{Born}}(\xi, \phi_0) = \frac{j}{4\pi} \int_{-\infty}^{\infty} d\alpha \frac{1}{\beta} e^{j(\alpha\chi + \beta l_0)} \bar{O}(k, k_0[\hat{s}(\alpha) - \hat{s}_0]), \tag{14.21}$$

$$\hat{s}(\alpha) = \frac{\alpha}{k_0}\hat{\xi} + \frac{\sqrt{k_0^2 - \alpha^2}}{k_0}\hat{\eta}, \tag{14.22}$$

where $\bar{O}(k, \mathbf{u})$ is the 2D Fourier transform of $O(k, \mathbf{r})$. From Eq. (14.21), the 1D spatial Fourier transform of $p^{\text{sc}}_{\text{Born}}(\xi, \phi_0)$ is given by

$$P^{\text{sc}}_{\text{Born}}(\kappa, \phi_0) = \int_{-\infty}^{\infty} d\xi\, p^{\text{sc}}_{\text{Born}}(\xi, \phi_0) e^{-j\kappa\xi} = \frac{j}{2} \frac{e^{j\gamma l_0}}{\gamma} \bar{O}(k, k_0[\hat{s}(\kappa) - \hat{s}_0]), \tag{14.23}$$

where $\gamma = \sqrt{k_0^2 - \kappa^2}$. From Eq. (14.23) one can observe that the 1D Fourier transform of the measured scattered pressure field is related to samples of the 2D Fourier transform of the scattering potential function (see Fig. 14.4). Further, these 2D Fourier samples lie along semi-circular arcs of radius k_0 whose centers in turn lie on a circle of radius k_0 centered at the origin of the 2D k-space. Therefore, by using different transmitter/receiver combinations one can sample a disk of radius $\sqrt{2}k_0$ in 2D k-space. By placing additional receiver lines at $\eta = -l_0$ one can readily measure in k-space full circles instead of semi-circular arcs per transmitted plane wave, effectively increasing the k-space coverage to a circle of radius $2k_0$. This fundamental result is termed the Fourier diffraction theorem, and was quickly acknowledged to be a generalization of the Fourier slice theorem (that applies to non-diffracting tomographic imaging) to the case of imaging with diffracting sources. One can also show that for a circular array of receivers with large radius

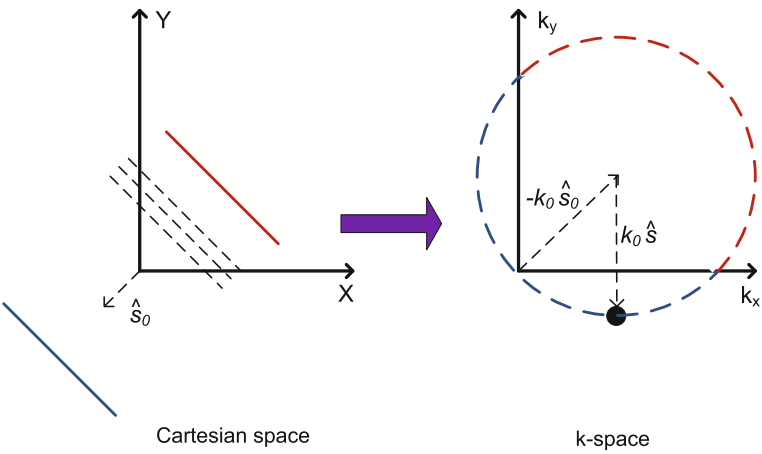

Fig. 14.4 k-space coverage of first order Born diffraction tomography. Scattered field data are related to the 2D Fourier transform of $O(\mathbf{r})$ at spatial frequencies $k = k_0(\hat{s} - \hat{s}_0)$. Using scattered field measurements at $\eta = l_0$ (blue) and $\eta = -l_0$ (red) provides samples over a full circle of radius k_0 centered at $-k_0\hat{s}_0$

such that measurements are collected in the far field, the actual values of $p^{\text{sc}}_{\text{Born}}(\mathbf{r}_r)$ are proportional to $\bar{O}(k, k_0[\hat{r}_r - \hat{s}_0])$ with $\hat{r}_r$ the unit vector in the direction of $\mathbf{r}_r$ (Naidu et al. 1995).

14.3.2 The First-Order Rytov Approximation

The first-order Born approximation is not the only way to linearize the wave equation. In particular, the first-order Rytov approximation was also applied to obtain analytical solutions to the wave inversion problem (Iwata and Nagata 1975; Devaney 1981; Kak and Slaney 2001). If the total pressure field is written as $p(\mathbf{r}) = \exp(\Phi(\mathbf{r}))$, then Eq. (14.3) can be written as

$$\nabla^2 \Phi(\mathbf{r}) + k_0^2 = -O(k, \mathbf{r}) - |\nabla \Phi(\mathbf{r})|^2. \tag{14.24}$$

Further, if the total complex phase is rewritten as $\Phi(\mathbf{r}) = \Phi^{inc}(\mathbf{r}) + \Phi^{\Delta}(\mathbf{r})$ with $p^{inc}(\mathbf{r}) = \exp(\Phi^{\text{inc}}(\mathbf{r}))$, Eq. (14.24) can be written as

$$\nabla^2 \Phi^{\Delta}(\mathbf{r}) + 2\nabla \Phi^{\text{inc}}(\mathbf{r}) \cdot \nabla \Phi^{\Delta}(\mathbf{r}) = -O(k, \mathbf{r}) - |\nabla \Phi(\mathbf{r})|^2. \tag{14.25}$$

Using the fact that $\nabla^2 p^{\text{inc}}(\mathbf{r}) = -k_0^2 p^{\text{inc}}(\mathbf{r})$, it can be shown that

$$\nabla^2 (p^{\text{inc}}(\mathbf{r}) \Phi^{\Delta}(\mathbf{r})) = p^{\text{inc}}(\mathbf{r}) \left[\nabla^2 \Phi^{\Delta}(\mathbf{r}) + 2\nabla \Phi^{\Delta}(\mathbf{r}) \cdot \Phi^{\text{inc}}(\mathbf{r}) - k_0^2 \Phi^{\Delta}(\mathbf{r})\right]. \tag{14.26}$$

Combining Eqs. (14.25) and (14.26) results in

$$\nabla^2 (p^{\text{inc}}(\mathbf{r}) \Phi^{\Delta}(\mathbf{r})) + k_0^2 p^{\text{inc}}(\mathbf{r}) \Phi^{\Delta}(\mathbf{r}) = -p^{\text{inc}}(\mathbf{r}) \left(O(k, \mathbf{r}) - |\nabla \Phi(\mathbf{r})|^2\right). \tag{14.27}$$

Equation (14.27) can be written in integral form as

$$p^{\text{inc}}(\mathbf{r}) \Phi^{\Delta}(\mathbf{r}) = \int_{\Omega} d\mathbf{r}' p^{\text{inc}}(\mathbf{r}') \left(O(k, \mathbf{r}') - |\nabla \Phi(\mathbf{r}')|^2\right) G_0(\mathbf{r}, \mathbf{r}'). \tag{14.28}$$

Up to this point, no simplifications have been made. If $O(k, \mathbf{r}) \gg |\nabla \Phi(\mathbf{r})|^2$, then the complex excess phase can be approximated as

$$\Phi^{\Delta}_{\text{Rytov}}(\mathbf{r}) = \frac{1}{p^{\text{inc}}(\mathbf{r})'} \int_{\Omega} d\mathbf{r}' p^{\text{inc}}(\mathbf{r}) O(k, \mathbf{r}') G_0(\mathbf{r}, \mathbf{r}') = \frac{p^{\text{sc}}_{\text{Born}}(\mathbf{r}_r)}{p^{\text{inc}}(\mathbf{r})} \tag{14.29}$$

Equation (14.29) implies that the Fourier diffraction theorem can also be used to reconstruct tomograms from measurements of the pressure field phase. Therefore, diffraction tomography under either the first-order Born or Rytov approximations can be used to reconstruct images of sound speed and acoustic attenuation by mapping measurements of scattered fields to k-space samples of the scattering potential function.

14.3.3 Multi-Frequency Diffraction Tomography

In order to reconstruct an N-dimensional object, N degrees of freedom in the measurements are needed. Conventional diffraction tomography exploits three degrees of freedom (i.e., transmitter position and two angular orientations between transmitter and receivers) to reconstruct 3D imaging targets. However, frequency diversity can also be exploited as a degree of freedom. For a fixed transmitter/receiver pair location, changing the angular frequency of the incident field will provide a different sample of the scattering potential function in k-space. This was exploited by Kenue and Greenleaf (1982) in order to increase k-space coverage when a limited number of transmitter/receiver locations is allowed. Other researchers exploited frequency diversity more aggressively by using bistatic scanning configurations (i.e., a fixed angular separation between transmitter and receiver) with broadband transducers (Norton 1983).

14.3.4 Frequency-Domain Interpolation Methods

Diffraction tomography under the Born and Rytov approximations provided an elegant solution to the wave inversion problem. The most direct approach for reconstructing tomograms under first order scattering assumptions is to use the Fourier diffraction theorem to obtain samples of the 2D Fourier transform of the scattering potential function. In order to reconstruct images of the scattering potential function on a Cartesian grid, samples of $\bar{O}(k, \mathbf{u})$ distributed on a Cartesian grid in k-space are needed. Therefore, the use of interpolation methods is required given that measurements of scattered fields provide Fourier samples in circular arcs as described in Sect. 14.3.1. Frequency-domain interpolation was one of the first algorithms proposed for acoustic diffraction tomography (Mueller et al. 1979). Pan and Kak reported that good results in terms of reconstruction quality can be obtained by using bilinear interpolation after increasing sampling density using zero-padding (Pan and Kak 1983). The unified Fourier reconstruction (UFR) method performs the frequency-domain interpolation exploiting the limited spatial support of the scattering potential function (Kaveh et al. 1984; Soumekh 1988).

14.3.5 The Filtered Backprojection Method

The filtered backpropagation algorithm was proposed by Devaney as the analogous of filtered backprojection when imaging with diffracting sources (Devaney 1982). Consider the case depicted in Fig. 14.3. From the results in Sect. 14.3.1, the scattering potential function can be reconstructed from its Fourier components using

$$O^{\mathrm{bp}}(k,\mathbf{r}) = \frac{1}{(2\pi)^2}\int_{|\mathbf{k}|<\sqrt{2}k_0} d\mathbf{k}\bar{O}^{\mathrm{bp}}(\mathbf{k})\mathrm{e}^{j\mathbf{k}\cdot\mathbf{r}}, \tag{14.30}$$

$$\mathbf{k} = k_0(\hat{s}-\hat{s}_0), \tag{14.31}$$

where $O^{\mathrm{bp}}(\mathbf{r}) = -O(k,\mathbf{r})/k_0^2$ and $\bar{O}^{\mathrm{bp}}$ is the spatial Fourier transform of O^{bp}. Introducing χ such that $\hat{s} = (\cos\chi, \sin\chi)$, Eq. (14.30) can be rewritten as

$$O^{\mathrm{bp}}(\mathbf{r}) = \frac{k_0^2}{2(2\pi)^2}\int_{-\pi}^{\pi} d\phi_0 \int_{-\pi}^{\pi} d\chi\sqrt{1-\cos^2(\chi-\phi_0)}\bar{O}^{\mathrm{bp}}(\mathbf{k})\mathrm{e}^{j\mathbf{k}\cdot\mathbf{r}}. \tag{14.32}$$

The integral in χ can be written in terms of κ by noticing that in the $\hat{\xi}-\hat{\eta}$ frame, $\cos\chi = \kappa/k_0$ ($\kappa \in [-k_0, k_0]$) and $\phi_0 = \pi/2$. As a result,

$$O^{\mathrm{bp}}(\mathbf{r}) = \frac{k_0}{2(2\pi)^2}\int_{-\pi}^{\pi} d\phi_0 \int_{-k_0}^{k_0} d\kappa\frac{|\kappa|}{\gamma}\bar{O}^{\mathrm{bp}}(\mathbf{k})\mathrm{e}^{j\mathbf{k}\cdot\mathbf{r}}. \tag{14.33}$$

Using the Fourier diffraction theorem in (14.23), Eq. (14.33) can be written as

$$O^{\mathrm{bp}}(\mathbf{r}) = \frac{1}{(2\pi)^2}\int_{-\pi}^{\pi} d\phi_0 \int_{-k_0}^{k_0} d\kappa|\kappa|\bar{G}(\kappa,\eta)\bar{\Gamma}(\kappa,\phi_0)\mathrm{e}^{j\kappa\xi}, \tag{14.34}$$

$$\bar{\Gamma}(\kappa,\phi_0) = \frac{j}{k_0}\mathrm{e}^{-jk_0l_0}P^{\mathrm{sc}}_{\mathrm{Born}}(\kappa,\phi_0), \tag{14.35}$$

$$\bar{G}(\kappa,\eta) = \mathrm{e}^{j(\gamma-k_0)(\eta-l_0)}. \tag{14.36}$$

According to Eq. (14.34), the scattering potential function can be reconstructed using a modified filtered backprojection algorithm. The modification consists of including an additional filter $\bar{G}(\kappa,\eta)$ prior to backpropagating the measured scattered pressure data. Also, the angular integration uses angles in $[-\pi,\pi]$ as opposed to $[0, \pi]$ in Eq. (14.9).

The need for depth-dependent filtering causes the filtered backpropagation method to be more computationally expensive than its filtered backprojection counterpart. Further, early studies found that Fourier interpolation methods were able to produce images of comparable quality but reduced computational cost when compared to filtered backpropagation (Pan and Kak 1983). In order to reduce the computational cost of the method, Devaney proposed an approximate solution that consisted of replacing the backpropagation filter $\bar{G}(\kappa,\eta)$ with $\bar{G}(\kappa,\eta_0 = x_0\cos\phi_0 + y_0\sin\phi_0)$, where (x_0, y_0) are the coordinates of the center of the region where good image quality is desired (Devaney 1983). Therefore, the modified filtered backpropagation method enables a reduction of computational cost at the expense of image quality.

Other variations of the filtered backpropagation method were later developed. In particular, the hybrid filtered backpropagation method by Sponheim et al.

preserved the essence of the original filtered backpropagation method while allowing the use of data from a circular array of receivers and better handling Rytov data for image reconstruction (Sponheim et al. 1991, 1994).

14.3.6 Algebraic Reconstruction Methods

Diffraction tomography as described in Sect. 14.3.1 was developed assuming plane wave illumination and receivers arranged in a straight line. These are very restrictive conditions, and therefore algorithms were later developed to handle more complex incident fields and receiver apertures (Devaney and Beylkin 1984; Devaney 1985; Gelius et al. 1991; Anastasio and Pan 2003). A particular approach to handle more general imaging configurations consisted of casting the linearized wave equation in (14.18) as a matrix equation. This approach allows the use of algebraic methods to solve the diffraction tomography problem (Devaney 1986; Ladas and Devaney 1991). An additional benefit of using algebraic methods is the possibility of incorporating *a priori* information about the scattering potential function during the reconstruction process. These approaches are usually simplified versions of methods for the inversion of the full integral wave equation, which will be discussed in Sect. 14.4.

14.3.7 Advantages and Limitations

The most significant advantage of diffraction tomography is its spatial resolution. If the scattered pressure is measured with full angular coverage on reception (i.e., transmitters and receivers distributed over a fully enclosed surface) the k-space can be fully covered within a sphere of radius $2k_0$. Therefore, the achievable spatial resolution is approximately $\lambda/2$ and as a result diffraction tomography is expected to produce tomograms with better spatial resolution than ray-based acoustic tomography. Diffraction tomography methods were also developed to reconstruct images of parameters other than sound speed and acoustic attenuation. Examples include density imaging (Devaney 1985; Moghaddam and Chew 1993; Mensah and Lefebvre 1997; Anastasio et al. 2005) and acoustic nonlinear parameter (Kai et al. 1992).

However, the main limitation of diffraction tomography is its convergence properties. Given that diffraction tomography is based on approximate expressions of the full wave equation, it is expected to provide accurate quantitative images only under weakly scattering conditions. The convergence of diffraction tomography was analyzed in detail in the early 1980s (Slaney et al. 1984; Robinson and Greenleaf 1986). Different convergence behavior was found depending on whether the first order Born or Rytov approximations were used to linearize the wave equation.

For the first order Born approximation it is required that $|p^{sc}| \ll |p^{inc}|$ within the imaging target. A somewhat equivalent condition was adopted by Slaney et al. (Slaney et al. 1984) regarding the quantity $\Delta\phi$, which represents the maximum phase change that the incident field suffers when propagating through an inhomogeneity. Slaney et al. found through simulations that diffraction tomography based on the first order Born approximation breaks down as $|\Delta\phi| \to 0.8\pi$. This bound was consistent with the expectation of the first order Born approximation breaking down for $|\Delta\phi| \geq \pi$ (Iwata and Nagata 1975; Slaney et al. 1984). An example of the degradation of reconstruction quality with increasing $\Delta\phi$ values is given in Fig. 14.5.

The first order Rytov approximation is derived under the assumption that $|\nabla\Phi|^2 \ll k_0^2 \max(c/c_0 - 1)$ (Slaney et al. 1984; Tsihrintzis and Devaney 2000). Unlike the Born approximation, the Rytov approximation imposes no restriction on the size of the scatterer, and therefore it is usually valid for a wider class of

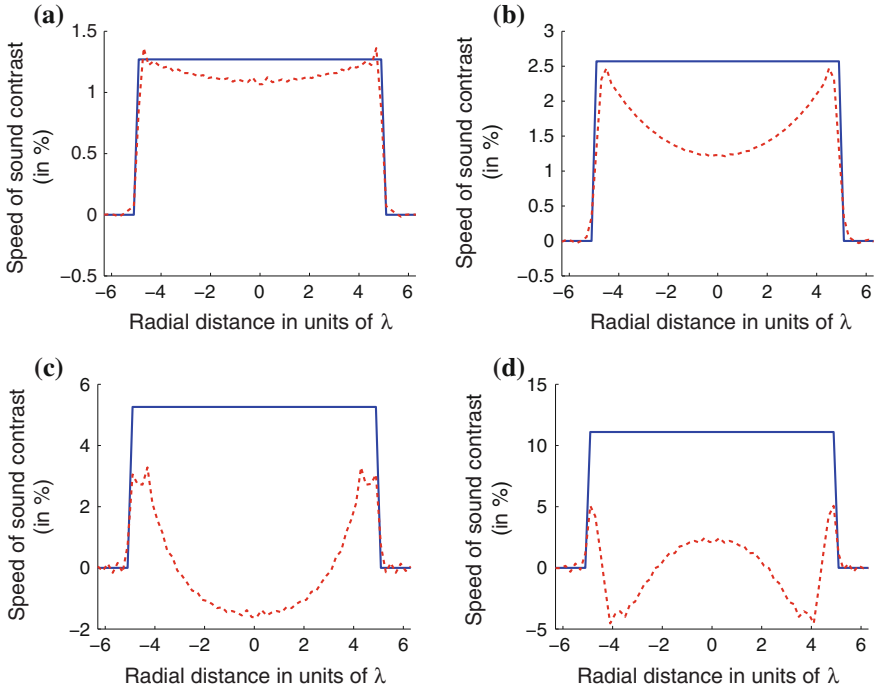

Fig. 14.5 Diffraction tomography under the first order Born approximation. The imaging targets are circular cylinders of radius 5λ and $\Delta\phi$ values of (**a**) 0.25π, (**b**) 0.5π, (**c**) π, and (**d**) 2π. Radial profiles corresponding to the ideal (*solid lines*) and reconstructed (*dash lines*) sound speed images are shown

imaging targets. However, inversions using the Rytov approximation suffer from phase wrapping problems caused when estimating Φ from measurements of the scattered pressure data. Tomograms obtained with the Rytov approximation are usually of better quality than the ones obtained with the Born approximation, but phase wrapping causes a sudden and catastrophic failure in the inversion (Slaney et al. 1984; Robinson and Greenleaf 1986). Phase unwrapping algorithms have been proposed in order to improve the performance of Rytov-based methods (Kaveh et al. 1984; Wedberg and Stamnes 1995) but only with limited success.

Therefore, just like for the case of ray-based acoustic tomography, diffraction tomography is better suited for imaging regions composed exclusively by soft tissues. However, unlike the case of ray-based tomography, non-convergence of diffraction tomography may lead to unusable tomograms due to the distortion of the underlying structures in the image (Robinson and Greenleaf 1986).

Several researchers have studied methods to extend the region of convergence of diffraction tomography. A particular approach is to use a non-uniform background that accounts for large structures of the imaging target when linearizing the wave equation. If both the incident field and Green's function can be calculated for such a background, then diffraction tomography can be used to image the fine details of the object. A gross estimate of the scattering potential function can be obtained from ray-based tomography. In order to retain the mathematical simplicity of diffraction tomography, researchers have proposed to modify both the free-space incident field and Green's function by using time delays that model the time-of-flight difference between the homogeneous and inhomogeneous backgrounds. This approach has been explored with the delays calculated using straight and refracted ray theory, and interesting results can be found in the literature (Gelius et al. 1991; Mast 1999; Astheimer and Waag 2008).

However, the limitations of diffraction tomography caused the attention of the research community to shift towards approaches that invert the full wave equation and therefore account for refraction, diffraction, and multiple scattering.

14.4 Full Wave Inversion Methods

The pioneering studies on full acoustic wave inversion were conducted almost simultaneously with the development of ultrasonic diffraction tomography. It was during the early 1980s that initial reports of methods designed to invert the wave equation were reported. These methods have a much higher computational cost than diffraction tomography approaches, and were therefore not widely explored until continued reports of the limitations of single-scattering tomography were made available.

14.4.1 The Alternating Variables Method

Diffraction tomography under the first-order Born approximation will fail if the condition $p(\mathbf{r}) \approx p^{\text{inc}}(\mathbf{r})$ is not met. If one were to exactly know the total pressure field $p(\mathbf{r})$ inside the imaging target, then the Born approximation would not be needed and the scattering potential function could be determined. In a seminal series of articles (Johnson and Tracy 1983; Tracy and Johnson 1993), Johnson et al. (1984) provided full details on an algorithm designed for the simultaneous estimation of $p(\mathbf{r})$ and $O(k, \mathbf{r})$. This method is known as the alternating variables algorithm, and is also known as the iterative Born method in the microwave imaging community (Wang and Chew 1989).

To illustrate the alternating variables method, it is convenient to express the integral wave equation (14.17) in operator notation as

$$\begin{aligned} p^{\text{inc}}(\mathbf{r}, \mathbf{r}_t) &= p(\mathbf{r}, \mathbf{r}_t) - \int_\Omega d\mathbf{r}'\, O(k, \mathbf{r}') p(\mathbf{r}', \mathbf{r}_t) G_0(\mathbf{r}, \mathbf{r}') \\ &= p(\mathbf{r}, \mathbf{r}_t) - \mathcal{G}Op(\mathbf{r}, \mathbf{r}_t) \end{aligned} \tag{14.37}$$

in which the total and incident pressures are explicit functions of $\mathbf{r}_t \in \Omega_t$ for some set Ω_t characterizing a variety of incident fields. Equation (14.37) is called the forward problem, and solutions to the forward problem for distinct sources corresponding to unique points $\mathbf{r}_t$ are independent. The operator $\mathcal{G}$ characterizes interactions among points within the scattering domain Ω and, in practice, is usually well conditioned.

For a known total field $p(\mathbf{r}, \mathbf{r}_t)$, the scattered field observed at some observation location $\mathbf{r}_r \in \Omega_r$ may be written

$$p^{\text{sc}}(\mathbf{r}_r, \mathbf{r}_t) = \int_\Omega d\mathbf{r}\, G_0(\mathbf{r}_r, \mathbf{r}) p(\mathbf{r}, \mathbf{r}_t) O(k, \mathbf{r}) = \mathcal{G}_r Op(\mathbf{r}_r, \mathbf{r}_t). \tag{14.38}$$

The operator $\mathcal{G}_r$ maps the total field within the domain Ω to an observed scattered field within the set Ω_r. $\mathcal{G}_r$ may be inverted to compute the scattering potential O if the total pressure p within Ω is known. Unlike in the forward problem, the inverse problem is ill-posed and is rarely well determined. A generalized solution to the inverse problem (14.38) is given by

$$O(k, \mathbf{r}) = \underset{O \in L^2(\Omega)}{\arg\min} \int_{\Omega_r} d\mathbf{r}_r \int_{\Omega_t} d\mathbf{r}_t \left(p^{\text{sc}}(\mathbf{r}_r, \mathbf{r}_t) - \mathcal{G}_r Op(\mathbf{r}_r, \mathbf{r}_t)\right)^2. \tag{14.39}$$

The alternating variables algorithm consists of iterating through the following steps: (1) calculate the total field p using Eq. (14.37) and an estimate of O, (2) calculate O using Eq. (14.39) and the current estimate of p, and (3) repeat steps (1)–(2) until O does not change significantly between consecutive iterations.

14.4.1.1 Variable Density Case

Consider the wave equation in (14.1). By applying the change of variables $p(\mathbf{r}) = f(\mathbf{r})\rho^{1/2}(\mathbf{r})$ (Johnson et al. 1982; Pourjavid and Tretiak 1992), Eq. (14.1) can be rewritten in integral form as

$$f(\mathbf{r}) = f^{inc}(\mathbf{r}) + \int_{\Omega} d\mathbf{r}' O_{\rho}(k, \mathbf{r}') f(\mathbf{r}') G_0(\mathbf{r}, \mathbf{r}'), \tag{14.40}$$

where $O_{\rho}(k, \mathbf{r})$ is given by

$$O_{\rho}(k, \mathbf{r}') = \left(k^2(\mathbf{r}) - k_0^2\right) - \rho^{1/2}(\mathbf{r})\nabla^2\rho^{-1/2}(\mathbf{r}). \tag{14.41}$$

By comparing Eqs. (14.17) and (14.40), it is clear the only difference between the constant and variable density cases is the form of the scattering potential function. Therefore, the alternating variables algorithm can be used to reconstruct tomograms of $O_{\rho}(k, \mathbf{r})$. If one assumes a non-dispersive medium for which $\left(k^2(\mathbf{r}) - \mathbf{k_0^2}\right)$ scales as ω^2, the term $\mathcal{F}_{\rho} = \rho^{1/2}(\mathbf{r})\nabla^{\mathbf{2}}\rho^{-\mathbf{1/2}}(\mathbf{r})$ can be isolated from the algebraic combination of reconstructions of $O_{\rho}(k, \mathbf{r})$ at two or more frequencies.[4] Density tomograms can be constructed by solving the differential equation

$$\begin{aligned} \nabla^2 u(\mathbf{r}) - \mathcal{F}_{\rho}(\mathbf{r}) u(\mathbf{r}) &= \mathcal{F}_{\rho}(\mathbf{r}), \mathbf{r} \in \Omega \\ u(\mathbf{r}) &= 0, \mathbf{r} \notin \Omega \end{aligned} \tag{14.42}$$

with $u(\mathbf{r}) = \left(\rho_r^{-1/2}(\mathbf{r}) - 1\right)$. This approach for density imaging using the alternating variables algorithm was proposed in (Berggren et al. 1986).

14.4.1.2 Convergence

This algorithm was extensively studied by Cavicchi et al. in the late 1980s. Initial results showed that the alternating variables algorithm could provide improved results in terms of reconstruction error when compared to diffraction tomography based on the first-order Born approximation (Cavicchi et al. 1988). However, it was found that the alternating variables algorithm suffered from divergence when $|\Delta\phi| \geq \pi$ (Cavicchi and O'Brien, Jr. 1989), which is only marginally better than the $|\Delta\phi| \to 0.8\pi$ condition found for first-order Born diffraction tomography in (Slaney et al. 1984).

[4] Density information from dispersive media can also be isolated from $O_{\rho}(k, \mathbf{r})$ profiles at different frequencies if the dispersion can be properly modeled as a function of ω.

14.4.2 Newton-Type Methods

The shortcomings of the alternating variables approach are caused by the nonlinearity of the inverse problem as a function of the total pressure. The solution to the wave equation is unique, but inverse scattering is generally ill-posed (Colton et al. 2000). The ill-posed nature of the acoustic tomography problem becomes more problematic for moderate to large complex wave number contrast with respect to the background. Therefore, the key to improving the convergence of the inverse scattering problem is to update not only the scattering potential function and total pressure field, but also the background and its corresponding Green's function.

Iterative updates of a background contrast profile were explored for electromagnetic inverse scattering by Chew and Wang (1990) and the approach was termed the distorted Born iterative method (DBIM). For acoustic tomography, Borup et al. (Borup et al. 1992) independently developed an inversion method based on Newton-type iterations. Both the distorted Born and Newton-type approaches have been found to be exactly equivalent (Remis and van den Berg 2000). Due to its more intuitive nature, the DBIM approach will be presented here.

Although a homogeneous background k_0 was used to write the integral wave equation in Sect. 14.3.1, one can use any inhomogeneous function $k_b(\mathbf{r})$ to characterize the acoustic background. Therefore, the integral wave equation can be written

$$p(\mathbf{r},\mathbf{r}_t,k)-p(\mathbf{r},\mathbf{r}_t,k_b)=\int_\Omega d\mathbf{r}'\,\Delta O(\mathbf{r}')p(\mathbf{r}',\mathbf{r}_t,k)G_b(\mathbf{r},\mathbf{r}'), \tag{14.43}$$

where $p(\mathbf{r},\mathbf{r}_t,k)$ is the total pressure field produced by a source characterized by $\mathbf{r}_t$ in a medium with wave number k, $\Delta O(\mathbf{r})=O(k,\mathbf{r})-O(k_b,\mathbf{r})$, and G_b is an inhomogeneous Green's function that characterizes the response of a point source in the presence of the background. A first-order Born approximation can be applied to linearize Eq. (14.43), which yields

$$\begin{aligned}\Delta p^{\mathrm{sc}}(\mathbf{r},\mathbf{r}_t)&=p^{\mathrm{sc}}(\mathbf{r},\mathbf{r}_t,k)-p^{\mathrm{sc}}(\mathbf{r},\mathbf{r}_t,k_b)=p(\mathbf{r},\mathbf{r}_t,k)-p(\mathbf{r},\mathbf{r}_t,k_b)\\&\approx\int_\Omega d\mathbf{r}'\,\Delta O(\mathbf{r}')p(\mathbf{r}',\mathbf{r}_t,k_b)G_b(\mathbf{r},\mathbf{r}')=\mathcal{G}_b\Delta O p(\mathbf{r},\mathbf{r}_t),\end{aligned} \tag{14.44}$$

in which $p^{\mathrm{sc}}(\mathbf{r},\mathbf{r}_t,k)=p(\mathbf{r},\mathbf{r}_t,k)-p^{\mathrm{inc}}(\mathbf{r},\mathbf{r}_t)$ is the scattered field relative to a homogeneous background with wave number k_0. This approach has been termed the distorted-wave Born approximation (Devaney and Oristaglio 1983) and was proposed as a tool for introducing prior knowledge about the scattering strength function into diffraction tomography.

Just as with Eq. (14.38), it is possible to invert Eq. (14.44) to obtain ΔO provided that the total field p is known throughout Ω. Because p^{sc} and, therefore, Δp^{sc} are generally observed on a set Ω_r that is distinct from Ω, a generalized solution

$$\Delta O(\mathbf{r}) = \underset{\Delta O \in L^2(\Omega)}{\arg\min} \int_{\Omega_r} d\mathbf{r}_r \int_{\Omega_t} d\mathbf{r}_t \left(\Delta p^{\mathrm{sc}}(\mathbf{r}, \mathbf{r}_t) - \mathcal{G}_b \Delta O p(\mathbf{r}_r, \mathbf{r}_t)\right)^2 \tag{14.45}$$

must be sought. The DBIM consists of iterating through the following steps: (1) calculate p using Eq. (14.37) and a current estimate of k_b, (2) calculate the scattered field corresponding to k_b using Eq. (14.38), (3) compute Δp^{sc} by subtracting the measured scattered field from the result of step (2), (4) estimate ΔO using Eq. (14.45), (5) update $k_b \leftarrow k_b + \Delta O$, (6) repeat steps (1)–(5) until the L^2 norm of ΔO drops below a specified threshold, (7) set $k = k_b$.

Given a background k_b, it is possible to numerically compute the Green's function G_b and, therefore, the operator $\mathcal{G}_b$. However, it is often preferable to avoid explicit construction of the Green's operator $\mathcal{G}_b$ in favor of a representation that describes the DBIM in terms of solutions of homogeneous, rather than inhomogeneous, scattering problems. From Eq. (14.44), is is possible to represent the inverse problem in the form (Borup et al. 1992)

$$\Delta p^{\mathrm{sc}}(\mathbf{r}_r, \mathbf{r}_t) = \mathcal{F} \Delta O(\mathbf{r}_r, \mathbf{r}_t), \tag{14.46}$$

where $\mathcal{F}$ is the Fréchet derivative of the scattering operator $\mathcal{G}_r$ in Eq. (14.38) (Ghosh Roy et al. 2007). For iterative solutions of Eq. (14.46), it is not required to explicitly invert $\mathcal{F}$, but rather to repeatedly compute products of $\mathcal{F}$ (and, generally, $\mathcal{F}^\dagger$) with test solutions. The product of $\mathcal{F}$ with some test solution ΔO can be shown to be equivalent to (Hesford and Chew 2010)

$$\mathcal{F} \Delta O(\mathbf{r}_r, \mathbf{r}_t) = \mathcal{G}_r \left[O(1 - \mathcal{G})^{-1} \mathcal{G} + 1 \right] \Delta O p(\mathbf{r}_r, \mathbf{r}_t), \tag{14.47}$$

where $p = p(\mathbf{r}, \mathbf{r}_t, k_b)$ and $O = O(k_b, \mathbf{r})$ correspond to the background medium with wave number k_b and $\mathcal{G}_r$ and $\mathcal{G}$ are the free-space Green's operators in Eqs. (14.37) and (14.38), respectively. Similarly, the adjoint Fréchet derivative product is equivalent to

$$\mathcal{F}^\dagger Y(\mathbf{r}) = \left[\int_{\Omega_t} d\mathbf{r}_t \, p(\mathbf{r}, \mathbf{r}_t, k_b) (1 - \mathcal{G}O)^{-1} \left(\mathcal{G}_r^\dagger Y^* \right)(\mathbf{r}, \mathbf{r}_t) \right]^*, \tag{14.48}$$

in which $(\cdot)^*$ denotes complex conjugation. Therefore, it is possible to invert Eq. (14.46) without explicit knowledge of an inhomogeneous background Green's function G_b. This operation can be made efficient provided that solutions of the forward problem, represented by the operators $(1 - \mathcal{G})^{-1}$ and $(1 - \mathcal{G}O)^{-1}$, and products of the operators $\mathcal{G}$ and $\mathcal{G}_r$ can be computed efficiently. This topic will be discussed more thoroughly in Sect. 14.5.

14.4.2.1 Convergence and Frequency-Hopping Approach

The DBIM also suffers from divergence if the initial guess is far from the true solution such that approximately $\left|\Delta\phi(k) - \Delta\phi(k_b^0)\right| > \pi$, where $\Delta\phi(k)$ and $\Delta\phi(k_b^0)$ are the maximum excess phases for the true and initial guess wave number profiles. However, this condition is less restrictive than the condition corresponding to the alternating variables algorithm. Therefore, the DBIM can provide an extended convergence region if a good initial guess is available. The simplest scheme is the frequency-hopping approach, i.e., the sequential use of multiple frequency data, processing first the low frequency data to achieve convergence and then the high frequency data to refine the spatial resolution of the resulting tomograms (Kim et al. 1987; Borup et al. 1992; Chew and Lin 1995; Haddadin and Ebbini 1998; Lavarello and Oelze 2008). An example taken from (Lavarello and Oelze 2008) is shown in Fig. 14.6, where DBIM and frequency hopping were used to

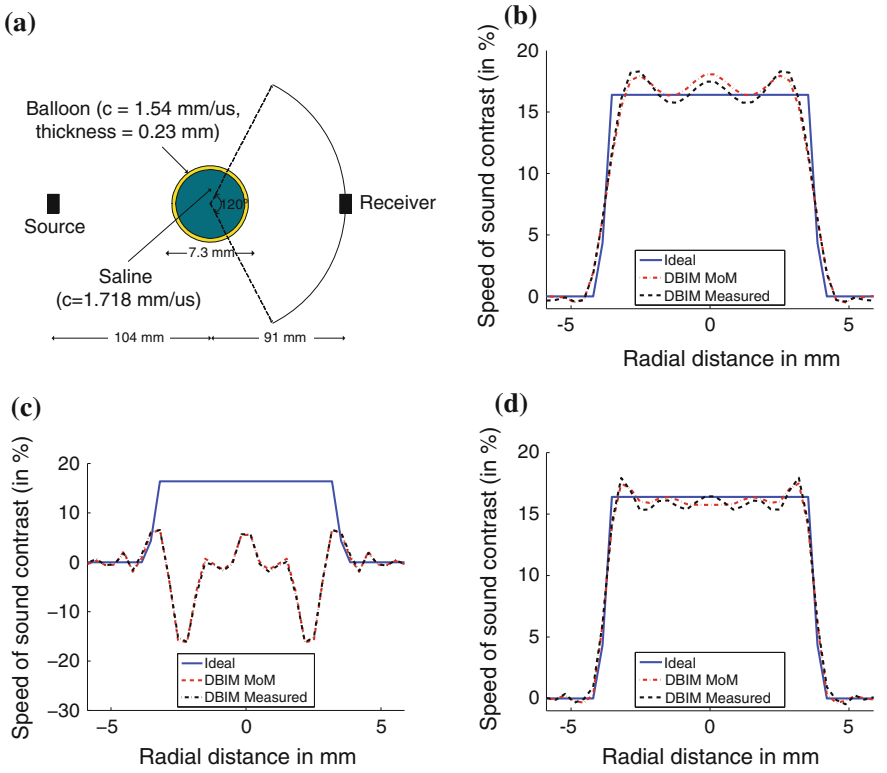

Fig. 14.6 (**a**) Experimental DBIM reconstructions of a balloon phantom containing a saline solution. In the frequency-hopping reconstruction, both 0.64- and 1.2-MHz data were used to produce an image ((**b**) reconstruction using 0.64-MHz data only, (**c**) reconstruction using 1.2-MHz data only, and (**d**) reconstruction using 0.64-MHz data initially followed by 1.2-MHz data). Results show the actual profile of the model and reconstructions using both ideal (computed) and measured data. Adapted from Lavarello and Oelze (2008)

reconstruct the cross-section of a cylindrical rubber balloon filled with a saline solution.[5] The low frequency (0.64 MHz, $\Delta\phi = 0.85\pi$) data reconstruction exhibits limited spatial resolution, whereas the high frequency (1.2 MHz, $\Delta\phi = 1.6\pi$) reconstruction diverged from the expected sound speed profile. The use of frequency hopping resulted in a convergent sound speed tomogram with improved resolution with respect to the low frequency reconstruction.

14.4.3 Conjugate Gradient Methods

An alternative way to invert the full wave equation is to use conjugate gradient approaches. This approach was studied in the early 1990s by researchers in the electromagnetics community (Kleinman and van den Berg 1992; Harada et al. 1995; Lobel et al. 1997). Conjugate gradient approaches have been used in UCT as well. Zhang et al. studied the performance of different methods to estimate the conjugate gradient directions (Zhang et al. 2004) as well as regularization methods for improved robustness (Zhang et al. 2002). Wiskin et al. (2007) have successfully demonstrated the application of the conjugate gradient method for obtaining clinical ultrasonic tomograms.

The conjugate gradient method consists of iterating through the equations

$$\bar{O}^{(n+1)} = \bar{O}^{(n+1)} + \alpha_n \bar{d}^{(n)} \tag{14.49}$$

$$\bar{d}^{(n+1)} = -\bar{g}^{(n+1)} + \beta_n \bar{d}^{(n)}, \tag{14.50}$$

where $\bar{O}$ and $\bar{g}$ are vector representations of the scattering potential function and the Fréchet derivative of the residual minimized in Eq. (14.39), respectively,[6] $\bar{d}$ is a vector pointing in the search direction, and α and β are scalar parameters. Numerical methods for calculating $\bar{d}$, α and β are discussed in (Wiskin et al. 2007).

A notable variation of the conjugate gradient method is the contrast source inversion (CSI) method, developed by van den Berg and Kleinman (van den Berg and Kleinman 1997). The residual R to be minimized in the CSI approach is given by

$$\begin{aligned} R = & \frac{\int_{\Omega_t} d\mathbf{r}_t \int_{\Omega_r} d\mathbf{r}_r \left(p^{\mathrm{sc}}(\mathbf{r}_r, \mathbf{r}_t) - \mathcal{G}_r w(\mathbf{r}_r, \mathbf{r}_t)\right)^2}{\int_{\Omega_t} d\mathbf{r}_t \int_{\Omega_r} d\mathbf{r}_r \left(p^{\mathrm{sc}}(\mathbf{r}_r, \mathbf{r}_t)\right)^2} \\ & + \frac{\int_{\Omega_t} d\mathbf{r}_t \int_{\Omega} d\mathbf{r} \left(w^{\mathrm{inc}}(\mathbf{r}, \mathbf{r}_t) - w(\mathbf{r}, \mathbf{r}_t) + O\mathcal{G} w(\mathbf{r}, \mathbf{r}_t)\right)^2}{\int_{\Omega_t} d\mathbf{r}_t \int_{\Omega} d\mathbf{r} \left(w^{\mathrm{inc}}(\mathbf{r}, \mathbf{r}_t)\right)^2} \end{aligned} \tag{14.51}$$

[5] In general, distortions may arise when reconstructing cross-sections of non-cylindrical objects using 2D data. The interested reader may refer to (Lavarello and Oelze 2009; Duncan et al. 2009).

[6] See Sect. 14.5 for a discussion on the discretization of the wave equation.

where $w = Op$ and $w^{\text{inc}} = Op^{\text{inc}}$. More recent versions of the technique, such as the multiplicative regularized contrast source inversion method (van den Berg et al. 1999; Pelekanos et al. 2003), added further robustness to the original CSI formulation.

14.4.4 Kaczmarz-Like Inverse Scattering

In the early days of X-ray tomography, algebraic methods were also studied for constructing tomograms. Even though the X-ray CT imaging problem is linear, the limited computing resources available at the time made it necessary to use iterative methods for matrix inversion. The algebraic reconstruction technique (ART) (Gordon 1974), one of the most celebrated iterative methods for the inversion of the Radon transform, is based on Kaczmarz's method. In short, Kaczmarz's method successively refines a current estimate of the solution by performing orthogonal projections on the hyper-planes corresponding to the equations given by each row of the matrix operator. If the system $\mathbf{R} \cdot \bar{\mathbf{f}} = \bar{\mathbf{g}}$ is to be inverted, starting from an initial guess $\bar{\mathbf{f}}_0$ an updated solution $\bar{\mathbf{x}}_{(n)}$ is calculated as

$$\bar{\mathbf{f}}^{(n)} = \bar{\mathbf{f}}^{(n-1)} + \beta \frac{\bar{\mathbf{g}}_m - \mathbf{R}_m \cdot \bar{\mathbf{f}}^{(n-1)}}{\mathbf{R}_m \cdot \mathbf{R}_m^{\mathrm{H}}} \mathbf{R}_m^{\mathrm{H}}, \tag{14.52}$$

where $\bar{\mathbf{g}}_m$ and $\mathbf{R}_m$ are the m-th entry of the measurement vector $\bar{\mathbf{g}}$ and the m-th row of the matrix $\mathbf{R}$, respectively, and β is a relaxation factor. This is a row-action method because only one row of the matrix equation is used at a time. Similar methods for inverse scattering that avoid constructing the Fréchet derivative matrix are therefore of potential benefit for ultrasonic tomography.

14.4.4.1 The Propagation-Backpropagation Method

Natterer and Wübbeling (Natterer and Wübbeling 1995) proposed in 1995 a method for inverse scattering that updated the scattering potential function using scattered data from one transmission at a time. In essence, the method is a nonlinear version of Kaczmarz's method. The imaging configuration corresponds to Fig. 14.3, with the incident plane wave propagating with different direction vectors $\theta_m = (\cos\theta_m, \sin\theta_m)$. The wave equation in (14.2) is written in the form

$$\nabla^2 u_\theta + k_0^2(1-f)u_{\theta_m} = 0 \tag{14.53}$$

$$u_{\theta_m} = \mathrm{e}^{jk\theta_m \cdot \mathbf{r}}(1 + v_{\theta_m}). \tag{14.54}$$

From Eq. (14.54) it can be derived that the scaled scattered field v_{θ_m} for the m-th transmission satisfies

$$\nabla^2 v_{\theta_m} + 2jk_0\theta_m \cdot \nabla v_{\theta_m} = k_0^2 f(1 + v_{\theta_m}) \tag{14.55}$$

for points inside the computational domain. In operator form, Eq. (14.55) can be written as $R_m(f) = g_m$, where $g_m = v_{\theta_m}$ at the receiver locations $\mathbf{r}_r$. This equation indirectly represents the scattered pressure field as a nonlinear transformation of the scattering potential function. The proposed algorithm, termed the propagation-backpropagation method, consists of updating f as

$$f^{(n)} = f^{(n-1)} + \omega R_m'(f^{(n-1)})^* C_m^{-1}\left(g_m - R_m(f^{(n-1)})\right), \tag{14.56}$$

where $R_m'(f)$ is the derivative of the operator $R_m(f)$, $R_m'(f)^*$ is the adjoint of $R_m'(f)$, and $C_m = R_m'(f)R_m'(f)^*$.[7]

The operator C_m can be simplified considering the limit $k_0 \to \infty$ for which $C_m \to R_m'(0)R_m'(0)^* = k_0^2/\rho\mathbf{I}$ and ρ is the radius of the reconstructed region (Natterer 1997). In order to calculate the updates, $R_m'(f)^* g$ needs to be calculated. This is performed indirectly by using the relationship

$$R_m'(f)^* g = k_0^2\left(1 + v_{\theta_m}^*\right)z, \tag{14.57}$$

where z satisfies the differential equation

$$\nabla^2 z + 2jk_0\theta_m \cdot \nabla z = k_0^2 f^* z. \tag{14.58}$$

The boundary conditions for both Eqs. (14.55) and (14.58) are given in (Natterer and Wübbeling 1995). As a result, this method allows reconstruction of the scattering potential function by successively solving two initial-value problems. Both (14.55) and (14.58) were solved using five-point finite difference marching schemes. A key detail of the actual marching implementations is that in order for the recursion to be stable the condition $h \geq \pi/k_0\sqrt{1-f}$ has to be met, with h the discretization step. Therefore, Natterer and Wübbeling suggested filtering high spatial frequency components after each step of the iteration.

Finally, the propagation-backpropagation method has been reported to converge as long as the initial guess f_0 satisfies the heuristic rule $|\int ds\,(f - f_0)| \leq \lambda$ (Natterer 2008). For low sound speed contrasts $\Delta c_r = |c - c_0|/c_0$, *i.e.*, $\Delta c_r \ll 1$, this convergence rule is equivalent to the one provided for DBIM in Sect. 14.4.2.

[7] Direct algebraic manipulation reveals that, for the linear-operator case (i.e., $R_m(f) = \mathbf{R}_m \cdot \bar{\mathbf{f}}$), (14.56) reduces to (14.52).

14.4.4.2 Kaczmarz-Like DBIM

The fundamental principals of the propagation-backpropagation method can also be applied to the DBIM to yield a Kaczmarz-like, round-robin scheme (Hesford and Chew 2010). Rather than attempt to invert the entire Fréchet derivative to arrive at an update to the background contrast, the round-robin scheme considers only the portion of the Fréchet derivative constrained to a limited number of source positions. The constrained Fréchet derivative problem will be severely underdetermined. In this case, the problem must be solved in the minimum-norm sense by forcing the solution to exist in the adjoint space of the Fréchet derivative. Unlike the propagation-backpropagation method, the round-robin DBIM does not require planar incident fields. Furthermore, the round-robin technique is readily incorporated into existing DBIM solvers without requiring a reformulation of the wave equation.

In analogy with frequency hopping, the round-robin technique attempts to avoid local minima associated with the solution of a single, restricted inverse problem (e.g., involving a single imaging frequency and a limited set of transmit angles) by using a previously obtained solution as a starting guess for a subsequent inversion. If local minima associated with distinct transmit angles do not coincide, a solution stagnating in a local minimum for one transmit angle may move away from the local minimum and toward the global minimum when the transmit angle is shifted.

14.4.5 Eigenfunction Methods

Eigenfunction methods for inverse scattering (Mast et al. 1997; Lin et al. 2000; Waag et al. 2007) rely on eigenfunctions of the far-field operator

$$A(\hat{s}_R, \hat{s}_T) = \lim_{r\to\infty} C \frac{e^{ik_0 r}}{r^{(d-1)/2}} p_s(\mathbf{r}_R, \hat{s}_T), \tag{14.59}$$

where C is an arbitrary constant, k_0 is the wave number of a homogeneous background material, $\hat{s}_R$ and $\hat{s}_T$ are points on the d-dimensional unit sphere Ω, $\mathbf{r}_R = r\hat{s}_R$, and the scattered pressure p_s is expressed as a function of the observation point $\mathbf{r}_R$ and the direction $\hat{s}_T$ of an incident plane wave. Thus, the far-field operator relates the angle $\hat{s}_T$ of an incident plane wave to the far-field scattering behavior observed at an angle $\hat{s}_R$.

For arbitrary focusing functions φ_i and φ_j, a measurement is defined as

$$M_{ji} = \langle \varphi_j, A\varphi_i \rangle = \int_\Omega d\hat{s}_R \, \varphi_j^*(-\hat{s}_R) \int_\Omega d\hat{s}_T \, A(\hat{s}_R, \hat{s}_T)\varphi_i(\hat{s}_T), \tag{14.60}$$

in which $(\cdot)^*$ represents complex conjugation. In the presence of an assumed background with wave number $k_b(\mathbf{r})$ and corresponding contrast profile O_b, the eigenfunction method is concerned with solving the differential far-field scattering problem (Waag et al. 2007)

$$M_{ji} - \langle \varphi_j, A_b \varphi_i \rangle = \langle \varphi_j, A_\Delta \varphi_i \rangle \tag{14.61}$$

for a differential update ΔO, where the far-field operator A_b corresponds to the scattering behavior of O_b relative to the homogeneous background k_0 and the far-field operator A_Δ corresponds to the scattering behavior of the unknown contrast ΔO relative to O_b. The problem is regularized to ensure a unique solution by minimizing

$$\|\Delta O(\mathbf{r})\|^2_{W_R} = \int_V d\mathbf{r}\, |\Delta O(\mathbf{r})|^2 W_R(\mathbf{r}), \tag{14.62}$$

where V contains the support of ΔO, for a suitable weighting function W_R.

The unknown far-field operator A_Δ may be written as

$$A_\Delta(\hat{s}_R, \hat{s}_T) = \int_V d\mathbf{r}\, G_b^f(\hat{s}_R, \mathbf{r}) \Delta O(\mathbf{r}) p(\mathbf{r}, \hat{s}_T), \tag{14.63}$$

in which p is the acoustic pressure at a point $\mathbf{r}$ due to a plane wave incident from an angle $\hat{s}_T$ and G_b^f is a far-field representation of the Green's function corresponding to the background O_b and is, in analogy with Eq. (14.59), given by

$$G_b^f(\hat{s}_R, \mathbf{r}) = \lim_{r \to \infty} C \frac{e^{ik_0 r}}{r^{(d-1)/2}} G_b(\mathbf{r}_R, \mathbf{r}). \tag{14.64}$$

Thus, Eqs. (14.43) and (14.63) are equivalent when the former is restricted to incident plane waves and far-field observations.

The differential scattering operation Eq. (14.43) that forms the basis of the distorted Born iterative method may be generalized to transmission focusing with an envelope function α and receive focusing with an envelope function β by writing

$$\begin{aligned} \int_R d\mathbf{r}\, \beta(\mathbf{r})_s(\mathbf{r}) = \int_V d\mathbf{r}' \left[\int_R d\mathbf{r}\, \beta(\mathbf{r}) G_b(\mathbf{r}, \mathbf{r}') \right] \\ \times \Delta O(\mathbf{r}') \left[\int_T d\mathbf{r}_T\, \alpha(\mathbf{r}_T) p(\mathbf{r}', \mathbf{r}_T) \right], \end{aligned} \tag{14.65}$$

where the total acoustic pressure p is now expressed as an explicit function of the source corresponding to a position $\mathbf{r}_T$ in some transmission domain T and the point $\mathbf{r}$ now exists in some measurement domain R. In the far-field limit, $G_b \to G_b^f$, $R = \Omega$ and $\mathbf{r} \mapsto \hat{s}_R$. If only plane-wave incidence is considered, then $T = \Omega$ and $\mathbf{r}_T \mapsto \hat{s}_T$. When $\alpha = \varphi_i$ and $\beta(\hat{s}) = \varphi_j^*(-\hat{s})$, Eqs. (14.61) and (14.65) are equivalent. The eigenfunction method employs a distorted Born approximation to linearize Eq. (14.61); therefore, the eigenfunction method is mathematically equivalent to a DBIM that employs focused plane-wave transmissions and focused far-field measurements.

The eigenfunction method is so named because artificial focusing envelopes φ_i and φ_j are chosen to be eigenfunctions of the measured scattering operator A.

These eigenfunctions concentrate energy within the support of the contrast function. When coupled with an explicit representation of the inverse scattering solution using Lagrange multipliers, the advantage of this choice of focusing profiles is a reconstruction that uses minimal unnecessary information (Mast et al. 1997).

Because the operator A characterizes far-field scattering of incident plane waves, focused transmissions or receptions are not directly applicable to the eigenfunction method. Instead, focused measurements would need to be suitably transformed into the required far-field operator, or the method would need to be reformulated to directly incorporate focusing. Such modifications to the eigenfunction method have not been described in the literature.

14.4.6 The T-matrix Formulation

The methods described so far are designed to reconstruct a single functional that depends on the complex wave number function. From this functional, sound speed and attenuation tomograms can be obtained. As described in Sect. 14.4.1.1, the functional can be made dependent on density variations with a proper change of variables. Although density tomograms can be reconstructed with this approach and the use of DBIM (Kwon and Jeong 1998; Lavarello and Oelze 2010; Lavarello et al. 2010), the solution of Eq. (14.42) can cause instabilities in the presence of noise. Alternatively, methods have been designed to natively take both compressibility and density variations into account when inverting the wave equation (van Dongen and Wright 2007).

One of these methods is the T-matrix formulation, presented by Lin and Chew in Lin and Chew (1996). Unlike the methods considered so far in Sect. 14.4 that directly use the wave equation in continuous differential or integral form, the T-matrix formulation is based on the harmonic expansion of the acoustic pressure field. Consider the case of a harmonic acoustic wave incident on an object. The computational domain is divided into N homogeneous subscatterers distributed on a rectangular grid of pixel size h. The total acoustic field produced at some point $\mathbf{r}_p$ in space is given by

$$p(\mathbf{r}_p) = \psi^t(\mathbf{r}_p - \mathbf{r}_s) \cdot \bar{f}_s + \sum_{m=1}^{N} \psi^t(\mathbf{r}_p - \mathbf{r}_m) \cdot \bar{a}_m, \tag{14.66}$$

where $\mathbf{r}_s$ is the location of the source, $\mathbf{r}_m$ is the location of the m-th subscatterer, $\psi(\mathbf{r})$ is a vector whose elements are cylindrical harmonics, i.e.,

$$[\psi(\mathbf{r})]_l = H_l^{(1)}(k_0 r) e^{il\theta}, \tag{14.67}$$

and $\bar{f}_s$ and $\bar{a}_m$ are vectors containing the amplitudes of the cylindrical harmonic fields generated by the source and the m-th subscatterer, respectively.

The equation above can be rewritten using the j-th subscatterer as the spatial origin for all the cylindrical harmonics. Using the vector $\hat{\psi}(\mathbf{r})$ whose elements are defined as $\left[\hat{\psi}(\mathbf{r})\right]_k = J_k(k_0|\mathbf{r}|)e^{il\angle\mathbf{r}}$, Eq. (14.66) can be rewritten as

$$p(\mathbf{r}_p) = \psi^t(\mathbf{r}_p - \mathbf{r}_j) \cdot \bar{a}_j + \hat{\psi}^t(\mathbf{r}_p - \mathbf{r}_j) \cdot \left(\sum_{m \neq j} \bar{\alpha}_{jm} \cdot \bar{a}_m + \bar{e}_{js} \right) \tag{14.68}$$

where the elements of matrix α_{jm} and vector $\bar{e}_{js}$ can be obtained using the addition theorem of Bessel functions (Chew 1995) as detailed in Lin and Chew (1996).

If $h \ll \lambda$, the coefficient that relates the amplitude of the source waves $J_k(\mathbf{r})$ with the outgoing waves $H_k^{(1)}(\mathbf{r})$ in Eq. (14.68) can be approximated by the scattering coefficient $R_k(\kappa_j, \rho_j)$ by a sphere of radius $h/\sqrt{\pi}$, where κ_j and ρ_j are the compressibility and density of the j-th subscatterer, respectively. Further, under the same condition $h \ll \lambda$ the harmonics $l = 0, 1, -1$ have been reported to be sufficient to characterize the scattering process (Lin and Chew 1996). Consequently, and considering Eq. (14.68) at all subscatterer locations $\mathbf{r_j}, j = 1, 2, \cdots N$, the $N \times 1$ vectors of equivalent induced sources $\bar{a}_k^s$ whose elements are given by $\bar{a}_m$ satisfy the equation

$$\{\bar{I} - \mathcal{D}(\bar{R}) \cdot \bar{A}\} \cdot \bar{a}^s = \mathcal{D}(\bar{R}) \cdot \bar{e}^s \tag{14.69}$$

$$\bar{a}^s = \begin{bmatrix} \bar{a}^s_{l=0} \\ \bar{a}^s_{l=1} \\ \bar{a}^s_{l=-1} \end{bmatrix}, \bar{e}^s = \begin{bmatrix} \bar{e}^s_{k=0} \\ \bar{e}^s_{k=1} \\ \bar{e}^s_{k=-1} \end{bmatrix}, \mathcal{D}(\bar{R}) = \begin{bmatrix} \mathcal{D}(\bar{R}_{k=0}) & 0 & 0 \\ 0 & \mathcal{D}(\bar{R}_{k=1}) & 0 \\ 0 & 0 & \mathcal{D}(\bar{R}_{k=-1}) \end{bmatrix},$$

with $\bar{R}_k$ an $N \times 1$ vector whose elements are equal to $R_k(\kappa_j, \rho_j)$, $\bar{A}$ a $3N \times 3N$ matrix whose coefficients are taken from matrices $\bar{\alpha}_{jm}$, and $\bar{e}_k^s$ an $N \times 1$ vector whose elements taken from vectors $\bar{e}_{js}$. If the total field $\bar{e}^{ts}$ at the scatterer is defined such that $\bar{a}^s = \mathcal{D}(\bar{R}) \cdot \bar{e}^{ts}$, then from Eq. (14.69),

$$\bar{e}^{ts} = [\bar{I} - \bar{A} \cdot \mathcal{D}(\bar{R})]^{-1} \cdot \bar{e}^s. \tag{14.70}$$

Assuming that the receiver positions $\mathbf{r_r}$, $r = 1, 2, \cdots, N_r$ are held constant for all transmissions, the corresponding scattered field vector $\bar{p}_s^{sc}$ can be computed as

$$\bar{p}_s^{sc} = \bar{\psi} \cdot \bar{a}^s = \bar{\psi} \cdot \mathcal{D}(\bar{R}) \cdot \bar{e}^{ts} \tag{14.71}$$

$$\bar{\psi} = \left[\bar{\psi}_{l=0} \bar{\psi}_{l=1} \bar{\psi}_{l=-1}\right] \tag{14.72}$$

with $\bar{\psi}_l$ an $N_r \times N$ matrix whose rows can be calculated using Eq. (14.67) with $\mathbf{r} = \mathbf{r}_r - \mathbf{r}_i$, $i = 1, 2, \cdots, N$.

The matrix equations in Eqs. (14.70) and (14.71) are counterparts to the integral equations in Eqs. (14.37) and (14.38), and can be solved for $\bar{R}$ using Newton-type or gradient descend methods as described in Lin and Chew (1996a, b).

14.4.6.1 Convergence

The convergence of the T-matrix formulation has been studied by Lavarello and Oelze (Lavarello and Oelze 2009). It was found that sound speed images derived using the T-matrix formulation follow the same convergence rules that the DBIM does, i.e., sound speed imaging convergence is dependent upon the maximum phase shift induced by the scatterer on the incident field. Density imaging using the T-matrix approach diverges due to a different mechanism, namely the weak dependence of the scattering pattern on ρ for large ka values. When imaging circular cylinders of radius a, the convergence condition was heuristically approximated as $k_0 a < 1$.[8] Therefore, for practical biomedical imaging applications the condition for convergence in κ and ρ is likely to be more restrictive than that for convergence in c. This restriction was later found to be valid for more complex imaging targets exhibiting structures of different sizes, as shown in Fig. 14.7. Further studies showed that the convergence of the T-matrix formulation is also dependent on the acoustical properties of the imaging target, i.e., the actual values of sound speed and density (Lavarello and Oelze 2010).

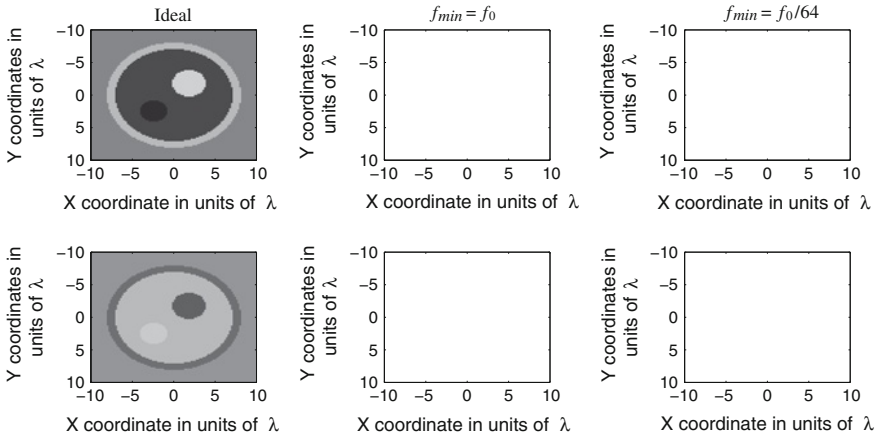

Fig. 14.7 Speed of sound (*top row*) and density (*bottom row*) images obtained using the multiple frequency T-matrix approach. First column: ideal profiles. Second and third columns: reconstructions using single frequency data and multiple frequency data with $f_{min} = f_0/64$, respectively. Even though the sound speed tomograms converged for both cases, multiple frequency data was needed to obtain a convergent density tomogram. Adapted from Lavarello and Oelze (2010)

[8] Like in the case of sound speed imaging with DBIM, frequency hopping can be used to improve the spatial resolution of density tomograms constructed with the T-matrix formulation.

14.4.7 Results

The complexity of both algorithmic implementations and required experimental setup has prevented widespread implementations of full wave inversion techniques. However, experimental validation of some of these methods using acoustic waves have been reported. An example is the laboratory system at the University of Rochester (Waag and Fedewa 2006), which consists of 2048 elements operating at 2.5 MHz with 67 % −6-dB bandwidth and distributed in a 150 mm diameter ring. Using this ring system, reconstructions of large scale phantoms using eigenfunction methods have been performed (Lin et al. 2000). Another notable system is the scanner by Techniscan Inc. (Johnson et al. 1999), which consists of linear arrays facing each other operating at frequencies up to 2.5 MHz. Mechanical rotation is used in order to obtain full angular coverage on transmission. Using this system, Techniscan Inc. researchers have successfully implemented inverse scattering methods based on Newton-type and gradient descent approaches and obtained breast images in vivo (Johnson et al. 2007; Wiskin et al. 2012). These encouraging results suggest full wave inversion methods have reached a level of maturity that allows them to be explored for clinical applications.

14.5 Numerical Forward Scattering Solutions

Full-wave inversion techniques such as the alternating variables method and the distorted Born iterative method require repeated solutions of the integral equation of scattering (14.17). For practical application of full-wave inverse scattering methods, efficient methods should be employed to solve the acoustic scattering problem with minimal computational effort. Among a wide variety of techniques developed to address these issues, fast Fourier convolution methods (Johnson et al. 1984; Borup and Ghandi 1985; Cui and Chew 1999; Xu and Liu 2002) and the fast multipole method (FMM) (Greengard and Rokhlin 1987; Rokhlin 1990; Chew et al. 2001; Michielssen and Jin 2008) are popular choices. These methods are here presented because they provide a complete solution to the wave equation and because they illustrate a number of the efficiency issues present in forward and inverse scattering problems. Simplified methods that trade accuracy for efficiency by solving a restricted version of the scattering problem may offer greatly improved performance and still provide sufficient accuracy for desired applications.

A generalized representation of the method-of-moments formulation of the wave scattering equation takes the form (Harrington 1993)

$$[A - G]f = f^i, \tag{14.73}$$

in which the $N \times N$ matrices A and G are given by

$$A_{kj} = \int_{\Omega} d\mathbf{r}\, t_k(\mathbf{r})\chi_j(\mathbf{r}), \tag{14.74a}$$

$$G_{kj} = \int_{\Omega} d\mathbf{r}\, t_k(\mathbf{r}) \int_{\Omega} d\mathbf{r}'\, G_0(\mathbf{r}, \mathbf{r}')O(\mathbf{r}')\chi_j(\mathbf{r}') \tag{14.74b}$$

for a Green's function G_0, a domain Ω that contains the support of a scattering contrast profile O, a basis function χ_j and a testing function t_k. The N-element vectors f and f^i are discrete representations of the total and incident fields, respectively, such that

$$f(\mathbf{r}) = \sum_{j=0}^{N-1} f_j \chi_j(\mathbf{r}), \tag{14.75a}$$

$$f_k^i = \int_{\Omega} d\mathbf{r}\, t_k(\mathbf{r}) f^i(\mathbf{r}). \tag{14.75b}$$

Using an iterative method such as GMRES (Saad and Schultz 1986) or BiCG-STAB (Van der Vorst 1992), the inverse of the matrix $A - G$ does not need to be directly computed. Instead, the solution is obtained through repeated products of $A - G$ with a succession of test vectors. Because the basis and testing functions are often localized, the matrix A tends to be sparse and, therefore, products of the form Af are inherently efficiently computed. Consequently, fast Fourier convolution methods and the FMM are each concerned with efficiently representing the matrix product Gf.

14.5.1 Fast Fourier Convolution Methods

Methods that employ fast Fourier convolution of the Green's function require that the basis functions χ_j and the testing functions t_k in a method-of-moments formulation (14.73) have supports that are positioned at regular intervals throughout the domain. Most commonly, a three-dimensional scattering domain Ω is subdivided into a collection $\{c_j : 0 \leq j < N\}$ of N disjoint cubic cells coincident with an $M_x \times M_y \times M_z = N$ grid. Each cell c_j has a volume Δ and is associated with a constant contrast value O_j and a constant field value f_j. Hence, the basis function χ_j is the characteristic function, or pulse basis function, associated with cell c_j. In this case, the contrast function O is separable from the Green's matrix G in Eq. (14.73):

$$f^s = Gf = G_s O f, \tag{14.76}$$

where O is interpreted as a diagonal matrix with elements O_{jj} that correspond to samples O_j of the contrast for cell c_j.

Let c_i represent a target cell that has an index (l, m, n) within the $M_x \times M_y \times M_z$ grid, while a source cell c_j has an associated grid index (t, u, v). The scattering contribution to the matrix-vector product (14.76) at cell c_i may be expressed as

$$f_i^s = \sum_{j=0}^{N-1} G_{s,ij} O_j f_j = \sum_{t=0}^{M_x-1} \sum_{u=0}^{M_y-1} \sum_{v=0}^{M_z-1} G(l-t, m-u, n-v) O_{tuv} f_{tuv}, \tag{14.77}$$

where $O_{tuv} f_{tuv} = O_j f_j$ for the global index j corresponding to the local grid index (t, u, v) and the Green's function

$$G(l-t, m-u, n-v) = \int_\Omega d\mathbf{r}\, \chi_0(\mathbf{r}) \int_\Omega d\mathbf{r}'\, G_0(\mathbf{r}, \mathbf{r}' + \Delta\mathbf{r}) \chi_0(\mathbf{r}). \tag{14.78}$$

Translational invariance and the equivalence of all cells c_i allows the characteristic functions χ_i and χ_j in the definition of the Green's matrix element $G_{s,ij}$ to be replaced with an arbitrary characteristic function such as χ_0. Hence, elements of the Green's function are functions only of the separation of two cells, rather than their absolute positions. The offset in Eq. (14.78) is given by

$$\Delta\mathbf{r} = [(l-t)\Delta x, (m-u)\Delta y, (n-v)\Delta z], \tag{14.79}$$

where each scattering cell has x, y, and z lengths Δx, Δy, and Δz, respectively. Since the grid is cubic, $\Delta x = \Delta y = \Delta z = \sqrt[3]{\Delta}$.

The three-dimensional convolution (14.78) can be evaluated in the Fourier domain if G satisfies the cyclic properties

$$G(-t, u, v) = G(M_x - t, u, v), \tag{14.80a}$$

$$G(t, -u, v) = G(t, M_y - u, v), \tag{14.80b}$$

$$G(t, u, -v) = G(t, u, M_z - v). \tag{14.80c}$$

To satisfy these criteria, the pairwise Green's function G defined on the local $M_x \times M_y \times M_z$ grid must be replaced with a modified Green's function G' defined on an expanded $2M_x \times 2M_y \times 2M_z$ grid. The modified Green's function

$$G'(t, u, v) = G(t', u', v'), \tag{14.81}$$

in which the mappings

$$t' = \begin{cases} t & \text{if } 0 \le t < M_x, \\ t - 2M_x & \text{if } M_x \le t < 2M_x, \end{cases} \tag{14.82a}$$

$$u' = \begin{cases} u & \text{if } 0 \le u < M_y, \\ u - 2M_y & \text{if } M_y \le u < 2M_y, \end{cases} \tag{14.82b}$$

$$v' = \begin{cases} v & \text{if } 0 \le v < M_z, \\ v - 2M_z & \text{if } M_y \le v < 2M_z, \end{cases} \tag{14.82c}$$

relate indices (t', u', v') on the original $M_x \times M_y \times M_z$ grid to indices (t, u, v) on the expanded $2M_x \times 2M_y \times 2M_z$ grid. The product of the contrast and pseudo-pressure must similarly be expressed on an expanded grid as

$$O'_{tuv} f'_{tuv} = \begin{cases} O_{tuv} f_{tuv}, & \text{if } 0 \le t < M_x, 0 \le u < M_y, \text{ and } 0 \le v < M_z; \\ 0 & \text{otherwise.} \end{cases} \tag{14.83}$$

The expressions (14.81) and (14.83) allow contributions to the field observed at c_i (14.77) to be represented as a Fourier-domain multiplication:

$$f_{s,i} = \mathbb{F}^{-1}\left[\mathbb{F}\left(O'_{tuv} f'_{tuv}\right) \cdot \mathbb{F}G'(t, u, v)\right]_{lmn}, \tag{14.84}$$

where $\mathbb{F}$ represents the discrete Fourier transform and the index triple (l, m, n) corresponds to a linearized index i. Thus, rather than requiring $O(N^2)$ computer time storage to evaluate products of the Green's matrix with some vector f, fast Fourier convolution reduces the computational cost to that of the fast Fourier transform (FFT): $O(N \log N)$. Likewise, rather than computing the Green's function for all pairwise interactions on the computational grid, which would require $O(N^2)$ memory storage, the convolutional Green's function G' is defined only once for each point on the extended $2M_x \times 2M_y \times 2M_z$ grid, which requires $O(N)$ storage.

14.5.2 The Fast Multipole Method

Like fast Fourier convolution methods, the FMM provides a mechanism for evaluating the product of a discrete Green's matrix and an arbitrary vector with computational and storage complexities better than the $O(N^2)$ complexities of a direct matrix-vector multiplication and without requiring explicit computation of the full Green's matrix G. This facilitates large-scale solutions even on modest computer hardware. Although a hierarchical implementation provides optimum performance, a single-level FMM highlights the fundamentals of the technique.

The FMM is derived by replacing the Green's function represented in the method of moments with a truncated expansion derived from Gegenbauer's addition theorem (Coifman et al. 1993):

$$\frac{e^{ik|\mathbf{D}+\mathbf{d}|}}{|\mathbf{D}+\mathbf{d}|} \approx \frac{ik}{4\pi}\int_{S_0} d\hat{s}\, e^{i\mathbf{k}\cdot\mathbf{d}}\tilde{\alpha}(k,\mathbf{D},\hat{s}), \tag{14.85}$$

in which $|\mathbf{d}|<|\mathbf{D}|$ and the spectral translator

$$\tilde{\alpha}(k,\mathbf{D},\hat{s}) = \sum_{l=0}^{L} i^l(2l+1)h_l(kD)P_l(\hat{D}\cdot\hat{s}). \tag{14.86}$$

The substitution in Eq. (14.85) decomposes the Green's function into local shifts $\mathbf{d}$ and a long-distance translation $\mathbf{D}$.

The number of terms in the translator sum (14.86) is determined by the excess bandwidth formula bandwidth formula (Koc et al. 1999; Song and Chew 2001; Chew et al. 2001)

$$L \approx k|\mathbf{d}| + 1.8d_0^{2/3}(k|\mathbf{d}|)^{1/3}, \tag{14.87}$$

in which $d_0 = -\log\epsilon$ is the number of digits of accuracy for a desired error ϵ. The formula (14.87) results in an approximate addition theorem (14.85) that exhibits the desired accuracy provided that the translation distance $k|\mathbf{D}| > L$. If this constraint cannot be satisfied, more sophisticated methods, such as that described in Hastriter et al. (2003), are required to select the truncation point. The excess bandwidth formula (14.87) balances the need to incorporate sufficiently many terms to accurately approximate an unbounded sum in the underlying addition theorem with the tendency for Hankel functions to become unbounded with increasing order, which can result in inaccurate finite-precision evaluation of Eq. (14.86).

The FMM is made efficient by subdividing the scattering domain into some number of distinct interaction groups that are each associated with a collection of unique basis and testing functions. Define a source group of basis functions $J = \{\chi_j : 0 \le j < M\}$ with center $\mathbf{r}_J$ and an observation group of testing functions $K = \{t_k : 0 \le k < M'\}$ with center $\mathbf{r}_K$, such that K is sufficiently distant from J for an appropriate definition of "sufficiently distant". Typically, two groups are deemed sufficiently distant if the smallest spheres that contain the groups do not overlap; the minimum acceptable distance may be increased to improve accuracy at the expense of efficiency. The indices k and j refer to a local enumeration of the functions within groups K and J, respectively. For each group, a one-to-one mapping exists such that $j \mapsto j'$ and $k \mapsto k'$, where the primed indices j' and k' are used to refer to the respective global enumeration for basis and testing functions.

The contribution to the total Green's matrix product in Eq. (14.73) for an element $t_k \in K$ due to the source group J takes the form

$$[Gf]_{k',J} = \sum_{j=0}^{M-1} G_{k'j'} f_{j'} \approx \frac{ik}{(4\pi)^2} \int_{S_0} d\hat{s}\, R_k(\mathbf{r}_K, \hat{s}) \tilde{\alpha}(k, \mathbf{r}_{KJ}, \hat{s}) \sum_{j=0}^{M-1} f_{j'} F_j(\mathbf{r}_J, \hat{s}) \\ = \frac{ik}{(4\pi)^2} \int_{S_0} d\hat{s}\, R_k(\mathbf{r}_K, \hat{s}) \tilde{\alpha}(k, \mathbf{r}_{KJ}, \hat{s}) F_J(\hat{s}), \tag{14.88}$$

where f is an arbitrary discrete function being multiplied by the Green's matrix and the functions F_j and R_k are called, respectively, the radiation and receiving patterns defined by

$$F_j(\mathbf{r}_J, \hat{s}) = \int_\Omega d\mathbf{r}\, O(\mathbf{r}) \chi_j(\mathbf{r}) e^{ik\hat{s}\cdot(\mathbf{r}_J - \mathbf{r})}, \tag{14.89a}$$

$$R_k(\mathbf{r}_K, \hat{s}) = \int_\Omega d\mathbf{r}\, t_k(\mathbf{r}) e^{ik\hat{s}\cdot(\mathbf{r} - \mathbf{r}_K)}. \tag{14.89b}$$

The radiation patterns of all basis functions of the group J have been aggregated to yield the group radiation pattern

$$F_J(\hat{s}) = \sum_{j=0}^{M-1} f_{j'} F_j(\mathbf{r}_J, \hat{s}) = \int_\Omega d\mathbf{r}\, O(\mathbf{r}) \left[\sum_{j=0}^{M-1} f_{j'} \chi_j(\mathbf{r}) \right] e^{ik\hat{s}\cdot(\mathbf{r}_J - \mathbf{r})}. \tag{14.90}$$

The radiation pattern in Eq. (14.90) is a Fourier transform, restricted to the unit sphere, of the product of the contrast function O with the discrete approximation of f within J, and is here called the far-field transform of J.

Accumulation of radiation patterns using the far-field transform in Eq. (14.90) prior to translation is one key aspect of the FMM. This allows the fields radiated by all elements within one group to be translated *en masse*, avoiding redundant calculations in Green's function expansions in Eq. (14.85). Further redundancy may be eliminated by considering the aggregate interaction of all source groups $J \in \text{far}\, K$, in which $\text{far}\, K$ denotes the collection of all groups that are sufficiently distant from the observation group K, The total far-field contribution to the Green's matrix product for an element $t_k \in K$ is written

$$[Gf]_{k',\text{far}\,K} \approx \frac{ik}{(4\pi)^2} \sum_{J \in \text{far}\,K} \int_{S_0} d\hat{s}\, R_k(\mathbf{r}_K, \hat{s}) \tilde{\alpha}(k, \mathbf{r}_{KJ}, \hat{s}) F_J(\hat{s}) \\ = \frac{ik}{(4\pi)^2} \int_{S_0} d\hat{s}\, R_k(\mathbf{r}_K, \hat{s}) \sum_{J \in \text{far}\,K} \tilde{\alpha}(k, \mathbf{r}_{KJ}, \hat{s}) F_J(\hat{s}). \tag{14.91}$$

Hence, radiation patterns from all source groups $J \in \text{far}\, K$ may be successively translated to the observer group K and accumulated before being distributed *en masse* to the testing function t_k using the receiving pattern R_k. Still greater efficiency is obtained when the summation in Eq. (14.91) is reused for calculations $[Gf]_{k',\text{far}\,K}$ for all $t_k \in K$. Because the sum depends only on the center $\mathbf{r}_K$ and not on the individual testing functions t_k, radiation patterns for all source groups $J \in \text{far}\, K$

need only be translated to K once; this translated field, which is expanded in terms of incoming plane waves, may be successively distributed to every testing function in K by simply changing the receiving pattern R_k.

The FMM fails to accurately compute interactions between an observation group K and source groups $J \notin \text{far}\, K$. Entries in the Green's matrix corresponding to these near-field interactions must be directly computed using the method of moments. Thus, the total action of the Green's matrix product on an element $t_k \in K$ may be written

$$[Gf]_{k'} = [Gf]_{k',\text{far}\, K} + \sum_{J \notin \text{far}\, K} \sum_{j=0}^{M_J - 1} G_{k',j'} f_{j'}, \tag{14.92}$$

where M_J is the number of basis functions in source group J and, as before, the mapping $(\cdot)'$ converts a local index into a global index.

The FMM can be improved by recursively subdividing the scattering domain into a hierarchy of cubic scattering groups. The hierarchical implementation facilitates multiplication of a vector by an $N \times N$ Green's matrix in $O(N)$ time and with $O(N)$ storage (Chew et al. 2001). A (finer) level-l hierarchy is obtained by dividing each group of the (coarser) level-$(l-1)$ hierarchy into eight "child" subgroups, halving the length of the cube edges along each dimension. The level-0 group contains the entire scattering domain; thus, the l-th level of the hierarchy contains 2^l cubic groups.

In the hierarchical FMM, diagonal translators are used to carry fields between groups at the coarsest possible level in the hierarchy. Near-field interactions, being unsuitable for diagonal translations, are deferred to the next finer level, where a portion of the interactions now exist between children of neighboring groups that are, in the finer level, now suitable for diagonal translation of a lower bandwidth. This is possible because, according to the excess bandwidth formula (14.87), the approximate bandwidth of diagonal translators, and hence the minimum translation distance, at any level is proportional to the size of the groups, relative to the acousti wavelength, in that level. The deferment of any remaining near-field interactions continues recursively until the finest level of the hierarchy is reached. At this level, all remaining near-field interactions are directly computed using the summation in Eq. (14.92).

Key to the efficiency of this technique are interpolation and filtering schemes that alter the sampling rate of outgoing radiation patterns and incoming group fields. Because the possible bandwidth of outgoing and incoming wave expansions depends on the size of the FMM group, these expansions should be sampled at the minimum rate necessary for accurate representation. Radiation patterns for each group at a particular level may be recursively aggregated from interpolated and shifted forms of the radiation patterns of the group's children. Likewise, incoming waves may be recursively distributed among the children of each group at a particular level by shifting and then filtering the waves to reduce their sampling rates. A schematic representation of these procedures is provided in Fig. 14.8.

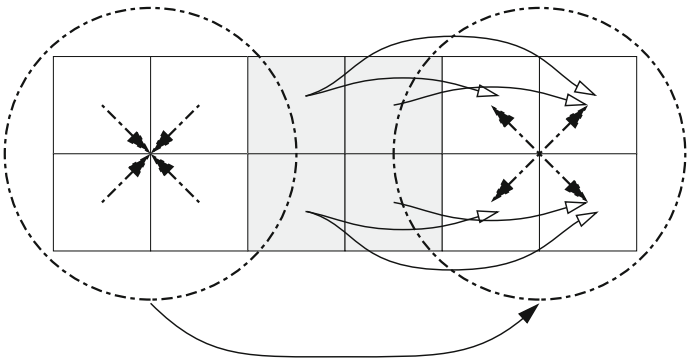

Fig. 14.8 Graphical depiction of aggregation and distribution (*dashed arrows*) and diagonal translations (*curved arrows*) in a two-level, hierarchical FMM

Radiation patterns of source groups at the finer level are aggregated, following the converging, dashed arrows at the left, to form the radiation pattern of the circled source group at the coarser level. The resulting radiation pattern is translated via the curved, solid arrow to an observer group at the right. The incoming plane-wave envelope is distributed via the diverging, dashed arrows to constituent observer groups at the finer level. At the finer level, interactions at each observer group that were not represented at the coarser level are carried via diagonal translations along the curved, hollow arrows.

14.5.2.1 Optimizations for Inverse Scattering Applications

Because the contrast profile is unknown during inverse scattering reconstructions, the use of basis and testing functions specialized to the shape of the scatterer is unwarranted. It is therefore convenient and computationally beneficial to employ the same discrete representation used in fast Fourier convolution methods; namely, that pulse basis functions χ_j and testing functions $t_k = \chi_k$ are defined on a collection of N disjoint cubic cells regularly spaced to cover the scattering domain Ω. While Eq. (14.91) still approximates the elements of the Green's matrix in this arrangement, the radiation pattern (14.89a) of a basis function $\chi_j \in J$ for some group J can be altered to remove its dependence on the contrast function, leaving

$$F_j(\mathbf{r}_J, \hat{s}) = R_j^*(\mathbf{r}_J, \hat{s}) = \int_{c_{j'}} d\mathbf{r}\, e^{ik\hat{s}\cdot(\mathbf{r}_J - \mathbf{r})}, \tag{14.93}$$

where j now refers to a local index of the basis function within group J and j' is the corresponding global index. Thus, only one of the radiation or receiving patterns for each group must be computed. The group far-field transform (14.90) becomes

$$F_J(\hat{s}) = \sum_{j=0}^{M-1} \left[f_{j'} O_{j'} \right] F_j(\mathbf{r}_J, \hat{s}), \tag{14.94}$$

in which the contrast O now modifies the source distribution f within the group rather than the radiation patterns of its constituent basis functions. The total far-field contribution to the Green's matrix product is still governed by Eq. (14.91) with the redefined group radiation patterns (14.94). The integration in Eq. (14.91), generalized as

$$f_k = \int_{S_0} d\hat{s}\, R_k(\mathbf{r}_K, \hat{s}) \gamma_K(\hat{s}), \tag{14.95}$$

in which γ_K is an arbitrary function that describes the complex amplitude of plane waves converging on $\mathbf{r}_K$ from directions $\hat{s}$, is the adjoint of the far-field transform when the far-field transform is viewed as an operator acting on the product $\tilde{f} = Of$. Thus, a discrete representation of the far-field transform operator (14.94) is sufficient to represent both the forward and adjoint transforms.

Even greater savings in memory and computation are realized when the grid of scattering cells aligns with the grid of FMM groups at the finest level. In that case, for two groups $J = \{\chi_j : 0 \le j < M\}$ and $K = \{\chi_k : 0 \le k < M\}$ with respective centers $\mathbf{r}_J$ and $\mathbf{r}_K$, $j = k \Rightarrow \mathbf{r}_j - \mathbf{r}_J = \mathbf{r}_k - \mathbf{r}_K$, where $\mathbf{r}_j$ and $\mathbf{r}_k$ represent, in turn, the centers of the globally indexed cells $c_{j'}$ and $c_{k'}$. Hence, the radiation and receiving patterns in Eq. (14.93) are independent of the group center $\mathbf{r}_J$ and a single representation of the group far-field transform (14.94) applies to every FMM group.

The use of gridded basis and testing functions means that near-field evaluations among finest-level groups that each contain $O(M)$ elements can be computed in $O(M \log M)$ time, with $O(M)$ storage, using an FFT-accelerated convolution (Hesford and Waag 2010) that extends the approach described in Sect. 14.5.1 to accommodate pairwise Green's functions that depend on the separation between source and observer groups in the FMM hierarchy. If the total number of scattering elements is N, then the number of finest-level FMM groups will be $O(N/M)$. The total cost for the evaluation of neighboring interactions using FFT convolution is therefore $O(N \log M)$, compared to the $O(NM)$ total cost for dense-matrix multiplication of neighboring interaction matrices. Thus, for a fixed problem size N, FFT convolution dramatically reduces the dependence of calculations of neighboring interactions on the group size M.

Another limiting factor in the size of the finest-level groups of a hierarchical FMM is the cost of evaluating far-field transforms and of distributing incoming plane waves to testing functions in each group. In a cubic, gridded arrangement of scatterers, the diameter of each group is $d = O(M^{1/3})$. Because the excess bandwidth formula (14.87) is used to predict the bandwidth L of the radiation and receiving patterns for a group, and $L = O(d)$, the total number of samples of the patterns is $O(M^{2/3})$. Thus, the far-field transform (14.94) may be represented by a

matrix $F \in \mathbb{C}^{m\times n}$, where $m = O(M^{2/3})$ and $n = O(M)$. Similarly, the adjoint far-field transform (14.95) may be represented as a matrix $R = F^\dagger \in \mathbb{C}^{n\times m}$, where $(\cdot)^\dagger$ represents the matrix adjoint.

The band-limited nature of the radiation and receiving patterns suggests that an accurate, but approximate, reduced-rank decomposition of the far-field transform may be obtained in the form

$$F \approx UV^\dagger, \tag{14.96}$$

with $U \in \mathbb{C}^{m\times k}$, $V \in \mathbb{C}^{n\times k}$ and the rank $k = O(L) = O(M^{1/3})$. This approximation reduces the cost of applying a far-field transform or its adjoint from $O(M^{5/3})$ to $O(M^{4/3})$. The adaptive cross approximation (ACA) (Bebendorf 2000; Zhao et al. 2005; Shaeffer 2008) provides a method for computing an approximation of the form in Eq. (14.96). The effective use of adaptive-cross approximated far-field transforms, together with recompression based on an efficient singular value decomposition, was explored in Hesford and Waag (2011) and shown to significantly reduce the computational cost of the FMM. Conceptually, the ACA works by alternatively constructing columns to populate the column matrix U and the row matrix V. Columns for U and V are selected as the most significant of the remaining columns and rows, respectively, of the matrix F to be approximated; for this purpose, "most significant" means the column or row of F that contributes the largest element of the column of U or V that is currently being analyzed, neglecting elements contributed by previously analyzed columns or rows.

14.6 Parallel Computing

Modern computer systems are inherently parallel. Low-cost desktop systems often contain at least two CPU cores that share access to a common memory store, while supercomputers are most commonly composed of many interconnected nodes that each contain distinct memory stores and multiple CPUs. More recently, graphics processing units (GPUs) have been adapted to general-purpose computations that exploit low memory latency, rapid context switching and massive parallel processing abilities to provide excellent computational power. Algorithms that compute large-scale forward and inverse scattering solutions should leverage such parallel facilities to be most effective.

Each parallel computing methodology has distinct advantages and drawbacks. Shared-memory algorithms, for example, provide multiple computing threads access to all data within a shared memory store. While such algorithms do not require communication between the threads, threads must be synchronized to prevent conflicting attempts to modify the same data. Distributed-memory systems provide each task with its own locally relevant data that eliminates the need for synchronization. However, operations that require the cooperation of more than one task must use communication (typically over a network) of data. Both

synchronization and communication result in serial bottlenecks that can limit the effectiveness of massive parallelization. Furthermore, distributed-memory communication often exhibits relatively high latency. To some extent, latency can be concealed by initiating non-blocking communication that can be completed while each task processes its local data.

General-purpose GPU computing takes a different approach than those of classical shared- or distributed-memory parallel systems. A typical GPU may have hundreds of lightweight, individual processing units capable of manipulating floating-point numbers, but each performs optimally on independent data accessed through a graphics memory store. Interactions with system memory must be performed over a comparatively slow bus, and the graphics memory, while fast, can have comparatively high latency with respect to the floating-point performance of the GPU. To conceal this latency, GPUs offer fast context switches, and dispatch hundreds of independent tasks that can be quickly interchanged while they await memory accesses. When multiple tasks must collaborate on blocks of data, special care must be taken to avoid redundant memory access or performance can suffer greatly. GPU computing has been reported to significantly speed-up the execution of full wave inverse scattering methods (Garland et al. 2008; Roy et al. 2010; Wiskin et al. 2010).

The choice of algorithm and the selection of parallel hardware are closely linked. The independence of the multiple forward solutions required for each iteration of the DBIM makes for an ideal parallelization scheme, without the need for substantial communication or synchronization, on either shared- or distributed-memory systems (Hesford and Chew 2006). In contrast, the fast Fourier transforms in the FFT-based methods described above are not ideal in distributed-memory systems, since all elements in the FFT interact. Alternative forward solvers like the FMM, with appropriate consideration, can be efficiently implemented on distributed-memory systems without requiring communication among all tasks.

In practice, modern algorithms often require hybrid parallelization to take advantage of supercomputers with multiple, distributed-memory nodes that each house several shared-memory CPUs. For example, a distributed-memory FMM that subdivides the scattering object among multiple nodes can be readily adapted to shared-memory nodes by assigning to each CPU a portion of the scattering object assigned to that node. With careful ordering of computations, it is possible to update representations of the field confined to the local portion of the object in parallel without the need for synchronization. Figure 14.9 provides an illustration of the benefit of multiple shared-memory threads and distributed-memory processes when solving an acoustic scattering problem involving approximately 440 million unknowns on a supercomputer. The reported parallel speed-up is the ratio of some reference solution time to the time required to compute a solution with the number of parallel tasks (threads or processes) scaled by a task multiplier. For the distributed-memory experiment, a minimum of 16 supercomputer nodes were required to store the problem in memory; therefore, the reference solution (with a unity task multiplier) employed 16 distributed processes. In all experimental configurations, each distributed process employed six shared-memory

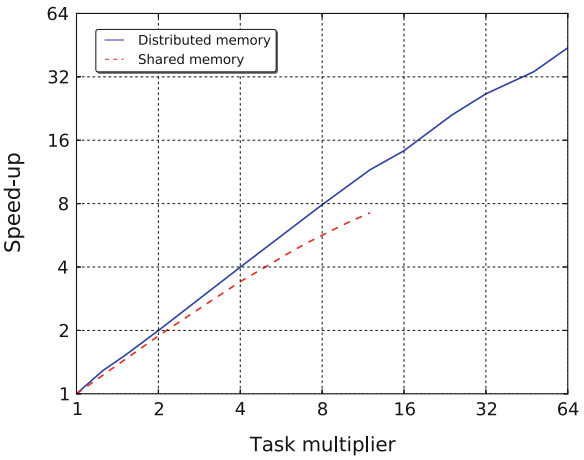

Fig. 14.9 Shared- and distributed-memory parallel speed-up of an FMM solution of an acoustic scattering problem involving approximately 440 million unknowns

threads. In the shared-memory experiment, a total of 64 distributed processes were used for all experimental configurations; the unity task multiplier corresponds to one shared-memory thread per process.

14.7 Closing Remarks

Acoustic tomography has reached a high level of maturity over the past four decades. A wide variety of reconstruction algorithms exist that represent different trade-offs between accuracy and computational cost. Several of these algorithms have been described in this chapter, but the list should not be considered to be complete.

Over the years, several engineering aspects of acoustic tomography have been successfully implemented. Even with the use of full wave inversion methods, the reconstruction of computational regions with hundreds of thousands to millions of unknowns is now possible (Lavarello and Oelze 2008; Haynes and Moghaddam 2010; Hesford and Chew 2010; Wiskin et al. 2012). However, certain implementation aspects still require additional developments. The vast majority of research in acoustic tomography involves the use of synthetic measurements, whereas system calibration for measuring phase-sensitive data is a non-trivial problem (Andre et al. 1997; Johnson et al. 1997; Waag and Fedewa 2006; Parhizkar et al. 2011) which may impair imaging of sensitive parameters such as attenuation coefficients and density. Although 3D imaging has been successfully demonstrated, proper handling of boundary conditions needs to be addressed for

certain applications such as breast imaging where inspection in the axillary region and near the chest wall may be required.

Perhaps the biggest challenge remaining for ultrasonic tomography is the validation of its usefulness in clinical practice. The significance of imaging sound speed, attenuation, or mass density for applications such as breast cancer detection has not been properly addressed yet. Specifically, the contrast associated with diseased tissue in terms of sound speed, density, and attenuation has not been explicitly established and conflicting reports in the literature exist. Therefore, the next chapter will provide a comprehensive discussion on the lessons learned from experimental acoustic tomography studies.

References

Green PS, Schaefer LF, Jones ED, Suarez JR (1974) A new high-performance ultrasonic camera system, in Acoustical Holography, 5th edn. Wiley, New York, pp 493–504

Marich KW, Green PS, Suarez JR, Zatz LM, Macovski A (March 1975) Real-time imaging with a new ultrasonic camera: Part I, in vitro experimental studies on transmission imaging of biological structures. J Clin Ultrasound 3(1):5–16

Heyser R, Le Croissette D (1973) Transmission ultrasonography. In: Proceedings of the IEEE ultrasonics, symposium, pp 7–9

Heyser RC, Croissette DHL (1974) A new ultrasonic imaging system using time delay spectrometry. Ultrasound Med Biol 1(2):119–131

Hounsfield GN (December 1973) Computerized transverse axial scanning (tomography): I. Description of system. Br J Radiol 46(552):1016–1022

Kuhl DE, Edwards RQ (April 1963) Image separation radioisotope scanning. Radiology 80(4):653–662

Phelps ME, Hoffman EJ, Mullani NA, Higgins CS, Ter Pogossian MM (February 1976) Design considerations for a positron emission transaxial tomogram (PETT III). IEEE Trans Nucl Sci 23(1):516–522

Damadian R (March 1971) Tumor detection by nuclear magnetic resonance. Science 171(3976):1151–1153

Lauterbur PC (1974) Magnetic resonance zeugmatography. Pure Appl Chem 40(1):149157

Pierce AD (1989) Acoustics: an introduction to its physical principles and applications. Acoustical Society of America, Woodbury

Carson PL, Oughton TV, Hendee WR, Ahuja AS (1977) Imaging soft tissue through bone with ultrasound transmission tomography by reconstruction. Med Phys 4(4):302–309

Dines KA, Fry FJ, Patrick JT, Gilmor RL (October 1981) Computerized ultrasound tomography of the human head: experimental results. Ultrason Imaging 3(4):342–351

Goss SA, Johnston RL, Dunn F (1978) Comprehensive compilation of empirical ultrasonic properties of mammalian tissues. J Acoust Soc Am 64(2):423–457

Goss SA, Johnston RL, Dunn F (1980) Compilation of empirical ultrasonic properties of mammalian tissues II. J Acoust Soc Am 68(1):93–108

Greenleaf J, Johnson S, Samayoa W, Duck F (1975) Algebraic reconstruction of spatial distributions of acoustic velocities in tissue from their time-of-flight profiles in Acoustical Holography vol 6. pp 71–90

Bracewell RN (1956) Strip integration in radio astronomy. Aust J Phys 9(2):198–217

Bracewell RN, Riddle AC (1967) Inversion of fan-beam scans in radio astronomy. Astrophysl J 150(2):427–434

Ramachandran GN, Lakshminarayanan AV (1971) Three-dimensional reconstructions from radiographs and electron micrographs: application of convolutions instead of fourier transforms. Proc Nat Acad Scie USA 68(9):2236–2240

Shepp LA, Logan BF (1971) The fourier reconstruction of a head section. IEEE Trans Nucl Sci 68(9):2236–2240

Andersen AH, Kak AC (1984) Simultaneous algebraic reconstruction technique (SART): a superior implementation of the ART algorithm. Ultrason Imaging 6(1):81–94

Glover GH (1978) Ultrasonic fan beam scanner for computerized time-of-flight tomography. U.S. Patent 4,075,883

Greenleaf J, Johnson S, Lee S, Herman G, Wood E (1974) Algebraic reconstruction of spatial distributions of acoustic absorption within tissue from their two-dimensional acoustic projections, in Acoustical Holography vol 5. pp 591–603

Dines KA, Kak AC (1979) Ultrasonic attenuation tomography of soft tissues. Ultrason Imaging 1(1):16–33

Klepper JR, Brandenburger GH, Mimbs JW, Sobel BE, Miller JG (1981) Application of phase-insensitive detection and frequency-dependent measurements to computed ultrasonic attenuation tomography. IEEE Trans Biomed Eng 28(2):186–201

Greenleaf JF, Johnson SA, Lent AH (1978) Measurement of spatial distribution of refractive index in tissues by ultrasonic computer assisted tomography. Ultrasound Med Biol 3(4):327–339

Jakowatz CV, Kak AC (1976) Computerized tomographic imaging using X-rays and ultrasound. School of Electrical Engineering, Purdue University, Tech Rep TR-EE 76–26

Johnson SA, Greenleaf JF, Samayoa WA, Duck FA, Sjostrand J (1975) Reconstruction of three-dimensional velocity fields and other parameters by acoustic ray tracing. In: Proceedings of the IEEE Ultrasonics, Symposium, pp 46–51

Andersen AH, Kak AC (1982) Digital ray tracing in two-dimensional refractive fields. J Acoust Soc Am 34(10):1562–1582

Andersen AH (1986) A top-down philosophy for accurate numerical ray tracing. J Acoust Soc Am 80(2):656–660

Norton SJ (1987) Computing ray trajectories between two points: a solution to the ray-linking problem. J Opt Soc Am 4(10):1919–1922

Julian BR, Gubbins D (1977) Three-dimensional seismic ray tracing. J Geophys 43(1–2):95–113

Schomberg H (1978) An improved approach to reconstructive ultrasound tomography. J Phys D: Appl Phys 11(15):L181–L185

Lytle RJ, Dines KA (1980) Iterative ray tracing between boreholes for underground image reconstruction. IEEE Trans Geosci Remote Sens 18(3):234–240

Andersen AH (1987) Ray linking for computed tomography by rebinning of projection data. J Acoustl Soc Am 81(4):1190–1192

Moser TJ (1991) Shortest path calculation of seismic rays. Geophysics 56(1):59–67

Klimes L, Kvasnicka M (1994) 3-D network ray tracing. Geophys J Intl 116(3):726–738

Song L, Zhang S (1998) Stabilizing the iterative solution to ultrasonic transmission tomography. IEEE Trans Ultrason, Ferroelectr, Freq Control 45(4):1117–1120

Li S, Jackowski M, Dione DP, Varslot T, Staib LH, Mueller K (2010) Refraction corrected transmission ultrasound computed tomography for application in breast imaging. Med Phys 37(3):201–233

Denis F, Basset O, Gimenez G (1995) Ultrasonic transmission tomography in refracting media: reduction of refraction artifacts by curved-ray techniques. IEEE Trans Med Imaging 14(1):173–188

Norton SJ, Linzer M (1982) Correcting for ray refraction in velocity and attenuation tomography:a perturbation approach. Ultrason Imaging 4(3):201–233

Farrell EJ (1981) Tomographic imaging of attenuation with simulation correction for refraction. Ultrason Imaging 3(2):144–163

Pan KM, Liu CN (1981) Tomographic reconstruction of ultrasonic attenuation with correction for refractive errors. IBM J Res Dev 25(1):71–82

Jensen JA (1990) A model for the propagation and scattering of ultrasound in tissue. J Acoustl Soc Am 89(1):182–190

Norton S, Linzer M (1979a) Ultrasonic reflectivity tomography: reconstruction with circular transducer arrays. Ultrason Imaging 1(2):210–231

Norton SJ, Linzer M (1979b) Ultrasonic reflectivity imaging in three dimensions: reconstruction with spherical transducer arrays. Ultrason Imaging 1(3):210–231

Soumekh M (1999) Synthetic aperture radar signal processing with matlab algorithms. Wiley, New York

Trahey GE, Smith SW, von Ramm OT (1986) Speckle pattern correlation with lateral aperture translation: experimental results and implications for spatial compounding. IEEE Trans Ultrason, Ferroelectr, Freq Control 33(3):257–264

Ashfaq M, Ermert H (2007) Acoustic tomography scheme for small animal tissue characterization. In: Proceedings of the IEEE ultrasonics, symposium, pp 977–980

Schmidt S, Duric N, Li C, Roy O, Huang Z-F (2011) Modification of Kirchhoff migration with variable sound speed and attenuation for acoustic imaging of media and application to tomographic imaging of the breast. Medl Phys 38(2):998–1007

Koch A, Koch I, Hansen C, Lerch R, Ermert H (2012) Numerical ray-tracing in full angle spatial compounding. Acoust Imaging 31:103–113

Glover GH (1977) Computerized time-of-flight ultrasonic tomography for breast examination. Ultrasound Med Biol 3(2–3):117–127

Carson PL, Meyer CR, Scherzinger AL, Oughton TV (1981) Breast imaging in coronal planes with simultaneous pulse echo and transmission ultrasound. Science 214(4525):1141–1143

Greenleaf JF, Bahn RC (1981) Clinical imaging with transmissive ultrasonic computerized tomography. IEEE Trans Biomed Eng 28(2):177–185

Schreiman JS, Gisvold JJ, Greenleaf JF, Bahn RC (1984) Ultrasound transmission computed tomography of the breast. Radiology 150(2):523–530

Duric N, Littrup P, Babkin A, Chambers D, Azevedo S, Kalinin A, Pevzner R, Tokarev M, Holsapple E, Rama O, Duncan R (2005) Development of ultrasound tomography for breast imaging: technical assessment. Med Phy 32(5):1375–1386

Duric N, Littrup P, Poulo L, Babkin A, Pevzner R, Holsapple E, Rama O, Glide C (2007) Detection of breast cancer with ultrasound tomography: first results with the computed ultrasound risk evaluation (CURE) prototype. Med Phys 34(2):773–785

Li C, Duric N, Littrup P, Huang L (2009) In vivo breast sound-speed imaging with ultrasound tomography. Ultrasound Med Biol 35(10):1615–1628

Jeong J-W, Kim T-S, Shin DC, Do S, Singh M, Marmarelis VZ (2005) Soft tissue differentiation using multiband signatures of high resolution ultrasonic transmission tomography. IEEE Trans Medl Imaging 24(3):399–408

Jeong J-W, Shin DC, Do S-H, Blanco C, Klipfel NE, Holmes DR, Hovanessian-Larsen LJ, Marmarelis VZ (2008) Differentiation of cancerous lesions in excised human breast specimens using multiband attenuation profiles from ultrasonic transmission tomography. J Ultrasound Med 27(3):435–451

Jeong J-W, Shin DC, Marmarelis VZ (2009) Image fusion methodology for efficient interpretation of multiband images in 3D high-resolution ultrasonic transmission tomography. Intl J Imaging Syst Technoly 19(4):277–282

Gemmeke H, Ruiter NV (2007) 3D ultrasound computer tomography for medical imaging. Nucl Instrum Methods Phys Res A 580(2):1057–1065

Jirík R, Peterlík I, Ruiter N, Fousek J, Dapp R, Zapf M, Jan J (2012) Sound-speed image reconstruction in sparse-aperture 3-D ultrasound transmission tomography. IEEE Trans Ultrason, Ferroelectr, Freq Control 59(2):254–264

Zhang D, Gong X-F (1999) Experimental investigation of the acoustic nonlinearity parameter tomography for excised pathological biological tissues. Ultrasound Med Biol 25(4):593–599

Zhang D, Chen X, Gong X-F (2001) Acoustic nonlinearity parameter tomography for biological tissues via parametric array from a circular piston source: theoretical analysis and computer simulations. J Acoust Soc Am 109(3):1219–1225

Quan Y, Huang L (2007) Sound-speed tomography using first-arrival transmission ultrasound for a ring array. In: Proceedings of the SPIE, vol 6513. pp 651 306.1-651 306.9
Leach Jr RR, Azevedo SG, Berryman JG, Bertete-Aguirre HR, Chambers DH, Mast JE, Littrup P, Duric N, Johnson SA, Wuebbeling F (2002) Comparison of ultrasound tomography methods in circular geometry. In: Proceedings of the SPIE, vol 4687. pp 362–377
Mueller RK, Kaveh M, Wade G (1979) Reconstructive tomography and applications to ultrasonics. Proc IEEE 67(4):567–587
Mueller RK (1980) Diffraction tomography I: the wave equation. Ultrason Imaging 2(3):213–222
Wolf E (1969) Three-dimensional structure determination of semi-transparent objects from holographic data. Opt Commun 1(4):153–156
Kak A, Slaney M (2001) Principles of computerized tomographic imaging. SIAM, Philadelphia
Chew WC (1995) Waves and fields in inhomogeneous media. IEEE Press, Piscataway
Naidu P, Vasuki A, Satyamurthy P, Anand L (1995) Diffraction tomographic imaging with a circular array. IEEE Trans Ultrason, Ferroelectr, Freq Control 42(4):787–789
Iwata K, Nagata R (1975) Calculation of refractive index distribution from interferograms using the Born and Rytov's approximations. Japan J Appl Phys 14(14–1):379–383
Devaney A (1981) Inverse-scattering theory within the Rytov approximation. Opt Lett 6(8):374–376
Kenue SK, Greenleaf JF (1982) Limited angle multifrequency diffraction tomography. IEEE Trans Sonics Ultrason 29(4):213–216
Norton SJ (1983) Generation of separate density and compressibility images in tissue. Ultrason Imaging 5(3):240–252
Pan S, Kak A (1983) A computational study of reconstruction algorithms for diffraction tomography: interpolation versus filtered-backpropagation. IEEE Trans Acoust, Speech Signal Process 31(5):1262–1275
Kaveh M, Soumekh M, Greenleaf JF (1984) Signal processing for diffraction tomography. IEEE Trans Sonics and Ultrason 31(4):230–239
Soumekh M (1988) Band-limited interpolation from unevenly spaced sampled data. IEEE Trans Acoust, Speech Signal Process 36(1):110–122
Devaney A (1982) Inversion formula for inverse scattering within the Born approximation. Opt Lett 7(3):111–112
Devaney AJ (1983) A computer simulation study of diffraction tomography. IEEE Trans Biomed Eng 30(7):377–386
Sponheim N, Gelius L-G, Johansen I, Stamnes JJ (1991) Quantitative results in ultrasonic tomography of large objects using line sources and curved detector arrays. IEEE Trans Ultrason, Ferroelectr, Freq Control 38(4):370–379
Sponheim N, Gelius L-J, Johansen I, Stamnes JJ (1994) Ultrasonic tomography of biological tissue. Ultrason Imaging 16(1):19–32
Devaney AJ, Beylkin G (1984) Diffraction tomography using arbitrary transmitter and receiver surfaces. Ultrason Imaging 6(2):181–193
Devaney AJ (1985) Generalized projection-slice theorem for fan beam diffraction tomography. Ultrason Imaging 7(3):264–275
Gelius L-G, Johansen I, Sponheim N, Stamnes JJ (1991) A generalized diffraction tomography algorithm. J Acoust Soc Am 89(2):523–528
Anastasio M, Pan X (2003) An improved reconstruction algorithm for 3-D diffraction tomography using spherical-wave sources. IEEE Trans Biomed Eng 50(4):517–521
Devaney AJ (1986) Reconstructive tomography with diffracting wavefields. Inverse Prob 2(2):161–183
Ladas KT, Devaney AJ (1991) Generalized ART algorithm for diffraction tomography. Inverse Prob 7(1):109–125
Devaney AJ (1985) Variable density acoustic tomography. J Acoust Soc Am 78(1):120–130
Moghaddam M, Chew W (1993) Variable density linear acoustic inverse problem. Ultrason Imaging 15(3):255–266

Mensah S, Lefebvre JP (1997) Enhanced compressibility tomography. IEEE Trans Ultrason, Ferroelectr, Freq Control 44(6):1245–1252
Anastasio MA, Shi D, Deffieux T (2005) Image reconstruction in variable density acoustic tomography. In: Proceedings of the SPIE, vol 5750. pp 326–331
Kai A, Sun J, Wade G (1992) Imaging the acoustic nonlinear parameter with diffraction tomography. IEEE Trans Ultrason, Ferroelectr, Freq Control 39(6):708–715
Slaney M, Kak A, Larsen L (1984) Limitations of imaging with first-order diffraction tomography. IEEE Trans Microwave Tech 32(8):860–874
Robinson B, Greenleaf J (1986) The scattering of ultrasound by cylinders: Implications for diffraction tomography. J Acoust Soc Am 80(1):40–49
Tsihrintzis GA, Devaney AJ (2000) Higher-order (nonlinear) diffraction tomography: inversion of the Rytov series. IEEE Trans Inf Theory 46(5):1748–1765
Wedberg TC, Stamnes JJ (1995) Comparison of phase retrieval methods for optical diffraction tomography. Pure Appl Opt 4(1):39–54
Mast TD (1999) Wideband quantitative ultrasonic imaging by time-domain diffraction tomography. J Acoustl Soc Am 106(6):3061–3071
Astheimer JP, Waag RC (2008) Born iterative reconstruction using perturbed-phase field estimates. J Acoust Soc Am 124(4):2353–2363
Johnson S, Tracy M (1983) Inverse scattering solutions by a sinc basis, multiple source, moment method - part I: theory. Ultrason Imaging 5(4):361–375
Tracy M, Johnson S (1983) Inverse scattering solutions by a sinc basis, multiple source, moment method - part II: numerical evaluations. Ultrason Imaging 5(4):376–392
Johnson S, Zhou Y, Tracy M, Berggren M, Stenger F (1984) Inverse scattering solutions by a sinc basis, multiple source, moment method - part III: fast algorithms. Ultrason Imaging 6(1):103–116
Wang YM, Chew WC (1989) An iterative solution of two-dimensional electromagnetic inverse scattering problem. Int J Imaging Syst Technol 1(1):100–108
Johnson SA, Stenger F, Wilcox C, Ball J, Berggren MJ (1982) Wave equations and inverse solutions for soft tissue. Acoust Imaging 11:409–424
Pourjavid S, Tretiak OJ (1992) Numerical solution of the direct scattering problem through the transformed acoustical wave equation. J Acoust Soc Am 91(2):639–645
Berggren MJ, Johnson SA, Carruth BL, Kim WW, Stenger F, Kuhn PK (1996) Ultrasound inverse scattering solutions from transmission and/or reflection data. In: Proceedings of the SPIE, vol 671. pp 114–121
Cavicchi T, Johnson S, O'Brien WD Jr (1988) Application of the sinc basis moment method to the reconstruction of infinite circular cylinders. IEEE Trans Ultrason, Ferroelectr, Freq Control 35(1):22–33
Cavicchi T, O'Brien WD Jr (1989) Numerical study of higher-order diffraction tomography via the sinc basis moment method. Ultrason Imaging 11(1):42–74
Colton D, Coyle J, Monk P (2000) Recent developments in inverse acoustic scattering theory. SIAM Rev 42(3):369–414
Chew WC, Wang YM (1990) Reconstruction of two-dimensional permittivity distribution using the distorted Born iterative method. IEEE Trans Med Imaging 9(2):218–225
Borup D, Johnson S, Kim W, Berggren M (1992) Nonperturbative diffraction tomography via Gauss-Newton iteration applied to the scattering integral equation. Ultrason Imaging 14(1):69–85
Remis RF, van den Berg PM (2000) On the equivalence of the Newton–Kantorovich and distorted Born methods. Inverse Prob 16(1):L1–L4
Devaney AJ, Oristaglio ML (1983) Inversion procedure for inverse scattering within the distorted-wave Born approximation. Phys Rev Lett 51(4):237–240
Ghosh Roy DN, Roberts J, Schabel M, Norton SJ (2007) Noise propagation in linear and nonlinear inverse scattering. J Acoust Soc Am 121(5):2743–2749
Hesford AJ, Chew WC (2010) Fast inverse scattering solutions using the distorted Born iterative method and the multilevel fast multipole algorithm. J Acoust Soc Am 128(2):679–690

Kim W, Borup D, Johnson S, Berggren M, ZhouY (1987) Accelerated inverse scattering algorithms for higher contrast objects. In: Proceedings of the IEEE Ultrasonics, Symposium, pp 903–906

Chew WC, Lin JH (1995) A frequency-hopping approach for microwave imaging of large inhomogeneous bodies. IEEE Microwave Guided Wave Lett 5(12):440–441

Haddadin O, Ebbini E (1998) Imaging strongly scattering media using a multiple frequency distorted Born iterative method. IEEE Trans Ultrason, Ferroelectr, Freq Control 45(6):1485–1496

Lavarello RJ, Oelze ML (2008) A study on the reconstruction of moderate contrast targets using the distorted Born iterative method. IEEE Trans Ultrason, Ferroelectr, Freq Control 55(1):112–124

Lavarello RJ, Oelze ML (2009) Tomographic reconsruction of three-dimensional volumes using the distorted Born iterative method. IEEE Trans Med Imaging 28:1643–1653

Duncan DP, Astheimer JP, Waag RC (2009) Scattering calculation and image reconstruction using elevation-focused beams. J Acoust Soc Am 125(5):3101–3119

Kleinman RE, van den Berg PM (1992) A modified gradient method for two-dimensional problems in tomography. J Comput Appl Math 42(1):17–35

Harada H, Wall DJN, Takenaka T, Tanaka M (1995) Conjugate gradient method applied to inverse scattering problem. IEEE Trans Antennas Propag 43(8):784–792

Lobel P, Pichot C, Blanc-Feraud L, Barlaud M (1997) Microwave imaging: reconstructions from experimental data using conjugate gradient and enhancement by edge-preserving regularization. Int J Imaging Syst Technol 8(4):337–342

Zhang X, Broschat S, Flynn PJ (2004) A numerical study of conjugate gradient directions for an ultrasound inverse problem. J Comput Acoust 12(4):587–604

Zhang X, Broschat S, Flynn P (2002) A comparison of material classification techniques for ultrasound inverse imaging. J Acoust Soc Am 111(1):457–467

Wiskin J, Borup D, Johnson S, Berggren M, Abbott T, Hanover R (2007) Full wave, non-linear, inverse scattering: High resolution quantitative breast tissue tomography. Acoust Imaging 28:183–193

van den Berg PM, Kleinman RE (1997) A contrast source inversion method. Inverse Prob 13(6):1607–1620

van den Berg PM, van Broekhoven AL, Abubakar A (1999) Extended contrast source inversion method. Inverse Prob 15(5):1325–1344

Pelekanos G, Abubakar A, van den Berg PM (2003) Contrast source inversion methods in elastodynamics. J Acoust Soc Am 114(5):2825–2834

Gordon R (1974) A tutorial on ART (algebraic reconstruction technique). IEEE Trans Nucl Sci 21(3):78–93

Natterer F, Wübbeling F (1995) A propagation-backpropagation method for ultrasound tomography. Inverse Prob 11(6):1225–1232

Natterer F (1997) An algorithm for 3D ultrasound tomography. In: Chavent G, Sabatier PC (eds) Lecture Notes in Physics, Vol 486: inverse problems of wave propagation and diffraction. Springer, New York, pp 216–225

Natterer F (2008) Reflectors in wave equation imaging. Wave Motion 45(6):776–784

Mast TD, Nachman AI, Waag RC (1997) Focusing and imaging using eigenfunctions of the scattering operator. J Acoust Soc Am 102(2):715–725

Lin F, Nachman AI, Waag RC (2000) Quantitative imaging using a time-domain eigenfunction method. J Acoust Soc Am 108(3):899–912

Waag RC, Lin F, Varslot TK, Astheimer JP (2007) An eigenfunction method for reconstruction of large-scale and high-contrast objects. IEEE Trans Ultrason, Ferroelectr, Freq Control 54(7):1316–1332

Kwon S, Jeong M (1998) Ultrasound inverse scattering determination of speed of sound, density and absorption. In: Proceedings of the IEEE Ultrasonics, Symposium, pp 1631–1634

Lavarello RJ, Oelze ML (2010) Density imaging using a multiple frequency DBIM approach. IEEE Trans Ultrason, Ferroelectr, Freq Control 57(11):2471–2479

Lavarello R, Bond S, Oelze M (2010) Regularized tomographic density imaging using multiple frequency information. In: Proceedings of the IEEE Ultrasonics, Symposium, pp 2336–2339

van Dongen KWA, Wright WMD (2007) A full vectorial contrast source inversion scheme for three-dimensional acoustic imaging of both compressibility and density profiles. J Acoust Soc Am 121(3):1538–1549

Lin J, Chew W (1996a) Ultrasonic imaging by local shape function method with CGFFT. IEEE Trans Ultrason, Ferroelectr, Freq Control 43(5):956–969

Lin JH, Chew WC (1996b) Three-dimensional microwave imaging by local shape function method with CGFFT. In: IEEE antennas and propagation society international. Symposium 3:2148–2151

Lavarello RJ, Oelze ML (2009) Density imaging using inverse scattering. J Acoust Soc Am 125(2):793–802

Lavarello RJ, Oelze ML (2010) Scattering by an arrangement of eccentric cylinders embedded on a coated cylinder with applications to tomographic density imaging. J Acoust Soc Am 127(2):645–648

Waag RC, Fedewa RJ (2006) A ring transducer system for medical ultrasound research. IEEE Trans Ultrason, Ferroelectr, Freq Control 53(10):1707–1718

Johnson SA, Borup DT, Wiskin JW, Natterer F, Wubeling F, Zhang Y, Olsen SC (1999) Apparatus and method for imaging with wavefields using inverse scattering techniques. U.S. Patent 6,005,916

Johnson SA, Abbott T, Bell R, Berggren M, Borup D, Robinson D, Wiskin J, Olsen S, Hanover B (2007) Noninvasive breast tissue characterization using ultrasound speed and attenuation. Acoust Imaging 28:147–154

Wiskin J, Borup DT, Johnson SA, Berggren M (2012) Non-linear inverse scattering: high resolution quantitative breast tissue tomography. J Acoust Soc Am 131(5):3802–3813

Borup DT, Ghandi OP (1985) Calculation of high-resolution SAR distributions in biological bodies using the FFT algorithm and conjugate gradient method. IEEE Trans Microwave Theory Tech 33(5):417–419

Cui TJ, Chew WC (1999) Fast algorithm for electromagnetic scattering by buried 3-D dielectric objects of large size. IEEE Trans Geosci Remote Sens 37:2597–2608

Xu XM, Liu QH (2002) The BCGS-FFT method for electromagnetic scattering from inhomogeneous objects in a planarly layered medium. IEEE Antennas Wireless Propag Lett 1:77–80

Greengard L, Rokhlin V (1987) A fast algorithm for particle simulations. J Comput Phys 73:325–348

Rokhlin V (1990) Rapid solution of integral equations of scattering theory in two dimensions. J Comput Phys 86(2):414–439

Chew WC, Jin J, Michielssen E, Song J (eds) (2001) Fast and efficient algorithms in computational electromagnetics. Artech House, Boston

Michielssen E, Jin J-M (2008) Guest editorial for the special issue on large and multiscale computational electromagnetics. IEEE Trans Antennas Propag 56(8):2146–2149

Harrington RF (1993) Field computation by moment methods. IEEE Press, New York

Saad Y, Schultz MH (1986) GMRES–a generalized minimal residual algorithm for solving nonsymmetric linear-systems. SIAM J Sci Stat Comput 7:856–869

Van der Vorst HA (1992) Bi-CGSTAB: a fast and smoothly converging variant of Bi-CG for the solution of nonsymmetric linear systems. SIAM J Sci Stat Comput 13(2):631–644

Coifman R, Rokhlin V, Wandzura S (1993) The fast multipole method for the wave equation: a pedestrian prescription. IEEE Antennas Propag Mag 35(3):7–12

Koc S, Song JM, Chew WC (1999) Error analysis for the numerical evaluation of the diagonal forms of the scalar spherical addition theorem. SIAM J Numer Anal 36(3):906–921

Song J, Chew WC (2001) Error analysis for the trunction of multipole expansion of vector Green's functions. IEEE Microwave Wirel Compon Lett 11:311–313

Hastriter ML, Ohnuki S, Chew WC (2003) Error control of the translation operator in 3D MLFMA. Microwave Opt Technol Lett 37(3):184–188

Hesford AJ, Waag RC (2010) The fast multipole method and Fourier convolution for the solution of acoustic scattering on regular volumetric grids. J Comput Phys 229:8199–8210

Bebendorf M (2000) Approximation of boundary element matrices. Numerische Mathematik 86:565–589

Zhao K, Vouvakis MN, Lee J-F (2005) The adaptive cross approximation algorithm for accelerated method of moments computations of EMC problems. IEEE Trans Electromagn Compatibility 47:763–773

Shaeffer J (2008) Direct solve of electrically large integral equations for problem sizes to 1 M unknowns. IEEE Trans Antennas Propag 56(8):2306–2313

Hesford AJ, Waag RC (2011) Reduced-rank approximations to the far-field transform in the gridded fast multipole method. J Comput Phys (submitted)

Garland M, Le Grand S, Nickolls J, Anderson J, Hardwick J, Morton S, Phillips E, Zhang Y, Volkov V (2008) Parallel computing experiences with CUDA. IEEE Micro 28(4):13–27

Roy O, Jovanovic I, Hormati A, Parhizkar R, Vetterli M (2010) Sound speed estimation using wave-based ultrasound tomography: theory and GPU implementation. In: Proceedings of the SPIE, vol 7629. pp 76 290J.1–76 290J.12

Wiskin J, Borup D, Johnson S, Berggren M, Robinson D, Smith J, Chen J, Parisky Y, Klock J (2010) Inverse scattering and refraction corrected reflection for breast cancer imaging. In: Proceedings of the SPIE, vol 7629. pp 76 290K.1–76 290K.12

Hesford AJ, Chew WC (2006) A frequency-domain formulation of the Frechet derivative to exploit the inherent parallelism of the distorted Born iterative method. Waves Random Complex Media 16(4):495–508

Haynes M, Moghaddam M (2010) Large-domain, low-contrast acoustic inverse scattering for ultrasound breast imaging. IEEE Trans Biomed Eng 57(11):2712–2722

Andre MP, Janee HS, Martin PJ, Otto GP, Spivey BA, Palmer DA (1997) High-speed data acquisition in a diffraction tomography system employing large-scale toroidal arrays. Int J Imaging Syst Technol 8(1):137–147

Johnson SA, Borup DT, Wiskin JW, Berggren MJ, Zhdanov MS, Bunch K, Eidens R (1997) Application of inverse scattering and other refraction corrected methods to environmental imaging with acoustic or electromagnetic energy. In: Dolic G, Wheeler MJ (eds) Next generation environmental models and computational methods. SIAM, Philadelphia, pp 295–312

Parhizkar R, Karbasi A, Vetterli M (2011) Calibration in circular ultrasound tomography devices. In: Proceedings of the IEEE international conference on acoustics, speech and, signal processing. pp 549–552

Chapter 15
Clinical Results with Ultrasound Computed Tomography of the Breast

Michael André, James Wiskin and David Borup

Abstract Although the science and engineering of ultrasound computed tomography (USCT) has been explored for over four decades, there have been relatively few instances of a system being developed and applied to patients. Nonetheless, there have been notable results from the clinical setting, especially recently, that illustrate how a successful USCT scanner may provide significant advances to women's health. For practical anatomical reasons, this work has almost exclusively addressed imaging of the female breast. Other quantitative ultrasound techniques have been applied to characterizing the female breast, including quantitative backscatter analysis, shear wave speed, computer-aided diagnosis, etc., but USCT is the focus of this chapter. We highlight the evolution of scanner design and image reconstruction by presenting key results from patient measurements by the major researchers in the field. There has been steady progress in electronics, parallel processors, reconstruction algorithms, understanding of the physical properties of breast tissue and a resurgence of interest in the medical community for dedicated breast ultrasound systems. It is understood today that USCT may be able to contribute in many aspects of the medical management of breast disease including detection, diagnosis and treatment of breast cancer.

M. André (✉)
Radiology, Physics & Engineering Division 114, VA Healthcare/University of California, San Diego, 3350 La Jolla Village Drive, San Diego, CA 92161, USA
e-mail: mandre@ucsd.edu

J. Wiskin · D. Borup
CVUS, LLC, 3216 Highland Dr.Suite 100, Salt Lake City, UT 84106, USA
e-mail: jwiskin.cvus@gmail.com

D. Borup
e-mail: dborup@comcast.net

J. Mamou and M. L. Oelze (eds.), *Quantitative Ultrasound in Soft Tissues*, DOI: 10.1007/978-94-007-6952-6_15,

15.1 The Medical Problem

The American Cancer Society estimated in 2011 that the lifetime risk for breast cancer is 12.15 % or 1 in 8 and the death rate is exceeded only by lung cancer in women (American Cancer Society 2011). In addition, about 1 % of all breast cancers occur in men. The National Cancer Institute estimated that in 2008 approximately 2.6 million women with a history of breast cancer were alive in the U.S. (Howlader et al. 2011). Breast cancer originates in the glandular tissue, called lobules, and in the ducts that connect them to the nipple. The remainder of the breast is connective tissue and fat, the relative composition of which may change with age and other factors. There are many known relative risk factors for breast cancer but the dominant one is age; incidence and death rates increase with age such that 97 % of breast cancer deaths occur in women 40 years of age and older. The majority of masses that occur in the breast are benign, not threatening and many may be identified with confidence on mammograms or sonograms. However, a significant number of masses are either not seen on screening mammography or the findings are not conclusive without further workup. Early detection of breast cancer when the mass is small is very important to survival rate; 5 year survival for women with cancer $\geq$20 mm is 80 % compared to 98 % for masses 10 mm (American Cancer Society 2011).

15.1.1 Current Breast Cancer Imaging

Mammography is the primary screening tool for breast cancer together with physical examination, while breast sonography is the principal adjunctive imaging modality. As a general rule, a screening test is desired to have very high sensitivity to disease with few or no false negative results. This often results in lower specificity, leading to higher false positives that require further clinical evaluation. A suspected finding in screening may advance the patient to a diagnostic examination. In this case the patient has additional specialized mammograms or very commonly, a diagnostic breast sonogram is obtained possibly of only a portion of one breast in the region where the finding is located. The handheld transducer used in the diagnostic sonogram is also well suited to provide guidance for performing a needle aspiration or core biopsy when a mass is identified that is suspicious for cancer. In some instances the patient may undergo a magnetic resonance imaging (MRI) breast examination that entails injection of a vascular contrast enhancing material incorporating gadolinium, although it is impractical for use in general screening. MRI has high sensitivity and is considered to provide the most accurate depiction of the margins of a malignant mass so it is often used for surgical planning and monitoring response to therapy. As a screening test applied to many millions of patients, mammography is relatively inexpensive, sonography costs approximately 2–3 times more, while breast MRI is up to 10 times more expensive

than mammography. Representative mammograms, sonograms and MRI images are compared later in the chapter.

15.1.2 Breast Sonography

Conventional sonography systems produce images of reflected and backscattered ultrasound energy, or relative "echogenicity," that occur at interfaces between the different breast tissues. Image formation assumes straight-line propagation, 180° backscatter and constant sound speed, usually 1,540 m/s, all of which are known to be incorrect. Breast ultrasound is recognized to be a difficult exam to perform and interpret while image quality is known to be dependent on the skill of the operator as well as technical features of the scanner. A major strength of breast ultrasound and its most common clinical use is differentiation of cystic and solid lesions with nearly 100 % accuracy (Stavros et al. 1995, 2005; Hong et al. 2005; Brogoch et al. 2010). Nonetheless, numerous studies of conventional breast ultrasound show substantial variance in diagnostic accuracy due to variability in radiologists' skill levels (Baker et al. 1999) and technical features of the scanner (Berg et al. 2006).

Work to improve the accuracy of diagnostic breast ultrasound led to the development of a well-defined rule-based system for mass assessment based on parameters describing the ultrasound appearance of breast lesions. Sonographic features of a mass are described in accordance with the ACR Breast Imaging Reporting and Data System® (BI-RADS®) (Mendelson et al. 2003). The BI-RADS sonographic categories include size, shape, margin, relative echogenicity, lesion boundary, orientation to the skin, posterior features (shadowing or enhancement due to different attenuation), vascularity, and surrounding tissue. A final numerical assessment is reported on an increasing scale of risk for cancer, 1–5, as well as 0 where more information is needed and 6 where the finding is a known cancer. Precise application of the BI-RADS approach was shown to be helpful in differentiating benign versus malignant solid masses, particularly when performed by experts, although there is variability between readers (Brogoch et al. 2010; Baker et al. 1999; Berg et al. 2006; Mendelson et al. 2003; Kwak et al. 2006; Kolb et al. 2002). Mass characterization with ultrasonography is highly dependent on technical factors and settings of the scanner. Example images of three masses are shown in Fig. 15.1. Posterior "enhancement" is evident for the fluid-filled simple cysts (Fig. 15.1a), while posterior "shadowing" is seen for the malignant mass (Fig. 15.1c). These effects are artifacts due to application of time-gain compensation in regions where attenuation and reflection losses are not uniform with depth.

The American College of Radiology (ACR) published breast ultrasound practice guidelines to establish standards for indications of use, qualifications and responsibilities of the practitioner, examination procedures, quality control, minimum equipment specifications and more (ACR 2011). Following these standards breast ultrasound should be performed with linear array transducers of 10 MHz or more and with variable focal zones. In order to obtain the needed high resolution,

Fig. 15.1 Three sonograms of breast masses where the transducer is applied to the skin at the top of the images. **a** Simple cystic mass with distinct margins. **b** Large complex cystic mass with internal echoes and debris. **c** Spiculated solid malignant mass. The field of view and range for these images is 4 cm

the field of view and range in sonography is small, which greatly complicates interpretation, localization of masses and comparison to prior exams. The sonogram is performed with the patient supine in order to minimize the thickness of the breast in accommodation of the high attenuation and small field of view at high frequency. It can be difficult to precisely describe or record the location of a finding in the breast since the tissue can be mobile. This complicates serial monitoring of a mass over time and in some cases it is difficult to find a mass at the time of biopsy that was seen in an earlier visit. BI-RADS uses a "face-of-the-clock" scheme for sonography with the nipple at the center and the caudal direction at 12:00, but of course the breast is three dimensional. These same issues may complicate other quantitative enhancements to breast sonography including shear wave speed (Berg et al. 2012) or elastography methods, and computer-aided diagnosis (Andre et al. 2011).

15.1.3 Whole-Breast Ultrasound Imaging

Even with the best imaging methods available today, up to 80 % of breast biopsies performed turn out to be benign (Silverstein et al. 2005; Kolb et al. 2002; Stavros 2004). Combined mammography and targeted breast ultrasound is still the most effective approach for breast cancer screening in women at normal risk (Silverstein et al. 2005; Stavros 2004). Adding a single screening ultrasound to mammography yields an additional 1.1–7.2 detected cancers per 1000 in high risk women, but at an increase in false positive findings (Silverstein et al. 2005; Shetty et al. 2003).

Despite the potential benefits, sonography is not usually employed for screening due to several factors including procedural complexity, additional skill and training required, a long procedure time, the requirement that a radiologist perform it, the large number of images that need to be reviewed and cost. Nonetheless sonography is being more widely employed particularly for younger women for whom mammography may not be recommended and women with dense breasts

where mammography is less sensitive. For women with particular risk factors, breast sonography may be indicated as a secondary screening modality.

The American College of Radiology Imaging Network (ACRIN) Trial 6666 examined the role of whole-breast ultrasound (WBU) screening with conventional scanners at multiple centers for several thousand patients with moderate risk factors for cancer (Berg et al. 2008). In this procedure, a high frequency hand-held transducer is slowly scanned across the entire breast in an overlapping raster fashion while the patient lies supine. The ACRIN protocol for scanning both breasts took 20–40 min and required that the procedure be performed and interpreted by a radiologist with special proficiency. A semi-automated system to facilitate this procedure was developed by Sonocine (Reno, NV) that has received approval from the U.S. Food and Drug Administration (Kelly et al. 2010). Any suitable breast ultrasound transducer system is attached to a mechanically-driven arm manipulated by the sonographer while the system records the position, angle and tip of the linear array. Overlapping passes are made of the breast while the sequence of up to 1,000 or more closely-spaced images of the breast is recorded. The radiologist reviews the images while they are displayed in rapid sequence, at a rate of a few per second, in two-dimensional (2D) mode as a cine loop. ACRIN 6666 and studies published by Sonocine show that there is a significant increase in the number of cancers detected by WBU over mammography alone.

A particularly noteworthy substudy of ACRIN 6666 examined the effect of supplementing annual mammography screening with annual ultrasound over a three-year period in 2809 women at elevated risk due to radiographically dense breast tissue and at least one additional risk factor such as personal and/or family history of breast cancer (Berg et al. 2012). Adding ultrasound to mammography each year significantly increased the chance of finding invasive cancer before it spread to the lymph nodes. Of the 111 breast cancer diagnoses in this group, mammography failed to see about half of the cancers present in women with dense breasts although it did detect 33 cancers not seen on sonography. 32 cancers were seen only by ultrasound of which 94 % were node-negative invasive. 26 were detected on both mammograms and sonograms, while 9 were seen only by a single MRI exam performed after three years of mammography and sonography. 11 were not detected by any imaging screen during this period. Adding annual sonography and a single MRI increased false positives by 5 % but they provided a significant detection benefit for these women. Neither ultrasound or MRI are recommended as a replacement for mammography, but it is important to emphasize that the vast majority of additional cancers detected by supplemental sonography were early-stage invasive cancers that had not spread to the lymph nodes. If a patient has an MRI the ultrasound is probably not needed and possibly vice versa for reasons of practicality.

In the U.S. 14 states have passed legislation requiring breast imaging centers to inform patients if they have mammographically dense breast tissue. The legislation is based on the proposition that breast density is a strong risk factor for breast cancer. When the breast is comprised of less fat and more glandular tissue it represents a challenge for mammography to detect masses. Categorizing breast

tissue is a component of the mammographic BI-RADS protocol but it is highly qualitative and variably applied. WBU has been shown to precisely differentiate between fat and fibroglandular tissues while in addition USCT can provide quantitative volumetric measurements of the tissues.

15.1.4 Opportunity for Ultrasound Computed Tomography

The discussion in the two previous sections describes many of the benefits and limitations of conventional breast sonography. It also illustrates there is an opportunity for new technology to play an important clinical role in breast cancer detection, diagnosis and management. Whole breast USCT using transmission and/or reflection techniques has been proposed for many years as a means to address the shortcomings but also to provide entirely new ways to assess and characterize masses and other findings in the breast.

The promise of USCT is based on several key attributes including:

- ability to provide global views of both breasts in a standard frame of reference for detailed contralateral and serial comparisons
- operator independence
- uniform high resolution independent of range and location
- minimal refraction, spatial distortion or multiple scattering effects
- no speckle
- quantitative tissue properties of sound speed, attenuation and scatter
- ability to precisely locate findings to facilitate follow-up exams
- volumetric images to aid monitoring changes due to therapy
- anatomic breast positioning with no compression or distortion
- fast scans of the entire breast
- characterization of masses based on quantitative properties and accurate morphometry
- accurately measures relative volumes of fat and glandular tissues
- significant improvements in both high speed data multi-channel acquisition systems and powerful multi-processor computing.

The experimental basis for this promising opportunity is summarized in the next section in which some of the notable clinical studies of USCT are reviewed.

15.2 Breast Ultrasound Computed Tomography

Research in a number of laboratories in the 1970s and 1980s showed potential for USCT to provide accurate spatial registration, high spatial and contrast resolution, few artifacts and quantitative tissue measurements, particularly of sound speed,

attenuation and morphometry. However, with over four decades of research there have been relatively few instances of practical systems being developed and applied to patients. Instead the majority of the research work addressed theoretical and computational developments. These early prototype scanners were mostly very slow, with few data channels, sparse spatial sampling and long reconstruction times limited by available technology. The U.S. medical community largely concluded this work was premature or unnecessary given the success of high-quality, fast, automated array technology that had multiple medical uses beyond breast imaging (Carson and Fenster 2009). The research also illustrated USCT is a highly complex, inherently non-linear problem that probably requires consideration of the three-dimensional (3D) nature of sound propagation. With steady scientific progress and new technology there is a revival of effort in this field and the latest results are impressive. The developments described earlier that are expanding the role for ultrasound in breast imaging have also enhanced the opportunity for USCT to emerge from the laboratory.

Four approaches to USCT will be considered in three categories described in Chap. 1: (a) ray-based backprojection, (b) diffraction tomography with an annular array and (c) full-wave inverse-scatter tomography (IST) with reflection tomography (RT). With the exception of recent work in IST, all of the approaches used 2D linear approximations to obtain sequential coronal planes through the breast. Two USCT systems developed by the authors are explored in some detail; one early diffraction tomography unit and the current full-wave inverse-scattering tomography system.

15.3 Ray-Based Backprojection Tomography

The earliest attempts at USCT used transmission time of flight (TOF) and amplitude measurements along straight rays combined with CT reconstruction methods analogous to x-ray CT. Greenleaf et al. (1974, 1975, 1978) were probably the first to describe results with ultrasound transmission tomography, while Glover and Sharp (1977); Glover (1977) may have been the first to show results in patients. Carson et al. (1981) was also actively imaging patients with a similar system. Others worked with B-mode methods to produce reflection tomograms (Carson et al. 1981; Mueller et al. 1979; Hiller and Ermert 1980).

In 1981, Greenleaf and Bahn (1981) published clinical results from approximately 150 patients, 30 of whom had biopsy-confirmed breast cancer. The scanner employed 5 MHz single-element transmit-receive pairs, initially one pair and later additional stacked in a vertical line that could acquire multiple planes of 2D data with each rotation (Fig. 15.2). 2.4×10^4 transmission rays were acquired to produce a 118×118 image matrix using filtered backprojection, examples of which are shown in Fig. 15.3 for an adenocarcinoma. The patient lay supine with one breast suspended in a water bath while the transducer pairs rotated 360°.

Fig. 15.2 Rotating transmit-receive pair of transducers obtained time-of-flight and signal amplitude data for reconstruction by filtered backprojection. Adapted from Greenleaf et al. (1978)

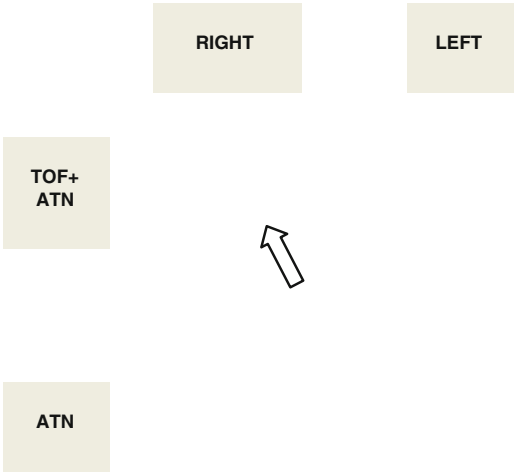

Fig. 15.3 Sound speed (*TOF*) is displayed in *blue* and attenuation (*ATN*) in *red* for *right* and *left* breast. The two are superimposed in the *top row* to emphasize the location of the mass (*arrow*). Adapted from Greenleaf et al. (1978)

The researchers carefully analyzed the calculated ultrasonic properties and pathological findings of both normal breast tissues and masses for patients who later had mastectomy. All solid lesions were found to have relatively higher sound speed in association with varied patterns of attenuation. Figure 15.4 demonstrates

Fig. 15.4 Relationship between sound speed and attenuation for normal tissues and masses. Adapted from Greenleaf and Bahn (1981)

the results of their analysis showing the relationship between sound speed (velocity) and attenuation. Overall a broad distribution of values was found with overlap of benign and malignant masses using only these two features. Several different classification schemes were tested with resulting specificity of 80–90 % (Greenleaf and Bahn 1981).

Carson et al., developed a system employing opposing 3.5 MHz transducers in a 20 °C water tank that used a translate-rotate motion around the breast to acquire 90 views or linear profiles with filtered backprojection reconstruction (Carson et al. 1981). Both transmission tomograms and compounded pulse-echo images were produced, the latter formed on an analog scan converter. Figure 15.5 shows images for a 41 year-old patient with a 1.8 cm infiltrating ductal carcinoma in the

Fig. 15.5 Coronal images of compounded pulse echo (*PE*), attenuation (*ATTEN*) and speed of sound (*SOS*) were obtained 9 cm from the nipple in a breast with infiltrating ductal carcinoma. The mass is indicated by the arrows and readily seen in the SOS image as a bright white irregular shape at 9:00 (Carson et al. personal communication)

9:00 location (arrows). Image features include high sound speed (1,531 m/s) surrounded by low speed fat (1,445 m/s). The mass is less echogenic than the surrounding tissue in the pulse-echo image and it appears to have attenuating borders (ATTEN). Not surprisingly, detection of malignancy was found to be more difficult with smaller masses and in younger patients with denser breasts.

Analysis similar to that of Fig. 15.4 was performed of the ultrasonic properties of 40 lesions. The speed of sound and attenuation relative to the surrounding mammary tissue are plotted in Fig. 15.6 for normal tissues, unclassified benigns and fibroadenomas (all solid dots), for cysts (open circles) and for cancers (5). In this three-group analysis it is apparent that four benign lesions including one cyst are classified with cancers. The overall sensitivity and specificity are quite good, both greater than 90 % (Carson et al. 1983, Scherzinger et al. 1989).

A recent clinical prototype imaging system was developed that employs a ray-based tomographic reconstruction but utilizes a stationary circular array without rotation (Duric et al. 2005, 2007). It bears some resemblance to the design of a previous diffraction tomography system (André et al. 1997) described in the next section but has numerous improvements. The array consists of 256 elements operating at 1.5 MHz, equally spaced on a diameter of 20 cm that is translated vertically to acquire successive planes. There are 256 data acquisition channels sampling at 6.25 MHz. This design affords very fast acquisition for a single slice ($\sim$100 ms) with about 45 slices acquired per breast for a total exam time of 5 min. Transmitted and reflected data are acquired to produce a reflection tomogram and

Fig. 15.6 Measured ultrasound characteristics of tissues and lesions. Adapted from Carson et al. (1983)

coincident images of sound speed and attenuation. Performance in phantoms met expectations with in-plane resolution for the transmission images of 4 mm, 0.5 mm in the reflection mode ($\sim \lambda/2$) and with effective slice thickness of 12 mm. Spatial resolution is limited by the size and spacing of the elements plus the large slice thickness (Fig. 15.7).

Sample images are shown in Fig. 15.8 from a patient whose subsequent biopsy proved invasive ductal carcinoma. The mass shows higher sound speed and attenuation compared to surrounding tissues (whiter) with apparent architectural distortion evident in the higher resolution reflection image. In a small patient study six features were found to be associated with malignancy: ratio of width to height $<$1.4, irregular shape, irregular margins, architectural distortion, elevated sound speed of 50–150 m/s relative to fat and elevated attenuation of 0.5 dB/cm relative to fat at 1.5 MHz (Duric et al. 2006). In addition to characterizing masses, this prototype scanner has shown potential value of the sound speed images for monitoring response to neoadjuvant chemotherapy. Inability to account for out-of-plane scattering and refraction limits accuracy of the attenuation measurements. The group has designed a production level scanner with apparently 2,048 elements that will be capable of much higher resolution and better in-plane focusing.

Although the results were very encouraging, these studies showed that the breast contains considerable complexity with as much as ± 8 % variation in sound speed and 4 dB/cm/MHz attenuation. Given the long path length, variations in refractive index are not negligible nor are refraction and multiple scattering. Consequently, the straight-ray image inversion methods are likely to prove inadequate for most clinical use.

Fig. 15.7 Ring transducer array in the water tank that is positioned below the patient table for scanning. From Duric et al. (2005)

Fig. 15.8 Images of a 10 mm invasive ductal carcinoma located inside the oval. **a** Reflection image. **b** Sound speed. **c** Attenuation. **d** Sound speed fused with reflection. **e** Close up of edge enhanced reflection image showing distortion. **f** Close up of (**d**). From Duric et al. (2006)

15.4 Diffraction Tomography

In ultrasound computed tomography, the wavelength of sound in tissue is on the order of 1 mm and the effects of diffraction are not negligible. In general, due to limitations of instrumentation and algorithms, the second stage in development of ultrasound transmission imaging was to solve wave equations using two-dimensional linearization techniques rather than geometrical ray models for reconstruction. In its simpler forms this approach usually fails for breasts because it is based on first-order perturbation approximations (Born or Rytov) that are valid only for unrealistically small variations in sound speed and attenuation. Diffraction tomography attempts to reconstruct an image from the scattered acoustic field with consideration of diffraction effects by utilizing approximations to the wave equation. Diffraction tomography received substantial theoretical treatment but with only a few researchers exploring medical applications for its potential to characterize tissue on the basis of physical properties. It is potentially able to account for the inherent diffraction in sound propagation and is not limited by assumptions of straight-line ray geometry. The method involves illuminating an object with ultrasound and measuring a set of scattered wave data around the object.

The approach described in this section used a wave-based diffraction tomography (DT) technique in a clinical prototype system developed in 1994 that addressed many of the shortcomings of previous work. It provided a large field of view (20 cm diameter) with high resolution ($\sim$1 mm) at low acoustic intensities ($<$10 mW cm^2), it was not strongly dependent on operator expertise, it provided a standardized sequential tomographic approach to surveying the entire breast, and it provided quantitative tissue properties in vivo. The methods of image

reconstruction employed were similar to previous diffraction tomography work in which the wave equation for the propagation of sound through a spatially variant medium is solved approximately (Kaveh et al. 1980; Devaney 1982; Wolf 1969). One significant difference is that this method acquired the 360° 2D scatter field around the object in a very short time interval plus it employed much lower frequencies (0.3–1.0 MHz) and continuous wave transmission. The researchers developed several approaches to image reconstruction that are closely tied to the annular array transducer configuration and data acquisition methods (André et al. 1995, 1996).

15.4.1 Clinical DT Prototype Design

This method of diffraction CT used steady-state sound to illuminate the medium from which the amplitude and phase of the scattered sound waves emanating from the medium and object were measured at the perimeter of the field. The system used much lower frequencies than were attempted previously by most researchers. By operating at 1 MHz and below, absorption and phase aberration are diminished permitting simplifications in image reconstruction. Cylindrical geometry of the transducer array allowed a compact design compared to plane-wave systems (Fig. 15.9). The transducer elements emitted a concentric cylindrical beam pattern that, together with the geometry of the receiver array, allowed transformation to a plane wave basis for efficient reconstruction. The toroidal array was designed to ensure adequate sampling of the entire 2D scattered field. The data acquisition system was capable of recording, digitizing at 30 MHz (12 bits) and storing a large amount of acoustic data quickly (<1 s at 0.5 MHz).

Fig. 15.9 Clinical DT prototype scanning system with annular array mounted on a vertical translation stage below a modified breast biopsy table. From André et al. (1997)

The patient scanning system is shown in Fig. 15.9 in which the cylindrical array is mounted below a modified breast biopsy table. Two separate arrays with 20 cm diameter were developed: 512 elements with center frequency at 0.5 MHz, and 1,024 elements with center frequency at 1.0 MHz. The entire measurement procedure is normally repeated at 10 discrete frequencies, ω_α ($\alpha = 1,2,\ldots,A$) where $A = 10$, spaced at 62.5 kHz intervals from 687 to 1.250 MHz for the 1,024 array. 20 discrete frequencies were typically used with the 512 array, spaced at 31 kHz from 300 to 600 kHz. The arrays had 60 % bandwidth and center frequencies of 1 and 0.4 MHz, respectively, in which the transducers were spaced evenly at slightly less than $\lambda_0/2$ (0.5 mm transducer width with 0.75 mm spacing for the 1 MHz array, 1.0 mm width and 1.5 mm spacing for the 0.5 MHz array). The elements were 12 mm in height to encourage a dipole ($\cos\theta$) pattern of wave propagation and were on a locus of a circle of radius 102 mm in both arrays. The transducers each act in turn as transmitter on a plane (r,θ), while the remaining elements act as receivers (Fig. 15.10). The z-direction is perpendicular to this plane. The full-width half-maximum of the slice sensitivity profile was approximately 8 mm across the field of view. The large 20 cm ring of transducers illuminated the tissue via a heated coupling bath (Fig. 15.9). The acoustic properties and temperature of the bath are adjusted to better match the acoustic properties of tissue and enhance penetration through the skin.

The transmitter is operated in one of two modes: (1) a continuous-wave mode in which single discrete frequencies (ω_α) were transmitted one at a time; (2) a broadband mode in which a periodic signal was used that is timed to repeat in concert with the receiver such that discrete frequency bands may be deconvolved from the measurements. The second procedure provides a rapid way to acquire the equivalent of many (usually 10 or more) discrete frequencies with a single transmission. The desired single- frequency waves are combined in the arbitrary waveform generator with varying phases between the different frequency cycles. This wideband signal was developed experimentally to maximize the peak-to-peak

Fig. 15.10 Annular transducer array geometry (**a**) for a cylindrical wavefront emitted by transducer k and received by transducer j. Water tank and array with cover removed (**b**)

transmitted energy at each frequency. The Fourier transform of this wideband signal is a comb-shaped pattern. The acquired information is in the form of an N × N complex matrix, $m_{jk}(\omega_\alpha)$ (j, k = 1,… N), for data acquired at in sonification frequency ω_α. A full set of receiver data for a complete transmit sequence is obtained in approximately 1 s for the 512 array (64 MB) and <3 s for the 1,024 array (128 MB). Detailed description of the data acquisition procedures is given in André et al. (1997).

15.4.2 DT Image Reconstruction

The complex amplitude, $m_{jk}(\omega_\alpha)$ (j, k = 1,… N), of the scattered acoustic wave measured at transducer k due to transmission from transducer j acquired for the medium may be described by the sound speed c(r, θ) and attenuation coefficient μ(r, θ) of the medium. The resulting image is based on the calculation of an approximation of the complex scattering potential, S^α(r, θ), at all locations (r, θ) throughout the slice of the medium (Fig. 15.10a). This algorithm has been described in detail elsewhere (André et al. 1995, 1996) but will be summarized here.

A solution to the wave equation due to single frequency illumination of the medium can be expressed in terms of a two-dimensional integral equation involving the complex scattering potential S^α(r, θ), the position of the transducers (r_0, θ), and the tabulated Hankel (H) and Bessel (J) functions (Devaney 1982), where the radiation pattern of the transducers is approximated well by a linear dipole such that

$$g(|r - r', \theta - \theta'|) = H_0^{(1)'}(k|\rho - \rho'|) \tag{15.1}$$

$g(|r - r', \theta - \theta''|)$ is the free-space Green's function, which describes a source transducer that acts as a dipole transmitter and receiver, ρ is density and k is the wave number. This takes the form

$$m_{jk}(\omega_\alpha) = \sum_{m,n}^{N} H'_m(k_0 r_0) H'_n(k_0 r_0) e^{-im\theta_j - in\theta_k} \int_V J_m(k_0 r) J_n(k_0 r) e^{i\theta(m+n)} S^\alpha(r, \theta) r dr d\theta \tag{15.2}$$

In the above equation, H_n' is the first derivative of the Hankel function of the integer order n representing the antenna pattern of the transmitter j, and H_m' represents the antenna pattern of receiver k. H_n' can be shown by Gegenbauer's addition theorem (Abramowitz and Stegun 1965; Devaney 1982) to be indicative of a dipole antenna pattern for both the transmitters and receivers. This antenna pattern has a complex dipole amplitude with a cylindrically symmetric phase and a magnitude in the imaging plane in the form of cos ϕ where ϕ is the angle from the vector normal to each transducer face. Different transducer radiation patterns may

be accommodated by substituting a weighted sum of monopole, dipole, etc., patterns or by using measured values. $J_m(k_0r)$ and $J_n(k_0r)$ are Bessel functions determined for all values r within the plane (r, θ). Equation 15.2 is derived in the Born approximation, which assumes that the medium is a weak scatterer of acoustic waves and induces small phase-shift variations in the incident wave front. Attenuation and phase shift in tissue are proportional to frequency; attenuation for breast tissue averages about 0.5 dB/cm/MHz while breast tissue exhibits fairly small fluctuations (±8 %) in sound speed. The use of frequencies lower than commonly employed in medical breast ultrasound, 0.5–1.5 MHz compared to 7–15 MHz, helps to constrain the breast properties to a range more appropriate for inversion techniques within range of the Born approximation as illustrated in the simple analysis of Fig. 15.11. The wave number, $k_0 = \omega/c_0$, was set to be the wave vector of the coupling fluid.

Several methods have been described to invert Eq. 15.2 but one of the most efficient methods is backpropagation that can be adapted to the specific geometry of the DT system. This may be viewed as beam forming in which a sound beam is formed in the medium by summing the set of N source transducers (j = 1,2,…,N), such that the signals add coherently at the point (r, θ).

The beam pattern of the transducer elements is removed by transforming the cylindrical data set into a form analogous to plane wave transmitters and receivers:

$$S_{pq}^{\alpha} = \left[\frac{1}{H_m'(k_0r_0)H_n'(k_0r_0)}\right]\sum_{j,k=1}^{N} m_{jk}(\omega_\alpha)e^{-\left(ip\theta_j - iq\theta_k\right)} \tag{15.3}$$

From reciprocity, we expect m_{jk} and S_{pq} to be symmetric matrices. At this point it is possible to filter S_{pq} to reduce the contribution from waves undergoing large diffraction. There is no preferred measurement direction in the transducer array so it can be shown that the convolution in the azimuthal domain is one dimensional such that

Fig. 15.11 Range of validity for the Born approximation at 0.5 and 1.0 MHz. At these frequencies up to 10 % variation in sound speed is accommodated for objects sizes up to the 20 cm diameter of the arrays (*red arrow*)

$$S_{pq}^{\alpha\prime} = \sum_{n} S_{p+n,q-n} C_n \tag{15.4}$$

where C_n are the filter coefficients in the azimuthal mode domain that simplify to

$$C_n = \frac{4\,k}{\pi} \frac{1}{1-4n^2} \tag{15.5}$$

The backpropagation reconstruction utilizes the filtered azimuthal mode data to obtain the scattering potential or object function $S^{\alpha}(r, \theta)$ in terms of a large azimuthally symmetric set of measured acoustic data $m_{jk}(\omega_\alpha)$, the known positions of the transducers, and tabulated Hankel functions. This process is summarized as follows. First compute the discrete two-dimensional Fourier transform of the filtered data:

$$\tilde{S}^{\alpha}(r,\theta) = \frac{1}{\Im_2\left\{\left[J_0(k_0 r)\right]^2\right\}} \Im_2 \left\{ \sum_{p,q=-N/2}^{N/2} J_p(k_0 r) J_q(k_0 r) e^{-i\theta(p+q)} S_{pq}^{\alpha\prime} \right\} \tag{15.6}$$

The discrete inverse two-dimensional Fourier transform of Eq. 15.6 recovers S^{α},

$$S^{\alpha}(r,\theta) = \Im_2^{-1}\left[\tilde{S}^{\alpha}(r,\theta)\right] \tag{15.7}$$

In Eq. 15.7, $\Im_2$ represents the two-dimensional Fourier transform operation: $g(\kappa, \phi) \equiv \Im_2\{f(r, \theta)\} \equiv f(r, \theta)e^{-i\kappa r\cos(\theta-\phi)}rdrd\theta$, and $\Im_2^{-1}$ represents the inverse Fourier transform: $f(r, \theta) \equiv \Im_2^{-1}\{g(\kappa, \phi)\} \equiv g(\kappa, \phi)e^{-i\kappa r\cos(\theta-\varphi)}\kappa d\kappa d\phi$. This algorithm produces an image or map of $S^{\alpha}(r, \theta)$ with a spatial bandwidth of $2k_0$, which is equivalent to a theoretical quantization limit of $\lambda/4$ or approximately 0.4 mm at 1 MHz in water. The basic steps of the image reconstruction process are shown in the flow chart of Fig. 15.12.

The reconstructed complex scattering potential $S^{\alpha}(r, \theta)$ given by Eq. 15.7 has a real part with an inverse quadratic dependence on the sound speed, $c(r, \theta)$, and an imaginary part with a linear dependence on the attenuation coefficient, $\mu(r, \theta)$. However, for the range of sound speeds found in breast tissue, the real part of $S^{\alpha}(r, \theta)$ can be linearized to reasonable accuracy. The linearized scattering potential, $I^{\alpha}(r, \theta)$, is given by:

$$I^{\alpha}(r,\theta) = -2\omega_{\alpha}^2 \left[\frac{\Delta c(r,\theta)}{c_0^3}\right] - i\omega_{\alpha}\Delta\mu(r,\theta) - \rho(r,\theta)^{1/2}\nabla^2\rho(r,\theta)^{-1/2} \tag{15.8}$$

In Eq. 15.8, $\Delta c(r, \theta) = c(r, \theta) - c_0$ and $\Delta\mu(r, \theta) = \mu(r, \theta) - \mu_0$, which are spatially dependent perturbations from the average sound speed, c_0, and attenuation coefficient, μ_0, of the entire medium including the object and coupling fluid. The attenuation coefficient represents energy loss mechanisms including absorption and scattering of acoustic energy out of the field of view of the transducers.

With this approach it was possible to define different ways of combining multiple reconstructed images $S^{\alpha}(r, \theta)$ acquired at different discrete frequencies ω_α

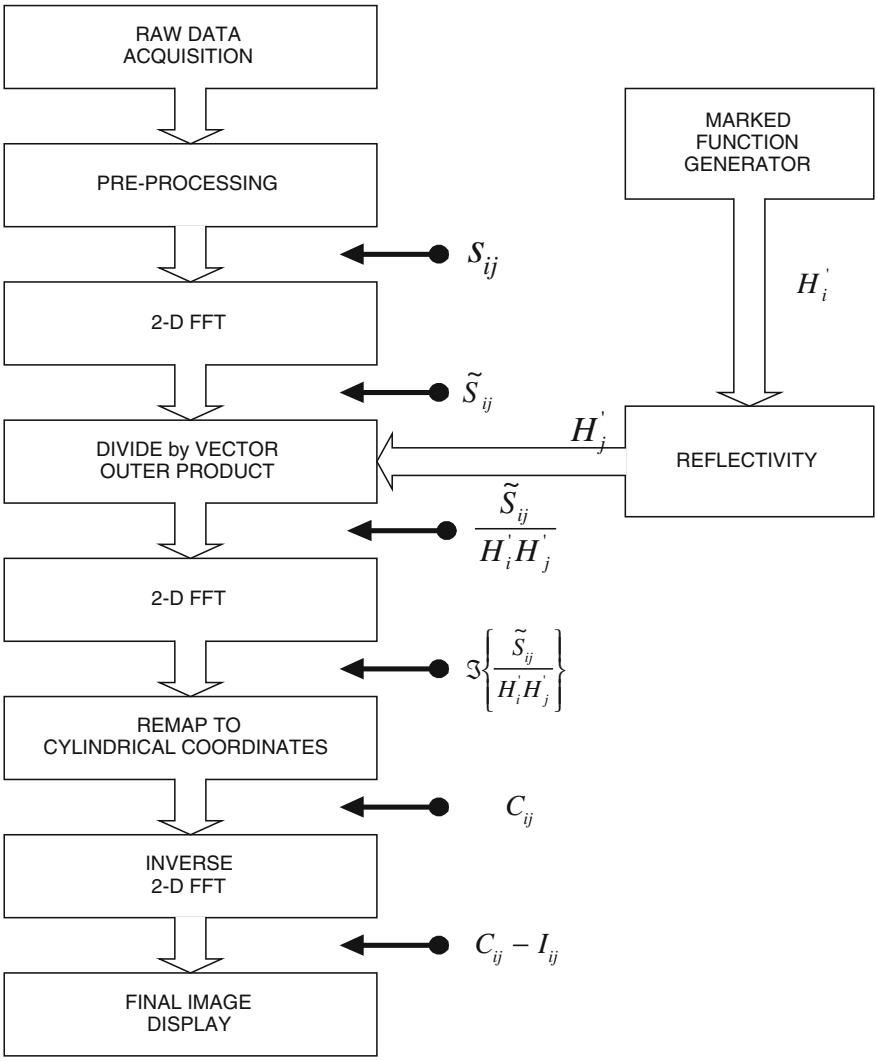

Fig. 15.12 Outline of the basic steps of image reconstruction

($\alpha = 1,2,\ldots,A$). The researchers found that summing the complex images $S^{\alpha}(r, \theta)$ or summing the magnitudes of these complex images reduces image artifacts due to reflections of acoustic energy from the receiver transducer faces and from multiple scattering events within the object being imaged.

As an extension to the above solution that is based in the Born approximation, they developed a hybrid reconstruction scheme that performs phase aberration correction to reduce distortion (André et al. 1997, 1996). This was accomplished by synthesizing pulse data at each point in the image field from a multiple-

frequency acquisition, summed as a Fourier series. These synthetic beams from all transmitters sequentially focus at each point in the object and then propagate back to all receivers. A time-of-flight map, $\tau(r, \theta)$, is calculated to each point in the object for each transmit–receive transducer pair and the attenuation of the pulse peak value relative to the background water bath is determined. These maps are essentially low-spatial frequency images of sound speed and attenuation. A phase correction, $e^{-j\omega\tau(r,\theta)}$, is applied to each single frequency backpropagation image, which results in higher spatial frequency images. The corrected single-frequency images were then summed to reduce aberration artifacts.

15.4.3 DT Results

Forty-five women, both symptomatic and asymptomatic, were successfully imaged with the DT system in a small pilot study. Images for an asymptomatic 65 year old patient with average density breasts were acquired at the same level with both arrays (Fig. 15.13). The real (sound speed), imaginary (attenuation) and scatter density components are displayed left to right. The images are frequency compounded from 330 to 640 kHz for the 0.5 MHz data (top row) and from 630 to 1,200 kHz for the 1 MHz array (bottom row). Fibroglandular tissues appear with bright signal while fat is dark.

A series of sequential tomographic slices for the left breast of a 42 year old subject are shown in Fig. 15.14 acquired with the 1 MHz array. Images were reconstructed from the nipple to maximum posterior level (bottom row to top) with 4 mm overlap at 10 mm intervals. The most posterior slices towards the chest wall in the top row show increasing amounts of retroglandular fat with diminishing bright signals from fibroglandular structures. Figure 15.15 shows polar plots of angular scatter data for the same subject acquired at 0.5 MHz for transmission from a single transducer at 0° acquired in the scan tank medium (a) and the medium plus breast scanned at approximately the middle of the breast (b). The data from this subject reveal high spatial frequency fluctuations that are believed to be acoustical signals possibly due to diffraction effects, multiple scattering and reflections. These data show significant attenuation and energy scattered at angles larger than those subtended by the breast. This suggests that such large-angle scattering is due to compressibility fluctuations, which gives rise to monopole terms. The patient had dense breast tissue on mammography (BI-RADS Category 3) with regions of very dense tissue, scattered microcalcifications but no abnormalities. The shape of scatter amplitude distribution was found to be closely represented by the Rayleigh distribution, suggesting a strong scattering condition. Other patient breasts with higher fat-gland ratios (BI-RADS 1 and 2) were found to exhibit relatively weaker scattering.

The advantages of summing data from multiple frequencies (10) is demonstrated in Fig. 15.16 for a 15 cm uniform saline phantom with sound speed of

Fig. 15.13 Images for a 65 yo patient with average density breasts acquired with both arrays. *Top row* was acquired with 1 MHz array, *bottom row* with 0.5 MHz array at approximately the same level in the breast

Fig. 15.14 Sequential series of images from a 42 yo subject with dense to very dense breast tissue. 1 MHz array

Fig. 15.15 Angular scatter distribution for the same subject with dense breast tissue (scattered fibroglandular density, BI-RADS 3). 0.5 MHz array

1,510 m/s. Non-uniformity is suppressed, the maximum effect of which occurs with frequency separation $\Delta\omega < c_0/D$, where c_0 is the average sound speed in the medium + object, D is the diameter of the field of view, and the total frequency range should be as large as possible. This image was acquired with the 0.5 MHz array.

Tissue contrast (relative units) compared to the water bath medium for sound speed images was measured in eight patients and is plotted in Fig. 15.17. Fat presents low values, fibroglandular tissues that are high in collagen show intermediate to higher sound speed values while the few cancerous masses all had very high values. In phantoms, the minimum sound speed sensitivity was found to be 0.5 %, which provides excellent performance.

Fig. 15.16 Images from the 0.5 MHz array for a 15 cm diameter saline-filled phantom showing artifact reduction with 10-frequency averaging (*right image*)

Fig. 15.17 Relative sound speed contrast for fat, fibroglandular (parenchyma) and confirmed cancer masses measured in eight patients

In general, the results of this work demonstrated a DT system sufficiently fast to be practical for clinical research. Image quality was promising despite artifacts inherent with coherent imaging methods and the low transmit power. The system design allowed simplifications in the algorithms for more efficient computation necessary with available computing resources and the researchers developed iterative methods to reduce aberrations and extend the limits imposed by the Born approximation. It was found to provide reproducible sound speed contrast but the methods used to achieve this reduced the accuracy of the attenuation (imaginary) component. It was concluded that the 2D geometric approximations in the algorithms as well as the inability to acquire signals scattered out of plane were significant limitations on performance.

15.5 Inverse Scatter Tomography (IST)

The third stage of development is the introduction of true wave equation based methods, not linear perturbation approximations, as models of ultrasound wave propagation (Berg et al. 2012; Carson and Fenster 2009). The wave equation approach described in this section provides a non-linear model of considerable accuracy, compensates for multiple scattering and provides uniform resolution throughout the image plane. This model is inverted by an iterative simultaneous determination of the breast tissue parameters and internal total fields (Fig. 15.18). Until recently, the mathematical and technical challenges for full-wave 3D IST were so complex that practical results in humans were not realized.

Fig. 15.18 General principle of inverse scatter algorithm

To achieve a solution of the inverse scattering problem the algorithm implements a fast forward solver and concomitant methods for large scale ($\sim$20 million unknowns) minimization of a functional F. The minimization is based on the Ribiere-Polak version of nonlinear conjugate gradients and therefore requires a fast way to calculate the gradient of F and the step length. The inversion algorithm is based on a type of approximate factorization of the Helmholtz wave equation that leads to a form of the phase screen approach (U.S. Patent No. 6,636,584). To solve the numerically ill-conditioned problem of full-wave inversion, increasing discrete frequency data are used and the number of iterations can be reduced by preconditioning to a practical level of 5–8 to achieve a 5 % residual. The method does not account for density variations but for scatter in the forward direction this approximation has proven reasonable. Detailed description of the 2D and 3D IST algorithm is published elsewhere (Borup et al. 1992; Wiskin et al. 2007, 2011, 2012; Johnson et al. 2007).

15.5.1 IST Theory

The attainment of an inversion or imaging algorithm that utilizes the full waveform and the inherent nonlinearity of the inversion process in a potentially useful time frame has been lacking. Furthermore, for medical application the inversion should take place on a computational engine that can accompany the data acquisition device, and be reasonably inexpensive, if the device is to be clinically useful as a self-contained device.

The inverse scattering algorithm is based on the minimization of the functional F, a function of the object function $\gamma(\mathbf{x}) \equiv (1/k_o)(k(\mathbf{x}) + i\alpha(\mathbf{x}))$ where $k_o \equiv \omega/c_o$ and $k(\mathbf{x}) \equiv \omega/c(\mathbf{x})$ are the wave-numbers in water and inhomogeneous tissue, respectively, at frequency $\omega = 2\pi f$ and α is the attenuation coefficient in Np/mm.

$$\min F_{\omega_j}(\gamma(\mathbf{x})) = \min \frac{1}{2} \sum_{\substack{\theta=1,\ldots N_{views} \\ l=1,\ldots,N_{levels}}} \overline{\mathbf{r}^l_{\omega_j\theta}(\gamma)} \mathbf{r}^l_{\omega_j\theta}(\gamma) \tag{15.9}$$

at successive frequencies, ω_j, $j = 1, \ldots N_{freq}$. We proceed from low frequencies to high frequencies to avoid local minima. We image at 0.35, 0.4, 0.45, 0.5, 0.6, 0.7, and 0.8 MHz successively for the 2D case, and 0.5, 0.6, 0.7, 0.8, 0.9, 1.0, 1.1, 1.2, and 1.25 MHz successively for the 3D volume image. The vectors

$$\mathbf{r}^l_{\omega\theta}(\gamma) \equiv \left(\hat{\mathbf{d}}^l_{\omega\theta}(\gamma) - \mathbf{d}^l_{\omega\theta} \right) \in C^{N_R} \tag{15.10}$$

represent the residual between the predicted field, $\hat{\mathbf{d}}^l_{\omega\theta}(\gamma)$, and the measured field, $\mathbf{d}^l_{\omega\theta}$, at each receiver position, for each transmitter position, θ, level l, and at the fixed frequency ω. Note that this functional involves all views and all levels simultaneously; that is, it is a true 3D algorithm.

The algorithm at the highest level is described in (Wiskin et al. 2007). It is a series of updates to γ. $\gamma^{(n+1)} = \gamma^{(n)} + \alpha_n \mathbf{d}_n$, where the descent direction $\mathbf{d}_n \equiv -\mathbf{g}_n + \beta_n \mathbf{d}_{n-1}$, and where $\mathbf{g}_n$ is the gradient, β_n is the Ribiere-Polak coefficient ($\beta_0 = 0$),

$$\beta_n \equiv \frac{(\mathbf{g}_n - \mathbf{g}_{n-1})^T \mathbf{g}_n}{\|\mathbf{g}_{n-1}\|^2} \tag{15.11}$$

and α_n is the step-length. The calculation of the step-length and the gradient are detailed below.

15.5.1.1 Initial Estimates

Due to the minimization nature of the algorithm an initial estimate is required. First a time of flight algorithm is used to create a series of initial distributions for speed of sound and attenuation *at each level.* These initial estimates are used in a series of 2D inverse scattering algorithms to create a series of 2D inverse scattering images at each level, which are the distributions that minimize the functional for *one particular level, l.* These 2D images are then concatenated together to form a 3D volume. The 3D volume is the *starting estimate* for the full 3D inverse scattering algorithm. The 3D algorithm is required to account for energy that is refracted or scattered out of plane; when ignoring these signals, the 2D-algorithm gives an anomalously high result for the attenuation estimate.

15.5.1.2 Forward Problem

As mentioned above, a very fast solution of the forward problem is required. To achieve this we rewrite the Helmholtz equation (15.44):

$$\frac{\partial^2 p(\mathbf{x})}{\partial x^2}+\frac{\partial^2 p(\mathbf{x})}{\partial y^2}+\frac{\partial^2 p(\mathbf{x})}{\partial z^2}+(k(\mathbf{x})+i\alpha(\mathbf{x}))^2 p(\mathbf{x})=0 \tag{15.12}$$

$$\text{as} \qquad [(A+iB)(A-iB)-i[B,A]]p(\mathbf{x})=0 \tag{15.13}$$

where: $A \equiv \frac{\partial}{\partial x}$, is a partial differential operator, and $B \equiv \sqrt{\frac{\partial^2}{\partial y^2}+\frac{\partial^2}{\partial z^2}+k^2(x,y,z)}$ is a pseudo-differential operator. $[B,A]$ is the commutator of these operators.

Under the assumption that this commutator can be ignored, we can approximately 'factor' the Helmholtz equation to yield (15.4):

$$\frac{\partial}{\partial x}p(x,\mathbf{r}_\perp)=i\mathbf{H}(x,\mathbf{r}_\perp)p(x,\mathbf{r}_\perp) \tag{15.14}$$

a 'Schroedinger' equation in 'time' x, with the unusual "Hamiltonian",

$$\mathbf{H}(x,\,\mathbf{r}_\perp)=\sqrt{\frac{\partial^2}{\partial y^2}+\frac{\partial^2}{\partial z^2}+k^2(x,\,y,\,z)} \tag{15.15}$$

in transverse co-ordinates $\mathbf{r}_\perp \equiv (y,z), x$ (the direction of propagation) plays the role of time.

A symbolic solution for the propagator from initial state (wave field) at x_o to final state (wave field) at x, is given as the phase-space path integral:

$$\left\langle p(x,\mathbf{r}_\perp)\middle|p\left(x^o,\mathbf{r}_\perp^o\right)\right\rangle=\int D\mathbf{r}_\perp(x)\int D\mathbf{p}_\perp(x)e^{iS(\mathbf{r}_\perp,\mathbf{p}_\perp)} \tag{15.16}$$

with "action", $S(\mathbf{r}_\perp,\mathbf{p}_\perp)\equiv\int_{x^o}^{x}dx\left(\mathbf{p}_\perp\frac{d\mathbf{r}_\perp}{dx}-\mathbf{H}(x,\mathbf{r}_\perp,\mathbf{p}_\perp)\right)$.

Discretizing the 'time' from x_o to x, $x_0<x_1<\cdots<x_{N-1}<x_N<x_{N+1}=x$, and utilizing standard properties of the exponential gives for the propagator:

$$\prod_{j=1}^{N}\int d\mathbf{p}_j e^{i\mathbf{r}_{j+1}\mathbf{p}_j}e^{-i\mathbf{H}\left(x,\mathbf{r}_j,\mathbf{p}_j\right)\Delta x}\int d\mathbf{r}_j e^{-i\mathbf{r}_j\mathbf{p}_j} \tag{15.17}$$

We approximate this with the following form of the propagator acting on the initial field at x_o: $p\left(x_o,\mathbf{r}_o^\perp\right)$, to give the total field at the receivers:

$$p\left(x_N,\mathbf{r}_N^\perp\right)=\prod_{j=1}^{N}t\left(x_j,\mathbf{r}_\perp\right)\odot\mathbf{F}^{-1}P\odot\mathbf{F}p\left(x_o,\mathbf{r}_o^\perp\right) \tag{15.18}$$

The $\odot$ indicates element-wise multiplication of two matrices: i.e. if $A_{\lambda\mu}$, $P_{\lambda\mu}$ are components of 2D matrices, $(P\odot A)_{\lambda\mu}\equiv\left(P_{\lambda\mu}A_{\lambda\mu}\right)$. F indicates Fourier Transform. P is the 2D matrix with elements, $P_{\lambda\mu}\equiv e^{i\varepsilon\sqrt{k_0^2-(\lambda\Delta_k)^2-(\mu\Delta_k)^2}}$, ε is step length in x, Δ_k is step length in transform space: k_y, k_z, and

$$t\left(x_j,\mathbf{r}_\perp\right)\equiv t_j(y,z)\equiv e^{i\varepsilon\left(k\left(x_j,y,z\right)-k_0\right)}\equiv e^{i\varepsilon k_0\left(\gamma\left(x_j,y,z\right)-1\right)} \tag{15.19}$$

is the "phase mask" element-wise multiplication operator discussed in U.S. Patent No. 6,636,584.

15.5.1.3 Gradient of the Functional *F*

The Polak-Ribiere version of the nonlinear conjugate gradient algorithm requires the gradient of functional *F:*

$$\frac{\partial}{\partial\overline{\gamma}}F(\gamma)=\sum\nolimits_{l\theta}\left(\overline{\frac{\partial}{\partial\gamma}\mathbf{r}_{l\theta}}\right)^{T}\mathbf{r}_{l\theta}\equiv\overline{J}_{\omega}^{T}\mathbf{r} \tag{15.20}$$

where $J\equiv\frac{\partial\mathbf{r}_{l\theta}}{\partial\gamma}$ is the Jacobian operator. This is obtained in the following manner. $\delta\gamma_j^{\omega\theta}=\mathbf{v}_j\odot f_{\mathbf{r}_{\omega\theta}}^{j}$ is the contribution to the gradient, from view angle θ and *x-coordinate,* x_j. It is the point-wise product of two 2-dimensional arrays of size (N_y, N_z). viz., $\mathbf{v}_j\equiv\mathbf{F}^{-1}P\odot\mathbf{F}p\left(x_{j-1},\mathbf{r}_{j-1}^{\perp}\right)$, the total field at propagation distance *j−1,* propagated through water, to propagation distance *j*. $f_{\mathbf{r}_{\omega\theta}}^{j}$ is the field at x_j, resulting from treating all receivers, at tomographic view angle θ, as transmitters, at frequency ω. The strength of each 'transmitter' is: $f_{\mathbf{r}_{\omega\theta}}^{N}\equiv\overline{\delta\mathbf{f}}_N$, i.e., the difference between the measured and predicted fields at the receivers, and we recursively define $f_{\mathbf{r}_{\omega\theta}}^{j}=\mathbf{F}^{-1}\overline{P}\odot\mathbf{F}\overline{\mathbf{t}}_j f_{\mathbf{r}_{\omega\theta}}^{j+1}$, for $j=N-1,\ldots,0$.

15.5.1.4 Step Length Calculation for Ribiere-Polak Conjugate Gradients

Step length $\alpha_n\approx\frac{\mathbf{g}_n^T\mathbf{d}_n}{\|J_n\mathbf{d}_n\|^2}$, $\mathbf{d}_\mathrm{n}$ is the RP descent direction. $\mathbf{g}_n$ is the gradient of the functional *F,* and $J\equiv\frac{\partial\mathbf{r}_{l\theta}}{\partial\gamma}$is the associated Jacobian.

The action of the Jacobian on the descent direction is given by

$$J_n\mathbf{d}_n=\left[\frac{\partial\mathbf{r}_{l\theta}}{\partial\gamma}\right]\mathbf{d}=\delta\mathbf{p}_N \tag{15.21}$$

where: $\delta\mathbf{p}_j=\mathbf{A}\mathbf{p}_{j-1}\odot\delta\mathbf{t}_j+t\left(x_j,\mathbf{r}_{\perp}\right)\odot\mathbf{A}\left(\delta\mathbf{p}_{j-1}\right)$, $j=1,..,N$, and where $\mathbf{A}\equiv\mathbf{F}^{-1}P\odot\mathbf{F}$ propagates a field a distance ε through water, and $\delta\mathbf{t}_j\left(\mathbf{r}^{\perp}\right)\equiv i\varepsilon k_0\mathbf{t}_j(y,z)\delta\gamma\left(x_j,y,z\right)$ from the definition of the phase mask $\boldsymbol{t}_\mathrm{j}$.

Having determined the step length and descent direction the update is given by

$$\gamma^{(n+1)}=\gamma^{(n)}+\alpha_n\mathbf{d}_n \tag{15.22}$$

15.5.2 IST/RT Scanner

A practical scanner employing IST imaging was developed by Techniscan Medical Systems (now by CVUS LLC, Salt Lake City, UT) (Greenleaf et al. 1974, 1975, 1978; Glover and Sharp 1977). The current scanner that is the subject of this section was employed in clinical research at the University of California, San Diego (UCSD), Mayo Clinic, Rochester, MN, and University of Freiburg, Germany to evaluate clinical feasibility of using IST and RT to analyze and detect breast masses as well as monitor changes due to therapies. All of the data presented here are from UCSD where the majority of the work was done.

The TMS scanner (Fig. 15.19) provides an automated, standardized scan of the whole breast nearly independent of operator expertise. The patient lies prone with her breast pendant but docked to a retention rod in a controlled 31 °C water bath within the field of view of several transducer arrays. The IST transmitter and receiver array rotate around 360° to collect 180 tomographic views of ultrasound wave data (Fig. 15.20). The transmitter emits broad-band planar pulses (0.3–2 MHz) while the receiver array, comprised of 1,536 elements in 8 vertical rows, digitizes the time signal. Total scan time is ∼10–20 s per level, ∼8 min for the average breast. 3D transmission and aberration-corrected RT reconstructions are accomplished in ∼40 min employing 2 nVidia GPUs for a portion of the process.

Fig. 15.19 IST/RT scanner with transducer arrays in water tank

Fig. 15.20 IST/RT transducers arrangement. 1, 2, 3 are the reflection transceivers coincident with the transmission arrays

15.5.3 Reflection Tomography (RT)

The scanner includes a set of three transceiver arrays that are coincident with the transmission arrays to simultaneously acquire conventional B-scan data. The arrays have bandwidths of ~2–8 MHz and are focused at depths of 2.5, 4.0 and 7.5 mm to provide complete depth of coverage of the breast. The three coincident RT arrays (3.6 MHz center frequency, 80 % bandwidth) spaced at 48° are angled upward at 12° to access the chest wall. A high-resolution RT algorithm was developed that utilizes the sound speed image to correct for refraction and attenuation images to adjust amplitude along the ray. The resulting backprojected RT image is a 360° B-scan image compounded from 60 views. The speed of sound and attenuation images resulting from the 3D inverse scattering algorithm are used to correct for refraction effects in the reflection algorithm. The canonical ray-tracing equations derived from the eikonal equation

$$\frac{d}{ds}\left(n\frac{d\mathbf{r}}{ds}\right) = \nabla n,\ n(\mathbf{x}) = c_o/c(\mathbf{x}) \tag{15.23}$$

are solved to give the energy path corrected for refraction due to speed variation. The attenuation images are used to adjust the displayed amplitude of the back-scattered energy along the computed ray.

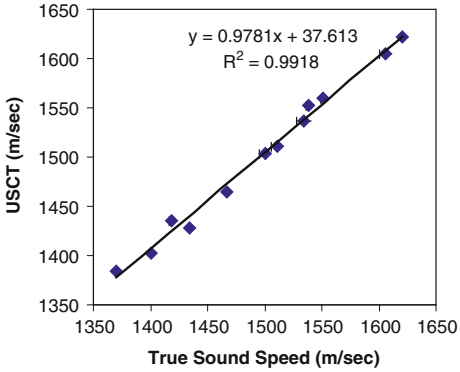

Fig. 15.21 Measured sound speed accuracy. Minimum detectability is ~7.5 m/s

15.5.4 IST and RT Results

15.5.4.1 Scanner Performance

2D reconstruction is completed in seconds, while the full 3D reconstruction is accomplished in ~24 min for average size breast using 2 GPUs. Image quality is excellent with resolution measured as FWHM of LSF of 0.8 mm for RT and 1.5 mm for IST. As shown in Fig. 15.21 sound speed detectability is 7.5 m/s and is highly linear from 1,325 to 1,700 m/s ($R^2 = 0.992$). Sound speed is a function of tissue stiffness, analogous to but not equal to bulk modulus. Attenuation tomograms are a function of tissue structure and composition while providing image contrast over a wide range (0–4 dB/cm/MHz) to assist in classification of masses.

Reflection tomography provides approximately twice the in-plane resolution as the transmission IST images as expected from theory. Image artifacts from compounding 60 views during 360° rotation are greatly reduced by the refraction

Fig. 15.22 Breast shaped urethane phantom scanned and reconstructed with RT algorithm. The *right image* is with refraction correction using the IST sound speed map while the *left image* is without

correction as shown in Fig. 15.22 for a urethane phantom with a range of inclusions (breast size and shape but not entirely tissue equivalent).

15.5.4.2 Patient Study Population

Female patients recruited to the IRB-approved protocol were referred for a diagnostic breast sonogram as the result of prior findings on mammography, physical exam or previously known conditions. The purpose of the study was to measure a range of tissue properties in women with widely varying breast sizes and mammographic densities, to assess reproducibility of findings and to examine depiction and quantitative properties of masses confirmed by biopsy for suspicious lesions or long-term follow-up for benign findings in comparison to hand-held sonography. The statistical design was to assess equivalence to sonography (93 % power).

15.5.4.3 Clinical Evaluation

Although more than 450 patients have been scanned with versions of IST in the past 5 years, under the current IST/RT protocol 172 patients with an age range of 19–78 years were scanned by the end of 2011, including thorough validation with other clinical findings and long-term follow-up (André et al. 2008; Wiskin et al. 2011; Callahan et al. 2007). The distribution of lesions imaged is as follows: 21 % simple cysts, 17 % complicated cysts, 36 % various solid benign, 26 % cancers, 12 no findings. By study design, this mix of cases very closely matched the three-year average of cases in the UCSD diagnostic breast imaging clinic. Mass sizes ranged from 2–39 mm and there was good agreement in size ($R^2 = 0.7$) between sonography and IST. Not surprisingly, the 3D representation of IST allowed a more accurate representation of the maximum mass diameter where sonography normally only reports radial and anti-radial dimensions. Even more importantly, for 13 patients who also had contrast enhanced MRI there was nearly perfect agreement of size, shape and margins to the IST sound speed images. This high correlation to MRI, which presently serves as the standard for delineating the margins and extent of cancerous breast masses, is a promising opportunity for IST to impact patient care with a much less expensive, less invasive but equivalent imaging modality.

The general quantitative IST attributes of masses can be summarized as follows:

- Simple cysts: low sound speed compared to water, low attenuation
- Complicated cysts: low to intermediate sound speed compared to water, low attenuation
- Solid benign masses: higher sound speed and attenuation
- Malignancies: highest sound speed and attenuation

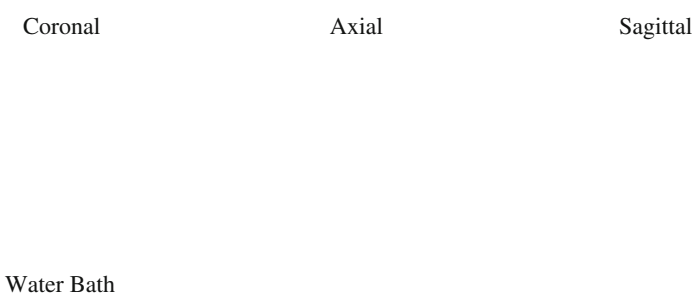

Fig. 15.23 Simple cyst in the right breast

The highest sound speed values that were measured in any patient were all associated with malignant masses, never with normal structures or benign masses. In addition, the three sets of IST/RT images provide reproducible information about mass shape, margins, volume, architectural distortion, texture, relative echogenicity, etc.

A sample of the range of findings found in patients is presented in the following sections. Images are usually presented to the Radiologist in rows with sound speed at the top in vertical columns of coronal, axial and sagittal views from left to right as shown in Fig. 15.23.

15.5.4.4 Research Subject: Simple Cyst

The patient is a 57 year-old female with history significant for profound nipple discharge of the left breast. The images in Fig. 15.23 above are of the right breast, which had a negative biopsy five years prior to the IST scan. The patient complained of a palpable abnormality on the right lasting for approximately one month. A mass was detected in the retroareolar region on mammography and was confirmed by sonogram to be cystic. USCT shows a large mass with distinct margins readily seen just posterior to the nipple. The sound speed values of the mass (upper row Fig. 15.23) are slightly higher (1,540 m/s) than that of water (1,510) while the attenuation images show a black void representing low attenuation values consistent with that of fluid ($\sim$0 dB/cm) (Fig. 15.23).

Fig. 15.24 Biopsy confirmed fibroadenoma, palpable mass at 3:00, 5 cm from nipple, 10 mm solid

15.5.4.5 Research Subject: Benign Fibroadenoma

In this case a 40 year old subject had a persistent biopsy-confirmed fibroadenoma in the left breast that was followed with a series of diagnostic sonograms. The mass was 10 mm, it was hypoechoic on sonography with posterior shadowing, distinct margins consistent with a solid mass, and it was found 5 cm from the nipple at the 3:00 position (Fig. 15.24). On IST/RT (Fig. 15.25) the mass is seen at 3:00, 8 × 9 × 6 mm diameter with intermediate sound speed (1,560 m/s), intermediate attenuation (1.6 dB/cm/MHz), and hypoechoic with distinct margins on RT.

15.5.4.6 Research Subject: Invasive Ductal Carcinoma

This case was of a 33 year old woman, with no family history of cancer, seen for a lump or thickening of the breast. Mammography (Fig. 15.26, left) showed a heterogeneously dense, spiculated 2 cm mass with malignant-appearing micro calcifications in the left breast in the middle outer quadrant. The sonogram (Fig. 15.26, right) shows at the 1:00 position in the breast, 2 cm from the nipple an irregular, heterogeneous, highly suspicious mass with angular margins and abrupt interface, 1.9 × 1.2 cm in diameter. Biopsy confirmed it was invasive ductal carcinoma.

The IST sound speed and RT images (Fig. 15.27) show the mass at 1:00 in the coronal view, 2.2 × 1.1 × 1.6 cm, corresponding well to the measurements by sonogram. The mass has very high sound speed (mean 1,570 m/s), bright compared to water, high attenuation (2.3 dB/cm/MHz) and appears hypoechoic with spiculated margins and irregular shape on RT with architectural distortion similar

Fig. 15.25 UST images with sound speed on the *top row*, attenuation on the middle row, reflection tomography on the *bottom row*. The fibroadenoma is seen as a mass, marked by the *red cross* hairs, with high sound speed at 3:00 on the coronal view, intermediate attenuation and hypoechoic on the reflection tomogram

Fig. 15.26 Mammogram (*left*), sonogram (*right*)

to the mammogram. Precisely as the IST/RT images, the coronal T1-weighted contrast-enhanced MRI (Fig. 15.28, right) showed a mass in the same location with dimensions 2.1 × 1.7 × 1.8 cm. The fluid-filled void from the core biopsy is visible in both sound speed and MR images.

Fig. 15.27 Sound speed IST in *upper row*, RT *lower row*. Coronal (*left*), cranio-caudal (*middle*), sagittal (*right*)

Fig. 15.28 RT (*left*), sound speed (*middle*), T1 weighted MRI (*right*)

As shown in Fig. 15.29, normal tissues and masses may be characterized by their acoustic properties. Fatty normal tissues (indicated by unfilled diamonds) are consistently very low sound speed with lower attenuation, therefore, fatty tissues appear dark on sound speed and attenuation images. Fibroglandular tissues (shown by the clear triangles) have intermediate sound speed and attenuations values. Simple cystic masses (shown by green circles) have consistently low attenuation with intermediate sound speed close to that of water, while complex cystic masses (shown by the blue circles) are higher in attenuation. Solid benign masses such as fibroadenomas (shown by the purple triangles) are wide ranging in sound speed.

To date, cancers (shown by the red squares) have shown both high sound speed (highest sound speed values ever measured were confirmed cancers) and high

Fig. 15.29 Summary of results for sound speed vs. attenuation values for normal tissues in 75 subjects. Data for the three sample cases above are indicated by the *red*, *blue* and *green boxes*

attenuation. Clearly there is some overlap in the acoustic properties of masses, but these data show promise that the quantitative WBU images may be helpful in differentiating masses.

A 98 % agreement that a mass was present in the correct location was found between IST/RT and sonography. It was determined from comparison to mammography and physical exam that three masses were outside the field of view of IST, either immediately at the chest wall or in the upper outer quadrant in the axillary tail. No statistically significant differences were observed between the two modalities in terms of sensitivity and specificity.

15.5.5 Summary

The attributes of whole breast IST and RT present the following potential clinical advantages: (1) operator independence with automated scanning, (2) true anatomic breast positioning, i.e., no breast compression or distortion, (3) no ionizing radiation, (4) true quantitative 3D imaging algorithms (not just stacked 2-D images), (5) accurately registered 3D IST and RT images, (7) global views of both breasts for detailed contralateral and serial comparisons, and (8) ability to provide quantitative tissue characteristics that have thus far, not been available in medicine. These characteristics provide unique advantages in the clinical setting for applications including, but not limited to, repeat breast imaging that is safe and cost-effective, whole-breast screening for high-risk women, young women or women with dense breasts, accurate volumetric analysis for detailed surgical planning, and monitoring over time of response to surgery and therapy.

15.6 Conclusion

USCT has long history so it is a fair question to ask if the technology will soon be ready for clinical use. The image quality, speed and performance of the IST/RT scanner described in Sect. 2.5 appear to be suitable and practical enough to play a role in breast cancer detection, diagnosis and management. Certainly in the very near future it will be ready for thorough objective clinical testing and with clinical success may come commercial viability. In addition, a new scanner is imminent from Delphinus Medical Technologies (Detroit, MI) that encompasses many design changes over the early prototype described in (Duric et al. 2005, 2006, 2007), which should lead to significant improvements in image quality. It is an interesting and important time for USCT, with perhaps an opportunity to finally advance from the laboratory to routine clinical use.

Acknowledgments We gratefully acknowledge the support and contributions of Melissa Ledgerwood, B.S., Melanie Aiken, B.A., Laura Brogoch, B.S., Karleen Callahan, Ph.D. and the National Institutes of Health, National Cancer Institute SBIR Program and Academic-Industry Partnership Program.

References

Abramowitz A, Stegun I (1965) Handbook of mathematical functions. Dover Publications, New York, p 363

ACR (2011) Practice guideline for the performance of a breast ultrasound examination. American College of Radiology, Reston

American Cancer Society (2011). Breast cancer facts & figures 2011–2012. American Cancer Society, Inc, Atlanta

Andre MP, Galperin M, Berry A, Taylor A, Ojeda-Fournier H, O'Boyle M, Olson L, Comstock C (2011) Performance of a method to standardize breast ultrasound interpretation using image processing and case-based reasoning. Acoust Imaging 30:3–10

André MP, Martin PJ, Otto GP, Olson LK, Barrett TK, Spivey BA, Palmer DA (1995) A new consideration of diffraction computed tomography for breast imaging: Studies in phantoms and patients. Acoust Imaging 21:379–390

André MP, Janée HS, Otto GP, Martin PJ, Jones P (1996) Reduction of phase aberration in a diffraction tomography system for breast imaging. Acoust Imaging 22:151–157

André M, Janee H, Otto G, Martin P (1997) High speed data acquisition in a diffraction tomography system with large-scale toroidal arrays. Int J Imaging Syst Technol 8(1):137–147

André M, Barker C, Sekhon N, Wiskin J, Borup D, Callahan K (2008) Pre-clinical experience with full-wave inverse scattering for breast imaging: sound speed sensitivity. Acoust Imaging 29:73–80

Baker J, Kornguth P, Soo M et al (1999) Sonography of solid breast lesions: observer variability of lesion description and assessment. AJR 172:1621–1625

Berg W, Blume J, Cormack J et al (2006) Operator dependence of physician performed whole breast US: lesion detection and characterization. Radiology 241:355–365

Berg WA, Blume JD, Cormack JB et al (2008) Combined screening with ultrasound and mammography vs mammography alone in women at elevated risk of breast cancer. JAMA 299:2151–2163

Berg W, Cosgrove DO, Doré CJ et al (2012a) Shear-wave elastography improves the specificity of breast US: The BE1 multinational study of 939 masses. Radiology 262(2):435–449

Berg W, Zhang Z et al (2012b) Detection of Breast Cancer with addition of annual screening ultrasound or a single screening mri to mammography in women with elevated breast cancer risk. JAMA 307(13):1394–1404

Borup DT, Johnson SA, Kim WW, Berggren MJ (1992) Nonperturbative diffraction tomography via Gauss-Newton iteration applied to the scattering integral equation. Ultrason Imaging 14(1):69–85

Brogoch L, André M, Ledgerwood M, Ojeda-Fournier H et al (2010) Reader variability and predictive value of breast imaging reporting and data system descriptors for lesions in breast sonography. J Ultrasound Med 29:S47

Callahan KS, Borup DT, Johnson SA, Wiskin J, Parisky Y (2007) Transmission breast ultrasound imaging: representative case studies of speed of sound and attenuation of sound computed tomographic images. Am J Clin Oncol 30(4):458–459

Carson PL, Fenster A (2009) Anniversary paper: evolution of ultrasound physics and the role of medical physicists and the AAPM and its journal in that evolution. Med Phys 36(2):411–428

Carson P, Meyer C, Scherzinger A, Oughton T (1981) Breast imaging in coronal planes with simultaneous pulse-echo and transmission ultrasound. Science 214:1141–1143

Carson PL, Scherzinger AL, Bland PH, Meyer CR, Schmitt RM, Chenevert TL, Bookstein FL, Bylski DI, Silver TM (1983) Advanced ultrasonic imaging for breast cancer diagnosis. In: Jellins J, Kobayashi T (eds) Ultrasonic Examination of the Breast, pp 187–199

Devaney A (1982a) Inversion formula for inverse scattering within the Born approximation. Opt Lett 7:111–112

Devaney A (1982b) A filtered backpropagation algorithm for diffraction tomography. Ultrason Imaging 4:336–350

Duric N, Littrup P, Babkin A, Chambers D, Azevedo S, Kalinin A, Pevzner R, Tokarev M, Holsapple E, Rama O, Duncan R (2005) Development of ultrasound tomography for breast imaging: technical assessment. Med Phys 32(5):1375–1386

Duric N, Littrup PJ, Rama O, Holsapple ET (2006) Computerized ultrasound risk evaluation CURE: first clinical results. Acoust Imaging 28:177–185

Duric N, Littrup P, Poulo L, Babkin A et al (2007) Detection of breast cancer with ultrasound tomography: first results with the computed ultrasound risk evaluation prototype. Med Phys 34(2):773–785

Glover GH (1977) Computerized time-of-flight ultrasonic tomography for breast examination. Ultrasound Med Biol 3(2–3):117–127

Glover G, Sharp J (1977) Reconstruction of ultrasound propagation speed distributions in soft tissue: time of flight tomography. IEEE Trans Sonics Ultrason SU-24:229–234

Greenleaf J, Bahn R (1981) Clinical imaging with transmissive ultrasonic computerized tomography. IEEE Trans Biomed Eng BME-28(2):231

Greenleaf J, Johnson S, Lee SL et al (1974) Algebraic reconstruction of spatial distributions of acoustic absorption in tissue from their two-dimensional acoustic projections. Acoust Holography 5:591–603

Greenleaf J, Johnson S, Samayoa W, Duck F (1975) Algebraic reconstruction of spatial distributions of acoustic absorption in tissue from their two-dimensional acoustic projections. Acoust Holography 6:71–90

Greenleaf JF, Johnson SA, Lent AH (1978) Measurement of spatial distribution of refractive index in tissues by ultrasonic computer assisted tomography. Ultrasound Med Biol 3(4):327–339

Hiller D, Ermert H (1980) Tomographic reconstruction of B-scan images. Acoust Imaging 10:347–364

Hong A, Rosen E, Soo M et al (2005) BI-RADS for sonography: Positive and negative predictive values of sonographic features. AJR 184(4):1260–1265

Howlader N, Noone AM, Krapcho M et al (eds) (2011) SEER cancer statistics review, 1975–2008. National Cancer Institute, Bethesda http://seer.cancer.gov/csr/1975_2008/, based on Nov 2010 SEER data submission, posted to the SEER web site

Johnson S, Abbott T, Bell R, Berggren M, Borup D et al (2007) Non-invasive breast tissue characterization using ultrasound speed and attenuation: in vivo validation. Acoust Imaging 28:147–154

Kaveh M, Mueller RK, Rylander R, Coulter TR, Soumekh M (1980) Experimental results in ultrasonic diffraction tomography. Acoust Imaging 9:433–450

Kelly KM, Dean J, Comulada WS, Lee S.-J. (2010) Breast cancer detection using automated whole breast ultrasound and mammography in radiographically dense breasts. Eur Radiol 20:734–742

Kolb T, Lichy J, Newhouse J (2002) Comparison of the performance of screening mammography, physical examination, and breast US and evaluation of factors that influence them: an analysis of 27,825 patient evaluations. Radiology 225:165–175

Kwak Y, Kim E, Park H et al (2006) Application of the breast imaging reporting and data system final assessment system in sonography of palpable breast lesions and reconsideration of the modified triple test. J Ultrasound Med 25(10):1255–1261

Mendelson EB, Baum JK, Berg WA, Merritt CB, Rubin E (2003) Breast imaging reporting and data system BI-RADS: ultrasound. In: D'Orsi CJ, Mendelson EB, Ikeda DM et al (eds) Breast imaging reporting and data system, 1st edn. American College of Radiology, Reston

Mueller RK, Kaveh M, Wade G (1979) Acoustical reconstructive tomography and applications to ultrasonics. Proc IEEE 67:567–586

Scherzinger AL, Belgam RA, Carson PL, Meyer CR et al (1989) Assessment of ultrasonic computed tomography in symptomatic breast patients by discriminant analysis. Ultrasound Med Biol 15:21–28

Shetty M, Shah Y, Sharman R (2003) Prospective evaluation of combined mammographic and sonographic assessment in patients with palpable abnormalities of the breast. J Ultrasound Med 22(3):263–268

Silverstein M, Lagios M, Recht A et al (2005) Image-detected breast cancer: state of the art diagnosis and treatment. J Amer Coll Surg 201(4):586–597

Stavros AT (2004) Breast ultrasound. Lippincott Williams & Wilkins, New York, pp 1–1015

Stavros A, Thickman D, Rapp C et al (1995) Solid breast nodules: use of sonography to distinguish between benign and malignant lesions. Radiology 196(1):123–134

Wiskin J, Borup D, Johnson S et al (2007) Full wave, non-linear, inverse scattering: high resolution quantitative breast tissue tomography. Acoust Imaging 28:183–194

Wiskin J, Borup D, Johnson S (2011a) Inverse scattering theory. Acoust Imaging 30:53–60

Wiskin J, Borup D, André M et al (2011b) Inverse scattering results. Acoust Imaging 30:61–68

Wiskin J, Borup D, Johnson S, Berggren M (2012) Nonlinear inverse scattering: high resolution quantitative breast tissue tomography. J Acoust Soc Am 131(5):3802–3813

Wolf E (1969) Three-dimensional structure determination of semi-transparent objects from holographic data. Opt Comm 1:153–156

Index

J. Mamou and M. L. Oelze (eds.), *Quantitative Ultrasound in Soft Tissues*, DOI: 10.1007/978-94-007-6952-6,